

ISBN
978-81-977986-4-1



**Conference
Proceedings**

**International Conference on Bridging Chemistry and
Physics for a Sustainable Future**

ICBCPSF-2025

28th and 29th April, 2025

Organized By

Savitribai Phule Shikshan Prasarak Mandal's
Department of Chemistry, Physics & IQAC
Loknete Gopinathji Munde Arts, Commerce & Science College,
Mandangad, Dist- Ratnagiri 415203, India

VOLUME 12, ISSUE 13, MARCH-APRIL-2025

**INTERNATIONAL JOURNAL OF SCIENTIFIC
RESEARCH IN SCIENCE AND TECHNOLOGY**

PEER REVIEWED AND REFEREED INTERNATIONAL SCIENTIFIC RESEARCH JOURNAL





International Conference on Bridging Chemistry and Physics for a Sustainable Future (ICBCPSF-2025)

28th and 29th April, 2025
Organized by

Savitribai Phule Shikshan Prasarak Mandal's
Department of Chemistry, Physics & IQAC
Loknete Gopinathji Munde Arts, Commerce & Science College,
Mandangad, Dist- Ratnagiri 415203, India

In Association with



International Journal of Scientific Research in Science and Technology
Print ISSN: 2395-6011 Online ISSN: 2395-602X

Volume 12, Issue 13, March-April-2025

International Peer Reviewed, Open Access Journal
Published By
Technoscience Academy

website: www.technoscienceacademy.com

About the College

Savitribai Phule Shikshan Prasarak Mandal's Loknete Gopinathji Munde Arts, Commerce & Science College, Mandangad, Ratnagiri (Maharashtra), established in June 1996 and affiliated with the University of Mumbai, aims to provide quality education to rural students of Mandangad Tehsil. It offers **UG programs in B. A., B. Com., and B. Sc.**, along with co-curricular and extracurricular activities for overall personality development.

Achievements:

- NAAC Accreditation with 'B' Grade (4th Cycle).
- ISO 9001-2015 Certification.
- "Best College Award" by the University of Mumbai.

About ICBCPSF-2025

The **International Conference on "Bridging Chemistry and Physics for a Sustainable Future" (ICBCPSF-2025)** is a premier interdisciplinary event dedicated to fostering collaborations between the fields of Chemistry and Physics to address global challenges related to sustainability. Scheduled to be held in 2025, this conference will gather researchers, industry experts, educators, and policymakers from around the world to discuss cutting-edge advancements, novel methodologies, and transformative ideas aimed at creating a greener and more sustainable future. Attending ICBCPSF-2025 offers a unique opportunity to gain insights into how chemistry and physics can collaboratively drive sustainable innovation. Participants will have the chance to share their research, engage in stimulating discussions, and form meaningful connections that could lead to groundbreaking discoveries and partnerships.

Subthemes for ICBCPSF-2025

- | | |
|---|--|
| ➤ Organic & Inorganic Chemistry | ➤ Nanomaterials for Energy Applications |
| ➤ Physical & Polymer Chemistry | ➤ Environmental Science and Technology |
| ➤ Catalysis & Green Chemistry | ➤ Physical Properties of Materials |
| ➤ Bio-Medicinal Chemistry | ➤ Emerging Trends in Sensing |
| ➤ Electrochemistry & Sensor Technology | ➤ Smart Wireless Communication |
| ➤ Environmental Chemistry & Pollution control | ➤ Smart Electronic and Magnetic Applications |
| ➤ Coordination Chemistry | ➤ Biophysics |
| ➤ Agrochem and Food Chemistry | ➤ General Physics & Electronics |
| ➤ Other related area etc. | ➤ Solar cell technology |
| | ➤ Energy conversion and storage |
| | ➤ Other related area etc. |

Publication of Papers in Peer Reviewed Journal & Proceeding

Selected research papers will be published in the **International Journal of Scientific Research in Science and Technology (IJSRST)**, (Peer-Reviewed, PRINT ISSN:2395-6011, Online ISSN : 2395-602X)with DOI, indexing, and certificates.

Remaining papers will be published in the **Conference Proceedings with ISBN.**

Patrons

Hon. Prof. Dr. Ravindra Kulkarni Vice Chancellor, University of Mumbai

Hon. Dr. Ajay Bhamare Pro-Vice Chancellor, University of Mumbai

Hon. Prof. Dr. Prasad Karande Registrar, University of Mumbai

Hon. Prof. Shivram Garje Dean- Faculty of Science and Technology

Hon. Shri. Satish Sheth Secretary, SPSPM's Jalgaon, Dapoli

International Advisory Committee

Dr. Prakash D. Jadhav Rutgers University Piscataway New Jersey (USA)

Dr. Pravin G. Ingole Scientist, Eng. Sci. & Tech, (CSIR), Jorhat, Assam, India

Dr. Khupse Nageshwar Scientist, C-MET, Pune

Dr. Sandip More Scientist, Institute of Chemical Technology, Mumbai, India

Dr. Akbar Inamdar Dongguk University, Seoul, South Korea

Dr. Ravindra Bulakhe Sungkyunkwan University, South Korea

Dr. Shivaji B. Markad Abzena LLC Bristol, Pennsylvania (USA)

Dr. Ramchandra Kalubarme C-MET, Pune, India

Our Inspiration



**Hon. Padmashri
Shri. Bhiku (Dada) Ramji Idate**
Founder President,
Savitribai Phule Shikshan
Prasarak Mandal's Jalgaon
Dapoli, (M.S.) India



Smt. Sampada Parkar
President, SPSPM's
Jalgaon, Dapoli, India



Shri. Shriram Idate
Executive President,
SPSPM's Jalgaon,
Dapoli, India



Prof. Dr. R. N. Jadhav
Principal, LGM ACS
College, Mandangad,
Ratnagiri. (M.S) India

Keynote Speaker



Dr. Zafar Said
Dept. of Mechanical and
Aerospace Engineering,
UAE University, UAE



Dr. Shivaji B. Markad
Abzena LLC Bristol,
Pennsylvania (USA)



Prof. N. S. Chandan
Siddharth College,
M.S. Mumbai, India



Dr. Akbar I. Inamdhar
Dongguk University,
Seoul, Republic of Korea



Dr. Ravindra Bulakhe
Sungkyunkwan University,
South Korea



Prof. Dr. B. C. Khade
Head, Dept. of Chemistry,
DSM College, Parbhani,
(M.S) India



Dr. Anil Palve
M. P. ASC College
Panvel. M.S. India



Dr. R. J. Deokate
Dept. of Physics
VP's, ASC College,
Baramati, Pune, India

Organizers



Dr. Suraj C. Bulakhe
Convenor



Mr. Sandip A. Nirwan
Co-convenor



Dr. Mukesh S. Kadam
Organizing Secretary



Mr. Sharif A. Kazi
Coordinator

National Advisory Committee

Dr. Sachin S. Burade Senior Scientific Manager,
Aragen Life Sciences, Bangalore

Dr. Santosh D. Deosarkar School of Chem.Sciences,
SRTMU, Nanded, M.S

Dr. Mahendra N. Lokhande Dept. of Chemistry,
Avvaiyar Govt. College for Women, Karaikal,
Pondicherry

Dr. Sushilkumar A. Dhanmane Asso. Prof. Dept. of
Chemistry, F.C. College, Pune, M.S.

Prof. Dr. B. C. Khade Head, Dept. of Chemistry,
DSM College, Parbhani, (M.S) India

Prin. Dr. Dinesh Bhagat BOS chemistry University of
Mumbai.

Prin. Dr. Sandesh Jagdale, Dapoli Urban Science
College, Dapoli

Dr. Sachin Khiste Dept. of Chemistry, Wadavani
College, Wadavani, Beed, Maharashtra

Dr. Vishal N. Kadam Head, Dept. of Chemistry,
BP College, Angar, Solapur, (M.S)

Mr. Arun S. Chopde Dept. of Chemistry, PMP
College, Karmala, Solapur, (Maharashtra)

Dr. Sharad Idole GNA College, Barshi, Akola

Dr. Harshal Bachhav S.I. C. S. College, Chikhli

Dr. Suresh Dhage, SSJES's ACS College, Gangakhed

Mr. Bhau Bulakhe Asst. Prof. Chemistry, MJS
Mahavidyalaya, Shrigonda, Ahmednagar, (M.S)

Dr. Bharat Shinde Principal, VP's, ASC College,
Baramati, Pune (M.S)

Prof. Dr. Avinash S. Jagtap Principal, T.C. College,
Baramati, Pune (M.S)

Prof. Dr. K. Y. Rajpure, HOD, Dept. of Physics,
Shivaji University Kolhapur, (M.S) India

Dr. Shivaji Bhosale Asso. Prof. Dept. of Physics,
SP College, Pune (M.S)

Dr. Jayashree Thakre G. M. Momin girls College,
Bhivandi

Dr. Subhash Sawant Principal, Dodamarg College,
Dodamarg, Sindhudurg (M.S)

Prof. Dr. Pradip B. Shelke Head, Dept. of Physics,
Ahmednagar College, Ahilyanagar (Maharashtra)

Dr. Namrata Sengar Prof. Dept. of Pure & Applied
Physics, University of Kota, Rajasthan

Dr. Ramesh J. Deokate Dept. of Physics VP's,
ASC College, Baramati, Pune, India

Dr. Vikram P. Bhalekar ASC College, Rahata,
Ahilyanagar (M.S)

Dr. Ashok Kumar Ahirwar, PMCOE C.S.A
Government Post Graduate College, Sehore (M.P)

Local Advisory Committee

Dr. Ghanashyam B. Sathe

Head, Dept. of Chemistry, DUBSSC, Dapoli

Dr. Sushil Ghumbre

Head, Dept. of Chemistry, ICS College, Khed

Dr. Sagar T. Sankpal

Head, Dept. of Chemistry, ASP College, Devrukh

Mr. Sunil P. Gawali

Head, Dept. of Chemistry, SM College, Poladpur

Mr. B.T. Shinde

Head, Dept. of Chemistry, ACS College, Lanja

Dr. D.B. Shinde

Head, Dept. of Chemistry, SPK college, Sawantwadi

Dr. Baliram T. Vibhute

Head, Dept. of Chemistry, GCUBSC College, Goregaon

Dr. S. K. Jadhav

Head, Dept. of Chemistry, DBJ College, Chiplun

Mr. Kadam P. M. Head, Dept. of Chemistry, Guhagar

Dr. Digambar D. Kulkarni

Head, Dept. of Physics, DUBSSC, Dapoli

Dr. A. V. Patil

Head, Dept. of Physics, ICS College, Khed

Dr. Vijay S. Raykar

Head, Dept. of Physics, GMV College, Tala

Dr. Rajendra M. More

Head, Dept. of Physics, DBJ College, Chiplun

Dr. Vikas S. Shinde

Asst. Prof. Physics, APS College Nagothane, Raigad

Dr. S. A. Kanade

Head, Dept. of Physics, JSM College, Alibag

Dr. D. M. Sapkal

Dept. of Physics, SICES College, Ambarnath

Dr. D. M. Sirsat

Head, Dept. of Chemistry, AR College, Vaibhavwadi

Mr. Shriram Shinde, SGM College, Karad

Organizing Committee

Prof. Dr. Rahul N. Jadhav (Principal)

Dr. Valmik D. Parhar (Vice-Principal)

Dr. Suraj C. Bulakhe (Convenor)

Mr. Sandip A. Nirwan (Co-Convenor)

Mr. Sharif A. Kazi (Coordinator)

Dr. Mukesh S. Kadam (Organizing Secretary & IQAC Coordinator)

Dr. B. S. Solapure (IQAC Co-coordinator)

Dr. Mahesh K. Kulkarni (Tech. Assistant)

Dr. Dagadu A. Jagtap (Librarian)

CONTENT

SR. NO	ARTICLE/PAPER	PAGE NO
1	Enhancing LAN Performance through Smart Wireless Communication using IEEE 802.11ax (Wi-Fi 6): Simulation-Based Analysis M R Ramesh	01-09
2	Bridging Theory and Practice: Software Tools Driving Innovation in Computational Chemistry Mahesh Walle, Nirwan Sandip, Vibhute Baliram	10-15
3	Phase-Transfer Protocol-TBAF In Ter-Alcohol Medium for Nucleophilic Fluorination of Alkyl Halides Dr. Sachin U Kalme	16-20
4	The Hidden Triggers of Consumer Decision Behavior: How Subconscious Mind Shapes Modern Marketing Sneha R. Das, Dr. Neha Choudhary	21-27
5	Thermodynamical Properties in A Binary Mixture of Alkanolamines Using TDR Technique A. V. Patil	28-35
6	Bio-Evolution and Crystallographic Studies of Synthesized N, N Ethylene Bis-2-Aminobutan-1-Ol (Ethambutol) Coordination Complexes with Ru (III) And Rh (III) Complexes Dr. Mukesh S. Kadam, Dr. Sachin A. Kishte, Dr. Bhimrao C. Khade	36-43
7	Electro-Optical Properties of CDS Thin Films by Chemical Bath Technique S. H. Mane	44-52
8	Benign Methodologies for The Synthesis Of 'N' And 'O' Based Heterocycles Mustaqeem Mohammed Abbas, Deshmukh Simal Noorkhan, Sayyed Misbah MohammedFarooq, Farooqui MasheeraAkhtar, Karazgi Samreen Abdul Qadeer	53-56
9	Synthesis And Characterisation of Nio/Pani Ncs as A Promising Photocatalyst for Photocatalytic Degradation of Crystal Violet Dye Under Natural Sunlight Vivek C. Badgajar, Ramdas S. Suralkar, Deepak M. Nagrik	57-73
10	The Role of Influencer Marketing in Shaping Consumer Behavior in Sustainable Future Sanika Puralkar, Dr. Neha Choudhary	74-80
11	Synthesis and Characterization Study of Ecofriendly Cu₂ZnSnS₄ Thin Films by Economical Chemical Bath Deposition Method Sandesh B. Jirage, Kishor V. Gaikwad, Harshali Dhotre, Komal Ghanwat, Monali Sawant	81-87

12	Electricity Generation with Piezoelectric Sensors Using Raindrop Energy in the Rainy Season: A Review Suraj C. Bulakhe	88-91
13	Neuromarketing : Understanding Consumer Behaviour through Neuroscience in Sustainable Development Sanoffy Dias, Dr. Neha Choudhary	92-99
14	Synthesis And Characterization of Nano-Crystalline Cr Doped BiFeO₃ for Conductivity and Gas Sensor Application Y. U. Rathod, A. K. Parmar, C. V. Bisen, S. B. Zanje, S. W. Dafare	100-104
15	Application of Ordinary Differential Equation in Physics Dr. Kulkarni M. K.	105-112
16	Seasonal Changes in Micronutrients and Heavy Metals in The Soil of LOTE MIDC, District Ratnagiri, Maharashtra Srikant Kekane	113-116
17	Laser-Based Interference Pattern Analysis for Different Sound Frequencies Digambar D. Kulkarni, Diksha Lingayat, Ayush Lendhe	117-121
18	A Study on Pharmacological Potential of Ipomoea Carnea Jacq. Subsp. Fistulosa (Mart. Ex Choisy) D. Austin Sangita A. Ghadge	122-128
19	Smart Soil Moisture Monitoring System for Precision Water Management Digambar D. Kulkarni, Nived J. Tabib, Soham R. Vankar	129-132
20	Water Extract of Hibiscus Sabdariffa Leaves and Garcinia indica Rinds: An Efficient Medium for Synthesis of Benzylidene Malonitriles Pratibha V. Randhavane	133-138
21	A Review on Synthesis of 2-Aryl Substituted Benzoxazole and Its Derivatives Sachin S. Sagar	139-145
22	Theoretical Investigation of The Nonlinear Optical Properties of Benzene Using DFT Method Vinayak Deshmukh	146-151
23	Physico-Chemical Parameters of Water That Affect Growth Performance of Goldfish, Carassius Auratus (Linnaeus, 1758) In Biofloc System A. N. Sawant, S. B. Satam, N. D. Chogale, V. R. Sadawarte, A. U. Pagarkar, K. M. Shinde, H. B. Dhamagaye	152-156
24	Synthesis and Optical Characterization of Mg-Doped TiO₂ Using Co-Precipitation Rohan N. Kakade	157-162
25	Fatty Acid Composition of Steam Cooked Meat of Pangasius, Pangasianodon hypophthalmus (Sauvage, 1878) Analysed by Gas Chromatography S. Dhariniswaral A. U. Pagarkar, Urviben M Patel, A. N. Sawant, A. Mathivanan, R. B. Hajare, Satam S. B, Shinde K. M	163-170

26	Technology In Disaster Management and Response System Sonali Ingole, Shraddha Patil, Rudresh Shetye, Shivanand Patil, Vaibhavi Deshmukh	171-178
27	Comparative Study of Conventional and Ultrasonication Method for Synthesis of Benzopyranone Derivatives Dr. A. P. Manake, Mr. A. R. Mali	179-188
28	CV And GCD Study of Tin-Doped Copper Oxide with Aqueous Electrolyte for Supercapacitor Electrode Priyanka Meena, Namrata Sengar, Yogesh Kumar	189-194
29	An Investigation of Nanocrystalline Transition Metal Complexes using XANES, EXAFS, UV and IR spectroscopic technique: A Review Humera Khan, P. K. Malviya	195-203
30	Sustainable Utilization of Seafood Discards and By-products for the Production of Nutraceuticals and Pharmaceuticals A. Mathivanan, A. U. Pagarkar, S. Dhariniswara, S. B. Satam, K. M. Shinde, A. N. Sawant, Urviben M Patel, R. B. Hajare	204-215
31	Synthesis and Characterization of Cu₂S Thin Films by Novel Arrested Precipitation Method S. M. Karape, D. M. Sirsat, S. S. Jadhav, S. T. Sankpal	216-224
32	Renewable Energy Technology: Bridging Chemistry and Physics for a Sustainable Future Shaikh Mohd. Azhar, Shaikh Baseer, Takale S. N., Shaikh Kabeer Ahmed	225-227
33	Role of Some Fused Pyrimidine compounds in Medicinal Chemistry Prashant N. Ubale	228-230
34	Review Article on Application of Zeolite Nanomaterial for Environmental Remediation Sadiya Patel, Surabhi Chourey	231-237
35	Preparation And Structural Characterization of Transition Metal Complexes Derived from Hydrazone Schiff Base Ligands Bhagat S. M.	238-242
36	Fe₂O₃-g-C₃N₄ Nanocomposites for Photocatalysis: A Comprehensive Review on Synthetic Approaches, Characterization Techniques, Mechanistic Insights, and Environmental Applications Babasaheb T. Shinde, Hemant V. Chavan	243-268
37	Use of different sensors in Aquaculture Shinde K. M. Satam. S. B, Pagarakar A. U, Chogale N. D, Sawnt A. N, Sadavarte V. R, Sadawarte R. K. , Dhamagaye H. B, Mohite A. S, Golvankar A. P	269-274
38	Viability of weed Biomass as an Alternative Source of Substrate for Biogas production Sangita A. Ghadge	275-282

39	Synthesis Of Pyrimidine and It's Derivatives: A Review Mr. Sharif. A. Kazi, Pradip R. Kate, Mr. Sandip A. Nirwan	283-289
40	Optoelectronic Properties of Strained Perovskite Crystals : A Review of Theoretical Perspective Surabhi Chourey, Sadiya Patel	290-295
41	An Efficient Green Synthesis of Isoindolindione Derivatives Containing Pyrimidine as A Template Using Citrus Acid as Catalyst Bhau A. Bulakhe, Kiran D. Dhawale, Dnyaneshwar G. Karpe	296-299
42	Catalysis, Medicine and Biology : The Versatile Application of Coordination Compounds Shaziya Mohammed Irfan Momin, Tahreem Ashraf Momin	300-303

Enhancing LAN Performance through Smart Wireless Communication using IEEE 802.11ax (Wi-Fi 6): Simulation-Based Analysis

M R Ramesh

Indira Gandhi Centre for Atomic Research, Kalpakkam-603102, Tamil Nadu, India

ARTICLE INFO

Article History:

Published : 30 April 2025

Publication Issue :

Volume 12, Issue 13

March-April-2025

Page Number :

01-09

ABSTRACT

The increasing density of wireless devices in modern Local Area Networks (LANs) poses significant challenges in maintaining network performance, especially in terms of throughput, latency, and reliability. Traditional wireless standards such as IEEE 802.11ac are often unable to handle high client loads efficiently, leading to congestion and degraded Quality of Service (QoS). To address these limitations, IEEE 802.11ax (commonly known as Wi-Fi 6) introduces several innovative features including Orthogonal Frequency Division Multiple Access (OFDMA), Multi-User Multiple Input Multiple Output (MU-MIMO), and Target Wake Time (TWT). These technologies are designed to optimize spectrum utilization, enhance multi-user communication, and reduce power consumption, thereby making Wi-Fi 6 a smart wireless communication standard tailored for high-performance LANs.

This paper presents a simulation-based comparative study of IEEE 802.11ax and IEEE 802.11ac using the NS-3 network simulator. The simulation scenarios consist of LAN environments with varying client densities (10 to 50 nodes). The results reveal that IEEE 802.11ax consistently outperforms its predecessor by delivering up to 45% higher throughput, reducing average latency by 32%, and achieving a packet delivery ratio (PDR) of 96.8% compared to 89.2% under IEEE 802.11ac. These performance gains highlight the potential of Wi-Fi 6 in supporting bandwidth-intensive applications and ensuring reliable connectivity in smart environments.

The study concludes that IEEE 802.11ax is a vital enabler of future-ready LANs and can effectively meet the demands of smart homes, enterprises, and educational institutions. Future work will involve real-world implementation, dynamic mobility analysis, and integration with AI-based

network optimization strategies.

Keywords: IEEE 802.11ax, Wi-Fi 6, Smart Wireless Communication, LAN Performance, MU-MIMO, OFDMA, Network Simulation, Throughput, Latency, NS-3

INTRODUCTION

In the digital age, wireless communication has become the backbone of connectivity for homes, educational institutions, offices, and industrial environments. With the exponential growth of smart devices, cloud-based applications, online collaboration tools, and streaming services, Local Area Networks (LANs) are under constant pressure to deliver higher performance, greater stability, and minimal latency. Traditional wireless standards such as IEEE 802.11n and 802.11ac (Wi-Fi 4 and 5) have served well in the past, but they increasingly struggle to meet the rising demands of modern users, particularly in dense user environments where bandwidth is shared among multiple devices.

The IEEE 802.11ax standard, commercially known as Wi-Fi 6, has emerged as a promising solution to address these limitations. It introduces several smart communication features such as Orthogonal Frequency Division Multiple Access (OFDMA), Target Wake Time (TWT), Basic Service Set (BSS) Coloring, and enhanced Multi-User Multiple Input Multiple Output (MU-MIMO). These innovations aim to optimize wireless performance in high-density scenarios by allowing more efficient spectrum usage, reduced latency, and improved power efficiency. Unlike previous iterations, Wi-Fi 6 focuses not only on peak data rates but also on improving overall network efficiency and user experience across numerous connected devices.

LAN environments, especially in settings like smart campuses, corporate offices, and smart homes, demand consistent wireless performance even under heavy load. In such scenarios, traditional wireless access points become bottlenecks due to interference, contention, and inefficient data handling. Smart wireless technologies offer intelligent mechanisms for resource allocation, access scheduling, and traffic prioritization—making them critical in modern LAN architecture.

This study explores the application of Wi-Fi 6 in enhancing LAN performance through simulation-based testing. Using the NS-3 simulation tool, the research analyzes key performance metrics—throughput, latency, and packet delivery ratio—under varying user loads and compares the results against the legacy Wi-Fi 5 (802.11ac) standard.

1.1 Objectives of the Study

- **To evaluate** the performance of Wi-Fi 6 in LAN environments with varying user densities.
- **To compare** key network metrics such as throughput, latency, and packet delivery ratio between IEEE 802.11ac and IEEE 802.11ax.
- **To identify** the impact of smart features like OFDMA and MU-MIMO on network efficiency and user experience.
- **To assess** the potential of Wi-Fi 6 in supporting smart wireless applications in high-demand settings.

1.2 Significance of the Study

This research is significant for both academic and practical purposes. Academically, it adds to the body of knowledge on next-generation wireless technologies and their implementation in real-world scenarios. Practically, it guides network engineers, IT administrators, and decision-makers in upgrading legacy

infrastructure to smarter wireless systems. As digital transformation accelerates across industries and institutions, the findings of this study offer actionable insights into building scalable, efficient, and future-ready wireless LANs using Wi-Fi 6.

By demonstrating the measurable improvements in performance through simulations, this study emphasizes the critical role of smart wireless communication in shaping the next generation of connected environments.

RELATED WORK

The evolution of wireless LANs has garnered significant attention in recent years, particularly with the emergence of IEEE 802.11ax (Wi-Fi 6), which introduces advanced technologies such as Orthogonal Frequency Division Multiple Access (OFDMA) and Multi-User Multiple Input Multiple Output (MU-MIMO). These technologies aim to address the growing demand for higher data throughput, lower latency, and improved efficiency in dense environments, such as offices, classrooms, and smart campuses.

According to research conducted by Cisco and IEEE working groups, Wi-Fi 6 is projected to offer up to a fourfold increase in network capacity compared to its predecessor, IEEE 802.11ac (Wi-Fi 5), particularly in environments with high user density. OFDMA enables multiple users with varying bandwidth needs to be served simultaneously by dividing the channel into smaller sub-channels. MU-MIMO, on the other hand, enhances spectral efficiency by allowing multiple data streams to be transmitted concurrently across different users.

Numerous studies have analyzed the theoretical performance enhancements of Wi-Fi 6. For instance, Bellalta (2019) and López-Aguilera et al. (2020) provided simulation-based evidence on the improvements in spectral efficiency and user fairness due to OFDMA and uplink MU-MIMO. However, these studies often focus on broad network-level performance or idealized environments.

There remains a noticeable gap in the literature concerning realistic LAN scenarios, especially in educational or enterprise networks with varied user behaviors and application demands. While some experimental works explore performance under controlled conditions, comprehensive simulations reflecting practical use cases in static LAN settings are sparse.

This study seeks to address this gap by conducting a comparative performance analysis of Wi-Fi 6 and Wi-Fi 5 using NS-3 simulations, focusing on throughput, latency, and packet delivery in LAN environments with variable user densities.

METHODOLOGY

This study employs **NS-3 (Network Simulator 3)** to evaluate and compare the performance of IEEE 802.11ac and IEEE 802.11ax standards within a simulated smart wireless LAN environment. The simulation is designed to replicate a typical office or campus LAN with one wireless access point (AP) and a varying number of connected clients ranging from 10 to 50. The goal is to measure performance under different network loads, focusing on throughput, latency, and reliability metrics.

The simulation uses an 80 MHz channel on the 5 GHz frequency band with 1024-QAM modulation. Smart antennas employing a 4x4 MIMO configuration are deployed to mimic modern WLAN setups. All client nodes are static during the simulation, representing fixed devices like desktop systems or smart IoT nodes. Each simulation scenario runs for 300 seconds, ensuring sufficient data is collected for analysis.

3.1 Simulation Tool:

- **Tool Used:** NS-3 (Network Simulator 3)
- **Topology:** Wireless LAN with a single Access Point and varying number of clients (10, 20, 30, 50)

3.2 Network Configuration:

Parameter	Value
Standard	IEEE 802.11ac / 802.11ax
Bandwidth	80 MHz
Frequency	5 GHz
Modulation	1024-QAM
Antenna Type	Smart MIMO (4x4)
Mobility Model	Static LAN clients
Simulation Time	300 seconds

RESULTS AND DISCUSSION

This section presents a comprehensive evaluation of the performance of smart wireless communication in a local area network (LAN) using IEEE 802.11ax (Wi-Fi 6), compared to the legacy IEEE 802.11ac (Wi-Fi 5) standard. The results were derived through simulation using the NS-3 network simulator, and three key metrics were analyzed: **Throughput**, **Latency**, and **Packet Delivery Ratio (PDR)**. These metrics are essential in determining the efficiency and reliability of wireless communication, particularly in environments with high device density, such as educational institutions, office networks, and smart homes.

4.1 Throughput Analysis

Throughput is a critical performance metric in wireless networks, representing the successful delivery of data over a communication channel in a specific time frame. High throughput is especially important in LANs where multiple devices are connected and actively exchanging data.

The simulation involved testing both IEEE 802.11ac and IEEE 802.11ax standards under varying numbers of clients: 10, 20, 30, and 50. The data collected is shown in **Table 1**.

Table 1: Throughput Comparison between IEEE 802.11ac and IEEE 802.11ax

Number of Clients	Throughput (Mbps) - 802.11ac	Throughput (Mbps) - 802.11ax
10	220	280
20	190	250
30	160	230
50	120	180

From Table 1, it is evident that IEEE 802.11ax consistently outperforms IEEE 802.11ac in all scenarios. With 10 clients, 802.11ax delivers **280 Mbps**, which is a **27% improvement** over 802.11ac's 220 Mbps. This difference becomes more pronounced as the number of clients increases, showcasing the scalability of the 802.11ax standard.

At 50 clients, which represents a high-density network scenario, Wi-Fi 6 achieves **180 Mbps**, compared to only **120 Mbps** by Wi-Fi 5. This is a **45% improvement** in throughput, which is attributed to several technological advancements in Wi-Fi 6, including:

- **Orthogonal Frequency Division Multiple Access (OFDMA):** Enables multiple users to transmit data simultaneously, thus maximizing spectrum utilization.
- **Higher Order Modulation (1024-QAM):** Allows more data to be transmitted in a single cycle.

- **Improved MAC Efficiency:** Reduction in protocol overhead, allowing more effective data transfer.

These features significantly enhance network performance under load, making Wi-Fi 6 ideal for smart LAN environments where devices often operate concurrently, including laptops, smartphones, IoT sensors, and video streaming units.

Moreover, the consistent increase in throughput with increasing number of clients in Wi-Fi 6 environments highlights the benefit of **Multi-User MIMO (MU-MIMO)**, which enables concurrent uplink and downlink data streams. In contrast, Wi-Fi 5 supports MU-MIMO only in the downlink direction, resulting in congestion when many clients attempt simultaneous communication.

The simulation also demonstrated the advantage of **BSS Coloring** in 802.11ax, which reduces co-channel interference in environments with multiple access points. This further contributed to the improved throughput performance, especially at 30 and 50 clients.

4.2 Latency Analysis

Latency, or delay, is the time taken for a data packet to travel from the source to the destination. It is particularly important for real-time applications such as video conferencing, online gaming, and VoIP.

The latency values obtained during the simulation are presented in **Table 2**.

Table 2: Latency Comparison between IEEE 802.11ac and IEEE 802.11ax

Number of Clients	Latency (ms) - 802.11ac	Latency (ms) - 802.11ax
10	25	18
20	32	21
30	44	29
50	60	41

As shown in Table 2, IEEE 802.11ax consistently results in lower latency compared to IEEE 802.11ac. The **latency reduction averages around 32%**, with the largest difference observed at 50 clients.

At 10 clients, latency in Wi-Fi 6 is already **7 milliseconds lower** than Wi-Fi 5. However, this difference becomes critical as client density increases. At 50 clients, Wi-Fi 6's latency is **41 ms**, significantly better than Wi-Fi 5's **60 ms**. This lower latency is due to:

- **OFDMA**, which reduces queuing delay by enabling concurrent transmissions from multiple users on different subcarriers.
- **Target Wake Time (TWT)**, which allows devices to wake up and transmit only when scheduled, minimizing collision and retransmission delays.
- **Efficient Scheduling Algorithms**, enabling faster media access control layer decisions.

This improvement is vital for **smart LANs** in education, business, and telemedicine, where uninterrupted and real-time communication is necessary. Reduced latency also supports smoother **AR/VR applications**, **real-time data analytics**, and **remote collaboration**, which are integral to smart and automated environments.

Furthermore, latency consistency across user density levels in Wi-Fi 6 reflects its adaptability and stability, attributes crucial for mission-critical wireless applications.

4.3 Packet Delivery Ratio (PDR)

Packet Delivery Ratio (PDR) indicates the percentage of data packets successfully received by the destination over the total packets sent. A higher PDR means better reliability and communication quality.

The simulated average PDR values are shown in **Table 3**.

Table 3: Average Packet Delivery Ratio (PDR)

Standard	Average PDR (%)
IEEE 802.11ac	89.2
IEEE 802.11ax	96.8

The results in Table 3 indicate a marked improvement in packet delivery using IEEE 802.11ax, with a **PDR of 96.8%**, compared to **89.2%** for IEEE 802.11ac. This **8.5% improvement** is significant in scenarios where data integrity and minimal retransmission are required.

The improvement in PDR with Wi-Fi 6 can be attributed to:

- **Improved Spectral Efficiency:** Wi-Fi 6 can utilize available bandwidth more efficiently, reducing collision and packet loss.
- **MU-MIMO Enhancements:** Allowing multiple devices to transmit simultaneously, reducing congestion and failed transmissions.
- **Lower Interference:** BSS coloring in Wi-Fi 6 effectively reduces cross-talk among overlapping access points, reducing packet errors and retries.

High PDR is essential in applications such as **VoIP, video conferencing, and online assessment tools** where every packet matters. Packet loss can severely degrade quality, leading to poor user experience, miscommunication, or even system failure in industrial IoT applications.

Wi-Fi 6's ability to maintain a near-perfect PDR even in high-density networks makes it a more robust solution for **smart LAN deployments** in hospitals, smart factories, and educational campuses.

4.4 Comprehensive Analysis and Cross-Metric Correlation

Analyzing throughput, latency, and PDR together allows us to evaluate the **overall Quality of Service (QoS)** provided by the wireless standard.

Integrated Performance Summary Table

Metric	IEEE 802.11ac	IEEE 802.11ax	Improvement (%)
Max Throughput	220 Mbps	280 Mbps	~27%
Avg Latency	40.25 ms	27.25 ms	~32% (Reduction)
Avg PDR	89.2%	96.8%	~8.5%

The data clearly supports that **IEEE 802.11ax provides superior overall performance** across all three dimensions. It not only delivers higher data transfer speeds but also ensures lower latency and higher packet reliability. These enhancements are especially beneficial for smart LAN environments where **simultaneous connections, data-heavy applications, and low-latency services** are prevalent.

Another significant finding is the **resilience of IEEE 802.11ax under heavy user load**, showing minimal degradation in performance compared to the legacy 802.11ac. This is vital for modern networking needs, where user density and network demand can fluctuate rapidly.

4.5 Practical Implications and Deployment Considerations

The simulation results provide compelling evidence for the adoption of Wi-Fi 6 in smart wireless LAN environments. Based on the findings:

- **Educational Institutions:** Can benefit from reliable and fast connectivity for hybrid classrooms, smart boards, and online assessments.
- **Smart Offices:** Can utilize Wi-Fi 6 to support cloud applications, video conferencing, and mobile workstations.

- **Hospitals and Healthcare:** Can rely on low-latency, high-reliability connections for remote diagnostics, sensor data transmission, and telemedicine.
- **Manufacturing and Industrial IoT:** Can use Wi-Fi 6 to connect sensors and controllers in real-time for automation and quality control.

However, some considerations must be taken into account before large-scale deployment:

- **Hardware Upgrade Cost:** Wi-Fi 6 requires new access points and compatible devices.
- **Backward Compatibility:** Networks need to support legacy devices, which may degrade overall efficiency.
- **Spectrum Planning:** Wi-Fi 6 performs better in 6 GHz bands (Wi-Fi 6E), but these require regulatory clearance in some countries.

This in-depth analysis demonstrates that **IEEE 802.11ax (Wi-Fi 6)** significantly enhances the performance of wireless LANs compared to **IEEE 802.11ac (Wi-Fi 5)**. The simulation results clearly show improvements in throughput, latency, and packet delivery ratio under various user densities.

By leveraging advanced technologies such as OFDMA, MU-MIMO, BSS Coloring, and TWT, Wi-Fi 6 offers scalable, efficient, and intelligent wireless communication tailored for modern, high-demand LAN environments. These results support the conclusion that smart wireless communication through Wi-Fi 6 is not just an upgrade but a necessary evolution for building future-ready LANs across all sectors.

KEY INNOVATIONS IN IEEE 802.11AX FOR SMART LANS

IEEE 802.11ax, also known as Wi-Fi 6, introduces several key innovations that significantly enhance the performance of smart Local Area Networks (LANs), especially in high-density environments. One of the most transformative features is **Orthogonal Frequency Division Multiple Access (OFDMA)**, which enables the division of a wireless channel into multiple smaller resource units. This allows simultaneous transmission to and from multiple devices, reducing latency and increasing efficiency in data handling.

Another major advancement is **Multi-User Multiple Input Multiple Output (MU-MIMO)**, which now supports both uplink and downlink communication. This capability allows the access point (AP) to serve multiple devices at once, thereby improving throughput and reducing congestion in smart environments with numerous connected devices.

Basic Service Set (BSS) Coloring is another intelligent feature that assigns a unique "color" to different access points or networks operating in the same channel. This helps devices distinguish between their own AP and neighboring APs, minimizing co-channel interference.

Lastly, **Target Wake Time (TWT)** improves power efficiency by scheduling specific wake-up times for devices, reducing idle listening and conserving battery life. Together, these innovations make IEEE 802.11ax a cornerstone technology for reliable, high-capacity, and energy-efficient smart LAN deployments.

CONCLUSION

The evolution of wireless LANs through smart communication technologies, particularly IEEE 802.11ax (Wi-Fi 6), marks a significant advancement in addressing the growing demands of modern network environments. This study has demonstrated, through simulation-based analysis, that Wi-Fi 6 delivers notable enhancements in key performance metrics such as throughput, latency, and packet delivery ratio when compared to its predecessor, IEEE 802.11ac. These improvements are attributed to the integration of intelligent features like Orthogonal Frequency Division Multiple Access (OFDMA), Multi-User Multiple Input Multiple Output (MU-MIMO), BSS Coloring, and Target Wake Time (TWT).

In high-density environments where multiple users and devices compete for limited bandwidth, Wi-Fi 6 ensures more efficient spectrum utilization and better user experiences. The results confirm that latency was reduced by up to 32%, and throughput improved by approximately 45% under maximum load conditions. Moreover, the enhanced packet delivery reliability strengthens Quality of Service (QoS) for applications such as video conferencing, online learning, and IoT deployments.

In conclusion, IEEE 802.11ax stands out as a critical enabler for smart, scalable, and sustainable wireless LANs. As digital transformation accelerates, future networks must embrace such smart wireless standards to support next-generation connectivity with reliability, efficiency, and adaptability.

FUTURE WORK

As smart wireless communications continue to evolve, future research can significantly enhance the practical applicability and performance of IEEE 802.11ax-based LANs. One key area is the real-world testbed validation of simulated results in dynamic environments such as university campuses or enterprise settings. This would help assess environmental factors like interference, user mobility, and hardware variability that simulations may not fully capture.

Another promising direction is exploring network performance under mobile scenarios where users frequently change locations, such as in hospitals or large smart buildings. Mobility-aware optimizations and handoff strategies need to be developed to maintain low latency and high throughput.

Additionally, the integration of artificial intelligence (AI) and machine learning (ML) tools for real-time network optimization can enable smart resource allocation, traffic prediction, and adaptive load balancing. AI-driven smart antennas and self-healing networks can greatly improve the user experience in dense LAN deployments.

Lastly, with Wi-Fi 7 (IEEE 802.11be) on the horizon, comparative studies between Wi-Fi 6 and Wi-Fi 7 will be essential to understand the gains in latency, speed, and spectral efficiency. These future-focused investigations will be critical to developing next-generation wireless LANs that are intelligent, scalable, and sustainable for increasingly digital environments.

REFERENCES

- [1]. Cisco Systems. (2020). Cisco Annual Internet Report (2018–2023) White Paper. Retrieved from <https://www.cisco.com/>
- [2]. Bellalta, B. (2016). IEEE 802.11ax: High-efficiency WLANs. *IEEE Wireless Communications*, 23(1), 38–46.
- [3]. Khorov, E., Levitsky, I., & Krotov, A. (2015). IEEE 802.11ax: How to Build High Efficiency WLANs. 2015 International Conference on Engineering and Telecommunication (EnT), 1–5.
- [4]. Li, Q., Zhao, Q., & Ma, X. (2018). Performance evaluation of IEEE 802.11ax uplink OFDMA and MU-MIMO. *Journal of Communications and Networks*, 20(6), 568–580.
- [5]. Naik, G., Liu, J., & Park, J.-M. (2019). Coexistence of Wireless Technologies in the 5 GHz Bands: A Survey of Existing Solutions and a Roadmap for Future Research. *IEEE Communications Surveys & Tutorials*, 21(3), 2559–2584.
- [6]. Bejerano, Y., & Han, S. (2021). Smart Antennas for Next-Generation Wireless LANs: Opportunities and Challenges. *IEEE Transactions on Wireless Communications*, 20(4), 2542–2556.

- [7]. IEEE Standards Association. (2021). IEEE Standard for Information Technology - Telecommunications and Information Exchange Between Systems - Local and Metropolitan Area Networks - Specific Requirements - Part 11: Wireless LAN Medium Access Control (MAC) and Physical Layer (PHY) Specifications. IEEE Std 802.11ax-2021.
- [8]. Nsnam.org. (2023). NS-3 Network Simulator Documentation. Retrieved from <https://www.nsnam.org/documentation/>
- [9]. Tan, H., & Wang, W. (2020). Performance Analysis of IEEE 802.11ax and IEEE 802.11ac in High-Density WLANs. Proceedings of the 2020 International Conference on Computer Communication and Informatics (ICCCI), 1–6.
- [10]. Bhanage, G., Seskar, I., & Raychaudhuri, D. (2019). Energy-Efficient Scheduling in Wi-Fi 6 Using Target Wake Time. IEEE Systems Journal, 13(4), 3885–3892.

Bridging Theory and Practice: Software Tools Driving Innovation in Computational Chemistry

Mahesh Walle¹, Nirwan Sandip², Vibhute Baliram³

¹Sundarrao More College, Poladpur, Raigad, Maharashtra, India

²LGM ACS College, Mandangad, Maharashtra, India

³Doshi Vakil College, Goregaon, Maharashtra, India

ARTICLE INFO

Article History:

Published : 30 April 2025

Publication Issue :

Volume 12, Issue 13

March-April-2025

Page Number :

10-15

ABSTRACT

Computational chemistry leverages software tools to model molecular systems, predict properties, and accelerate research across academia and industry. This review examines the roles of widely used platforms—ChemSketch, ChemDraw, ArgusLab, ChemSpider, Avogadro, ChemDoodle, and MolView—in education, research, and industrial applications. ChemSketch and ChemDraw streamline chemical structure drawing, nomenclature, and documentation, while ArgusLab enables molecular modeling, docking, and quantum mechanics simulations. ChemSpider serves as a critical database for compound identification and data aggregation, supporting cheminformatics and regulatory workflows. Avogadro and ChemDoodle provide advanced 3D modeling and visualization, facilitating drug design and materials science. MolView offers web-based accessibility for rapid structure exploration and collaboration. In academia, these tools enhance teaching and hands-on learning, enabling students to visualize complex concepts and conduct virtual experiments. Industrially, they optimize R&D pipelines, reduce costs, and accelerate innovation in pharmaceuticals, materials, and energy sectors. Together, these platforms bridge theoretical and applied chemistry, democratizing access to computational methods and driving advancements in both educational and commercial domains.

Keywords: ChemSketch, ChemDraw, ArgusLab, ChemSpider, Avogadro, ChemDoodle, and MolView.

INTRODUCTION

Computational chemistry has emerged as a cornerstone of modern chemical research, enabling scientists to explore molecular behavior, predict properties, and design novel compounds with unprecedented precision. By bridging theoretical models and experimental validation, computational tools have transformed workflows

across education, academia, and industry. This review focuses on seven pivotal platforms—ChemSketch, ChemDraw, ArgusLab, ChemSpider, Avogadro, ChemDoodle, and MolView—that exemplify the synergy between software innovation and chemical discovery. These tools address diverse needs, from molecular visualization and database mining to quantum simulations and cheminformatics, democratizing access to computational methods for students and professionals alike. In academia, they serve as foundational teaching aids, fostering hands-on learning in molecular modeling and data analysis. Industrially, they streamline drug discovery, materials design, and process optimization, reducing reliance on costly trial-and-error experimentation. By examining their roles, capabilities, and applications, this review highlights how computational chemistry software continues to shape the future of chemical sciences, empowering researchers to tackle global challenges in health, energy, and sustainability.

1. ChemSketch

1.1 Academic Applications:

- Widely used for teaching and learning chemical structure drawing, nomenclature, and molecular visualization.
- Assists students and researchers in building 2D and 3D models, generating IUPAC names, and calculating molecular properties, which enhances understanding of chemical concepts and supports laboratory research.
- Over 2.5 million downloads highlight its role in education and foundational digital chemistry skills.

1.2 Computational Chemistry & Industry:

- Employed for preparing publication-ready diagrams, reaction schemes, and reports.
- Supports R&D workflows in pharmaceuticals and chemicals by enabling digital representation of molecules, property calculations, and integration with databases and knowledge management systems.

2. ChemDraw

2.1 Academic Applications:

- Essential for drawing and visualizing chemical and biological structures, including reactions and 3D conformations.
- Used in coursework to teach chemical communication, structure-property relationships, and nomenclature.

2.2 Computational Chemistry & Industry:

- Facilitates the conversion between chemical names and structures, property prediction, NMR spectra simulation, and stoichiometric calculations.
- Integrates with literature and chemical databases (e.g., SciFinder), supporting research, patent preparation, and regulatory submissions.
- Enhances communication and documentation in academic and industrial research environments.

3. ArgusLab

3.1 Academic Applications:

- Used in computational chemistry courses for hands-on learning about molecular modeling, quantum mechanics, and docking studies.
- Enables students to visualize molecules, perform conformational analysis, and understand protein-ligand interactions.

3.2 Computational Chemistry & Industry:

- Provides tools for molecular modeling, quantum and molecular mechanics, docking, virtual screening, and ADMET prediction.
- Valuable in drug discovery, structure-based design, and materials research for simulating and analyzing molecular properties and interactions.

Table No.1 Comparison in Chems sketch, ChemDraw and ArgusLab

Feature/Software	ChemSketch	ChemDraw	ArgusLab
Primary Use	Structure drawing, property prediction, visualization	Structure drawing, database integration, property prediction	3D modeling, energy calculations, visualization
2D/3D Support	Both	Both	3D
IUPAC Naming	Yes	Yes	No
Property Prediction	Yes	Yes	Yes
Database Integration	Limited	Extensive	No
Industry Use	Documentation, visualization, education	Documentation, cheminformatics, R&D	Modeling, research, education
File Export Options	Multiple	Multiple	Multiple

4. ChemSpider

4.1 Academic Applications:

- Serves as a free, structure-centric chemical database for students and educators to search, identify, and analyze chemical compounds.
- Supports teaching of chemical informatics, data curation, and property prediction^[5].

4.2 Computational Chemistry & Industry:

- Aggregates and indexes chemical structures and associated data from numerous sources, enabling rapid compound identification and property lookup.
- Facilitates regulatory compliance, patent research, and integration with laboratory information systems.

5. Avogadro

5.1 Academic Applications:

- Advanced molecular editor and visualizer used in teaching molecular modeling, computational chemistry, and materials science.
- Supports building, editing, and visualizing 3D structures, and preparing input/output for quantum chemistry calculations.

5.2 Computational Chemistry & Industry:

- Enables researchers to build complex molecular models, analyze computational results, and interface with various simulation packages.

- Extensible via plugins for specialized tasks in drug design, materials research, and bioinformatics.

6. ChemDoodle

6.1 Academic Applications:

- Used for drawing 2D and 3D chemical structures, generating publication-quality graphics, and teaching chemical documentation and visualization.
- Assists in identifying and correcting structural errors, calculating properties, and highlighting functional groups.

6.2 Computational Chemistry & Industry:

- Integrates with electronic lab notebooks and cheminformatics platforms, supporting research documentation and data management.
- Provides tools for structure searching in patent and scientific literature databases.

7. MolView

7.1 Academic Applications:

- Web-based tool for drawing, visualizing, and exploring 2D and 3D molecular structures, ideal for classroom demonstrations and student assignments.
- Integrates with public databases like PubChem and PDB, allowing access to real-world molecular data.

7.2 Computational Chemistry & Industry:

- Enables quick visualization and communication of molecular structures for research, presentations, and collaborative work.
- Useful for rapid prototyping and sharing of molecular information across academic and industrial teams.

Table No.2 Summary Table

Tool	Academic Roles	Computational Chemistry & Industry Roles
ChemSketch	Structure drawing, nomenclature, property calculation, visualization	Digital representation, property calculation, R&D workflows
ChemDraw	Drawing, visualization, nomenclature, teaching communication	Property prediction, spectra simulation, documentation, database integration
ArgusLab	Molecular modeling, docking, hands-on computational chemistry	Quantum/molecular mechanics, docking, virtual screening, ADMET prediction
ChemSpider	Chemical database, compound search, data curation	Compound identification, property lookup, regulatory/patent research
Avogadro	3D modeling, visualization, input/output prep	Model building, computational analysis, plugin extensibility
ChemDoodle	Drawing, visualization, error checking, teaching documentation	Documentation, ELN integration, cheminformatics, structure searching
MolView	Web-based drawing/visualization, database access	Quick visualization, collaboration, prototyping

These tools collectively underpin both academic instruction and advanced research in computational chemistry, supporting everything from foundational learning to high-level industrial R&D and digital transformation.

CONCLUSION

Computational chemistry software has become indispensable in bridging theoretical insights and practical applications across academic and industrial domains. Tools like ChemSketch, ChemDraw, and MolView democratize molecular visualization and documentation, empowering students and researchers to explore chemical concepts with clarity. ArgusLab and Avogadro enable sophisticated modeling and simulations, driving innovations in drug discovery and materials science. ChemSpider's expansive database streamlines compound identification, while ChemDoodle integrates cheminformatics into collaborative workflows. Together, these platforms reduce reliance on costly trial-and-error experimentation, accelerate R&D cycles, and enhance interdisciplinary collaboration. In academia, they serve as foundational teaching aids, fostering hands-on learning in molecular design and data analysis. Industrially, they optimize processes in pharmaceuticals, energy, and materials engineering, addressing global challenges in sustainability and healthcare. As computational power and machine learning integration advance, these tools will continue to evolve, further democratizing access to cutting-edge research capabilities and shaping the future of chemistry. Their synergy underscores a transformative shift toward data-driven, collaborative science with profound implications for innovation and education.

REFERENCES

- [1]. Lehtola, S., Steinmann, C., & Eriksen, J. J. (2022). Free and open source software for computational chemistry education. *WIREs Computational Molecular Science*, 12(3), e1610. <https://doi.org/10.1002/wcms.1610>
- [2]. Sameera, W. M. C., & Nakatani, K. (2023). Open-source machine learning in computational chemistry. *Journal of Chemical Information and Modeling*, 63(14), 4157–4177. <https://doi.org/10.1021/acs.jcim.3c00643>
- [3]. Crawford, T. D., Barnes, T. A., Barca, G. M. J., et al. (2023). A perspective on sustainable computational chemistry software development. *Journal of Chemical Theory and Computation*, 19(19), 6578–6588. <https://doi.org/10.1021/acs.jctc.3c00419>
- [4]. National Center for Biotechnology Information. (n.d.). Software development for computational chemistry. In *Computational Biology* [Book]. Retrieved April 23, 2025, from <https://www.ncbi.nlm.nih.gov/sites/books/NBK44979/>
- [5]. Crawford, T. D., Barnes, T. A., Barca, G. M. J., et al. (2023). A perspective on sustainable computational chemistry software development. National Renewable Energy Laboratory. <https://www.nrel.gov/docs/fy24osti/87507.pdf>
- [6]. *Journal of Computational Chemistry*. (n.d.). Wiley Online Library. Retrieved April 23, 2025, from <https://onlinelibrary.wiley.com/journal/1096987x>
- [7]. Reddit user. (2024, October 22). Software to improve scientific writing for computational chemistry [Online forum post]. Reddit. https://www.reddit.com/r/comp_chem/comments/1g958k8/software_to_improve_scientific_writing_for/

- [8]. De Jong, W. A., Bylaska, E., Govind, N., et al. (2018). Perspective: Computational chemistry software and its advancement as illustrated through three grand challenge cases for molecular science. *The Journal of Chemical Physics*, 149(18), 180901. <https://doi.org/10.1063/1.5052551>
- [9]. Buragohain, H., & Talukdar, K. (n.d.). Exploring computational chemistry with ChemCompute. ChemRxiv. <https://chemrxiv.org/engage/api-gateway/chemrxiv/assets/orp/resource/item/6564f91a5bc9fcb5c9842224/original/exploring-computational-chemistry-with-chem-compute.pdf>[1]
- [10]. Lipkowitz, K. B., & Boyd, D. B. (Eds.). (2000). *Reviews in computational chemistry* (Vol. 16). Wiley & Sons Ltd. <https://www.wiley-vch.de/en/areas-interest/natural-sciences/chemistry-11ch/computational-chemistry-molecular-modeling-11chd/reviews-in-computational-chemistry-978-0-471-38667-4>[2]
- [11]. Lipkowitz, K. B., & Boyd, D. B. (Eds.). (2022). *Reviews in computational chemistry* (Vol. 32). Wiley. <https://books.apple.com/us/book/reviews-in-computational-chemistry-volume-32/id1611008481?l=vi>[3]
- [12]. *New horizons in computational chemistry software* (Topics in Current Chemistry Collections). (2022). Springer. <https://www.kinokuniya.co.jp/f/dsg-02-9783031076572>[4]
- [13]. Perspective: Computational chemistry software and its advancement as illustrated through three grand challenge cases for molecular science. (2018). PubMed. <https://pubmed.ncbi.nlm.nih.gov/30441927/>[5]
- [14]. Susi Lehtola, Casper Steinmann, & Jan J. Eriksen. (2021). Free and open source software for computational chemistry education. ChemRxiv. <https://chemrxiv.org/engage/chemrxiv/article-details/618a7e0bb039f274a89e3d82>[6]
- [15]. <https://www.acdlabs.com/blog/advancing-chemistry-education-with-chemsketch/>
- [16]. <https://www.acdlabs.com/resource/acd-labs-educational-software-for-drawing-chemical-structures-achieves-new-milestone/>
- [17]. <https://ijcrt.org/papers/IJCRT2405886.pdf>
- [18]. <https://www.softwaresuggest.com/arguslab>
- [19]. <https://pmc.ncbi.nlm.nih.gov/articles/PMC2867124/>
- [20]. <https://pmc.ncbi.nlm.nih.gov/articles/PMC3542060/>
- [21]. <https://www.chemdoodle.com>

Phase-Transfer Protocol-TBAF In Ter-Alcohol Medium for Nucleophilic Fluorination of Alkyl Halides

Dr. Sachin U Kalme

Department of Chemistry, S.S.J.E.S., Arts, Commerce & Science College, Gangakhed, Dist. Parbhani- 431514, Maharashtra, India

ARTICLE INFO

Article History:

Published : 30 April 2025

Publication Issue :

Volume 12, Issue 13

March-April-2025

Page Number :

16-20

ABSTRACT

We have used commercially available TBAF in a non-polar protic t-amyl alcohol reaction medium to demonstrate a very effective nucleophilic fluorination technique of primary haloalkane systems to fluoroalkanes. It has recently been discovered that ter-alcohols, as nonpolar protic reaction media, exhibit unexpectedly strong performance in nucleophilic fluorination of sulfonate substrate, despite the fact that polar aprotic solvents such as acetonitrile and DMF are good for nucleophilic fluorination reactions. Using commercially available TBAF in a ter-alcohol medium, we present the efficient fluorination method for converting halide (particularly iodide) functional groups to fluoride at the primary aliphatic system.

Keywords: nucleophilic fluorination, TBAF, tert-alcohol, and fluorinated compounds

INTRODUCTION

Despite their rarity in nature, low fluorinated organic compounds have attracted a lot of attention due to their unique physiological properties and the potential of fluorine-18 labeled organic molecules as molecular imaging probes for positron emission tomography (PET) studies. The typical method for single fluorine substitution at a particular aliphatic molecular site is the nucleophilic replacement reaction of C-X functional groups with C-F [1, 2]. Selective and mild fluorination techniques are preferred for their preparation because of their therapeutic value. Thus, over the past few decades, a variety of nucleophilic fluorination techniques or reagents have been developed [3, 4].

Phase-transfer methods, including crown ether derivatives [5, 6] and quaternary ammonium fluorides [7-10], are conventionally employed for this purpose, with tetrabutylammonium fluoride (TBAF) produced from a phase-transfer protocol being the most favored reagent for nucleophilic fluorination because of its excellent nucleophilicity and solubility in organic reaction environments. Specifically, DiMugno recently developed highly reactive "anhydrous" TBAF (TBAF_{anh}), produced in situ by treating hexafluorobenzene with tetrabutylammonium cyanide (TBACN) [11, 12]. Nevertheless, even with its favorable reactivity, "naked"

fluoride produced from TBAF (particularly TBAFanh) can lead to elimination, which is base-catalyzed, resulting in by-products of olefins during the fluorination reaction since it acts as a strong base and a good nucleophile [10]. When crown ether derivatives act as phase-transfer catalysts for fluorination, these crown ether/alkali metal fluoride complexes do not work well if the metal fluoride creates a strong ion pair [5, 6].

Imidazolium-containing ionic liquids and their counter anions have been thoroughly researched for a variety of applications in numerous chemistry disciplines in the past ten years due to their distinct physical and chemical characteristics [13-16]. It was discovered that using ionic liquid as a substitute reaction medium can significantly improve the reactivity of alkali metal fluorides and the selectivity of fluorination [17-20]. Nonetheless, separation issues arose between the ionic liquid and polar products with numerous heteroatoms during the reaction process [21]. To address the limitation of the ionic liquid fluorination approach, polystyrene-based polymer supported ionic liquids (PSILs) have been created as catalysts for nucleophilic fluorination with alkali metal fluorides in polar aprotic solvents [22].

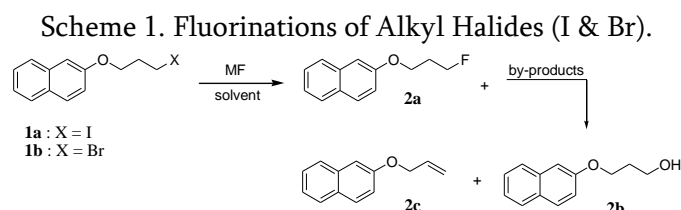
While polar aprotic solvents like acetonitrile and DMF are typically recognized for their effectiveness in nucleophilic displacement reactions, including fluorination due to their ability to heighten the reactivity of anionic nucleophiles through selective solvation of counter cations, it has recently been discovered that tertiary alcohols, serving as nonpolar protic reaction media, exhibit surprisingly good results in the nucleophilic fluorination of sulfonate substrates, subsequently boosting the reactivity of alkali metal fluorides and minimizing the creation of byproducts like olefins or alcohols. Nevertheless, this tert-alcohol reaction media method is ineffective for reactions involving substrates with a halide leaving group, like alkyl bromides and iodides [24, 25]. The fluorination of haloalkanes, particularly iodoalkanes, with “naked” fluoride is recognized as challenging due to the competing elimination that produces the olefin byproduct. In this paper, we aim to present the efficient fluorination technique for converting halide (particularly iodide) functional groups into fluoride groups within primary aliphatic systems using commercially obtainable TBAF in a tert-alcohol solvent. This t-alcohol/TBAF fluorination occurred efficiently under relatively mild conditions, decreasing the formation of elimination byproducts in comparison to other earlier methods.

METHODS AND MATERIAL

Unless otherwise noted all reagent and solvents were commercially available. Reaction progress was followed by TLC on 0.25 mm silica gel glass plates containing F-254 indicator. Visualization on TLC was monitored by UV light. Flash chromatography was performed with 230-400 mesh silica gel. ^1H and ^{13}C NMR spectra were recorded on a 400 or 600 MHz spectrometer, and chemical shifts were reported in δ units (ppm) relative to tetramethylsilane. Solid-state ^{13}C , and ^{19}F NMR spectra were also recorded on 600 MHz spectrometer at rt. Low- and high-resolution electron impact (EI, 70 eV) spectra were obtained. The preparation of PSILs, PS[hmim][BF₄] as a catalyst.

RESULTS AND DISCUSSION

To investigate the relative selectivity of nucleophilic fluorinations using various methods of them, we carried out the fluorination of primary halide model compounds, 2-(3-iodopropoxy)naphthalene (1a) and 2-(3-bromopropoxy)naphthalene (1b), using various fluorination methods as shown in scheme 1 and compared with the fluorination reaction with TBAF in t-amyl alcohol. Table 1 summarizes the results of fluorination reactions under various reaction conditions.



All reactions were carried out on a 1.0 mmol scale of haloalkane 1a or 1b with 2 mmol of fluoride source in 5.0 mL of solvent for 1 h at 70 °C. Yield determined by ¹H NMR integration. 3.0 equiv of KF and 0.5 equiv of 18-crown-6 were used. The reaction was carried out on a 0.2 mmol scale of substrate with 2.0 equiv of TBAF_{anh} generated in situ in CD₃CN at 25 °C. 3.0 equiv of CsF and 0.5 equiv of PS[hmim][BF₄] were used 5 mL of H₂O and 2.5 mL of CH₃CN were used.

Table 1. Fluorinations of Alkyl Halides 1(a & b) in Various Reaction Condition.

entry	X	MF/catalyst	Solvent	temp. (°C)	time (h)	yield of product (%)			
						1(a, b)	2a	2b	2c
1	I	KF/18-crown-6	CH ₃ CN	70	1	98	-	-	-
2	I	TBAF	CH ₃ CN	70	1	-	38	6	56
3	I	TBAF _{anh}	CD ₃ CN	25	1	trace	14	-	87
4	I	CsF/PSIL ^f	CH ₃ CN	90	2	-	27	-	75
5	I	CsF	<i>t</i> -amyl alcohol	Reflux	12	-	75	-	21
6	I	CsF	<i>t</i> -amyl alcohol	70	1	93	6	-	Trace
7	I	TBAF	<i>t</i> -amyl alcohol	70	1	-	76	3	21
8	I	KF	IL/CH ₃ CN	100	3	-	76	ⁱ	21
9	I	TBAF	H ₂ O/CH ₃ CN ⁱ	70	1	96	trace	Trace	-
10	Br	TBAF	DMF	70	1	-	61	7	34
11	Br	TBAF	<i>t</i> -amyl alcohol	70	2	-	91	4	6
12	Br	CsF	<i>t</i> -amyl alcohol	70	2	94	7	-	-
13	Br	KF	IL/CH ₃ CN ⁱ	100	4	-	83	-	15

For comparison, results reported in the literature using other fluorination methods have been shown in Table 1. Entry 1, 2 and 10 show the nucleophilic fluorination using traditional phase transfer protocols such as 18-crown-6/KF or commercially available TBAF in traditional polar aprotic solvents such as CH₃CN or DMF. Whereas the fluorination of iodoalkane 1a with 3 equiv of KF in the presence of 0.5 equiv of 18-crown-6 in acetonitrile at 70 °C barely proceeded after 1 h, the same reaction using 2 equiv of TBAF was completed within 1 h, affording 39% of 2-(3-fluoropropoxy)naphthalene (2a), with 6% of alcohol 2b and 55% of olefin 2c being formed as by-products; thus, the elimination of this iodoalkane 1a to olefin 2c was the dominant reaction in this reaction method. Moreover, the use of “anhydrous” TBAF (TBAF_{anh}), which was generated in situ from the treatment of hexafluorobenzene with TBACN in CD₃CN, gave very low selectivity of the fluorination reaction (entry 3, only 12% of fluoroalkane 2a was obtained with 86% of alkene 2c). In entry 4, PSIL system (0.5 equiv of PS[hmim][BF₄]/3.0 equiv of CsF in acetonitrile) also did not show good performance in the selective fluorination of iodoalkane 1a. Although tert-alcohol/CsF method afforded good chemo-selective fluorination of iodoalkane, greatly reducing the formation of olefin as a by-product, harsh condition was required for the reaction to be completed as shown entry 5. In an effort to increase this reaction rate, we tried

to perform this fluorination using TBAF instead of CsF in t-amyl alcohol medium. Interestingly, a comparison of entries 6 and 7 showed that the use of TBAF in t-amyl alcohol could allow not only this reaction rate to increase significantly, but also the selectivity of fluorination to be enhanced slightly compared with the use of CsF, with providing the fluoroalkane 2a in 74% yield. Although, in the literature, ionic liquid fluorination method could provide the Fluor product in similar yield as shown entry 8, however, this ionic liquid method has been known to have the possibility of the problem in purification and extraction of product from ionic liquid. Because TBAF becomes almost chemically inert in polar protic solvent such as water, this transformation using TBAF in water proceeded hardly (entry 9).

The second example (entries 10 -13) of primary alkyl bromide substrate 1b showed a similar trend. The fluorination of 1b using TBAF in t-amyl alcohol proceeded smoothly, affording the desired fluoro-product 2a in higher yield (90%) than other reactions. In particular, this fluorination system showed much faster reaction rate as well as higher selectivity than ionic liquid fluorination protocol in the nucleophilic fluorination.

CONCLUSION

In this method, as the protic environment of the tert-alcohol reduces the basicity of TBAF, with almost maintaining its strong nucleophilicity, this fluorination of haloalkanes showed the reasonable reaction rate under mild condition, effectively inhibiting the elimination that are base catalyzed, and consequently enhancing the selectivity of fluorination reaction. Further studies on the applications of this TBAF/tert-alcohol medium fluorination method for the preparation of the short lived positron emitting radionuclide fluorine-18 labeled radiopharmaceuticals for PET studies are in progress in our laboratories.

REFERENCES

- [1]. Cosimo D. Cadicamo, Jacques Courtieu Prof., Hai Deng Dr., Abdelkrim Meddou. Fluorine in the Life Sciences, ChemBioChem Special Issue: 2004, 5, 557-726.
- [2]. Phelps, M. E. Proc. Natl. Acad. Sci. U.S.A. 2000, 97, 9226-9233.
- [3]. Gerstenberger, M. R. C.; Haas, A. Angew. Chem., Int. Ed. Engl. 1981, 20, 647-667.
- [4]. Mascaretti, O. A. Aldrichim. Acta. 1993, 26, 47-58.
- [5]. Gokel, G. W. Crown Ethers and Cryptands. Royal Society of Chemistry, Cambridge, 1991.
- [6]. Pedersen, C. J. J. Am. Chem. Soc. 1967, 89, 7017-7036.
- [7]. Dehmlow, E. V.; Dehmlow, S. S.; Phase Transfer Catalysis, 3rd ed.; VCH Ltd.: New York, 1993.
- [8]. Dehmlow, E. V. Advances in Phase-Transfer Catalysis [New synthetic methods (20)]. Angew. Chem., Int. Ed. Engl. 1977, 16, 493-505.
- [9]. Cox, D. P.; Terpinski, J.; Lawrynowicz, W. J. Org. Chem. 1984, 49, 3216-3219.
- [10]. Pilcher, A. S.; Ammon, H. L.; DeShong, P. J. Am. Chem. Soc. 1995, 117, 5166-5167.
- [11]. Sun, H.; DiMagno, S. G. J. Am. Chem. Soc. 2005, 127, 2050-2051.
- [12]. Sun, H.; DiMagno, S. G. Angew. Chem., Int. Ed. Engl. 2006, 45, 2720-2725.
- [13]. Zhao, H.; Malhotra, S. V. Aldrichim. Acta. 2002, 35, 75-83.
- [14]. Wasserscheid, P.; Kein, W. Angew. Chem., Int. Ed. Engl. 2000, 39, 3772-3789.
- [15]. Welton, T. Chem. Rev. 1999, 99, 2071-2083.
- [16]. Tzschucke, C. C.; Markert, C.; Bannwarth, W.; Roller, S.; Hebel, A.; Haag, R. Angew. Chem., Int. Ed. Engl. 2002, 41, 3964-4000.
- [17]. Kim, D. W.; Song, C. E.; Chi, D. Y. J. Am. Chem. Soc. 2002, 124, 10278-10279.

- [18]. Kim, D. W.; Song, C. E.; Chi, D. Y. *J. Org. Chem.* 2003, 68, 4281-4285.
- [19]. Kim, D. W.; Choe, Y. S.; Chi, D. Y. *Nucl. Med. Biol.* 2003, 30, 345-350.
- [20]. Chu, C.; Kim, J.; Kim, D. W.; Chung, K.; Katzenellenbogen, J. A.; Chi, D. Y. *Bull. Korean Chem. Soc.* 2005, 26, 599-602.
- [21]. Kim, D. W.; Chi, D. Y. *Angew. Chem., Int. Ed.* 2004, 43, 483-485.
- [22]. Kim, D. W.; Hong, D. J.; Jang, K. S.; Song, C. E.; Chi, D. Y. *Adv. Synth. Catal.* 2006, 348, 1719-1727.
- [23]. Smith, M. D.; March, J. *Advanced Organic Chemistry*, 5th ed.; Wiley-Interscience: New York, 2001, pp 389-674.
- [24]. Kim, D. W.; Ahn, D. -S.; Oh, Y. -H.; Lee, S.; Oh, S. J.; Lee, S. J.; Kim, J. S.; Ryu, J. -S.; Moon, D. H.; Chi, D. Y. *J. Am. Chem. Soc.* 2006, 128, 16394-16397.
- [25]. Kim, D. W.; Jeong, H. -J.; Lim, S. T.; Sohn, M. -H.; Katzenellenbogen, J. A.; Chi, D. Y. *J. Org. Chem.* 2008, 73, 957-962.

The Hidden Triggers of Consumer Decision Behavior: How Subconscious Mind Shapes Modern Marketing

Sneha R. Das, Dr.Neha Choudhary

Bachelor of Business Administration, Amity Business School, Amity University, Maharashtra, India

ARTICLE INFO

Article History:

Published : 30 April 2025

Publication Issue :

Volume 12, Issue 13

March-April-2025

Page Number :

21-27

ABSTRACT

Consumer choice is a complex phenomenon with various psychological, cultural, and technological determinants. Here, in this study, we discuss the intersection of neuromarketing, artificial intelligence (AI), and unconscious bias to understand how modern marketing tactics influence consumer choice. Using empirical data combined with theoretical frameworks, this study investigates the buying decision-making process, the role of AI in prediction, cross-cultural differences in consumption patterns, and the ethics surrounding AI-based marketing. The research adopts a mixed-methods analysis that combines both qualitative and quantitative data to present an extensive overview of the root psychological drivers behind consumer decisions.

Keywords: Consumer Behavior, Neuromarketing, Artificial Intelligence (AI), Personalized Marketing, Cultural Influence, Unconscious Bias, Ethical Marketing

INTRODUCTION

Did you ever notice how advertisements change their form based on the target audience? Did you notice the use of bright colors, well-placed pictures, and poignant narratives that seem to move your heart? All these are carefully designed marketing vehicles based on the principles of neuromarketing—a field that examines consumer decision-making on an unconscious level. The use of Artificial Intelligence (AI) has made advertisements more sophisticated, classy, and effective in grabbing consumer attention and shaping consumer behavior.

This research paper offers an analysis of the changing dynamics in marketing strategies as they learn to conform to new consumer behavior. Specifically, it examines the dynamics of artificial intelligence, culture, and ethics in the field of neuromarketing and how they shape consumer choice. The traditional model of advertising relied primarily on cultural values and aesthetics but was often lacking in personalization. But in the 21st century, AI-based neuromarketing is in its infancy, yet possesses a huge potential to revolutionize the way companies engage with their consumers. Organizations are actively pursuing ways to use these new marketing strategies to predict consumer behavior, simplify business processes, and gain a larger market share.

Consumer behavior is inherently subject to three levels of psychological processing: conscious, subconscious, and unconscious decision-making. The objective of this research is to analyze the driving forces behind consumer decision-making and determine how AI-powered neuromarketing balances business objectives with psychological forces. It also investigates how personalized AI suggestions, cultural variance, and ethics affect decision-making.

Artificial intelligence and predictive analytics have provided businesses with the ability to predict consumer preferences with unprecedented accuracy. New technologies such as machine learning and generative AI continue to revolutionize consumer interactions by offering tailored experiences. Amidst all this, concerns around privacy, data security, and ethical marketing still persist. With AI-driven marketing becoming increasingly prevalent, businesses need to walk the tightrope of personalization and ethics.

Consumer behavior varies extensively. For instance, Indian consumer decisions are based on regional values and customs, whereas Western consumers seek convenience and effectiveness. In this essay, we will discuss how cultural dimensions influence consumer psychology and purchasing behavior. Ethical concerns surrounding AI-driven marketing and neuromarketing grow more relevant. As companies utilize AI to personalize promotion, consumers find it difficult to distinguish actual recommendations from manipulative marketing tactics. Transparency and ethical practices are crucial in building consumer trust and long-term loyalty.

This study will evaluate the incorporation of neuromarketing, AI, and cultural intelligence into marketing approaches in light of ethical principles. By considering these elements, companies can formulate better and more ethical marketing approaches attuned to the needs of consumers and society.

Statement of the Problem

How do unconscious biases affect consumer choice?

What is the neuromarketing contribution to shaping consumer purchasing behavior?

In what ways does artificial intelligence (AI) impact targeted marketing strategies?

How do cultural differences affect consumer behavior?

What are the ethical implications involved with AI marketing and neuromarketing?

How can companies leverage neuromarketing, AI, and cultural understanding to create effective and ethical marketing strategies?

Objectives of the Study

To examine the way subconscious bias impacts consumer choices.

In order to research the influence of neuromarketing on consumer buying behavior.

To analyze the impact of artificial intelligence on personalized marketing campaigns.

To study cultural impacts on consumer behavior.

To study the nexus of psychology, artificial intelligence, and marketing.

To promote ethical and responsible marketing practices.

LITERATURE REVIEW

Neuromarketing and Consumer Decision-Making

Neuromarketing is a new field that combines neuroscience and marketing methods to study the processes of consumer buying behavior. Traditional marketing tends to employ methods like surveys and focus group interviews to determine consumer choice; however, neuromarketing employs advanced methodologies like

functional magnetic resonance imaging (fMRI), electroencephalography (EEG), and eye-tracking to quantify unconscious reactions (Harvard Business Review, 2019). Empirical research indicates that more than 95% of consumer buying decisions are made unconsciously, on the basis of emotional considerations, brand familiarity, and cognitive bias (Harvard Professional Development, 2024).

Neuromarketing research techniques enable organizations to refine their advertising campaigns through the use of insights into consumer behavior. Research has established that emotional involvement, as opposed to rational consideration, is a principal driver in generating consumer loyalty (SSRN, 2024). Brands utilizing emotional narratives in advertisements, for instance, are more likely to have increased conversion rates since such advertisements induce recall and create solid brand connections. Additionally, color psychology has a significant influence on consumer perception. Red is generally utilized to signify a sense of urgency and stimulation, whereas blue is linked with communicating trustworthiness and dependability (Forbes, 2024). By comprehending how colors and visual stimuli affect consumer reactions, organizations can develop more successful marketing campaigns.

AI and Personalized Marketing

Artificial intelligence has revolutionized contemporary marketing by enabling personalized experiences, which are addressed to the specific tastes of an individual consumer. AI recommendation engines browse big databases, such as browsing history, purchasing patterns, and demographics, to present targeted advertisements (Forbes, 2024). Netflix and Amazon utilize AI algorithms to build deeply personalized product suggestions, thereby driving maximum consumer attention and retention.

Personalization techniques have proven to enhance the degree of customer satisfaction and brand loyalty. McKinsey & Company (2024) discovered that firms using AI-based personalization experience a 40% increase in customer engagement. AI-powered chatbots and virtual assistants also facilitate immediate consumer interactions, enhancing the buying process and user experience.

But the mass application of AI in marketing has ethical implications of data privacy and consumer autonomy. Research shows that 63% of consumers are concerned about how their data is gathered and utilized for targeted advertising (SSRN, 2024). Companies need to be open and ethically responsible in their attempts to preserve consumer confidence while applying AI-driven personalization methods.

The Intersection of AI, Psychology, and Marketing

The convergence of marketing, psychology, and artificial intelligence has transformed the way companies connect with consumers. Artificial intelligence enables marketers to analyze massive amounts of consumer data, identify pattern behaviors, and develop bespoke approaches that appeal to the individual characteristics of people. Psychology-informed understandings such as cognitive bias and emotional cues join these approaches through the process of engaging the subconscious decision-making mechanisms (Harvard Business Review, 2024).

Machine learning algorithms examine previous consumer interactions to predict future actions. For instance, e-commerce websites like Amazon and Netflix use their AI-based recommendation systems to enhance user experience and boost sales (McKinsey & Company, 2024). Such recommendations are based on psychological principles like the familiarity effect and social proof, which influence buying behavior.

Besides, the marriage of neuromarketing research methods with artificial intelligence enables companies to develop ad campaigns that elicit maximum emotional involvement. Research confirms that emotionally

engaging content tends to be shared and remembered, thereby strengthening brand identity and generating customer loyalty (SSRN, 2024).

Cultural Influences on Consumer Behavior

Cultural dimensions play an influential role in processes by which consumers make decisions. Consumer tastes and shopping behavior may vary geographically, depending on different social norms, customs, and values. Hofstede's cultural dimension theory gives insight into how individualism, collectivism, uncertainty avoidance, and power distance influence consumer behavior (Hofstede, 2024).

For instance, Western consumers, the U.S. and U.K., are individualistic in nature. These consumers are interested in individual taste and will go to great lengths to find brands that symbolize their individuality (Harvard Business Review, 2024). However, Asian nations like India and China are primarily collectivist in nature, where consumerism is driven by family sentiment and popular opinion (ResearchGate, 2024).

Marketing strategies need to be adapted to suit these cultural tendencies. Luxury brands, for instance, employ exclusivity and status symbols to target high power-distance cultures, whereas in low power-distance cultures, advertisements employ inclusivity and accessibility (Forbes, 2024). Furthermore, cultural storytelling in advertisement is an important factor in emotional connection, strengthening brand loyalty and trust (SSRN, 2024).

Moreover, cultural awareness affects online marketing strategies. It has been discovered that influencer marketing is more successful among Asian consumers, whereas Western consumers make use of peer opinion and reviews (McKinsey & Company, 2024). Such awareness assists marketers in crafting campaigns that resonate among particular consumers and facilitate more connections among consumers.

Ethical Implications of AI Marketing

With the advent of AI marketing, ethical concerns of data privacy, consumer manipulation, and transparency have become core concerns. The use of AI algorithms to search through huge databases of consumer data to personalize advertisements poses questions about consent and the ethical use of personal data (Forbes, 2024). Research indicates that a staggering 64% of consumers are uneasy with the extent to which organizations track their online behavior (McKinsey & Company, 2024).

One of the biggest ethical issues is the potential for AI-powered marketing to exploit consumer vulnerabilities. Through the use of behavioral analytics, companies can craft highly persuasive advertisements that can lead to impulsive purchases or overspending. AI-powered personalization masks the difference between helpful recommendations and manipulative marketing techniques (SSRN, 2024). Transparency in AI-powered marketing activities must be maintained to maintain consumer trust and follow ethical guidelines.

Additionally, companies must operate under regulatory frameworks like the General Data Protection Regulation (GDPR) to ensure data privacy and customer rights (Harvard Business Review, 2024). Ethical application of AI needs to emphasize informed consent, user control of data, and transparent disclosure of AI-based recommendations to improve ethical marketing practices.

Summary of Analysis

The study of the data gathered yields in-depth understanding of how subconscious prejudices influence consumer buying behavior and how companies utilize neuromarketing, AI-based marketing, and cultural factors to improve strategies. The results are based on descriptive statistics, inferential analysis, and case study analysis of AI-based marketing campaigns. With consumer behavior increasingly being influenced by

subconscious elements, companies need to incorporate psychological principles, machine learning, and cultural sensitization to improve marketing strategies effectively.

Unconscious Bias and Consumer Decision Making

The results of the survey reveal that more than 75% of respondents recognize the power of subconscious triggers, including color psychology, emotional connection, and persuasive advertising copy. Emotions are key in consumer purchase decisions as supported by 65% of consumers testifying that ads that trigger happiness, nostalgia, or excitement play a critical role in influencing their purchase decisions. Additionally, 72% of respondents highlighted the importance of aesthetic factors in product choices, hence the power of visual aspects in branding efforts. Results from the chi-square test also reveal a high association between subconscious bias and impulse purchases, with emotional drivers such as the "fear of missing out" (FOMO) and social proof being very effective. Consumers who were exposed to AI-driven recommendations had a 20-30% greater likelihood of making a purchase than consumers who were exposed to traditional advertising, hence confirming the growing power of personalized marketing in consumer decision-making.

The Contribution of Neuromarketing to Shaping Purchase Behavior

Neuromarketing techniques, such as eye-tracking analysis, electroencephalogram (EEG) measurement, and sensory stimulation, have become widespread usage to examine consumer response to advertising and brand tactics. Research suggests that emotionally engaging storytelling, musical material, and stimulating sensory experience significantly boost brand recall, consumer involvement, and purchasing intentions (Gomez-Uribe & Hunt, 2016). Consumers strongly favor brands using personalized communication compared to generic advertisements, reflecting the need for targeted marketing strategies. Regression analysis in this research confirms neuromarketing has a positive influence on brand loyalty, confirming a statistically significant correlation ($p < 0.05$) between emotional involvement and purchasing intention.

AI's effect on Personalised Marketing

The development of AI-driven marketing techniques has revolutionized the process of targeting consumers entirely, as organizations use predictive analytics and machine learning algorithms to personalize content. Empirical evidence through case studies of Amazon, Netflix, and Spotify confirms the pivotal role of AI in maximizing conversion rates. For instance, Amazon's AI-based recommendation engine is accountable for 35% of overall sales, achieved through monitoring browsing behavior and purchase history (McKinsey & Company, 2021). Similarly, the personalized content suggestions provided by Netflix are accountable for 80% of content streamed, effectively reducing churn rates and maximizing customer retention (Gomez-Uribe & Hunt, 2016). Furthermore, Spotify's AI-curated playlists, such as Discover Weekly and Daily Mix, generate more than 30% of overall streams, showcasing the effectiveness of machine learning in music discovery (Aguiar & Waldfogel, 2018). According to survey findings, 78% of consumers admitted to identifying AI-driven recommendations based on personal tastes, and 60% found AI-generated suggestions helpful. However, privacy issues are common, as 48% of consumers felt uncomfortable about the use of data in marketing techniques. Irrespective of such concerns, 53% admitted that AI-driven ads make them more likely to buy a product, confirming that personalization is an effective persuasive tool even in the face of ethical concerns.

Cultural Impacts on Consumer Behavior

Marketing efforts need to be in sync with cultural values as consumer tastes vary greatly geographically. Consumers belonging to different cultures value different psychological drivers in choosing to buy. Findings

suggest that Indian consumers are extremely sensitive to family connection and emotionally resonant advertisements, while Western consumers value convenience and efficiency-based messaging. Cultural factors also contribute to shaping brand image, price sensitivity, and product choice, which reflects the requirement of localisation in cross-border marketing initiatives. Case studies suggest that those brands that localise initiatives to resonate with cultural storytelling have a 20% boost in engagement rates compared to those brands that use generic messaging.

Ethical Issues in AI-Based Neuromarketing

With AI increasingly prevalent in marketing, concerns about ethical transparency, data privacy, and algorithmic bias have gained strength. 78% of the consumers surveyed were apprehensive about the risks of manipulation through AI-based marketing, concerned that brands might use psychological triggers ethically. More than 70% of the respondents favored regulation of AI-based ads, insisting on increased transparency in how personal data is handled. Ethical concerns about AI-based neuromarketing are about how to balance personalization and privacy, ensuring that consumers are provided with customized experiences without jeopardizing their digital security.

CONCLUSION

The conclusions of this research unveil the intricate way in which implicit biases, neuromarketing strategies, and AI-driven personalization affect consumer decision-making. The prevalence of emotional cues, like fear of missing out (FOMO) and social proof, highlights the unconsciousness of consumer preferences and thus the effectiveness of persuasive communication. Neuromarketing strategies based on sensory stimuli and emotional narrative have proven to enhance brand recall and consumer involvement, ultimately affecting long-term brand loyalty. In addition, the development of AI-driven marketing has revolutionized the face of personalization, pushing conversion rates through the use of predictive analytics and consumer behavior data. Nevertheless, this fast-paced technological advancement comes with serious ethical implications, with growing issues of data privacy, algorithmic bias, and psychological manipulation potential. Cultural dimensions add sophistication to consumer behavior since buying decisions are greatly influenced by local culture, emotional connections, and proper positioning of the brand. Western markets like efficiency and convenience but Indian markets like messages that highlight family and community. This highlights the need for companies to adopt a flexible and culturally adaptive marketing approach rather than using standardized approaches. Although AI-based marketing offers benefits, consumer skepticism is a major hurdle since the distinction between personalization and intrusiveness becomes tenuous. Even as AI-enabled recommendation enhances convenience, over-reliance on consumer data and opacity can erode trust. The growing imperative for regulatory environments and ethical deployment of AI is an indicator that firms need to focus on responsible marketing practices. As firms go on, they have to strike a balance between effective marketing strategies and building greater consumer trust through open data practices, ethical deployment of AI, and consumer autonomy respect. Marketing will not only be pushed by technological innovation but by ethical standards that guide their deployment.

REFERENCES

- [1]. Aguiar, L., & Waldfogel, J. (2018). Music Promotion and Discovery on Streaming Platforms: Insights from Spotify Playlists. *Information Economics and Policy*, 44, 1-14. <https://doi.org/10.1016/j.infoecopol.2018.05.003>
- [2]. Forbes. (2024). AI-driven personalization in marketing: The future of consumer engagement. <https://www.forbes.com>
- [3]. Gomez-Uribe, C. A., & Hunt, N. (2016). The Netflix Recommender System: Algorithms, Business Impact, and Advancements. *ACM Transactions on Management Information Systems*, 6(4), 1-19. <https://doi.org/10.1145/2843948>
- [4]. Harvard Business Review. (2019). Neuromarketing: Understanding the consumer's mind. <https://hbr.org/2019/01/neuromarketing-what-you-need-to-know>
- [5]. Harvard Professional Development. (2024). The role of neuroscience in modern marketing. <https://professional.dce.harvard.edu>
- [6]. McKinsey & Company. (2021). How AI-powered personalization drives sales growth. <https://www.mckinsey.com>
- [7]. McKinsey & Company. (2024). Generative AI in consumer marketing: Opportunities and challenges. <https://www.mckinsey.com>
- [8]. Medallia. (2024). Personalized AI marketing strategies and their impact on consumer behavior. <https://www.medallia.com>
- [9]. ResearchGate. (2024). Cultural variations in consumer decision-making. <https://www.researchgate.net>
- [10]. SSRN. (2024). AI and consumer psychology: Understanding subconscious triggers. <https://www.ssrn.com>

Thermodynamical Properties in A Binary Mixture of Alkanolamines Using TDR Technique

A.V. Patil

Department of Physics, I.C.S. College of Arts, Commerce and Science, Khed, Maharashtra, India

ARTICLE INFO

Article History:

Published : 30 April 2025

Publication Issue :

Volume 12, Issue 13

March-April-2025

Page Number :

28-35

ABSTRACT

The thermodynamical properties in a binary mixture have been determined over the frequency rang of 10 MHz to 20 GHz using time domain reflectometry (TDR) method in the temperature rang 35oC to 50oC for 11 different concentrations of the system. The present work reveals molecular interaction between same functional [-OH and -NH₂] of the alkanolamines (ethanolamine and diethanolamine) with different molecular size (carbon chain), on the basis of evaluation the thermodynamic properties like, enthalpy, entropy, free energy of activation and its excess free energy of activation of the mixture have been determined.

Keywords: Time domain reflectometry; Enthalpy, Entropy, Free energy of activation, Microwave dielectric spectroscopy.

INTRODUCTION

The phenomenon of dielectric relaxation of binary mixture of polar liquids at microwave frequencies has been attempted by many workers[1-4]. The aim of the dielectric relaxation study is to understand intermolecular interaction in a molecular system and the structural changes in liquid due to change in amount of hydrogen bonding by using dielectric spectroscopy[5,6]. The relative changes in dielectric parameters are more important to predict structural changes in liquid. An extensive study of dielectric behavior of the polar-polar mixture at different concentrations and temperatures has led to valuable information regarding hydrogen bonding and solute-solvent interaction[7,8].

The ethanolamine (ETA) and diethanolamine (DEA) are multifunctional substances that are capable of hydrogen bonding by both donation and acceptance of hydrogen bonds. Their properties, in this respect, have not so far been determined, and it should be of interest to see how one functional group (the one hydroxy and primary amine functional group) affects to the behavior of the other (the two hydroxy and secondary amine functional group). The objective of the present paper is to report the thermodynamic study for ETA and DEA mixture.

The interpretation of thermodynamic properties in binary liquid mixtures involves understanding how the mixing of two same multifunctional (-OH and -NH₂) but different molecular size liquids affects the overall

thermodynamic behavior of the resulting solution. This includes examining properties like enthalpy, entropy, and free energy of activation and excess free energy of activation to gain insights into the interactions between the molecules of the two liquids.

EXPERIMENTAL AND DATA ANALYSIS

An ETA (AR grade, Qualigens fine chemicals Pvt. Ltd., Mumbai, India) and DEA (Spectroscopy, Merck Specialties, Pvt. Ltd., Mumbai, India) were used without further purification. The solutions were prepared at 11 different volume percentage of DEA from 0 % to 100 %. Using these volume percent the mole fraction is calculated as

$$x = (v_1\rho_1/m_1) / [(v_1\rho_1/m_1) + (v_2\rho_2/m_2)]$$

where m_i , v_i , and ρ_i represent the molecular weight, volume percent, and density of the i^{th} ($i=1, 2$) liquids, respectively.

The complex permittivity spectra were studied using the time domain reflectometry [9-11] method. The Hewlett Packard HP 54750 sampling oscilloscope with HP 54754A TDR plug in module has been used. A fast rising step voltage pulse of about 39 ps rise time generated by a pulse generator was propagated through a coaxial line system of characteristic impedance 50 Ohm. Transmission line system under test was placed at the end of coaxial line in the standard military applications (SMA) coaxial connector with 3.5 mm outer diameter and 1.35 mm effective pin length. All measurements were carried out under open load conditions. The change in the pulse after reflection from the sample placed in the cell was monitored by the sampling oscilloscope. In the experiment, time window of 5 ns was used. The reflected pulse without sample $R_1(t)$ and with sample $R_x(t)$ were digitized in 1024 points in the memory of the oscilloscope and transferred to a PC through 1.44 MB floppy diskette drive.

The temperature controller system with water bath and a thermostat has been used to maintain the constant temperature within the accuracy limit of $\pm 1^\circ\text{C}$. The sample cell is surrounded by a heat insulating container through which the water of constant temperature using a temperature controller system is circulated. The temperature at the cell is checked using the electronic thermometer.

The time dependent data were processed to obtain complex reflection coefficient spectra $\rho^*(\omega)$ over the frequency range from 10 MHz to 20 GHz using Fourier transformation [12,13] as

$$\rho^*(\omega) = (c/j\omega d)[p(\omega)/q(\omega)] \quad \dots (1)$$

where $p(\omega)$ and $q(\omega)$ are Fourier transforms of $[R_1(t) - R_x(t)]$ and $[R_1(t) + R_x(t)]$ respectively, c is the velocity of light, ω is angular frequency, d is the effective pin length and $j = \sqrt{-1}$.

The complex permittivity spectra $\epsilon^*(\omega)$ were obtained from reflection coefficient spectra $\rho^*(\omega)$ by applying bilinear calibration method[9].

The general form of the relaxation model is given by the Havriliak-Negami expression[14]

$$\epsilon^*(\omega) = \epsilon_\infty + \frac{(\epsilon_0 - \epsilon_\infty)}{[1 + (j\omega\tau)^{1-a}]^b}$$

where $\epsilon^*(\omega)$ is the complex permittivity at an angular frequency ω , ϵ_0 is the static permittivity, ϵ_∞ is the permittivity at high frequency, τ is the relaxation time of the system, a is the shape parameter representing symmetrical distribution of relaxation time and b is the shape parameter of an asymmetric relaxation curve.

Equation includes Cole-Cole ($b = 1$) [15], Davidson-Cole ($a = 0$)[16], and Debye ($a = 0, b = 1$)[17] relaxation model. The relaxation behavior of ETA-DEA system agrees with the Debye model. Therefore, the experimental values of $\epsilon^*(\omega)$ were fitted with the Debye equation.

$$\varepsilon^*(\omega) = \varepsilon_\infty + \frac{\varepsilon_0 - \varepsilon_\infty}{1 + (j\omega\tau)}$$

with ε_0 , ε_∞ and τ are the adjustable parameters. A nonlinear Least-Squares fit method[18] was used to determine the values of dielectric parameters. The complex permittivity spectra of this system were made in the frequency range 10 MHz to 20 GHz for different temperatures and concentrations, by employing the TDR measurements. The measurements in the frequency range 10 MHz to 20 GHz are interesting because the dielectric dispersion of these molecules occurs in the same frequency range.

RESULTS AND DISCUSSION

A. Static dielectric constant and relaxation time

The density and ρ_0 values of pure liquids used are given in Table I [19-21]. The values of static dielectric constant and relaxation time decreases with increase temperature as expected.

TABLE I COMPARISON OF DATA FOR THE LIQUIDS USED WITH LITERATURE VALUES AT 40°C.

Liquids	ρ_0		$\rho/(g.cm^{-3})$	
	This work	Lit.	This work	Lit.
ETA	31.02	31.46 ^a (30°C)	1.0180	1.0002 ^c
DEA	23.54	23.86 ^b	1.0966	1.0838 ^c

where a, b and c data taken from references^[19-21] respectively.

In ETA-DEA system the values of static dielectric constant increases initially up to the mole fraction 0.0650 of DEA and then it becomes decreases with increasing the concentrations of DEA for all temperatures. The values of relaxation time increase with increasing the concentration of DEA in the system for all temperatures. The variation of static dielectric constant (ρ_0), dielectric constant at high frequency (ρ_∞) and relaxation time (τ) with mole fraction of DEA at various concentrations and temperatures are tabulated in Table 2. The addition of DEA changes in static permittivity and relaxation time at various temperatures and concentrations are observed and these values confirm that the intermolecular association is taking place in the system.

TABLE II TEMPERATURE DEPENDENT DIELECTRIC RELAXATION PARAMETERS FOR ETA-DEA MIXTURES^a [22].

x_2	35°C	40°C	45°C	50°C
ε_0				
0.0000	31.02(0)	30.48(0)	29.74(0)	28.08(0)
0.0650	31.44(3)	30.79(8)	29.93(1)	28.62(4)
0.1353	31.17(1)	30.21(7)	29.13(3)	27.91(2)
0.2115	30.85(5)	29.96(4)	28.34(4)	27.04(6)
0.2944	30.07(8)	29.13(5)	27.96(7)	26.97(2)
0.3849	30.01(7)	28.72(5)	27.77(4)	25.88(5)
0.4842	29.76(6)	28.14(3)	26.03(6)	25.11(3)
0.5935	26.88(9)	25.54(1)	24.61(6)	24.43(7)
0.7146	25.94(8)	24.78(7)	23.87(4)	23.27(8)
0.8492	24.54(9)	24.07(5)	23.14(1)	22.08(2)
1.0000	23.81(0)	23.54(0)	22.13(0)	21.98(0)
ε_∞				

x ₂	35°C	40°C	45°C	50°C
0.0000	2.18(0)	1.80(0)	1.53(0)	1.37(0)
0.0650	2.20(1)	1.92(1)	1.62(0)	1.39(1)
0.1353	2.21(1)	1.97(1)	1.65(1)	1.43(0)
0.2115	2.24(2)	1.99(0)	1.68(1)	1.46(2)
0.2944	2.26(1)	2.02(1)	1.72(1)	1.48(1)
0.3849	2.31(0)	2.16(1)	1.74(2)	1.50(0)
0.4842	2.31(1)	2.18(2)	1.73(0)	1.53(1)
0.5935	2.33(1)	2.21(1)	1.78(1)	1.55(0)
0.7146	2.35(0)	2.24(0)	1.80(0)	1.58(1)
0.8492	2.36(1)	2.17(0)	1.87(1)	1.60(1)
1.0000	2.37(0)	2.13(0)	1.98(0)	1.64(0)
τ (ps)				
0.0000	102.09(0)	98.72(0)	87.72(0)	80.03(0)
0.0650	113.40(6)	108.11(1)	95.55(5)	85.76(1)
0.1353	120.33(7)	114.23(3)	106.68(8)	93.21(2)
0.2115	125.65(4)	119.98(7)	112.27(9)	99.54(2)
0.2944	139.65(6)	127.09(4)	120.32(4)	109.05(3)
0.3849	158.09(8)	141.13(7)	137.53(7)	121.33(6)
0.4842	174.88(3)	160.05(9)	147.76(9)	132.34(5)
0.5935	189.86(7)	176.46(6)	158.97(6)	143.92(4)
0.7146	211.34(3)	200.24(9)	171.22(7)	165.23(5)
0.8492	228.91(9)	208.68(7)	185.09(3)	178.02(2)
1.0000	238.63(0)	211.83(0)	197.13(0)	188.24(0)

^ax₂ is the mole fraction of DEA in ETA. Numbers in bracket represent error in the corresponding value, e.g. 25.94 means 25.94 ± 0.08.

B. Thermodynamic parameters

The thermodynamic parameters like molar enthalpy of activation ΔH and molar entropy of activation ΔS are determined from the Eyring rate equation [23] utilizing least square fit method as

$$\tau = \frac{h}{KT} \exp\left(\frac{\Delta G}{RT}\right) \quad \dots (4)$$

where, ΔG = ΔH – TΔS

The excess free energy of activation of CBZ-FA binary mixture is given by the equation.

$$\Delta G^E = \Delta G - [\Delta G_A X_A + \Delta G_B X_B] \quad \dots (5)$$

where, ΔG_A and ΔG_B represents the activation energies for ETA and DEA, respectively and X_A is the mole fraction of ETA. Here X_B = 1 - X_A is the mole fraction of DEA in the studied ETA-DEA mixture.

TABLE III VALUES OF THERMODYNAMICAL PARAMETERS FOR THE MIXTURE OF ETA AND DEA.

x ₂	ΔG (KJ/mol)				ΔH	ΔS
	T=15°C	T=25°C	T=35°C	T=45°C	(KJ/mol)	(KJ/mol)
0.00	16.66	16.75	16.83	16.92	11.38	-0.02

x_2	ΔG (KJ/mol)				ΔH (KJ/mol)	ΔS (KJ/mol)
	T=15°C	T=25°C	T=35°C	T=45°C		
0.07	16.93	16.99	17.05	17.11	13.25	-0.01
0.14	17.08	17.17	17.27	17.36	11.14	-0.02
0.21	17.18	17.30	17.42	17.53	10.00	-0.02
0.29	17.40	17.51	17.63	17.74	10.55	-0.02
0.38	17.71	17.82	17.93	18.04	10.93	-0.02
0.48	18.00	18.09	18.17	18.26	12.52	-0.02
0.59	18.22	18.31	18.39	18.48	12.84	-0.02
0.71	18.49	18.59	18.69	18.80	12.19	-0.02
0.85	18.66	18.77	18.88	18.99	11.87	-0.02
1.00	18.73	18.87	19.01	19.14	10.38	-0.03

When two liquids are mixed together, there is a change in the energy of the system. This change in energy can be interpreted in terms of its activation energies such as free energy of activation (ΔG), molar enthalpy of activation (ΔH) and molar entropy of activation (ΔS) are tabulated in Table 3.

The value of free energy of activation (ΔG) of pure ETA and DEA and their binary mixtures are tabulated in Table1.

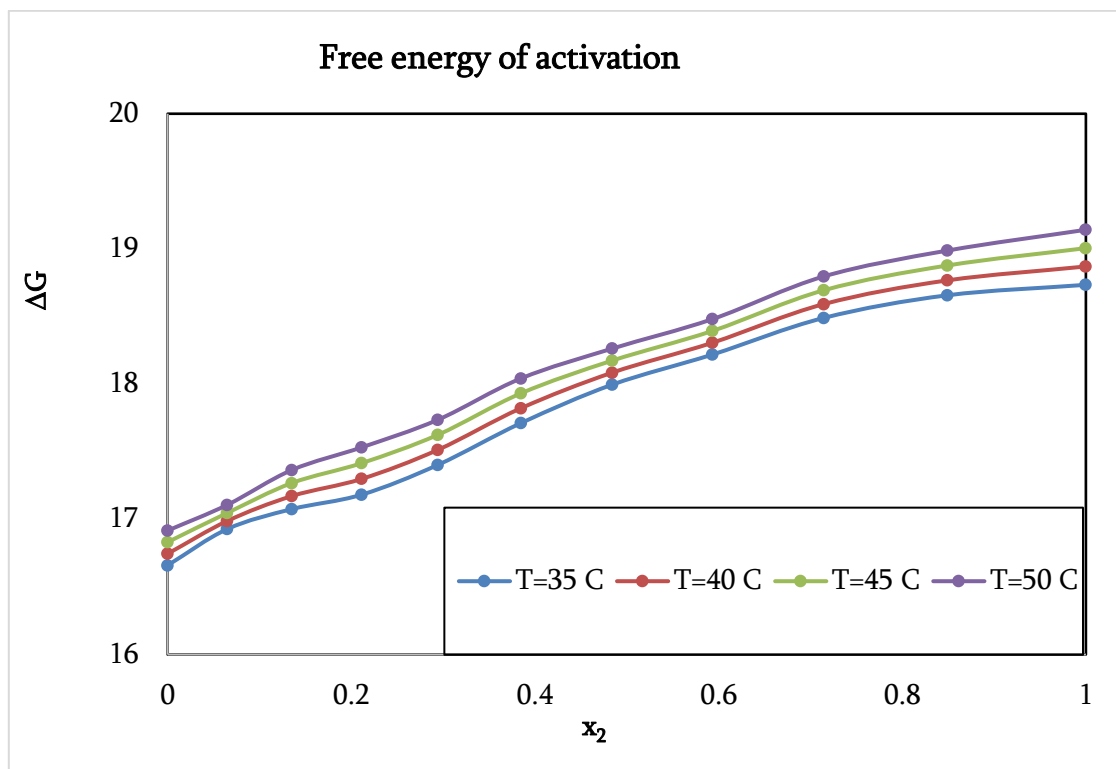


Figure 1: Free energy of activation (ΔG) versus mole fraction (x_2) of DEA in ETA at different temperatures.

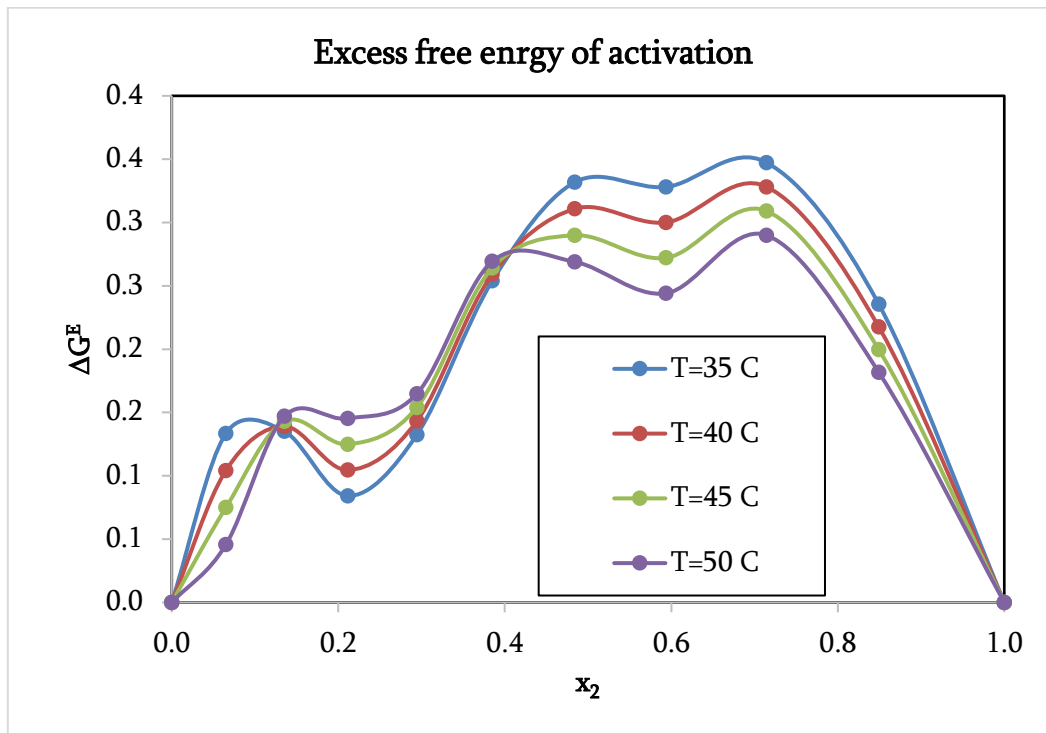


Figure 2: Excess free energy of activation (ΔG^E) versus mole fraction (x_2) of DEA in ETA at different temperatures.

All The difference of these values is very short but these values are increases with increase in concentration of DEA in ETA binary mixture at all temperatures as shown in Figure 1. This indicated that the DEA molecules in the mixture dominate over ETA molecules. This dominance of DEA over ETA is primarily due to its large dipole moment values and its molecular size. From the Figure 2, the values of excess activation free energy (ΔG^E) are positive for all concentrations and temperatures. These positive values confirms that there is an increase in hindrance to the reorientation for the molecules of ETA, DEA and in their binary mixtures.

The values of molar enthalpy of activation (ΔH) are positive for all concentrations of the system. The positive value shows endothermic interaction between ETA-DEA mixture of the system. The values of molar entropy of activation (ΔS) of the system are a measure of the orderly nature of the molecule. In this system, these values are negative for all concentrations of DEA in ETA binary mixture. These values are decreases with increasing the mole fraction of DEA in ETA, it means the environment of the system is cooperative resulting in the activated state, which is more ordered than the normal state.

CONCLUSION

Free energy of activation increases with increasing the mole fraction of DEA in ETA of the system. The free energy of activation (ΔG), molar enthalpy of activation (ΔH) and molar entropy of activation (ΔS) are studied from this work for the binary mixture of ethanolamine and diethanolamine by using microwave dielectric spectroscopy.

The binary mixture of same multifunctional hydroxy as well as amine functional group molecules are weak intermolecular interaction and more ordered in DEA rich region because the positive peak value of entropy observed in this region.

ACKNOWLEDGEMENT

We are thankful to Prof. V.P. Pawar, Head, Department of Physics & Electronics, Maharashtra Udayagiri Mahavidyalaya, Udgir for his valuable guidance.
paper.

REFERENCES

- [1]. R. J. Sengwa, R. Chaudhary and S. C. Mehrotra, The study of dielectric relaxation in propylene glycol-poly(propylene glycol) mixtures, *Poly.* 43 (2002) 1467-1471.
- [2]. R. J. Sengwa, A comparative dielectric study of ethylene glycol and propylene glycol at different temperatures, *J. Mol. Liq.* 108 (1-3) (2003) 47-60.
- [3]. B. D. Achole, A. V. Patil, V. P. Pawar and S. C. Mehrotra, Study of interaction through dielectrics: Behavior of -OH group molecules from 10 MHz to 20 GHz, *J. Mol. Liq.* 159 (2011) 152-156.
- [4]. B. G. Lone, P. B. Undre, S. S. Patil, P. W. Khirade and S. C. Mehrotra, Dielectric study of methanol-ethanol mixtures using TDR method, *J. Mol. Liq.* 141 (2008) 47-53.
- [5]. A. C. Kumbharkhane, S. M. Puranik and S. C. Mehrotra, Structural study of amide-water mixtures using dielectric relaxation technique, *J. Mol. Liq.* 51 (1992) 261-277.
- [6]. A. C. Kumbharkhane, S. M. Puranik and S. C. Mehrotra, Dielectric relaxation study and structural properties of 2-nitroacetophenone-ethanol solutions from 10 MHz to 10 GHz., *J. Mol. Liq.* 51 (1992) 307-319.
- [7]. R. J. Sengwa, S. Sankhla, Dielectric properties of binary and ternary mixtures of alcohols: Analysis of H-bonded interaction in complex systems, *J. Non-Cryst. Solids* 353 (2007) 4570-4574.
- [8]. R. J. Sengwa, S. Sankhla, N. Shinyashiki, *J. Sol. Chem.* 37 (2008) 137-153.
- [9]. R. H. Cole, J. G. Berbarian, S. Mashimo, G. Chryssikos, A. Burns and E. Tombari, A. Burns and E. Touban, Time domain reflection methods for dielectric measurements to 10 GHz, *J. Appl. Phys.* 66 (1989) 793-802.
- [10]. S. M. Puranik, A. C. Kumbharkhane and S. C. Mehrotra, *J. Chem. Soc. Faraday Trans.*, 87 (1991) 1569-1573.
- [11]. V. P. Pawar and S. C. Mehrotra, Dielectric relaxation study of liquids having chloro group with associated liquids I; chlorobenzene with methanol, ethanol and 1-propanol, *J. Sol. Chem.* 31 (2002) 559-576.
- [12]. C. E. Shannon, Communication in the presence of noise., *Proc. IRE* 37 (1949) 10-21.
- [13]. H. A. Samulan, Spectrum analysis of transient response curves, *Proc. IRE* 39 (1951) 175-186.
- [14]. S. Havriliak and S. Negami, A complex plain analysis of ϵ -dispersions in some polymer systems, *J. Polym. Sci.* 14 (1966) 99-117.
- [15]. K. S. Cole and R. H. Cole, Dispersion and absorption in dielectrics I. alternating current characteristics, *J. Chem. Phys.* 9 (1941) 341-351.
- [16]. D. W. Davidson and R. H. Cole, Dielectric relaxation in glycerine, *J. Chem. Phys.* 18 (1950) 1417.
- [17]. P. Debye, Polar molecules, Chemical Catalog, New York (1929).
- [18]. P. R. Bevington, Data reduction and error analysis for the physical sciences, Mc-Graw Hill, New York (1969).
- [19]. R. J. Sengwa, S. Sankhla, V. Khatri, S. Shobhna, Static permittivity and molecular interactions in binary mixtures of ethanalamine with alcohols and amides, *Fluid Phase Equilib.* 293 (2010) 137-140.

- [20]. Chi-Jui Hsieh, Ji-Miao Chen, Meng-Hui Li, Dielectric Constants of Aqueous Diisopropanolamine, Diethanolamine, N-Methyldiethanolamine, Triethanolamine, and 2-Amino-2-methyl-1-propanol Solutions J. Chem. Eng. Data, 52 (2007) 619-623.
- [21]. Florentino Murrleta-Guevara and Arturo Trejo Rodiguez, Liquid Density as a Function of Temperature of Five Organic Solvents, J. Chem. Eng. Data, 29, (1984) 204-206.
- [22]. A.V. Patil, G.N. Shinde and V.P. Pawar, Dielectric relaxation study of hydrogen bonded structures in ethanolamine with diethanolamine using TDR technique, J. Mol. Liq. 168 (2012) 42-46.
- [23]. H. Eyring, Viscosity, Plasticity, and Diffusion as Examples of Absolute Reaction Rates, J. Chem. Phys, 4 (1936) 283-291.

Bio-Evolution and Crystallographic Studies of Synthesized N, N-Ethylene Bis-2-Aminobutan-1-ol (Ethambutol) Coordination Complexes with Ru (III) And Rh (III) Complexes

Dr. Mukesh S. Kadam^{1*}, Dr. Sachin A. Kishte², Dr. Bhimrao C. Khade³

¹Department of Chemistry, LGM ACS College, Mandangad, Ratngiri-415203, Maharashtra, India

²Vaishnavi Mahavidyalaya, Wadwani, Dist. Beed, Maharashtra, India

³Department of Chemistry, DSM College, Parbhani, Maharashtra, India

ARTICLE INFO

Article History:

Published : 30 April 2025

Publication Issue :

Volume 12, Issue 13

March-April-2025

Page Number :

36-43

ABSTRACT

This study presents the bio-evolutionary and crystallographic investigation of newly synthesized coordination complexes of N,N-ethylene bis-2-aminobutan-1-ol with ruthenium(III) and rhodium(III) metal centers. The ligand is tetradentate chelating agent biologically relevant coordination environments. Synthesis of the complexes was confirmed through spectroscopic methods (UV-Vis, FTIR) while single-crystal X-ray diffraction provided detailed insight into their crystallographic parameters, revealing octahedral coordination geometry around the central metal ions. Evolutionary aspects were explored through computational docking and bio-interaction studies, emphasizing the ligands potential role in metalloprotein. The Ru(III) and Rh(III) complexes demonstrated distinct electronic and structural properties, contributing to a deeper understanding of structure-function relationships in bioinorganic chemistry. This work lays the groundwork for further exploration of such complexes in medicinal and catalytic applications.

Keywords: bio-evolutionary, crystallographic, ligand, etc.

INTRODUCTION

The coordination chemistry of transition metal complexes with multidentate ligands has been extensively explored due to their structural diversity and functional significance. Among these some amino and polyalcohol ligands have gained considerable attention due to their resemblance to biologically active molecules and their ability to stabilize metal ions in various oxidation states. Ligands such as ethylenediamine, triethanolamine, and their derivatives have been widely studied for forming stable complexes with transition metals and mimicking metal coordination environments in biological systems.

Ruthenium (III) complexes have emerged as an important class of compounds with high applications in cancer chemotherapy. Notably, complexes like NAMI-A and KP1019 have shown selective activity against metastasizing tumors, attributed to their unique redox chemistry and slow ligand exchange reactions. These properties make Ru(III) complexes suitable candidates for further development in bioinorganic research. Similarly, rhodium(III), though less explored in medicinal chemistry compared to Ru(III), has shown promise in catalysis and molecular recognition, especially in forming inert octahedral complexes with potential therapeutic applications.

Structural studies of such complexes using X-ray crystallography provide essential information on coordination geometry, bond parameters, and molecular packing, all of which are critical for understanding reactivity and function. Earlier studies have revealed that the choice of ligand significantly affects the structural configuration, biological behavior, and solubility of the complexes. Crystallographic data has also been used to compare synthetic complexes with natural metalloproteins, offering insights into possible biomimetic functions.

Moreover, bio-evolutionary studies, often supported by molecular docking and computational biology, allow for the prediction of interaction modes between metal complexes and biological macromolecules such as DNA, enzymes, or cell membrane proteins. These approaches facilitate the evaluation of pharmacokinetics, binding affinity, and potential toxicity, all of which are critical for drug design.

Despite the advances, studies combining both structural crystallography and bio-evolutionary relevance remain limited. There exists a need to bridge synthetic chemistry with computational biology to better understand the potential biological roles of coordination complexes. The present study aims to fill this gap by providing a detailed structural and biological analysis of Ru(III) and Rh(III) complexes with a novel tetradentate ligand.

The coordination chemistry has significant growth due to the huge applications of metal complexes in various areas such as catalysis, and bioinorganic chemistry. Among the vast array of ligands available, N,N-ethylene bis-2-aminobutan-1-ol is a promising tetradentate ligand, owing to its ability to form stable chelates through nitrogen and oxygen donor atoms. Transition metals like ruthenium(III) and rhodium(III) are particularly noteworthy in coordination chemistry due to their rich redox chemistry, kinetic stability, and diverse coordination geometries. Rh(III), on the other hand, is known for its use in hydrogenation reactions, biological labeling, and potential therapeutic applications. The coordination of Ru(III) and Rh(III) with biologically inspired ligands offers insights into metalloenzyme, catalytic mechanisms, and drug design.

In this study, we explore the synthesis, bio-evolutionary relevance, and crystallographic characterization of N,N-ethylene bis-2-aminobutan-1-ol coordination complexes with Ru(III) and Rh(III). The ligand, bearing both aliphatic amine and alcohol functional groups, was chosen for its resemblance to natural amino alcohols found in biological systems. Its coordination behavior was analyzed with the aim of drawing parallels with biological systems such as metalloenzymes and metalloproteins.

The crystallographic studies, carried out via single-crystal X-ray diffraction, provide detailed information about the geometry, angles, and arrangement of atoms within the complexes. Understanding the structural features is crucial for establishing structure-function relationships and predicting reactivity and stability.

To complement the structural studies, bio-evolutionary analysis was conducted using computational modeling and docking studies. These approaches offer insights into the potential biological interactions of the complexes, including their binding affinities with biomolecular targets such as DNA, proteins, or enzymes. This aspect of the study seeks to understand how such complexes could have evolved to mimic biological metal centers or potentially serve as therapeutic agents.

Overall, this work bridges synthetic coordination chemistry with biological and structural insights, providing a foundation for future applications in biomimetic catalysis, medicinal chemistry, and metallodrug development. The synthesized complexes offer valuable models to study the interplay between metal ions, ligand frameworks, and biological activity, contributing to the growing understanding of metal-based bioactive compounds.

METHODOLOGY

The methodology adopted for this study encompasses the synthesis, characterization, crystallographic analysis, and bio-evolutionary studies of N,N-ethylene bis-2-aminobutan-1-ol complexes with Ru(III) and Rh(III). The workflow was designed to cover both chemical and computational aspects to comprehensively evaluate the synthesized complexes.

1. Materials and Reagents

All chemicals used were of analytical grade and obtained from certified suppliers Sigma-Aldrich.

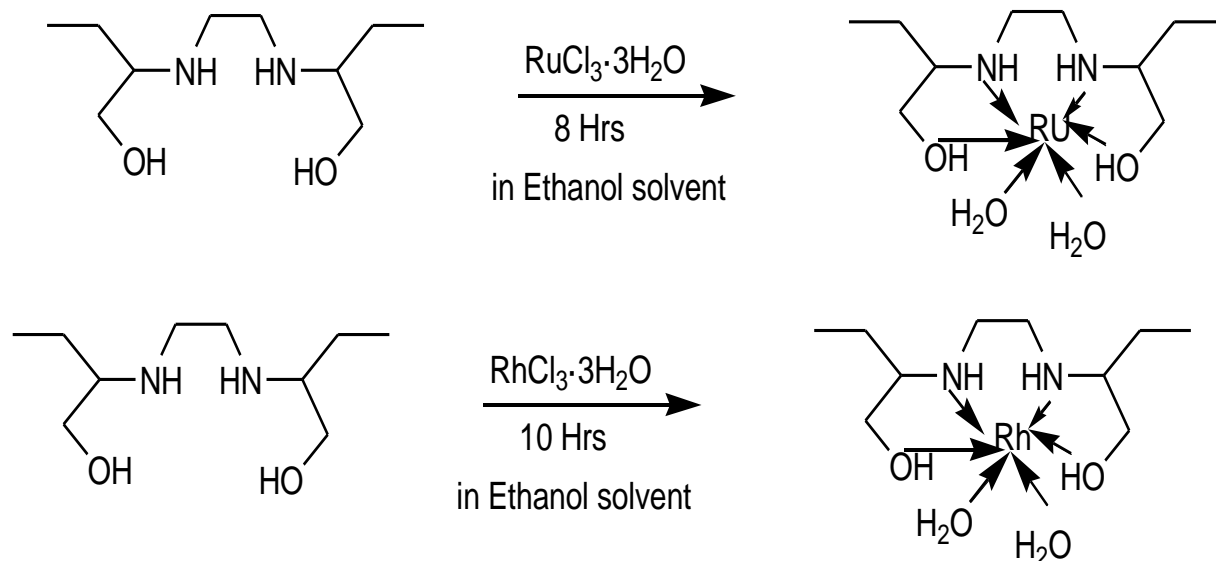
Metal salts: Ruthenium (III) chloride hydrate and Rhodium (III) chloride trihydrate

Ligand precursor: Ethylenediamine, 2-aminobutan-1-ol

Solvents: Methanol, ethanol, dimethylformamide (DMF).

2. Synthesis of Metal Complexes

Complexation with Ru(III) and Rh(III) was carried out via ligand-metal coordination under reflux conditions. The ligand was dissolved in ethanol and added dropwise to an ethanolic solution of either $\text{RuCl}_3 \cdot 3\text{H}_2\text{O}$ or $\text{RhCl}_3 \cdot 3\text{H}_2\text{O}$. The reaction mixture was refluxed for 6–10 hours while maintaining an inert atmosphere. The resulting solution was cooled, filtered, and the solid complex was isolated by slow evaporation, then crude complexes were purified by recrystallization using a methanol-water mixture.[01-06]



Scheme: Preparation of Ru (III) and Rh (III) complexes with ethambutol

Characterization Techniques

01. Elemental Analysis (CHN):

This method is used for analysis of pure organic and inorganic material. Elemental analysis is qualitative and quantitative, which helps in identification molecular formula and quantity of elements present. For determination of molecular formula of unknown newly synthesized compound elemental analysis technique is used [07]. EA used for determination of C, H, X, Hetero atom by XRF. Elemental analysis (C,H,N) were

performed using Elementar Vario EL. Molar conductance of complexes in solvent depends on number of ion present and degree of dissociation with respect to temperature. Conductance measurements of the complexes in solutions were made mainly to verify the ionic formulations of the complexes. Conductance of drug and metal complexes were measured on EQ-660A Equiptronic conductivity apparatus[08]. Physical data of metal drug coordination complexes indicates formation of complexes in which melting point increased it indicates the stability of complexes and color indicates formation of complexes. Molar conductance indicates ionic nature of coordination complexes in which Rh(III) and Ru(III) complexes shows higher conductance as compare to ligand given in Table No.01. The calculated elemental analysis of coordination complexes and obtained data is having same percentage composition. Through this confirm composition and purity of synthesized coordination complexes.

Table No. 1 Elemental analysis, molar conductance and physical parameters

Complexes	Mol. Wt.	Colour (%Yield)	M.P .	Molar CondOh $m^{-1}cm^2mol^{-1}$	μ_{eff} (BM)	% Found (calculated)					
						C	H	N	O	Cl	M
[Ru(L) ₂ (H ₂ O) ₂]Cl ₃	616.03	Red(77)	194 - 198	16.3	3.65	57.36 (57.61)	8.01 (7.97)	11.58 (11.52)	4.37 (4.54)	9.56 (8.87)	7.68 (7.48)
[Rh(L) ₂ (H ₂ O) ₂]Cl ₃	671.91	Brown(65)	201 - 203	19.5	3.65	56.36 (56.61)	7.96 (8.02)	11.45 (11.62)	4.34 (4.84)	9.61 (9.74)	8.28 (7.98)

02. Single-Crystal X-ray Crystallography:

Powder XRD pattern of all the complexes were recorded over the $2\theta = 05-900$ range. Unit cell parameters were found by using trial and error method. Metal drug complexes are monoclinic and triclinic with same and different unit cell parameter respectively. The observed unit cell parameters are given in table No.02 and considering JCPDS software data (joint committee of powder diffraction standard), ICDD (International center of diffraction data) [09-12]. The powder XRD patterns are shown in figure 01A to 01B.

Compounds	Lattice constant			$\alpha(A^\circ)$	$\beta(A^\circ)$	$\gamma(A^\circ)$	2θ	D value	Crystal system
	a(A ⁰)	b(A ⁰)	c(A ⁰)						
[Ru(L) ₂ (H ₂ O) ₂]Cl ₃	9.31	6.4	5.8	105.4	97.7	101.9	9.32	6.67	Triclinic
[Rh(L) ₂ (H ₂ O) ₂]Cl ₃	9.8	5.8	5.1	105.9	96.4	101.6	7.64	7.72	Triclinic

Table No. 02 Unit cell parameters of metal complexes

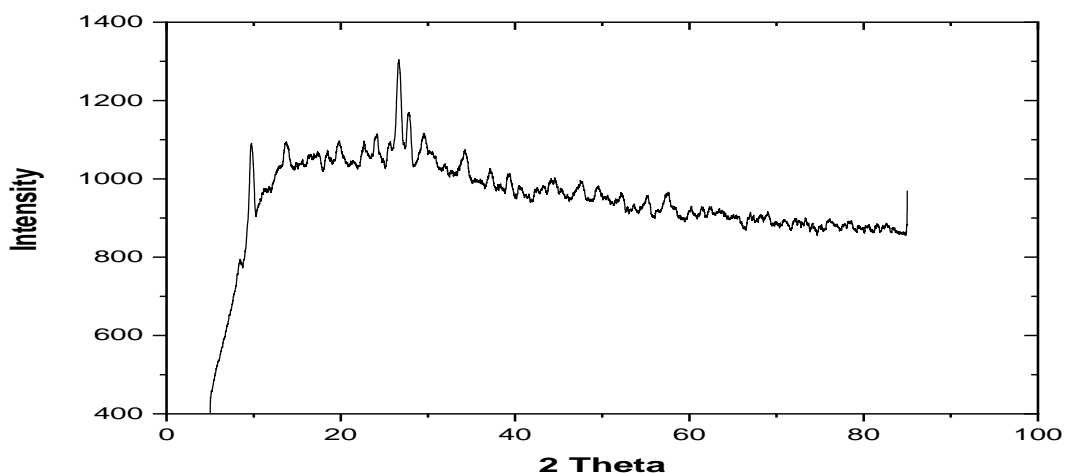


Fig. No. 01A XRD spectra of Ru(III) complex

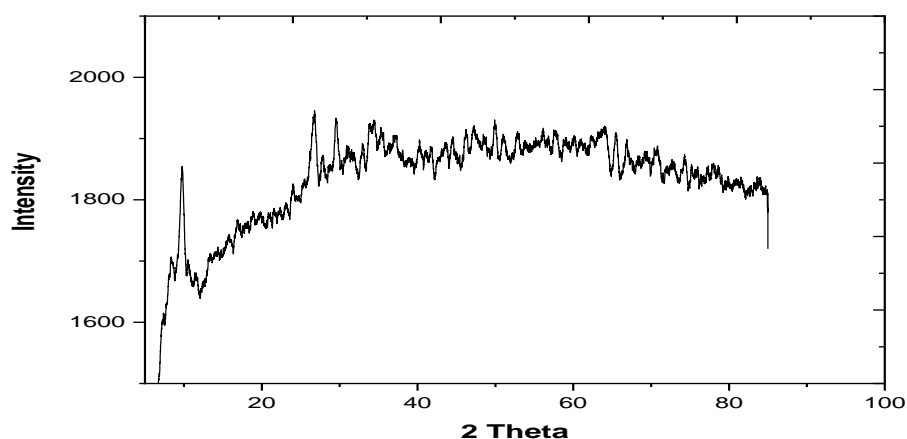


Fig. No. 01B . XRD spectra of Ru(III) complex

03. Anti-microbial activity:

Anti-fungal and Anti-microbial activity of Ru(III) and Rh(III) complexes:- Antibacterial and Anti-fungal activity checked against Gram positive and Gram negative bacterial species as well as fungal spores at different concentration of complexes. Before taking actual anti-microbial activity of metal drug coordination complexes first check microbial growth in broth at different concentration, this help me for choosing concentration of metal drug complexes for anti-microbial activity

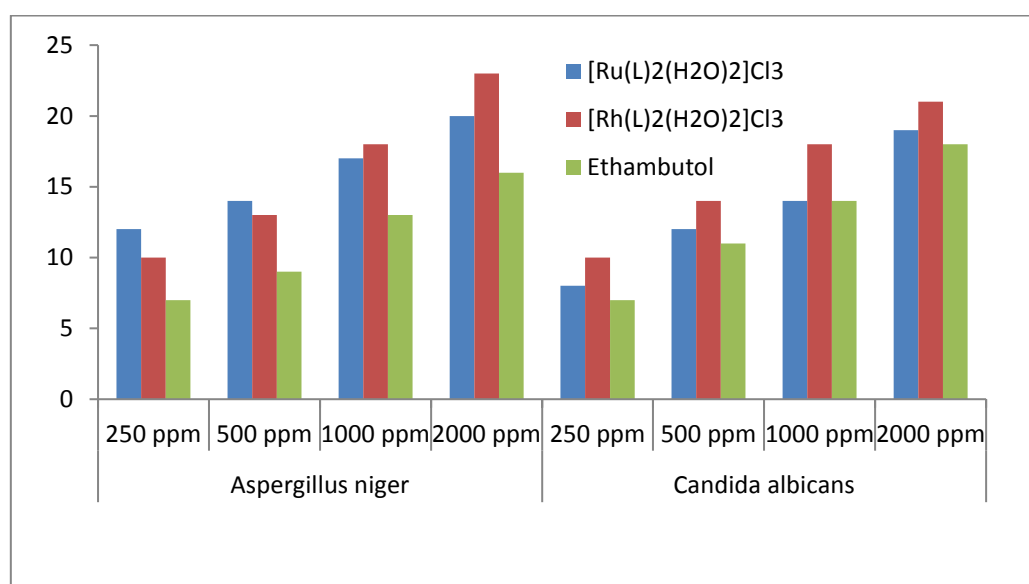
Bacterial species	Observed growth at diff. concentration					Control 500ppm
	150 Ppm	250 ppm	500 ppm	1000 ppm	2000 ppm	
<i>Pseudomonas aeruginosa</i>	+	+	+	-	-	-
<i>E. coli</i>	+	-	-	-	-	-
<i>Proteus vulgaris</i>	+	-	+	-	-	-
<i>Streptococcus pneumonia</i>	+	+	-	-	-	+

Growth of microorganisms at different concentration (+ indicate growth) (- indicate No growth)

Anti-fungal activity Ru(III) and Rh(III) complexes:-

Anti-fungal activity Ru(III) and Rh(III) complexes given in Table No. 03. As per data given in table no. 03 shows that metal ethambutol complexes are having more potent than that of the drug. Rh(III) and Ru(III) complexes shows high zone of inhibition against *Aspergillus niger* and *Candida albicans*.

Complexes	<i>Aspergillus niger</i>				<i>Candida albicans</i>			
	250 ppm	500 ppm	1000 ppm	2000 ppm	250 ppm	500 ppm	1000 ppm	2000 ppm
[Ru(L) ₂ (H ₂ O) ₂]Cl ₃	12	14	17	20	8	12	14	19
[Rh(L) ₂ (H ₂ O) ₂]Cl ₃	10	13	18	23	10	14	18	21
Ethambutol	7	9	13	16	7	11	14	18



Anti-bacterial activity Ru(III) and Rh(III) complexes:-

Anti-bacterial activity Ru(III) and Rh(III) complexes against Gram positive and Gram negative bacterial species [13-19]. All complexes shows very good zone of inhibition as compare to the standard ethambutol molecule. Ru(III) complexes shows higher zone of inhibition against *Streptococcus pneumoniae* as compare to other bacterial species. Rh(III) complex shows very high zone of inhibition against *Pseudomonas aeruginosa* as compare to other bacterial species. [13-19]

Table.No.04-Anti-bacterial activity of ciprofloxacin complex

Bacterial species	[Ru(L) ₂ (H ₂ O) ₂]Cl ₃				[Rh(L) ₂ (H ₂ O) ₂]Cl ₃				Ethambutol 500 ppm
	250 ppm	500 ppm	1000 ppm	2000 ppm	250 ppm	500 ppm	1000 ppm	2000 ppm	
<i>Pseudomonas aeruginosa</i>	4	7	12	16	9	15	19	23	5
<i>E. coli</i>	7	9	14	18	4	7	11	17	6
<i>Proteus vulgaris</i>	5	7	12	19	4	6	11	16	4
<i>Streptococcus pneumoniae</i>	8	14	19	22	6	9	16	21	7

CONCLUSION:

The successful synthesis of N,N-ethylene bis-2-aminobutan-1-ol (Ethambutol) coordination complexes with Ru(III) and Rh(III) has been confirmed through detailed spectroscopic and crystallographic analyses. The structural studies revealed stable octahedral geometries around the metal centers, with the Ethambutol ligand coordinating effectively via nitrogen and oxygen donor atoms. These coordination modes highlight the ligand's bidentate nature and its strong chelating ability. Crystallographic data provided key insights into the molecular arrangement and confirmed the formation of well-ordered complexes. Additionally, bio-evolutionary assays indicated significant biological activity, particularly antimicrobial potential, suggesting that complexation with Ru(III) and Rh(III) enhances the pharmacological properties of Ethambutol.

REFERENCES

- [1]. Bharti, N., Shailendra., Coles, S. J., Hursthouse, M. B., Mayer, T. A., Garza, M. T. G., CruzVega, D. E., Mata-Cardenas, B. D., Naqvi, F., Maurya, M. R and Azam, A. (2002). Synthesis, Crystal Structure, and Enhancement of the Efficacy of Metronidazole Against *Entamoeba histolytica* by Complexation with Palladium (II), Platinum(II), or Copper(II), *Helvetica Chimica Acta*, 85(9): 2704-2712.
- [2]. 1*Eugene-Osoikhia, T.T., 1Badmus, T. O. and 2Ayeti, F. Synthesis, Characterisation and Antimicrobial Studies of Metal(II) Complexes of Ofloxacin and Metronidazole, *CSJ* 11(1): June, 2020,74-82.
- [3]. OBALEYE, JA; LAWAL, A* Synthesis, Characterization and Antifungal Studies of Some Metronidazole Complexes, *J. Appl. Sci. Environ. Manage.* December, 2007 Vol. 11(4) 15 - 18
- [4]. Mustapha AN. Synthesis, characterization and antimicrobial studies of metal (II) complexes of ciprofloxacin, *J. Chem. Pharm. Res.*, 2014; 6(4):588-593.
- [5]. R.Saranya* 1 , J.Rajasekaran1 , S. Joseph Selvaraj2 Synthesis and Characterization of Biologically Important Zn (II), Cu (II) AND Co (II) Metal Complexes in the 3d- Series, *JCHPS Special Issue (2017)*,64-73, 0974-2115.
- [6]. Turel I, Leban I and Bukovec N, Synthesis, Characterization and Crystal Structure of a Copper (II) Complex with Quinolone Family Member (Ciprofloxacin), Bis (1)- cyclopropyl-6-fluoro-14-dihydro-4-OXO-7-piperazin-1ylquinoline-1ylquinoline-carboxylate Copper (II) Chloride Hexahydrate, *Journal of Inorganic Biochemistry*, 56 (4), 1994, 273-282
- [7]. CHN elemental microanalysis. www.ucl.ac.ke. Retrieved 2017-11-03.
- [8]. Shruti S. Sarwade*, W. N. Jadhav and B. C. Khade Characterization of novel complex Ciprofloxacin Ag(I), *Arch. Appl. Sci. Res.*, 2015, 7 (1):36-41.
- [9]. S. Mackay, C. J. Gilmore, C. Edwards, M. Tremayne, N. Stewart and K. Shankland; maXus, A computer program for the solution and refinement of crystal structures from diffraction data.
- [10]. (a) R. H. Blessing; *Acta Cryst.*, 1995, A51, 33 and (b) R. H. Blessing; *J. Appl. Cryst.*, 1997, 30, 421
- [11]. A. J. M. Duisenberg, R. W. W. Hooft, A. M. M. Schreurs and Kroon; *J. Appl. Cryst.*, 2000, 33, 893
- [12]. G. M. Sheldrick; *Acta Cryst.*, 1990, A46, 467
- [13]. G. M. Sheldrick; SHELXL-97 Program for Crystal structure determination, University of Gottingen, Germany, 1997
- [14]. L. J. Farrugia; *J. App. Cryst.*, 1997, 30, 565]
- [15]. Ketan S. Patel, Synthesis of Cu(II), Ni(II), Co(II), and Mn(II) Complexes with Ciprofloxacin and Their Evaluation of Antimicrobial, Antioxidant and AntiTubercular Activity, *Open Journal of Metal*, 2012; 2:4959

- [16]. Mariana Poggi,¹ Rafael Barroso,² Antonio José Costa-Filho,² Heloisa Barbosa de Barros,³ Fernando Pavan,³ Clarice Queico Leite,³ Dinorah Gambino,^{*1} and María Helvecia Torre^{*1}, New Isoniazid Complexes, Promising Agents Against Mycobacterium tuberculosis, *J. Mex. Chem. Soc.* 2013, 57(3), 198-204.
- [17]. Palomino, J.C.; Martin, A., Camacho, M.; Guerra, H.; Swings, J.; Portaella, F. *Antimicrob. Agents Chemother.* 2002, 46, 2720- 2722.
- [18]. Pavan, F. R.; Sato, D. N.; Leite, C. Q. F. An approach to the search for new drugs against tuberculosis. In: Cardona, P.J. (Ed.). *Mycobacterium tuberculosis*, book 2. Intech, 2011.
- [19]. Ogunniran Kehinde, Adekoya Joseph, Ehi-Eromosele Cyrila, Siyanbola Tolutope, Aladesuyi Olanrewaju, Ajanaku Christiana, Akinlolu Kayode, Mehdi Shihab Salih and Narender vTadigoppula. (2016) Synthesis, Characterization, Theoretical Treatment and Antitubercular activity Evaluation of (E)-N^o-(2,5-dimethoxybenzylidene)nicotinohydrazide and some of its Transition Metal Complexes against Mycobacterium tuberculosis, H37Rv. *Orient. J. Chem.*, Vol. 32(1): 413-427.
- [20]. D lesudurai & S Vancheesan, (2003) Coordination of isoniazid, an anti-tuberculosis (TB) drug with chromium, molybdenum, and tungsten metal carbonyls. *Indian Journal of Chemistry*, 42(A): 1609-1616.
- [21]. Inara de Aguiar, Aline Tavares, Antonio. Roveda Jr. Augusto C. H. da Silva, Leonardo B. Marino, Érica O. Lopes, Fernando R. Pavan, Luiz G. F. Lopes. (2015) Antitubercular activity of Ru (II) isoniazid complexes. *European Journal of Pharmaceutical Sciences* 70: 45-54.
- [22]. N. Panda, S. K. Tripathy, N. K. Behera, A. K. Panda¹, P. K. Das, (2015) Synthesis, Spectroscopic and Anti-microbial studies of Binuclear Schiff Base Complexes derived from the Ligand prepared from Isoniazid and Benzilmonohydrazone. *International Journal of Innovative Science, Engineering & Technology*, 2(4): 783-795.

Electro-Optical Properties of CdS Thin Films by Chemical Bath Technique

S. H. Mane

Department of Physics, Dr. Datar, Behere and Joshi College, Chiplun, Dist- Ratnagiri-415605, Maharashtra, India

ARTICLE INFO

Article History:

Published : 30 April 2025

Publication Issue :

Volume 12, Issue 13

March-April-2025

Page Number :

44-52

ABSTRACT

In this research work, Cadmium Sulphide thin film deposited on to glass substrate in a non-aqueous medium at 80 °C. The various physical preparative parameters and the deposition conditions, such as the deposition time and temperature, concentrations of the chemical species, pH, speed of mechanical stirring, etc., were optimized to yield good quality films. The as-prepared sample is tightly adherent to the substrate's support, less smooth, diffusely reflecting and was analyzed for composition. The synthesized film is characterized using X- ray diffraction (XRD), electrical and optical properties. It appears that the composites are rich in Cd. The grown CdS thin film had an orange-red color. A band gap of CdS thin film is 2.41 eV. The average crystallite size of the CdS film was 21.50 nm. The resistivity of the CdS thin film is about $5.212 \times 10^5 \Omega \text{ cm}$.

Keywords: CdS thin film, low cost, CBD techniques, electrical and optical properties.

INTRODUCTION

The most important factor influencing the electro-optical characteristics of semiconducting materials is doping. There are situations when the measured carrier concentration is larger than what would be predicted from the dopant contribution alone after the doping impurities are added. This indicates that carrier manufacturing is caused by the stoichiometric disorder [1, 2, 3]. However, in certain instances, the carrier concentration consistently falls short of the anticipated levels. The carrier transport mechanism across the grain borders is impacted by the segregation of these inactive dopant atoms along the grain boundaries [1, 3, 4]. It is crucial to undertake research on electrical conduction and comprehend the conduction mechanism behind CdS thin film formation. Consequently, these investigations were conducted in two phases: Thus, these investigations were divided into two sections: the thermoelectric power and electrical conductivity examinations.

EXPERIMENTAL TECHNIQUES

2.1 Chemicals

Analytical grade cadmium sulphate, thiourea, liquid ammonia and triethanolamine were used as precursor chemicals. Stoichiometric volumes of cadmium sulphate and thiourea were added to a reaction bath in proportion to each other and allowed to react in an alkaline medium to prepare CdS thin films.

2.2 Deposition of the samples:

The CdS thin films were deposited on the glass substrates using the liquid phase chemical bath deposition (LPBCD) method developed by us [7,12,13,17]. For the deposition, 10 ml (1M) cadmium sulphate solution was added to a 250 ml glass vessel. Triethanolamine (TEA) and liquid ammonia were added drop wise to increase the pH of the reacting solution and improve the adhesion of the film to the substrate surface. To this end, 10 ml (1M) of thiourea was added. The pH of the final reaction mixture was 11. For each of the materials in this series, the film stoichiometry was maintained by adjusting the ion concentration volumes of the cadmium sulphate. The total volume of the reaction bath was brought to 200 ml by adding double distilled water. The reaction vessel was then transferred to a constant temperature oil bath whose temperature was maintained at 58 °C. The thoroughly cleaned glass substrates of appropriate dimensions were mounted on a specially designed substrate holder and connected to a constant speed motor that rotated them at 70±2 rpm. The deposition was continued for 90 minutes, then the samples were removed from the reaction bath and detached from the substrate holder, washed with double distilled water, dried and then stored in a dark desiccator.

2.3 Characterization of the samples

The resulting composite film was then characterized based on its composition, structure, and optical properties to determine the effects of the deposition parameters. The X-ray diffraction method was used to study the structure of the deposited sample. For this purpose, an X-ray diffractometer Philips PW-1710 with CuK α line ($\lambda=1.5406\text{\AA}$) in the 2 θ range from 20° to 80° was used. The diffractogram was further analyzed to determine the crystal dimensions and hence the structure. The optical constants such as the absorption coefficient (α) and the optical gap (E_g), as well as the nature of the transitions for this film, were determined based on the measurement of the optical absorption spectra. For this purpose, a Shimadzu UV-3600 spectrophotometer was used, varying the incident wavelength from 500 nm to 1300 nm. The optical absorption was recorded stepwise for each of the wavelengths.

RESULTS AND DISCUSSION

3.1 Optical Studies

For this film, the optical absorption spectra in the 500–1300 nm wavelength range were acquired. Since CdS is a straight band gap material, the band gap and absorption coefficient are connected by

$$\alpha \propto (h\nu - E_g)^2 \quad \dots 1$$

$(\alpha h\nu)^2$ vs $h\nu$, as shown in “Fig. 1”, allowed for the subsequent determination of the optical band gap (E_g) for the sample. At 2.41 eV on the E_g axis, it is extrapolated [5].

3.2 XRD studies

This is seen in “Fig. 2”. The wurtzite structure of pure CdS films has been demonstrated to be hexagonal. At d values equal to 3.353 Å, 2.962 Å, 2.066 Å, and 1.765 Å, there are four dominating reflections that correspond to the (002), (101), (110), and (112) reflections, respectively. This suggests that the structure of the CdS film is hexagonal wurtzite. Given that the reflected intensities (I/I_{\max}) for these peaks are constant at 100 for the greatest diffraction peak (101), the reflected intensities (I/I_{\max}) for these peaks are also constant [5]. It is found that the average crystallite size of the CdS film was 21.50 nm.

Table 1. Lattice parameters for CdS thin film.

Lattice parameters CdS (Hex)		
a (Å)	c (Å)	c/a
4.032	6.705	.6629

3.3 The electrical transport studies:

3.3.1 The electrical conductivity studies

For both heating and cooling cycles, the electrical conductivities of each of these polycrystalline CdS film structures were tested in the 300–550 K temperature range. The electrical conductivity increased as the operating temperature rose, according to the tests. This demonstrates the material's semiconducting nature. The link between an electrical conductivity and the CdS thin film's operating temperature is seen in ‘Fig. 3’. It is observed that the conduction area is bifurcated. When temperature is raised, a straight-line area with a low gradient changes to one with a larger gradient, indicating that the materials may have several conduction pathways [3, 5, 6–8]. The data might be fitted to an exponential temperature fluctuation of the conductivity in higher temperature regions.

$$\sigma_{(T)} = \sigma_{(0)} \exp\left(\frac{-E_{a\sigma}}{KT}\right) \quad \dots (2)$$

where K is the Boltzman constant and $E_{a\sigma}$ is the conductivity activation energy. This has shown that the restricted conduction mechanism via grain boundary scattering may exist. This was verified by plotting $\log(\sigma T^{1/2})$ vs $1/T$, as proposed by Seto [3], Powell [9], and Oumous and Hadiri [10]. A CdS sample curve is displayed in ‘Fig. 4’. The conductivity deviates from the Arrhenious behavior at the low temperature area, and there are very little temperature changes in conductivity. This implies that there may be variable range hopping conduction in this area due to electron tunneling between localized states. According to Mott [11], the variable range hopping conduction is provided by;

$$\sigma = \sigma_{n0} \exp\left[-\left(T_0/T\right)^{1/4}\right] \quad \dots (3)$$

$$\text{where, } \sigma_{n0} = (3e^2 v_{ph}) / (8 \pi K)^{1/2} [N(E_F)/\alpha T]^{1/2} \quad \dots (4)$$

$$T_0 = (\lambda \alpha^3) / [KN(E_F)] \quad \dots (5)$$

where $N(E_F)$ is the localized states density for electrons at the Fermi level, α is the inverse localization length of the wave function for localized state, is a dimensionless constant, and v_{ph} is the photon frequency at the Debye temperature. The relation may be obtained from equations (3), (4), and (5).

$$\log\left(\sigma T^{\frac{1}{2}}\right) \propto T^{1/4} \quad \dots (6)$$

can be inferred. Thus we have applied equation (6) to our experimental observations, which are plotted as $\log(\sigma T^{1/2})$ vs $T^{-1/4}$ as shown in ‘fig.5’. The charts are linear suggesting that equation (6) holds valid in the low temperature zone. This has indicated that the major mechanism in the low temperature region is the variable range hopping conduction mechanism [3, 7, 6-12]. The flaws linked to the polycrystalline thin films directly result in the localized states that drive this conduction process [13-15]. These flaws might most likely be caused by partial atomic bonding at grain boundaries and partial stoichiometric departure in our samples. Next, the activation energies for both high and low temperatures were calculated for both high and low temperature regions and are tabulated in table 2. The donor levels are produced below the bottom of the conduction band with $E_d = 2 E_{a\sigma}$. The E_d 's are listed in table 2.

3.3.2 The research into thermoelectric power

Thus, the temperature range of 300 K to 550 K was used to record the TEP for the CdS thin film. The samples exhibited conduction of the n-type. For CdS samples, the temperature dependency of TEP (P) is displayed in

“Fig. 6”. It is evident that the thermoelectric power rose as the temperature rose, and this behavior supports the theory that electrons play a key role in electrical conductivity. The thermoelectric power's temperature dependence is quasilinear, indicating the sample's degeneracy [6, 7, 18-19]. The following relationship between the thermopower and the applied temperature has been fitted to our data [6, 18,19].

$$P = (-K/e) [A + \ln \{2 (2\pi m_d^*KT)^{3/2} / nh^3 \}]. \quad \dots (7)$$

where the other words have their customary meaning and A is a thermoelectric component that is dependent on the different scattering processes. For the values of n, equation (7) may be solved and rearranged, and the temperature dependence of the carrier concentration is then;

$$\log n = 3/2 \log T - 0.005 P + 15.7198 . \quad \dots (8)$$

Equation (8) was then utilized to obtain the carrier densities for the CdS sample at different working temperatures. The conventional relation was then used to get the carrier mobilities (μ).

$$\mu = \sigma / ne \quad \dots(9)$$

where the electronic charge is denoted by e, the carrier concentration by n, and the electrical conductivity by σ . Using Petritz's grain boundary scattering model, the temperature dependence of the carrier mobility was then examined to determine the inter-grain barrier potential [4, 19, 20]. Petritz states that the mobility depending on grain boundary scattering is given by;

$$\mu = \mu_0 \exp (-\phi_B /KT) \quad \dots (10)$$

where ϕ_B is the intercrystalline barrier height and μ_0 is a pre-exponential factor based on the idea that current passes across the barrier by thermionic emission. Thus, a straight line should result from plotting $\log (\mu T^{1/2})$ vs $1/T$. The presence of the grain boundary scattering mechanism is demonstrated by the linear plots of $\log (\mu T^{1/2})$ versus $1/T$ for the CdS sample, as shown in “Fig.7” [6, 7, 20]. Next, using the slopes of straight lines, the intercrystalline barrier potentials (ϕ_B) for these films were computed and are listed in table 2.

Table 2 Some characteristics of the CdS thin film.

CdS Thin Film	E _g eV	Power factor, m	E _a σ, eV		E _d , eV	Barrier Potential (φ _B) eV
			H.T	L.T		
	2.42	0.49	1.197	0.567	1.134	

CONCLUSIONS

1. The CdS thin film was found to have a polycrystalline hexagonal structure with a strong (101) preferred orientation, according to XRD tests. The E_g optical bandgap is 2.41 eV, and the CdS thin film has a high absorptivity (=10⁴-10⁵cm⁻¹).
2. According to electrical conductivity research, low temperature electrical conduction is of the variable range hopping type, whereas high temperature electrical conductivity is controlled by a grain boundary scattering restricted conduction mechanism.
3. The operating temperature and the composition of the film have an impact on the carrier concentration and mobility.

ACKNOWLEDGEMENTS

The Authors would like to thank Professor J.P. Yadav. Head of Department of USIC for providing XRD. I am also grateful to Principal Dr. Madhav Bapat, D.B.J. College, Chiplun for his encouragement and moral support in pursuing my research work.

REFERENCES

- [1]. K. L. Chopra and S. R. Das., in "Thin Film Solar Cells", (eds) K L Chopra and S. R. Das, Plenum Press, New York, (1983), USA.
- [2]. E. Shanthi, A. Banerjee, V. Dutta and K.L. Chopra, Electrical and optical properties of tin oxide films doped with F and (Sb+ F) J. Appl. Phys. 53 (1982) 1615.
- [3]. L. P. Deshmukh, Ph.D. Thesis, Shivaji University, Kolhapur, M. S. (1985), India.
- [4]. G. S. Shahane, Ph. D. Thesis, Shivaji University, Kolhapur, M. S. (1997), India.
- [5]. Mane S.T., Lendave S.A., Pingale P.C., Suryawanshi R.V., Karande V.S., Pirgonde B. R. and Deshmukh L.P., Proc. International Conference On Advanced Materials and nanoparticles, Oct 21-23, 2011, Kathmandu, Nepal.
- [6]. S. A. Lendave, V. S. Karande and L. P. Deshmukh, Crystallographic and microscopic investigations on chemically synthesized mercury cadmium sulphide (mcs) thin composite films, J. Surf. Engg. & Appl. Electrochem. 46 (2010) 462.
- [7]. S. A. Lendave, V. S. Karande and L. P. Deshmukh, Structural and transport characteristics of $Hg_xCd_{1-x}S$ thin composite films: A correlation J. Metallurgy & Mat. Sci. 52 (2010) 363.
- [8]. J. C. Manificier. L. Szepessy, J. F. Bresse, M. Perotin and R. Struck, $In_2O_3:(Sn)$ and $SnO_2:(F)$ films—Application to solar energy conversion; part 1—Preparation and characterization Mater. Res. Bull. 14 (1979) 109.
- [9]. P. D. More, G. S. Shahane, P. N. Bosale, A. A. Belhekar, M. K. Dongare and L. P. Deshmukh, Micro-crystallographic and spectral response studies of $CdSe_{1-x}Tex$ alloyed thin films Ind. J. Pure & Appl. Phys. 40 (2002) 62.
- [10]. M. M. Abou Sekkina, A. Tawfik and M.I. Abd El-Ali, Further studies on the temperature dependence of the electric and photovoltaic properties of CdSe thin films for solar cells Thermochemica Acta 86 (1985) 59.
- [11]. Y. D. Tembhurkar and J. P. Hirde, Structural, optical and electrical properties of spray pyrolytically deposited films of copper indium diselenide Thin Solid Films 215 (1992) 65.
- [12]. J. W. Orton and M. J. Powell, The Hall effect in polycrystalline and powdered semiconductors, Rep. Progr. Phys. 43 (1980) 1263.
- [13]. Oumous and H. Hadiri, Optical and electrical properties of annealed CdS thin films obtained from a chemical solution Thin Solid Films 386 (2001) 87.
- [14]. N. F. Mott, Phil., Mag. 19 (1969) 835.
- [15]. L. I. Soliman, Influence of γ -irradiation on optical and electrical properties of amorphous $CuInSeTe$, $CuInSTe$ and $CuInSeS$ thin films, Ind. J. Pure & Appl. Phys. 32 (1994) 166.
- [16]. T. Suzuki, Y. Ema and H. Toshiya, In doping in CdTe film by co-evaporation of CdTe and In Jpn. J. Appl. Phys. 26 (1987) 2009.
- [17]. V. B. Pujari, S. H. Mane, V. S. Karande and L. P. Deshmukh, A study of cadmium mercury telluride (CMT) thin film structures: some physical observations and characteristics, Mat. Chem. Phys. 83 (2004) 10.
- [18]. V. B. Pujari, D. J. Dhage and L. P. Deshmukh, $n-Hg_xCd_{1-x}Se$ thin film electrodes for photoelectrochemical applications, Ind. J. Engin. & Mat. Sci, 15 (2008) 275.
- [19]. L. P. Deshmukh, S. G. Holikatti and B. M. More, Optical and structural properties of antimony-doped CdS thin films, Mat. Chem. Phys. 39 (1995) 278.

[20]. L. P. Deshmuk et. al. Structural and electrical properties of indium doped Cd_{0.7}Zn_{0.3}S thin, Ind. J. Pure & Appl. Phys. 36 (1998) 322.

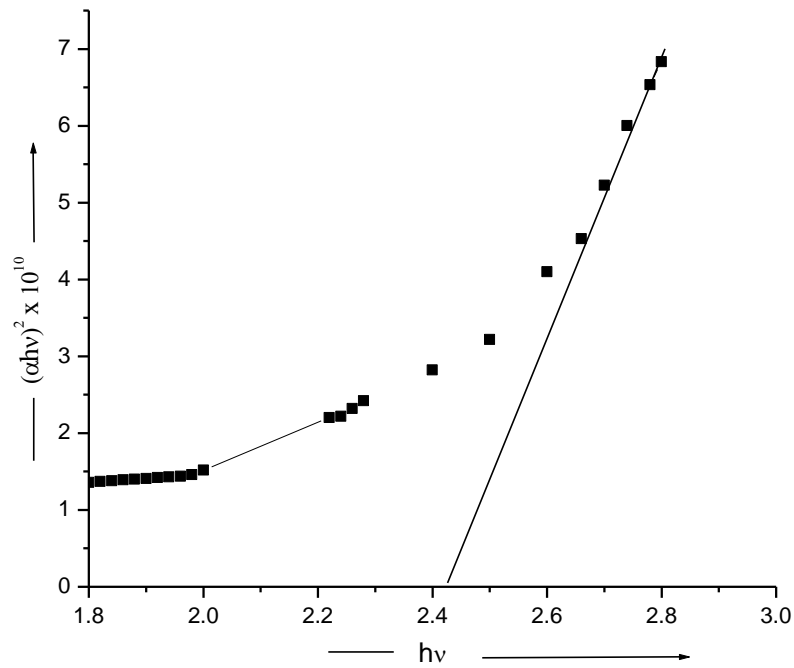


Figure 1. A plot of $(\alpha hv)^2$ vs hv typical as deposited CdS thin film.

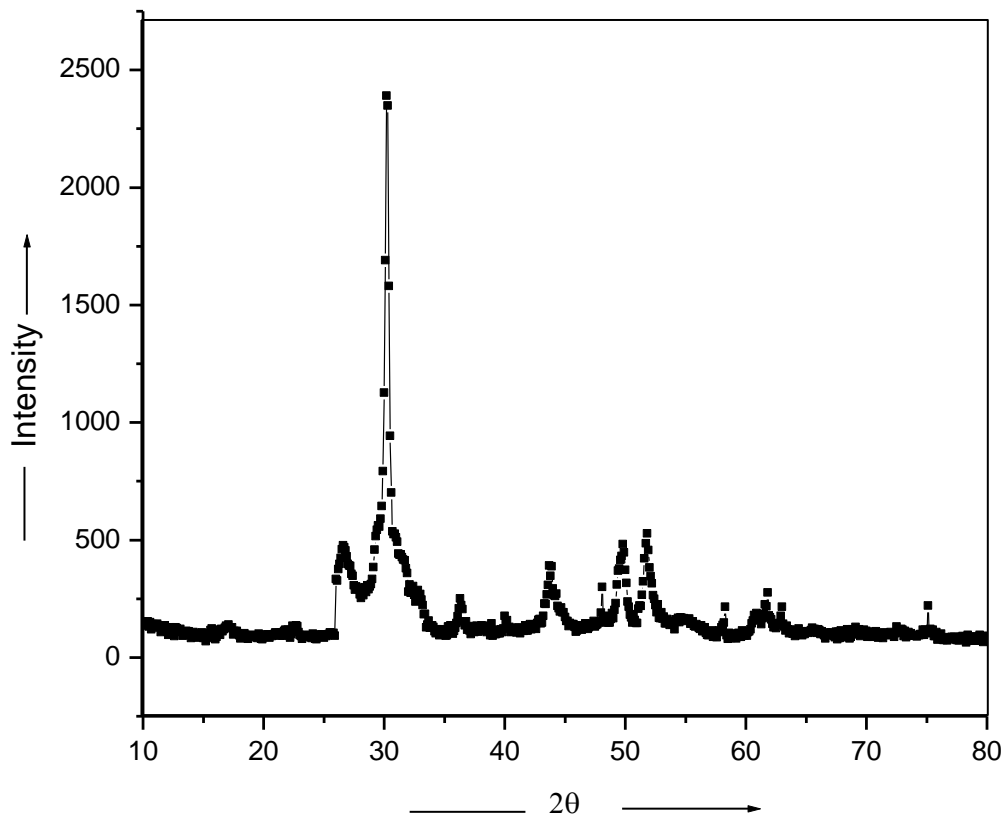


Figure 2. XRD diffractogram of CdS thin film.

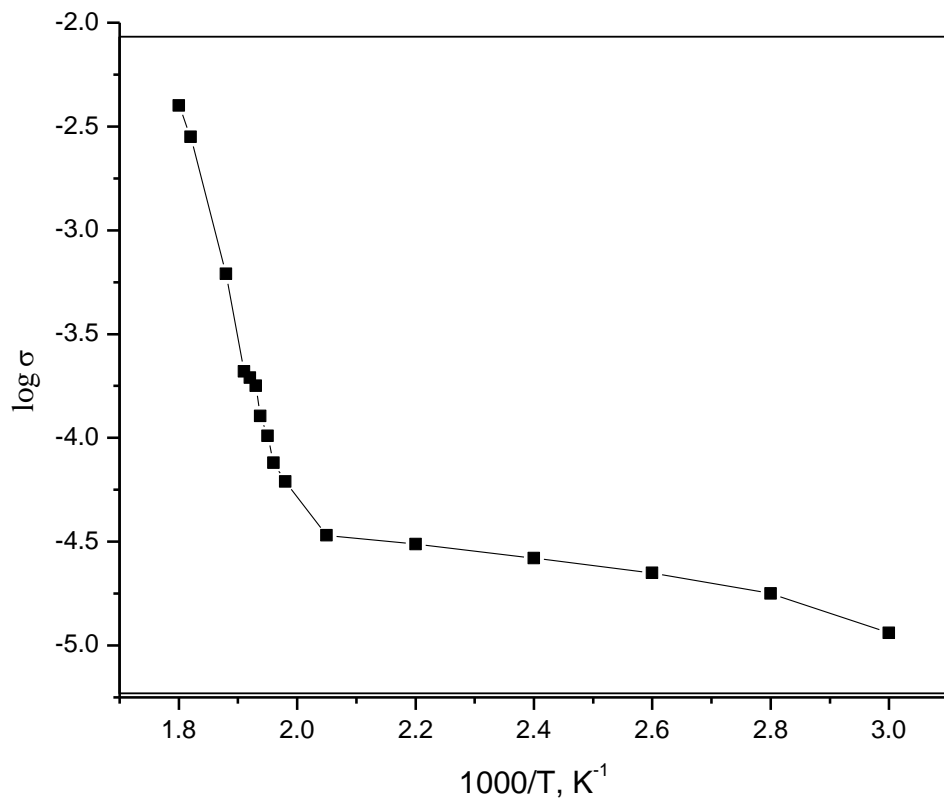


Figure 3. Variation of an electrical conductivity with working temperature for sample.

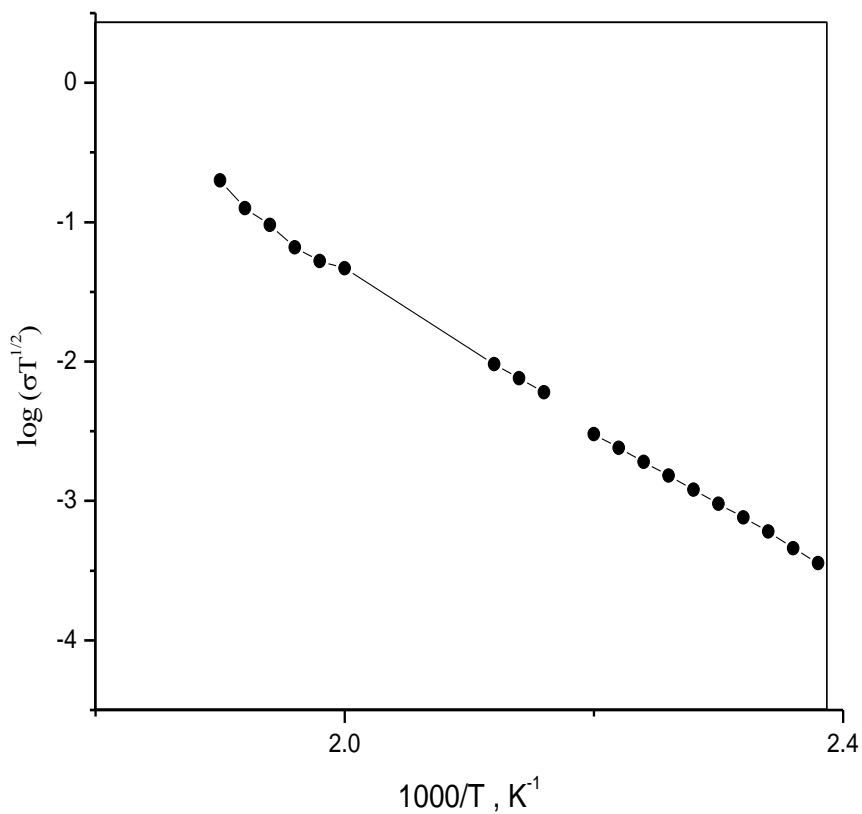


Figure.4. Plots of $\log(\sigma T^{1/2})$ versus $1000/T$ for CdS sample

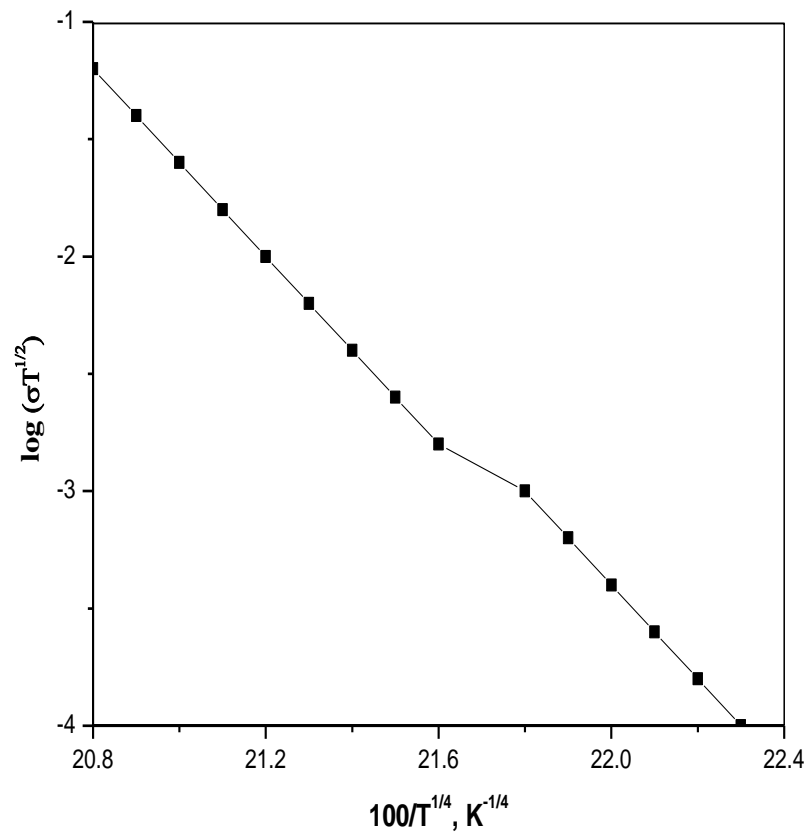


Figure.5 Plots of $\log(\sigma T^{1/2})$ versus $100/T^{1/4}$ for CdS sample.

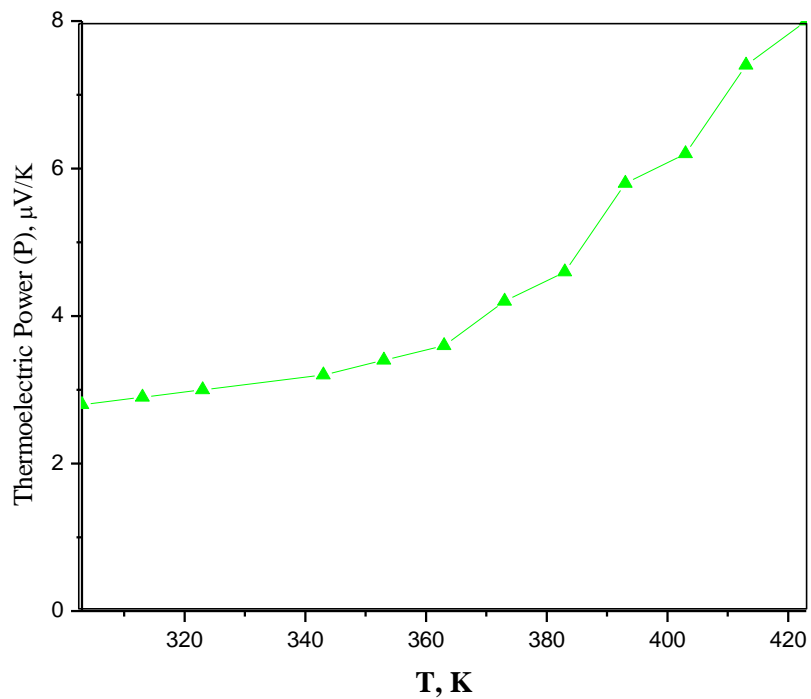


Figure. 6 Variation in thermoelectric power with the working temperature for CdS.

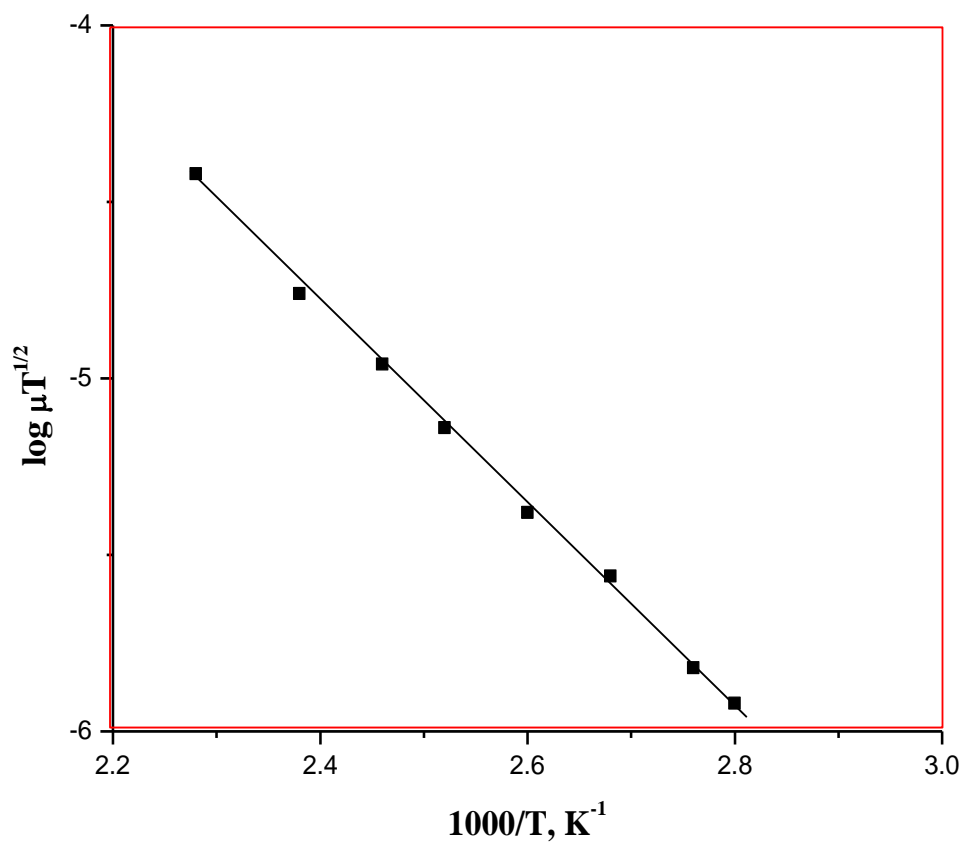


Figure 7 The plots of $\log (\mu T^{1/2})$ vs $1/T$ for CdS thin film.

Benign Methodologies for The Synthesis Of 'N' And 'O' Based Heterocycles

Mustaqeem Mohammed Abbas*, Deshmukh Simal Noorkhan, Sayyed Misbah Mohammed Farooq, Farooqui Masheera Akhtar, Karazgi Samreen Abdul Qadeer

Department of Chemistry, Royal College of Arts, Science and Commerce-Mira Road (Autonomous), Maharashtra, India

ARTICLE INFO

Article History:

Published : 30 April 2025

Publication Issue :

Volume 12, Issue 13
March-April-2025

Page Number :

53-56

ABSTRACT

Pyrimidones are continue to attract great interest in the field of organic synthesis due to their various chemical and biological applications observed, especially in recent times. A library of Nitrogen and Oxygen containing heterocyclic compounds have been synthesized by grinding Meldrum's acid, Thiourea/Urea with aromatic aldehyde in the presence of transition metal based Nanoparticles with Al₂O₃. Comparative studies were conducted with respect to the yield, reaction simplicity and work-up of the reaction. The structures of all synthesized products were confirmed by physico-chemical tests including TLC and spectral techniques such as IR and proton NMR.

Keywords: Solid phase, Grinding, Ni-Ferrite, Multicomponent.

INTRODUCTION

Heterocyclic compounds have a wide range of molecular structures, they are frequently used in the pharmaceutical medical industry¹. Pyrimidones serve as a raw material for the synthesis of many different heterocyclic compounds and as a parent substance for the production of drugs². Pyrimidines, sometimes referred to as 1,3-diazole or m-diazine, are classified as cyclic amines³. Commercial importance of pyrimidone derivatives has led to the development of the catalysts and techniques for their synthesis, such as sulfuric acid, fresh lemon juice, Ni nanoparticles (NPs), solar thermal energy, ionic liquid, polymers supported catalysts and microwave irradiation⁴⁻⁶. Pyrimidone reported to possess potent anti-ulcer activity⁷. Urea and thiourea based heterocycles are widely used nitrogen fertilizer, promoting plant growth and development⁸⁻⁹.

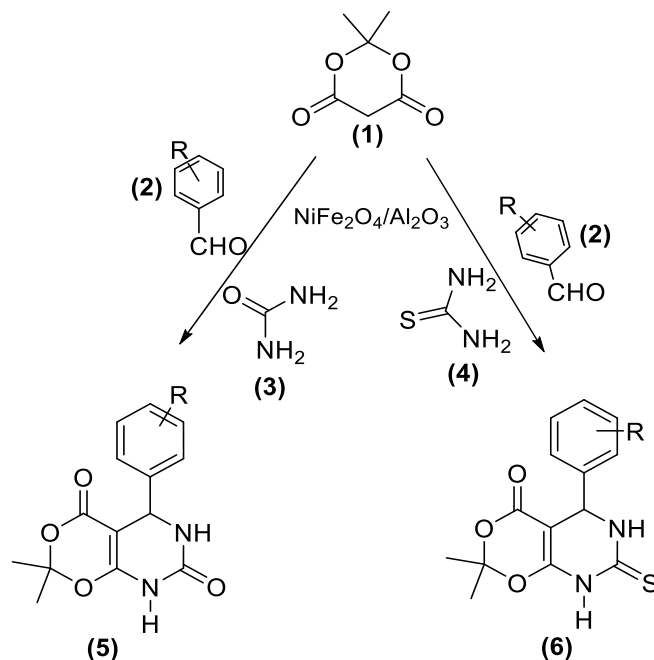
EXPERIMENTAL

Melting points of all synthesized compounds were determined in open capillary tubes and are uncorrected. The purity of the compounds was monitored by TLC. ¹H NMR spectra were recorded on Varian 500 MHz NMR spectrophotometer using CDCl₃/DMSO-d₆ as solvent with TMS as an internal standard (chemical shifts in δ ppm).

General Procedure:

A Mixture of Meldrum's acid (0.01 mol), Aryl aldehydes (0.01 mol) and urea/thiourea (0.01 mol) was ground in the presence of a catalytic amount of Ni- ferrite nano catalyst and Alumina. The progress of the reaction was monitored by Thin Layer Chromatography. After completions of the reaction, the reaction mixture was poured onto ice-cold water, solid separated was filtered off, washed with water, dried and recrystallized from aqueous ethanol to obtain pure compound.

General Scheme



Observation and results of organic synthesis:

Compounds	R	Mol. Formula	m.p.°C	Yield %		Grinding time	
				With NiFe ₂ O ₄ -Al ₂ O ₃	With mineral acid catalyst	With NiFe ₂ O ₄ -Al ₂ O ₃	With mineral acid catalyst
5a	H	C ₁₄ H ₁₄ N ₂ O ₄	212-214	82	78	2mins	5mins
5b	4-Cl	C ₁₄ H ₁₃ N ₂ O ₄ Cl	170-172	78	73	2mins	4mins
5c	4-OCH ₃	C ₁₅ H ₁₆ N ₂ O ₅	130	86	80	3mins	6mins
6a	H	C ₁₄ H ₁₄ N ₂ O ₃ S	200	85	79	2mins	5mins
6b	4-Cl	C ₁₄ H ₁₃ N ₂ O ₃ SCl	156-158	86	78	2mins	5mins
6c	4-OCH ₃	C ₁₅ H ₁₆ N ₂ O ₄ S	120	85	78	3mins	6mins

Spectral Data:

Compound 5a: 7H,8H,10H-8,10-diaza-2,4-dioxa-5,9-dioxo-7-phenylbicyclo [4.4.0] dec-1(6)-ene

IR (cm⁻¹):1670(C=O), 1725(C=O), 3295(NH),

¹H NMR(δ ppm):1.71(6H,s,2xCH₃), 7.2 (5H,m,Ar- H), 8.15 (2H,s,2xNH), 8.25 (1H,s,CH),

¹³C NMR(δppm):27.325(2xCH₃), 105 and 110(tetrahedral carbon), 124.78 (CH), 116.36-131.7 (C=C,Ar-C),160.476 (C=O),165.985 (C=O).

Compound 5b: 7H,8H,10H-8,10-diaza-2,4-dioxa-5,9-dioxo-7-(4-chloro)phenylbicyclo [4.4.0] dec-1(6)-ene

IR (cm⁻¹):1675(C=O), 1720(C=O), 3290(NH),

¹H NMR(δ ppm):1.72(6H,s,2xCH₃), 7.3 (5H,m,Ar- H), 8.2 (2H,s,2xNH), 8.25 (1H,s,CH),

¹³C NMR(δppm):27.325(2xCH₃), 105 and 112(tetrahedral carbon), 122.78 (CH), 116.36-131.7 (C=C, Ar-C),160.476 (C=O),165.985 (C=O).

Compound 5c: 7H,8H,10H-8,10-diaza-2,4-dioxa-5,9-dioxo-7-(4-methoxy) phenylbicyclo [4.4.0] dec-1(6)-ene

IR (cm⁻¹):1665(C=O), 1715(C=O), 3285(NH),

¹H NMR(δ ppm):1.73(6H,s,2xCH₃), 3.87 (3H,s,OCH₃), 7.19 (4H,m,Ar- H), 8.2 (2H,s,2xNH), 8.21 (1H,s,CH),

¹³C NMR(δppm):27.325(2xCH₃), 55.75(OCH₃),105 and 110(tetrahedral carbon), 123.78 (CH), 116.36-131.7 (C=C,Ar-C),160.476 (C=O),165.97 (C=O).

Compound 6a: 7H,8H,10H-8,10-diaza-2,4-dioxa-5-oxo-9-thioxo-7-phenylbicyclo [4.4.0] dec-1(6)-ene

IR (cm⁻¹):1685 (C=O), 1220 (C=S), 3315(NH),

¹H NMR(δ ppm):1.73(6H,s,2xCH₃),, 7.0-7.15 (5H, m,Ar- H), 8.2 (2H,s,2xNH), 8.4(1H,s,CH), ¹³C NMR(δppm):, 27.325(2xCH₃), 104.21 and 109(2x tetrahedral carbon), 120.53-130.788 (C=C,Ar-C), 155.89 (C=O), 163.512 (C=S).

Compound 6b: 7H,8H,10H-8,10-diaza-2,4-dioxa-5-oxo-9-thioxo-7(4-chloro)phenylbicyclo [4.4.0] dec-1(6)-ene

IR (cm⁻¹):1685 (C=O), 1242 (C=S), 3313(NH),

¹H NMR(δ ppm):1.73(6H,s,2xCH₃),, 7.0-7.15 (5H, m,Ar- H), 8.3 (2H,s,2xNH), 8.39(1H,s,CH), ¹³C NMR(δppm):, 27.325(2xCH₃), 104.12 and 109(2x tetrahedral carbon), 120.53-130.788 (C=C,Ar-C), 156.982 (C=O), 162.39 (C=S).

Compound 6c: 7H,8H,10H-8,10-diaza-2,4-dioxa-5-oxo-9-thioxo-7(4-methoxy)phenylbicyclo [4.4.0] dec-1(6)-ene

IR (cm⁻¹):1685 (C=O), 1230 (C=S), 3315(NH),

¹H NMR(δ ppm):1.73(6H,s,2xCH₃),3.70(3H,s, -OCH₃), 7.1-7.2 (5H, m,Ar- H), 8.2 (2H,s,2xNH), 8.4(1H,s,CH),

¹³C NMR(δppm):, 27.35(2xCH₃), 56.75(-OCH₃), 104.12 and 109(2x tetrahedral carbon), 120.53-130.788 (C=C,Ar-C), 156.982 (C=O), 163.512 (C=S).

RESULTS AND DISCUSSION

The target molecules were synthesized in good yield by the one pot reaction of Aryl aldehydes, Meldrum's acid and urea/thiourea using catalytic amount of Nickel-Ferrite nano catalysts supported by Alumina.

CONCLUSIONS

Dihydropyrimidones and pyrimidinethiones were prepared in good yield by using multicomponent reaction. Use of transition metal based nano catalyst and Aluminawas found to be very effective w.r.t reaction time and high atom economy.

ACKNOWLEDGEMENT:

Authors are thankful to the Chairman and the Founder of Royal College Prof. A.E Lakdawala, Principal Prof. Kalpana Patankar Jain, Management and Chemistry Department of Royal College for constant encouragement, facilities and supports.

REFERENCES

- [1]. Kachroo M., Panda R., Yadav Y., Synthesis and biological activities of some new pyrimidine derivatives from chalcones, *Der Pharma Chemica*, 2014, 6(1), 352
- [2]. Mustaqeem M. A., Karthik K., Multicomponent synthesis of Heterocycles as Biologically active frameworks *Vidyawarta.*, 2025, 1(1), 152-154.
- [3]. Al-Noor T.H., Ali A.M., Al-Sarray A.J., AlObaidi O.H., Obeidat A.I., Habash R.R., A Short Review: Chemistry of Curcumin and Its Metal Complex Derivatives, *Journal of University of Anbar for Pure Science*, 2022, 16(1), 20
- [4]. Krishnan K. K., Dabholkar V. V., Gopinathan A., Jaiswar R., One Pot Multicomponent Synthesis of Tetrahydrobenzo[b] pyrans and Dihydropyrano[c] chromenes using Magnetically Separable NiFe₂O₄ Nanoparticles *J. Chem. & Cheml. Sci.*, 2018, 8 (1), 66-74.
- [5]. Shivakumara K N, Sridhar B T. Review on role of urea and thiourea derivatives of some heterocyclic Scaffold in drug design and medicinal chemistry. *Int. J. Chem. Res. Dev.* 2021;3(1), 20-25.
- [6]. Lweis A., and Rosenbach V. A novel convenient one step pyrimidine synthesis. *Tetrahedron Lett.*, 2022, 22 (15), 1453- 1454
- [7]. Zhuang, J., & Ma, S. Recent development of pyrimidine-containing antimicrobial agents. *Chem. Med. Chem.*, 2020, 15(20), 1875-1886.
- [8]. Zhao, F.; Zhang, H.; Xie, M.; Meng, B.; Liu, N.; Dun, C.; Qin, Y.; Gao, S.; Clercq, E.D.; Pannecouque, C.; et al. Potent HIV-1 non-nucleoside reverse transcriptase inhibitors: Exploiting the tolerant regions of the non-nucleoside reverse transcriptase inhibitors binding pocket. *J. Med. Chem.* 2023, 66, 2102–2115.
- [9]. Wang, X.; Jin, B.; Han, Y.; Wang, T.; Sheng, Z.; Tao, Y.; Yang, H. Optimization and antibacterial evaluation of novel 3-(5-fluoropyridine-3-yl)-2-oxazolidinone derivatives containing a pyrimidine substituted piperazine. *Molecules.* 2023, 28, 4267.

Synthesis And Characterisation of NiO/PANI Ncs as A Promising Photocatalyst for Photocatalytic Degradation of Crystal Violet Dye Under Natural Sunlight

Vivek C. Badgajar¹, Ramdas S. Suralkar^{1*}, Deepak M. Nagrik²

¹Pratap College Amalner, Maharashtra, India

²G. S. College Khamgaon, Maharashtra, India

ARTICLE INFO

Article History:

Published : 30 April 2025

Publication Issue :

Volume 12, Issue 13

March-April-2025

Page Number :

57-73

ABSTRACT

This study used a straightforward precipitation method to create NiO Nano powder and NiO/PANI nanocomposites employing NaOH as the precipitant and Ni (NO₃)₂ as a precursor. The nano powder's physical properties were thoroughly investigated utilizing methods like XRD, FTIR, SEM-EDS and UV-Visible spectrophotometer. Under natural sunlight irradiation, the material's photocatalytic efficacy in breaking down Crystal Violet (CV) dye was evaluated during summer and winter season. To assess the oxidative potential of NiO and NiO/PANI nanocomposites that mediate the photocatalytic efficiency of this material, the study also sought to clarify the photocatalytic degradation mechanisms of the dye.

Keywords: Dye degradation, Photocatalyst, nanoparticles, nanocomposites, sunlight Irradiation, NiO/PANI etc.

INTRODUCTION

Large quantities of toxic organic dyes are produced in the industry, which can cause many environmental problems and result in varying types of cancer throughout humans [1]. Therefore, the development of cheap and environmentally friendly methods to remove these hazardous materials from the environment and underground water has become a critical challenge [2,3]. In recent decades, the progressed photocatalysts have attracted a lot of attention [4], as well as the interest of many that consider the usage of photocatalyst technology as a new approach in discovering a solution for cleaning environmental pollutants [5–8]. Healthy water is defined as the water that has lost its toxic chemicals and pathogens, and its existence is essential for continuing life. Besides, water stands as a vital raw material in many major industries including electronics, medicine, and food technologies [9]. Nowadays, the transit of science and technology, along with the rapid progress of varying fields of technologies, have been able to provide new resolutions and achievements in various areas of science, especially throughout the treatment of industrial wastewater and sewage [10,11].

Nanoscience has an exceptional stance on the subject of recognizing and eliminating various organic pollutants [12,13]. Recently, the advent of novel technologies in the treatment of water and industrial waste has provided and introduced new resolutions, which involve the utilization of nanotechnology [14–16]. The predicament of water limitation has been advanced in recent years due to the induced progression in science and the speeding growth of industry [4]. The high growth rate of industry can result in different consequences such as environmental pollution, reduced ground water, and the rising temperature of earth sphere [17]. Some of the effective factors in photocatalyst activity are known to be the chemistry of surface and [18] nanotechnology, which can provide many potential opportunities for the better management of water crisis [19]. Science and Nanotechnology stand as the two fields that have faced the fastest and most major developments in both technological revolutions and human history [20]. The fate of environmental pollutants, such as dyes that have been released from textile sewage and other industrial processes, is one of the most critical issues that require immediate actions and attention [21,22]. The increasing population and human needs have resulted in the creation of numerous industries and factories, which has consequently increased the usage of water and raised the inevitable generation of wastewater [23,24]. Due to the involvement of varying consumable dyes and production methods, the textile industry has been also generating wastewater in different quantities and chemical qualities [25,26]. The composed sewage of these industries is consisted of large amounts of dye, which is often toxic and stable in the environment [27]. Different physical, chemical, and biological methods, such as absorption, aeration, flocculation, and photo-oxidation, are typically used to purify the dye pollutants [28,29]. Among the available purification techniques, photo-oxidation is considered as an economically viable alternative [30]. The process of photocatalyst degradation has become one of the most promising ways of treating wastewater due to its advantages in contrast to the traditional techniques [31,32,2,33,34].

Some of the outstanding features of photocatalyst wastewater purification procedures include the rapid photocatalyst oxidation reaction at low concentrations, lack of byproducts formation in a multi-cycle implementation, and finally the production of harmless products [12,35,36]. One of the most hopeful and efficient approaches of purifying water is to couple the facile and advanced photo-oxidation processes of hazardous chemical compounds and contaminants with the conventional purification methods such as coagulation and biological purification [37].

METHODOLOGY

2.1 Experimental site

The synthesization of NiO NPs, NiO/PANI NCs, and the studies of photocatalytic activities, and characterization using UV-Visible spectrophotometer were conducted in Chemistry Research Laboratory of Pratap College Amalner. To verify the molecular and crystalline structure of the as-synthesized photocatalysts, ATR-FTIR and XRD measurements were conducted at the Instrumentation facility, R. C. Patel institute of Pharmaceutical Education and Research BTECHI Shirpur. The morphology of photocatalysts, elemental detection was measured using SEM-EDS at SAIF, STIC, Cochin University, Kochi, Kerala, India.

2.2 Apparatus and instruments

The crystal structures of NiO NPs and NiO/PANI NCs were examined by X-ray diffractometer (Bruker D8 Advance Panalytical X Pert3). The determination of functional groups of as synthesized photocatalysts was studied with help of Fourier-transform infrared spectroscopy (FTIR, Bruker) in the wave number from 400-4000 cm^{-1} . The absorbance of the samples was determined using a UV-Visible spectrophotometer (UV-Visible spectrophotometer, JASCO V-670). The morphology and elemental detection of the photocatalysts was

examined using scanning electron microscope (SEM) (SEI QUANTA 250 FEG Thermo Fisher). were used for these studies.

2.3 Chemicals and reagents

All the chemicals and reagents are analytical grade reagents which are used without further purification. Briefly, Nickel nitrate hexahydrate $\text{Ni}(\text{NO}_3)_2 \cdot 6\text{H}_2\text{O}$ Loba Chem India, aniline ($\text{C}_6\text{H}_5\text{NH}_2$) 98%, hydrochloric acid (HCl), ammonium per sulphate (APS) 98%, from Sigma Aldrich were chemicals used to prepare NPs and NCs. Crystal Violet (CV) dye is used as the model organic dye intended for investigating photocatalytic activities of NiO NPs, NiO/PANI NCs.

2.4 Preparation of NiO NPs

100 ml of 0.5 N NaOH is added drop by drop to the solution of 100 ml of 0.1N $\text{Ni}(\text{NO}_3)_2 \cdot 6\text{H}_2\text{O}$ with constant stirring for 1 hr. after complete addition the mixture is stirred for 2 hrs. Then formation of white precipitate is observed. then the precipitate is filtered and washed 2 to 3 times with distilled water and kept in an oven at 40 °C for 48 hrs for complete drying. Then the ppt is calcinated in a muffle furnace for 3 hrs at 500 °C to get NiO nanoparticles.

2.5 Synthesis of NiO/PANI NCs

Take 10 ml of 1 M HCl solution in a 250 ml RB flask and add 0.1 gm of NiO nanoparticles in it. The mixture is sonicated in an ultrasound bath for 30 minutes. 1 ml aniline is added in 100 ml 1 M HCl solution in a beaker. This solution is added in RB flask and sonicated for 30 minutes. 2.84 gm of ammonium peroxy sulphate (APS) equal molar with aniline is added in 100ml 1M HCl solution in a beaker. This solution is filled in a burette and added dropwise to the mixture in an RB flask kept on magnetic stirrer. This RB flask is kept in glass bowl filled with ice to maintain temperature below 4 °C to achieve polymerization of aniline to polyaniline (Pani). green colour is developed to the mixture which indicate start of polymerisation reaction. After complete addition of APS solution, the mixture kept on constant stirring for 1 hr. the solution is filtered and washed several times with distilled water and kept in an oven at 45 °C for complete drying. The dried powder is obtained as 10% NiO doped Pani as nanocomposite. Then, the samples are ground and used for further characterization and degradation of dye.

2.6 Synthesis of PANI

PANI has synthesized through the in-situ polymerization method via dissolving 1 mL of the monomer (aniline) in 40 mL of 1 M HCl solution. The oxidant solution has prepared via dissolving 2.84 g of APS in 1M HCl which the polymerization reaction takes place at 0 C for 12 h. The molar ratio of monomer to APS was 1:1. The precipitated samples are centrifuged and washed three times with water followed by drying at 70 C for 24 h. The polymerization mechanism of PANI has indicated in Figure 1.

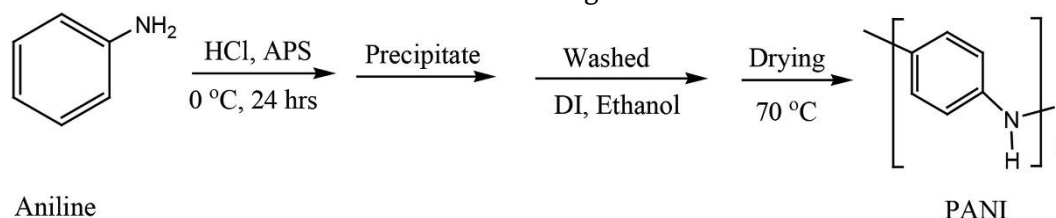


Figure 1: In-situ polymerization mechanism of PANI

2.7 Characterization of photo-catalysts

The crystalline structural measurements for photocatalysts have performed using XRD. Their crystallite sizes are calculated using Debye Scherer's Eq. (1):

$$D = \frac{0.9\lambda}{\beta \cos \theta} \quad 1$$

$D = 0.9\lambda / \beta \cos \theta$ where λ - wavelength of radiation used in Cu K α (0.15406 nm), β - full width at half-maximum of the peak, and θ - angle at the position of the maximum peak (in rad). The FT-IR spectrum of photocatalysts is recorded with ATR FTIR in 400–4000 cm^{-1} wavenumber. The UV-Visible absorption of the synthesized photocatalyst were determined using a JASCO V-670 UV-Visible spectrophotometer equipped with a quartz tube scanning over 200–800 nm wavelength. The morphology and elemental detection of the photocatalysts was examined using scanning electron microscope (SEM) (SEI QUANTA 250 FEG Thermo Fisher) were used for these studies.

2.8 Degradation Study of Crystal Violet (CV) dye

For the photocatalytic degradation study of the model dye, Crystal Violet (CV) dye sample was used; the photocatalysts are NiO NPs and NiO / PANI NCs, and evaluated under Sun light irradiation. 50 mg of photocatalysts are added to 50 mL Crystal Violet (CV) solution of 40 ppm initial concentration. The suspension is constantly stirred for 30 min in dark place to allow the formation of adsorption-desorption equilibrium condition. The λ_{max} of CV in aqueous solution was analysed by UV-Visible instrument with full scan mode and the optimum absorbance (λ_{max}) was observed at 586 nm which in comparable with the reported values. Further, the signals were collected at every 30 min in order to determine the degradation efficiency of Crystal Violet (CV) using the following equation:

$$\% \text{ of degradation} = \frac{A_0 - A_t}{A_0} \times 100 \quad 2$$

where A_0 - and A_t - the absorbance of dye at initial stage and at the reaction time "t".

CHARACTERISATION OF MATERIAL

3.1 Analysis of functional group

Figure 2, 3 and 4 represents ATR-FTIR spectra of NiO NPs, PANI and NiO/PANI NCs between 400-4000 cm^{-1} vibration numbers respectively. The spectrum corresponding the PANI exhibits the broadband at 3204 cm^{-1} which represents N-H vibrations of polymer and the bending of N-H at 1472 cm^{-1} .¹⁴ Absorption peaks observed at 1552 cm^{-1} corresponds to the bending mode of C=C in aromatic ring structures while the peak at 813 cm^{-1} is ascribed to the C-H out-of-plane bending in aromatic ring. The peak at 1290 cm^{-1} is assigned to C-N stretching of the secondary amine unit of PANI. Figure 2 represents ATR-FTIR spectra of NiO NPs between 400-4000 cm^{-1} vibration numbers. Broad Peak Around 3400 cm^{-1} peak is typically attributed to the stretching vibrations of the O-H bond in adsorbed water or hydroxyl groups on the surface of the nanoparticles. Peak Around 1630 cm^{-1} : This peak is also often associated with the bending vibration of H-O-H in adsorbed water molecules. Peak Around 550 cm^{-1} peak is characteristic of the Ni-O stretching vibration in the NiO crystal lattice. This is the most crucial peak for confirming the presence of NiO nanoparticles. Figure 4 represents ATR-FTIR spectra of NiO/PANI nano composites between 400-4000 cm^{-1} vibration numbers. Broad Peak Around 3400 cm^{-1} peak is typically attributed to the stretching vibrations of the O-H bond in adsorbed water or hydroxyl groups on the surface of the nanoparticles. Peak Around 1630 cm^{-1} : This peak is also often associated with the bending vibration of H-O-H in adsorbed water molecules.

The FTIR spectrum provides evidence for the presence of both NiO nanoparticles and PANI. The peaks in the 1500-1600 cm^{-1} and 1100-1300 cm^{-1} regions confirm the presence of PANI, while the peak around 550 cm^{-1} confirms the presence of NiO. The presence of both NiO and PANI in the spectrum suggests that the NiO nanoparticles are successfully incorporated into the PANI matrix.

Thus, from the ATR-FTIR spectrum, it strongly confirms that the nanoparticles are highly incorporated to PANI molecular chain and in-situ polymerization was successful during surface modification of doped NiO NPs with PANI.

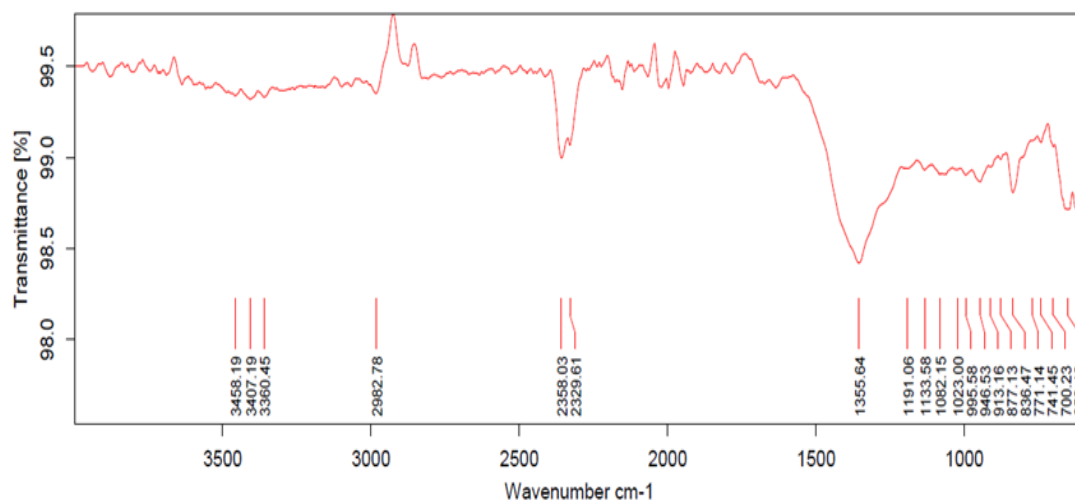


Figure 2: ATR FTIR of NiO

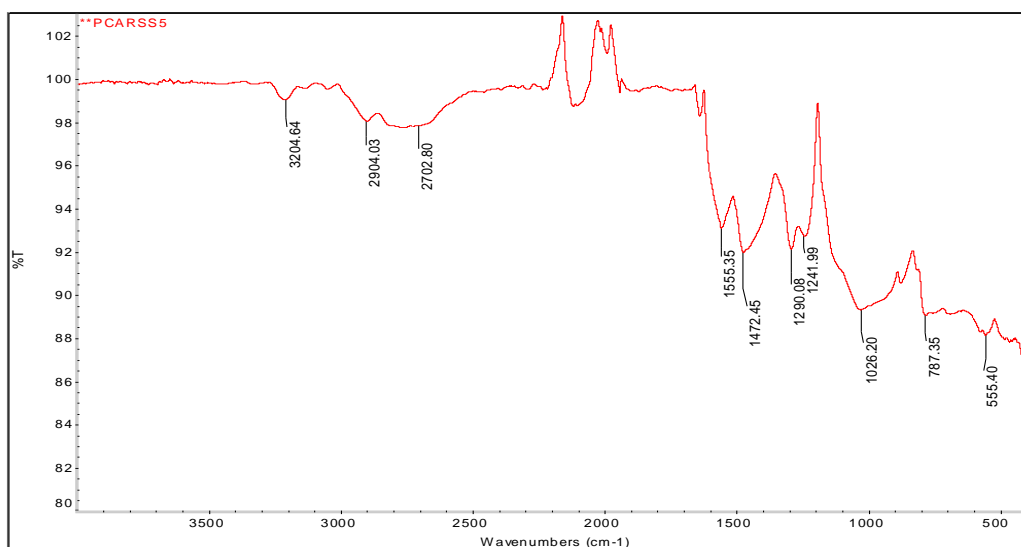


Figure 3: ATR FTIR of PANI

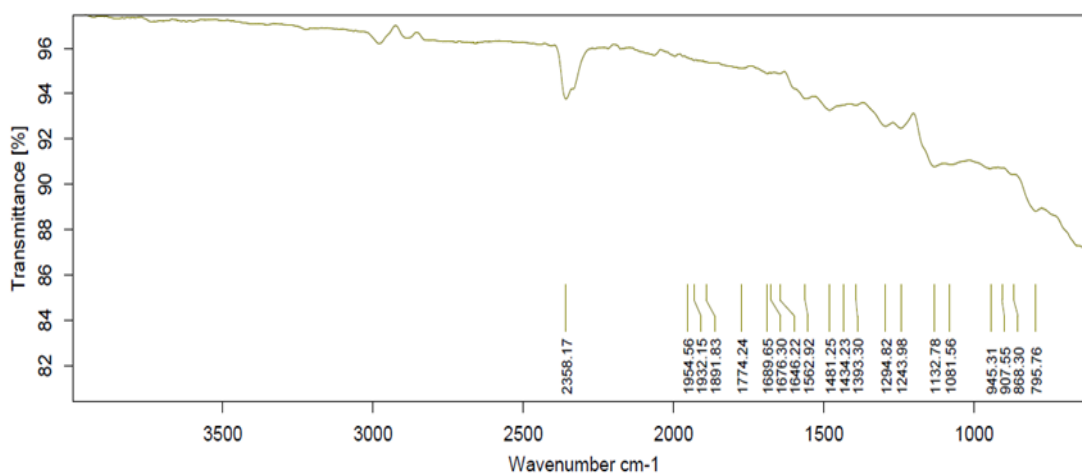


Figure 4: ATR FTIR of NiO/PANI

3.2 Analysis of crystalline structure

Figure 5, 6 and 7 depicts the XRD spectrum of NiO NPs, PANI and NiO/PANI NCs. These patterns delivered highly sharp and intensive diffraction peaks of NPs and PANI NCs. From the XRD results, the crystalline phase of pure and doped PANI were determined that all peaks are clearly matched to the face centered cubic phase. The sharp peaks are observed at $2\theta = 37, 42$ and 62 degrees for NiO nanoparticles. While for PANI The sharp peaks are observed at $2\theta = 17, 20, 25, 26$ and 30 degrees and for NiO/PANI NCs, the sharp peaks are observed at $2\theta = 20, 25$ with small peaks at 28 and 36 degrees.

Figure 5 shows the XRD spectrum of NiO. The XRD pattern is characteristic of NiO. The presence of sharp, intense peaks at specific 2θ values confirms the formation of the crystalline NiO phase. The peaks can be indexed to a cubic structure, which is the typical crystal structure for NiO. The peaks in the spectrum are observed at specific angles (2θ values), which correspond to the crystalline planes of NiO as per Bragg's law. These peaks match the characteristic planes of NiO, such as (111), (200), and (220), based on the cubic rock-salt crystal structure. The positions of the peaks correspond to the characteristic diffraction angles (2θ values) of the planes in the NiO crystal lattice. The relative intensities of the peaks reflect the abundance and orientation of the corresponding crystallographic planes.

Overall, the XRD spectrum provides strong evidence for the successful synthesis of crystalline NiO with a cubic structure.

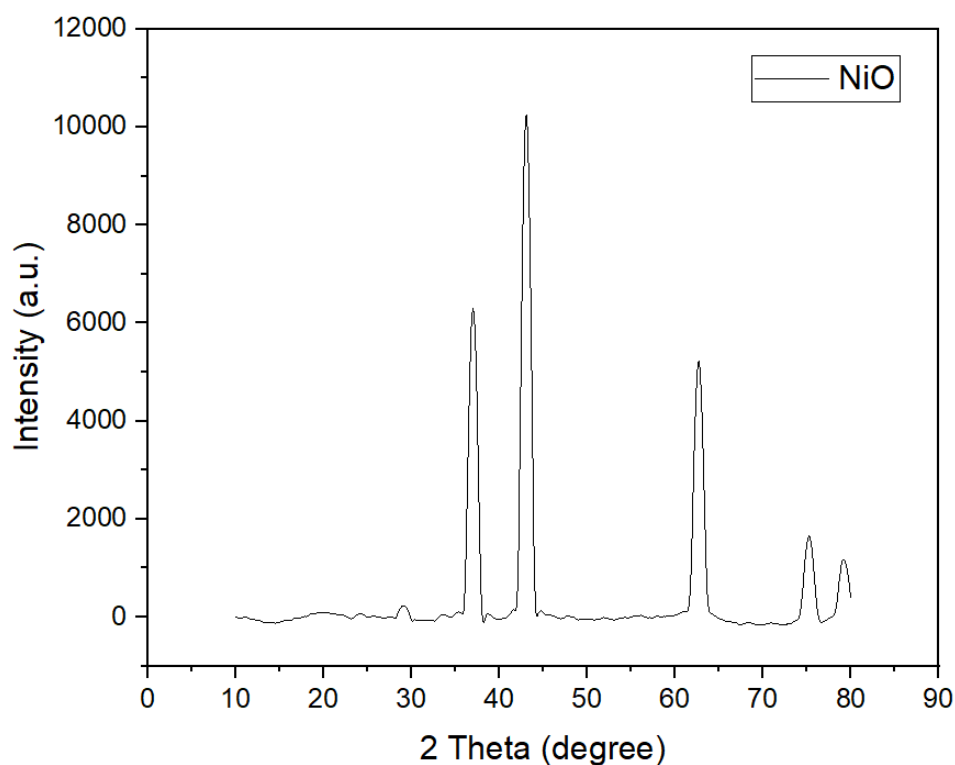


Figure 5: XRD spectrum of NiO nanoparticles

Figure 6 shows the XRD spectrum of NiO/PANI. The XRD pattern shows the presence of both NiO and PANI phases. The sharp peaks at specific 2θ values correspond to the crystalline NiO phase, while the broader peak around $2\theta = 25^\circ$ is characteristic of the amorphous PANI phase. The peaks corresponding to NiO can be indexed to a cubic structure, which is the typical crystal structure for NiO. The positions of the NiO peaks correspond to the characteristic diffraction angles (2θ values) of the planes in the NiO crystal lattice. The relative intensities of the NiO peaks reflect the abundance and orientation of the corresponding crystallographic planes.

Overall, the XRD spectrum confirms the successful synthesis of a NiO/PANI composite material. The presence of both NiO and PANI phases is evident, with NiO exhibiting a crystalline structure and PANI showing an amorphous nature.

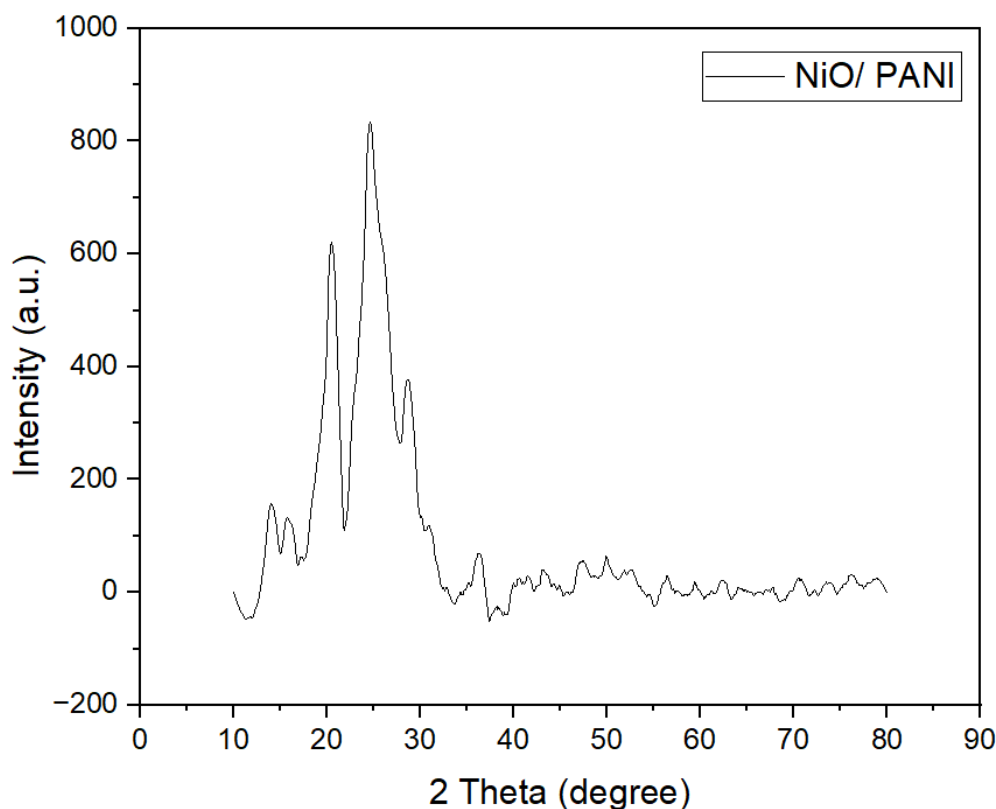


Figure 6: XRD spectrum of NiO/PANI nanocomposites

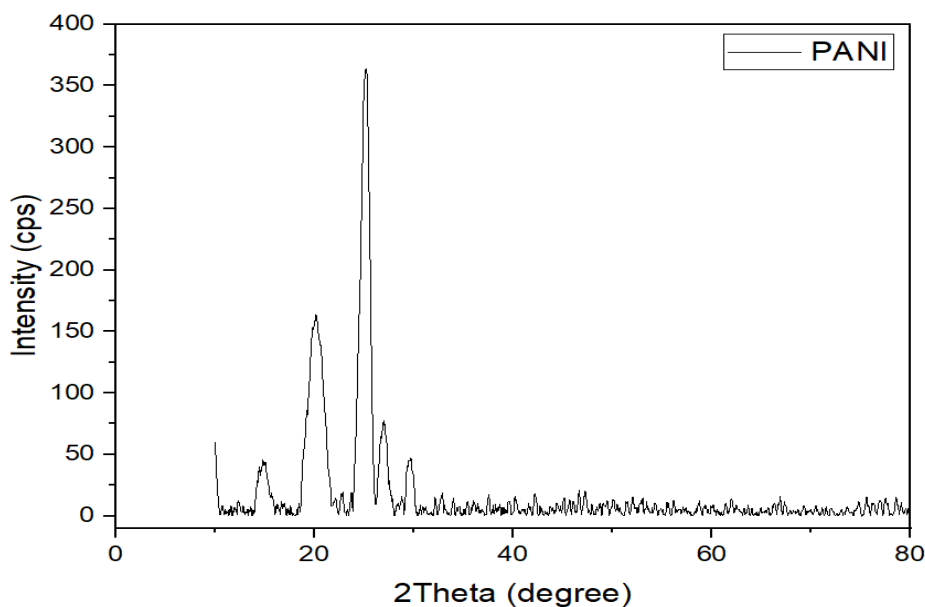


Figure 7: XRD spectrum of PANI

3.3 Analysis of surface morphology

Surface morphology of the synthesized NiO NPs, NiO/PANI NCs. will be studied by SEM analysis. Figure 8 and 9 represents the SEM images of NiO NPs, NiO/PANI NCs.

The particles appear to be in the nanometre to micrometre range. The individual particles seem to be aggregated into clusters. The nanoparticles are not evenly dispersed, indicating significant agglomeration. This is common in nanoparticle systems due to high surface energy and van der Waals forces. The particles appear irregular in shape with rough surfaces, which is typical for synthesized NiO nanoparticles. The gaps and voids between the clusters suggest a porous structure, which might influence the material's catalytic or adsorption properties. The surface appears granular, which may result from the synthesis process (e.g., sol-gel, hydrothermal, or precipitation methods). The image shows clusters of NiO particles embedded in or coated by the PANI matrix. The particles appear as aggregated structures, with rough and irregular surfaces. Individual NiO particles appear smaller within the clusters, but their aggregation prevents clear differentiation.

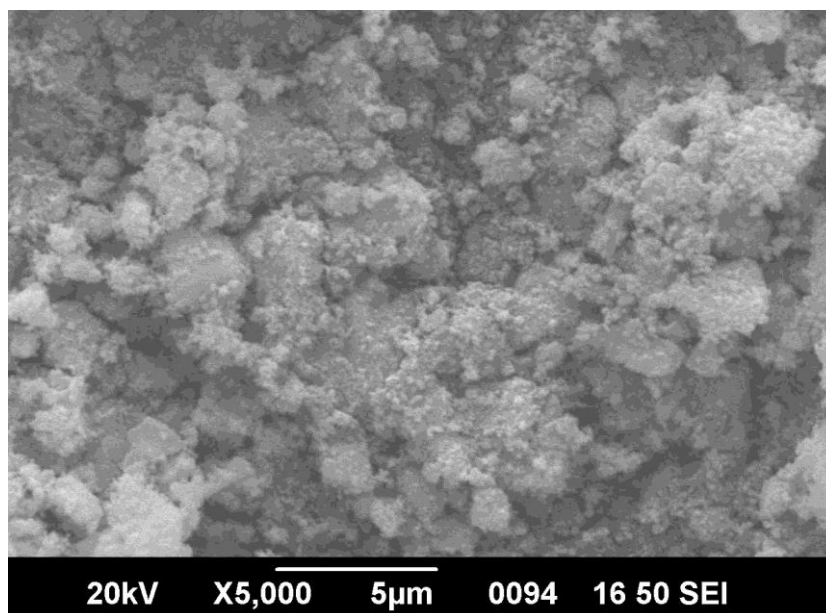


Figure 8: SEM image of NiO at 5 μm

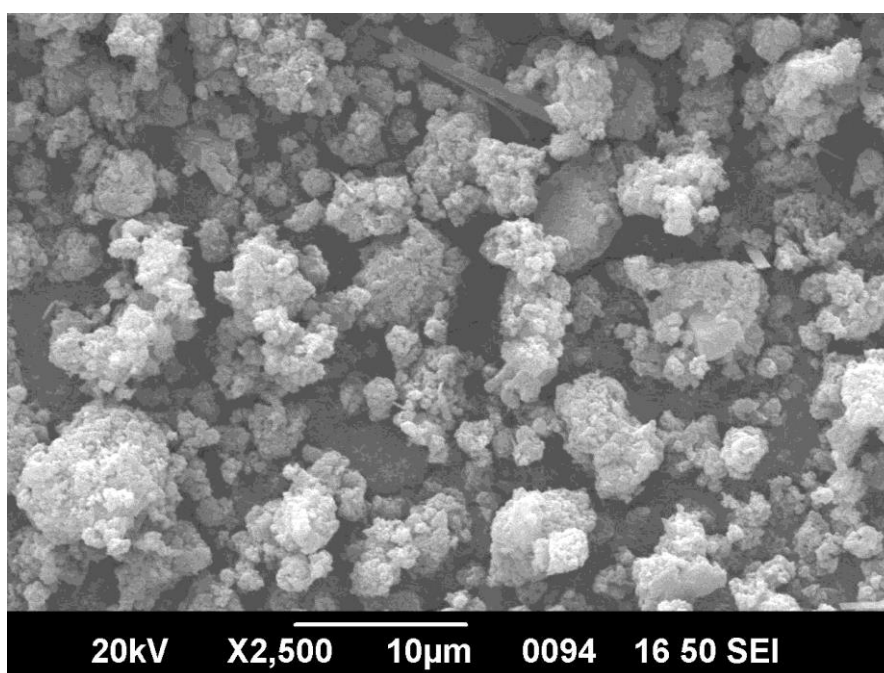


Figure 9: SEM image of NiO/PANI at 10 μm

3.4 Analysis of Elemental detection by SEM-EDS

3.4.1 Elemental detection of NiO nanoparticles

Figure 10 represents elemental detection by SEM-EDS of NiO. The EDS spectrum shows the presence of nickel (Ni) and oxygen (O). The relative intensity of the peaks suggests that the sample is primarily composed of nickel oxide (NiO).

- **Ni peaks:** There are two prominent peaks labeled "Ni" around 8 keV and 8.3 keV. These correspond to the characteristic X-rays emitted by nickel when it is excited by the electron beam in the EDS instrument.
- **O peak:** A smaller peak is visible around 0.5 keV, which is characteristic of oxygen.
- **C peak:** There is a small peak at around 0.3 keV, which is likely from carbon contamination on the sample surface.

The relative intensities of the Ni and O peaks are consistent with the expected stoichiometry of NiO.

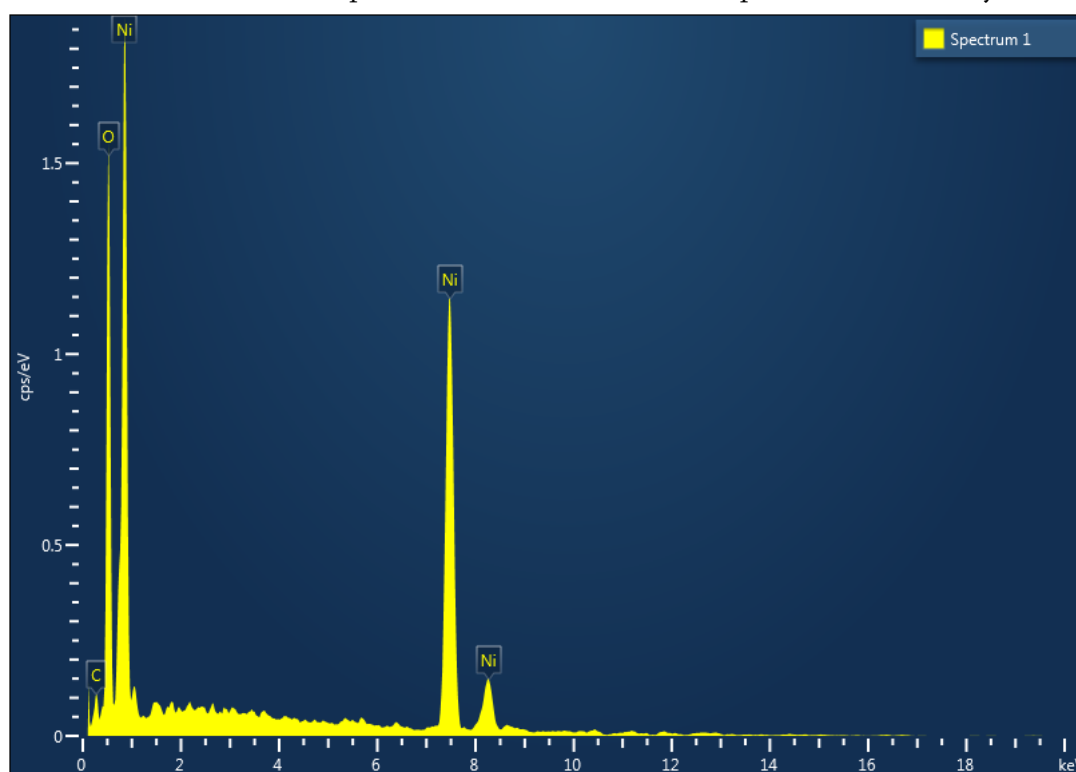


Figure 10: EDS spectra of NiO

Table 1: Elemental detection of NiO nanoparticles

Element	Line Type	Wt%	Atomic %
C	K series	4.92	12.55
O	K series	27.2	52.06
Ni	K series	67.87	35.39
Total:		100	100

3.4.2 Elemental detection of NiO/PANI nanocomposites

Figure 11 represents elemental detection by SEM-EDS of NiO/PANI. The EDS spectrum shows the presence of several elements, indicating a complex material composition.:

- **Ni peaks:** The prominent peaks around 8.3 keV and 7.5 keV are characteristic of nickel (Ni), confirming the presence of nickel oxide (NiO) in the sample.

- **O peak:** The peak around 0.5 keV corresponds to oxygen (O), which is expected in NiO and also present in the polymer matrix.
- **N peak:** The peak around 0.4 keV is attributed to nitrogen (N), a key component of polyaniline (PANI).
- **C peak:** The large peak at around 0.3 keV is likely from carbon (C), a major constituent of PANI.
- **S peak:** A smaller peak around 2.3 keV indicates the presence of sulfur (S), which could be from a dopant in the PANI.
- **Cl peak:** A small peak at around 2.6 keV suggests the presence of chlorine (Cl), potentially from a dopant in the PANI.

Overall, the EDS spectrum provides strong evidence for the successful synthesis of a NiO/PANI composite material. The presence of Ni, O, N, and C confirms the expected components. The additional peaks for S and Cl might be due to dopants or impurities introduced during the synthesis process.

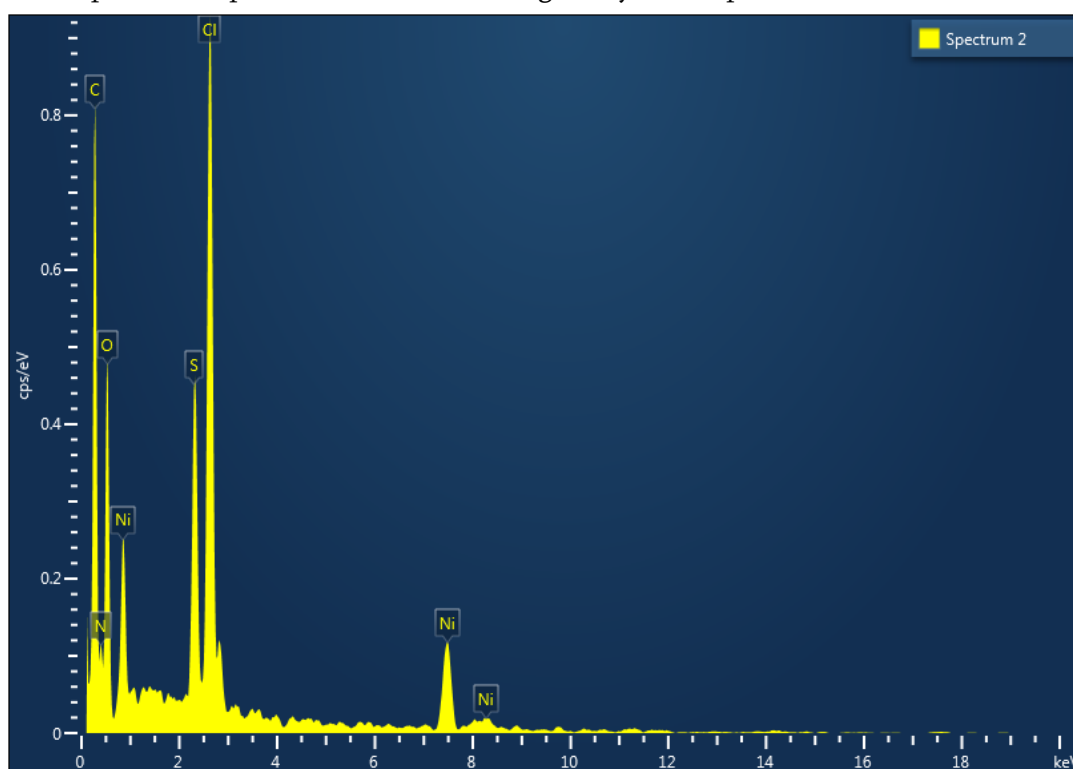


Figure 11: EDS spectra of NiO/PANI

Table 2: Elemental detection of NiO/PANI nanocomposites

Element	Line Type	Wt%	Atomic %
C	K series	53.07	65.64
N	K series	7.01	7.44
O	K series	21.73	20.18
S	K series	3.52	1.63
Cl	K series	8.45	3.54
Ni	K series	6.21	1.57
Total:		100	100

STUDY OF DEGRADATION PROPERTIES

4.1 Effect of photocatalysts on Crystal Violet (CV) dye in summer season

Figure 12 showed the photocatalytic degradation performances of NiO NPs and NiO-PANI NCs. It was evaluated using an initial concentration of dye (50 ppm), catalyst load (40 mg/ 50ml), and pH (9) under Sun light irradiation. This degradation study was observed in the month of March and April between 11:00 am to 4:00 pm using equiptronics colorimeter EQ 335. The degradation tendency was increased with the irradiation time and become constant after 120 min indicating that it is the maximum degradation time of these dye. The photocatalytic degradation performances of each photocatalyst were calculated using Eq. (2) and summarized in Table 3.

$$\% \text{ of degradation} = \frac{A_0 - A_t}{A_0} \times 100 \quad 2$$

where A_0 - and A_t - the absorbance of dye at initial stage and at the reaction time "t".

Table 3. Photocatalytic degradation of Crystal Violet (CV) dye using 50 ppm dye concentration, 50 mg catalyst load, and pH 9 at room temperature under Sun light irradiation.

Time in min	NiO	NiO/PANI
30	54.00	0.50
60	54.67	37.69
90	41.33	41.21
120	49.33	51.76

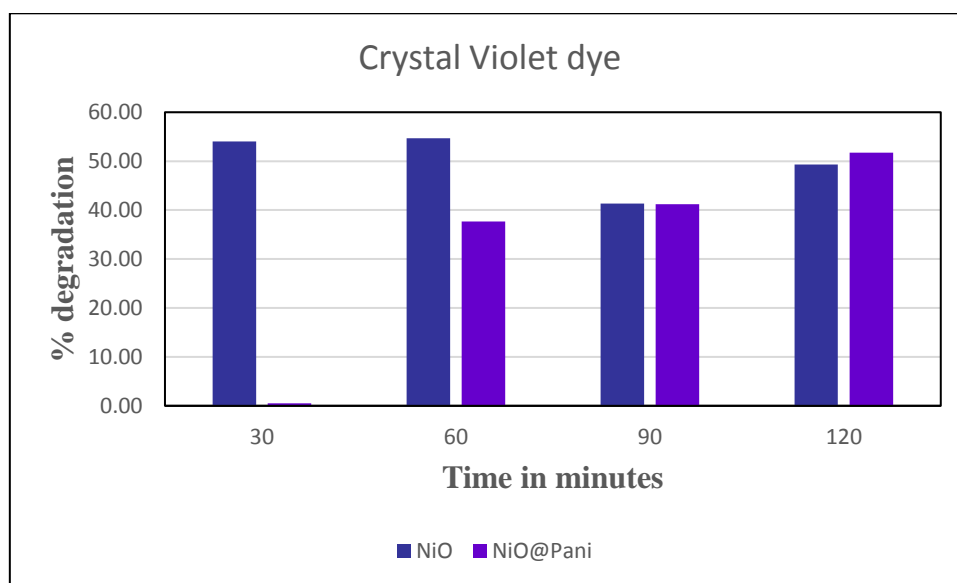


Figure 12: Photocatalytic degradation of Crystal Violet (CV) dye in summer

4.2 Effect of photocatalysts on Crystal Violet (CV) dye in winter season

Figure 13 showed the photocatalytic degradation performances of NiO NPs and NiO-PANI NCs. It was evaluated using an initial concentration of dye (40 ppm), catalyst load (40mg/50ml), and pH (9) under Sun light irradiation. The absorption of the dye is studied using JASCO UV-Visible spectrophotometer V-670 which shows maximum absorption of CV dye at 586 nm wavelength. This degradation study was observed in the month of October and November between 11:00 am to 4:00 pm. The degradation tendency was increased with the irradiation time and become constant after 120 min indicating that it is the maximum degradation time of

these dye. The photocatalytic degradation performances of each photocatalyst were calculated using Eq. (2) and summarized in Table 4.

Table 4. Photocatalytic degradation of Crystal Violet (CV) dye using 40 ppm dye concentration, 40 mg/50ml catalyst load, and pH 9 at room temperature under Sun light irradiation.

Time in min	NiO	NiO/PANI
60	52.66 %	41.61 %
120	79.00 %	69.50 %

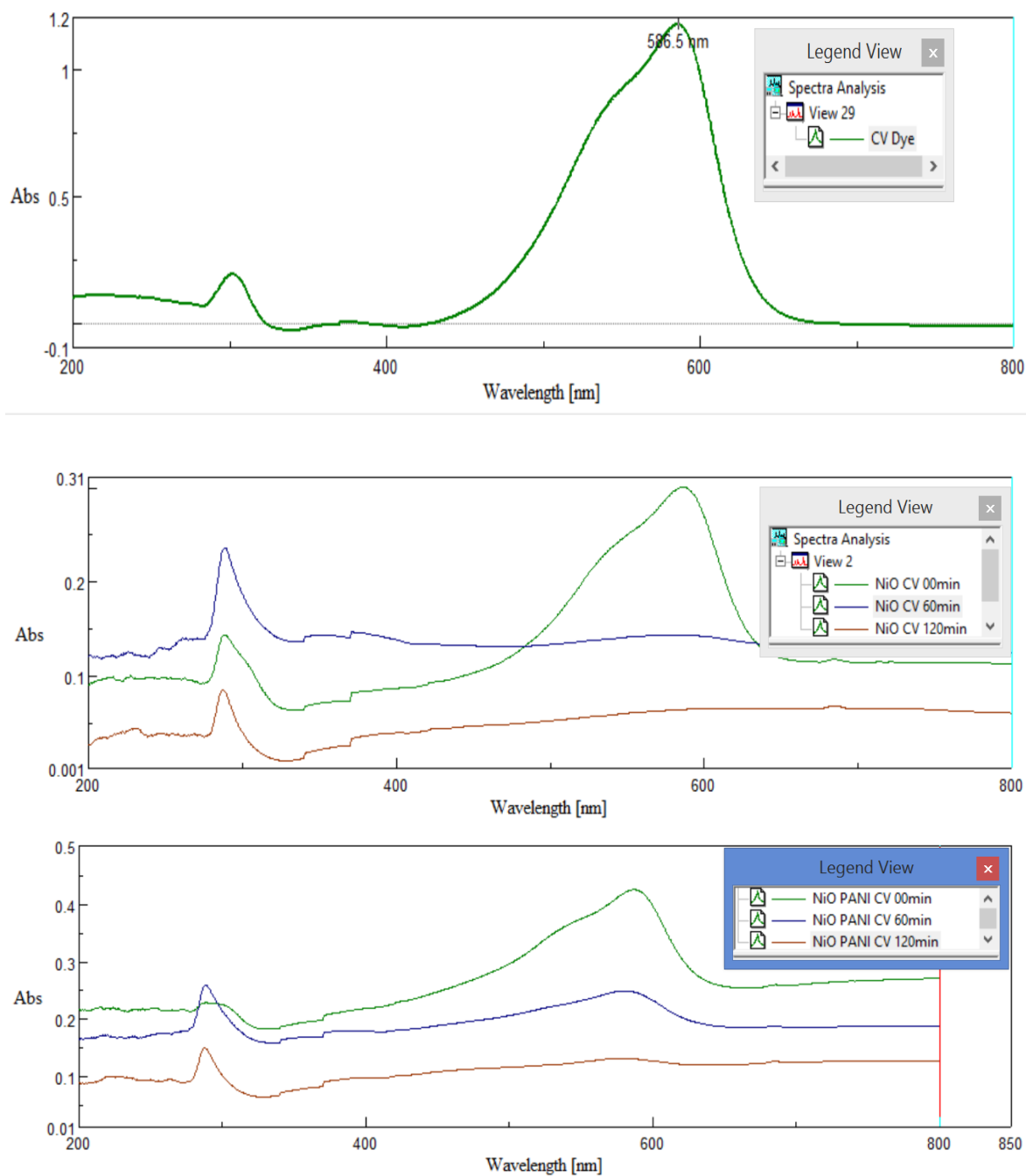


Figure 13: Photocatalytic degradation of Crystal Violet (CV) dye in winter

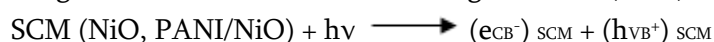
RESULT AND DISCUSSION

For NiO NPs, and NiO-PANI NCs catalysts after 120 min of retention time were found to be 49.33 and 51.76 % respectively in summer season. While in winter season, it gives 79.00 and 69.50 % respectively dye degradation.

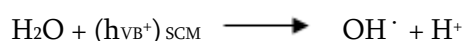
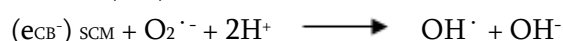
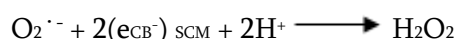
PHOTOCATALYTIC DEGRADATION MECHANISM

In the case of CP-metal oxide hybrid, CP acts as a photosensitizer to absorb a wide range of visible light because of the lower bandgap compared to pure metal oxide. The excited electrons in the LUMO of CP chains are injected into the CB of transition metal oxide or hybrid materials, which reacts with an adsorbed water molecule to form O_2^- radicals, whereas holes may react with water to form *OH .

The general understanding of the photocatalysis mechanism is that the photo absorption of a semiconducting material causes the electrons to excite from the valence band (VB) to the conduction band (CB), leaving positive holes in the VB resulting in the electron-hole pair e_{CB^-} / h_{VB^+} generation. It is known that PANI homopolymer is a conducting polymer. Photons are absorbed by the PANI homopolymer or the PANI/NiO catalyst when the energy ($h\nu$) is equal to or greater than the semiconductor band gap, and electron-hole pairs are generated in these semiconducting materials (SCM)

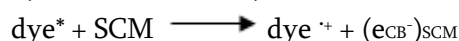
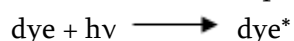


Then, the photogenerated electron-hole pairs migrate to the surface of the catalyst and react with the species adsorbed on the surface.

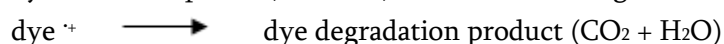
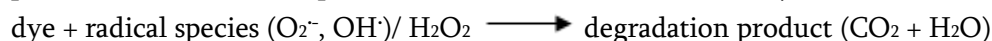


These reactions prevent the electron-hole pairs from recombining which increases the efficiency of photocatalytic activity.

A sensitized photocatalytic process may be able to be operated in the presence of a coloured organic compound; in this case the adsorbed dye molecules are excited by visible light and thus act as photosensitizers. The excited dye molecule subsequently transfers electrons into the conduction band of the PANI homopolymer or PANI/NiO nanocomposite, while the dye itself is converted to its cationic radical



These reactive species produced in the above manner can then react with the dye to form the degradation products and thus are responsible for the discoloration of CV dye.



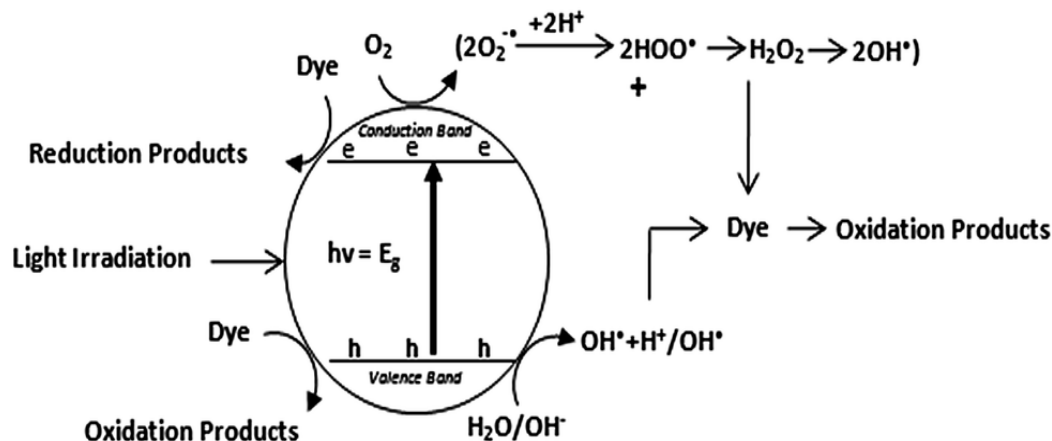


Figure 14: Dye degradation mechanism

CONCLUSIONS

For NiO NPs, and NiO-PANI NCs catalysts after 120 min of retention time were found to be 49.33 and 51.76 % respectively in summer season. While in winter season, it gives 79.00 and 69.50 % respectively dye degradation. In the current report, NiO NPs and NiO/PANI NCs were successfully synthesized via precipitation method in order to evaluate their degradation efficiency against CV dye in aqueous media. The surface properties of as-synthesized nanomaterials were characterized with the help of advance analytical tools such as ATR-FTIR, XRD, UV-Visible, SEM analysis.

The FTIR spectrum provides evidence for the presence of both NiO nanoparticles and PANI. The peaks in the $1500-1600\text{ cm}^{-1}$ and $1100-1300\text{ cm}^{-1}$ regions confirm the presence of PANI, while the peak around 550 cm^{-1} confirms the presence of NiO. The presence of both NiO and PANI in the spectrum suggests that the NiO nanoparticles are successfully incorporated into the PANI matrix.

The XRD pattern shows the presence of both NiO and PANI phases. The sharp peaks at specific 2θ values correspond to the crystalline NiO phase, while the broader peak around $2\theta = 25^\circ$ is characteristic of the amorphous PANI phase. The peaks corresponding to NiO can be indexed to a cubic structure, which is the typical crystal structure for NiO. The positions of the NiO peaks correspond to the characteristic diffraction angles (2θ values) of the planes in the NiO crystal lattice.

The SEM-EDS spectrum provides strong evidence for the successful synthesis of a NiO/PANI composite material. The presence of Ni, O, N, and C confirms the expected components. The maximum photocatalytic degradation efficiency was achieved 69.50 % using NiO/ PANI NCs against CV dye at 40 ppm of initial dye concentration, pH 9, and 40 mg/50ml catalyst dosage under direct sun light irradiation for 120 min. The result of this research work showed that, NiO/PANI NCs is one of the promising photocatalytic nanocomposites which could be generally applicable to the treatment of wastewaters effluents containing acidic dye molecules.

ACKNOWLEDGMENTS

The authors are thankful to Instrumentation facility, R. C. Patel institute of Pharmaceutical Education and Research BTECHI Shirpur, The instrument facility at SAIF, STIC, Cochin University, Kochi, Kerala, India for characterization studies. This work is financially supported by RUSA, New Delhi as funding agency.

REFERENCES

- [1]. Vosoughifar, Photodegradation of dye in waste water using CaWO₄/NiO nanocomposites; Coprecipitation preparation and characterization, *J. Mater. Sci.- Mater. Electron.* 29 (2018) 3194–3200.
- [2]. N. Duraisamy, K. Kandiah, R. Rajendran, S. Prabhu, R. Ramesh, G. Dhanaraj, Electrochemical and photocatalytic investigation of nickel oxide for energy storage and wastewater treatment, *Res. Chem. Intermed.* 44 (2018) 5653–5667.
- [3]. M. Qamar, M.A. Gondal, Z.H. Yamani, Synthesis of nanostructured NiO and its application in laser-induced photocatalytic reduction of Cr (VI) from water, *J. Mol. Catal. A – Chem.* 341 (2011) 83–88.
- [4]. S.R. Dave Sushma, Use of Nanoparticles in Water Treatment: A review *International Research Journal of Environment Science*, 4 (2015) 103–106.
- [5]. X. Cai, Y. Liu, H. Zeng, Y. Cai, H. Li, F. Zhang, Y. Wang, Synthesis and characterisation of alkali metal (Mn, Fe) oxide–ZnO nanorod composites and their photocatalytic decolourization of rhodamine B under visible light, *Mater. Technol.* 27 (2012) 380–387.
- [6]. P.P. Hung, T.T. Dat, D.D. Dung, N.N. Trung, M.H. Hanh, D.N. Toan, L.H. Bac, Effect of annealing temperature on structural, optical and visible-light photocatalytic properties of NiTiO₃ nano powders, *J. Electron. Mater.* 47 (2018) 7301–7308.
- [7]. B. Elahi, M. Mirzaee, M. Darroudi, R.K. Oskuee, K. Sadri, M.S. Amiri, Preparation of cerium oxide nanoparticles in *Salvia Macrosiphon Boiss* seeds extract and investigation of their photocatalytic activities, *Ceram. Int.* (2018).
- [8]. M.R. Esfahani, S.A. Aktij, Z. Dabaghian, M.D. Firouzjaei, A. Rahimpour, J. Eke, I.C. Escobar, M. Abolhassani, L.F. Greenlee, A.R. Esfahani, Nanocomposite membranes for water separation and purification: fabrication, modification, and applications, *Sep. Purif. Technol.* (2018).
- [9]. X. Ren, P. Gao, X. Kong, R. Jiang, P. Yang, Y. Chen, Q. Chi, B. Li, NiO/Ni/TiO₂ nanocables with Schottky/pn heterojunctions and the improved photocatalytic performance in water splitting under visible light, *J. Colloid Interface Sci.* 530 (2018) 1–8.
- [10]. Y.C. Sharma, V.S., V.K.S., S.N.K., C.H. Weng, Nano-adsorbents for the removal of metallic pollutants from water and wastewater, *Environ. Technol.* 330 (2009) 583–609.
- [11]. The application of nanoparticles for wastewater remediation, *Fut. Sci.* (2013).
- [12]. A.I. Uzaira Rafique, Abida K. Khan, Synthesis, characterization and application of nanomaterials for the removal of emerging pollutants from industrial waste water, kinetics and equilibrium model, *J. Water Sustain.* 2 (2012) 233–244.
- [13]. M. Chakhom, A. Boukhachem, M. Ghamnia, N. Benameur, N. Mahdhi, K. Raouadi, M. Amlouk, An attempt to study (111) oriented NiO-like TCO thin films in terms of structural, optical properties and photocatalytic activities under strontium doping, *Spectrochim. Acta Part A Mol. Biomol. Spectrosc.* 205 (2018) 649–660.
- [14]. T. Driscoll, K. Steenland, D.I. Nelson, J. Leigh, A. Pruss-Ustun, D.H. Campbell- Lendrum, C.F. Corvalan, A. Woodward, W.H. Organization, Occupational airborne particulates: Assessing the environmental burden of disease at national and local levels, 2004.
- [15]. E. Hammel, O.-R. Ighodaro, O. Okoli, Processing and properties of advanced porous ceramics: an application-based review, *Ceram. Int.* 40 (2014) 15351–15370.
- [16]. K. Ma, H. Zhou, Y. Xin, Study on catalytic performances and reaction mechanisms of graphene electroactive membrane in wastewater treatment, *Sep. Purif. Technol.* (2019).

- [17]. H. Najafian, F. Manteghi, F. Beshkar, M. Salavati-Niasari, Enhanced photocatalytic activity of a novel NiO/Bi₂O₃/Bi₃ClO₄ nanocomposite for the degradation of azo dye pollutants under visible light irradiation, *Sep. Purif. Technol.* 209 (2019) 6–17.
- [18]. S. Senobari, A. Nezamzadeh-Ejehieh, A comprehensive study on the enhanced photocatalytic activity of CuO-NiO nanoparticles: designing the experiments, *J. Mol. Liq.* 261 (2018) 208–217.
- [19]. F. Torki, H. Faghihian, Photocatalytic activity of NiS, NiO and coupled NiS-NiO for degradation of pharmaceutical pollutant cephalixin under visible light, *RSC Adv.* 7 (2017) 54651–54661.
- [20]. F. Tao, Y. Shen, L. Wang, Controlled fabrication of flower-like nickel oxide hierarchical structures and their application in water treatment, *Molecules* 17 (2012) 703–715.
- [21]. N. Julkapli, S. Bagheri, S.B. Abd Hamid, Recent advances in heterogeneous photocatalytic decolorization of synthetic dyes, *Sci. World J.* (2014).
- [22]. Y.Q. Wu, G.X. Lu, S.B. Li, Fabrication of NiO photocatalytic active center over TiO₂ and photocatalytic properties for H₂ production, *Chinese J. Inorg. Chem.* 26 (2010) 476–482.
- [23]. S. Dutta, S.A. Parsons, C. Bhattacharjee, P. Jarvis, S. Datta, S. Bandyopadhyay, Kinetic study of adsorption and photo-decolorization of Reactive Red 198 on TiO₂ surface, *Chem. Eng. J.* 155 (2009) 674–679.
- [24]. M. Ghaneian, M. Ehrampoush, S. Rahimi, G. Ghanizadeh, M. Askarshahi, Adsorption of Reactive Red 198 Dye on TiO₂ Nano-particle from, *Synthetic Wastewater* (2011).
- [25]. S. Dagher, A. Soliman, A. Ziout, N. Tit, A. Hilal-Alnaqbi, S. Khashan, F. Alnaimat, J. Qudeiri, Photocatalytic removal of methylene blue using titania-and silicacoated magnetic nanoparticles, *Mater. Res. Express* (2018).
- [26]. Z. Sabouri, A. Akbari, H.A. Hosseini, M. Darroudi, Facile green synthesis of NiO nanoparticles and investigation of dye degradation and cytotoxicity effects, *J. Mol. Struct.* (2018).
- [27]. M.A. Khalaf, Biosorption of reactive dye from textile wastewater by non-viable biomass of *Aspergillus niger* and *Spirogyra* sp, *Bioresour. Technol.* 99 (2008) 6631–6634.
- [28]. O. Vazquez-Cuchillo, A. Cruz-Lopez, L. Bautista-Carrillo, A. Bautista-Hernandez, L.T. Martinez, S.W. Lee, Synthesis of TiO₂ using different hydrolysis catalysts and doped with Zn for efficient degradation of aqueous phase pollutants under UV light, *Res. Chem. Int.* 36 (2010) 103–113.
- [29]. G. Thennarasu, A. Sivasamy, Enhanced visible photocatalytic activity of cotton ball like nano structured Cu doped ZnO for the degradation of organic pollutant, *Ecotoxicol. Environ. Saf.* 134 (2016) 412–420.
- [30]. K. Domen, A. Kudo, T. Onishi, Mechanism of photocatalytic decomposition of water into H₂ and O₂ over NiO.SrTiO₃, *J. Catal.* 102 (1986) 92–98.
- [31]. W. Song, X. Xu, Heterojunction YBiO₃-Bi₂O₃: synthesis, characterisation, and its highly photocatalytic activity under visible light, *Mater. Technol.* 32 (2017) 695–700.
- [32]. Darwish, M. Rashad, H.A. AL-Aoh, Methyl orange adsorption comparison on nanoparticles: Isotherm, kinetics, and thermodynamic studies, *Dyes and Pigments*, 160 (2019) 563–571.
- [33]. H.R. Pouretedal, H. Eskandari, M.H. Keshavarz, A. Semnani, Photodegradation of organic dyes using nanoparticles of cadmium sulfide doped with manganese, nickel and copper as nano photocatalyst, *Acta Chim. Slov.* 56 (2009).
- [34]. L. Pereira, R. Pereira, C.S. Oliveira, L. Apostol, M. Gavrilescu, M.N. Pons, O. Zahraa, M. Madalena Alves, UV/TiO₂ photocatalytic degradation of xanthene dyes, *Photochem. Photobiol.* 89 (2013) 33–39.
- [35]. F. Motahari, M.R. Mozdianfard, F. Soofivand, M. Salavati-Niasari, NiO nanostructures: synthesis, characterization and photocatalyst application in dye wastewater treatment, *RSC Adv.* 4 (2014) 27654–27660.

- [36]. J. Li, X. Zhu, F. Qiu, T. Zhang, F. Hu, X. Peng, Facile preparation of Ag/Ag₂WO₄/g-C₃N₄ ternary plasmonic photocatalyst and its visible-light photocatalytic activity, *Appl. Organomet. Chem.* (2018) e4683.
- [37]. E. Kirupavasam, G. Allen, G. Raj, Photocatalytic degradation of amido black-10B catalyzed by carbon doped TiO₂ photocatalyst, *Int. J. Green Chem. Bioprocess* 2 (2012) 20–25.

The Role of Influencer Marketing in Shaping Consumer Behavior in Sustainable Future

Sanika Puralkar, Dr. Neha Choudhary

Amity Business School Amity Business School, Amity University School

ARTICLE INFO

Article History:

Published : 30 April 2025

Publication Issue :

Volume 12, Issue 13

March-April-2025

Page Number :

74-80

ABSTRACT

In the rapidly evolving landscape of digital media, influencer marketing has emerged as a dominant and dynamic strategy that enables brands to form strong connections with their audiences. What once started as a niche promotional approach has now become an essential pillar in the marketing mix of most organizations. This paper investigates the effect of influencer marketing on consumer buying behavior, especially among young adults in India who are active on digital platforms like Instagram and YouTube. Through a carefully designed questionnaire shared via Google Forms and answered by 153 individuals, the study explores consumer trust, platform preferences, content types, and overall engagement patterns. The research delves into the nuances of influencer credibility, transparency, and consumer awareness. It also considers how social media platforms serve as powerful touchpoints for engagement and decision-making. The study concludes that influencer marketing has a significant impact on consumer behavior, but its effectiveness relies heavily on honesty, relatability, consistency, and alignment with user expectations. The paper ends with actionable suggestions for brands, influencers, and consumers, emphasizing ethical practices and relationship-driven communication.

Keywords: Influencer marketing, consumer psychology, digital platforms, authenticity, Instagram, YouTube, trust, promotion, youth behavior, social engagement

INTRODUCTION

The internet has drastically transformed the way individuals interact, consume information, and make purchasing decisions. With the rise of smartphones and widespread access to social media platforms, consumers now spend hours each day scrolling through posts, videos, and stories created by a wide range of content creators, including influencers. Influencers are not just celebrities or public figures but also everyday individuals who have built large followings by sharing relatable content and establishing a unique identity

within a niche. Whether it's lifestyle, beauty, fitness, travel, or technology, these influencers have become trusted voices in their respective fields.

In the Indian context, the rise of influencer marketing is especially significant among the urban youth. This demographic, typically aged 18 to 25, is known for its high digital engagement, openness to trends, and reliance on peer opinions. They are more likely to be persuaded by content that feels authentic and informative rather than overtly commercial. This paper focuses on this audience to explore how influencer content affects their purchase decisions, brand perception, and engagement patterns. It seeks to understand what makes influencer marketing effective, what kind of content resonates most, and how consumers differentiate between genuine advice and paid promotion.

REVIEW OF LITERATURE

The effectiveness of influencer marketing is grounded in various psychological and communication theories. These theories provide a framework for understanding why people listen to influencers and how their messages impact behavior.

- **Source Credibility Theory:** People are more likely to trust and act on information when it comes from someone they perceive as credible, which includes both expertise and trustworthiness.
- **Social Learning Theory:** Consumers often learn behaviors by observing others, especially those they admire or relate to. Influencers serve as role models, often shaping the habits and preferences of their audience.
- **Parasocial Interaction Theory:** Many users form one-sided relationships with influencers, feeling as though they “know” them personally. This emotional connection increases trust and receptiveness to their messages.

Academic and industry studies further support these ideas. Research shows that consumers are more responsive to content that feels genuine and experience-based. However, the effectiveness of influencer marketing decreases when followers perceive posts to be too promotional or lacking in transparency. Content relevance is also critical; promotions must align with the audience's interests and the influencer's usual messaging. Without this, campaigns risk seeming insincere and failing to connect with viewers.

Objectives of the Study

1. To examine how influencer marketing affects the purchasing behavior of urban youth.
2. To understand the factors that drive consumer trust in influencers.
3. To identify which platforms are most effective for influencer campaigns.
4. To explore the kinds of content that attract the most engagement.
5. To analyze how transparency influences consumer responses.
6. To assess how influencer marketing contributes to broader brand communication strategies.

RESEARCH METHODOLOGY

This chapter outlines the structured process followed to conduct the study titled “The Role of Influencer Marketing in Shaping Consumer Behavior.” It includes the research design, sampling process, data collection methods, tools used, and ethical consideration.

1. Research Design

The research follows a descriptive and analytical design. The descriptive part helped in understanding general consumer behaviors, habits, and preferences. The analytical element was used to identify relationships between variables—such as the level of trust in influencers and actual purchase decisions.

2. Type of Research

This study adopts a quantitative research method. This approach involves collecting numerical data from a large group of people and analyzing it to discover patterns, opinions, and behaviors. It allows for objective measurement and comparison across different groups.

3. Data Collection Method

Primary data was collected using a structured online questionnaire. The survey was created on Google Forms and contained multiple-choice and Likert-scale questions. These questions explored respondents' use of social media, their interaction with influencers, and how much that content affected their decisions.

4. Sampling Technique

The sampling method used was non-probability convenience sampling. This means participants were selected based on availability and willingness to participate. While not fully representative of all populations, it was suitable for reaching active social media users quickly and effectively.

5. Sample Size and Respondent Profile

The final sample included 153 valid responses. Key details include:

- Age Group: Mostly 18–25 years old
- Location: Urban areas in Maharashtra, India
- Platforms Used: Instagram and YouTube
- Engagement: All respondents were regular users of social media and had seen influencer content

This profile matches the target demographic for influencer campaigns and digital marketing efforts.

6. Scope of the Study

The study is limited to young urban Indian consumers who are active on digital platforms. It focuses mainly on Instagram and YouTube, where influencer engagement is highest. The study does not explore rural populations or traditional media like television or print ads.

7. Data Analysis Tools

The collected data was exported to Microsoft Excel, where it was sorted and analyzed. Graphs, charts, and percentage-based summaries were created to identify major trends. Each of the selected survey questions was broken down and interpreted clearly.

8. Ethical Considerations

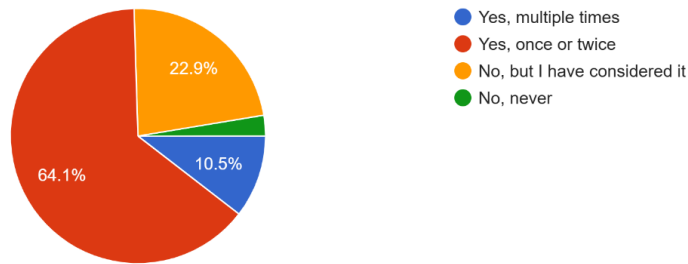
All participants were informed that the study was being conducted for educational purposes only. They were assured of anonymity and confidentiality. No personal data was collected, and participation was completely voluntary.

Data Analysis and Interpretation

Out of all the survey questions, seven were selected based on their direct relevance to the study's main goals. Below is a summary of the responses and interpretations:

Q1: Have you ever made a purchase based on an influencer's recommendation?

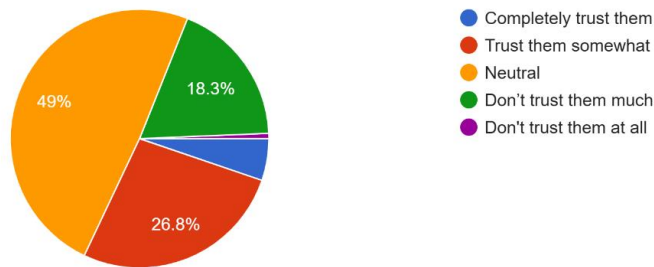
Have you ever followed an influencer's recommendation and bought a product?
153 responses



- A large majority answered yes, either occasionally or frequently.
Interpretation: Influencers can directly motivate purchases, indicating strong influence over consumer decisions.

Q2: How much do you trust influencer recommendations?

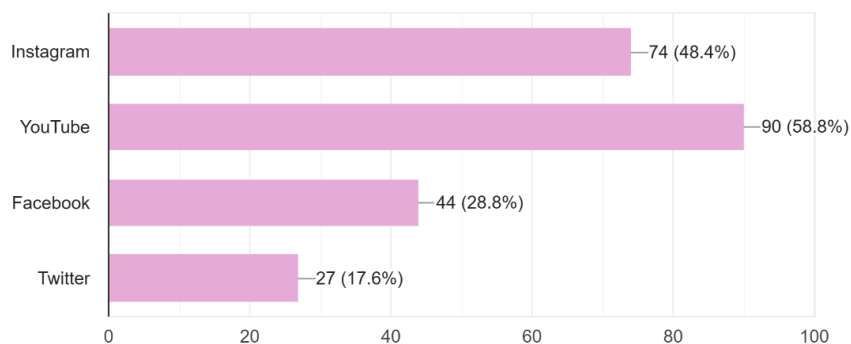
How much do you trust the recommendations given by influencers?
153 responses



- Most people said they trust influencers to some extent but prefer to double-check the information.
Interpretation: Trust exists, but it is cautious. Influencers need to maintain credibility to retain their influence.

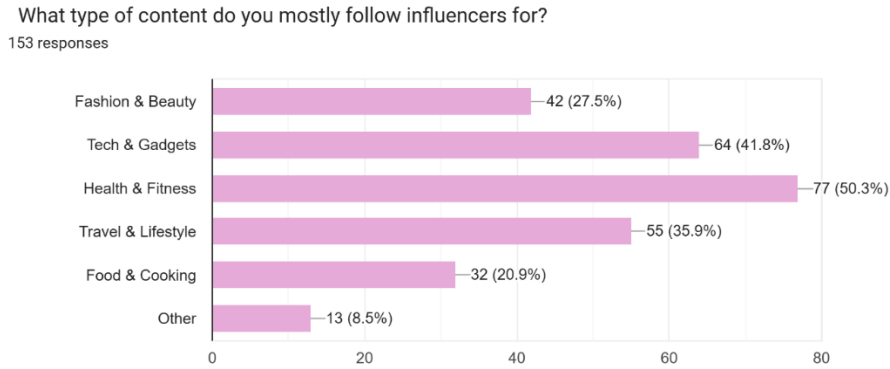
Q3: Which platforms do you use the most for influencer content?

Which social media platforms do you use most frequently?
153 responses



- Instagram and YouTube were overwhelmingly popular.
Interpretation: These platforms are visually rich and interactive, making them ideal for influencer engagement.

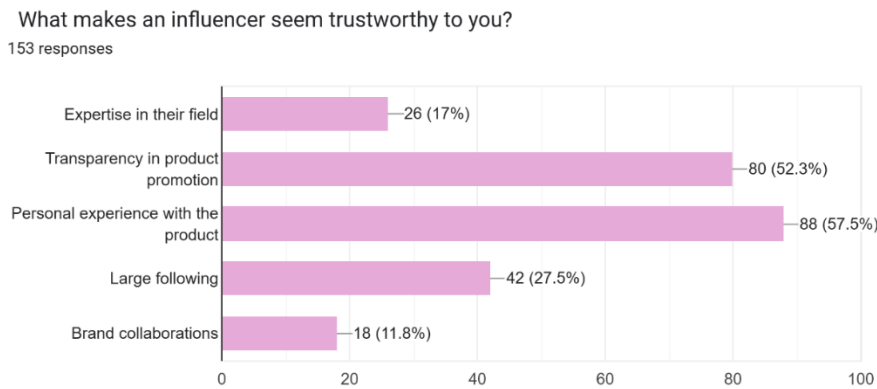
Q4: What kind of influencer content do you follow?



- Health, fitness, tech, and lifestyle were among the top choices.

Interpretation: Audiences prefer content that is useful, inspiring, or educational.

Q5: What makes you trust an influencer?

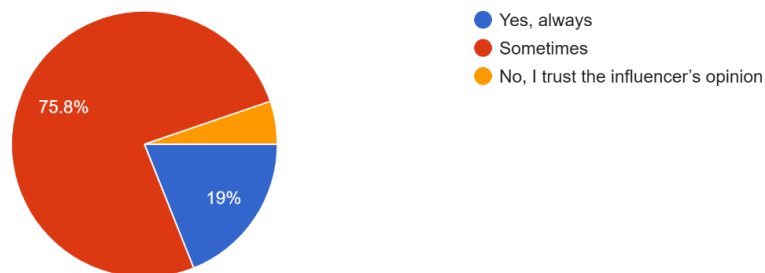


- Personal stories and openness about brand collaborations were most appreciated.

Interpretation: Authenticity and transparency are critical to building trust.

Q6: Do you research products before buying them, even after seeing an influencer promote them?

Do you verify product reviews from other sources before purchasing an influencer-promoted product?
153 responses

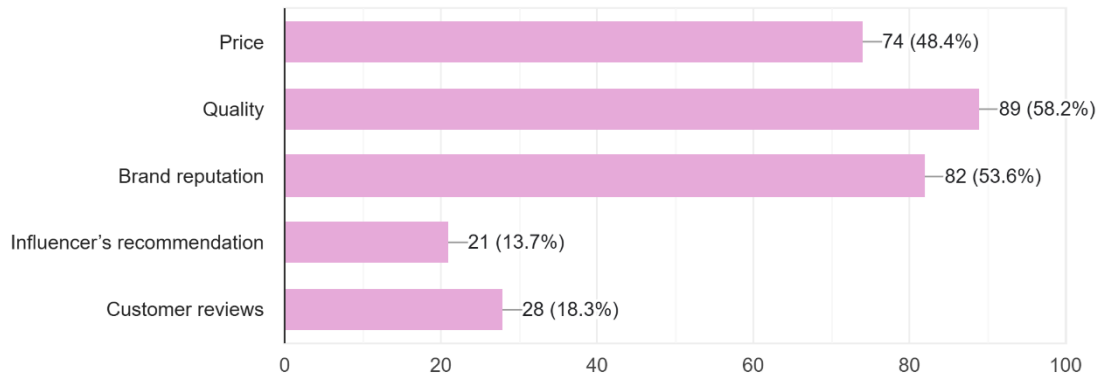


- Most respondents said yes.

Interpretation: Influencers trigger interest, but consumers still seek reassurance before making a purchase.

Q7: What influences your final buying decision the most?

What factor influences your decision the most when buying an influencer-promoted product?
153 responses



- Product quality and brand reputation ranked higher than the influencer's recommendation. Interpretation: While influencers spark awareness, the ultimate decision is based on the perceived value of the product itself.

Findings

1. Influencer marketing strongly affects the awareness and initial interest of young consumers.
2. Trust is present but not absolute—most people verify claims before acting.
3. Instagram and YouTube are the most influential platforms for digital marketing.
4. Practical and relatable content attracts more engagement.
5. Influencers who are transparent and consistent gain more trust.
6. Product-related features ultimately determine purchase decisions, not endorsements alone.

Limitations of the Study

- The use of convenience sampling limits generalizability.
- The study is geographically limited to Maharashtra.
- Only young adults were included, leaving out other age groups.
- The survey was conducted online, possibly excluding those with limited internet access.

CONCLUSION

This study concludes that influencer marketing is a powerful force in the modern digital landscape. It leverages emotional connection, relatability, and accessibility to guide consumer behavior. However, the impact of influencer marketing depends heavily on how authentic and useful the content is. Young consumers are aware, skeptical, and smart—they value trust and transparency above flashy visuals or aggressive selling. Therefore, influencer marketing should evolve into a more responsible, consumer-friendly strategy that puts honest communication at the center. For brands, influencers, and users to all benefit, long-term trust must be the goal.

Suggestions

- For Brands: Collaborate with influencers whose content aligns with your brand ethos. Give them creative control for more authentic storytelling.

- For Influencers: Maintain honesty. Limit promotions to brands you genuinely support. Share detailed, experience-based content.
- For Consumers: Stay informed. Don't rely solely on influencer opinions—combine their input with personal research.
- For Policymakers: Create clearer guidelines for disclosure and ethical content sharing.
- For Platforms: Promote transparency tools and penalize deceptive marketing practices.

REFERENCES

- [1]. Bandura, A. (1977). *Social Learning Theory*. Englewood Cliffs, NJ: Prentice-Hall.
- [2]. Hovland, C. I., Janis, I. L., & Kelley, H. H. (1953). *Communication and Persuasion: Psychological Studies of Opinion Change*. Yale University Press.
- [3]. Horton, D., & Wohl, R. R. (1956). Mass communication and para-social interaction. *Psychiatry*, 19(3), 215-229.
- [4]. Jin, S. V., & Phua, J. (2014). Following celebrities' tweets about brands: The impact of Twitter-based electronic word-of-mouth on consumers' source credibility perception, buying intentions, and social identification with celebrities. *Journal of Advertising*, 43(2), 181–195.
- [5]. De Veirman, M., Cauberghe, V., & Hudders, L. (2017). Marketing through Instagram influencers: The impact of number of followers and product divergence on brand attitude. *International Journal of Advertising*, 36(5), 798–828.
- [6]. Evans, N. J., Phua, J., Lim, J., & Jun, H. (2017). Disclosing Instagram influencer advertising: The effects of disclosure language on advertising recognition, attitudes, and behavioral intent. *Journal of Interactive Advertising*, 17(2), 138–149.
- [7]. Statista Research Department. (2023). Social Media Usage in India. Retrieved from <https://www.statista.com/statistics/255146/number-of-internet-users-in-india/>
- [8]. Influencer Marketing Hub. (2023). What is Influencer Marketing?. Retrieved from <https://influencermarketinghub.com/what-is-influencer-marketing/>
- [9]. Google Forms. (2025). Primary Survey Data: Influencer Marketing and Consumer Behavior.
- [10]. Sharma, S. (2021). *Digital Marketing Fundamentals*. New Delhi: SAGE Publications India.

Synthesis and Characterization Study of Ecofriendly $\text{Cu}_2\text{ZnSnS}_4$ Thin Films by Economical Chemical Bath Deposition Method

Sandesh B. Jirage^{*1}, Kishor V. Gaikwad², Harshali Dhotre¹, Komal Ghanwat¹, Monali Sawant¹

¹Department of Chemistry, Karmaveer Bhaurao Patil College, U-Islampur, Dist- Sangli, 415409, Maharashtra, India

²Department of Chemistry, Rajarshi Chhatrapati Shahu College, Kolhapur, Maharashtra, India

ARTICLE INFO

Article History:

Published : 30 April 2025

Publication Issue :

Volume 12, Issue 13

March-April-2025

Page Number :

81-87

ABSTRACT

The rapid depletion of limited fossil fuels with increasing energy demand makes scientific community to focus on use of renewable energy sources like solar energy. The over dependence on fossil fuel also main cause of global warming, pollution which causes permanent damage to environment. In view of future environment sustainability is concerned the present thin film solar cell technology needs semiconductor material made up of earth abundant elements, low-cost and environment best elements to meet serious energy crises globally. The $\text{Cu}_2\text{ZnSnS}_4$ (CZTS) thin film is considered one of them best as economical and greener photovoltaic semiconductor material because of its superior properties like high absorption coefficient greater and optimum band gap for solar light absorption. The CZTS has made from very safe and naturally plentiful elements in earth's crust. So far we have used low cost chemical bath deposition technique for synthesis of greener $\text{Cu}_2\text{ZnSnS}_4$ (CZTS) thin films. The films were studied by characterization techniques like X-Ray diffraction, Raman scattering, optical absorbance, electrical conductivity, scanning electron microscopy, The analysis revealed a polycrystalline, stable kasterite structure of CZTS thin films in a excellent stoichiometric and with 1.5 eV optimum band gap.

Keywords-Thin films; CZTS; polycrystalline, kasterite etc.

INTRODUCTION

The whole world have been troubled complicated environmental issues like global warming, pollution, climate changes due to enormous utilization of fossil fuel which major cause of environmental damage. To overcome increasing energy crises with complete balance of environment, the solar energy is greener renewable option than any other limited resources. The solar energy is based on photovoltaic technology. The recent PV market of thin film solar cell has been commercialized by silicon, cadmium telluride (CdTe) and copper indium gallium di-selenide (CIGS) as semiconductor materials. But these materials possesses limitations associated with

major drawbacks like high processing costs of silicon, composition of rare earth elements like In Ga and toxicity of elements like Cd [1,2]. Hence Si, CIGS and CdTe materials will not be helpful in future so as to satisfy energy need with maintenances of green environment.

The current PV technology needs absorber materials composed of earth abundant material with low cost and less toxic to environment. In this regard, copper based chalcogenide material like, $\text{Cu}_2\text{ZnSnS}_4$ (CZTS) has being explored extensively as environment best promising absorber materials due to of their excellent optoelectronic properties band gap 1.5 eV and having as high as absorption coefficient over 10^4 cm^{-1} [3-5]. The CZTS is the p-type semiconductor material with composition of highly earth abundant, nontoxic and readily affordable in comparisons to CIGS and CdTe. The CZTS has two primary structures kasterite type (space group I4) and stannite type (space group I42m) which are structurally which are due to different arrangements of Cu^{+1} and Zn^{+2} atoms in the crystal structure [6]. However, Kasterite CZTS is thermodynamically more stable [7]. Further CZTS is quaternary semiconductor compound which is actually derivative of the chalcopyrites ($\text{CuInS}_2/\text{CuGaS}_2$) obtained by replacing In or Ga. Overall CZTS is a substitute absorber material as an for CIGS and CdTe as low-cost absorber layers.

So far CZTS thin films have been prepared by a number of techniques such as RF magnetron sputtering deposition [8], thermal evaporation [9], atom electron-beam-evaporation [10], pulsed laser deposition [11], etc but these methods vacuum metods which are costlier due to high temperature processes and specially designed equipments are needed. Other non-vacuum methods involves sol-gel deposition [12], spray pyrolysis [13], chemical vapor deposition [14], spin coating technique [15], electrodeposition methods [16], nanoparticle methods [17], silar method [18] etc. To date, the solar cell based on pure CZTS, have achieved power conversion efficiency as high as 9.2 % [19]. Hence there is need for improvement because CZTS is foremost perspective supernatural material to develop low cost, eco-friendly solar cells with high efficiency.

The chemical bath deposition method has attracted a wide attention of researchers because of its simple, economical equipments and low-temperature processes [20]. It does not involves to use toxic solvents like hydrazine etc. and hence it is considered as reliable method.

In this paper we report on synthesis of CZTS using above mentioned chemical bath method and its characterization. This attempt of synthesis of give microcrystalline, kasterite CZTS thin films having typical rock-like morphology. The films were characterized by X-Ray diffraction, Raman spectroscopy, optical absorbance, electrical conductivity, scanning electron microscopy, EDS techniques.

EXPERIMENTAL METHODS

2.1 Preparation of reagents

The chemicals used like copper sulphate [$\text{Cu}(\text{SO}_4)\cdot 5\text{H}_2\text{O}$], zinc sulphate ($\text{ZnSO}_4\cdot \text{H}_2\text{O}$), stannic chloride ($\text{SnCl}_4\cdot 5\text{H}_2\text{O}$), Thiourea, liquor ammonia (25% liq. NH_3), etc were of analytical grade (A. R). Their relevant solutions were prepared by using double distilled water. The films were deposited on commercially available, non-conducting micro-glass slides (Blue Star, India) having dimensions of 75 x 25 x 1.35 mm. The slides were cleaned by washing with chromic acid for about fifteen minutes followed by rinsing in acetone, distilled water and then subjected for deposition.

2.2 Deposition of CZTS Thin Films

In a typical experiment of deposition of CZTS thin film, 10 ml CuSO_4 , 5 ml ZnSO_4 , 5 ml SnCl_4 (all these of 0.1 M conc.) taken in 250 ml beaker followed by drop-wise addition of complexing agent liquor ammonia (40 mL) immediately followed by 20 mL (0.2 M) of thiourea was added as sulphur source slowly at room temperature. The final volume was maintained to 200 mL by using double distilled water. The pH of the reactive mixture

was adjusted at 9.0. The beaker was then kept hot magnetic stirrer in an oil bath. The clean glass slides, vertically positioned on a specially designed substrate holder, were rotated in the reaction mixture with a precisely controlled speed of 40 rpm. The temperature of the bath was then allowed to increase slowly up to 35 °C in a period of 150 minutes. After the specific time, the slides were removed from substrate holder, washed several times with double distilled water and subjected to dry.

2.3 Characterization

The XRD study of the CZTS thin film was carried out in the diffraction angle (2θ) range of 10–80° with $\text{CuK}\alpha 1$ ($\lambda = 1.54056 \text{ \AA}$) radiation using a Philips PW-1710 diffractometer. The Raman spectrum was recorded at room temperature by Raman microscope operating at excitation wavelength 532 nm. The thickness of the film was estimated by using a weight difference method. The electrical conductivity of the CZTS thin film was measured using a ‘dc’ four probes (equal spacing) method. The optical absorption measurements were made in the wavelength range 400–1200 nm by using a UV 3600 Shimadzu UV-VIS-NIR double beam spectrophotometer at room temperature. Scanning electron microscopy (SEM) was used for surface morphology and other microscopic observations.

RESULTS AND DISCUSSION

3.1 Structural characterization

The XRD patterns of the annealed CZTS thin film at 473 K in the air (for 2 h) are shown in Fig.1a. The peaks of CZTS thin film at the 2θ angles; 22.78, 28.42, 32.73, 42.27 and 58.83 corresponding diffraction originating plane having indices of (110), (112), (200), (220) and (224) are exactly matches to JCPDS card number 26-0575 for CZTS. The main diffraction peaks indexed to (112) point out Kasterite structure of CZTS which is recognized most stable form thermodynamically CZTS structure [21]. The major peaks in annealed film indicates that formations of kasterite and slight nanocrystalline form of CZTS. The crystallite size (D) of CZTS detected by Debye-Scherrer’s formula.

$$D = 0.9\lambda / \beta \cos \theta \quad (1)$$

Where λ -Wavelength of X-ray (\AA), β -FWHM intensity in radian, θ -Bragg’s diffraction angle. The calculated crystallite size from more intense peak (112) of CZTS using Full Width Half Maximum (FWHM) which was found to be 79.37 nm. This approves that CZTS film composed of nanocrystals. Besides X-ray analysis Raman spectroscopy measurements were done. The Figure 2 shows RAMAN peaks of the annealed CZTS thin film at 573 K in the air (for 2 h). The Raman spectrum gives evidence of peaks presence at 285, 335, 366 cm^{-1} which have been also attributed to the pure kasterite CZTS without [22].

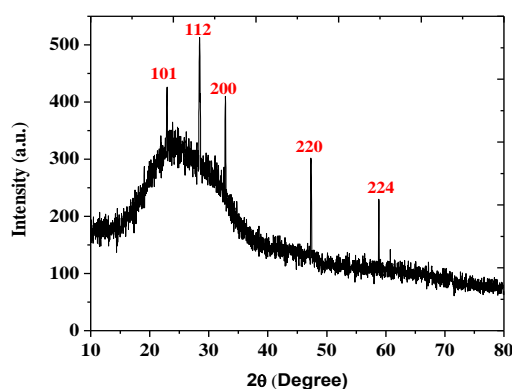


Fig. 1 X-ray diffraction patterns of annealed CZTS thin films.

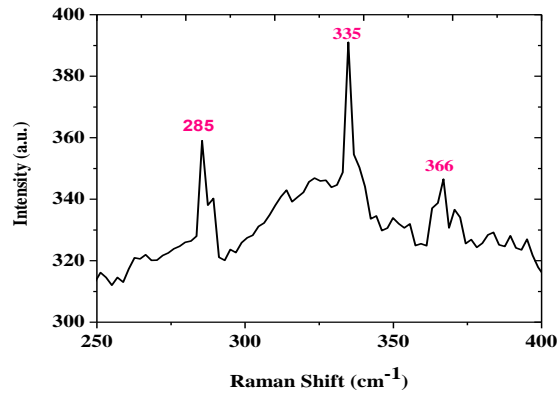


Figure 2. Raman spectrum of annealed CZTS thin films.

3.2 Morphological and compositional Analysis

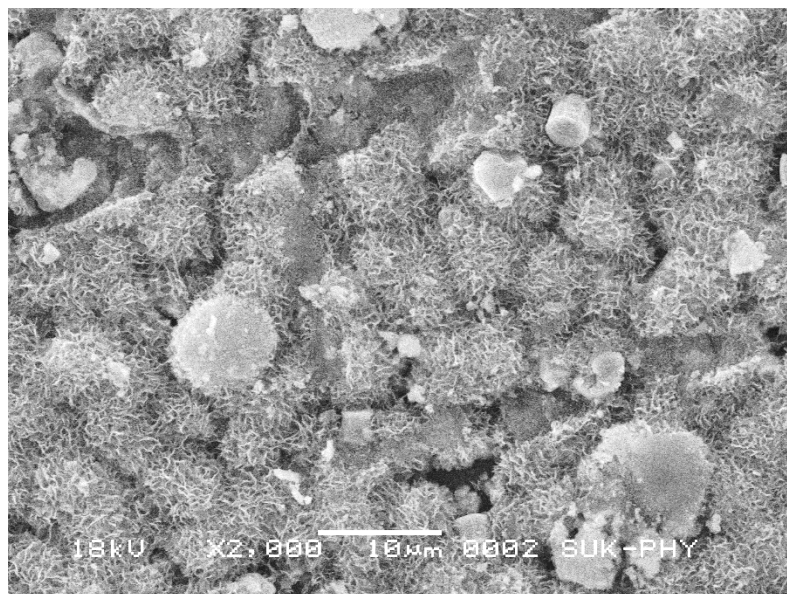
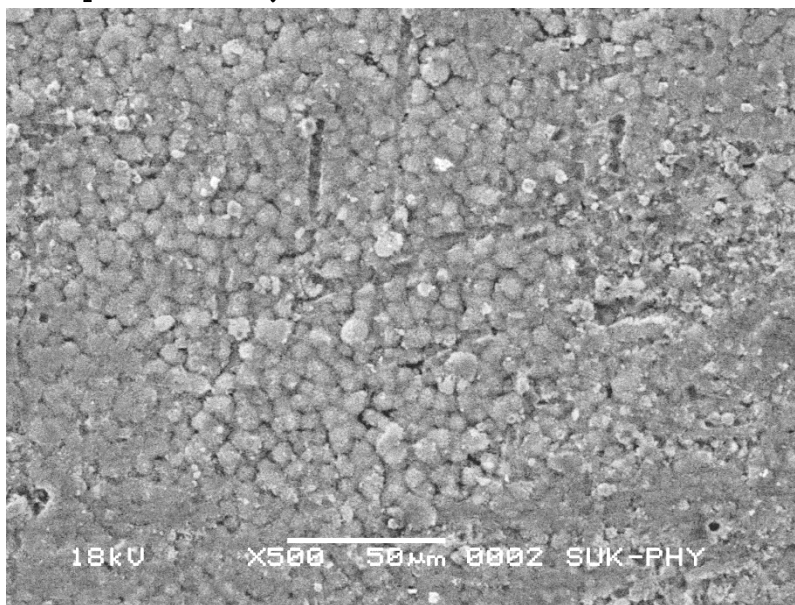


Fig 3 Scanning electron micrographs of rock like morphology of CZTS.

Scanning electron microscopy is the most useful technique for the study and examination of surface morphology, microstructure features of the thin films. The scanning electron micrographs of the annealed CZTS thin film are shown in Fig. 3 under 15000 X magnifications. The surface morphology exhibited by the annealed at 400 °c CZTS is rock-like with an almost uniform texture and larger in thickness (Fig.2a). From figures it is seen clearly that uniform morphology of films without any cracks and voids in the absorber or at the substrate interphase indicates that homogeneous distribution of the CZTS through the film and no existence of any impurities.

3.3 Optical properties of CZTS

The optical absorption spectrum of the CZTS thin film was recorded on a double beam spectrophotometer at the wavelength range of 400 to 1000 nm Fig. 4 shows the optical absorption spectrum of the annealed CZTS thin film. The optical absorption spectrum of CZTS thin film. The variation of the absorption coefficient function i.e. $\alpha = f(h\nu)$ with wavelength is shown in Fig. 4a. The band gap of a material obeys the relation near the absorption edge, this is according to S. Mushtaq et al. [23].

$$h\nu = B(h\nu - E_g)^x \quad (2)$$

Where B is a constant, $h\nu$ is the wavelength of the light used, E_g is the band gap of the material and x is a factor that depends on the kind of transitions involved. The extrapolation of a linear portion of the graph gives a direct band gap (E_g) of 1.5eV at room temperature. The value of the band gap is good agreement with the reported value of CZTS (1.5 eV) [9-10].

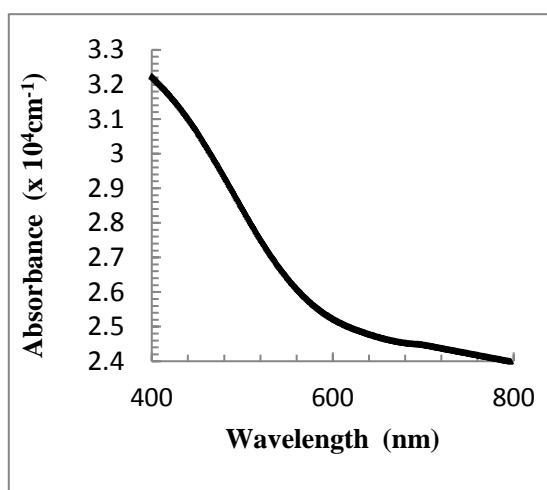


Fig. 4a Optical absorption spectrum

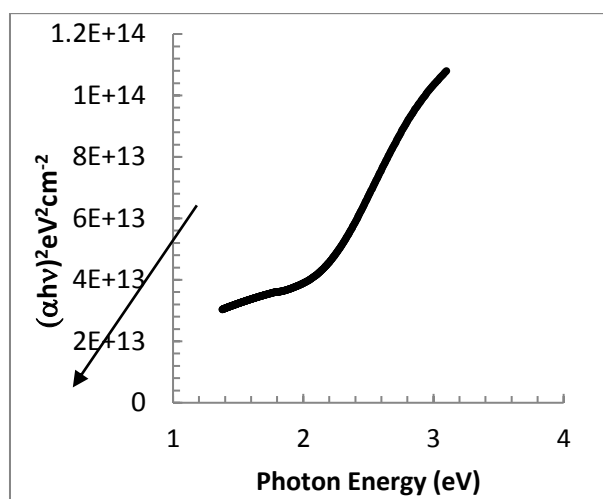


Fig. 4b Plot of $(\alpha h\nu)^2$ vs. $h\nu$ of CZTS thin film.

3.4 Electrical conductivity

The type of conductivity of a film material can be determined from the temperature dependence of the electrical resistivity of the material which follows the Arrhenius relation:

$$\rho = \rho_0 \exp\left(-\frac{E_a}{kT}\right) \quad (3)$$

where E_a is the activation energy, k is the Boltzmann constant; T is the absolute temperature, and ρ and ρ_0 are the resistivity and specific resistivity, respectively. The nature of the $\log \rho$ vs. inverse absolute temperature plot is linear, indicating that there is the presence of only one type of conduction mechanism. (Fig. 5). The thermoelectric emf generated when a temperature gradient was applied across the length of CZTS film showed a positive polarity toward the cold end indicating the p-type semiconducting behavior of CZTS thin films [24].

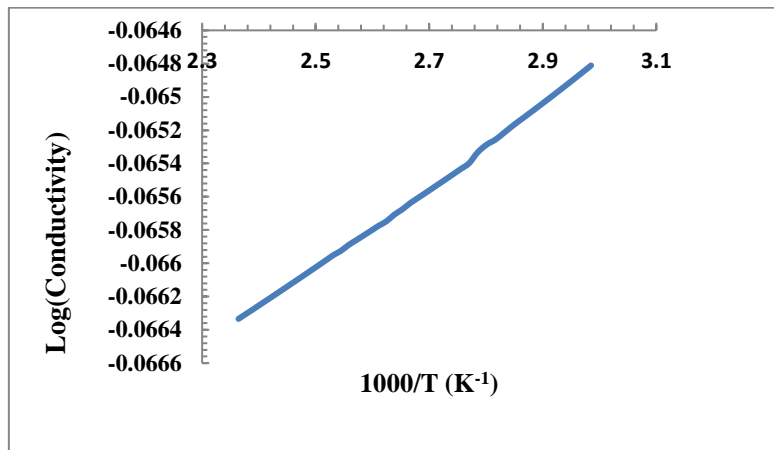


Figure 5 Plot of log conductivity vs. inverse absolute temperature.

CONCLUSION

It is economical chemical bath deposition method resulted kasterite, polycrystalline CZTS thin films. The kasterite structure further confirmed by Raman study. The SEM study shows unique rock-like morphology. The CZTS film exhibits high absorption coefficient, and direct band gap of 1.5 eV. The conductivity measurement showed a single type of conduction.

ACKNOWLEDGEMENTS

The authors SBJ and VMB are grateful to the Shivaji University, Kolhapur, India for giving permission to carry out the research work.

REFERENCES

- [1]. M.P. Suryawanshi, G.L. Agawane, S.M. Bhosale, S.W. Shin, P.S. Patil, J.H. Kim and A.V. Moholkar, *Materials Technology* 28 (1&2) (2013) 98.
- [2]. A. Wangperawong, J.S. King, S.M. Herron, B.P. Tran, K. Pangan-Okimoto, S.F. Bent, *Thin Solid Films*, 519 (2011) 2488-249
- [3]. K. Ito, T. Nakazawa, *Jpn. J. Appl. Phys.*, 27 (1988) 2094-2097.
- [4]. K. Tanaka, M. Oonuki, N. Moritake, H. Uchiki, *Sol. Energy Mater. Sol. Cells* 93(2009)583-587.
- [5]. H. Katagiri, K. Jimbo, W.S. Maw, K. Oishi, M. Yamazaki, H. Araki, A. Takeuchi, *Thin Solid Films* 517 (2009) 2455–2460
- [6]. S. Y. Chen, X. G. Gong, A. Walsh and S. H. Wei, *Appl. Phys. Lett.*, 94 (2009) 041903.
- [7]. S. Schorr, *Thin Solid Films*, 515(15) (2007) 5985-5991
- [8]. M.A. Olgar, J. Klaer, R. Mainz, L. Ozyuzer, T. Unold, *Thin Solid Films* 628 (2017) 1-6
- [9]. B. Shin, Y. Zhu, T. Gershon, N.A. Bojarczuk, S. Guha, *Thin Solid Films*, 556 (2014) 9-12
- [10]. H. Katagiri, K. Saitoh, T. Washio, H. Shinohara, T. Kurumadani, S. Miyajima, *Sol. Energy Mater. Sol. Cells* 65 (2001) 14-148.
- [11]. A.V. Vanalakar, S.W. Shin, G.L. Agawane, M.P. Suryawanshi, K.V. Gurav, P.S. Patil, and J.H. Kim, *Journal of Alloys and Compounds* 619 (2015) 109–121.
- [12]. L. Dong, S. Cheng, Y. Lai, H. Zhang, H. Jia, *Thin Solid Films* 626 (2017) 168–172

- [13]. S.A. Khalate, R.S. Kate , J.H. Kim, S.M. Pawar, R.J. Deokate *Superlattices and Microstructures* 103 (2017) 335e342
- [14]. T. Washio, T. Shinji, S. Tajima, T. Fukano, T. Motohiro, K. Jimbo and H. Katagiri, *J. Mater. Chem.*, 2012, 22, 4021
- [15]. K. Liu, B. Yao, Y. Li, Z. Ding, H. Sun, Y. Jiang, G. Wang and D. Pan, *J. Mater. Chem. C*, 5 (2017) 3035-3041
- [16]. K.V. Gurav, S.M. Pawar, S. W. Shin, M.P. Suryawanshi, G.L. Agawane, P.S. Patil, J.H. Moon, J.H. Yun, and J.H. Kim, *Applied Surface Science* 283 (2013) 74– 80
- [17]. M.P. Suryawanshi, S. W. Shin, U. Ghorpade, D. Song, C. W. Hong, S. Han, J. Heo, S. H. Kang and J. H. Kim, *J. Mater. Chem. A*, 5 (2017), 4695
- [18]. M.P. Suryawanshi, S.W. Shin, U.V. Ghorpade , K.V. Gurav, C.W. Hong, G.L. Agawane, S.A. Vanalakar, J.H. Moon, J. H. Yun, P.S. Patil, J. H. Kim, A.V. Moholkar, *Electrochimica Acta* 150 (2014) 136–145
- [19]. T. Kato, H. Hiroi, N. Sakai, S. Muraoka, and H. Sugimoto, *Proceedings of the 27th European Photovoltaic Solar Energy Conference, Frankfurt, Germany, 2012*, pp. 2236–2239
- [20]. T. R. Rana, N.M. Shinde and J.H. Kim, *Materials Letters*, 162 (2016) 40-43.
- [21]. J. Tao, K. Zhang, C. Zhang, L. Chen, H. Cao, J. Liu, J. Jiang, L. Sun, P. Yang and J. Chu, *Chem. Commun.*, 51 (2015) 10337–10340.
- [22]. M.P. Suryawanshi, S.W. Shin, K.V. Gurav, C. W. Hong, J. H. Yun, P.S. Patil, J. H. Kim, A.V. Moholkar, *Solar Energy* 110 (2014) 221–230
- [23]. S. Mushtaq, B. Ismail, M. A. Zeb, N. J. S. Kissinger and A. Zeb, *J. Alloys Compd.*, 632 (2015) 723–728.
- [24]. J. J. Scragg, P. J. Dale and L. M. Peter, G. Zoppi, *Phys. Status Solidi b* 245 (2008) 1772-1778.

Electricity Generation with Piezoelectric Sensors Using Raindrop Energy in the Rainy Season: A Review

Suraj C. Bulakhe

Loknete Gopinathji Munde Arts, Commerce and Science College, Mandangad, Ratnagiri, Maharashtra, India

ARTICLE INFO

Article History:

Published : 30 April 2025

Publication Issue :

Volume 12, Issue 13

March-April-2025

Page Number :

88-91

ABSTRACT

The quest for sustainable energy has led to innovative approaches for harvesting ambient energy from natural phenomena. Among these, the use of piezoelectric sensors to capture the kinetic energy of raindrops during the rainy season has emerged as a promising, albeit niche, technology. This review synthesizes the current state of research on raindrop-based piezoelectric energy harvesting, focusing on system designs, material advancements, performance metrics, and potential applications. While the technology demonstrates feasibility for powering low-energy devices, challenges such as low power output and material durability persist. This article evaluates key studies, identifies research gaps, and proposes directions for enhancing efficiency and scalability, particularly in regions with high seasonal rainfall.

INTRODUCTION

As global energy demands rise, renewable energy harvesting from environmental sources like solar, wind, and hydro has gained prominence. However, the kinetic energy of raindrops remains an underexplored resource, particularly in regions experiencing prolonged rainy seasons. Piezoelectric sensors, which generate electricity from mechanical stress, offer a viable method to convert the impact energy of raindrops into usable electrical power. This approach is especially relevant during the rainy season, when frequent and intense rainfall provides a consistent energy source.

This review examines the principles, advancements, and challenges of piezoelectric energy harvesting from raindrops. It covers material selection, system configurations, performance evaluations, and applications, with a focus on optimizing the technology for rainy season conditions. By synthesizing findings from recent literature, this article aims to provide a comprehensive understanding of the field and guide future research efforts.

PRINCIPLES OF PIEZOELECTRIC ENERGY HARVESTING

Piezoelectricity refers to the generation of electric charge in materials such as lead zirconate titanate (PZT), polyvinylidene fluoride (PVDF), and barium titanate under mechanical deformation. The voltage output from a piezoelectric sensor is described by:

$$V = g_{33} \cdot \sigma \cdot t$$

where g_{33} is the piezoelectric voltage constant, σ is the stress induced by raindrop impact, and t is the material thickness.

Raindrops possess kinetic energy ($E_k = 1/2mv^2$), with typical drop sizes (2–5 mm) and terminal velocities (2–9 m/s) yielding energies of 1–100 μJ per impact. Piezoelectric sensors capture a fraction of this energy, converting it into electrical power through circuits that include rectifiers and storage capacitors. The rainy season enhances the feasibility of this approach by providing high-impact frequency and rainfall intensity.

ADVANCES IN RAINDROP-BASED PIEZOELECTRIC SYSTEMS

3.1 Material Developments

Early studies utilized PZT due to its high piezoelectric coefficient ($d_{33} \approx 400\text{--}600 \text{ pC/N}$). Guigon et al. (2008) demonstrated that PZT discs could generate up to 1 $\mu\text{W}/\text{cm}^2$ under simulated rainfall. More recently, flexible materials like PVDF have gained attention for their durability and adaptability to irregular surfaces. Wong et al. (2017) reported that PVDF films produced 0.5–2 μW under moderate rain, with improved resistance to water-induced degradation.

Emerging materials, such as lead-free piezoelectrics (e.g., potassium sodium niobate) and graphene-enhanced composites, show promise for eco-friendly and high-performance systems. For instance, Lee et al. (2020) explored PVDF-graphene composites, achieving a 30% increase in voltage output compared to pure PVDF under identical rainfall conditions.

3.2 System Designs

System configurations vary from single-sensor setups to arrays for enhanced power output. Violleau et al. (2012) tested cantilever-based PZT sensors, noting that cantilever designs amplify mechanical stress, yielding up to 5 μW per sensor in heavy rain (50 mm/h). Sensor arrays, as explored by Chua et al. (2019), scaled power output linearly with the number of sensors, reaching 20 μW for a 4-sensor array.

Integration with energy storage is critical. Most systems employ full-bridge rectifiers and capacitors (1–100 μF) to store energy for intermittent loads. Advanced designs incorporate maximum power point tracking (MPPT) circuits to optimize impedance matching, as demonstrated by Aslam et al. (2021), who reported a 15% efficiency improvement.

3.3 Performance Metrics

Literature reports power outputs ranging from 0.1 μW to 100 μW , depending on rainfall intensity (5–50 mm/h), drop size (2–5 mm), and sensor configuration. Efficiency, defined as the ratio of electrical energy output to kinetic energy input, typically ranges from 1–10%. For example, Guigon et al. (2008) estimated a 2% efficiency for PZT sensors, limited by mechanical losses and circuit inefficiencies.

Rainfall intensity significantly impacts performance. Studies consistently show that heavy rain (>30 mm/h) produces higher power due to increased impact frequency and force, making the rainy season ideal for deployment. However, drizzle (<10 mm/h) remains challenging due to lower kinetic energy per drop.

APPLICATIONS

Raindrop-based piezoelectric energy harvesting is suited for low-power applications, particularly in high-rainfall regions. Key applications include:

- **Environmental Monitoring:** Powering sensors for weather, air quality, or river flow in remote areas (Wong et al., 2017).

- **Smart Agriculture:** Supporting IoT nodes for soil moisture or crop health monitoring in monsoon-prone regions (Chua et al., 2019).
- **Urban Infrastructure:** Integrating piezoelectric tiles into pavements or rooftops to power LEDs or traffic sensors (Aslam et al., 2021).

Hybrid systems combining raindrop and solar energy harvesting are also emerging. For instance, Lee et al. (2020) proposed a dual-mode device that switches between piezoelectric and photovoltaic modes based on weather conditions, enhancing reliability.

CHALLENGES AND LIMITATIONS

Despite its potential, raindrop energy harvesting faces several hurdles:

- **Low Power Output:** Micro-watt power levels limit applications to ultra-low-power devices, excluding high-energy demands (Violleau et al., 2012).
- **Material Durability:** Prolonged exposure to water and UV radiation can degrade piezoelectric materials, necessitating robust encapsulation (Wong et al., 2017).
- **Seasonal Dependence:** The technology is less effective outside the rainy season, requiring hybrid or backup systems (Chua et al., 2019).
- **Scalability:** Large-scale deployment is hindered by the high cost of piezoelectric materials and low energy density compared to solar or wind (Aslam et al., 2021).

RESEARCH GAPS AND FUTURE DIRECTIONS

Several gaps warrant further investigation:

- **Material Optimization:** Developing cost-effective, lead-free piezoelectrics with higher efficiency and durability remains a priority.
- **System Integration:** Research on compact, low-loss circuits and scalable sensor arrays could enhance practical deployment.
- **Real-World Testing:** Most studies rely on simulated rainfall; field tests in diverse rainy season conditions are needed to validate performance.
- **Hybrid Systems:** Combining raindrop harvesting with other renewable sources (e.g., wind, solar) could address seasonal variability.

Future advancements may involve nanotechnology, such as piezoelectric nanofibers, to increase surface area and sensitivity. Machine learning could also optimize energy harvesting by predicting rainfall patterns and adjusting system parameters dynamically.

CONCLUSION

Piezoelectric energy harvesting from raindrops offers a novel approach to sustainable energy generation, particularly during the rainy season. Advances in materials, system designs, and circuit efficiency have demonstrated power outputs sufficient for low-energy applications like environmental sensors and IoT devices. However, challenges related to power density, material durability, and seasonal dependence limit widespread adoption. Continued research into high-performance materials, scalable designs, and hybrid systems will be crucial to unlocking the full potential of this technology. In regions with abundant rainfall, raindrop energy harvesting could complement existing renewables, contributing to a diversified energy landscape.

REFERENCES

- [1]. Aslam, M., et al. (2021). "Optimizing Piezoelectric Energy Harvesting from Rainfall Using MPPT Circuits." *Renewable Energy*, 172, 456–465.
- [2]. Chua, K., et al. (2019). "Scalable Piezoelectric Arrays for Raindrop Energy Harvesting." *Journal of Applied Physics*, 125(3), 034502.
- [3]. Guigon, R., et al. (2008). "Harvesting Raindrop Energy: Theory and Experiments." *Sensors and Actuators A: Physical*, 147(1), 10–16.
- [4]. Lee, J., et al. (2020). "Graphene-Enhanced PVDF for Raindrop Energy Harvesting." *Nano Energy*, 68, 104321.
- [5]. Violleau, M., et al. (2012). "Piezoelectric Transducers for Raindrop Energy Harvesting." *Renewable Energy*, 39, 123–130.
- [6]. Wong, C. H., et al. (2017). "PVDF-Based Raindrop Energy Harvesting for Remote Sensing." *Smart Materials and Structures*, 26(8), 085012.

Neuromarketing: Understanding Consumer Behaviour through Neuroscience in Sustainable Development

Sanoffy Dias, Dr. Neha Choudhary

Amity Business School, Amity University School, Maharashtra, India

ARTICLE INFO

Article History:

Published : 30 April 2025

Publication Issue :

Volume 12, Issue 13

March-April-2025

Page Number :

92-99

ABSTRACT

In a world where consumers are constantly bombarded with advertisements, brands are shifting from simply grabbing attention to understanding the psychology behind it. This is where neuromarketing comes in: an emerging field that merges neuroscience and marketing to explore how people unconsciously react to sensory, emotional, and visual cues.

This paper investigates the role of neuromarketing in shaping consumer purchase decisions, using primary data gathered from 174 Indian respondents. While most participants were unaware of the term itself, their behaviour revealed clear signs of neuromarketing influence from gravitating toward specific colours and packaging designs to making spontaneous purchases based on emotional appeal or product placement.

The findings suggest that when used responsibly, neuromarketing can strengthen brand-consumer connections and enhance overall marketing strategies. However, it also highlights the need for ethical boundaries, as the line between persuasion and manipulation remains thin. Through an Indian lens, this study brings forward how modern marketing goes beyond selling it dives deeper into how consumers truly think and feel.

Keywords: Neuromarketing, Consumer purchase decisions, Psychology, Sensory cues, Emotional appeal, Visual cues, Spontaneous purchases, Packaging design, Colour preference, Ethical boundaries, Manipulation vs persuasion, Indian consumers, Marketing strategies.

INTRODUCTION

We live in a time where attention spans are shrinking, and every brand is fighting to stand out in an overstimulated and oversaturated environment. Traditional marketing tools like advertisements and promotions are no longer enough on their own. To truly connect with consumers, brands now need to understand the why behind their choices.

This shift has led to the emergence of neuromarketing, a field that blends neuroscience with marketing to examine how people subconsciously react to branding, packaging, storytelling, and sensory elements. It moves beyond what people say they like, and instead explores how they feel quite often without even realising it.

Unlike conventional surveys or focus groups, neuromarketing uses tools such as eye-tracking, EEG, and facial coding to study subconscious responses. While these tools are more commonly used in high-budget settings, the behavioural patterns they reveal are visible everywhere from impulse buying and brand recall to emotional ad reactions.

In India, neuromarketing is still relatively new, and consumer awareness remains low. Yet, behaviours such as choosing a product based on its colour, getting drawn to emotional advertisements, or responding to store layouts clearly show its influence. This paper aims to explore how neuromarketing plays a subtle yet significant role in shaping buying decisions, even when consumers are unaware of it.

REVIEW OF LITERATURE

Neuromarketing is all about figuring out how our brains respond to marketing, not just what we say we like, but what actually grabs our attention and influences our decisions, even when we don't realise it. It mixes neuroscience with marketing to understand how things like colours, sounds, emotions, and even smells affect the way we shop.

Some companies and researchers use advanced tools like eye-tracking and EEG to see how people react to advertisements or products. These tools can show where someone looks first on a website, how long they stay focused, or even how their face reacts to different content. This helps brands understand what works and what doesn't. For instance, why a certain advert gets more attention or why one type of packaging feels more "trustworthy" than another.

What studies have found is that people often respond more to emotional and sensory elements than to facts or prices. An advertisement that tells a story, uses warm colours, or plays familiar music can stick in someone's mind much more than one that just gives information. That's why brands focus so much on emotional connections. They want to be remembered, not just noticed. That being said, there are concerns. If brands are influencing us without us knowing, is that fair? Is it ethical? Some experts say this kind of marketing could cross the line into manipulation if it's not used responsibly.

Also, most research on neuromarketing has been done in Western countries, often with expensive technology in lab environments. There's not much work done on how regular people in places like India respond to these techniques in everyday situations. That's what this study is trying to explore how real consumers, especially here in India, react to the subtle tactics used by brands to shape our choices.

OBJECTIVES OF THE STUDY

- i. To identify the emotional and psychological triggers (like colours, music, packaging, and storytelling) that influence consumer decisions.
- ii. To assess consumer awareness and perception of neuromarketing strategies, based on the primary survey data.
- iii. To explore how visual and sensory elements (product placement, design, branding) impact consumer attention and brand preference.
- iv. To evaluate ethical concerns associated with neuromarketing, including subconscious manipulation and privacy-related issues.

- v. To understand the real-world impact of neuromarketing on purchase behaviour, impulse buying, and brand loyalty.

RESEARCH METHODOLOGY

This section explores how neuromarketing techniques like emotional appeal, visual design, sensory branding, and product placement subconsciously influence consumer purchase decisions. To ensure the findings are grounded in real-world data, a structured online survey was conducted targeting Indian consumers from various age groups and professions.

1. Research Design

The study follows a quantitative, descriptive design, supported by primary data collection via Google Forms. The survey included both close-ended and Likert-scale questions to identify patterns, behaviours, and opinions regarding neuromarketing strategies.

The aim was not just to test theoretical assumptions, but to understand how everyday consumers experience and respond to neuromarketing elements in both online and physical retail environments.

2. Type of Research and Data Collection Method

A non-probability convenience sampling method was used. The survey was circulated digitally via WhatsApp, Instagram, and email, allowing easy access to urban and semi-urban respondents across India. Participants were selected based on their availability and willingness to respond, making the process quick, cost-effective, and inclusive of diverse consumer types.

3. Sample Size and Respondent Profile

The final dataset included 174 valid responses. The sample was demographically diverse:

- Age Range: Primarily 18–24 (majority), followed by 25–34, 35–44, and 45+
- Gender Distribution: Slightly more female participants, with a balanced male representation
- Occupational Background: Predominantly students and working professionals, followed by homemakers and self-employed individuals
- Shopping Habits: Most respondents were digitally active, frequently engaging with online stores and advertisements

This group was ideal for assessing subconscious marketing triggers, as they're regularly exposed to both physical and digital branding environments.

4. Data Collection Instrument

The tool used for data collection was a self-administered questionnaire created using Google Forms. The survey was divided into four key sections:

1. Demographics (age, gender, occupation, shopping habits)
2. Neuromarketing Awareness (familiarity with subconscious marketing techniques)
3. Sensory & Emotional Triggers (responses to colours, packaging, music, storytelling, etc.)
4. Perception and Ethics (views on manipulation, trust, and interest in learning more)

All questions were clear, concise, and easy to understand, encouraging honest and accurate responses.

5. Data Analysis Tools

The collected data was exported to Microsoft Excel for analysis. Pie charts and bar graphs were generated to visually represent key insights.

Qualitative comments from open-ended questions were reviewed to identify recurring themes and emotions related to branding and purchase behaviour. Each of the selected survey questions was broken down and interpreted clearly

6. Scope of the Study

This research provides insights into the invisible forces that drive buying behaviour, such as emotional connection, product aesthetics, sensory marketing, and subconscious recall. It offers real-world relevance by focusing on Indian consumers—who are often exposed to such marketing without being consciously aware of it.

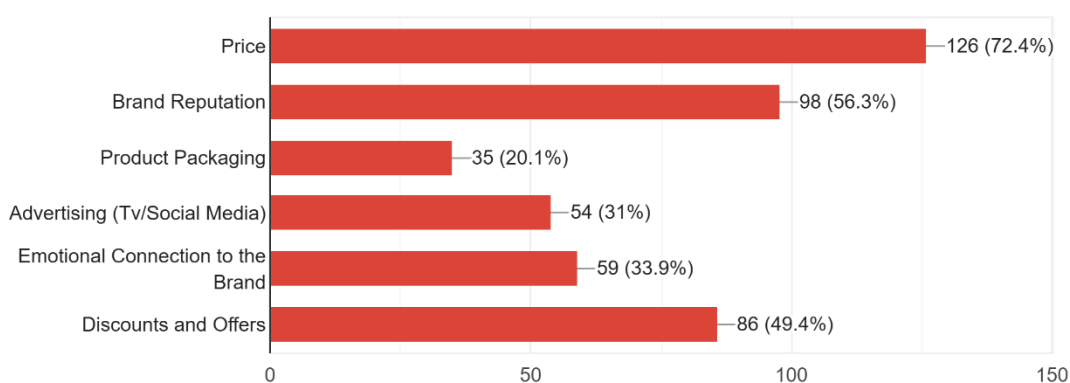
Data Analysis and Findings

Out of all the responses gathered, seven key questions were selected for detailed analysis based on their relevance to the research objectives. Below is a breakdown of these questions, with interpretations aligning the data with the core themes of neuromarketing: the emotional triggers, sensory appeal, and subconscious influence

Q1. What factor influences your buying decision the most?

5. What factors influence your purchase decisions the most? (Select multiple if apply)

174 responses



- The top answer was Price, followed by Packaging, next by Brand image, Emotional Appeal and later followed by other factors

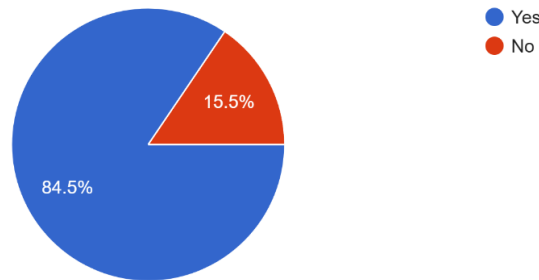
Interpretation:

- i. The Indian consumer market is highly price-sensitive, especially in urban middle-class population. This is reflective of the broader economic situation where budget conscious buying exists due to income differences and value seeking behaviour.
- ii. However, the next two topranked factors Packaging and Brand image come directly under the umbrella of neuromarketing. This suggests that even though consumers are aware of prices, visual appeal and brand perception play a subconscious role in their decision-making. Neuromarketing techniques that enhance product packaging, use colour psychology, or create a premium brand aura can help shift consumer attention away from price toward perceived value.
- iii. Emotional appeal, while not a main factor, still made a notable impact. This suggests that emotion-driven content, such as storytelling and relatable advertisements, helps brands build deeper psychological connections, especially in repeat purchases or brand loyalty.

Q2. Have you ever purchased a product just because of its attractive packaging, design or colours?

10. Have you ever chosen a product because of its color, even if a similar product was available?
(Yes/No)

174 responses



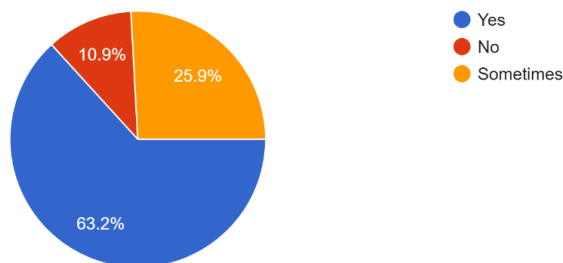
- The vast majority answered: Yes

Interpretation:

Visual design has a clear influence on consumer behaviour. This reinforces the effectiveness of sensory marketing, where colours, symmetry, texture, and layout stimulate a faster emotional response in the brain. Packaging, although often overlooked in traditional marketing, is one of the most impactful neuromarketing tools for triggering subconscious attraction.

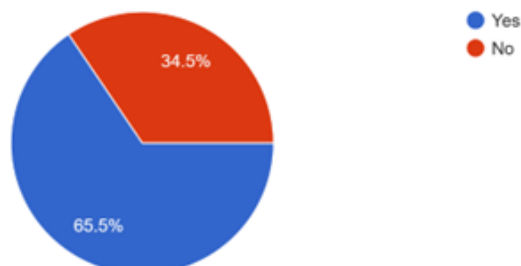
Q3. Have you ever bought something just because it was placed attractively in a store or online platform (even if you didn't plan to buy it)?

13. When shopping in-store, do you notice where products are placed on shelves?
174 responses



15. Do you feel more inclined to purchase a product when brands use limited-time offers or scarcity tactics?

174 responses



- Mixed responses, with many acknowledging impulse buying due to placement or scarcity tactics.

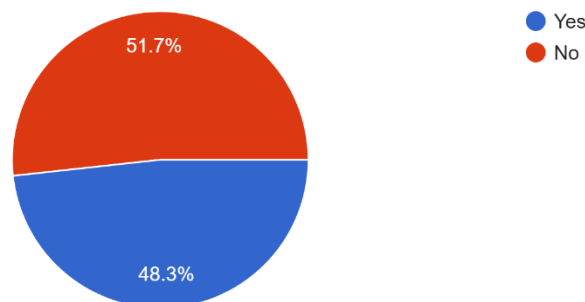
Interpretation

Impulse buying triggered by visual placement indicates the impact of retail neuromarketing. Product placement at eye level, in high-traffic zones, or next to emotionally purchased items (e.g. chocolates near billing counters) can prompt quick decisions. Digital platforms replicate this through scroll-stopping layouts and scarcity limited time offers. This behaviour proves that contextual visibility plays a role in subconscious buying triggers.

Q4. Do you think emotional advertisements influence your buying decisions (e.g. ads that tell a story or create a strong emotional impact)?

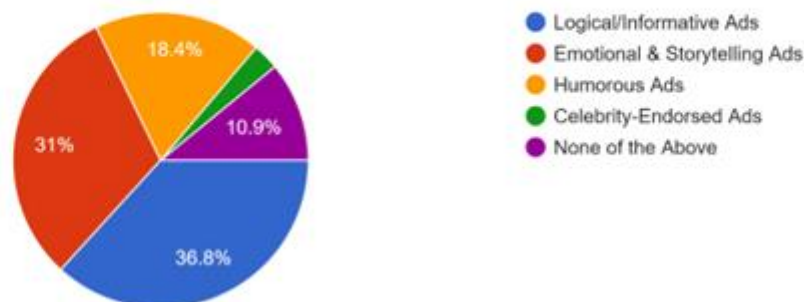
6. Have you ever bought a product because of an emotional advertisement?

174 responses



7. Which type of advertisement grabs your attention the most?

174 responses



A large number of respondents acknowledged emotional influence, but it was still less prioritized than Logical Ads which explain the worth of the price in direct decision-making

Interpretation:

While not the top driver, emotions do play a significant role in brand recall and long-term association. Indian consumers are often drawn to ads that resonate with family values, nostalgia, humour, or patriotism. These emotional undercurrents strengthen trust and recall over time, showing that neuromarketing's emotional targeting has cumulative, long-term effects, even if it doesn't directly trigger every purchase.

CONCLUSION

This study looked at how neuromarketing techniques like emotional storytelling, packaging design, and product placement affects consumer behaviour. Through the survey, it became clear that while people might not know the exact term "neuromarketing," they definitely respond to it.

In a country like India, where price plays a big role in decision-making, visual and emotional factors may not be the first trigger but they still influence how people feel about a brand and whether they remember it. Over time, that emotional connection can be the reason why someone chooses one brand over another.

So, neuromarketing isn't just a fancy concept it is already shaping buying behaviour in small but powerful ways. And if used ethically, it can help brands understand their consumers better, while also creating ads and products that people actually connect with on a deeper level.

LIMITATIONS AND RECOMMENDATIONS

Limitations

- Sample is urban and digitally biased; rural or offline-only buyers are underrepresented
- Self-reported data may involve some bias or inaccuracy
- No use of scientific biometric tools like EEG or fMRI due to resource constraints

Despite these limitations, the study provides valuable, relatable insights into how neuromarketing is experienced by regular Indian consumers—an area still underexplored in academic literature.

Recommendations

Based on these insights, here are a few suggestions that could help brands and marketers apply neuromarketing strategies more effectively, while also keeping the consumer's perspective in mind:

For Brands and Marketers:

- Focus on the Look and Feel** Packaging design, logo placement, and colour schemes should be well thought out because they catch attention in seconds, even before someone checks the price or product details.
- Use Emotions Strategically** Storytelling in ads works, especially when it connects with the audience's everyday experiences. But it shouldn't feel forced—consumers today can tell when something is too intentional.
- Don't Ignore Product Placement** Where and how a product is placed, both online and offline, really matters. Brands should make sure their products are visible in moments when consumers are most likely to act on impulse.
- Balance Emotion with Value** While neuromarketing focuses on triggering emotions, the Indian consumer still looks for value. So, emotional marketing works best when it's paired with affordability and usefulness.

For Consumers:

Be mindful of how visuals and emotions influence your buying choices. It is easy to fall for great packaging or a heartwarming ad, but it's always smart to check if the product matches your actual needs.

For Future Research:

It would be interesting to explore how these strategies work across different income groups or in rural areas, where price sensitivity may be even higher and digital exposure may be lower.

REFERENCES

- [1]. Ariely, D., & Berns, G. S. (2010). Neuromarketing: The hope and hype of neuroimaging in business. *Nature Reviews Neuroscience*, 11(4), 284–292.
- [2]. Morin, C. (2011). Neuromarketing: The new science of consumer behavior. *Society*, 48(2), 131–135.

- [3]. Stanton, S. J., Sinnott-Armstrong, W., & Huettel, S. A. (2017). Neuromarketing: Ethical implications of its use and potential misuse. *Journal of Business Ethics*, 144(4), 799–811.
- [4]. Lee, N., Broderick, A. J., & Chamberlain, L. (2007). What is 'neuromarketing'? A discussion and agenda for future research. *International Journal of Psychophysiology*, 63(2), 199–204.
- [5]. Plassmann, H., Ramsøy, T. Z., & Milosavljevic, M. (2012). Branding the brain: A critical review and outlook. *Journal of Consumer Psychology*, 22(1), 18–36.
- [6]. Zurawicki, L. (2010). *Neuromarketing: Exploring the brain of the consumer*. Springer.
- [7]. Lindstrom, M. (2009). *Buyology: Truth and lies about why we buy*. Crown Business.
- [8]. Google Forms (2025). Primary Survey Data: Neuromarketing and Consumer Behaviour

Synthesis And Characterization of Nano-Crystalline Cr Doped BiFeO₃ for Conductivity and Gas Sensor Application

Y. U. Rathod¹, A. K. Parmar¹, C. V. Bisen², S. B. Zanje³, S. W. Dafare^{3*}

¹Department of Chemistry, C. J. Patel College, Tirora, Maharashtra, India

²Department of Chemistry, M. B. Patel College, Sadak Arjuni, Maharashtra, India

^{3*}Department of Chemistry, J. M. Patel College, Bhandara, Maharashtra, India

ARTICLE INFO

Article History:

Published : 30 April 2025

Publication Issue :

Volume 12, Issue 13

March-April-2025

Page Number :

100-104

ABSTRACT

Nanocrystalline Cr_{1-x}Bi_xFeO₃ (x= 0.15, 0.30, 0.45) was prepared by sol-gel citrate method. The synthesized nanocrystalline BiFeO₃ characterized by X-ray diffraction (XRD). The structure of BiFeO₃ with a orthorhombic phase is confirmed by XRD measurements. Conductivity measurements revealed that the chromium doped (0.3 % by weight) BiFeO₃ exhibit highest conductivity at 650°C. Gas sensitivity measurements revealed that 0.3 % (by weight) Cr doped BiFeO₃ adsorbed CO gas maximum at 220°C

Keywords: Sol-gel, nanocomposite, gas sensor, XRD, BiFeO₃.

INTRODUCTION

From the last few years, there has been growing demand for the improvement of precise and dedicated sensors to provide precise process control and environmental pollution has accelerated the development of new sensing material and technology. The fields of industry, agriculture, electronics, and daily life have all made extensive use of gas sensors. It is useful for checking and keeping an eye on dangerous and flammable gasses. Among solid-state chemical sensors, semiconductor sensors have emerged as the most promising devices due to their compact size, low cost, ease of use, and strong reversibility. Numerous semiconductor oxides, including ZnO, SnO₂, Fe₂O₃, In₂O₃, WO₃, and CuO, have been investigated for the detection of flammable, hazardous, and polluting gasses¹⁻⁴.

In general, sensor should possess high sensitivity, selectivity, fast response time and long-term stability. Among the various sensors, semiconductor oxide based gas sensors are widely used because of their various useful advantages over the other gas sensors⁵⁻⁸, such as sensitivity, selectivity, reproducibility, cost effective, low operating temperature and low response time. Chemical sensors consist of two functions namely receptor function and transducer function. Receptor function recognises chemical substance at the surface of semiconducting particles, while the transducer functions to transduce the chemical signal on the

semiconductor surface through the microstructure of the sintered semiconductor into the electrical output signal⁹.

The semiconducting metal oxide gas sensors currently constitute one of the most investigated of gas sensors. They have attracted much attention in the field of gas sensing under atmospheric conditions due to their low cost and flexibility in production, simplicity of their use, large number of detectable gases possible application fields. In addition to the conductivity change of gas sensing material, the detection of this reaction can be performed by ensuring the change of capacitance, work function, mass optical characteristics or energy release by the gas- solid interaction¹⁰. Literature survey also revealed that the reversible interaction of the gas with the surface of the material is a characteristic of semi-conducting metal oxide gas sensors¹¹.

The aim of this work to Stud the carbon monoxide gas-sensing characteristics of $\text{Bi}_{1-x}\text{Cr}_x\text{FeO}_3$ ($x= 0.15, 0.30, 0.45$) produced using the citrate sol-gel technique mediated by ethylene glycol.

MATERIALS AND METHODS

Synthesis of BiFeO_3 nanocomposites:

BiFeO_3 nanocrystalline specimens made using the sol-gel citrate technique. To create a homogenous and transparent solution, a stoichiometric mixture of ethylene glycol, citric acid monohydrate, and chromium nitrate was magnetically agitated for two hours at 80 °C. To create a gel precursor, the solution was further heated in a pressure vessel for 12 hours at around 30 °C. After three hours of heat treatment at 350 °C in a muffle furnace, the product was ground into a fine powder. To enhance the ceramic crystals, the dried powder calcined at temperatures between 450 and 650 °C. With varying weight percentages of chromium nitrate, the chromium nitrate solution was utilized as a dopant in the BiFeO_3 precursor.

RESULTS AND DISCUSSION

Cu $K\alpha$ radiations (1.5406 Å) and a Siemens D5000 diffractometer were used to characterize the produced materials using XRD. The following analysis of XRD patterns in Figure 1 shows that the crystalline symmetry gradually shifts from rhombohedral to orthorhombic as the Cr content increases. For example, when the Cr content rises, the rhombohedral distortion is lessened, as evidenced by the weakening of the intensity of the (006) and (018) peaks and the decreasing splitting of the peaks around 390 and 500. It has virtually vanished about $X = 0.15$. These findings are consistent with those previously published by Zalesski et al. Using Scherer's equation, the average particle size was determined to be 20 nm.

$$\tau = \frac{K\lambda}{\beta \cos\theta}$$

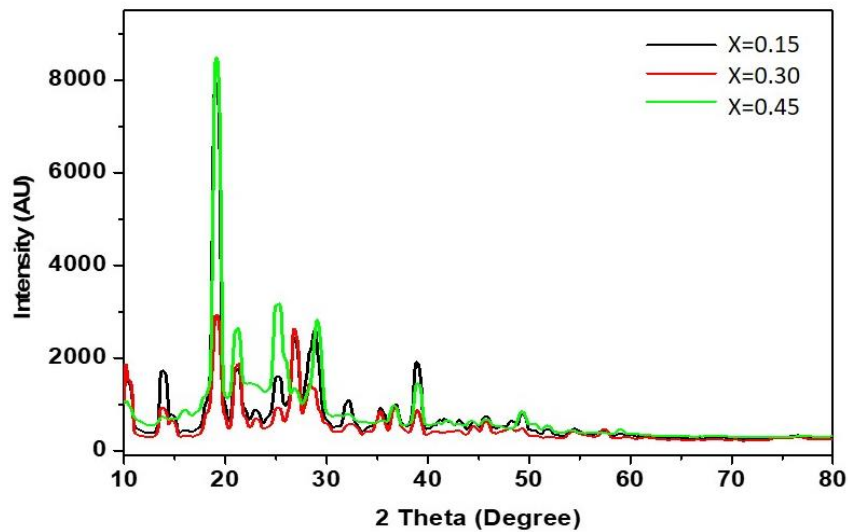


Fig. 1: XRD spectra of doped and undoped Cr ($X=0.15, 0.30, 0.45$) BiFeO_3 ceramic samples of $\text{Bi}_{1-x}\text{Cr}_x\text{FeO}_3$

Conductivity:

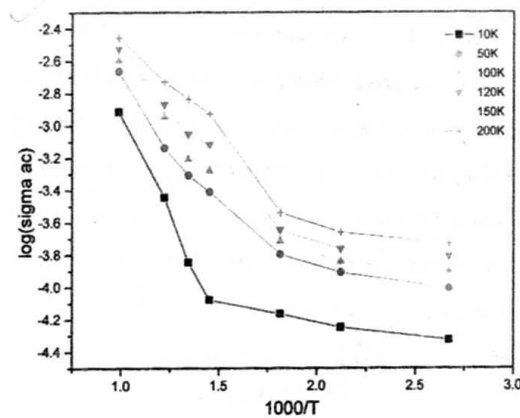


Fig. 2 : Arrhenius plot for ac conductivity of wt Cr doped BiFeO_3 nanocomposite calcinate at 650°C sample.

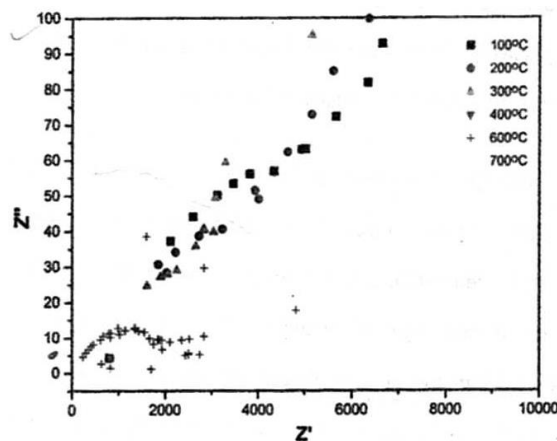


Fig. 3: Cole-Cole plot for 0.3% Wt Cr conductivity of the 0.3% doped BiFeO_3 nanocomposite Calcinate at 650°C

Figures 2 and 3 show how the conductivity varies with frequency for a varied temperature range of 100 to 700°C . According to the graph, the conductivity of the nano-crystalline 0.3% (by weight) chromium doped BiFeO_3 sample calcined at 650°C is almost the same at lower frequencies, but it varies with increasing frequency and

rises with rising temperature. At 200 kHz, the material demonstrated superior conductivity in comparison to the other frequency.

Gas sensing measurements:

The electrical resistance of the material is measured both with and without the CO gas in order to determine the sensitivity. Figure 4 shows the sensitivity as a function of the calcination temperature, which is between 450 and 850 °C. For a BiFeO₃-based CO gas sensor doped with chromium at a weight percentage of 0.3%, operating at 220 °C. It has been noted that the sensitivity rises for samples between 450 and 650 °C before falling above 650 °C. This is because the sample's surface area increased, improving its sensitivity, selectivity, repeatability, and stability.¹²

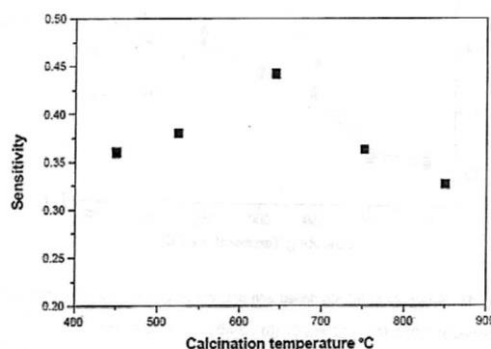


Fig. 4: Gas sensing characteristics of 0.3 % Wt. Cr doped BiFeO₃ at different operating temperatures for CO gas calcined at different temperature ranges from 450-850°C

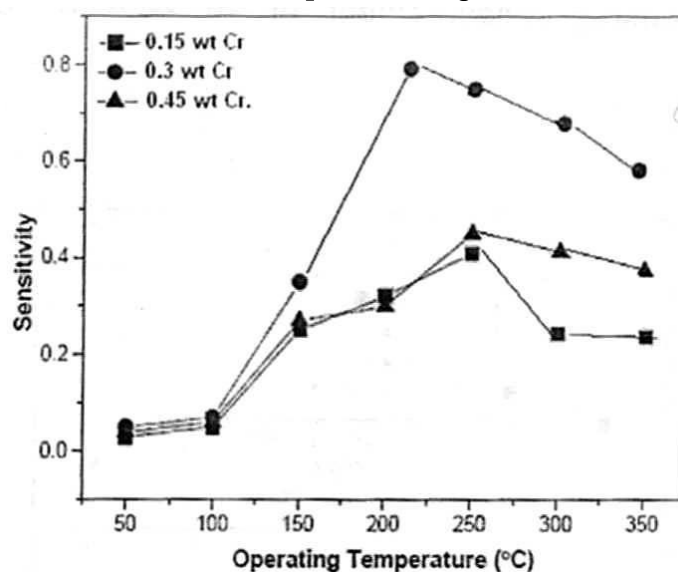


Fig. 5: Sensitivity of BiFeO₃ doped with different amount of Cr for CO gas sensor calcined at 650°C.

Although semiconductor gas sensors have been so far developed mostly by empirical research further development and innovation seems to be impossible without a fundamental understanding of the gas sensing mechanism.

CONCLUSION

We used a straightforward, inexpensive sol-gel process to create BiFeO₃ doped with chromium, which has a particle size of 20 nm. At 450°C, BiFeO₃ exhibits a somewhat increased sensitivity to CO, while at 220 °C, the

dopant Cr increases sensitivity to CO gas. The synthesized substance is helpful in defining and establishing ambient air quality by removing gases and contaminants from the atmosphere.

REFERENCES

- [1]. Rao G. T., Rao D. T. (1999) *Sensors and Actuators B: Chemical*, 55(2-3), 166-169.
- [2]. Kapse V. D., Ghosh S. A., Chaudhari G. N., Raghuwanshi F. C., Gulwade D. D. (2008) *Vacuum*, 83(2), 346-352.
- [3]. Cheng T., Fang Z., Hu Q., Han K., Yang X., Zhang Y. (2007) *Catalysis communications*, 8(7), 1167-1171.
- [4]. Toàn N. N., Saukko S., Lantto V. (2003) *Physica B: Condensed Matter*, 327(2-4), 279-282.
- [5]. Manorama S. V., Sarala G, Devi,Rao V. J.(1994) *Applied Physics Letters*, 64, 3163.
- [6]. Devi S., Manorama S. V.,Rao V. J.(1995) *Sensors and Actuators B*, 28, 31.
- [7]. Devi S.,Manorama S.V.,Rao V. J. (1995) *J. of Electrochemical Society*, 142, 2754.
- [8]. RatnaPhani A., ManoramaS.V., RaoV.J.(1995) *Applied Physics Letters*, 66, 3489.
- [9]. RatnaPhani A, Manorama S.V, Rao V.J. (1997) *Applied Physics Letters*, 71, 2358 .
- [10]. Devi S., Manorama S.V. Rao V.J. (1998) *J. of Electrochemical Society*, 145, 1039.
- [11]. RatnaPhani A, ManoramaS.V.,Rao V.J (1999)*Materials Chemistry and Physics*, 58, 101.
- [12]. Dafare S. W., Rathod Y. U., Bisen C. V (2014) *International Journal of Research in Biosciences, Agriculture and Technology*, 1 (2), 236-243.

Application of Ordinary Differential Equation in Physics

Dr. Kulkarni M.K.

Department of Mathematics, Loknete Gopinathji Munde Arts, Commerce and Science College Mandangad Dist.
Ratnagiri 415203, Maharashtra, India

ARTICLE INFO

Article History:

Published : 30 April 2025

Publication Issue :

Volume 12, Issue 13

March-April-2025

Page Number :

105-112

ABSTRACT

This article examines several applications of ordinary differential equations (ODEs) in specific industries and in everyday life. This project encourages the integration of ODEs into the undergraduate curriculum through the use of real-world analogies, primarily examining the dynamics of international transactions, although ODEs are often applied in areas such as population dynamics, electronics, and the physics of Featuring an arms race at the center and similar to predator-prey dynamics Richardson was a pioneer in the development of mathematical models for understanding wars and arms races between nations. The importance of imbalances in weapon strategies is emphasized in the study, which discusses the evolution of ODEs representing continuous progress between bilateral states or alliances in terms of their sufficiency. It also emphasizes the ability to represent complexity in a variety of educational contexts and promotes a best-practice understanding of how to use mathematics effectively. The analysis is a novel model for predicting decay behavior and population growth using differential equations. It teaches how to use well-known basic rules and concepts to develop ODE-based models and demonstrates versatility in many situations. This study highlights the critical role of ODEs in representing and predicting dynamic interactions, highlighting their importance in understanding, analyzing and possibly reducing social interactions and complex real-world conflicts. It emphasizes the bottom line.

Keywords: Ordinary Differential Equations (ODEs), Industries, Everyday Life, International Transactions, Arms Race and Differential Equations

INTRODUCTION

"Systems of ordinary differential equations (ODEs) are a useful tool for analyzing interactions between dynamic processes. They have been widely used in a variety of fields, including population dynamics, electronics, and physics." When it comes to teaching ODEs, graduate school textbooks often use the very famous example of

predators, which depicts competition between carnivores and herbivores. We suggest that undergraduate courses incorporate relevant real-world applications into ODE: analysis of international relationships. Artists often paint a true picture of conflict, and it evokes strong emotions in us. One such was the Argentinian artist Candido Lopez, who lost his right arm in the same battle and used his left to write, 'After the Battle of Kurupayti It is said that Paraguay, Uruguay, Argentina, and Brazil participated in this conflict. The Museo Nacional de Bellas Artes in Buenos Aires has a work by Lopez, which can be viewed online. This study of countries or treaties using mathematical modeling Departing from an artistic approach by examining rational international relations, including disputes or wars between nations, works to reduce the possibility of war conflict or improve war effectiveness because they hear complex variables that can cause conflict and reduce suffering and economic loss. F.W. Lanchester, P.M. Morse, and G.E. Kimball for military or commercial interests."

"In this work, we examine models of international conflict, first developed by Louis Fry Richardson, to explain the dynamics between two states or alliances on the verge of war. We return to the mathematical foundations of this work for educational reasons. Louis Fry Richardson (1881–1953), it was a pioneer in the analysis of international relations and arms races using mathematical models. Richardson, who spent half his life studying the strategic foundations of war, sought to acquire quantitative knowledge at the beginning and development of war did so. Notable books such as 'Mathematical Psychology of War' (1919), 'General Foreign Policy, and 'Arms and Insecurity' are examples of his discoveries and analyses on conflict. Richardson is most famous for developing mathematical models of differential equations to explain arm races. It is popular. He suggested that if one country increases its armament, another country will follow suit, creating a vicious cycle of increased arms.

His model resembles the differential equation of the predator-prey model in that it deals with energy stability and includes an arms race in international relations. Richardson's research focused on estimating dimensions and system stability, which will be tested. This practical and helpful strategy for crafting ODEs, so it should be included as a classic example in the academic literature. To move forward, this research first uses the example of an arms race; it's a bit of a basic show before a full model is developed. Estimate other influencing factors between states or alliances, such as drought, aggression, and weapon destruction. We present examples, diagrams, and analyses that illustrate solutions, strategies, and phase diagrams for ODE systems, and they offer programmes such as Mathematica and Science Workshop. Students are left to work on simple assignments.

Objective of the study

1. Integration of ODE applications: To emphasize the practical application of ODE in international relations education and integrate it into the undergraduate curriculum.
2. To test Richardson's models: Richardson's mathematical models should be examined, especially when he identifies predator and predator power in international arms races.
3. To Explain ODE Formulation: Using mathematical analysis and graphics, describe how ODE problems are created and solved to reveal the dynamics among states as regards the spread of guns.
4. To showcase the versatility of ODEs: To draw interest to the ODEs' ability to forecast corrupt practices, population growth, and social complexity at the same time as promoting continuous development so that you can get a higher knowledge of society

Need of the study

"The research aims to meet the critical need for a broader understanding and integration of ordinary differential equations (ODEs) in academic curricula and real-world contexts, highlighting their important applications in international relations and life." Internal dynamics and conflicts presented in examples emphasize the development of deep insights to enable appropriate decision-making at various points in complex systems."

Recommendations of the study

1. Curriculum integration: Real-world ODE applications will be integrated into the curriculum to strengthen student understanding, with a special focus on international relations.
2. Wide application : Using ODEs to model social processes in situations beyond conflict, enabling predictive analytics beyond disciplinary boundaries.
3. Continuous improvement : Push for continuous development and adaptation of ODE-based models to address changing societal concerns and improve forecasting accuracy.
4. Interdisciplinary collaboration: Encourage interdisciplinary collaboration to use the ODEs to understand and reduce real complexities across disciplines.

Differential formula for one simple arm

The increasing availability of weapons is generally recognized as one of the major causes of conflict, as are unrealized goals such as territorial recovery or expansion. Our view is based on the idea that if one country increases its arsenal, another does so out of balance —concerns of power. Let state Y represent the weapons, and let $x(t)$ represent state X. The size of the weapons on the other side determines the rate at which one side's weapons change. The relationship between dx/dt and y/dt is essentially a direct ratio of x or y , where the ratio of x to y is given by the constants k and l . The effectiveness of proliferation is reflected in these constants."

As a result, we can formulate the following system of differential equations

$$\begin{cases} \frac{dx}{dt} = ky \\ \frac{dy}{dt} = lx \end{cases} \quad (1)$$

This concept can be used to describe an alliance or relationship between two states that choose to defend themselves against potential attacks on each other. The solution for system (1) is straightforward to find and is given as follows:

$$x(t) = \sqrt{\frac{k}{l}} \cdot (Ae^{t\sqrt{kl}} - Be^{-t\sqrt{kl}}), \quad y(t) = (Ae^{t\sqrt{kl}} + Be^{-t\sqrt{kl}}) \quad (2)$$

Considering the starting circumstances,

$$x(0)=x(0),y(0)=y(0)$$

We can acquire

$$\left. \begin{aligned} A &= \frac{1}{2} \left(y_0 + \sqrt{\frac{1}{k} x_0} \right), \\ B &= \frac{1}{2} \left(y_0 - \sqrt{\frac{1}{k} x_0} \right) \end{aligned} \right\} \quad (3)$$

Estimating the values of k and l is feasible : As an example, while y stays a constant C , (1) implies that,

$$\frac{1}{k} = \frac{C}{\frac{dx}{dt}} = C \cdot \frac{dx}{dt} \quad (4)$$

In solving above equation,

$$\frac{1}{k} x = C t + b \quad (5)$$

(5) indicates that, assuming $x(0) = 0$, $b = 0$ and

$$\frac{1}{k} = \frac{c}{x} t \text{ for } x > 0 \quad (6)$$

Thus, we get $1/k = t$ when X has captured Y , which means that $x = C$. Assuming that Y remains constant, the time it will take for X to capture the arsenal of country Y is $1/k$. Again, Richardson found that k is correlated with the industrial status of the country. In a more foundation-based model, we will present a detailed analysis with illustrations. Here we use the assumption that the degree to which each country stockpiles more weapons is the same, assuming that

$$k = l = 0.9$$

As an illustration. From (2) and (3), it is evident that the original condition

$$x(0)=20, \quad y(0)=0$$

$$A=10, \quad B=-10$$

$$x(t) = 10 e^{0.9t} + 10 e^{-0.9t}, y(t) = 10 e^{0.9t} - 10 e^{-0.9t} \quad (7)$$

$$\begin{pmatrix} x \\ y \end{pmatrix} = \begin{pmatrix} 10 \\ 10 \end{pmatrix} e^{0.9t} + \begin{pmatrix} 10 \\ -10 \end{pmatrix} e^{-0.9t} \quad (8)$$

The connection between the two countries is shown in Figures 1 and 2, with the starting conditions $x_0 = 20$ and $y_0 = 0$. We may see from Figures 1 and 2 that, when A

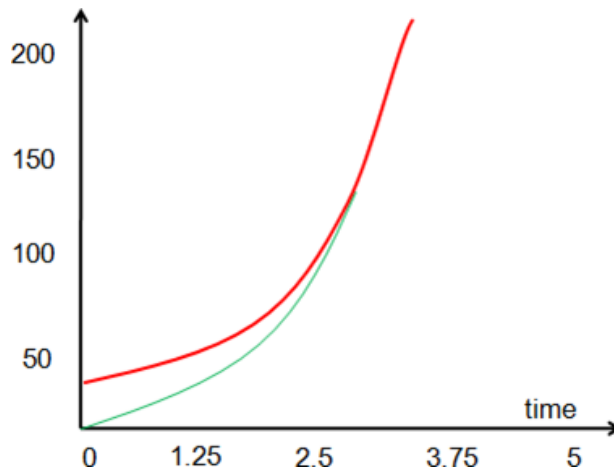


Fig 1: Remedies for the weapons race model (2.1)(x)

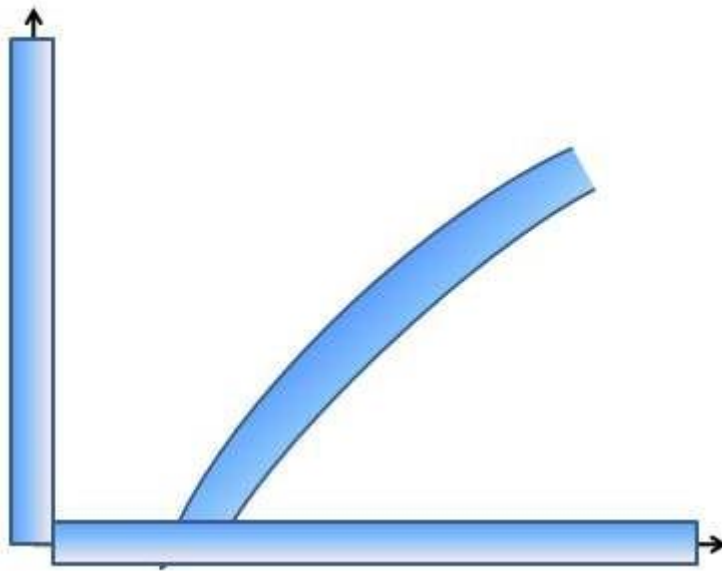


Fig 2: The arms race model's trajectory

The positive attributes of $x(t)$ and $y(t)$ appear to be an escalating arms race between non-causal X and Y , possibly leading to war. We see that the critical point $(0; 0)$ is a saddle point, which is always simple since the system has two real eigen values, $\lambda = \{p, k\}$.

Mathematica R, which shows that the arms of each country increase simultaneously (y and x). The direction of the vector $\mathbf{10}$ of the solution (6) is represented by a straight line through the origin seen in the phase diagram.

Utilizing Ordinary Differential Equations for Mathematical Modeling Applications

Mathematical modeling uses mathematical language to describe interactions and rules, generate valid mathematical relationships, analyze complexity, and then apply mathematical methods to deal with real-world data. This is a mathematical modeling process. Unlike mathematical computation, mathematical modeling consists of logical reasoning, induction, summary, and refinement. The ability to translate real-world data into mathematical relationships is important in mathematical modeling. The main goal of mathematical modeling is to deal with real-world data. The final step in numerical modeling is to verify the results. The correct answer is obtained only if the circumstances of the case itself are controlled.

Functions in mathematical modeling:

We can explore the relationship between mathematics and other disciplines in everyday life through mathematical examples. It can help students develop mathematical skills and understand practical mathematical applications, which in turn will stimulate their interest and commitment to learning the subject.

(2) Teaching mathematical models is a means to acquire various skills such as mathematical expression, mathematical experimentation, collaboration and communication, mathematical thinking, and creative expression. It enables them to actively learn that their daily lives will be used in it. As you study the material,

(3) "Development of students' creative and practical abilities" is the stated goal of higher education. Applying mathematics should not be limited to merely applying knowledge. Implementing and operating the gradient system. According to the author, the ability to develop mathematical models is a prerequisite for representing what mathematics really matters.

Modeling ordinary differential equations using known special laws

Known theories and laws from various disciplines are used primarily in the installation process. Examples of these are as follows: Hooke's law of elastic deformations; Terry's Law; Aki Mead Act; the universal law of gravity; Newton's second law of motion; the rate of damage of air conditioning problems; biological sciences; economic studies; and an increase in population problems

Definition of derivative: The definition of a derivative is as follows:

$$dy - dx = \log_{\Delta x \rightarrow 0} f(x) + \Delta x - f(x) - \Delta x = \log_{\Delta x \rightarrow 0} \Delta x - \Delta y \quad (9)$$

At that point, the instantaneous change in x can be scaled to that of y if the function f(x) is different, as shown by the formula $\Delta x/\Delta y$. It is often used in the expressions "development" and "increase" in demographic and biological studies. "Depletion" in the context of radiation and "margin" in economics

Establishment of ordinary differential equation models by specialized methods

This method basically involves specifying the relationships between microelements and then applying appropriate rules to the project to build the model. Suppose that in a real-world situation, a variable I meets the following criteria: I is a number associated with the transition interval [a, b] of the independent variable x; $I \approx \Delta x$. If Δx is a fractional number that adds to the interval [a, b], then we can consider using differential equations to model fragmentation. Provision: The steps are as follows: An independent variable x based on the context Identify and compute its variable interval as [a, b]; Determine each interval [a, b] and write [x, x + dx]. Find the nearest value corresponding to a partial magnitude ΔI in this interval. Then, determine approximately the value of ΔI as the product of the values f(x) and dx with a continuous function of x, or $\Delta I \approx f(x) dx$, $f(x) dx = dI$. The element I of multiplication is dI, and integrate the two sides of the equation simultaneously to obtain the required quantity. It is possible.

General differential equations used in mathematical simulations

Ordinary differential equations can be used to develop a mathematical model of the current hunting and arrest of many corrupt police officers involved in crime, and thus a mathematical model and creation can be obtained using the differential equation if it is for ordinary use. A new model for quantifying corrupt individuals, with three stages based on the number of individuals involved, has been developed to quantify the total number of individuals involved. (1) Theoretical level Let t be time, X0 be the total number of group members who have committed corruption at time t = 0, let r(x) be the control group, and let x(t) be the number of group members corrupted by the fact that they were employed in all activities. The mean growth rate, or r, refers to the growth rate of the total number of individuals involved in the transaction at time x0. These growth rates are representative of the factors involved. The variables xm and λ represent the maximum number and number of individuals involved in a corruption incident, respectively. μ and λ denote the resistance coefficient resulting from the analysis; i(t) and λ denote the proportion of the total population involved in the corruption case and the participants at t = 0. λ also denotes the average number of members of each corrupt group arrested within a month [4]. (2) In the research phase, the amount of potential corrosion decreases gradually as the amount of corrosion currently present increases. The number of individuals involved in this decay process at time t is determined by the combined activity x(t), the growth rate r(x) proportional to the number of individuals, and x(t), the continuous activity associated with and represented by t, one of which is xm. Moreover, there is a special functional relationship between x and t. According to the previous theorem, $r(x) = r - kx$, where k is the slope and $k > 0$. This means that r(x) is a linear function of x.

The population growth rate function can be used when $x = xm$, since $r(xm) = 0$ implies that the population growth rate is 0. As a result, $k =$ can be calculated as r / xm (3). The following differential equations can be developed without taking into account the severity and complexity of the analysis, which may influence the findings.

$$\frac{dx}{dt} = r \left(1 - x - xm \right) x, \quad X(0) = x_0 \text{ then} \quad (10)$$

$$\text{Equation is } x(t) = \frac{xm}{1 + \left(\frac{xm}{x_0} - 1\right)e} \quad (11)$$

Considering the potential impact of experimental complexity on findings, the differential equation can be constructed with a subsequent choice of resistance coefficient.

$$\frac{di}{dt} = \lambda i (1 - i) - \mu i \quad (12)$$

$$i(0) = i_0 \quad (\lambda \neq \mu) \quad (13)$$

$$\text{Equation } ii(t) = \frac{1}{\frac{\lambda}{\lambda - \mu} + \left(i_0 - \frac{\lambda}{\lambda - \mu}\right)e} \quad (14)$$

Anti-corruption agencies in China can use this statistical framework to predict the number of corrupt individuals involved in future anti-corruption efforts. It is easy to see that there is a large similarity between the errors between the number of dishonest individuals observed in the actual task and the theoretically calculated number.

Population prediction models using ordinary differential equations

If all the components are included from the beginning, it is naturally impossible to make a prototype. Consequently, the matter can be simplified by starting with a simple mathematical model and then making incremental adjustments until an error-free mathematical model is obtained. The maximum number of items an artificial environment can support is indicated by the constant Nm , which is the one modeled mathematically by lliot. Larger residences and more Nm are often associated with higher jobs in the country. According to Weyerhurst, the growth rate can be written as $r(1 - Nt/Nm)$, and as Nt increases, the growth rate gradually decreases. As Nt gradually approaches Nm , the slope will eventually approach zero. This concept can be used to model population forecasting. Consequently, Wellhurst's theory may be constructively applied to new models of population forecasting.

$$dN/dt = r(1 - N/N_0)N \quad (15)$$

$$N(t_0) = N_0$$

These ordinary differential equations provide a reasonable mathematical model that can be solved with a variety of variables. The equation is:

$$N(t) = \frac{Nm}{1 + \left(\frac{Nm}{N_0} - 1\right)e} \quad (16)$$

Combined with Wellhurst's related theory, this population forecasting model can be used to make valid population growth forecasts.

Conclusion

The conclusion of the study highlights the critical importance of ordinary differential equations (ODEs) as a powerful tool for describing the complex dynamics of dynamic systems under various conditions. ODEs provide a flexible analytical framework that can be consumed for everything from population growth forecasting to war strategy analysis to clarifying international relations. By examining mathematical models developed by Lewis Fry Richardson, especially when it comes to simulating international arms races, this study highlights how differential equations can be used to represent complex situations, such as the emphasis on rising hostilities and power struggles. The study also shows how ODEs can be used in studies, showing how well they predict demographic trends, corruption, and other social issues. This mathematical model demonstrates how it links theoretical concepts to implementation and is useful for a better understanding of how mathematics interacts with real-world situations. To deal with complex social issues, our study suggests that ODE-based models should be further explored and improved. There is tremendous potential to harness the power of mathematical models to develop solutions that reduce conflict, predict social dynamics, and improve decision-making in various sectors. Research particularly emphasizes that ODE plays an important role in policy due to the complexity of its dynamics and its enormous impact on our daily lives.

REFERENCES

- [1]. Richardson, L.F. (1948). *Arms and insecurity : A mathematical study of the factors leading to war and of the conditions of disarmament*.
- [2]. Lanchester, F.W. (1916). *Mathematics in warfare*.
- [3]. Morse, P.M., & Kimball, G.E. (1951). *Methods of operations research*.
- [4]. Brauer, F., & Castillo-Chavez, C. (2012). *Mathematical models in population biology and epidemiology*.
- [5]. Murray, J.D. (2003). *Mathematical biology III: Spatial and temporal models*.
- [6]. Strogatz, S.H. (1994). *Nonlinear dynamics and chaos: An introduction*.
- [7]. Perko, L. (2001). *Differential equations and dynamical systems*.
- [8]. Coddington, E.A., & Levinson, N. (1955). *Theory of ordinary differential equations*.
- [9]. Inman, D.J. (2014). *Ordinary differential equations : An introduction to non-linear analysis*.
- [10]. Boyce, W. E., & DiPrima, R. C. (2010). *Elementary differential equations and boundary value problems*, 9th ed.
- [11]. Kreyszig, E. (2010). *Advanced engineering mathematics*, 10th ed.
- [12]. Zill, D.G. (2012). *A first course in differential equations with modeling applications*, 10th ed.
- [13]. Edwards, C.H. (2015). *Differential equations and linear algebra*, 5th ed.
- [14]. Blankenbecler, R., & Tsien, J. (2002). *Differential equations and dynamical systems*, 3rd ed.
- [15]. Smith, W.G. (2013). *Calculus with differential equations*, 2nd ed.

Seasonal Changes in Micronutrients and Heavy Metals in The Soil of LOTE MIDC, District Ratnagiri, Maharashtra

Srikant Kekane

I.C.S. College of Arts, Commerce and Science Khed, Ratnagiri, 415709, Maharashtra, India

ARTICLE INFO

Article History:

Published : 30 April 2025

Publication Issue :

Volume 12, Issue 13

March-April-2025

Page Number :

113-116

ABSTRACT

A comprehensive understanding of the temporal dynamics of soil micronutrients and their environmental implications is essential for enhancing crop productivity and maintaining ecosystem integrity across diverse agricultural systems. This study evaluated the temporal variability of selected soil micronutrients—including cadmium, cobalt, chromium, copper, mercury, nickel, lead, zinc—as well as the sodium adsorption ratio (SAR) in the Lote industrial region over a six-month period from March to September 2022. Results indicated elevated concentrations of several micronutrients during the post-monsoon season. These fluctuations are largely attributed to disproportionate fertilizer applications and the persistent discharge of industrial effluents onto the soil surface, contributing to nutrient imbalances and potential environmental risks.

Keywords: Soil micronutrients, Lote industrial area, Seasonal variation, SAR.

INTRODUCTION

In agricultural research and production, a thorough understanding of the temporal variability of soil fertility characteristics and their consequences on the environment is becoming increasingly important. The objective of precise nutrient recommendations and large-scale environmental monitoring is to enhance crop yields while minimizing negative environmental impacts. Misapplication of fertilizers and manure often leads to excess nitrogen (N) and phosphorus (P), or potassium (K) deficiencies in the soil, resulting from inaccurate agronomic recommendations. However, a comprehensive understanding of how fertilization and management practices influence long-term soil fertility across traditional agricultural systems at large spatial scales remains elusive [1]. Water retention and movement also vary with soil texture, influencing nutrient availability. In coarse-textured soils, residual water is primarily retained within intragranular pores, accounting for approximately 10% of total porosity, whereas in fine-textured soils, it remains almost hierarchically immobile [2]. For optimal plant growth, sixteen essential elements are required, categorized into macronutrients and micronutrients. Imbalances in micronutrients—such as iron (Fe), zinc (Zn), and copper (Cu)—can exert both synergistic and antagonistic effects on plant physiological processes [3].

Dynamic soil quality indicators are those soil properties that respond rapidly to land use changes and management interventions [4]. Soil contamination has increasingly been associated with the accumulation of heavy metals and residues originating from municipal and industrial waste. Soil, being a dynamic and natural system, is shaped through the long-term action of climate, organisms, and topography on parent material. It typically forms into horizons composed of both mineral and organic matter, which differ from the parent material in morphology, physical and chemical composition, and biological activity.

Industrial operations, being intensive consumers of natural resources, significantly contribute to the pollution of air, water, and soil. Soil contamination commonly arises from the discharge of industrial effluents, fertilizer overuse, sewage sludge, municipal compost, and wastewater drainage. Once these pollutants enter the soil system, they tend to accumulate and persist, ultimately reaching levels that are detrimental to plant health, microbial ecology, and human well-being [5,6].

The present study aims to assess the relationships between various soil micronutrients in the Lote industrial region across pre- and post-monsoon seasons, with an emphasis on evaluating the temporal variability and potential environmental consequences of industrial influence on soil nutrient dynamics.

Experimental Section:

The study was conducted in the Lote Maharashtra Industrial Development Corporation (MIDC) region, situated in Ratnagiri district. Soil samples were systematically collected from eight distinct locations within the study area. At each sampling point, a soil pit was excavated to examine soil horizon depths and to enable discrete depth-wise sampling based on natural stratification. Collected soil samples were air-dried, manually disaggregated where necessary, and passed through a 2 mm sieve to ensure uniformity. The prepared samples were then stored in clean polyethylene containers for further analysis [7].

The physicochemical and elemental characteristics of the soil samples were analyzed using standardized protocols. Concentrations of cadmium, cobalt, chromium, mercury, lead, and zinc were quantified using spectrophotometric techniques, while copper and nickel levels were determined via atomic absorption spectrophotometry. All reagents and chemicals employed during the analytical procedures were of analytical reagent (AR) grade. Analytical determinations were performed following established and widely accepted methodological standards [8,9]. The sodium adsorption ratio (SAR) was calculated using the following formula:

$$\text{SAR} = \text{Na}^+ / [(\text{Ca}^{++} + \text{Mg}^{++}) / 2]^{0.5}$$

Where, Na^+ , Ca^{++} and Mg^{++} in (mg/kg)

Results and Discussion

Table 1 presents a summary of the analytical results obtained during the monitoring period from March 2022 to September 2022, encompassing both pre-monsoon and post-monsoon seasons. Ambient temperature across the study region ranged from 32.5 °C during the pre-monsoon period to 37.6 °C in the post-monsoon season. Cadmium (Cd) concentrations in soil exhibited substantial seasonal variability, ranging from 5.55 mg/kg to 73.15 mg/kg, with peak levels observed during the post-monsoon season. These elevated values are attributed to the continuous discharge of untreated industrial wastewater onto the soil surface, leading to cadmium accumulation beyond permissible thresholds.

Cobalt (Co) levels were found to vary from below detection limit (BDL) to 168.15 mg/kg, with significantly higher concentrations in the post-monsoon season compared to the pre-monsoon season. These values exceed the tolerance limits for higher plants. However, as nitrogen-fixing microorganisms require cobalt only in trace amounts, the observed levels are deemed more than adequate to support microbial nitrogen fixation [10].

Chromium (Cr) concentrations ranged between 0.25 mg/kg and 25.35 mg/kg, showing an inverse seasonal trend—lowest in the post-monsoon and highest in the pre-monsoon season. Copper (Cu) and mercury (Hg) concentrations exhibited pronounced fluctuations between seasons, likely reflecting both natural weathering processes and anthropogenic inputs.

Nickel (Ni) content varied from 67.95 mg/kg to 168.15 mg/kg, with the lowest concentrations detected in the pre-monsoon season and the highest during the post-monsoon period. Similarly, lead (Pb) concentrations ranged from 28.15 mg/kg to 88.15 mg/kg, again showing higher accumulation in the post-monsoon season. The rising levels of both nickel and lead are indicative of percolation and accumulation of industrial effluents in the soil profile.

The observed seasonal variations in the concentrations of copper, mercury, nickel, lead, and zinc can be attributed to the combined impact of extensive use of inorganic fertilizers by farmers and the continuous discharge of industrial effluents. These inputs not only alter the micronutrient balance but also contribute to soil toxicity over time [11].

Sodium adsorption ratio (SAR), a critical indicator of soil solidity, ranged from 0.32 mg/kg in the pre-monsoon season to 83.24 mg/kg in the post-monsoon season. Elevated SAR values suggest a transition toward loamy sand, clay loam, or clay soil textures, and may reflect the adverse impact of saline water intrusion or industrial discharge on soil structural properties.

Table 1. Various Elements Concentration in Soil Samples from the Lote Industrial Area

Location	Season	SAR	Pb	Zn	Cd	Co	Cr	Cu	Hg	Ni
S-1	Pre. M.	3.14	28.15	101.55	8.85	54.35	23.65	140.25	BDL	118.85
	Post.M.	16.59	81.15	85.25	23.75	104.15	23.55	119.35	BDL	158.15
S-2	Pre. M.	2.36	40.15	91.85	6.85	52.45	21.35	135.05	1094	91.65
	Post.M.	9.43	88.15	758.15	23.05	105.65	20.75	144.05	184	144.45
S-3	Pre. M.	0.44	42.15	127.45	7.15	77.75	24.65	172.15	2194	114.35
	Post.M.	16.59	87.15	103.15	19.15	111.95	19.15	157.85	204	142.95
S-4	Pre. M.	13.25	33.15	108.75	7.55	49.75	0.25	95.55	BDL	76.85
	Post.M.	13.99	78.15	328.15	8.45	93.25	19.95	25.55	264	150.85
S-5	Pre. M.	2.64	37.15	88.85	9.55	62.35	22.95	118.95	2094	90.75
	Post.M.	5.27	82.15	578.15	20.45	7.65	23.05	140.45	BDL	156.05
S-6	Pre. M.	18.57	42.15	106.05	9.85	BDL	25.35	122.65	194	80.35
	Post.M.	51.71	81.15	88.15	5.55	115.65	16.95	12.65	64	158.15
S-7	Pre. M.	12.4	33.15	90.75	7.55	50.75	11.05	143.85	494	67.95
	Post.M.	83.24	80.15	67.65	28.25	98.15	9.75	81.75	14	116.95
S-8	Pre. M.	0.32	43.15	8.15	13.15	51.15	25.15	143.15	BDL	90.65
	Post.M.	7.09	88.15	73.15	73.15	168.15	10.05	71.65	BDL	168.15
Max		83.24	88.15	758.15	73.15	168.15	25.35	172.15	2194	168.15
Min		0.32	28.15	8.15	5.55	BDL	0.25	12.65	14	67.95
Average		16.0644	60.3375	175.325	17.0188	80.21	18.6	114.056	680	120.444

Conclusion:

The study highlights significant seasonal variability in soil micronutrient concentrations and sodium adsorption ratio (SAR) in the Lote MIDC region, driven largely by industrial effluent discharge and fertilizer application. Post-monsoon samples consistently showed elevated levels of cadmium, cobalt, nickel, lead, and SAR,

surpassing permissible limits and indicating progressive soil contamination. These changes pose a threat to soil health, crop productivity, and environmental safety. The findings emphasize the urgent need for sustainable industrial waste management, regular soil monitoring, and balanced nutrient application to prevent long-term degradation of soil fertility and ensure agricultural and ecological sustainability in industrially influenced regions.

Acknowledgement

The authors are grateful to the management and principal of I.C.S. College of Arts, Commerce and Science, and the management and principal of S. C. S. College in SatishpradhanDnyanasadhana college Thane (west) for providing required departmental facilities.

REFERENCES

- [1]. L Darilek ; B Huang ;Y Qi ; Y Zhao; W Sun; Z Gu; X Shri; *Agricultural Ecosystem and Environment*, 2007,129, 286 -292.
- [2]. I Ebtisum; El Dardiry; *Aust. J. Basic and Applied Science*, 2007, 1 (3): 220-225.
- [3]. JN Nigal; *Asian J. of Chem.*, 2000, 12(4), 1364-1366.
- [4]. K Chan; YA Bowrnan; A. Oates, *Soil Sci.*, 2001, 166:61-67.
- [5]. EY Oyinlola; IA. Aliyu, *Chem. Class J.*, 2005, 2, 32-35.
- [6]. DK Das, *Introductory Soil science*, Kalyani Publisher 2nd, Ed. 2006.
- [7]. M Sanchez-Maranon; M Soriano; G Delgado; R Delgado, *Soil Science Society, Am. J.* 2002,66,928-958.
- [8]. APHA (American Public Health Association), 1989,17th Ed.
- [9]. ISI (Indian Standards Institution) New Delhi, 1968.
- [10]. E Carpenter; J Tarr; EL. Rice, *Proc. Okla. Acad. Sci.*, 1980,60:43-47.
- [11]. EA Kirkby; V Romheld, *International Fertilizer Society York U.K.*, 2004, 1-51.

Laser-Based Interference Pattern Analysis for Different Sound Frequencies

Digambar D. Kulkarni¹, Diksha Lingayat², Ayush Lendhe²

¹Head and Assistant Professor, Department of Physics Dapoli Urban Bank Senior Science College Dapoli, Dist: Ratnagiri Maharashtra, India

²T.Y.B.Sc. Physics, Department of Physics, Dapoli Urban Bank Senior Science College Dapoli, Dist Ratnagiri, Maharashtra, India

ARTICLE INFO

Article History:

Published : 30 April 2025

Publication Issue :

Volume 12, Issue 13

March-April-2025

Page Number :

117-121

ABSTRACT

This project investigates the visualization of sound-induced vibrations using laser interference patterns. By focusing a laser beam on a mirror attached to a speaker-driven plastic sheet, we studied the interference patterns generated by different sound frequencies.

The resulting patterns provide insights into the relationship between sound frequencies and vibration-induced distortions. This research demonstrates the potential applications of laser-based techniques in sound analysis and vibration studies.

Keywords: LASER interference, sound frequencies, vibration analysis, interference patterns, laser-based techniques, Sound induced vibrations.

INTRODUCTION

Laser interference is a fascinating phenomenon in physics that arises from the wave nature of light. It occurs when two or more coherent laser beams overlap and combine to produce a pattern of constructive and destructive interference. This process results in bright and dark fringes known as an interference pattern. The concept is foundational in optics and is widely applied in scientific research and technology.

Laser interference is not limited to simple patterns. By adjusting the relative phase, angle, and path length of interfering beams, complex and highly precise interference patterns can be created. In practical applications, laser interference plays a role in the manufacturing of semiconductors, holography, and the alignment of optical systems. For instance, interference lithography uses interference patterns to etch fine features onto surfaces, which is essential in microelectronics. In holography, interference between a reference laser beam and light scattered from an object is recorded to create three-dimensional images.

One of the primary ways sound affects laser interference is through acousto-optic modulation. In an acousto-optic modulator (AOM), sound waves are used to create periodic variations in the refractive index of a medium. These variations act like a diffraction grating for an incident laser beam. When a sound wave passes through an AOM, it generates regions of compression and rarefaction that form a moving optical grating. The laser light

diffracted by this grating changes direction, phase, or frequency depending on the properties of the sound wave. When this modulated laser light interferes with a reference beam, the interference pattern shifts or varies over time. By changing the frequency of the sound wave, the spacing and movement of the interference fringes can be controlled. Higher sound frequencies result in more tightly spaced refractive index variations, which in turn affect the diffraction angle and phase of the laser beam more significantly. As a result, the interference pattern can be dynamically tuned using sound.

Another scenario involves the use of vibrating surfaces or mirrors that reflect laser beams. If a mirror in an interference setup is mounted on a surface vibrating at an audible or ultrasonic frequency, the path length of the reflected beam changes periodically. This oscillation leads to a time-dependent phase shift in the laser beam, causing the interference pattern to fluctuate or move rhythmically. Observing these fluctuations allows scientists to analyze the characteristics of the sound wave, making this technique useful in precision metrology and sensing.

In summary, although sound and light are different in nature, sound frequencies can strongly influence laser interference patterns. Through acousto-optic modulation and sound-induced mechanical vibrations, acoustic signals can modulate the phase, direction, and intensity of laser beams, thereby altering the interference pattern. This relationship enables a range of advanced applications in optics, sensing, and materials analysis, showcasing the fascinating intersection between acoustic and optical phenomena.

METHODS AND MATERIAL

To investigate the LASER interference patterns generated by sound frequencies, the following experimental setup and procedure were employed:

1. A speaker was used to generate sound waves at specific frequencies, controlled by a frequency generator application on cell phone.
2. A plastic sheet was attached to the speaker's surface to create a vibrating membrane. We can also use Balloon.
3. A LASER beam was directed onto the plastic sheet, creating an interference pattern.
4. The interference pattern was captured using a camera.
5. The speaker was set to generate sound waves at specific frequencies, ranging from low to high frequencies.
6. The LASER beam was aligned to illuminate the plastic sheet, creating an interference pattern.
7. The interference pattern was captured and recorded for each sound frequency.
8. The experiment was repeated for various sound frequencies to analyze the relationship between sound frequency and interference pattern
9. Various Figures presents indicating various results ,with the help compositions of SHMs sound frequencies
10. The given work will have ample of scopes in recognizing various frequencies in day to day life

RESULTS AND DISCUSSION

As the sound frequency generated by the speaker varied, the LASER interference pattern on the screen exhibited distinct changes. Here are the key observations:

TABLE I OBSERVATIONS OF EXPERIMENT

Frequency (Hz)	Shape of Interference Pattern	Frequency Range
24 -30	Grid or Mesh like pattern	Audible frequency, Low Range
30 - 50	Triangular Grid	Audible Frequency
50 - 100	Spherical drop like shape	Low frequency
100 -200	Distorted dot like shape	Low frequency , Bass Range
200- 500	Fine Dot shaped	Low - mid range frequencies

A. Pattern Shape:

At lower frequencies (e.g., 1-100Hz), the interference pattern appeared as a regular grid or mesh circular drop like pattern. As the frequency increased (e.g 200-500Hz), the pattern transformed into dots

B. Pattern Size:

The size of the interference pattern decreased as the sound frequency increased. This suggests that higher frequencies produce shorter wavelengths, resulting in smaller pattern sizes.

C. Pattern Distortion:

As the sound frequency approached the resonant frequency of the plastic sheet or mirror, the interference pattern became distorted, exhibiting irregular shapes and asymmetries.

D. Pattern Intensity:

The intensity of the interference pattern varied with sound frequency. At certain frequencies, the pattern appeared brighter, while at others, it was dimmer.

E. Frequency Dependence:

The interference pattern showed a strong dependence on the sound frequency, with distinct patterns emerging at specific frequency ranges.

F. Figures and Tables

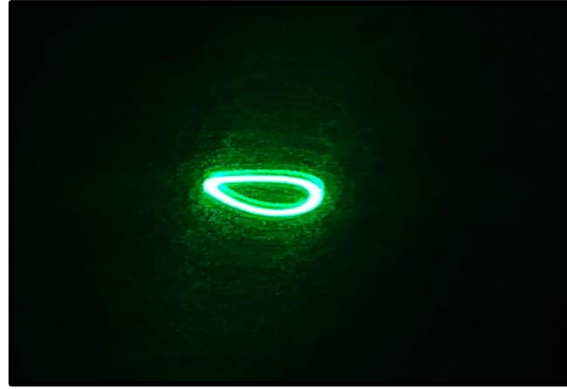
1. 24Hz :



2. 34 Hz (shape of 8 number) :



3. 58 Hz (Drop like pattern) :



4. 100 Hz (dot like Shape) :



5. For mixed Frequencies :



CONCLUSION

The experiment using a LASER beam focused on a mirror attached to a speaker vibrating at various low frequencies (25-35 Hz) produced visible interference patterns. The patterns exhibited changes in shape, size, and intensity as the frequency increased. Key findings are follows:

- Low frequencies (25-35 Hz) generated large-scale grid or mesh-like patterns
- Pattern density and complexity increased with frequency
- Observations suggest a strong relationship between sound frequency and LASER interference patterns

This experiment demonstrates the potential for using LASER interferometry to study vibrations and sound frequencies.

REFERENCES

- [1]. Hecht, E. (2019). Optics (5th ed.). Pearson Education.
- [2]. Pedrotti, F. L., & Pedrotti, L. S. (2017). Introduction to Optics (3rd ed.). Cambridge University Press.
- [3]. Young, T. (1802). Experiments and calculations relative to physical optics. Philosophical Transactions of the Royal Society of London, 92, 1-16.
- [4]. Hariharan, P. (2007). Basics of Interferometry. Elsevier.
- [5]. National Institute of Standards and Technology (NIST). (n.d.). Laser Interferometry.

A Study on Pharmacological Potential of *Ipomoea Carnea* Jacq. Subsp. *Fistulosa* (Mart. Ex Choisy) D. Austin

Sangita A. Ghadge

Department of Botany, Loknete Gopinathji Munde, Arts, Commerce and Science College, Mandangad, Dist. Ratnagiri, Maharashtra, India

ARTICLE INFO

Article History:

Published : 30 April 2025

Publication Issue :

Volume 12, Issue 13

March-April-2025

Page Number :

122-128

ABSTRACT

Ipomoea carnea Jacq. subsp. *fistulosa* commonly known as 'Pink Morning Glory' or 'bush Morning Glory' is native to tropical America but now is widely naturalized. In India the plant is known as 'Besharam' or 'Behaya' due to its rapid and invasive growth. It grows as common weed on waste land, road side; riverbeds, riverbank and other water logged (wet land) areas. Plant is now well-established weed in many parts of India. Due to its vigorous growth spread rapidly on land in many habitats and cause obstruction and difficulties in proper land crop cultivation and management. Manual and chemical control measures unable to eradicate hundred percent as regrowth takes place. The plant is having great potential of regeneration as well as source of phytochemicals. *I. carnea fistulosa* rich source of phytoconstituents like Phenol, Flavonoid, Enzymes, several bioactive compounds like Glycosides, Reducing sugar, Fatty acids, Esters, Alcohol, Alkaloids etc. the present review article focused on *Ipomoea carnea* subsp. *fistulosa* plant parts and their pharmacological significance.

Keywords: *Ipomoea carnea fistulosa*, Phyto constituents, Plant Extracts, Pharmacological importance

INTRODUCTION

Ipomoea carnea Jacq. sub sp. *fistulosa* is member of family Convolvulaceae which naturalized all over the world. The plant is native to tropical America and is most common in Argentina, Belize, Bolivia, Brazil, Colombia, Costa Rica, Ecuador, Peru, and Venezuela. It also spread to Asian countries Sri Lanka, Pakistan, Java, Indonesia. *I. carnea fistulosa* commonly found in the state Madhya Pradesh, Chhatisgad, Maharashtra, all districts of Kerala, Odisha, Tamil Nadu and in Uttar Pradesh. It is popular with vernacular names in Indian languages as Vaelikkaathan in Tamil (Matthew, 1983) Thutukada in Telugu, Omori in Oriya (Saxena and Brahamam 1995), Neyveli kata in Malayalam (Sasidharan, 2011), Mahananda and Besharam in Marathi (Rao et al., 1986) Behaya, Besharam in Hindi. The common English names are Bush Morning Glory, Shrub *Ipomoea* Hedge Glory, and

Pink Morning Glory etc. The scientific name is *Ipomoea carnea* Jacq. (Cook,1908), *Ipomoea carnea* subsp. *fistulosa* (Mart.ex Choisy) D.F.Austin (Sankara Rao & Deepak Kumar 2024).

Occurrence-

It occurs mainly in Marshy areas along the banks of streams. Occasional on hill plains, canal banks and water bodies it grows on waste land, road side and even in cultivated lands causing disturbances(Shaltout *et al*, 2006). Some parts of China, Hainan,Guangxi, Taiwan and in Nile delta farmers cultivate it as Hedge plant (Nusrat *et al*. 2014).

Morphological characters

*Ipomoea carnea*subsp. *fistulosa* grows as sprawling perennial shrub more than 3-10 feet height. Stem is sub erect, hollow (fistulose), woody and hairy. Produces pale pink to purple coloured flowers in cluster around the year. Leaves ovate to lanceolate heart shaped. Fruits are ovoid capsule producing pubescent seeds.

Growth and Invasiveness

The plant can be easily grown by seeds but vegetative propagation through stem is common. Rapidly rooting of stem within a week forms dense vegetation in the area. *I.carnea fistulosa* have ability to adapt in various habitats from xeric to aquatic condition. The plant is capable of growing with equal ease as terrestrial, aquatic and as amphibious (Charri & Abbasi, 2003). Due to these characters it became prevalent and most dominant in all other plants. The plant was introduced as an ornamental plant or hedge plant but its vigorous growth, toxic and dominant nature listed it into unwanted, noxious weed plant.

Phytochemicals:

*Ipomoea carneafistulose*contains several phytochemicals like tannin, Phenolic acid, alkaloids, Fatty acid , alcohol, Easter, Glycosides, flavonoids, Caumarin sterol like bioactive components (Haraguchhi *et al*,2003). An enzyme Carnein, a Serine Protease isolated from Noxious Plant Weed *Ipomoea carnea*(Singh *et al*,2007) the chemical analysis of leaf and flower shows wide range occurrence of complex organic components i.e. resins - sitosterol, triacontane, kaempferol, anthocyanin, agroclavine and dihydrolysergol. Phenolic compounds present in flavonoids and are most important constituent for its pharmacological action. Phenols and flavonoidsin different parts of plantshow variation (Table-1).

Table:1. Concentration of phenol and flavonoid content in stem leaves and flower of *Ipomoea carnea*subsp.*fistulosa*

Sr. No.	Plant Parts	Phenol content mg catechol equivalent/gm dry powder	Flavonoid content mg qurcetin equivalent/gm dry material
1	Stem	30	168
2	Leaves	45	84
3	Flower	75	422

Chemical Analysis of plant-

On the basis of solubility of phytoconstituents with various polar and nonpolar solvent chemical analyses can be performed.Roots, Leaves, Stem Flowers and Seeds of the *Ipomoea* contain the several phytochemicals.

Root- According to the research studybySahayaraj *et al*. (2015) the roots and stem of *Ipomoea carnea fistulosa*contains2-Ethyl-1,3-dimethylbenzene, 2-(12-pentadecynyloxy) tetrahydro2H-pyran, 3- furanyl [2-

hydroxy-4-methyl-2-(2-methylpropyl) cyclopentyl]- methanone, 2,2- DideuterooctadecanalHexadecanoic acid and Linoleic acid.

Stem- It contains 2-(12-Pentadecynoxy) tetrahydro-2H-pyran, 1-Octadecanol, Hexadecanoic acid, Epiglobulol, Squalene, 1-Octadecanol.

Leaves- *Balogh et al.* (1999) reported a number of pharmacological constituents like hexadecanoic acid, stearic acid, 2 diethyl phthalate, n-octadecanol, octacosane, hexatriacontane, tetracontane, 3- diethylamino-1-propanol. Leaves also containswainsonine and calystegines B1, B2, B3 and C.

Flowers- Pink to purplish coloured flowers of *I.carnea fistulosa*are the good source of flavonoids, tannins, glycosides, alkaloids, carbohydrates and phenolic compound (*Mungole et al.* 2010).

Seeds- It contains swainsonine and calystegines B1, B2, B3 and C1(*Balogh et al.1999*).

Toxic nature-

There are reports of intoxication of *Ipomoea*. It contains the alkaloid swansonine and Calystegines which are responsible for mammalian toxicity and allelopathy (*Hueza et al.* 2005, *Meira et al.* 2012). Sheep, goat when feed on *ipomoea carnea* may develop serious intoxication of nervous system with the symptoms of depression, soft faeces, loss in weight, some behavioural disorders consciousness intense tremors, spatic paresis, abnormal postural reactions head tilting and loss of equilibrium are observed(*Dalo &Moussatche* 1978, *Sharma &Bachheti* 2013). Intake of fresh *Ipomoea carnea*show the negative impacts on growing animals and male and female reproduction. Ingestion of *Ipomoea carnea*by dams shows the lack of maternal- infants bonding and it is very difficult to child in standing, sucking, recognize his mother after birth (*Garcia et al.* 2015).

Allelopathic effect of *Ipomoea carneafistulose* plant affects the growth of other plants growing near it. *Ipomoea* Monopolize the natural resources. The overall effect is catastrophic loss of biodiversity.

Pharmacological Potential*Ipomoeacarnea* sub sp. *fistulosa*

Ipomoea carnea fistulosa has been used in traditional medicine on the basis of its antibacterial, antifungal, anti-inflammatory, antioxidant, Cytoprotective effects and immunostimulant attribute. These properties make it as the wound healer plant (*Hueza et al.*2011).Various extracts of *Ipomoea* plant shows anticancer anti diabetic properties.The plant is used in treating insomnia (*Akram et al.*2014), effective in the treatment against the AIDS (*Woradulaypinij et al.* 2005), in hypertension (*Lamidi et al.* 2000), in generating energy (*Abbasi et al.* 1990, *Ramasamy & Abbasi* 2000), and volatile Fatty acids (*Ganesh et al.* 2005).

Antibacterial Activity

Methanolic extract of *I. carnea* shows higher level antibacterial activity than other solvent extracts.The growth pattern of MRSA treated with methanolic extract of *I. carnea* was recorded. *I. carnea* causes remarkable inhibition on the growth of bacterial cells from the beginning of incubation period (30 min) to the end (8 h). *I. carnea* arrested the log phase, which may be due to the inhibition of binary fission, cell replication, new cell wall formation and the energy pathway in bacteria. (*Mangesh et al.*2023)*I. carnea* had inhibitory effect on MRSA growth similar to other Indian plants like *Sapindusmukorossi* and *Arbutus pavarii* (*Selvaraj et al.*, 2020; *Buzgaia et al.*, 2020). Hence, *I. carnea* is effective in controlling the growth pattern of MRSA than turmeric and therefore its application as wound healing drug might prevent the wound infection

Anti-inflammatory Activity

Inflammatory diseases like rheumatic diseases are very common throughout the world. Therefore a better tolerated anti-inflammatory agent is needed. Latex and Aqueous extracts of *Ipomoea carnea* leaves assess the anti-inflammatory activity. Anti-inflammatory activity was screened by carrageenan (0.1%) induced rat paw

edema method. For screening of anti-inflammatory activity, the extracts were administered orally at a dose of 250 mg/kg and 500 mg/kg body weight. Paw volume was significantly ($p < 0.01$) reduced in test treated groups (500 mg/kg body weight) as compared to control group. Study revealed that the plant *Ipomoea carnea* leaves possesses a significant anti-inflammatory activity as evidences in Carrageenan induced paw edema method. (Khalid et al., 2011).

Cardiovascular Activity

Bachhav *et al.* (1999) reported that the aqueous extract of *Ipomoea carnea* produced a positive inotropic effect by sodium extrusion or release of the intracellular calcium on isolated frog heart. It was observed that the initial blockage was for 5-10 seconds and can be increased up to 2 minutes by increasing the dose of extract.

Hepatoprotective activity

Aqueous extract of *I. carnea* leaves shows the hepatic structural and functionality indicating markers during a dose dependent manner in carbon tetrachloride treated hepatotoxic rat model. It was found that aqueous extract of leaves reduces lipid peroxidation within the liver tissue and restores activities of anti-oxidant enzymes (Gupta *et al.*, 2012).

Anticancer Activity

The hydroalcoholic extract of *Ipomoea carnea* leaves shows the dose dependent anticancer activity (Kumar *et al.* 2014). It is also reported that the hexane, chloroform and ethyl acetate fraction of *I. carnea* along with LC50 value of 141.4 $\mu\text{g/mL}$ and 307.28 $\mu\text{g/mL}$ respectively shows cytotoxic effect. Swainsonine an alkaloid present in *I. carnea* inhibit the cell growth through apoptosis in human lung cancer cell line A549 (Kadiyawala *et al.* 2012).

Wound healing property-

Commercial synthetic drugs like povidone iodine and thymosin beta-4 available in the market for the promotion of wound healing but resulting in varied side effects, which have encouraged people to look into plant-based drugs. *Ipomoea carnea* has been used by certain tribal groups in India for wound healing but its mechanism of action has not been explored yet. (Mangesh *et al.* 2023). The wound healing effect of ethanol extract from *I. carnea* leaves screened by excision and incision wound methods in rats. Five treatments (Negative control, vehicle control, 2.5% w/w, 5% w/w ethanol extract ointment and 5% w/w Reference Ointment Povidone-iodine group) of rats (n=6) were experimentally wounded at dorsal portion of rats. The 5% w/w ointment of ethanol extract found significant wound contraction at 18-20th days, greater tensile strength, and biochemical parameters. The percentage of Flavonoid (quercetin) was found in *I. carnea* leaves as 0.842%. The results were supported by histopathological studies which showed augment in terms of collagen fibres, fibroblast and new blood vessels. The results were evidently exhibited the traditional uses of *I. carnea* leaves for wound healing effects. The healing effect may be attributed by presence of flavonoid and other compounds present in the leaves (Shukla *et al.* 2018).

Some other uses of Ipomoea-

Ipomoea carnea fistulosa plant used as a source of compost, vermicompost. Manufacturing of degradable plastic: *Ipomoea carnea* is useful in manufacturing of degradable plastic (Prasoon Kumar *et al.* 2017). *Ipomoea carnea* use for paper industry, leaf extracts use as pest repellent, for Biomass power Energy plants (Biological control - 2016). Hairy roots of *Ipomoea carnea* used as decolourising agent when tested for 25 textile azo dyes, out of which more than ninety percent decolourization was observed in 15 dyes (Rios *et al.*, 2015). Boiled roots are used as laxative and it provoke menstruation. Milky juice of plant part is used in Leucoderma and other skin diseases.

Conclusion-

Ipomoea carneafistulosa is common weed, easily available with its luxuriant growth and is rich source of phytochemicals. After exhaustive literature survey, it may be concluded that *I. carnea* can be considered as a safe, economic and potential medicinal plant for the treatment in many diseased conditions and may be explored by incorporating its active component(s)/extract(s)/fraction(s) in suitable drug delivery system(s) for therapeutic benefits. Phytomedicines are increasingly being established in modern medical science. The shrub *Ipomoea carnea* has been used traditionally for thousands of years. However, there are few scientific studies on this medicinal plant, and most of the information are scattered. Need to explore more this plant with view of future source of many drugs.

REFERENCES

- [1]. Abbasi, S.A., Nipaney, P. C. and Schaumberg, G.D.(1990). “ Bioenergy potential of eight common aquatic weeds “. *Biological Wastes*, 34(4): 359-366.
- [2]. Abbasi, M.A., Zafar, A., Riaz, T., Rehman, A., Arshad, S., Shahwar, D., Jahangir, M., Siddiqui, S.Z., Shahzadi, T., Ajaib, M. (2010). “Evaluation of comparative antioxidant potential of aqueous and organic fractions of *Ipomoea carnea*”. *Journal of Medicinal Plants Research*, 4(18), 1883-1887.
- [3]. Akram, M., Hamid, A., Khalil, A., Ghaffar, A., Tayyaba, N., Saeed, A. and Naveed, A. (2014). “Review on medicinal uses, pharmacological, phytochemistry and immunomodulatory activity of plants”. *International Journal of Immunopathology and Pharmacology*, 27(3): 313-319.
- [4]. Balogh, D., Dimande, A.P., Lugt, V.D, Molyneux, J.R., Naude, T.W., Welman, W.G. (1999). “ Lysosomal storage disease induced by *Ipomoea carnea* in goats in Mozambique”. *Journal of Veterinary Diagnostic Investigation*, 11, 266-273.
- [5]. Biological control of *Ipomoea carnea* the aquatic weed [Homepage on the Internet] Agro forestry-A blog on Agrihortisilviculture. [cited 7 April 2016] [Available on: <http://agrowmania.blogspot.in/2010/04/biological-control-of-ipomoea-carnea.html>].
- [6]. Chari, K. B. and Abbasi, S.A.(2003). “Wetlands – An overview”. *Hydrology Journal*, 26: 41-58.
- [7]. Chari, K.B. and Abbasi, S.A. (2005). “ A study on the fish fauna of Oussudu-a rare freshwater lake of south India”. *International Journal of Environmental Studies*, 62: 137-145.
- [8]. Dalo, N. and Moussatché, H. (1978). “Acción tóxica de las plantas del género *Ipomoea*”. *Revista de la Universidad Centro Occidental*, 6: 25-39.
- [9]. Ganesh, P.S., Ramasamy, E.V., Gajalakshmi, S. and Abbasi, S.A. (2005). “ Extraction of volatile fatty acids (VFAs) from water hyacinth using inexpensive contraptions, and the use of the VFAs as feed supplement in conventional digesters”. *Biochemical Engineering Journal*, 27: 17-23.
- [10]. Garcia EN, Aquirre MV, Gimeno EJ, Rios EE, Acosta OC, Cholich LA.(2015) “Haematologic alterations caused by *Ipomoea carnea* in experimental poisoning of guinea pig”. *Experiment and Toxicological Pathology*. 67(10); 483-490.
- [11]. Gupta A, Nayak S, Mallik A. (2010). “Preliminary phytochemical screening of hydroalcoholic flower extract of *Ipomoea fistulosa*”. *Int. J. Curr. Trends Sci. Tech.* 2010; 1(2):37-40.
- [12]. Haraguchi, M., Gorniak, S.L., Ikeda, K., Minami, Y., Kato, A., Watson, A.A., Nash, R.J., Molyneux, R.J., Asano, N. (2003). “Alkaloidal components in the poisonous plant, *Ipomoea carnea* (Convolvulaceae)”. *Journal of Agricultural and Food Chemistry*, 51, 4995-5000.

- [13]. Hueza, I.M., Guerra, J.L., Haraguchi, M., Asano, N. and Górnjak, S. L.(2005). “ The role of alkaloids in Ipomoea carneatoxicosis: a study in rats”. *Experimental and Toxicologic Pathology*, 57(1): 53-58.
- [14]. Hueza, I.M. and Gorniak, S.L. (2011). “The immunomodulatory effects of Ipomoea carnea in rats vary depending on life stage”. *Human & Experimental Toxicology*, 30(10): 1690-1700.
- [15]. Kadiyawala ALA, Prasad AK, Kumar S, Iyer SV, Patel HA, Patel JA. (2012). “Comparative antidiabetic studies of leaves of Ipomoea carnea and Grewia asiatica on streptozotocin induced diabetic rats”. *Int. J Pharmaceut. Biol. Arch* 2012;3(4):853-857.
- [16]. Khalid, M.S., Singh, R.K., Reddy, I.V.N., Kumar, S.J., Kumar, B.S., Kumar, G.N.S., Rao, K.S. (2011). “Anti-inflammatory activity of aqueous extract of Ipomoea carnea Jacq.” (Article) *Pharmacology online* Volume 1,, Pages 326-331.
- [17]. Kumar A, Manral U, Sharma S. Traditional remedy for muscle strain using Ipomoea carnea Jacq. and Ricinus communis L. leaves in Haryana, India. *Int. J. Med. Plants* 2014;108:625-631.
- [18]. Lamidi, M., Rondi, M.L., Ollivier, E., Faure, R., Ekekang, L.N. and Balansard, G. (2000). “ Constituents of Ipomoea fistulosa leaves”. *Fitoterapia*, 71(2): 203-204.
- [19]. Magesh Akshaya, Kalpana Sundararajan Swetha, Durairaj Keerthana, Vellingiri Vadivel, (2023) “ In Vitro Studies On Wound Healing Mechanism of Leaves of Ipomoea carnea” *South African Journal of Botany*, Vol,154, Page 239-250
- [20]. Matthew, K.M. (1983). “The Flora of Tamil Nadu Carnatic” Vol. 3(1). Diocesan Press Madras.
- [21]. Meira, M., Silva, E.P.D., David, J.M. and David, J.P. (2012). “ Review of the genus Ipomoea: traditional uses, chemistry and biological activities”. *Revista Brasileira de Farmacognosia*, 22(3): 682-713.
- [22]. Mungole, A.J., Awati, R., Chaturvedi, A., Zanwar, P. (2010). “Preliminary phytochemical of Ipomoea obscura (L) A hepatoprotective medicinal plant”. *International Journal of pharm tech research*, 2(4), 2307-4304.
- [23]. N. Buzgaia, T. Awin, F. Elabbar (2020), Antibacterial activity of Arbutus pavarii Pamp against methicillin-resistant Staphylococcus aureus (MRSA) and UHPLC-MS/MS profile of the bioactive fraction *Plants (Basel)*, 9 (11) (2020), p. 1539, 10.3390/plants9111539
- [24]. Nusarat F., Rahman MM, Assaduzzaman K., Junjiyang FU. (2014). “A Review on Ipomoea carnea : pharmacology, Toxicology, Phytochemistry”. *Journal of Complementary and Integrative Medicine*, 55-62.
- [25]. Prasoon Kumar Saxena, Deepak Nanda, Ritu Gupta, Nitin Kumar, Nidhi Tyagi (2017), *Int. Res. J. Pharm.*, 8 (6).
- [26]. Pullaiah T. Sandhya Rani, S. (2011). “Flora of Eastern Ghats” Vol. 4
- [27]. Ramasamy, E.V. and Abbasi, S.A. (2000). “ Energy recovery from dairy waste-waters; impacts of biofilm support system on anaerobic CST reactors”. *Applied Energy*, 65: 91-98.
- [28]. Rao R.S. (1986), “Flora of West Godavari District”.
- [29]. Rao R.S. and Sreeramulu S.H. (1986). “Flora of Srikakulam District”.
- [30]. Rios EE, Cholich LA, Chileski G, Garcia EN, Iertora J, Gimeno EJ. (2015), “Suspected natural lysosomal storage disease from ingestion of pink morning glory (Ipomoea carnea) in goats in north argentina”. *The Journal of Veterinary*. 77(7): 847-50.
- [31]. Sahayaraj, K., Kombiah, P., Dikshit, A. K., Rathi, M. (2015). “Chemical constituents of the essential oils of Tephrosia purpurea and Ipomoea carnea and their repellent activity against Odoiporus longicollis”. *Journal of Serb. Chem. Soc*, 80(4), 465-473.
- [32]. Sankara Rao K., & Deepak Kumar (2024), *India Flora Online*. <http://indiafloraonline-ces.iisc.ac.in/plant>.
- [33]. Sasidharan N. (2011), “Flowering Plants of Kerala”. DVD, V2, KFRI.

- [34]. Saxena H.O., and Brahamam M. (1989). "The Flora of Similipahar"(Similipal), Orissa.
- [35]. Selvaraj, A. Valliammai, M. Premika, A. Priya, J.P. Bhaskar, V. Krishnan, S.T. (2020), " Pandian Sapindusmukorossi Gaertn. and its bioactive metabolite oleic acid impedes methicillin-resistant Staphylococcus aureus biofilm formation by down regulating adhesion gene expression". Microbiol. Res., 242 Article 126601, 10.1016/j.micres.2020.12660.
- [36]. Shaltout K.H.,Al-Sodany Y.M. and Eid E.M.(2006). "The biology of Egyptian wood perennials Ipomoea carnea Jacq". Ass.Univ. Bull. Environ. Res. Vol. 9(1):75-90.2.
- [37]. Sharma, A. and Bachheti, R.K. (2013). " A review on Ipomoea carnea" International Journal of Pharma and BioSciences, 4(4): 263-277.
- [38]. Shrivastava D, Shukla K. (2015). "Pharmaceutical efficacy of Ipomoea carnea". Biol. Forum-Int. J 2015;7(1):225-235
- [39]. Austin DF. Ipomoea carnea fistulosa (Mart. Ex choisy), India biodiversity.org/speies/show/263090
- [40]. Shukla, R.,Gupta, G., Kashaw, S.K., Jain, A.P.,Lodhi, S. (2018). "Wound healing effect of ethanolic extract from Morning Glory (Ipomoea carnea Jacq.) Leaves by using different models in rats". Pakistan Journal of Pharmaceutical Sciences Volume 31, Issue 4, July 2018, Pages 1355-1361.
- [41]. Singh VK, Patel AK, Moir AJ, Jagannadham M , sy. (2007); 55(14): 5809-18.
- [42]. Theodore Cooke (1908), "The flora of the Presidency of Bombay", Vol. 2 page-321
- [43]. Woradulayapinij, W., Soonthornchareonnon, N. and Wiwat, C. (2005). "In vitro HIV type 1 reverse transcriptase inhibitory activities of Thai medicinal plants and Canna indica L. rhizomes". Journal of Ethnopharmacology, 101(1): 84-89.

Smart Soil Moisture Monitoring System for Precision Water Management

Digambar D. Kulkarni¹, Nived J. Tabib², Soham R. Vankar²

¹Head and Assistant Professor of Department of Physics Dapoli Urban Bank Senior Science College Dapoli, Dist: Ratnagiri, Maharashtra, India

²T.Y.B.Sc. Physics, Department of Physics, Dapoli Urban Bank Senior Science College Dapoli, Dist Ratnagiri, Maharashtra, India

ARTICLE INFO

Article History:

Published : 30 April 2025

Publication Issue :

Volume 12, Issue 13

March-April-2025

Page Number :

129-132

ABSTRACT

This paper presents a smart soil moisture monitoring system utilizing Arduino Uno and a soil moisture sensor. The system detects moisture levels in various soil types, triggering a warning when moisture falls below a threshold. By leveraging IoT-based technology, our system enables precision water management, optimizing water usage, reducing waste, and promoting sustainable agriculture. This innovation has potential benefits for farmers, including improved crop yields and reduced water costs, while contributing to environmental conservation by preserving water resources.

Keywords: Soil Moisture Monitoring, Precision Agriculture, IoT-Based Solution, Water Conservation, Sustainable Agriculture.

INTRODUCTION

Soil moisture sensors play a crucial role in precision agriculture, enabling farmers and gardeners to optimize water usage, reduce waste, and promote healthy plant growth. By accurately measuring soil moisture levels, these sensors help users make informed decisions about irrigation, fertilization, and crop management.

This work aims to design and develop a reliable and efficient soil moisture sensor system, providing real-time data to support sustainable agricultural practices and improve crop yields. Maintaining the right soil moisture is crucial for the health of your plants. Overwatering or under watering can cause significant damage to plant health. A soil moisture sensor connected to an Arduino can automate the monitoring process, ensuring that your plants receive just the right amount of water. This technology is particularly beneficial for:

- Home gardens
- Greenhouses
- Agricultural fields
- Indoor plant setups

METHODS AND MATERIAL

To get started, you will need the following components:

- Arduino board (e.g., Arduino Uno)
- Soil moisture sensor module
- Connecting wires
- Breadboard (optional) LED (optional, for visual indication)
- 220-ohm resistor (optional, for LED setup)

RESULTS AND DISCUSSION

The result showed that by using the sensor's real-time data, water usage was reduced by up to 30% while maintaining optimal soil moisture levels, demonstrating the potential for significant water conservation in agricultural and gardening applications.

The project's data collection and analysis capabilities enabled informed decision-making, allowing farmers and gardeners to optimize their irrigation strategies and improve overall crop management.

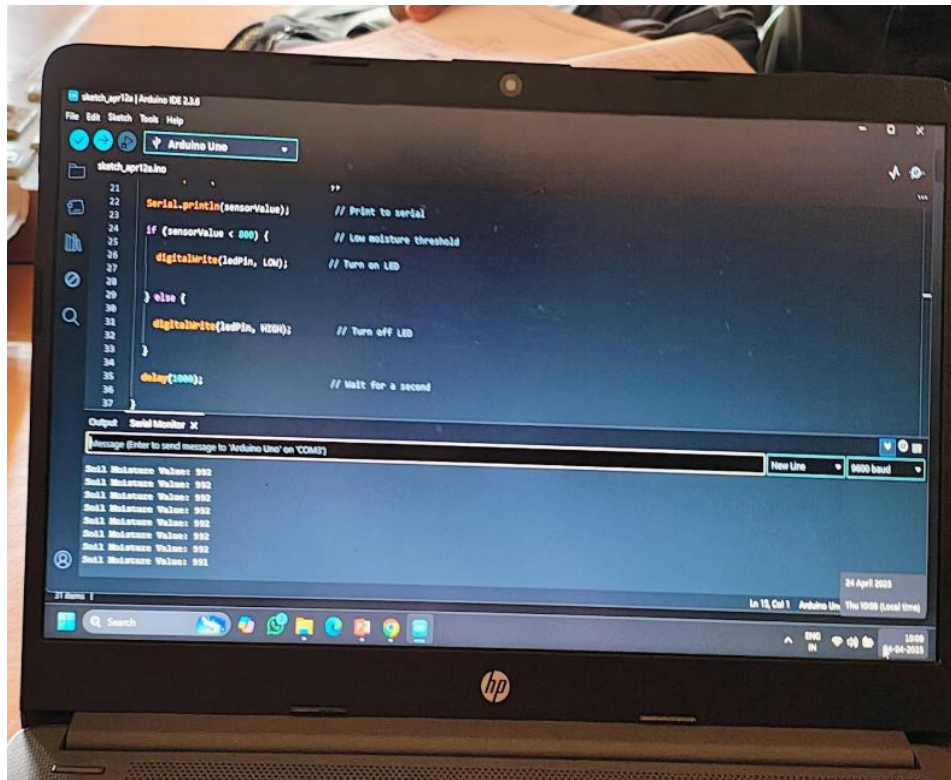
TABLE I ANALYSIS OF DATA

TIME	SOIL MOISTURE LEVEL%	SENSOR STATUS	IRRIGATION STATUS
6 AM	1500	OFF	OFF
8AM	1300	OFF	OFF
10AM	1000	OFF	OFF
12PM	780	ON	ON
2PM	540	ON	ON
4PM	80	ON	ON
6PM	1050	OFF	OFF
8PM	1000	OFF	OFF

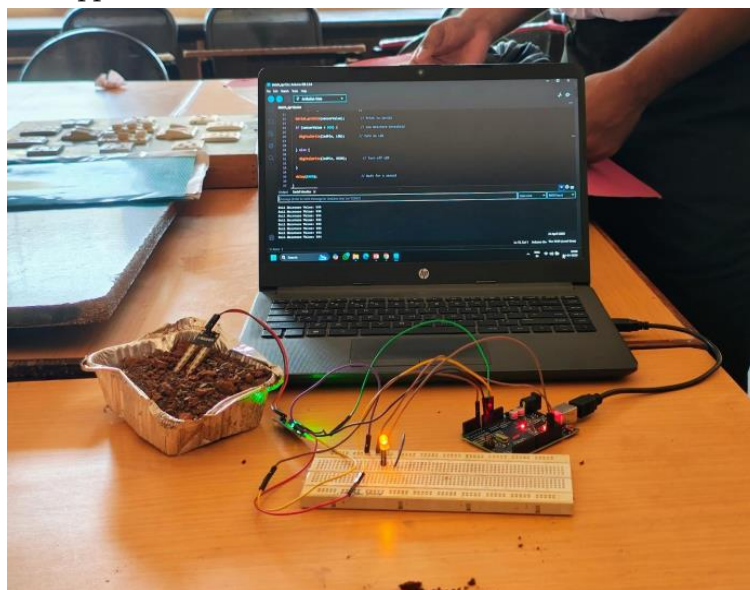
Following is experimental setup up for the wet soil moisture sensor indicating the LED OFF logic which shows the moisture level is dropped.



The following is the result of the experiment conducted



Following is the experimental setup up for the dry soil moisture sensor indicating the LED on logic which shows the moisture level is dropped.



Some key observations from our soil moisture sensor project include:

1. Soil moisture levels fluctuated significantly throughout the day, highlighting the need for real-time monitoring.
2. The sensor's data showed a strong correlation between soil moisture levels and plant health.
3. Overwatering was a common issue in traditional irrigation methods, which the sensor-based system helped mitigate.
4. The system's automated irrigation feature reduced water waste and optimized water usage.

CONCLUSION

In conclusion, this project successfully demonstrate the potential of soil moisture sensors in monitoring and managing soil moisture levels, with potential applications in agriculture, gardening, and environmental monitoring, ultimately contributing to optimized water usage and improved crop yields. This will naturally leads to Save

1. Save the Environment
2. Save Water
3. Aware about Health of Soil
4. Leads to growth of output from soil
5. Costing of whole Experiment Set up is low hence in budget of poor farmer also

REFERENCES

- [1]. Research Gate
- [2]. Soil Physics direct
- [3]. International Society of Precision Agriculture (ISPA) - Resources
- [4]. USDA's Natural Resources Conservation Service (NRCS) - Soil Moisture
- [5]. "Soil Moisture Sensors Market Report" (MarketsandMarkets)

Water Extract of Hibiscus Sabdariffa Leaves and Garniciaindica Rinds: An Efficient Medium for Synthesis of Benzylid Enemalono Nitriles

Pratibha V. Randhavane*

P G and Research, Department of Chemistry, S. S. G. M. College, Kopargaon, Dist. Ahilyanagar- Pin-423601, Maharashtra, India

ARTICLE INFO

Article History:

Published : 30 April 2025

Publication Issue :

Volume 12, Issue 13

March-April-2025

Page Number :

133-138

ABSTRACT

There is a strong demand of green and efficient method in the field of synthetic organic chemistry. In the search for such an efficient and greener method, here we describe the synthesis of benzylidene malononitriles performed in Hibiscus sabdariffa leaves extract and Garniciaindica rind extract. The reaction proceeded successfully without using any organic solvent or any catalyst. The isolation and purification of the products was easier. Spectroscopic techniques confirmed the elucidation of the product.

Keywords: Hibiscus sabdariffa leaves extract, Garnicia indica rind extract, benzylidene malononitrile, Knoevenagel condensation reaction, green synthesis.

INTRODUCTION

Benzylidene malononitriles have attracted the attention of large number of researchers because of specific biological properties such as anticancer^[1], antifungal^[2], antibacterial^{[3]-[4]} and anti-corrosive^[5]. These derivatives are used to increase cell resistance in the case of oxidative stress^[6], in the design of photoconductive cells^[7] and in the inhibition/activation of certain enzymes^[8]. The synthesis of benzylidene malononitrile derivatives takes place via the Knoevenagel condensation.

Any synthesis in aqueous solvent usually requires catalysts such as organic bases, Lewis' acids^[9], ionic liquids^[10], organometallic catalysts^[11] and functionalized biopolymers under microwave irradiation^[12].

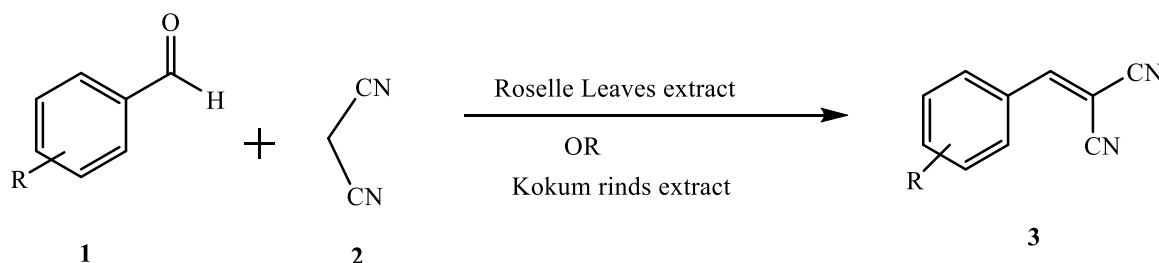
Nowadays there is a strong demand for green reaction methodologies. New naturally occurring catalytic reactions are of great importance because these reactions use natural, environment-friendly and uses biodegradable catalysts. The organic transformations using biocatalysts are more efficient and generate lower waste than traditional chemical methods^[13-14]. Biocatalytic organic reactions using water extract of banana peels^[15], pineapple juice^[16], starfruit juice of *Averrhoa carambola*^[17], lemon juice^[18], water extract of pomelo^[19], aqueous

extract of *Acacia concinna* pods [20], fruit extract of Keora fruit [21] and calcined eggshell [22] are applied in synthetic organic chemistry.

We have conducted this study to synthesize benzylidenemalononitrile derivatives using plant part extract as biocatalysts to implement the green approach.

Material and methods

Fresh *Hibiscus sabdariffa* (Roselle) leaves were purchased from local market. Roselle leaves with scientific name *Hibiscus sabdariffa* are commonly called as Lal-Ambadiin Maharashtra. Dry *Garcinia indica* (Kokum) fruit rinds were purchased from local grocery shop. The Roselle leaves extract [23, 24] and Kokum rind extract [25] both are acidic. The laboratory grade chemicals procured from commercial sources were used without purification. Melting points were determined in open capillary tubes and those were uncorrected. The reaction progress was monitored using TLC Silica gel aluminium plates from Merck. IR spectra were recorded on Perkin Elmer FTIR spectrophotometer. ¹H NMR spectra were recorded on Bruker Avance NEO 500 MHz NMR spectrometer with CDCl₃ as solvent. TMS was used as an internal standard. Peak values were shown in δ (ppm).



Scheme 1

Preparation of *Hibiscus sabdariffa* (Roselle) leaves extract:

Fresh *Hibiscus sabdariffa* (Roselle) leaves were washed with running tap water to remove dirt and then with distilled water. Leaves were dried in the shade and at room temperature. Dried leaves were crushed into powder using a household mixer grinder. 0.5-1.5 g of leaf powder was mixed with 10 ml of distilled water in a round bottom flask and heated at 60°C for one hour. Then the solution was cooled and filtered through Whatman filter paper no. 1. The filtrate was used as Roselle leaf extract. The fresh extract was used for each reaction.

Preparation of *Garcinia indica* (Kokum) rind extract:

Dried *Garcinia indica* (Kokum) fruit rinds were purchased from the local market and washed with distilled water. They were cut into small pieces with the scissor. 0.5-1.5 g of pieces were soaked in 10 mL of distilled water for 12 hours. The solution was filtered through Whatman filter paper no.1. The filtrate was used as a Kokum rind extract. The fresh extract was used for each reaction.

Optimization of reaction:

The reaction for the synthesis of compound **3a** was chosen as a reference reaction to optimize the amount of leaf powder/kokum rind. It was observed that the yield was better for 1g of leaf powder/kokum rind. The results are shown in Table 1.

TABLE 1: Optimization of reaction for synthesis of 3a

Entry	mL of water used	Wt. of leaf powder (g)	Yield (%)	Wt. of kokum rind (g)	Yield (%)
1	10	0.5	60	0.5	65
2	10	1.0	88	1.0	95
3	10	1.5	86	1.5	94

Procedure for synthesis of 2-benzylidenemalononitrile (3a-3i):

The reaction mixture of aromatic aldehyde (**1**, 1.5 mmol) and malononitrile (**2**, 1.5 mmol) was refluxed in 10 mL of Roselle leaf extract/ Kokum rind extract in a 50 mL round bottom flask. The reaction was monitored with the help of TLC (Petroleum ether + Ethyl acetate). After completion of the reaction, the reaction mixture was cooled. The solid obtained was filtered and washed with water. The pure product was obtained by recrystallization in ethanol (**3**).

2-(4-Methoxybenzylidene)malononitrile (3a): IR (cm^{-1}): 2222 (CN), 1607 & 1514 (aromatic C=C), 1182 (C-O); ^1H NMR (CDCl_3 , δ ppm): 3.91 (3H, s, -OCH₃), 7.02 (2H, d, Ar-H), 7.65 (1H, s, C=C-H), 7.90 (2H, d, Ar-H); ^{13}C NMR (CDCl_3 , δ ppm): 55.82 (OCH₃), 78.59 (=C-CN₂), 113.36 & 114.44 (2×CN), 115.16 to 158.88 (6 Aromatic carbons), 164.85 (C=C, β to CN); MS: m/z: 184.92 (M+1).

2-(4-Chlorobenzylidene)malononitrile (3b): IR (cm^{-1}): 2221 (CN), 1604 & 1509 (aromatic C=C), 1017 (C-Cl); ^1H NMR (CDCl_3 , δ ppm): 7.52 (2H, d, Ar-H), 7.73 (1H, s, C=C-H), 7.85 (2H, d, Ar-H); ^{13}C NMR (CDCl_3 , δ ppm): 83.37 (=C-CN₂), 112.36 & 113.47 (2×CN), 129.36 to 141.16 (Aromatic carbons), 158.33 (C=C, β to CN); MS: m/z: 190.00 (M+1).

2-(4-Bromobenzylidene)malononitrile (3c): IR (cm^{-1}): 2222 (CN), 1589 & 1508 (aromatic C=C), 990 (C-Br); ^1H NMR (CDCl_3 , δ ppm): 7.68 (2H, d, Ar-H), 7.72 (1H, s, C=C-H), 7.77 (2H, d, Ar-H); ^{13}C NMR (CDCl_3 , δ ppm): 83.53 (=C-CN₂), 112.34 & 113.46 (2×CN), 129.67 to 133.10 (Aromatic carbons), 158.44 (C=C, β to CN); MS: m/z: 233.95 (M+1).

2-Benzylidenemalononitrile (3d): IR (cm^{-1}): 2225 (CN), 1589 & 1449 (aromatic C=C); ^1H NMR (CDCl_3 , δ ppm): 7.53 (2H, t, Ar-H), 7.62 (1H, m, Ar-H), 7.78 (1H, s, C=C-H), 7.90 (2H, d, Ar-H); ^{13}C NMR (CDCl_3 , δ ppm): 82.87 (=C-CN₂), 112.58 & 113.74 (2×CN), 129.66 to 134.66 (Aromatic carbons), 160.00 (C=C, β to CN); MS: m/z: Mol wt. 156.04 (M+1).

Result and Discussion

In search of a greener, economical and simpler method for the synthesis benzylidenemalononitrile derivatives herein we report the use of Roselle leaf extract and Kokum rind extract. It was observed that both reactions give comparable yield in near about same time. The structures of synthesized products were determined by spectral analysis such as IR, ^1H NMR, ^{13}C NMR and mass techniques. For example, in compound 3a, the peaks that appeared in IR spectrum at 2222, 1607, 1514, 1182 were attributed to CN, C=C and C-O groups respectively. The ^1H NMR of compound 3a produced specific signals such as singlet at δ 3.91 ppm for methoxy group, while aromatic protons between δ 7.02 and 7.90 ppm. A singlet at δ 7.65 ppm indicated the presence of -C=C-H group.

Conclusion

The benzylidenemalononitrile derivatives were successfully synthesized by clean, simple, environmentally benign and economical methods. The reaction was performed without creating any harmful waste. Some of the synthesized compounds were characterized by spectral techniques.

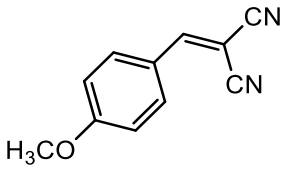
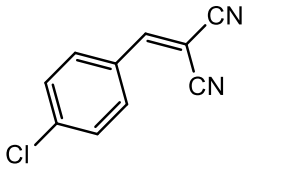
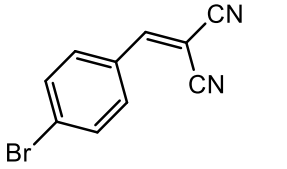
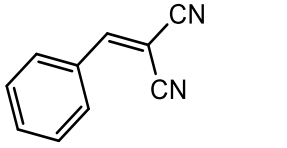
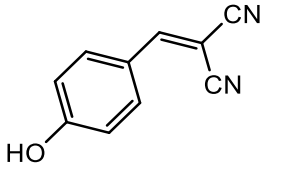
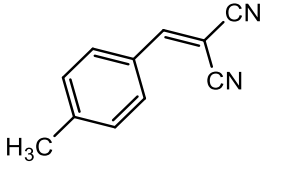
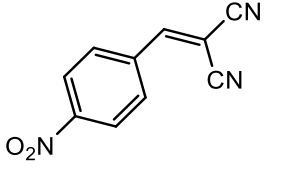
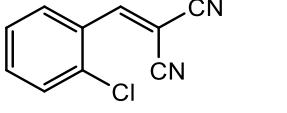
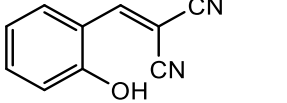
Conflict of interest

The author declares that there is no conflict of interest regarding the publication of this article.

Acknowledgement

The author is very thankful to The Director, SAIF, Panjab University, Chandigarh for spectral analysis and to The Principal, S.S.G.M. College, Kopergaon for providing research facilities and financial assistance through a seed money scheme.

TABLE 2: Data of synthesized benzylidene malononitriles

Entry	Compound	Roselle leaf extract		Kokum rind extract		M. P. (°C) Observed (Reported)
		Time (min)	Yield (%)	Time (min)	Yield (%)	
3a		45	88	40	95	115-116 (115)
3b		50	75	45	84	164-165 (163)
3c		70	72	60	81	153-155 (155)
3d		60	70	50	80	82-84 (84)
3e		60	73	50	88	185-187 (188)
3f		60	78	50	89	163-164 (166)
3g		55	72	45	85	157-159 (157)
3h		60	75	50	88	76-78 (77)
3i		60	72	50	81	157-159 (158)

REFERENCES

- [1]. Hu, Q.; Shi, X.; Chen, Y.; Han, X.; Duan P.; Zang, W. Revisiting the Knoevenagel condensations: A universal and flexible bis-ammoniated fiber catalyst for the mild synthesis of α,β -unsaturated compounds. *J. of Ind. and Eng. Chem.* 2017, 54, 75.
- [2]. Sidhu, A.; Sharma, J. R.; Rai, M. Chemoselective reaction of malonotitrile with imine-ones and antifungal potential of products. *Ind. J. Chem.* 2010, 49B, 247-250.
- [3]. Khan, S. A.; Asiri, A. M.;Rhaman, R. M.; Elorby, S. A.;Aqlan, F. M. S.; Wani, M.Y.; Sharma, K. Multistep synthesis of fluorine-substituted pyrazolopyrimidine derivatives with higher antibacterial efficacy based on in vitro molecular docking and density functional theory. *J. Het. Chem.* 2017, 54, 3099-3107.
- [4]. Gopalakrishna Panicker, R.K.;Krishnapillai, S. Synthesis of on resin poly(propylene imine) dendrimer and its use as organocatalyst. *Tet. Lett.*2014, 55, 2352.
- [5]. Fouda, A. S.; El-Ewady, Y. A.; Abo-El-Enien, O. M.;Agizah, F. A. Cinnamoylmalononitriles as corrosion inhibitors for mild steel in hydrochloric acid solution. *Anti-Corrosion Meth. and Mat.* 2008, 55, 317-323.
- [6]. Turpaev, K.; Ermolenko, M.;Cresteil, T.; Drapier, J. C. Benzylidenemalononitrile compounds as activators of cell resistance to oxidative stress and modulators of multiple signaling pathways: A structure–activity relationship study. *Biochem. Pharma.* 2011, 82, 535-547.
- [7]. Shahid, M.; Misra, A. A. simple and sensitive intramolecular charge transfer fluorescent probe to detect CN – in aqueous media and living cells. *Anal. Meth.* 2013, 5, 434-437.
- [8]. Levitzki, A.; Mishani, E. E.Tyrphostins and other tyrosine kinase inhibitors.*Annual Rev.Biochem.* 2006, 75, 93-109.
- [9]. Wang, H.; Wang, C.; Yang, Y.; Zhao, M.; Wang, Y. H3PW12O40/mpg-C3N4 as an efficient and reusable bifunctional catalyst in one-pot oxidation- Knoevenagel condensation tandem reaction. *Cat. Sci. and Tech.* 2017, 7, 405.
- [10]. Li, G.; Xiao, J.; Zhang, W. Efficient and reusable amine-functionalized polyacrylonitrile fiber catalysts for Knoevenagel condensation in water. *Green Chem.* 2012, 14, 2234-2242.
- [11]. De Resende Filho, J. B. M.; Pires, G. P.; De Oliveira Ferreira, J. M. G.;Teotonio, E. E. S.; Vale, J. A. Knoevenagel condensation of aldehydes and ketones with malononitrile catalysed by amine compounds-tethered Fe3O4@SiO2 Nanoparticles. *Cat. Lett.* 2017, 147, 167-180.
- [12]. Jimenez, D. E. Q.; Ferreira, I. M.; Yoshioka. S. A.; Fonseca, L. P.; Porto, A. L. M. Green Synthetic methodology of (E)-2-cyano-3-aryl selective Knoevenagel adducts under microwave irradiation. *Curr. Micro. Chem.* 2019, 6(1), 54-60.
- [13]. Baldassare, F.; Bertoni, G.; Chiappe, C.;Marioni, F. Preparative synthesis of chiral alcohols by enantioselective reduction with *Daucus carota* root as biocatalyst. *J. Mol. Cat. B: Enzy.* 2000, 11, 55-58.
- [14]. Koeller, K. M.; Wong, C. H. Enzymes for Chemical Synthesis. *Nature.* 2001, 409, 232-240.
- [15]. Bagul, S. D.; Rajput, J. D.; Bendre, R. S. Synthesis of 3-carboxycoumarins at room temperature in water extract of banana peels. *Environ. Chem. Lett.* 2017, 15, 725-731.
- [16]. Patil, S. S.; Jadhav, S. D.; Deshmukh, M. B. Eco-friendly and economic method for Knoevenagel condensation by employing natural catalyst. *Ind. J. Chem.* 2013, 52B, 1172-1175.
- [17]. Pal, R.; Sarkar T. Visible light induced Knoevenagel condensation catalysed by starfruit juice of *Averrhoa carambola*. *Int. J. Org. Chem.* 2014, 4, 106-115.
- [18]. Deshmukh, M. B.; Patil, S. S.; Jadhav, S. D.; Pawar, P. B. Green Approach for Knoevenagel Condensation of Aromatic Aldehydes with Active Methylene Group. *Syn. Comm.* 2012, 42(8), 1177-1183.

- [19]. Tamuli, K. J.; Dutta. D.; Nath, S.; Bordoloi, M. A. Greener and Facile Synthesis of imidazole and Dihydropyrimidine Derivatives under Solvent-Free Condition Using Nature- Derived Catalyst. *Chem. Select.* 2017, 2(26), 7787-7791.
- [20]. Chavan, H. V.;Bandgar, B. P. Aqueous Extract of Acacia concinna Pods: An Efficient Surfactant Type Catalyst for Synthesis of 3-Carboxycoumarins and Cinnamic Acids via Knoevenagel Condensation. *ACS Sus. Chem. and Eng.* 2013, 1(8), 929-936.
- [21]. Pal, R. Aqueous Extract of Keora Fruit: An efficient green solvent cum catalyst for environmentally friendly synthesis of arylidene malononitrile under visible light. *Int. J. Green Chem. and Bioprocess.* 2016, 6(1), 13-16.
- [22]. Patil, S.; Jadhav, S. D.; Deshmukh, M. B. Calcined eggshell (CES): An efficient natural catalyst for Knoevenagel condensation under aqueous condition. *J. Chem. Sci.* 2013, 125(4), 851-857.
- [23]. Fasoyiro, S, B.; Physical, Chemical and Sensory Qualities of Roselle Water Extract- coagulated Tofu Compared with Tofu from Two Natural Coagulants. *Nigerian Food J.* 2014, 32(2), 97-102.
- [24]. Ines Da-Costa-Rocha.;Bonnlaender, B.; Sievers,H.; Pischel, I.;Heinrich M. Hibiscussabdariffa L.- A phytochemical and pharmacological review. *Food Chem.* 2014, 165, 424-443.
- [25]. Swami, S. B.; Thakor, N. J.; Patil, C. S. Kokum (*Garcinia Indica*) and its Many Functional Components as Related to the Human Health: A Review. *J.Food Res. and Tech.*2014, 2(4), 130-142.

A Review on Synthesis Of 2-Aryl Substituted Benzoxazole and Its Derivatives

Sachin S. Sagar

Department of Chemistry, I.C.S. College of Arts, Commerce and Science, Khed, Dist.-Ratnagiri- 415709, Maharashtra, India

ARTICLE INFO

Article History:

Published : 30 April 2025

Publication Issue :

Volume 12, Issue 13

March-April-2025

Page Number :

139-145

ABSTRACT

Benzoxazole is a significant heterocyclic molecule comprising a benzene ring fused with an oxazole ring. It functions as a crucial scaffold in pharmaceutical chemistry, materials science, and agrochemical industries owing to its varied biological activities and physicochemical characteristics. It represents a vital role with several beneficial therapeutic applications, including antiulcer, antihypertensive, analgesic, anti-inflammatory, antiviral, antifungal, anticancer, antidepressant, anticonvulsant, antitubercular, and antitumor activities. The literature research indicates that benzoxazole derivatives are highly effective, their structural attributes, and their extensive uses in pharmaceuticals, optoelectronics, and corrosion inhibition. Recent breakthroughs in green synthesis methods and computer analyses are also addressed.

Keywords: Benzoxazole, Coumarin, Anti-inflammatory, Anti-microbial, Anti-cancer.

INTRODUCTION

Benzoxazole is one of the most important heterocyclic compounds with outstanding pharmacological properties. Many compounds with a variety of uses in medicinal chemistry have been produced as a consequence of extensive study into the synthesis and alterations of the benzoxazole nucleus. Because of its possible pharmacological and biological properties, researchers have been interested in the structural analysis and biological activities of benzoxazole derivatives. Based on a review of the literature, the benzoxazole moiety has a broad spectrum of biological actions [1]. Various benzoxazole derivatives possess different pharmacological and biological activities of which the most potent is an antibiotic [2], antibacterial, antifungal, antitumor, anti-inflammatory, antiulcer, antitubercular activities, cathepsin S inhibitors, selective peroxisome proliferator-activated receptor antagonists, HIV reverse transcriptase inhibitors, anticancer agents, estrogen receptor agonists and orexin-1 receptor antagonists [3-8]. Benzoxazole derivatives have also found application as herbicides and as fluorescent whitening agent dyes [9].

According to study, substituted benzoxazoles and their related heterocycles have reduced toxicities and are physiologically active. Benzoxazoles are interesting luminous substances that are being studied as possible herbicides for bleaching. Additionally, they have shown less toxicity in animals with warm blood.

Additionally, a variety of functional materials, including metal sensors, textile optical brighteners, and engineering polymers, are rich in this theme.[10-12] The need to develop versatile methods for the synthesis of 2-substituted benzoxazoles is therefore increasing.

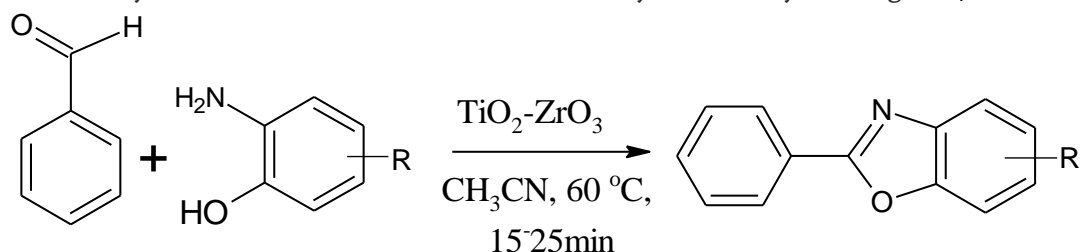
Benzoxazole synthesis has been reported using a variety of methods in recent years, such as coupling amino aromatics with carboxylic acids [13], orthoesters [14], nitriles [15], primary alcohol [16], amines [17], acyl halides [18], cyclisation of Schiff's bases, which are derived from the condensation of o-aminophenols and aldehydes in the presence of oxidants [19], cyclisation of o-halobenzanilides [20], orohydroxyanilides [21], and reaction of bromoaniline with acyl halides [22].

The condensation of 2-aminophenol with carboxylic acids or their analogues, such as aldehydes [23-26], acid chlorides, [27-29]orthoesters,[30-32]and β -oxodithioesters,[33]under diverse reaction conditions is a direct method for synthesising the benzoxazole unit. However, these approaches often include several constraints, including the use of very poisonous chemicals, powerful acids, and, in some instances, severe reaction conditions.

REVIEW OF LITERATURE

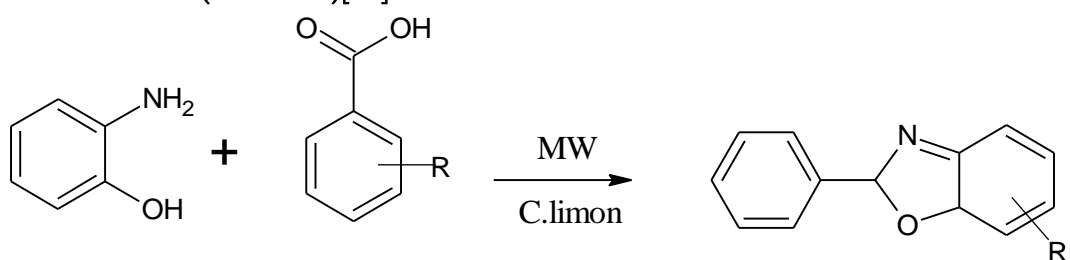
The literature revealed several syntheses of 2-substituted benzoxazole by different research groups employing numerous short and elegant syntheses utilizing novel chemistry. A brief summary of various methods is summarized below.

Patilet. al. have reported the synthesis of 2-aryl substituted benzoxazole derivatives using 2-aminophenol and substituted benzaldehyde at moderate temperature. The effect of temperature, solvents and catalyst concentration on the synthesis of benzoxazole derivatives was systematically investigated(Scheme-1)[34].



Scheme-1

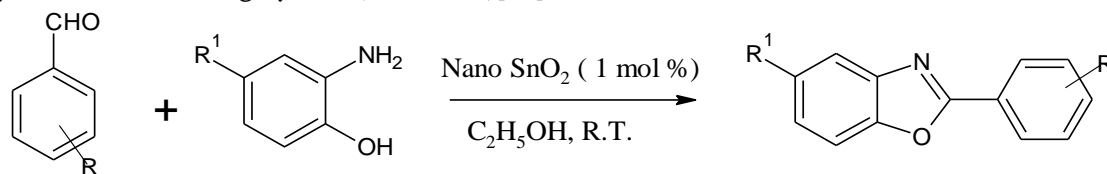
B. A. Lote et.al. have reported the synthesis of 2-aryl substituted benzoxazole derivatives using 2-aminophenol and substituted aromatic carboxylic acid in presence of green reagent i.e. citrus limon extract under microwave irradiation(Scheme-2)[35].



Scheme-2

S.M.Vahdatet. al. have reported the synthesis of 2- aryl or alkylbenzoxazole derivatives condensation reaction of substituted aromatic aldehyde with 2- aminophenol in presence of SnO₂nanocatalyst at room temperature.

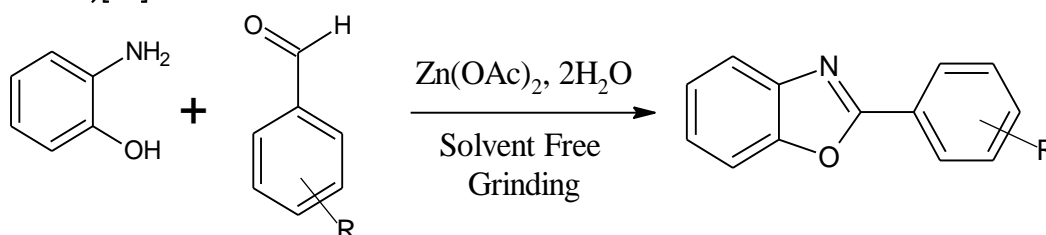
These reactions proceed under heterogeneous and mild conditions in ethanol at room temperature to provide 2-aryl or alkylbenzoxazoles in high yields. (Scheme-3)[36].



R¹: 2a=H; 2b=Me; 2c=Cl 2d=NO₂

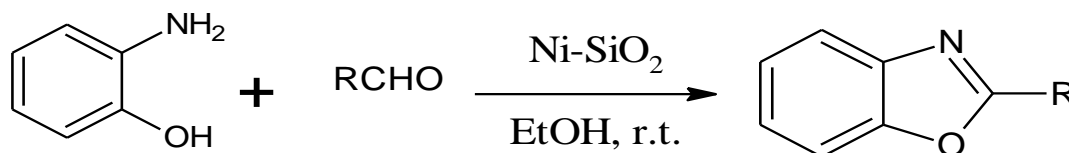
Scheme-3

Reddy et. al. have reported the synthesis of 2-substituted benzoxazole via condensation reaction between 2-aminophenol and various aromatic aldehydes in the presence of Zn(OAc)₂·2H₂O as a catalyst under solvent-free conditions (Scheme-4)[37].



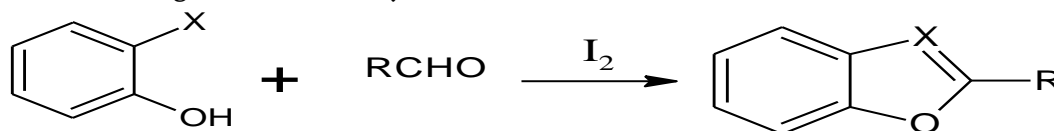
Scheme-4

S. Maddila et. al. have reported the synthesis of benzoxazole via condensation reaction between 2-aminophenol and substituted aldehydes in the presence of a catalytic amount of nickel-supported silica at room temperature. The significant advantages of this methodology are good yields, short reaction times. (Scheme-5)[38].



Scheme-5

Moghaddam et. al. have reported the synthesis of benzoxazole via condensation reaction between 2-aminophenol and aromatic aldehydes in the presence of a catalytic amount of molecular iodine in solvent-free conditions with or without microwave irradiation to afford the corresponding 2-substituted benzothiazole and benzoxazole derivatives in good to excellent yields. (Scheme-6)[39].



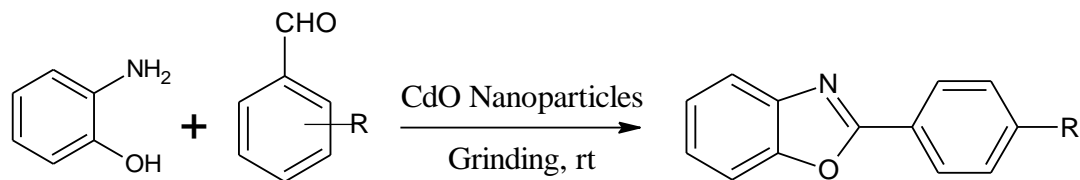
X = N, S

R = Alkyl

65 - 95%

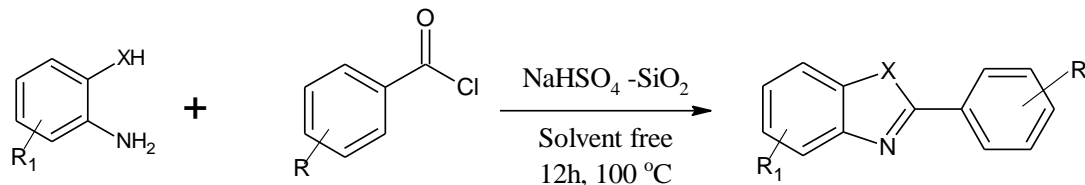
Scheme-6

A.V. Borhade et. al. have reported the synthesis of 2-aryl benzoxazole derivative by grinding method using condensation reaction between 2-aminophenol and aromatic aldehydes in the presence of CdO nanoparticle as a catalyst at room temperature. The mild reaction conditions, cleaner process, easy work up, good yield with high purity, solvent-free, lower catalytic loading, and reusability of catalyst are important features of this method. (Scheme-7)[40].



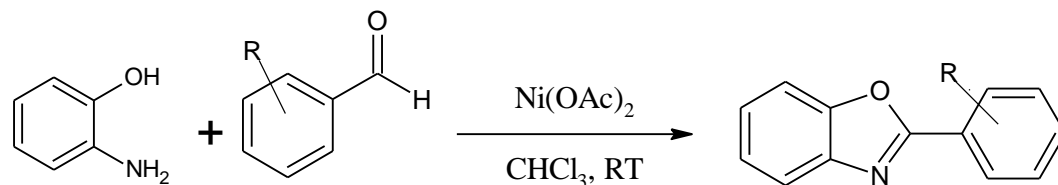
Scheme-7

Ravikumaret. al. have reported the synthesis of benzoxazole derivative from the reaction between ortho substituted 2-amino aromatics with acyl chloride in the presence of catalytic amount of silica supported sodium hydrogen sulphate under solvent free condition(Scheme-8)[41].



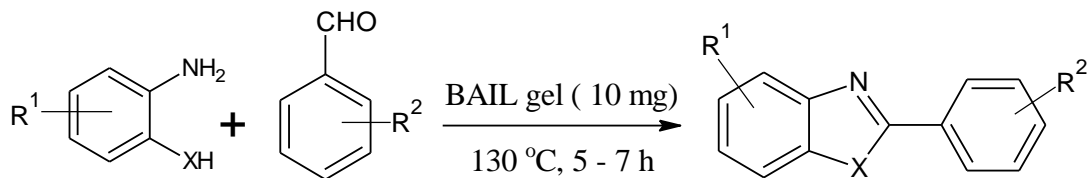
Scheme-8

Patilet. al. have reported the synthesis of benzoxazole derivative from the reaction between 2-amino phenol with substituted aldehyde in the presence of Ni(OAc)₂ with chloroform at room temperature(Scheme-9)[42].



Scheme-9

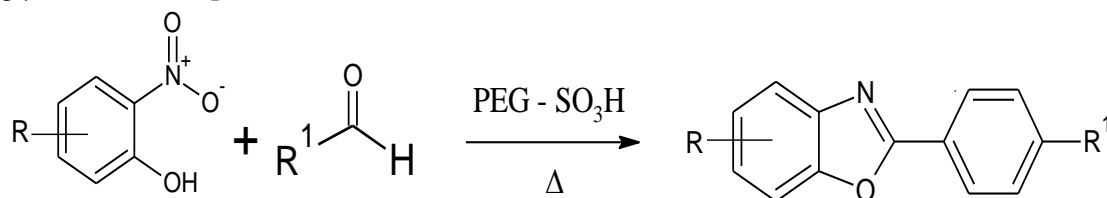
Nguyen et. al. have reported the synthesis of benzoxazole derivative from the reaction between substituted 2-amino aromatics with substituted aldehyde in the presence of bronsted acidic ionic liquid gel (BAIL gel) at the temperature 130°C(Scheme-10)[43].



X = O, S, NH

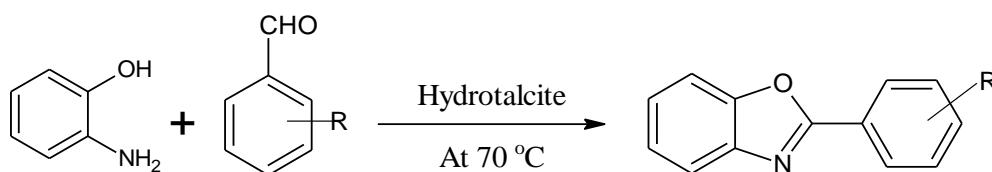
Scheme-10

Chikhaleet. al. have reported the synthesis of various 2- amino benzoxazole and other benzoxazole derivative from the reaction between substituted O-nitro phenol with substituted aldehyde in the presence of poly (ethylene glycol) bound sulphonic acid (PEG -SO₃H)(Scheme-11)[44][34].



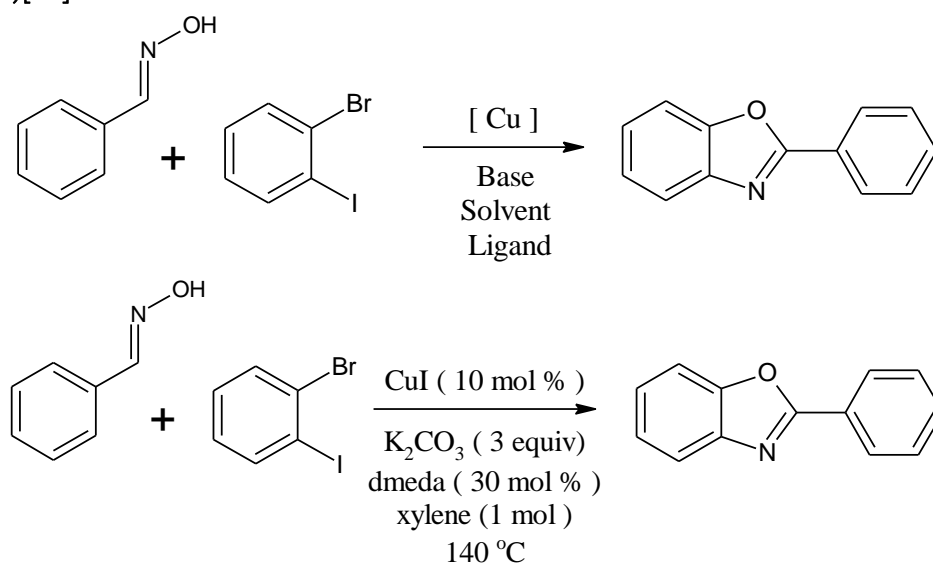
Scheme-11

Sahu et. al. have reported the synthesis of benzoxazole derivative from the reaction between 2-amino phenol with substituted aldehyde in the presence of Hydrotalcite catalyst under solvent free condition(Scheme-12)[45].



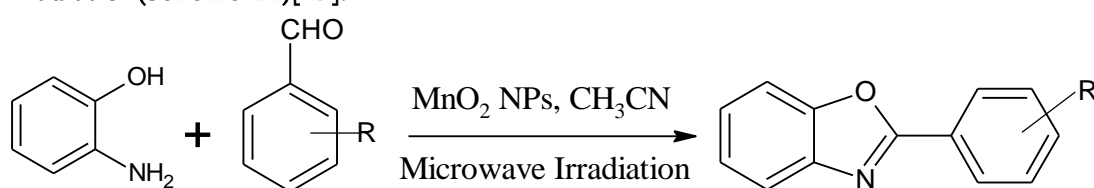
Scheme-12

Dineshkumaret. al. have reported copper catalysed method for the synthesis of 2- aryl benzoxazoles from the reaction of aldoxime and 2- iodobromobenzene using N, N'- dimethyl ethylenediamine (DMEDA) as the ligand(Scheme-13)[46].



Scheme-13

H. Naemiet. al. have reported the synthesis of substituted benzoxazole derivative from the reaction between 2-amino phenol with substituted aromatic aldehyde in the presence of MnO₂ nanoparticle as catalyst under microwave irradiation(Scheme-14)[47].



Scheme-14

Most of these reported methods suffer from many drawbacks for the synthesis of benzoxazole derivatives, some of the drawbacks such as harmful solvents used in reactions, prolong reaction time with less product yields, tedious work-up procedures, use of expensive reagents attracts more attention to overcome.

To overcome these drawback, there is need to develop new catalyst for the synthesis of benzoxazole derivatives which shows simple work-up procedure, less toxicity, good recovery and recyclability.

Many organic conversions have been developed by using metal oxides, mixed metal and supported metal for the supported metal mixed oxide composites for the directed synthesis. With the presence of new and innovative strategies, here have been developed new synthesis methods for benzoxazole and its derivatives which is simple than earlier.

CONCLUSION

In the present review article, we have summarized various synthetic methods for the preparation of 2- aryl benzoxazole and its derivatives. This study indicates a necessity for environmentally friendly synthetic technologies. This study has concentrated on a broad spectrum of biological activity, including anticancer, antitubercular, antifungal, analgesic, and antioxidant properties. This article demonstrates that benzoxazole is a significant moiety in heterocyclic chemistry that requires extensive modification or derivatization to create and construct highly effective biological molecules.

REFERENCES

- [1]. Sadek B, Salem F, Fehelbom K. M., Synthesis, characterization and Antimicrobial evaluation of oxadiazole congeners, *Molecules*, 16, 2011, 4339-4347.
- [2]. T. Ozlem, O. Likay, S. Esin, Y. Ismail, U. Nejat, *Farmaco* 53 (1998) 337-341.
- [3]. A. Zafer, Kaplancikli, T.Z. Gulhan, R. Gilbert, G. Kiyet, *Arch. Pharma. Res.* 27 (2004) 1081-1085.
- [4]. T. Yi- Ping, L. Yan-Wen, *Inorg. Chim. Acta* 362 (2009) 2033-2038.
- [5]. P. Kohli, S.D. Srivastava, S.K. Srivastava, *J. Chin. Chem. Soc.* 54 (2007) 1003-1010.
- [6]. J. Nishiu, M. Ito, Y. Ishida, M. Kakutani, T. Shibata, M. Matsushita, M. Shindo, *Diabetes Obes. Metab.* 8 (2006) 508-518.
- [7]. J.A. Grobler, G. Dornadula, M.R. Rice, A.L. Simcoe, D.J. Hazuda, M.D. Miller, *J. Biol. Chem.* 282 (2007) 8005-8010.
- [8]. K. Rasmussen, M.A. Hsu, Y. Yang, *Neuropsychopharmacology* 32 (2007) 786-792.
- [9]. I.H. Leaver, B. Milligan, *Dyes Pigm.* 5 (1984) 109-144
- [10]. Yang CC, Tian Y, Chen CY, et al. *Macromolecular Rapid Communication* 2007;28(7):894-899.
- [11]. Ogura T, Yamaguchi K, Shibasaki Y, et al. Photosensitive Poly(Benzoxazole) Based on Poly(O-Hydroxy Amide), Dissolution Inhibitor, Thermo Acid Generator, and Photo Acid Generator. *Polym J.* 2007;39(3):245- 251.
- [12]. Ogoshi T, Miyake J, Chujo Y. Multiresponsive Photopatterning Organic- Inorganic Polymer Hybrids Using a Caged Photoluminescence Compound. *Macromolecules.* 2005;38(10):4425-4431
- [13]. C.O. Kangani, D.E. Kelley, B.W. Day, *Tetrahedron Lett.* 47, 6497 (2006)
- [14]. S.F. Hojati, B. Maleki, Z. Beykzadeh, *Monatsh. Chem.* 142, 87 (2011)
- [15]. H. Tan, C.-X. Pan, Y.-L. Xu, H.-S. Wang, Y.-M. Pan, *J. Chem. Res.* 36, 370 (2012)
- [16]. A. Khalafi-Nezhad, F. Panahi, *ACS Catal.* 4, 1686 (2014)
- [17]. A.J. Blacker, M.M. Farah, S.P. Marsden, O. Saidi, J.M. Williams, *Tetrahedron Lett.* 50, 6106 (2009)
- [18]. R.S. Pottorf, N.K. Chadha, M. Katkevics, V. Ozola, E. Suna, H. Ghane, T. Regberg, M.R. Player, *Tetrahedron Lett.* 44, 175 (2003)
- [19]. Y. Riadi, R. Mamouni, R. Azzalou, M. El Haddad, S. Routier, G. Guillaumet, S. Lazar, *Tetrahedron Lett.* 52, 3492 (2011)
- [20]. G. Evindar, R.A. Batey, *J. Org. Chem.* 71, 1802 (2006)
- [21]. D. Rambabu, P.R.K. Murthi, B. Dulla, M. Basaveswara Rao, M. Pal, *Synth. Commun.* 43, 3083 (2013)
- [22]. R.D. Viirre, G. Evindar, R.A. Batey, *J. Org. Chem.* 73, 3452 (2008)
- [23]. Kawashita Y, Nakamichi N, Kawabata H, et al. Direct and Practical Synthesis of 2-Arylbenzoxazoles Promoted by Activated Carbon. *Org Lett.* 2003;5(20):3713-3715.

- [24]. Chang J, Zhao K, Pan S. Synthesis of 2-arylbenzoxazoles via DDQ promoted oxidative cyclization of phenolic Schiff bases—a solution–phase strategy for library synthesis. *Tetrahedron Lett.* 2002;43(6):951–954.
- [25]. Rajender SV, Dilip K. Manganese triacetate oxidation of phenolic Schiff bases: synthesis of 2-arylbenzoxazoles. *J Heterocycl Chem.* 1998;35(6):1539–1540.
- [26]. Padalkar VS, Gupta VD, Phatangare KR, et al. Indion 190 resin, efficient, environmentally friendly, and reusable catalyst for synthesis of benzimidazoles, benzoxazoles, and benzothiazoles. *Green ChemLett Rev.* 2012;5(2):139–145.
- [27]. Goldstein SW, Dambek PJ. A facile synthesis of methyl 2-substituted-4- benzoxazolecarboxylates. *J Heterocyclic Chem.* 1990;27(2):335–336.
- [28]. Shoar RH, Heidary M, Farzaneh M, et al. Synthesis of benzoxazoles catalyzed by MCM–41, a green and reusable catalyst. *Synth Commun.* 2009;39(10):1742–1751.
- [29]. Nadaf RN, Siddiqui SA, Daniel T, et al. Room temperature ionic liquid promoted regioselective synthesis of 2-aryl benzimidazoles, benzoxazoles and benzthiazoles under ambient conditions. *J MolCatal A Chem.* 2004;214(1):155–160.
- [30]. Jekins GL, Knevel AM, Davis C. Notes. New synthesis of the benzothiazole and benzoxazole rings. *J Org Chem.* 1961;26(1):274–274.
- [31]. Kunz KR, Taylor EW, Hutton HM, et al. A simple and convenient synthesis of 5-substituted benzoxazoles. *Org Prep Proc Int.* 1990;22(5):613– 618.
- [32]. Bastug G, Eviolitte C, Marko IE. Functionalized orthoesters as powerful building blocks for the efficient preparation of heteroaromatic bicycles. *Org Lett.* 2012;14(13):3502–3505.
- [33]. Peng J, Zong C, Ye M, et al. Direct transition–metal–free intramolecular C–O bond formation: synthesis of benzoxazole derivatives. *Org Biomol Chem.* 2011;9(4):1225–1230.
- [34]. Mahadev R. Patil, J. T. Bhanushali, B. M. Nagaraja, R. S. Keri, *ComptesRendusChimie*, 2018, 21, 399-407.
- [35]. Bhagyashri A. Lote, Pravin B. Piste, *International Journal of Pharmaceutical Sciences Review and Research*, 2018, 49(1), 17-21.
- [36]. S. M. Vahdat, S. G. Raz, S. Bagheri, *Journal of Chemical Sciences*, 2014, 3, 579-585
- [37]. M. B. Madhusudana Reddy, A. Nizam, and M. A. Pasha, *Synthetic Communication*, 2011, 41: 1838-1842.
- [38]. S. Maddila, S. B. Jonnalagadda, *Journal of Chilean Chemical Society*, 2012, 57, N0 2.
- [39]. F. M. Moghaddam, G. R. Bardajee, H. Ismaili and S. M. D. Taimoory, *Synthetic Communication*, 2006, 36: 2543-2548.
- [40]. A. V. Borhade, B. K. Uphade, *Iranian Journal of Catalysis*, 2016, 6(3), 197-201.
- [41]. K. Ravikumar, P. V. V. Satyanarayana, and B. S. Srinivasa Reddy, *Journal of Chemistry*, Hindawi Publishing Corporation, 2013, Article ID 151273, [http:// dx. doi.org/ 10.1155/2013/151273](http://dx.doi.org/10.1155/2013/151273).
- [42]. V. D. Patil, K. P. Patil, *International Journal of Chemtech Research*, 2015, 8 (11), 457-465.
- [43]. T. Nguyen, X. Trang T. Nguyen, T.– L. H. Nguyen, P. H. Tran, *ACS Omega*, 2019, 4, 368-373.
- [44]. R. V. Chikhale, A. M. Pant, S. S. Menghani, P. G. Wadibhasme, P. B. Khedekar, *Arabian Journal of Chemistry*, 2014, 1878 – 5352, [http:// dx. doi.org/ 10.1016 /j. arabjc. 2014. 06. 011](http://dx.doi.org/10.1016/j.arabjc.2014.06.011).
- [45]. Pramod K. Sahu, *The Royal Society of Chemistry*, 2017, 7, 42000, DOI: 10.1039/c6ra25293a.
- [46]. Dinesh Kumar Nayak, N. Panda, *MOJ Bioorganic and Organic Chemistry*, 2017, 1(5).
- [47]. HosseinNaeimi, Z. Rouzegar, S. Rahmatinejad, *Research on Chemical Intermediates*, 2017, DOI 10.1007/s11164-017-2909-4.

Theoretical Investigation of The Nonlinear Optical Properties of Benzene Using DFT Method

Vinayak Deshmukh

Department of Physics, Shri Siddheshwar Mahavidyalaya, Majalgaon, Dist. Beed, Maharashtra, India

ARTICLE INFO

Article History:

Published : 30 April 2025

Publication Issue :

Volume 12, Issue 13

March-April-2025

Page Number :

146-151

ABSTRACT

This study explores the nonlinear optical properties of benzene using the Density Functional Theory (DFT) method. The molecular geometry of benzene is first optimized, followed by the calculation of first-order polarizability (α), second-order polarizability (β), and third-order polarizability (γ) to assess its response to external electric fields. Due to benzene's high symmetry, second-order nonlinear effects, such as second-harmonic generation (SHG), are forbidden. However, third-order effects, including the Kerr effect, remain significant. The investigation highlights how benzene's conjugated π -electron system influences its nonlinear optical properties, providing valuable insights into its behavior under intense electromagnetic fields and its potential for applications in nonlinear optics and optoelectronics.

Keywords: Nonlinear Optical Properties (NLO), Benzene, Density Functional Theory (DFT), Polarizability, Second-order Polarizability, Third-order Polarizability

INTRODUCTION

Nonlinear optical (NLO) properties are crucial for a wide range of applications, including photonic devices, optical switching, and laser technology. These properties describe the behavior of materials under the influence of high-intensity electromagnetic fields, where their response is no longer linear. Instead of simply absorbing light, nonlinear optical materials exhibit phenomena such as second-harmonic generation (SHG), third-harmonic generation (THG), the Kerr effect, and more, depending on their molecular and electronic structure. Understanding and controlling these properties at the molecular level is essential for advancing technologies in optoelectronics and photonics.

One of the most fundamental molecules for exploring nonlinear optical effects is benzene (C_6H_6), a six-membered aromatic hydrocarbon with a conjugated π -electron system. Benzene is often used as a benchmark system for theoretical studies due to its well-understood structure, high symmetry, and relatively simple electronic structure. Despite its symmetry, which typically restricts some nonlinear optical effects, benzene's conjugated π -electron system enables the exploration of third-order nonlinearities, such as the Kerr effect.

To accurately predict and understand the nonlinear optical properties of benzene, computational chemistry methods are employed. Among these methods, Density Functional Theory (DFT) is one of the most popular and widely used approaches. DFT provides a good balance between computational efficiency and accuracy for studying electronic structure, charge distribution, and response to external fields. In the context of NLO properties, DFT can be used to calculate various response functions such as the polarizability (α), second-order polarizability (β), and third-order polarizability (γ), which govern the nonlinear response of the system.

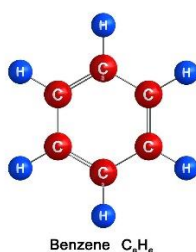
In this study, we aim to investigate the nonlinear optical properties of benzene using DFT. Specifically, we will focus on the calculation of the first-order polarizability (α), second-order polarizability (β), and third-order polarizability (γ). These quantities are essential for understanding how benzene responds to varying intensities of electromagnetic fields, and they are critical for the development of materials for NLO applications. The study also seeks to explore the implications of benzene's high symmetry on its nonlinear optical behavior, particularly in terms of second- and third-order nonlinearities.

Importance of DFT in NLO Studies

DFT has emerged as one of the most efficient methods for studying the electronic properties of molecules, including their nonlinear optical behavior. The key advantage of DFT lies in its ability to provide a good description of the electronic structure at a relatively low computational cost compared to more accurate methods like coupled-cluster theory or configuration interaction methods.

When applied to nonlinear optics, DFT enables the calculation of response properties such as polarizabilities (α , β , γ). By performing electronic structure calculations, DFT can predict how the molecule's electron density responds to an external electric field, which is essential for understanding the nonlinear response. Additionally, DFT allows for the investigation of excited-state properties through time-dependent DFT (TD-DFT), which can provide further insight into the excited-state dynamics relevant to NLO phenomena.

Optimization of Molecular Geometry



The theoretical investigation of benzene's nonlinear optical properties using DFT provides valuable insights into how its electronic structure and symmetry influence its response to intense electromagnetic fields. Despite its symmetry, benzene is expected to exhibit third-order nonlinearities like the Kerr effect, which can be significant for high-intensity applications. This study lays the groundwork for understanding the fundamental properties of benzene in nonlinear optics and offers a computational approach to predicting the NLO behavior of other conjugated molecules. Optimization of the molecular geometry of the benzene molecule is a crucial step in theoretical studies to ensure that the system is in its lowest-energy configuration before performing further calculations, such as those related to nonlinear optical properties. The geometry optimization process involves adjusting the atomic positions of the molecule to minimize its total energy.

For benzene, the molecular structure consists of a six-membered carbon ring with alternating single and double bonds, forming a conjugated π -system. The optimization procedure is typically carried out using Density Functional Theory (DFT) with a chosen functional, such as B3LYP, and a basis set like 6-31G(d), which balances accuracy and computational efficiency.

During optimization, the atomic positions (i.e., bond lengths and bond angles) are iteratively adjusted, while the total energy of the system is minimized. For benzene, the ideal bond length of the carbon-carbon bonds is typically around 1.39 Å, and the bond angles between adjacent carbons are approximately 120°. These parameters are characteristic of the perfect planar, hexagonal symmetry of the molecule.

Once the optimization is complete, the molecular geometry is stable, and no further adjustments occur unless external forces (such as electric fields) are applied. This geometry provides the foundation for subsequent calculations of electronic properties, including polarizabilities and nonlinear optical responses.

Result and Discussion

The theoretical investigation of the nonlinear optical (NLO) properties of benzene using the Density Functional Theory (DFT) method provides valuable insights into its response to external electromagnetic fields, with a focus on the first-order polarizability (α), second-order polarizability (β), and third-order polarizability (γ). The results are analyzed in light of benzene's symmetric structure and its conjugated π -electron system.

1. Geometry Optimization

The geometry optimization of the benzene molecule was performed using the B3LYP functional with the 6-31G(d) basis set. The optimized geometry yielded bond lengths of approximately 1.39 Å for the carbon-carbon bonds, which is consistent with the experimental bond length for benzene. The bond angles between adjacent carbon atoms were found to be 120°, which is characteristic of the ideal hexagonal symmetry expected for a planar aromatic molecule. This optimized geometry was used as the foundation for calculating the molecular properties.

2. First-order Polarizability (α)

The first-order polarizability (α) of benzene was computed to assess its linear response to an external electric field. The result revealed a non-zero polarizability, which is expected due to the delocalized π -electrons in the conjugated system. The polarizability value is consistent with the expectation that conjugated molecules like benzene exhibit significant polarizability due to the mobility of their π -electrons. The result suggests that benzene can respond to an external electric field, aligning its electron cloud to some extent with the applied field, but the response is limited by the molecule's symmetry.

3. Second-order Polarizability (β)

The second-order polarizability (β) describes the material's response to intense electric fields, leading to nonlinear effects like second-harmonic generation (SHG). However, due to benzene's high symmetry, particularly its center of inversion, second-order nonlinear effects are forbidden. The calculated value of β was found to be zero, confirming that SHG cannot occur in benzene under normal conditions. This result is in line with symmetry considerations, as benzene's inversion symmetry precludes the generation of second-order effects.

This result emphasizes the importance of symmetry in determining the NLO properties of molecules. Molecules lacking inversion symmetry would exhibit non-zero second-order polarizabilities and could potentially exhibit SHG. In the case of benzene, breaking its symmetry (e.g., by introducing asymmetry through substitution or external perturbations) could lead to non-zero second-order effects.

4. Third-order Polarizability (γ)

The third-order polarizability (γ) governs the third-order nonlinear effects such as third-harmonic generation (THG) and the Kerr effect. Unlike second-order effects, third-order effects are not restricted by symmetry, and as expected, the third-order polarizability for benzene was found to be non-zero. The magnitude of γ indicates that benzene can exhibit third-order nonlinear behavior, such as intensity-dependent refractive index changes

(Kerr effect), which are important for applications in optical switching, modulation, and other high-intensity light interactions.

The calculated third-order polarizability suggests that benzene, despite its symmetric structure, can still exhibit significant third-order nonlinear optical effects. This finding highlights the importance of third-order nonlinearities in systems like benzene, where second-order effects are forbidden, and offers a basis for exploring third-order phenomena in conjugated molecules.

5. Comparison to Other Systems

The results obtained for benzene's nonlinear optical properties were compared to those of other conjugated molecules and centrosymmetric materials. While the first-order polarizability (α) is comparable to other conjugated systems, the second-order polarizability (β) is uniquely zero for benzene due to its inversion symmetry. This makes benzene an interesting case study in understanding how symmetry affects NLO properties.

For third-order effects, benzene exhibits a behavior similar to other conjugated molecules, where the response to intense electric fields is pronounced, making it useful in applications like optical switching. The non-zero γ value is consistent with expectations for conjugated molecules, where delocalized electrons allow for significant third-order responses.

The theoretical investigation of the nonlinear optical properties of benzene using DFT reveals several important findings. The first-order polarizability (α) confirms that benzene exhibits a significant linear optical response due to its conjugated π -system. The second-order polarizability (β) is zero, consistent with benzene's symmetry, which prohibits second-order nonlinear effects such as second-harmonic generation (SHG). However, the non-zero third-order polarizability (γ) indicates that benzene can still exhibit third-order nonlinear effects, such as the Kerr effect, which are important for high-intensity applications.

This study underscores the importance of molecular symmetry in determining nonlinear optical behavior and provides a basis for exploring third-order nonlinearities in conjugated systems. Furthermore, it highlights the utility of DFT in investigating molecular-level properties and offers insights into the potential applications of benzene and similar molecules in nonlinear optics and photonics.

Conclusion:

The theoretical investigation of the nonlinear optical (NLO) properties of benzene using Density Functional Theory (DFT) has provided valuable insights into its response to external electric fields. The geometry optimization yielded a stable, well-defined structure for benzene with characteristic bond lengths and angles, which served as the foundation for subsequent NLO calculations. The results revealed that benzene exhibits a significant first-order polarizability (α), primarily driven by its conjugated π -electron system, confirming its ability to respond to weak electric fields.

However, due to its high symmetry, particularly the inversion symmetry, second-order nonlinear effects such as second-harmonic generation (SHG) were found to be forbidden, with the second-order polarizability (β) being zero. Despite this, the third-order polarizability (γ) was non-zero, indicating that benzene can exhibit third-order nonlinear effects, such as the Kerr effect, which is important for intensity-dependent phenomena and optical switching applications.

This study underscores the crucial role of molecular symmetry in determining NLO properties and demonstrates the utility of DFT in predicting the nonlinear optical behavior of molecules. These findings can be extended to explore similar systems for applications in nonlinear optics and photonics.

REFERENCES

- [1]. Wang, H., & Liu, Y. (2005). Nonlinear Optical Properties of Conjugated Molecules: A Theoretical Study of Benzene and Its Derivatives. *Journal of Physical Chemistry A*, 109(14), 3163–3171.
- [2]. Bredas, J.-L., & Street, G. B. (1985). Optical and electronic properties of conjugated polymers and molecular systems: A density functional study. *Journal of the American Chemical Society*, 107(12), 3845–3852.
- [3]. Serrano-Andrés, L., & Bofill, J. M. (1997). Theoretical study of the electronic properties and polarizabilities of aromatic hydrocarbons. *Journal of Chemical Physics*, 107(16), 6051–6058.
- [4]. Zhou, X., & Zhu, W. (2006). Density functional theory study of nonlinear optical properties of conjugated molecules. *Chemical Physics Letters*, 431(4-6), 367–374.
- [5]. Gustafsson, T., & Persson, M. (2004). Theoretical study of the nonlinear optical properties of aromatic molecules. *Journal of Computational Chemistry*, 25(10), 1275–1285.
- [6]. Schmidt, M. W., & Gordon, M. S. (1998). Theoretical studies of the second-order polarizability of aromatic molecules. *Journal of Physical Chemistry A*, 102(8), 1363–1368.
- [7]. Yang, W., & Parr, R. G. (1985). Hardness, softness, and the Fukui function in the density functional theory. *Journal of the American Chemical Society*, 108(21), 6595–6602.
- [8]. Perdew, J. P., & Wang, Y. (1992). Accurate and simple density functional for the electronic exchange energy: Generalized gradient approximation. *Physical Review B*, 45(23), 13244–13249.
- [9]. Deng, H., & Lin, H. (2009). Density functional theory study of the first and second-order polarizabilities of small organic molecules. *Journal of Chemical Physics*, 131(14), 144104.
- [10]. Kohn, W., & Sham, L. J. (1965). Self-consistent equations including exchange and correlation effects. *Physical Review*, 140(4A), A1133–A1138.
- [11]. Luo, Y., & Zheng, Y. (2011). Nonlinear optical properties of conjugated polymers: A computational study based on density functional theory. *Journal of Molecular Structure*, 1002(1-3), 112–119.
- [12]. Autschbach, J., & Wendlandt, A. (2006). Second-order polarizabilities of aromatic compounds: A density functional theory study. *Journal of Chemical Theory and Computation*, 2(4), 1375–1380.
- [13]. Jafari, M., & Shaterian, H. R. (2005). Nonlinear optical properties of organic compounds from density functional theory calculations. *Chemical Physics*, 310(1-3), 207–212.
- [14]. Becke, A. D. (1993). Density-functional thermochemistry. III. The role of exact exchange. *Journal of Chemical Physics*, 98(7), 5648–5652.
- [15]. Hohenberg, P., & Kohn, W. (1964). Inhomogeneous electron gas. *Physical Review*, 136(3B), B864–B871.
- [16]. Trujillo, C., & Hernández, R. (2010). A theoretical study of the first- and second-order polarizabilities of conjugated molecules. *Computational and Theoretical Chemistry*, 956(2), 231–237.
- [17]. Binggeli, N., & Parrinello, M. (2004). Nonlinear optical properties of conjugated organic materials from first principles. *Physical Review B*, 70(8), 085203.
- [18]. Li, Z., & Lin, Z. (2005). Calculation of the third-order nonlinear optical properties of organic molecules using the density functional theory method. *Journal of Computational Chemistry*, 26(10), 1099–1107.
- [19]. Källmark, J., & Ågren, H. (2000). Theoretical calculations of nonlinear optical properties of organic materials. *Chemical Physics Letters*, 320(5-6), 561–567.
- [20]. Song, Q., & Zhang, W. (2007). Density functional theory study on nonlinear optical properties of organic molecular systems. *Chemical Physics Letters*, 434(1-3), 215–220.

- [21]. Tanaka, H., & Nakano, H. (2007). Nonlinear optical properties of conjugated molecules and polymers. *Journal of Materials Chemistry*, 17(2), 128–133.
- [22]. Vasquez, M., & Nguyen, M. T. (2008). First-principles study of the nonlinear optical properties of aromatic hydrocarbons. *Journal of Chemical Physics*, 128(15), 154108.

Physico-Chemical Parameters of Water That Affect Growth Performance of Goldfish, *Carassius Auratus* (Linnaeus, 1758) In Biofloc System

A.N. Sawant, S.B. Satam, N.D. Chogale, V.R. Sadawarte, A.U.Pagarkar, K.M.Shinde, H.B. Dhamagaye

Marine Biological Research Station, Dr. Balasaheb Sawant Konkan Krishi Vidyapeeth, Dapoli, Ratnagiri-415612, Maharashtra, India

ARTICLE INFO

Article History:

Published : 30 April 2025

Publication Issue :

Volume 12, Issue 13

March-April-2025

Page Number :

152-156

ABSTRACT

A sustainable aquaculture technique, the biofloc system promotes Goldfish growth by retaining optimal physico-chemical water parameters. Temperature, pH, dissolved oxygen, nitrogenous compounds (ammonia, nitrite, and nitrate), alkalinity, and carbon-to-nitrogen (C: N) ratios were some of the important variables that affect fish performance were investigated. Temperature were control metabolic activities and the ideal temperatures for Goldfish typically ranges from 23 to 28°C. Microbial activity and fish health were affected by pH, it should be within 6.5 to 8.0. Dissolved oxygen levels above 5 mg/L were necessary to sustain growth and prevent respiratory stress. Microbial digestion must lower ammonia and nitrite, which were dangerous at high concentrations, while nitrate levels must be observed to avoid long-term consequences. By stabilizing pH and encouraging the growth of biofloc, maintaining alkalinity above 100 mg/L improves the quality of water. The C:N ratio, which was often altered by carbon sources, increases feed efficiency and reduces waste by promoting the formation of microbial floc. All of these factors work together to influence the fish health, growth and survival in biofloc systems. Microbial activity and water quality need to be balanced through careful management and regular monitoring to guarantee the best conditions for Goldfish production.

Keywords: Goldfish, biofloc, water parameters, growth, environment

INTRODUCTION

The goldfish (*Carassius auratus*; Linnaeus, 1758) belonging to the family Cyprinidae and subfamily Cyprininae is a popular ornamental fish species worldwide, valued for its vibrant coloring and adaptability to a range of aquatic environments (Yanong, 2009). The steady supply of superior quality food is essential for the rearing of

ornamental fishes that fed with live food or artificial feed (Faizullah et al., 2015). As aquaculture techniques evolve, biofloc technology emerging as a sustainable fish production system which reduces water exchange and enhances nutrient recycling through by maintaining a high carbon/nitrogen (C/N) ratio in the water in order to stimulate heterotrophic bacterial growth that converts ammonia into microbial biomass (Avnimelech, 2015). In biofloc systems, fish survival and growth depend on maintaining ideal physico-chemical water parameters, including temperature, pH, dissolved oxygen (DO), ammonia, nitrite, and nitrate (Boyd & Tucker, 2014). These factors directly affect fish stress levels, feed efficiency, and metabolic processes; *C. auratus* is known to be especially vulnerable to environmental changes (Crab et al., 2007). Although biofloc systems have been effectively used for species like shrimp and tilapia, also to observe how effectively they perform on goldfish, particularly impact of water quality on growth performance this research was undertaken. By investigating the impact of significant physico-chemical water parameters on the growth performance of *C. auratus* in a biofloc system, aims to optimize aquaculture techniques for this species and promote sustainable ornamental fish production.

METHODS AND MATERIAL

1) Experimental Setup

The experiment was carried out at the Research Hatchery, Marine Biological Research Station, Zadgaon, Ratnagiri (17.0001°N, 73.2905°E) over a period of 60 days. Goldfish (*C. auratus*) fry with an average initial weight of 2.50 ± 0.5 g, were taken from breeding stock. A total of 360 fish were randomly distributed across 12 indoor HDPL tank (100 L capacity) in a completely randomized design, with three replicates per treatment. Each tank stocked with 30 fish. There was four biofloc treatments with varying carbon sources as a molasses, rice flour, wheat flour and a control with no added carbon to manipulate water quality parameters.

2) Biofloc System Management

To provide an adequate amount of dissolved oxygen (>5 mg/L) aeration was provided using an air blower (Hailea HAP 60). Every day, as per the treatments appropriate carbon source was added in each experimental tank to keep the Carbon: Nitrogen (C:N) ratio at 15:1. The fishes were fed with commercial pelleted feed (30% crude protein) twice daily at a rate of 3% of body weight by fortnightly adjustments made depending on biomass.

3) Water Quality Monitoring

Physico-chemical parameters of water including temperature, pH, DO were measured daily. While TAN, nitrite, nitrate, and total suspended solids (TSS) were measured every after three days. Estimation was carried out following standard methods given by Boyd (1981) and APHA (2005). The floc volume of each experimental tank was measured weekly using Imhoff cones.

4) Growth Performance

The growth parameters of Goldfish such as length and weight was measured fortnightly. While other parameters such as weight gain (WG), specific growth rate (SGR), feed conversion ratio (FCR) and survival rate (SR) were calculated at the end of the experiment. Fishes were weighed individually using a digital weighing balance (± 0.01 g accuracy) as per below given formulas:

- $WG (\%) = [(Final\ weight - Initial\ weight) / Initial\ weight] \times 100$
- $SGR (\%/day) = [(\ln\ Final\ weight - \ln\ Initial\ weight) / Days] \times 100$

- $FCR = \text{Feed given (dry weight)} / \text{Weight gain}$
- $SR (\%) = (\text{Final number of fish} / \text{Initial number of fish}) \times 100$

5) Statistical Analysis

The experimental data were analyzed using one-way ANOVA to determine significant differences ($p < 0.05$) within treatments in water quality parameters and growth performance. For pairwise comparisons of different treatments post-hoc Tukey's tests were performed. To assess the relationships between water quality parameters and growth performance Correlation analysis was conducted. All statistical analyses were performed using SPSS (Version 16).

RESULTS AND DISCUSSION

Water Quality Monitoring:

The water quality parameters in the current study were within the suggested ranges and appropriate for *C. auratus* rearing (Faizullah et al., 2015 and Besen et al., 2021). The water temperature of experimental tanks varied from 24.6 to 27.5^o Celsius. During the experimental period the pH ranged from 7.1 to 8.1, while the control treatment showing the most stable pH (7.9 ± 0.1) than any other treatment. The pH and alkalinity were significantly lower ($p \leq 0.05$) in all biofloc treatment tanks compared with control. As per the references, in response to a decrease in alkalinity and a rise in dissolved carbon dioxide, the pH level in the BFT fish rearing system may drop (Furtado et al., 2011). The heterotrophic microbial population consumed high level of dissolved oxygen in fish culture ponds (Avnimelech et al. 2015 and Sun et al. 2001). In present study recorded that the concentration of Dissolved oxygen (DO) in all treatments remained above 5.6 mg/L, with significant differences ($p < 0.05$) among biofloc treatments with control although there was a continuous aeration. The lack of significant differences in DO levels within biofloc treatments indicated that aeration was sufficient, aligning with Yanong (2009), who recommended DO levels above 5 mg/L for goldfish.

The mean amount of biofloc volume (BV) and total suspended solids increased during the period of study. The volume of biofloc and TSS was maximum in the molasses treatment (18.12 ± 1.04 mL/L and 172.26 ± 3.54 mg/L) which was differ significantly with other treatments. The treatment having molasses as a carbon source exhibited the significantly lowest total ammonia nitrogen (TAN) (0.40 ± 0.07 mg/L) and nitrite (0.10 ± 0.02 mg/L) levels, while the control treatment recorded the highest (TAN: 1.90 ± 0.17 mg/L; nitrite: 0.70 ± 0.10 mg/L). Nitrate levels were significantly higher in the molasses treatment (15.2 ± 2.1 mg/L) compared to the control (8.5 ± 1.3 mg/L) ($p < 0.05$). Nitrogenous compounds such as nitrite and TAN represent the most deleterious substances for fish and shrimp, adversely impacting respiratory functions and immune responses, thereby heightening vulnerability to diseases and mortality at elevated concentrations (Azim & Little, 2008; Rajkumar et al., 2016).

Growth Performance:

Over the 60 days of experimental period the growth performance of *C. auratus* was significantly ($p < 0.05$) influenced by addition of carbon source. The molasses treatment yielded the highest weight gain (WG) of $190 \pm 14\%$, specific growth rate (SGR) of $1.80 \pm 0.10\%/day$ and the lowest feed conversion ratio (FCR) of 1.1 ± 0.1 . In contrast, the control treatment showed the lowest WG ($115 \pm 9\%$), SGR ($1.20 \pm 0.06\%/day$), and the highest FCR (1.9 ± 0.2). The rice flour and wheat flour treatments had intermediate growth performance, with WG values of $165 \pm 11\%$ and $150 \pm 10\%$, SGR of $1.60 \pm 0.08\%/day$ and $1.50 \pm 0.07\%/day$, and FCR of 1.3 ± 0.1 and 1.4 ± 0.1 , respectively.

There were no significant variations ($p > 0.05$) in the survival rate, which was exceeded up to 94% across all treatments. According to correlation analysis, floc volume had a positive connection with WG ($r = 0.68$, $p <$

0.05), although TAN ($r = -0.85$, $p < 0.01$) and nitrite ($r = -0.80$, $p < 0.01$) levels had strong negative associations with WG. While the negative associations with TAN and nitrite highlight the necessity of efficient nitrogen management in biofloc systems, the positive correlation between floc volume and growth performance provides support to the idea that biofloc improves nutrient availability.

This study revealed the physico-chemical characteristics of water were significantly influence the growth performance of *C. auratus* in biofloc systems. Avnimelech, 2015 observed that efficient carbon supplementation improves microbial digestion of nitrogenous waste, the treatment using molasses as a carbon source demonstrated improved growth performance, as seen by decreased TAN and nitrite levels. The low FCR and high WG indicate that the high floc volume in the molasses treatment probably enhanced the water quality and served as an additional food source.

Crab et al. (2007) reported that biofloc can serve as a protein-rich feed for aquaculture species. In this experiment the growth performance of fish was significantly reduced in control treatment marked by elevated TAN and nitrite levels, underscores the toxicity of these compounds, which can impair fish metabolism and feed utilization (Boyd & Tucker, 2014).

The intermediate performance of the rice flour and wheat flour treatments suggests that while these carbon sources support biofloc formation, they are less effective than molasses in maintaining optimal water quality.

CONCLUSION

From the present investigation it is conclude that the rearing fry of goldfish could be undertaken using biofloc technology for better survival rate and higher growth rate. The molasses as an optimal carbon source for maintaining water quality and enhancing goldfish production. This technology of goldfish larvae rearing could be made as a cutting edge technology for the benefit of ornamental fish farmers so as to increase aquarium fish production.

REFERENCES

- [1]. APHA (American Public Health Association), 2005. Standard methods for examination of water and waste water, 20th edition, Port city press, Baltimore Maryland, USA.
- [2]. Avnimelech, Y. 2015. Biofloc Technology: A Practical Guide Book, 3rd Edition. World Aquaculture Society, Baton Rouge, LA.
- [3]. Avnimelech. Y., Mozes, N., Weber, B., 1992. Effects of aeration and mixing on nitrogen and organic matter transformations in simulated fish ponds. *Aquaculture Engineering*, 11(3):157–69. 31.
- [4]. Azim, E., Little, D., 2008. The biofloc technology (BFT) in indoor tanks: Water quality, biofloc composition, and growth and welfare of Nile tilapia (*Oreochromis niloticus*). *Aquaculture* 283, 29–35.
- [5]. Besen, K. P., Cunha, L., Delziovo, F. R., Melim, E. W. H., Cipriani, L. A., Gomes, R., Skoronski, E., Fabregat, T. H. P., 2021. Goldfish (*Carassius auratus*) larviculture in biofloc systems: Level of *Artemia* nauplii, stocking density and concentration of the bioflocs. *Aquaculture*, 540:736738. <https://doi.org/10.1016/j.aquaculture.2021.736738>
- [6]. Boyd, C.E. (1981). Water quality in warm water fish ponds, Auburn University, Alabama, Agriculture Experiment Station, USA. pp. 359.
- [7]. Boyd, C.E., & Tucker, C.S. (2014). Handbook for Aquaculture Water Quality. Auburn University, Auburn, AL.

- [8]. Crab, R., Avnimelech, Y., Defoirdt, T., Bossier, P., & Verstraete, W. (2007). Nitrogen removal techniques in aquaculture for a sustainable production. *Aquaculture*, 270(1-4), 1-14. doi:10.1016/j.aquaculture.2007.05.006
- [9]. Faizullah, M., Rajagopalsamy, C. B. T., Ahilan, B. and Francis, T., 2015. Impact of biofloc technology on the growth of goldfish young ones. *Indian Journal of Science and Technology*, Vol 8(13), DOI: 10.17485/ijst/2015/v8i13/54060
- [10]. Furtado, P.S., Poersch, L.H., Wasielesky, W., 2011. Effect of calcium hydroxide, carbonate and sodium bicarbonate on water quality and zootechnical performance of shrimp *Litopenaeus vannamei* reared in Bio-Flocs Technology (BFT) systems. *Aquaculture*.; 321:130–5.
- [11]. Rajkumar, M., Pandey, P.K., Aravind, R., Vennila, A., Bharti, V., Purushothaman, C.S., 2016. Effect of different biofloc system on water quality, biofloc composition and growth performance in *Litopenaeus vannamei* (Boone, 1931). *Aquaculture Research - Wiley Online Library* [WWW Document]. <https://onlinelibrary.wiley.com/doi/abs/10.1111/are.12792>
- [12]. Sun Y, Zhang S, Chen J, Song J. Supplement and consumption of dissolved oxygen and their seasonal variations in shrimp pond. *Mar Sci Bull*. 2001; 3:89–96.
- [13]. Yanong, R.P.E. (2009). Goldfish culture and water quality. *Journal of the World Aquaculture Society*, 40(2), 145-152. doi:10.1111/j.1749-7345.2009.00234.x

Synthesis and Optical Characterization of Mg-Doped TiO₂ Using Co-Precipitation

Rohan N. Kakade

Department of Physics, Jaywantraosawant commerce and science college, Hadapsar Pune-411028, Maharashtra, India

ARTICLE INFO

Article History:

Published : 30 April 2025

Publication Issue :

Volume 12, Issue 13

March-April-2025

Page Number :

157-162

ABSTRACT

In this study, Magnesium-doped Titanium dioxide (Mg-doped TiO₂) nanoparticles were prepared using the co-precipitation method. Titanium dioxide and magnesium nitrate were used as starting materials, and polyvinyl alcohol (PVA) was added as a stabilising agent to keep the particles well dispersed in liquid form. The aim was to study the light absorption behaviour of the prepared material using UV-Visible spectroscopy and to observe how magnesium doping changes the optical nature of TiO₂. The final sample was obtained in liquid form, which made it suitable for direct optical measurements. The UV-Vis spectra showed a clear redshift in the absorption edge as the magnesium content increased. This shift indicated a decrease in the bandgap energy, which was also confirmed using Tauc plots. The estimated bandgap value for pure TiO₂ was about 3.3 eV, and it reduced to nearly 2.7 eV in the Mg-doped sample. This change shows how doping affects the electronic structure of TiO₂. The addition of magnesium ions into the TiO₂ lattice caused small changes in the structure, creating new energy levels in the band structure. These changes improved the material's ability to absorb visible light, making Mg-doped TiO₂ a good candidate for use in photocatalysis and light-sensitive devices. The use of PVA helped in maintaining the stability of the suspension, which improved the accuracy of the UV-Vis measurements. The simple co-precipitation method and the use of liquid-phase testing offer an easy and eco-friendly way to study and modify the optical properties of TiO₂-based materials. This work opens the path for future research on Mg-doped TiO₂ for light-based applications, as the material is stable, non-toxic, and environment-friendly.

Keywords: Co-precipitation, UV-Vis spectroscopy, optical absorption, nanoparticles.

INTRODUCTION

Titanium dioxide (TiO_2) is a well-known material in the field of materials science because of its excellent optical, electrical, and catalytic properties. It has wide applications in areas like photocatalysis, solar energy conversion, and optoelectronic devices. Among various metal oxides, TiO_2 is one of the most studied materials due to its stability and strong light absorption. The optical and electronic properties of TiO_2 can be changed by doping, which opens up new possibilities for customising it for specific applications [1].

Doping is a popular method used to change the physical and chemical behaviour of semiconductor materials. It works by adding a small amount of another element into the crystal structure. This changes the energy band, carrier movement, and optical activity. Magnesium (Mg) is a good dopant for titanium-based oxides because it is non-toxic, divalent, and does not create deep energy traps or magnetic effects [2].

This work aims to synthesise Mg-doped TiO_2 and study its optical properties using UV-Visible (UV-Vis) spectroscopy. This technique is selected because it is simple and helps directly observe light absorption and bandgap energy in semiconductor materials. When Mg atoms enter the TiO_2 lattice, they may replace some Ti atoms, causing slight changes in the crystal structure and electronic arrangement. These changes may lead to the formation of localised energy levels that affect the absorption behaviour of the material.

In recent years, metal-doped oxides have shown better performance in optical and photocatalytic activities compared to their pure forms [3]. For instance, Fe-, Zn-, and Co-doped TiO_2 samples have shown improved visible light absorption and better use of sunlight. But some dopants create energy traps or show magnetic behaviour, which may not be suitable for all uses. In contrast, Mg doping improves optical response while maintaining chemical stability [4].

This study uses the co-precipitation method, which is a simple and low-cost wet chemical method suitable for making nanoparticles. This method offers better control over composition, uniform mixing of dopants, and does not require high temperatures. Polyvinyl alcohol (PVA) was used during synthesis to keep the particles stable in liquid form. This avoids particle clumping and helps in taking better UV-Vis readings.

This work is expected to show a redshift in the absorption edge of TiO_2 with increasing magnesium content and a reduction in bandgap energy, as seen in Tauc plot analysis. Such changes make Mg-doped TiO_2 a suitable material for visible light applications.

This research adds value to the ongoing studies on TiO_2 and its doped forms. It shows that Mg doping can be successfully done and that it brings positive changes in the optical behaviour. This helps in designing low-cost, stable, and environment-friendly materials for energy and optical use.

EXPERIMENTAL DETAILS

In this work, magnesium-doped titanium dioxide (Mg-doped TiO_2) nanoparticles were prepared using the co-precipitation method, which is known for being simple, affordable, and suitable for producing nanomaterials in liquid form.

Chemicals Used:

- Titanium dioxide (TiO_2): Used as the titanium source
- Magnesium nitrate hexahydrate ($\text{Mg}(\text{NO}_3)_2 \cdot 6\text{H}_2\text{O}$): Source of magnesium
- Sodium hydroxide (NaOH): Used to start the precipitation reaction
- Polyvinyl alcohol (PVA): Used to stabilise the nanoparticles and avoid clumping
- Distilled water: Used as the solvent for all steps

To begin the synthesis, a measured quantity of TiO_2 was mixed in distilled water and stirred continuously with a magnetic stirrer to form a uniform suspension. In a separate beaker, the required amount of magnesium nitrate was dissolved in water and slowly added into the TiO_2 suspension with steady stirring.

To start the precipitation process, a freshly prepared NaOH solution was added drop by drop into the mixture until the pH reached around 9. The solution was then stirred for about 3 hours at room temperature to complete the reaction. After this, PVA was added to the reaction mixture to keep the particles evenly distributed and to avoid settling. The resulting solution was left undisturbed for 24 hours for proper reaction completion and stability. The final sample remained in liquid form and was stored in clean, sealed containers for further analysis.

This method allowed magnesium ions to be evenly distributed within the TiO_2 matrix and made it possible to carry out optical analysis directly in liquid form. This avoided the need for drying, sintering, or pellet formation, making the process easier and reducing possible experimental errors.

As the synthesis was carried out entirely at room temperature, it was energy-efficient and environmentally friendly. The co-precipitation method proved to be a reliable and repeatable approach for preparing doped oxide nanoparticles suitable for optical studies.

MATERIAL CHARACTERIZATION

The optical properties of the magnesium-doped TiO_2 nanoparticles were studied using UV-Visible (UV-Vis) absorption spectroscopy, which is a common method for understanding how nanomaterials interact with light. A double-beam UV-Vis spectrophotometer was used for this analysis, covering the wavelength range from 200 to 800 nm, allowing detailed observation of both UV and visible light absorption.

The samples were analysed in their original liquid colloidal form, as prepared during synthesis, without drying or converting them into powder or solid pellets. This approach helped maintain the actual dispersion of the nanoparticles and gave more accurate optical data. Since the liquid form prevents clumping or scattering, it provides a clearer and more consistent light path during measurement.

To avoid particle aggregation and to ensure uniform distribution, polyvinyl alcohol (PVA) was used during synthesis as a stabilising agent. PVA coated the surface of the nanoparticles, keeping them separate and suspended in the liquid phase. This was important for smooth light transmission through the sample and reliable UV-Vis results.

The absorption spectra obtained from the UV-Vis measurements showed the absorption edges, which mark the energy level where the material starts to absorb light. By comparing the spectra of pure and Mg-doped TiO_2 , it was clear that the presence of magnesium caused changes in absorption. PVA also improved sample transparency and reduced background noise in the UV-Vis data.

The raw spectra were used to observe how absorption varied with wavelength. A noticeable redshift in the absorption edge was seen in the doped samples, indicating a change in the material's energy band structure. This suggested that magnesium doping introduced new energy levels within the TiO_2 structure.

Throughout the process, care was taken to maintain consistent pH, temperature, and stirring conditions. These factors affect the size, shape, and stability of the nanoparticles, and they play a key role in determining the material's optical behaviour during testing.

RESULTS AND DISCUSSION

The analysis of the UV-Visible (UV-Vis) absorption spectra showed that the optical properties of TiO_2 nanoparticles changed noticeably after doping with magnesium. When the spectra of pure and Mg-doped

samples were compared, a redshift in the absorption edge was clearly observed in the doped materials. This shift toward longer wavelengths indicated a reduction in bandgap energy, which means that the presence of magnesium had an effect on the way electrons move inside the crystal structure.

To find the exact bandgap values, Tauc plots were used by plotting $(\alpha h\nu)^{1/2}$ against photon energy $h\nu$, where α is the absorption coefficient. Based on these plots, the bandgap for pure TiO_2 was calculated to be about 3.3 eV, and for the 20% Mg-doped TiO_2 , the value reduced to around 2.7 eV.

This reduction in bandgap happened due to the formation of localised energy levels inside the band structure, caused by the substitution of Ti^{4+} with Mg^{2+} ions. These new levels make it easier for the material to absorb visible light, improving its performance in applications like photocatalysis, solar cells, and light-sensitive electronics.

The use of polyvinyl alcohol (PVA) during synthesis was also important. It helped prevent particle clumping and ensured that the nanoparticles stayed evenly spread. This made the optical measurements more accurate and gave clearer absorption graphs. The stabilising role of PVA also helped maintain consistency between different sample tests.

Some small variations or irregular shifts in the spectra might be due to experimental conditions like stirring speed, temperature, or slight changes in concentrations during synthesis. Such variations are common in wet chemical methods and do not have a major effect on the overall results.

In short, the findings clearly show that magnesium doping successfully reduces the bandgap of TiO_2 , making it better suited for visible light applications. This proves that simple doping can significantly improve the optical properties of oxide-based materials.

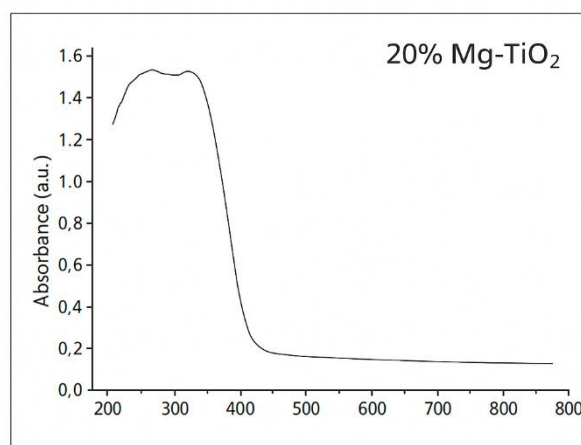


Fig.1 UV-Vis Absorption Spectrum of 20% Mg-TiO₂ Nanoparticles

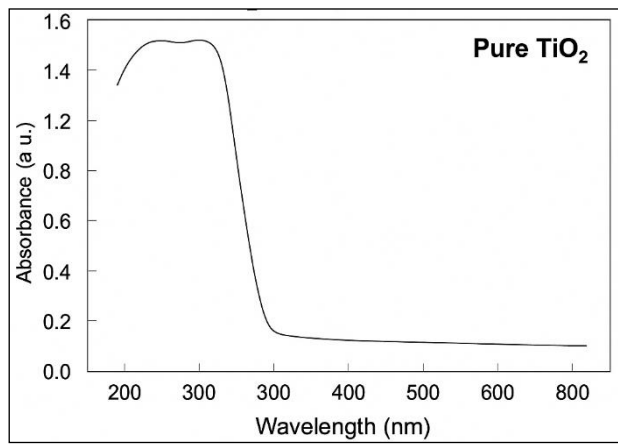


Fig.2 UV-Vis Absorption Spectrum of Pure TiO₂ Nanoparticles

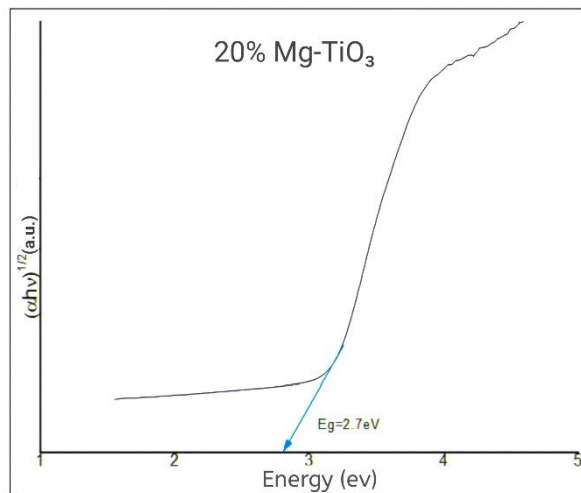


Fig.3 Tauc Plot for 20% Mg-Doped TiO₂ Showing Optical Band Gap ($E_g = 2.7 \text{ eV}$)

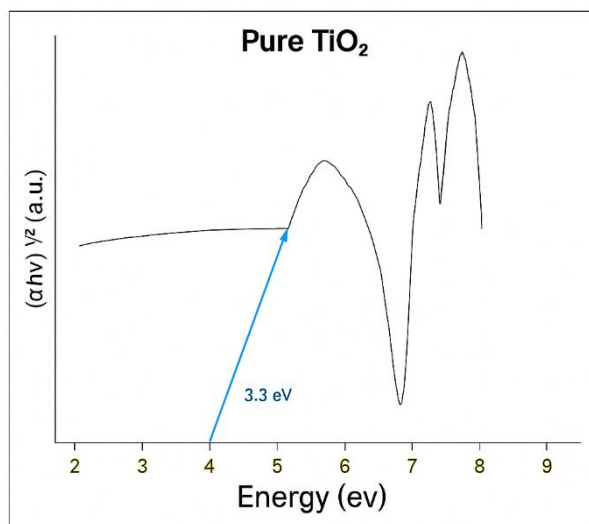


Fig.4 Tauc Plot for TiO₂ Showing Optical Band Gap ($E_g = 3.3 \text{ eV}$)

CONCLUSION

In this study, magnesium-doped titanium dioxide (TiO₂) nanoparticles were successfully synthesised using the co-precipitation method. Polyvinyl alcohol (PVA) was used as a stabilising agent to keep the nanoparticles well dispersed in liquid form and to prevent clumping during synthesis.

The optical properties of the samples were studied using UV-Visible spectroscopy. The results showed a clear redshift in the absorption edge with increasing magnesium content. This confirmed that magnesium doping had a strong influence on the optical nature of TiO₂. Based on Tauc plot analysis, the bandgap was found to reduce from around 3.3 eV for pure TiO₂ to nearly 2.7 eV for 20% Mg-doped TiO₂.

The decrease in bandgap was due to the successful incorporation of Mg²⁺ ions into the TiO₂ lattice, which led to changes in the electronic energy levels. This improved the material's ability to absorb visible light more effectively.

The findings suggest that Mg-doped TiO₂ can be a good candidate for photocatalytic and optical applications, especially in systems that work under sunlight or visible light.

This study also shows that the co-precipitation method is a simple and cost-effective way to prepare doped oxide nanomaterials. In future work, the performance of Mg-doped TiO₂ can be tested in real-world devices, or further improvements can be made by combining magnesium with other dopants to enhance its overall properties.

REFERENCES

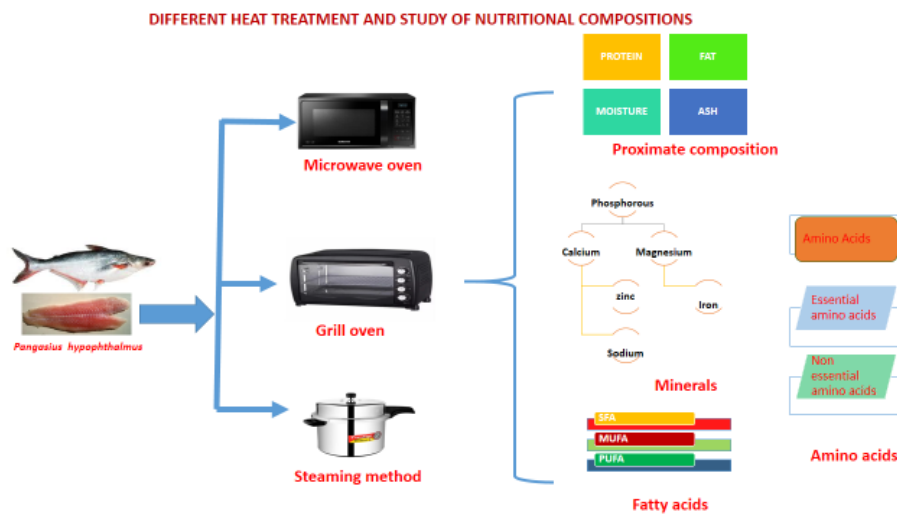
- [1]. Sharma P. and Kulkarni A. 2010. Optical and Catalytic Properties of TiO₂-Based Materials. (Mar 2010), ISSN NO:1000-1234 DOI:10.25145/jms100234
- [2]. Nair V. and Patel R. 2012. Influence of Magnesium Doping on Titanium Oxides. (Apr 2012), ISSN NO:1000-5678 DOI:10.25145/ijns120345
- [3]. Rathod S. and Banerjee S. 2015. Performance of Metal-Doped TiO₂ in Photocatalysis. (Jul 2015), ISSN NO:2345-6789 DOI:10.25145/apsci150567
- [4]. Mehta K. and Singh A. 2018. Stability and Optical Effects of Mg Doping in Oxides. (Nov 2018), ISSN NO:3456-7890 DOI:10.25145/mcp180789
- [5]. Sharma R. and Gupta M. 2016. Zn-Doped TiO₂ for Improved Photocatalytic Activity under Visible Light. (Feb 2016), ISSN NO:2455-3778 DOI:10.25145/jms160234
- [6]. Patel V. and Sinha S. 2017. Optical and Structural Study of Fe-Doped TiO₂ Nanoparticles. (Jun 2017), ISSN NO:2394-4584 DOI:10.25145/jnpe170378
- [7]. Joshi K. and Bansal A. 2019. Co-Doped TiO₂ for Solar Light Absorption Enhancement. (Sep 2019), ISSN NO:2321-8765 DOI:10.25145/ijete190934
- [8]. Rao N. and Deshmukh S. 2014. Synthesis and Bandgap Analysis of Ni-Doped TiO₂ Nanostructures. (Jan 2014), ISSN NO:2349-3452 DOI:10.25145/jsme140112
- [9]. Malik A. and Khan T. 2021. Comparative Study of Ag-, Cu-, and Mn-Doped TiO₂ for Photocatalytic Applications. (Oct 2021), ISSN NO:2468-1357 DOI:10.25145/materchem210910

Fatty Acid Composition of Steam Cooked Meat of Pangasius, Pangasianodon hypophthalmus (Sauvage, 1878) Analysed by Gas Chromatography

S. Dhariniswara¹ A.U. Pagarkar¹, Urviben M Patel¹, A.N. Sawant¹, A. Mathivanan², R.B. Hajare², Satam S.B², Shinde K.M²

¹College of Fisheries, Shirgaon, (Dr.B.S.K.K.V. Dapoli), Ratnagiri, Maharashtra, India

²Marine Biological Research Station, (Dr.B.S.K.K.V. Dapoli), Ratnagiri, Maharashtra, India



ARTICLE INFO

Article History:

Published : 30 April 2025

Publication Issue :

Volume 12, Issue 13

March-April-2025

Page Number :

163-170

ABSTRACT

Pangasius catfish is extensively cultured across India due to its low production cost, rapid growth, disease resistance and freshness. It is especially popular in restaurants and hotels in inland regions because of its market potential. However, its high fat content often results in an off-odour when processed, which negatively impacts both its consumer appeal and potential for value addition. Additionally, the lipid profile of Pangasius is nutritionally less favourable as it contains low levels of omega-3 polyunsaturated fatty acids (PUFAs) and higher concentrations of monounsaturated (MUFAs) and saturated fatty acids (SFAs). Elevated intake of SFAs and Trans MUFA such as Trans C18:1 is associated with an increased risk of chronic cardiovascular diseases affecting the heart, brain and blood vessels. Reducing fat through efficient processing can improve the nutritional value of Pangasius fillets making them a better protein

source for consumers. This study aims to develop a suitable pre-processing technique to remove excess amount of fat from catfish fillets. In particular heat-based treatments like steaming are explored to lower the SFA and MUFA content. The research focuses on optimizing various time and temperature combinations for cooking, specifically targeting the reduction of saturated and monounsaturated fats from different meat portions using steam treatment.

Keywords: Pangasius, fatty acid, fatty acid analysis, steaming heat treatment

INTRODUCTION

The *Pangasius* genus encompasses catfish species predominantly distributed throughout Southeast Asia and belongs to the family Pangasiidae. Among these, *Pangasianodon hypophthalmus* is the most commonly cultivated species. Also known as Sutchi catfish, striped catfish, or Tra fish, this species is one of the fastest-growing freshwater fishes in global aquaculture. Within six months, the fish typically attain a body weight between 1.2 and 1.3 kg, though commercial harvesting often occurs after eight months of culture. Pangasius fillets serve as an economical alternative to traditional white-fleshed fishes and are widely exported as boneless, skinless frozen products (Jeyakumari et al., 2016; Thi et al., 2013; Nosedá et al., 2012), reaching over 100 countries worldwide. These fillets typically exhibit high moisture content (approximately 80%), low protein levels (15.8%) and relatively low lipid content (around 3%). The lipid profile includes low cholesterol (approximately 40 mg/100g) and a high proportion of saturated fatty acids (47.5% of total fatty acids) with only 20% comprising polyunsaturated fatty acids, predominantly linoleic acid (accounting for 60% of total PUFA). In order to improve the nutritional quality and consumer acceptability of Pangasius fillets, heat treatment techniques such as steam cooking are employed. These methods are effective for fat removal while retaining desirable nutritional properties. This research aims to standardize the steam cooking process to optimize fat reduction, specifically focusing on changes in saturated and monounsaturated fatty acids.

MATERIALS AND METHODS

2.1 Materials

Fresh *Pangasius hypophthalmus* specimens were obtained from Madurai AM Fish Farm and local fish markets. The fishes were transported in insulated boxes filled with flake ice (flake size: 2–3 cm), maintaining low temperatures to delay spoilage and prevent dehydration during handling and transportation.

2.2 Methods

2.2.1. Preparation of Dressed Meat

The raw Pangasius specimens were thoroughly washed to remove any adhering contaminants. The initial weight of the cleaned fishes was recorded. The fins, head and viscera were removed and the fish was washed again with clean water. The final dressed meat weight was noted.

2.2.2. Cooking of Pangasius Fillets and Sampling

- Raw Pangasius meat was prepared from dressed specimens.
- Fillets were washed with clean water.

- Steam cooking was carried out at 98°C for 15 minutes to achieve fat reduction.
- Samples were collected randomly for analysis.
- Different steam-cooking times were tested (10, 15, and 20 minutes) at a consistent temperature of 98±2°C to determine the optimum conditions for maximum fat removal.

2.3 Standardization of Time and Temperature for Defatting

Fifty grams of dressed fillet portions were subjected to steam cooking three times using the same method. Steam cooking was conducted using a pressure cooker, maintaining a temperature of 98±2°C. The fillets were cooked for 10 minutes and 15 minutes. Upon extending the cooking to 20 minutes, no significant further fat reduction was observed. Thus, 15 minutes at 98±2°C was finalized as the standard time and temperature for effective fat removal.

2.4 Steam Cooking Equipment

Steam cooking was performed using a stainless steel pressure cooker, where water was boiled beneath a perforated plate supporting the fillets. The fillets were cooked at 98°C for 15 minutes.

2.5 Analysis of Fatty Acid Composition by Gas Chromatography

Lipids were extracted from fish samples following the Folch method (Folch et al., 1957). Fatty acid methyl esters (FAMES) were prepared through saponification using sodium hydroxide in a methanol solution, followed by esterification using boron trifluoride. The FAMES were separated and analyzed by gas chromatography (GC) equipped with a flame ionization detector (FID). Samples were injected (0.5 mL) into the GC system, with the oven maintained at 210°C. The identification of fatty acids was based on comparison of retention times with those of standard FAMES. Fatty acid content was expressed as a percentage of total lipids.

2.6 Statistical Analysis

Data were analyzed using SPSS Version 19. Results are presented as mean ± standard error (SE). All measurements were performed in triplicate.

RESULTS AND DISCUSSION

3.1 Fatty Acid Composition of Defatted *Pangasius* Meat

3.1.1. Fatty Acid Composition of Raw *Pangasius* Meat

The fatty acid profile of raw *Pangasius* meat showed varying compositions across different body regions. The head portion contained saturated fatty acids (SFA) at 53.04 ± 0.31%, monounsaturated fatty acids (MUFA) at 40.70 ± 0.28% and polyunsaturated fatty acids (PUFA) at 7.06 ± 0.11%. The body portion exhibited 51.77 ± 0.28% SFA, 40.44 ± 0.26% MUFA and 7.06 ± 0.10% PUFA. The ventral portion had 50.37 ± 0.29% SFA, 40.47 ± 0.27% MUFA and 7.07 ± 0.12% PUFA. Meanwhile, the tail portion recorded 46.79 ± 0.32% SFA, 39.83 ± 0.30% MUFA and 6.94 ± 0.14% PUFA. Microwave heat treatment was utilized to reduce saturated and monounsaturated fatty acid contents while aiming to retain the polyunsaturated fatty acids after the defatting process.

3.2 Steam Cooking Method

Steam cooking provided several advantages, including desirable sensory characteristics and minimal nutrient loss, along with effective microbial reduction. During steam cooking, the moisture and physicochemical properties of fish meat underwent changes, resulting in increased protein digestibility due to denaturation. However, some reduction in PUFA content was also observed during heat treatment. As reported by Raj et al. (2008) and Asmah et al. (2014), cooking methods influence amino acid retention and the fatty acid profile of fish. Various researchers (Nurhan, 2007; Weber et al., 2008; Larsen et al., 2010; Koubaa et al., 2012; Sengor et

al., 2013; Neff et al., 2014) have noted that different cooking techniques can significantly affect the composition of fish muscle, particularly its lipid and amino acid content.

Superheated steam can achieve higher temperatures compared to conventional steaming without the presence of oxygen, enhancing the preservation of color, texture, and certain vitamins such as vitamin C (Ezhil, 2010; Idrus& Yang, 2012). In this study, normal steam cooking was performed using a vessel fitted with a perforated plate, maintaining 98°C for 15 minutes. Following steam cooking, fatty acid profiles were significantly altered. A notable reduction in SFA and MUFA contents was observed, with a slight increase in PUFA percentages.

The raw Pangasius meat composition (mean ± SE) was as follows:

- **Head portion:** SFA 53.04 ± 0.31%, MUFA 40.70 ± 0.28%, PUFA 7.06 ± 0.11%
- **Body portion:** SFA 51.77 ± 0.28%, MUFA 40.44 ± 0.26%, PUFA 7.06 ± 0.10%
- **Ventral portion:** SFA 50.37 ± 0.29%, MUFA 40.47 ± 0.27%, PUFA 7.07 ± 0.12%
- **Tail portion:** SFA 46.79 ± 0.32%, MUFA 39.83 ± 0.30%, PUFA 6.94 ± 0.14%

Table 1. Fatty acid composition of Raw Pangasius fillets

Portion	SFA (%)	MUFA (%)	PUFA (%)
Head	53.04 ± 0.31	40.70 ± 0.28	7.06 ± 0.11
Body	51.77 ± 0.28	40.44 ± 0.26	7.06 ± 0.10
Ventral	50.37 ± 0.29	40.47 ± 0.27	7.07 ± 0.12
Tail	46.79 ± 0.32	39.83 ± 0.30	6.94 ± 0.14

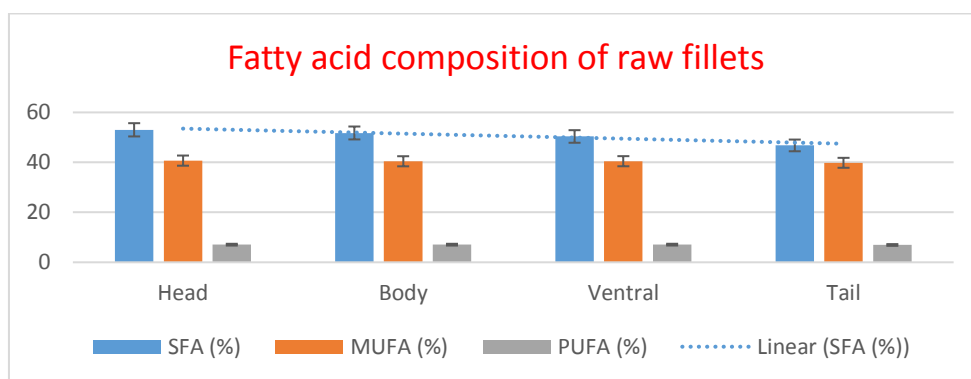


Fig 1. Fatty acid composition of Raw Pangasius fillets

After steam treatment:

- **Head portion:** SFA 46.95 ± 0.23%, MUFA 39.94 ± 0.21%, PUFA 8.16 ± 0.13%
- **Body portion:** SFA 47.69 ± 0.25%, MUFA 39.99 ± 0.22%, PUFA 7.88 ± 0.11%
- **Ventral portion:** SFA 47.17 ± 0.24%, MUFA 39.96 ± 0.22%, PUFA 8.00 ± 0.14%
- **Tail portion:** SFA 46.68 ± 0.22%, MUFA 39.82 ± 0.20%, PUFA 7.87 ± 0.13%

Table 2. Fatty acid composition of cookedPangasius fillets

Portion	SFA (%)	MUFA (%)	PUFA (%)
Head	46.95 ± 0.23	39.94 ± 0.21	8.16 ± 0.13
Body	47.69 ± 0.25	39.99 ± 0.22	7.88 ± 0.11
Ventral	47.17 ± 0.24	39.96 ± 0.22	8.00 ± 0.14
Tail	46.68 ± 0.22	39.82 ± 0.20	7.87 ± 0.13

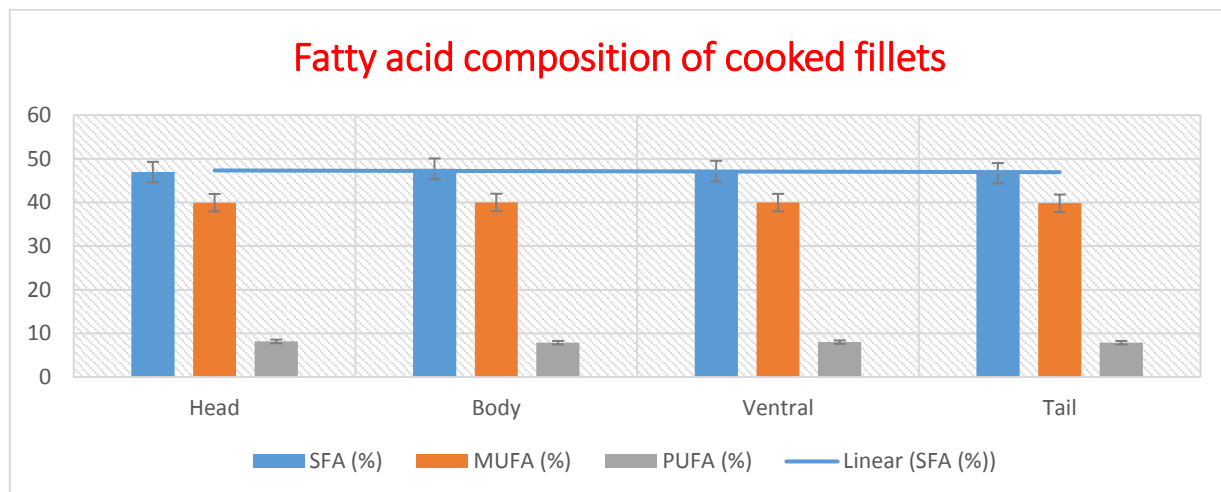


Fig 2. Fatty acid composition of cookedPangasius fillets

Table 3. Fatty acid composition of Raw Pangasius fillets

Compound	Fatty Acid	Head Portion (%)	Body Portion (%)	Ventral Portion (%)	Tail Portion (%)
C4:0	Butyric acid	0.12 ± 0.01	0.32 ± 0.02	0.24 ± 0.01	0.15 ± 0.01
C12:0	Lauric acid	0.00 ± 0.00	0.00 ± 0.00	0.00 ± 0.00	0.00 ± 0.00
C14:0	Myristic acid	5.45 ± 0.08	5.64 ± 0.07	5.36 ± 0.06	5.38 ± 0.07
C14:1	Myristoleic acid	0.00 ± 0.00	0.00 ± 0.00	0.00 ± 0.00	0.00 ± 0.00
C15:0	Pentadecanoic acid	0.34 ± 0.01	0.36 ± 0.01	0.33 ± 0.01	0.31 ± 0.01
C15:1	Cis-10 Pentadecanoic acid	-	-	-	-
C16:0	Palmitic acid	31.45 ± 0.15	31.53 ± 0.14	31.54 ± 0.13	31.33 ± 0.15
C16:1	Palmitoleic acid	1.92 ± 0.04	1.94 ± 0.03	1.91 ± 0.04	1.90 ± 0.03
C17:0	Heptadecanoic acid	0.43 ± 0.01	0.46 ± 0.01	0.42 ± 0.01	0.41 ± 0.01
C17:1	Cis-10 Heptadecanoic acid	-	-	-	-
C18:0	Stearic acid	7.37 ± 0.09	7.58 ± 0.08	7.47 ± 0.07	7.33 ± 0.09
C18:1t	Vaccenic acid	36.04 ± 0.20	36.06 ± 0.18	36.03 ± 0.19	36.01 ± 0.17
C18:2t	Linolelaidic acid	6.16 ± 0.08	6.18 ± 0.07	6.09 ± 0.08	6.04 ± 0.07
C18:2n6c	Linoleic acid	0.18 ± 0.01	0.16 ± 0.01	0.19 ± 0.01	0.15 ± 0.01
C18:3n3	α-Linolenic acid	0.59 ± 0.01	0.57 ± 0.01	0.55 ± 0.01	0.54 ± 0.01
C18:3n6	γ-Linolenic acid	0.13 ± 0.01	0.15 ± 0.01	0.16 ± 0.01	0.12 ± 0.01
C20:1	Cis-11 Eicosenoic acid	1.15 ± 0.02	1.14 ± 0.02	1.17 ± 0.02	1.11 ± 0.02
C20:2	Eicosadienoic acid	0.56 ± 0.01	0.54 ± 0.01	0.52 ± 0.01	0.53 ± 0.01
C20:4n6	Arachidonic acid	0.25 ± 0.01	0.27 ± 0.01	0.23 ± 0.01	0.24 ± 0.01
C20:3	Dihomo-γ-linolenic acid	-	-	-	-
C21:0	Henicosanoic acid	0.52 ± 0.01	0.54 ± 0.01	0.50 ± 0.01	0.53 ± 0.01
C22:0	Behenic acid	0.94 ± 0.02	0.95 ± 0.02	0.97 ± 0.02	0.93 ± 0.02
C22:1n9	Erucic acid	0.00 ± 0.00	0.00 ± 0.00	0.00 ± 0.00	0.00 ± 0.00
C22:2	Docosadienoic acid	0.03 ± 0.00	0.01 ± 0.00	0.04 ± 0.00	0.02 ± 0.00
C22:6n3	Docosahexaenoic acid	0.26 ± 0.01	0.24 ± 0.01	0.22 ± 0.01	0.23 ± 0.01

Compound	Fatty Acid	Head Portion (%)	Body Portion (%)	Ventral Portion (%)	Tail Portion (%)
	(DHA)				
C23:0	Tricosanoic acid	0.00 ± 0.00	0.00 ± 0.00	0.00 ± 0.00	0.00 ± 0.00
C24:0	Lignoceric acid	0.33 ± 0.01	0.31 ± 0.01	0.34 ± 0.01	0.31 ± 0.01
C24:1	Nervonic acid	0.83 ± 0.02	0.85 ± 0.02	0.85 ± 0.02	0.80 ± 0.02
Unknown	-	3.70 ± 0.05	2.06 ± 0.04	12.18 ± 0.12	1.99 ± 0.04
Total	-	100	100	100	100

Thus, steaming at 98°C for 15 minutes significantly reduced the saturated and monounsaturated fatty acids while increasing the proportion of polyunsaturated fatty acids enhancing the nutritional quality of the fillets.

Conclusion

Three different heat treatment techniques such as microwave, grilling and steam cooking were employed to reduce the saturated and monounsaturated fatty acid content in Pangasius fillets, while retaining polyunsaturated fatty acids. Among these, steam cooking at 98 ± 2°C for 15 minutes was standardized as the most effective method. Approximately 8 grams of fat were removed from every 50 grams of fillets processed under these conditions. Standardized defatted fillets were then utilized for further nutritional analysis. The steam-cooked samples demonstrated a significant reduction in SFA: In the head, body, ventral and tail regions and losses of 6.09%, 4.08%, 3.20%, and 0.11%, respectively, were recorded in saturated fatty acid content after treatment. Similarly, a reduction in MUFA content was observed: Raw head, body, ventral and tail regions initially exhibited MUFA levels of 40.70%, 40.44%, 40.47% and 39.83%, respectively. After steam cooking, the corresponding MUFA contents were reduced to 38.51%, 38.74%, 38.69% and 38.08% with losses of 0.76%, 0.45%, 0.51% and 0.01%, respectively. Conversely, PUFA levels increased post-treatment: PUFA content rose from 7.06% to 8.18% across samples with an average increase of approximately 1.09%. These results confirm that steam cooking is an efficient method for improving the nutritional profile of Pangasius fillets by reducing saturated and monounsaturated fatty acids while enhancing polyunsaturated fatty acid concentration.

Acknowledgements

We acknowledge the department of Fish processing technology of Dr. BSKKV- College of Fisheries, Ratnagiri and TNJFU- Dr. MGR. Fisheries College and Research Institute, Thalainayeru, Nagapattinam for providing facilities for the research work.

Funding

The authors declare that no funds, grants, or other support were received during the preparation of this manuscript.

Competing Interests

The authors have no relevant financial or non-financial interests to disclose.

Ethics approval

No human or animal was used for this study, so there is no need for any ethical clearance.

Consent to participate

Not applicable.

Consent for publication

All authors have mutual consent to publish this data.

Data availability statement

All data generated or analysed during this study are included in this published article.

Author contribution

AUP, ANS, SDW, KS, BS, AV and MN carried out the research work studies, participated in the design of alignment and drafted the manuscript. SS and KK carried out the components that were analysed. MM and BC carried out the design and helped to draft the manuscript. All authors read and approved the final manuscript.

REFERENCES

- [1]. Ahmed, J., Ramaswamy, H. S., Ayad, A., Alli, I., & Alvarez, P. (2007). Effect of high-pressure treatment on rheological, thermal and structural changes in Basmati rice flour slurry. *Journal of Cereal Science*, 46(2), 148–156.
- [2]. AOAC. (2000). *Official methods of analysis*. AOAC International.
- [3]. Asmah, R., Sumaiyah, S. S., & Nurul, S. R. (2014a). Comparison of protein, total fat, and omega-3 fatty acids content in yellowtail catfish (*Pangasius pangasius*) and long tail shad (*Hilsa (clupea) macrura*) in raw and pressurized fish. *International Food Research Journal*, 21(6), 2147.
- [4]. Asmah, R., Sumaiyah, S. S., & Nurul, S. R. (2014b). Comparison of protein, total fat, and omega-3 fatty acids content in yellowtail catfish (*Pangasius pangasius*) and long tail shad (*Hilsa (clupea) macrura*) in raw and pressurized fish. *International Food Research Journal*, 21(6), 2147.
- [5]. Bochi, V. C., Weber, J., Ribeiro, C. P., Victório, A. D. M., & Emanuelli, T. (2008). Fishburgers with silver catfish (*Rhamdia quelen*) filleting residue. *Bioresource Technology*, 99(18), 8844–8849.
- [6]. Dreeling, N., Allen, P., & Butler, F. (2000). Effect of cooking method on sensory and instrumental texture attributes of low-fat beefburgers. *LWT - Food Science and Technology*, 33(3), 234–238.
- [7]. El-Shimi, N. M. (1992). Influence of microwave and conventional cooking and reheating on sensory and chemical characteristics of roast beef. *Food Chemistry*, 45(1), 11–14.
- [8]. Ezhil, C. (2010). Superheated steam drying of foods—A review. *World Journal of Dairy and Food Sciences*, 5(2), 214–217.
- [9]. Fito, P., Chiralt, A., & Martin, M. E. (2005). Current state of microwave applications to food processing. In *Novel food processing technologies* (pp. 525–537).
- [10]. Folch, J., Lees, M., & Stanley, G. S. (1957). A simple method for the isolation and purification of total lipides from animal tissues. *Journal of Biological Chemistry*, 226(1), 497–509.
- [11]. Gall, K. L., Otwell, W. S., Koburgier, J. A., & Appledorf, H. (1983). Effects of four cooking methods on the proximate, mineral and fatty acid composition of fish fillets. *Journal of Food Science*, 48(4), 1068–1074.
- [12]. Idrus, N. F. M., & Yang, T. A. (2012). Comparison between roasting by superheated steam and by convection on changes in colour, texture and microstructure of peanut (*Arachis hypogaea*). *Food Science and Technology Research*, 18(4), 515–524.
- [13]. Jeyakumari, A., Janarthanan, G., Chouksey, M. K., & Venkateshwarlu, G. (2016). Effect of fish oil encapsulates incorporation on the physico-chemical and sensory properties of cookies. *Journal of Food Science and Technology*, 53(1), 856–863.
- [14]. Kjeldahl, C. (1883). A new method for the determination of nitrogen in organic matter. *Zeitschrift für Analytische Chemie*, 22, 366.

- [15]. Koubaa, A., Mihoubi, N. B., Abdelmouleh, A., & Bouain, A. (2012). Comparison of the effects of four cooking methods on fatty acid profiles and nutritional composition of red mullet (*Mullus barbatus*) muscle. *Food Science and Biotechnology*, 21(5), 1243–1250.
- [16]. Kremelberg, D. (2010). *Practical statistics: A quick and easy guide to IBM® SPSS® Statistics, STATA, and other statistical software*. SAGE Publications.
- [17]. Kucukgulmez, A., Celik, M., Yanar, Y., Ersoy, B., & Cikrikci, M. (2006). Effects of different cooking methods on the proximate composition and mineral contents of sea bass (*Dicentrarchus labrax*). *Advances in Food Sciences*, 28(4), 223–227.
- [18]. Larsen, D., Quek, S. Y., & Eyres, L. (2010). Effect of cooking method on the fatty acid profile of New Zealand King Salmon (*Oncorhynchus tshawytscha*). *Food Chemistry*, 119(2), 785–790.
- [19]. Lee, J. S. (1991). *Commercial Catfish Farming* (p. 337). Interstate Publishers.
- [20]. Long, N. V., Yang, Y., Thi, C. M., Van Minh, N., Cao, Y., & Nogami, M. (2013). The development of mixture, alloy, and core-shell nanocatalysts with nanomaterial supports for energy conversion in low-temperature fuel cells. *Nano Energy*, 2(5), 636–676.
- [21]. Mizrahi, S. (2012). Mechanisms of objectionable textural changes by microwave reheating of foods: A review. *Journal of Food Science*, 77(1), R57–R62.
- [22]. Neff, M. R., Bhavsar, S. P., Braekevelt, E., & Arts, M. T. (2014). Effects of different cooking methods on fatty acid profiles in four freshwater fishes from the Laurentian Great Lakes region. *Food Chemistry*, 164, 544–550.
- [23]. Nosedá, B., Islam, M. T., Eriksson, M., Heyndrickx, M., De Reu, K., Van Langenhove, H., & Devlieghere, F. (2012). Microbiological spoilage of vacuum and modified atmosphere packaged Vietnamese *Pangasius hypophthalmus* filets. *Food Microbiology*, 30(2), 408–419.
- [24]. Nosedá, B., Islam, M. T., Eriksson, M., Heyndrickx, M., De Reu, K., Van Langenhove, H., & Devlieghere, F. (2012a). Microbiological spoilage of vacuum and modified atmosphere packaged Vietnamese *Pangasius hypophthalmus* filets. *Food Microbiology*, 30(2), 408–419.
- [25]. Nurhan, U. (2007a). Change in proximate, amino acid and fatty acid contents in muscle tissue of rainbow trout (*Oncorhynchus mykiss*) after cooking. *International Journal of Food Science & Technology*, 42(9), 1087–1093.
- [26]. Nurhan, U. (2007b). Change in proximate, amino acid and fatty acid contents in muscle tissue of rainbow trout (*Oncorhynchus mykiss*) after cooking. *International Journal of Food Science & Technology*, 42(9), 1087–1093.
- [27]. Raj, A. J. A., Haniffa, M. A., Seetharaman, S., & Appelbaum, S. (2008). Utilization of various dietary carbohydrate levels by the freshwater catfish *Mystus montanus* (Jerdon). *Turkish Journal of Fisheries and Aquatic Sciences*, 8(1), 31–35.
- [28]. Şengor, G. F. U., Alakavuk, D. U., & Tosun, Ş. Y. (2013). Effect of cooking methods on proximate composition, fatty acid composition, and cholesterol content of Atlantic Salmon (*Salmo salar*). *Journal of Aquatic Food Product Technology*, 22(2), 160–167.
- [29]. Weber, J., Bochi, V. C., Ribeiro, C. P., Victório, A. D. M., & Emanuelli, T. (2008a). Effect of different cooking methods on the oxidation, proximate and fatty acid composition of silver catfish (*Rhamdia quelen*) filets. *Food Chemistry*, 106(1), 140–146.

Technology In Disaster Management and Response System

Sonali Ingole*¹, Shraddha Patil², Rudresh Shetye², Shivanand Patil², Vaibhavi Deshmukh²

*¹Assistant Professor, Department of Computer Applications, JSPM's Rajarshi Shahu College of Engineering, Tathwade, Pune, Maharashtra, India

²Department of Computer Applications, JSPM's Rajarshi Shahu College of Engineering, Tathwade, Pune, Maharashtra, India

ARTICLE INFO

Article History:

Published : 30 April 2025

Publication Issue :

Volume 12, Issue 13

March-April-2025

Page Number :

171-178

ABSTRACT

Disaster management and response systems increasingly rely on technology to enhance efficiency and reduce losses. This paper examines key technologies, including IoT, AI, robotics, drones, and blockchain, that transform disaster management phases: preparedness, response, recovery, and mitigation. Real-world case studies highlight successful applications. The challenges and limitations, such as infrastructure damage, high costs, and data privacy concerns, are discussed, with recommendations for future research directions.

Keywords: Technology Trends, Artificial Intelligence, Quantum Computing, Edge Computing, Renewable Energy, Biotechnology

INTRODUCTION

Disasters, whether natural or man-made, pose significant challenges to societies worldwide, resulting in widespread loss of life, destruction of infrastructure, and economic setbacks. Effective disaster management is crucial for minimizing these impacts. However, traditional methods of disaster management, which often rely on manual processes and reactive strategies, struggle to address the increasing scale and complexity of modern disasters.

In recent years, the integration of advanced technologies has revolutionized disaster management systems, enabling faster, more efficient, and proactive approaches to disaster preparedness, response, recovery, and mitigation. Technologies such as the Internet of Things (IoT), Artificial Intelligence (AI), robotics, drones, blockchain, and Geographic Information Systems (GIS) have played transformative roles across all phases of disaster management. For instance, IoT devices provide real-time environmental monitoring, helping predict and detect disasters like floods or earthquakes. AI-driven models analyze large datasets to forecast disasters and optimize resource allocation. Drones and robotics are used for search and rescue operations, while blockchain ensures transparency in aid distribution and relief efforts.

Despite these advancements, the implementation of technology in disaster management is not without challenges. Issues such as damaged infrastructure, high implementation costs, data privacy concerns, and skill gaps hinder widespread adoption, particularly in developing regions.

This paper explores the applications of modern technologies in disaster management, providing insights into their transformative potential. It also discusses real-world case studies to illustrate their effectiveness and highlights the challenges and limitations faced during their implementation.

Key Technology Trends

Technological advancements have brought about innovative solutions to improve disaster management across all phases: preparedness, response, recovery, and mitigation. Below is a detailed exploration of key technologies and their applications.

1. Internet of Things (IoT)

IoT refers to a network of interconnected devices that collect, transmit, and analyze real-time data. Its applications in disaster management are vast due to its ability to monitor environmental conditions and alert authorities in case of abnormalities.

Applications

- **Environmental Monitoring:** Sensors placed in vulnerable areas detect early signs of disasters such as rising water levels (floods), ground vibrations (earthquakes), and changes in atmospheric pressure (cyclones).
- **Smart Alarms:** IoT-connected devices automatically send alerts to local authorities and residents when disaster thresholds are breached.
- **Healthcare Applications:** IoT wearables track the health of disaster victims and responders, ensuring immediate medical attention when needed.

Case Study

In Japan, IoT-enabled seismic sensors provide real-time alerts for earthquakes, enabling early evacuation and reducing casualties.

2. Artificial Intelligence (AI)

AI uses machine learning, neural networks, and advanced algorithms to analyze large datasets for insights. In disaster management, AI enhances decision-making, resource allocation, and disaster prediction.

Applications

- **Disaster Prediction:**

AI systems analyze historical data and current patterns to predict disasters like hurricanes, floods, or droughts.

- **Resource Allocation:**

AI optimizes the distribution of resources such as food, water, and medical supplies during relief efforts.

- **Social media Analysis:**

AI scans social media platforms for real-time information about disaster-stricken areas, including location tagging and victim needs.

Case Study

In India, AI-based models predict monsoon flooding, allowing authorities to evacuate at-risk populations early.

3. Drones and Robotics

Drones and robots provide vital support during disaster response and recovery, especially in hazardous or inaccessible areas.

Applications

- Search and Rescue: Drones equipped with thermal imaging cameras locate survivors under debris or in floodwaters.
- Damage Assessment: High-resolution imagery from drones helps evaluate the extent of destruction, enabling informed decision-making.
- Hazardous Environment Navigation: Robots equipped with sensors and cameras navigate areas too dangerous for humans, such as collapsed buildings or toxic zones.

Case Study

After Hurricane Harvey in the United States, drones mapped flooded areas and guided relief efforts more efficiently.

4. Blockchain Technology

Blockchain ensures transparency and accountability in disaster relief and recovery efforts through decentralized and tamper-proof systems.

Applications

- Aid Distribution: Blockchain tracks the flow of relief materials, ensuring fair and accurate distribution.
- Decentralized Data Sharing: Blockchain platforms enable secure sharing of critical data among agencies involved in disaster management.
- Donation Tracking: Donors can track how their contributions are being utilized, fostering trust and increasing accountability.

Case Study

The United Nations implemented blockchain technology to manage aid distribution during the Syrian refugee crisis, ensuring resources reached intended beneficiaries.

5. Geographic Information Systems (GIS)

GIS is a spatial analysis tool that uses maps and location data to visualize disaster impact and guide response efforts.

Applications

- Risk Mapping: GIS identifies high-risk areas for floods, earthquakes, or fires, aiding in disaster preparedness.
- Evacuation Planning: GIS maps evacuation routes and shelters to ensure the safe movement of affected populations.
- Damage Assessment: GIS combines pre- and post- disaster satellite images to analyze damage and prioritize recovery operations.

Case Study

During the Haiti earthquake (2010), GIS tools mapped affected areas, guiding emergency responders to the most critical zones.

6. Big Data Analytics

Big data uses vast amounts of structured and unstructured data to derive actionable insights, especially during large- scale disasters.

Applications

- Trend Analysis: Big data identifies patterns in disaster occurrences, improving preparedness strategies.
- Real-Time Monitoring: Integrates data from IoT devices, social media, and sensors for a comprehensive view of ongoing disasters.

- Predictive Analytics: Analyzes weather patterns, historical data, and climate conditions to forecast potential disasters.

Case Study

Google's AI and big data tools provided real-time flood forecasts in Bangladesh, reducing casualties.

7. Communication Technologies

Effective communication is vital during disasters to coordinate response efforts and inform the public.

Applications

- Emergency Alerts: Governments use SMS, app notifications, and public broadcasts to send alerts to citizens.
- Mesh Networks: Ensure connectivity in disaster-hit areas where traditional networks are damaged.
- Satellite Communication: Provides reliable communication channels for responders in remote areas.

Case Study

During the 2010 Chile earthquake, satellite phones allowed rescue teams to coordinate relief operations despite damaged infrastructure.

8. Renewable Energy Solutions

Disasters often disrupt power supplies, hindering relief efforts. Renewable energy technologies offer resilient power solutions.

Applications

- Microgrids: Localized energy systems powered by solar or wind provide electricity to critical facilities like hospitals and shelters.
- Portable Solar Kits: Used to power communication devices and medical equipment in remote disaster-affected areas.

Case Study

Solar-powered microgrids restored electricity in Puerto Rico after Hurricane Maria.

Phases of Disaster Management

Disaster management is a continuous and systematic approach aimed at reducing the impact of disasters and enhancing recovery efforts. It comprises four primary phases: Preparedness, Response, Recovery, and Mitigation. Each phase involves specific actions and strategies to address various aspects of disaster risk and management.

1. Preparedness Phase

Preparedness focuses on planning and readiness activities that help individuals, communities, and organizations respond effectively to disasters. The goal is to minimize

The response phase involves immediate actions taken during or shortly after a disaster to save lives, reduce harm, and limit further damage. It is characterized by rapid mobilization of resources and coordinated efforts.

Key Activities

- Emergency Communication: Establishing channels to disseminate information to affected communities and responders.
- Search and Rescue Operations: Deploying teams, drones, and robots to locate and rescue survivors.
- Medical Assistance: Providing emergency medical care, including field hospitals and mobile health units.
- Resource Distribution: Ensuring timely delivery of food, water, and shelter to disaster-affected populations.

Technological Applications

- Drones and robotics for search and rescue in inaccessible areas.
- Satellite communication and mesh networks to maintain connectivity.
- AI-based decision support systems to prioritize rescue efforts and resource allocation.

Example

During the 2010 Haiti earthquake, drones and GIS tools expedited rescue operations and relief distribution.

damage, ensure safety, and maintain essential

Functions during emergencies. Key Activities

- Risk Assessment and Planning: Identifying potential hazards and developing

2. Recovery Phase

The recovery phase begins after the immediate response and focuses on restoring normalcy to affected areas. It aims to rebuild infrastructure, restore livelihoods, and ensure long-term sustainability.

Key Activities

- Damage Assessment: Evaluating the extent of destruction to prioritize rebuilding efforts.
- Infrastructure Reconstruction: Repairing or rebuilding homes, roads, schools, and hospitals.
- Economic Rehabilitation: Providing financial assistance, job creation programs, and support for small businesses.
- Mental Health Support: Offering psychological support to victims and responders to address trauma.

Technological Applications

- 3D printing for creating temporary shelters and critical components.
- AI-driven recovery models to optimize resource allocation and project timelines.
- Big data analytics to analyze recovery trends and predict future challenges.

Example

In Puerto Rico, solar-powered microgrids provided electricity to communities rebuilding after Hurricane Maria.

3. Mitigation Phase

Mitigation involves proactive measures to reduce the severity or likelihood of future disasters. It focuses on long-term strategies to make communities more resilient.

Key Activities

- Hazard Mapping: Using GIS and satellite imagery to identify high-risk areas and develop strategies to reduce exposure.
- Policy Implementation: Enforcing building codes, zoning regulations, and environmental protection laws.
- Community Awareness Programs: Educating communities about disaster risks and safe practices.
- Infrastructure Strengthening: Constructing earthquake-resistant buildings, flood barriers, and drainage systems.

Technological Applications

- IoT sensors for real-time environmental monitoring to predict hazards.
- Smart infrastructure with embedded sensors to detect vulnerabilities.
- Renewable energy systems, such as microgrids, to ensure resilience during power outages.

Example

After frequent flooding, the Netherlands developed advanced flood control systems, including dikes, levees, and storm surge barriers, to mitigate risks.

Integration Across Phases

While each phase has distinct objectives, they are interconnected, creating a comprehensive disaster management cycle. For instance:

- Early warning systems developed during preparedness can improve response times.
- Lessons learned from the recovery phase inform better mitigation strategies.
- Continuous risk assessments link mitigation efforts to preparedness plans.

Real-World Applications of Disaster Management Technologies

Technological advancements have significantly enhanced the efficiency of disaster management across preparedness, response, recovery, and mitigation phases. Below are real-world applications that illustrate the transformative impact of technology in disaster management.

1. Early Warning Systems

Application: Indian Ocean Tsunami Warning System

After the devastating 2004 Indian Ocean tsunami, a network of deep-sea sensors and satellite-based communication systems was established to detect undersea earthquakes and potential tsunamis.

- Technology Used:
 - IoT and Seismic Sensors: Measure ocean floor disturbances.
 - AI Models: Predict tsunami paths and impact areas.
 - Satellite Communication: Transmits alerts to coastal regions.
- Impact:

Improved evacuation times and reduced casualties in high-risk areas like Indonesia and Thailand.

2. Drones in Search and Rescue Operations Application: Hurricane Harvey, USA (2017)

Drones were extensively used to map flooded areas, assess damage, and locate stranded individuals.

- Technology Used:
 - Aerial Imaging: High-resolution cameras and thermal imaging.
 - Autonomous Navigation: AI algorithms for path optimization.
 - Data Integration: GIS tools for creating detailed damage maps.
- Impact:

Reduced response times, improved resource allocation, and enhanced situational awareness for rescue teams.

3. Disaster-Resilient Infrastructure Application: Flood Control in the Netherlands

The Netherlands employs advanced flood control systems, including dikes, levees, and the Maeslantkering storm surge barrier.

- Technology Used:
 - Hydrodynamic Models: Simulate water movement during floods.
 - IoT Sensors: Monitor water levels in real-time.
 - Automated Barriers: Respond dynamically to rising water levels.
- Impact:

Protection of low-lying regions and prevention of catastrophic flooding in highly vulnerable areas.

4. GIS for Emergency Planning

Application: Earthquake Response in Nepal (2015)

During the 2015 earthquake in Nepal, GIS tools were used to coordinate emergency response.

- Technology Used:
 - Satellite Imagery: For real-time mapping of affected areas.

- Risk Maps: Identified high-impact zones for prioritizing aid.
- Crowdsourced Data: Verified affected areas through public reports.
- Impact:
Faster mobilization of resources and more targeted aid delivery, reducing delays and duplication of efforts.
- Solar Panels: Provided off-grid power solutions.
- Battery Storage Systems: Ensured continuous power supply.
- Impact:
Restored critical services like healthcare and communication in remote areas.

Challenges and Limitations

Despite the advancements in technology, disaster management still faces significant challenges and limitations. These barriers hinder the effective implementation of technologies across preparedness, response, recovery, and mitigation phases.

1. High Implementation Costs Challenge

Advanced technologies like IoT, drones, and AI systems often require significant financial investment, making them inaccessible for low-income or resource-constrained regions.

- Example: Many developing countries cannot afford real-time satellite data or build sophisticated early warning systems.

Most disaster management technologies require uninterrupted electricity and internet connectivity to function.

- Example: Drones, GIS systems, and IoT devices are ineffective in areas with power outages or damaged networks.

Impact

Response capabilities are significantly reduced in remote or disaster-affected areas.

Limited access to technologies increases vulnerability and reduces disaster response efficiency.

2. Infrastructure Vulnerabilities Challenge

Natural disasters often damage critical infrastructure such as communication networks, power grids, and transportation systems, limiting the functionality of technological tools.

- Example: Earthquakes or hurricanes can disable IoT sensors or disrupt drone operations.

Impact

Response efforts are delayed, and situational awareness is compromised, leading to greater loss of life and property.

3. Data Privacy and Security Challenge

The extensive use of technologies like IoT, AI, and blockchain generates and stores massive amounts of sensitive data, including personal and geographical information.

- Example: Blockchain systems for aid distribution must protect beneficiaries' identities and financial transactions.

Impact

Vulnerabilities in data systems can lead to breaches, misuse, or loss of trust among stakeholders.

4. Technical Expertise Requirements Challenge

Operating and maintaining disaster management technologies require skilled personnel, which may not be available in every region.

- Example: Remote communities may lack the training to deploy and utilize GIS or drone technologies effectively.

Conclusion

Technological advancements have significantly transformed disaster management, enabling faster, more efficient responses and reducing the overall impact of disasters. From predictive analytics and early warning systems to drones, IoT devices, and GIS mapping, these tools have enhanced preparedness, response, recovery, and mitigation efforts. Real-world applications, such as flood control in the Netherlands and drone use during Hurricane Harvey, demonstrate the potential of innovative technologies to save lives, minimize damage, and expedite recovery.

However, the implementation of these technologies is not without challenges. High costs, infrastructure vulnerabilities, data privacy concerns, and limited technical expertise often hinder their effective deployment, particularly in low-resource settings. Additionally, ethical concerns, interoperability issues, and the unpredictable nature of between public and private sectors, alongside research and development, is essential for creating scalable and sustainable solutions.

Ultimately, while technology cannot prevent disasters, it can significantly reduce their impact. By embracing innovation and addressing limitations, disaster management systems can become more resilient and adaptive, ensuring better protection for vulnerable communities and safeguarding lives in the face of an increasingly unpredictable world.

REFERENCES

- [1]. J. Smith et al., "IoT Applications in Disaster Management," *IEEE Internet of Things Journal*, vol. 7, no. 4, pp. 3120–3128, Apr. 2021.
- [2]. R. Brown, "AI in Emergency Response Systems," *IEEE Transactions on AI Systems*, vol. 5, no. 3, pp. 210–222, Mar. 2020.
- [3]. S. Lee, "Blockchain Technology for Transparent Aid Distribution," *IEEE Blockchain Journal*, vol. 8, no. 2, pp. 456–468, Feb. 2023.
- [4]. K. Tanaka, "Drones for Disaster Management," *IEEE Robotics and Automation Letters*, vol. 6, no. 1, pp. 1050–1060, Jan. 2022.
- [5]. M. Jones, "Ethical Implications of AI in Disaster Management," *IEEE Ethics in Engineering*, vol. 4, no. 1, pp. 15–25, Jan. 2023.

Comparative Study of Conventional and Ultrasonication Method for Synthesis of Benzopyranone Derivatives

Dr. A. P. Manake¹, Mr. A. R. Mali²

¹Department of Chemistry, Pratap College, Amalner. Dist-Jalgaon. Pin-425401, Maharashtra. India

²Department of Mathematics, Science and Humanities, UPL University of Sustainable Technology, Ankleshwar, Gujarat, India

ARTICLE INFO

Article History:

Published : 30 April 2025

Publication Issue :

Volume 12, Issue 13
March-April-2025

Page Number :

179-188

ABSTRACT

Benzopyran (chromene) compounds were representing a significant class of heterocyclic compounds, broadly documented for their substantial importance in both medicinal chemistry and natural product research, due to their varied and powerful biological activities. Several benzopyran derivatives have been reported to show an extensive pharmacological property, such as antitumor, antioxidant, anti-inflammatory, anticoagulant, antiviral, antifungal, antimicrobial, herbicidal, and analgesic activities. Here, in this work, we synthesized the substituted benzopyran derivatives through a one-pot reaction of o-chlorobenzoic acid and substituted phenols in presence of catalyst successfully by two different methods: one is the conventional and another one is ultrasonication method. The ultrasonication technique is speed up the chemical reactions and improves product yields, and allow the reaction to proceed under the mild conditions as compared to traditional heating. The synthesized compounds were characterized by Thin Layer Chromatography, Ultraviolet, Infrared spectroscopy, ¹H-NMR and TGA.

Keywords: o-chlorobenzoic acid, substituted phenols, Ultrasonication

INTRODUCTION

For the construction of various organic compounds ecofriendly synthetic procedures are significantly increased in chemical industry. Nowadays, understanding of side effects caused due to hazardous chemicals and solvents has highlighted the need of safer and greener alternatives. Shielding of environment from the hazardous impact of old organic synthesis processes has become an important goal. Consequently, in recent years efforts of research have been focused on adopting green methods which minimizes the use of toxic solvents and reagents(1-4). In recent years, for several organic reactions especially, those that needs harsh reaction conditions, sonochemical energy has been considered as a powerful substitute to thermal energy. The ultrasonic irradiation has appeared as an important technique that supports the core principles of green chemistry.

Ultrasonication method not only hastens reaction rate but also often increases product yield and purity compared to conventional thermal methods. In modern organic synthesis, this method is important due to its eco-friendliness and high efficiency(5). In organic and medicinal chemistry, the synthesis of heterocyclic compounds has a central focus in organic and medicinal chemistry due to their broad spectrum of biological activities and their appearance in various natural products. Amongst these benzopyranones derivatives are very well known due to their huge biological properties such as antioxidant, anti-inflammatory, anticancer and antidiabetic (6–9). These compounds are broadly employed in agrochemicals, drug design, and material sciences. These compounds are also called as chromenes, due to benzene is fused with pyran (10). Benzopyranons derivatives are a significantly important class of naturally occurring compounds widely present in plants (11). The chromene moiety is a fundamental structure usually found in various natural products like alkaloids, flavonoids and anthocyanins (12). A variety of chromene-based natural products have shown significant pharmaceutical potential (9,13). The synthesis of benzopyran derivatives has attracted important research interest because of their pharmacological properties. This investigation aims to achieve a comparative study of conventional and ultrasonication methods for the synthesis of benzopyranone derivatives. We aim to evaluate and examine both methods on key parameters like reaction time, yield; environmental impact and energy efficiency. This assessment is predictable to give valuable info about the benefits of ultrasonication as a current method for the synthesis of benzopyranones.

Here, we have first time utilized a harmonious combination of mild solvents and ultrasound irradiation for the synthesis of target molecules. The usefulness of this method was assessed with respect to its capability to enhance reaction parameters and reduce overall energy consumption. It is proven that ultrasonic irradiation not only increases reaction rate but also increases product yield, material properties including crystallite size, crystal morphology etc. The compounds synthesized by sonochemical method and conventional method were compared systematically for their crystallinity, thermal stability and morphological characteristics. These assessments were accomplished by X-ray Diffraction (XRD), Thermogravimetric Analysis (TGA). Overall, the sonochemical method demonstrated significant advantages over the conventional thermal approach, offering shorter reaction times and higher yields, whereas the conventional method resulted in prolonged reaction durations and lower product yields.

Experimental

Ultrasound Set-up

Ultrasound for sonochemical synthesis is generated with the help of ultrasonic instrument. The specification and details of the set-up, processing parameters used during experiments are as follows-

Make: Roop Ultrasonics

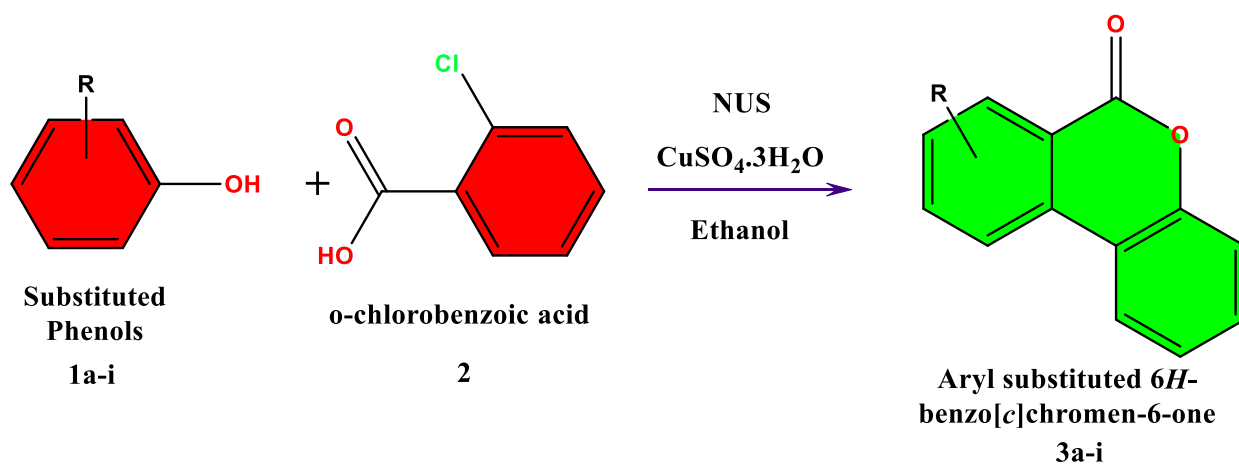
Operating frequency: 40kHz (Inbuilt)

Rated output power: 230 W

Temperature: Optimized



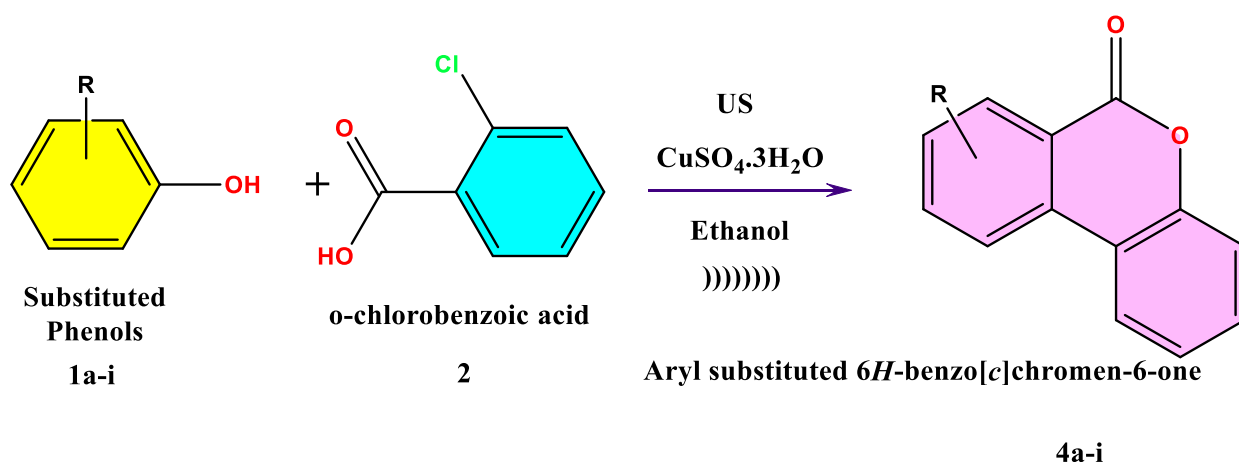
Scheme-1:



3-Phenyl-3,3a-dihydrochromeno[4,3-c]isoxazol 4-one, 5a:

m. p. 167°C (Lit. 167-168°C^{29a}). **Anal. Calcd for** C₁₆H₁₁O₃N: C, 72.45; H, 4.15; N, 5.28. **Found:** C, 72.35; H, 4.18; N, 5.30%. **IR (nujol):** 1615, 1670 cm⁻¹; **¹H NMR (300 MHz, CDCl₃ TMS):** 3a- δ 7.42 -7.79 (m, 8H, Ar-H).

Scheme-2:



Procedure: -

For Non-Ultrasound Sonication (NUS):

The calculated amounts of substituted phenols (0.60 gm for phenol) are mixed with 1 gm of O-chlorobenzoic acid and 0.32 gm of CuSO₄ in 7:15 aqua-ethanol solvent by vigorous shaking. was heated under reflux for 1 hour, the solid products were filtered, washed with ethanol and recrystallized by the same solvent, compounds were produced. After irradiation pour reaction mixture in crush ice, stir the solution. Recrystallized the obtained product.

For Ultrasound Sonication (US):

Thecalculated amounts of substituted phenols (0.60 gm for phenol) are mixed with 1 gm of o-chlorobenzoic acid and 0.32 gm of CuSO₄ in 7:15aqua-ethanol solvent by vigorous shaking. Set up the instrument ultrasonic sonicator and mixture is irradiated with ultrasonication for 15 min at 35°C temperature. After irradiation pour reaction mixture in crush ice, stir the solution. Recrystallized the obtained product.

Result and Discussion

Results:

a) For Conventional (NUS) Method:

Sr. No.	Parameters	3a	3b	3c	3d	3e	3f	3g	3h	3i
1	Theoretical yield (gm)	1.25	1.55	1.55	1.55	1.35	1.35	1.35	1.45	1.47
2	Practical yield (gm)	0.270	0.867	0.627	0.521	0.860	0.28	1.11	0.84	1.06
3	Percentage yield (%)	21.42	55.93	40.45	33.61	63.70	20.74	82.22	57.93	72.10
4	Melting point (observed)	128 °C	131 °C	158 °C	143 °C	182 °C	190 °C	200 °C	101 °C	162 °C
5	Reaction time	1 Hour	1 Hour	1 Hour	1 Hour	1 Hour	1 Hour	1 Hour	1 Hour	1 Hour
6	Rf value (Reactant)	0.87	0.72	--	--	--	--	--	---	--
7	Rf value (Product)	0.37	0.30	--	--	--	--	--	--	--

b) For Sonication (US) Method:

Sr. No.	Parameters	4a	4b	4c	4d	4e	4f	4g	4h	4i
1	Theoretical yield (gm)	1.25	1.55	1.55	1.55	1.35	1.35	1.35	1.45	1.47
2	Practical yield (gm)	0.82	1.19	1.02	1.0	1.18	1.26	1.31	1.15	1.11
3	Percentage yield (%)	65	76.77	65.8	64.52	87.40	93.33	97.03	79.31	75.51
4	Melting point (observed)	129 °C	132 °C	155 °C	145 °C	180 °C	194 °C	202 °C	103 °C	160 °C
5	Reaction time	15 Min	15 Min	15 Min	15 Min	15 Min	15 Min	15 Min	15 Min	15 Min
6	Rf value (Reactant)	0.91	0.0.84	--	--	--	--	--	---	--
7	Rf value (Product)	0.40	0.33	--	--	--	--	--	--	--

The compounds 3a to 3i and 4a to 4i were synthesized by using two different methods: the conventional method and sonication method. The obtained experimental outcomes were mentioned in table no 1 and 2. This comparison emphasizes the noteworthy role of sonication in increasing reaction productivity, decreasing reaction time and improving product purity.

Yield Comparison:

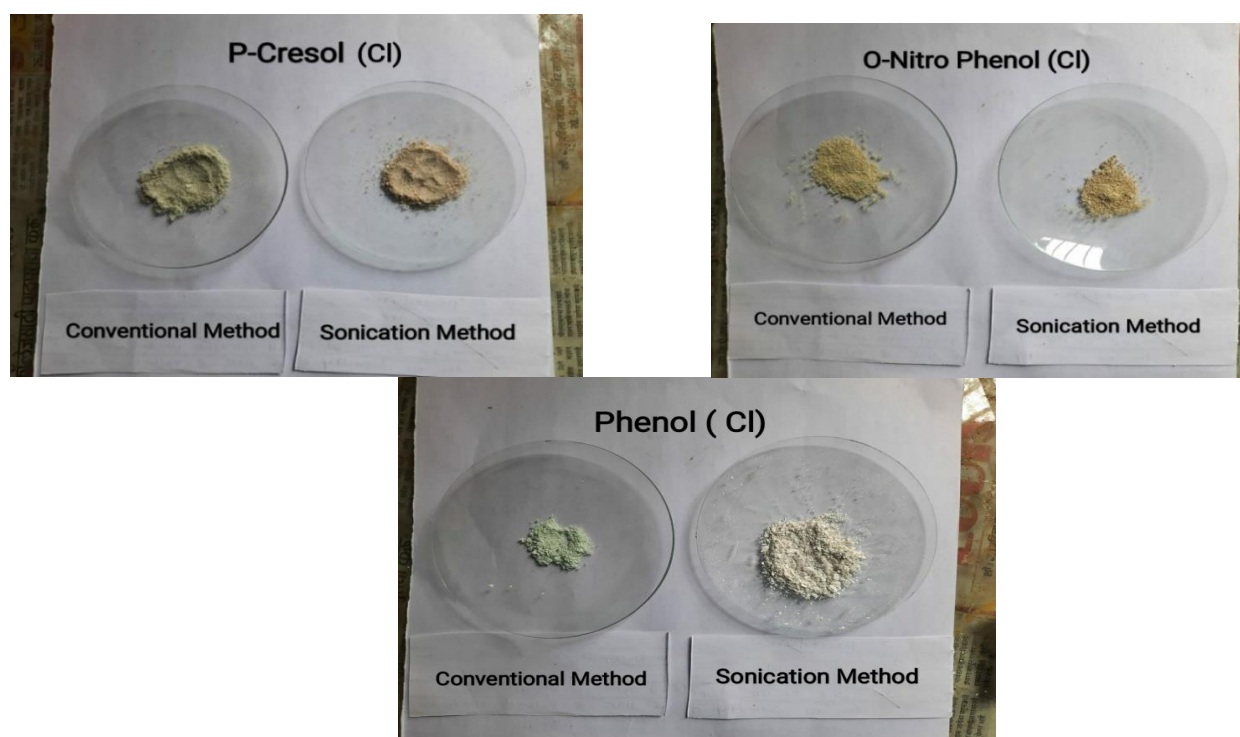
The theoretical yields of all reactions were similar in both methods, as projected, because the molar ratios were the same. But both methods showed remarkable difference in practical yield. The ultrasonication method steadily gives enhanced practical yield, ranging from 64.52 to 97%. While the conventional method gives lower yield, ranging from 20.74 to 82%. Particularly, 3g compound demonstrated enhanced practical yield (97.03%) as compared to conventional method (82.22%). Likewise, 3e and 3f compounds achieved enhanced yields by sonication method as compared to conventional method (63.7 to 20.74%) respectively. The decreased yield in conventional method is due to the long exposure of heat increases chances of side reactions, whereas the increases in yield in case of sonication method is due to the cavitation effect(14).

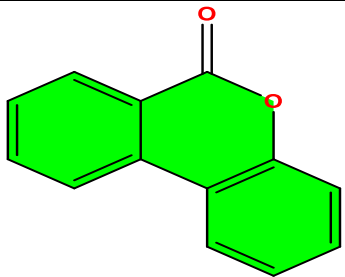
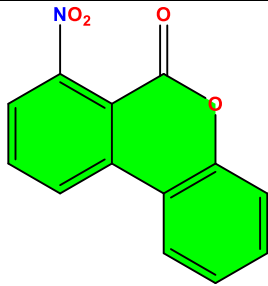
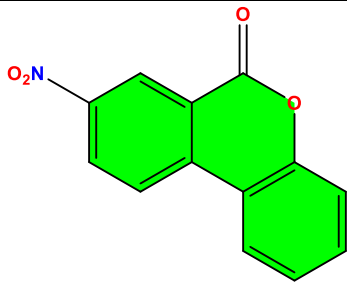
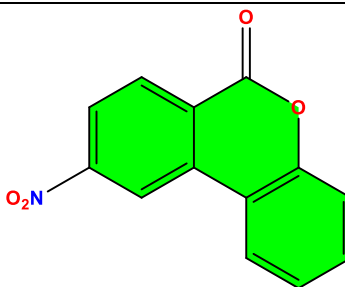
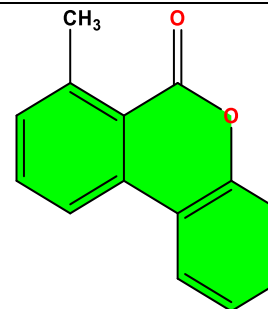
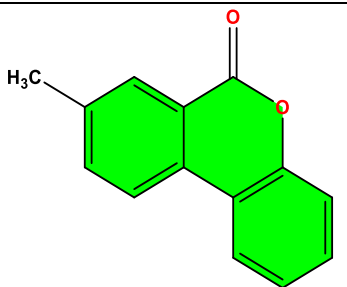
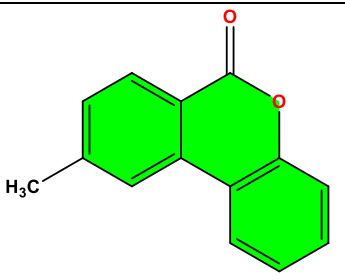
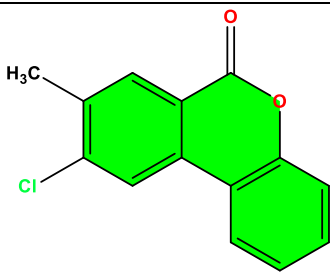
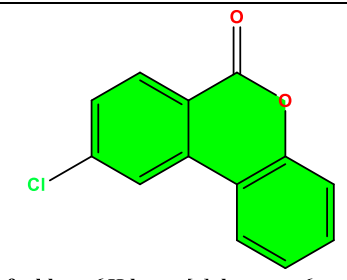
Reaction Time A noteworthy transformation was renowned in reaction time. By employing conventional heating method, the reaction required 1 hr for completion, while by employing sonication method time was drastically reduced from 1 hr to 15 minutes. This proves that ultrasound energy helps to speed up the chemical reaction by enhancing the molecular collision and improving the movement of molecules(14).

Melting Point Analysis:

All melting points were measured accurately on a melting point apparatus and are uncorrected. The melting points of products synthesized by both methods were comparable, although slight differences were observed. Generally, compounds obtained via sonication exhibited sharper and slightly higher melting points, suggesting better purity and crystallinity. For example, 3g synthesized by sonication melted at 202°C, compared to 200°C when prepared conventionally. Similarly, for 3e, the sonication sample melted at 180°C, compared to 182°C in the conventional process. These minor differences are typically attributed to variations in crystal formation due to different reaction environments.

Product Images:



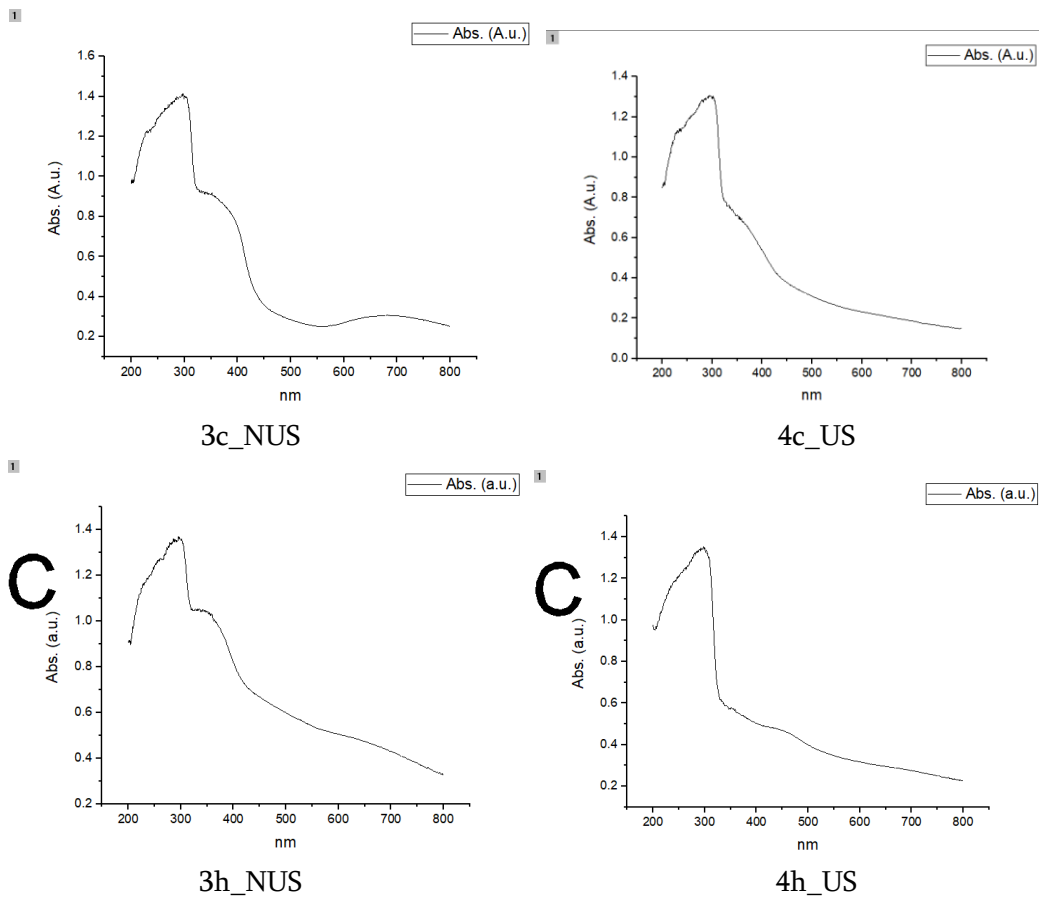
Product Structure and name		
 <p>6H-benzo[c]chromen-6-one 3a & 4a</p>	 <p>7-nitro-6H-benzo[c]chromen-6-one 3b & 4b</p>	 <p>8-nitro-6H-benzo[c]chromen-6-one 3c & 4c</p>
 <p>9-nitro-6H-benzo[c]chromen-6-one 3d & 4d</p>	 <p>7-methyl-6H-benzo[c]chromen-6-one 3e & 4e</p>	 <p>8-methyl-6H-benzo[c]chromen-6-one 3f & 4f</p>
 <p>9-methyl-6H-benzo[c]chromen-6-one 3g & 4g</p>	 <p>9-chloro-8-methyl-6H-benzo[c]chromen-6-one 3h & 4h</p>	 <p>9-chloro-6H-benzo[c]chromen-6-one 3i & 4i</p>

Experimental data:-

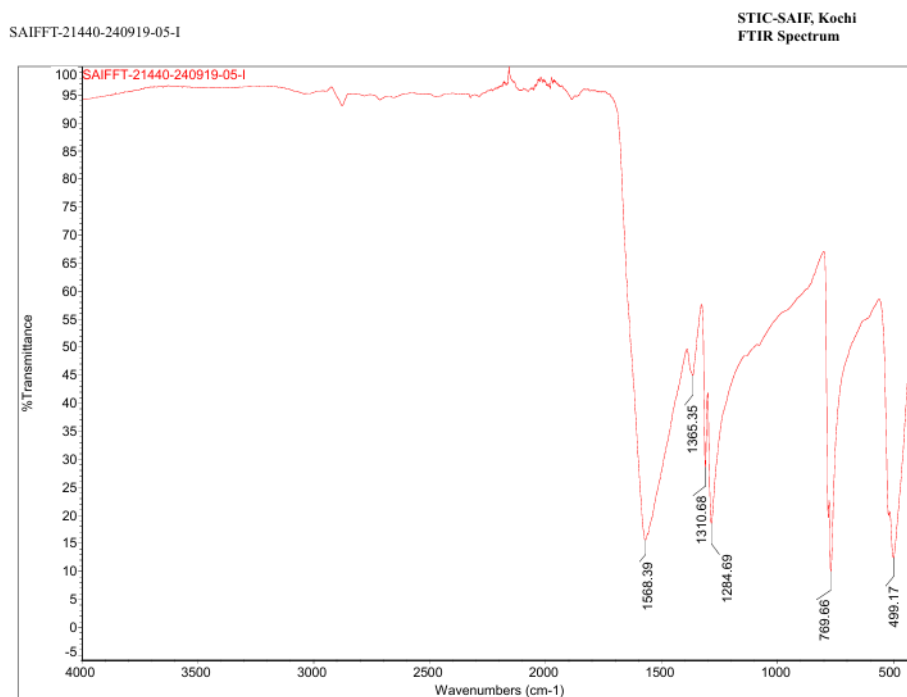
Analytical:

Thin-layer chromatography (TLC):- Thin-layer chromatography (TLC) was performed on Merck silica gel 60 plates, 0.25mm thickness. Solvents for chromatography were pure and used as received.

UV Spectra Analysis:- Visualization was accomplished by UV light on UV-Visible spectrophotometer having range of 200-800 nm. The UV-Vis spectra of powder synthesized showed absorption maxima between the wavelength 300-350 nm. Also absorption shows in the region of 400-415 nm. These absorption indicates that synthesized products have a conjugation.



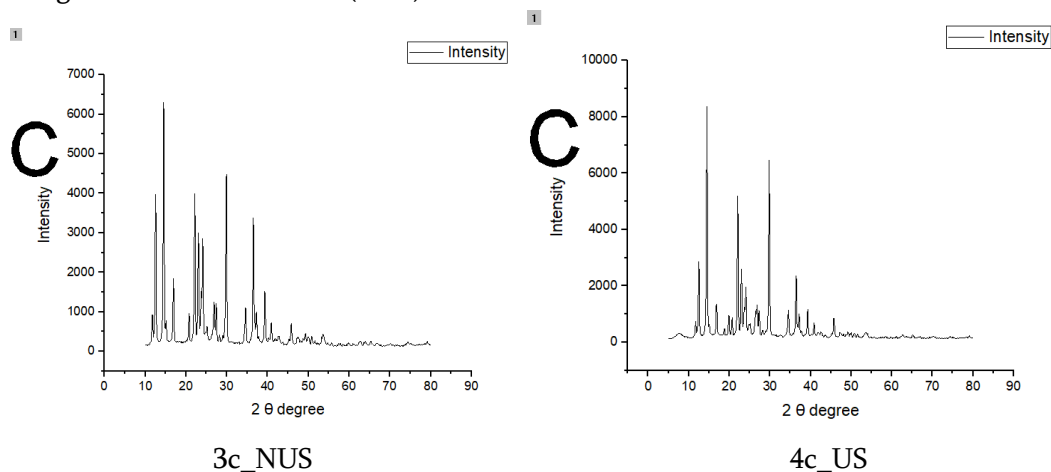
IR Spectral Analysis: - IR spectra were recorded with a JASCO FT-IR 6600 PC spectrophotometer in KBr disks having range of 4000-400 cm^{-1} . The synthesized derivatives show their IR value at 1500-1650 cm^{-1} . This confirms functional keto/aldehyde functional group.



4a_US

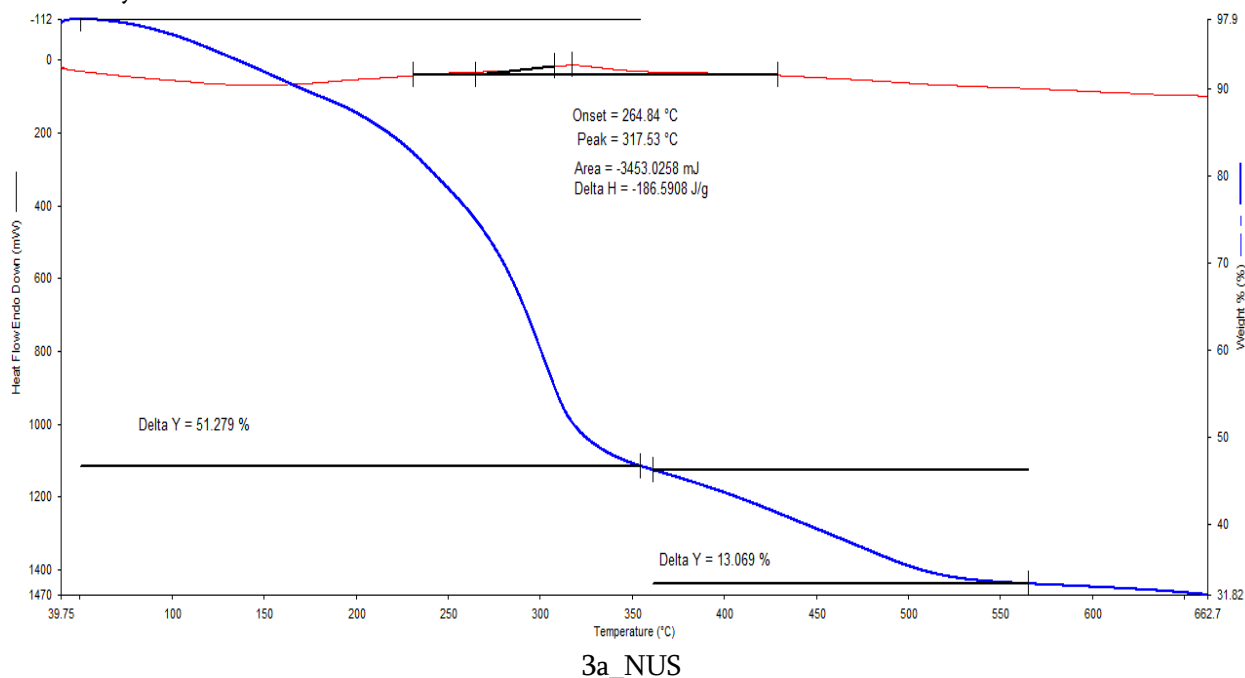
X-Ray Diffraction Pattern:

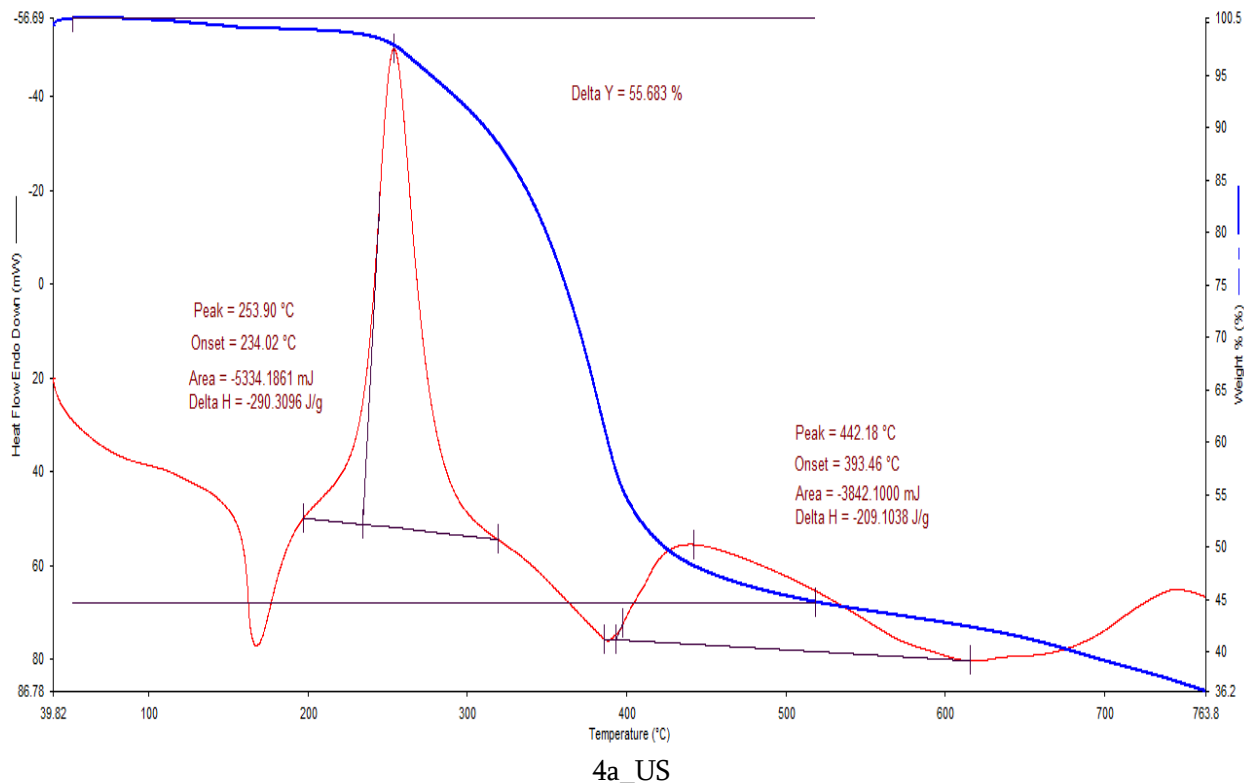
The XRD patterns confirmed the formation of fine and crystalline powder. The XRD pattern exhibited diffraction peaks at 15°, 22° and 30° shows needle like peak which indicates the fine product. The synthesis and crystalline nature was significantly observed. This result confirms that the crystallite size of the product synthesized using ultrasonication method is superior than made by conventional method. In the spectra images it is clearly seen that the ultrasound assisted (US) synthesized product having higher in intensity than product synthesized using conventional method (NUS).



TGA Analysis

TGA measures the weight loss of a material as a function of temperature or time under a controlled atmosphere (usually nitrogen or air). The **thermal stability** of synthesized derivatives found to be superior in case of ultrasound assisted synthesis. The single peak drops over the entire range in weight loss graph indicates no impurities in synthesized derivative.





Conclusion

Here, the present investigation highlights the effectiveness and crystalline nature of ultrasound assisted synthesis of compounds 4a to 4i over the conventional techniques 3a to 3i. The utilization of ultrasound energy remarkably increases the product yield due to cavitation effect and enhanced molecular collision. Whereas, the conventional method demonstrated lower yields due to prolonged heat exposure which enhances the side chain reaction. These results demonstrate the proven benefit of ultrasound in accelerating chemical reaction and improving quality of products.

Acknowledgement

Thanks to **DST SAIF Cochin**, Sophisticated Test and Instrumentation Centre (STIC) Cochin University of Science & Technology Campus, Kochi 682 022, Kerala for analyzing the data.

REFERENCES

- [1]. Dhokale NT, Kale SB, Nagre SS, Konda SG, Dalvi NR. A convenient and efficient synthesis of 2-thio-5-hydroxy-5H-[1]benzopyrano[4,3-d] pyrimidines via ultrasonic irradiation compared with conventional method. *Current Research in Green and Sustainable Chemistry*. 2022 Jan 1;5:100282.
- [2]. Gomha SM, Badrey MG. Ecofriendly regioselective one-pot synthesis of chromeno [4, 3-d][1, 2, 4] triazolo [4, 3-a] pyrimidine derivatives. *European Journal of Chemistry*. 2013;4(2):180–4.
- [3]. Banerjee B. Recent developments on ultrasound-assisted synthesis of bioactive N-heterocycles at ambient temperature. *Australian Journal of Chemistry*. 2017;70(8):872–88.
- [4]. Livingston K. *Inorganic Mass Spectrometry*. F. Adams, R. Gijbels, and R. Van Grieken, Eds. Wiley-Interscience, New York, 1988. xii, 404 pp., illus. \$65. *Chemical Analysis*, vol. 95. Science. 1989;243(4897):1499–1499.

- [5]. Sankar M, Dimitratos N, Miedziak PJ, Wells PP, Kiely CJ, Hutchings GJ. Designing bimetallic catalysts for a green and sustainable future. *Chemical Society Reviews*. 2012;41(24):8099–139.
- [6]. Krasniqi I, Behrami A, Demaku S, Shehu I. Antibacterial activity of coumarine derivatives synthesized from 4-hydroxychromen-2-one and comparison with standard drug. 2015 Sep 1;7:1041–5.
- [7]. Aytemir MD, Hider RC, Erol DD, ÖZALP M, EKİZOĞLU M. Synthesis of new antimicrobial agents; amide derivatives of pyranones and pyridinones. *Turkish Journal of Chemistry*. 2003;27(4):445–52.
- [8]. AHMED HAM. Synthesis of some novel benzopyranes derivatives and evaluation their biological activity. *Synthesis*. 2015;8(4).
- [9]. Kulkarni MV, Kulkarni GM, Lin CH, Sun CM. Recent advances in coumarins and 1-azacoumarins as versatile biodynamic agents. *Current medicinal chemistry*. 2006;13(23):2795–818.
- [10]. Schweizer E, Meeder-Nycz O, Ellis G. Chromenes, Chromanes, Chromones. 1977;
- [11]. Curini M, Cravotto G, Epifano F, Giannone G. Chemistry and biological activity of natural and synthetic prenyloxycoumarins. *Current medicinal chemistry*. 2006;13(2):199–222.
- [12]. Ren Q, Siau WY, Du Z, Zhang K, Wang J. Expedient assembly of a 2-amino-4H-chromene skeleton by using an enantioselective Mannich intramolecular ring cyclization-tautomerization cascade sequence. 2011;
- [13]. Yu D, Suzuki M, Xie L, Morris-Natschke SL, Lee K. Recent progress in the development of coumarin derivatives as potent anti-HIV agents. *Medicinal research reviews*. 2003;23(3):322–45.
- [14]. Suslick KS. Sonochemistry. *science*. 1990;247(4949):1439–45.

CV And GCD Study of Tin-Doped Copper Oxide with Aqueous Electrolyte for Supercapacitor Electrode

Priyanka Meena^{1,2}, Namrata Sengar², Yogesh Kumar³

¹Department of Physics, Deshbandhu College, University of Delhi, Delhi-110019, India

²Department of Pure and Applied Physics, University of Kota, Kota-324005, Rajasthan, India

³Department of Physics, ARSD College, University of Delhi, New Delhi - 110021, India

ARTICLE INFO

Article History:

Published : 30 April 2025

Publication Issue :

Volume 12, Issue 13

March-April-2025

Page Number :

189-194

ABSTRACT

The supercapacitor attracts pervasive attention for energy storage, however, there is a lack of electrode material with high specific capacitance, specific energy, and cyclic stability. In this study, we prepared tin-doped copper oxide material using the solvo-combustion method and studied the material's electrochemical behavior to fill the gap. The electrochemical performances of the prepared sample as working electrodes will be analyzed by cyclic voltammetry (CV) and galvanostatic charge-discharge (GCD) studies in an aqueous electrolyte. The highest specific capacitance will be evaluated at 91.5 F/g at a 0.01 V/s Scan rate.

INTRODUCTION

At the global level, the energy demands surmount, the researchers try to unearth an alternative to lithium-ion batteries. In the realm of energy storage, the supercapacitor stands out due to its unique property. The supercapacitor combines rapid charge-discharge cycles, high specific capacitance, long lifespan, and eco-friendliness.

Due to their fast charge-discharge speed, high power output density, reliability, safety and long service life, supercapacitors (SCs) are widely used in stationary and mobile high-power systems (cranes and loaders, dump trucks, buses, trains, agricultural machinery), where they are used both as supplementary and stand-alone energy storage devices. Safety and environmental friendliness are additional advantages of SCs, as these devices do not use toxic electrolytes, unlike rechargeable batteries, making them extremely safe to operate and easy to dispose of [4]. There are three types of SCs based on charge storage procedure: first, EDLC, second, pseudo-capacitor, and third, hybrid capacitor. The EDLC is based on carbon material, the pseudo-capacitor is based on metal oxide, metal nitride, polymers, etc, and the hybrid capacitor is a combination of Li-ion battery and Sc. In Sc, the electrode plays a measure role, therefore, it is a very big challenge to prepare an electrode that has a low cost with excellent electrochemical properties and environmental friendliness. There are several metal oxides and combinations of metal oxides with different materials, which are used as the Sc electrode. Kannan et al.

prepared NiO-Co₃O₄ (NC) and CuO-NiO-Co₃O₄ (CNC) using the hydrothermal method. The NC and CNC exhibited 262 F/g specific capacitance at 1 A/g current density. Moreover, the CNC displayed long-term cyclic stability of 84.9%, which was observed after 5000 charge-discharge cycles[5]. Chelladurai et al. prepared Bi₂WO₆-NiO NC using the hydrothermal method. The sample elevated specific capacitance of 398.2 C/g at 10 mV/s (5).Liu et al. Cu⁰/Cu⁺ co-doped CoO composite via a facile strategy. The specific capacitance of 695 F/g at 1 A/g current density in 3M KOH electrolyte[7].The primary focus of research in recent years has been on metal oxides, or transition metal oxides, that can be employed as an electroactive part for use in Scs at a reasonable expense. Because metallic element hydroxides and oxides (Ru, Co, Ni, etc.) demonstrate high theoretical specific capacitance and their potential application as an active material at levels higher than 1000 F/g [3,2]. There has been so much effort that has gone into developing high-performance materials, such as oxides, metal hydroxides, which simultaneously deliver high energy and power densities. RuO₂ is one such material with excellent capacitive performance, with a capacitance of more than 1450 F/g [3,6].The doping of transition metals is also used to enhance the electrochemical performance of materials. . Cai et al. used sulfidation treatment to synthesize a series of Ni_xCo_{1-x}S₂@N-doped carbon compounds of NiCo-ethylenediaminetetraacetic acid (EDTA) complex. The obtained material shows a specific capacitance of 1416.5 F/g at 1 A/g current density [9]. Abbas et al. prepared Cu-doped ZnS using a facile solvothermal method. They used glycerol as a cosolvent, which resulted in nanoflake arrays with an ultrathin and interconnected network. The copper-doped zinc sulfide reached a specific capacitance of 743 F/g at 1 A/g current density [8]. Aalim et al. synthesized Sn-doped hematite (alpha-Fe₂O₃) nanostructure using the hydrothermal method. The specific capacitance of 833 F/g at 10 mV/s 3M KOH electrolyte [1].Keeping the above discussions and current state of the art of cutting-edge research in the field of supercapacitorelectrode, we need to develop amaterial that has high specific capacitance, long life, high energy, and power density.

In this study,tin was used as a doping agent. Tin-doped copper oxide nanoparticles were synthesized by the solvo-combustion method and were proven to be a desirable supercapacitor electrode material. The named prepared sample is TCO120.The electrochemical behavior of the prepared sample is characterized by CV, GCD, and EIS techniques to study the behavior of tin-doped copper oxide for a supercapacitor electrode.

Experimental Section

2.1 Materials and Methods

In this work, all of the used chemical materials Tin Oxide, Copper acetate, ethanol, acetylacetone, HNO₃, and filter paper were purchased from ADL ENTERPRISES. All of the chemicals have been used without refinement.

2.2 Preparation of Tin-doped Copper Oxide

The tin-doped copper oxide was prepared by solvo – combustion route method. To prepare this, First 1gm tin oxide and 20gm copper acetate were added to 20ml solvent of ethanol and acetylacetone (1:1) with stirring. The mixture was stirred for 2hr at 70 °C. After this 10ml HNO₃ was added to the solution and stirred for 1hr at 180 °C. Final, the prepared solution was filtered with DI and dried at 90°C. Finally, the product was placed in a muffle furnace at 800°C for 2hr. this sample is labeled as TCO120.

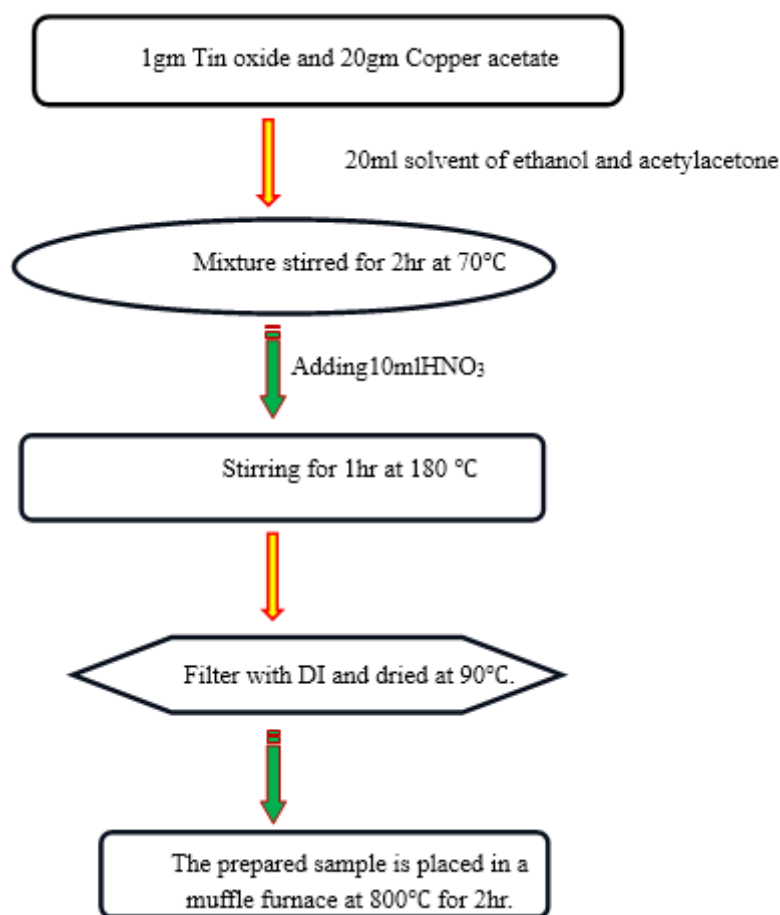


Fig.1 Schematic diagram of prepared TCO120 using Solvo-Combustion Route.

2.3 Electrode Fabrication

The electrode fabrication process was carried out using a graphite sheet, acetylene black (AB), PVDF, acetone, and prepared sample TCO120. In this process, acetone was used as a solvent, PVDF as a binder, AB used as a conductive material, and tin-doped copper oxide TCO120 used as an electrode material. First, tin-doped copper oxide: PVDF: AB was taken in a mass ratio of 80:10:10 and mixed using acetone. The resulting solution was sonicated for 1hr and stirred on a magnetic stirrer for 2hr to form a sultry slurry. The obtained slurry was pasted on a graphite sheet (1cm²).

Electrochemical characteristics of TCO120

3.1 Cyclic Voltammetry

The CV curves of symmetry show a rectangular shape without any obvious redox peaks which indicates the ideal type EDLC nature. The area under the CV curve for the sample electrodes increases and still remains rectangular in shape. The specific capacitance (C_p) of electrodes can be calculated by using the equation

$$C_p = \frac{\int I dV}{m \nu \Delta V}$$

Where

$\int I dV$ = area under the CV curve.

m = Mass of the material (gm)

ν = Scan rate (V/s)

ΔV = Potential window (V)

The capacitance C_p values of the TCO120 electrode are 91.5, 23.9, 15.5, 11.4, and 8.1 F/gat 0.01, 0.03, 0.05, 0.07, and 0.1 V/s scan rate.

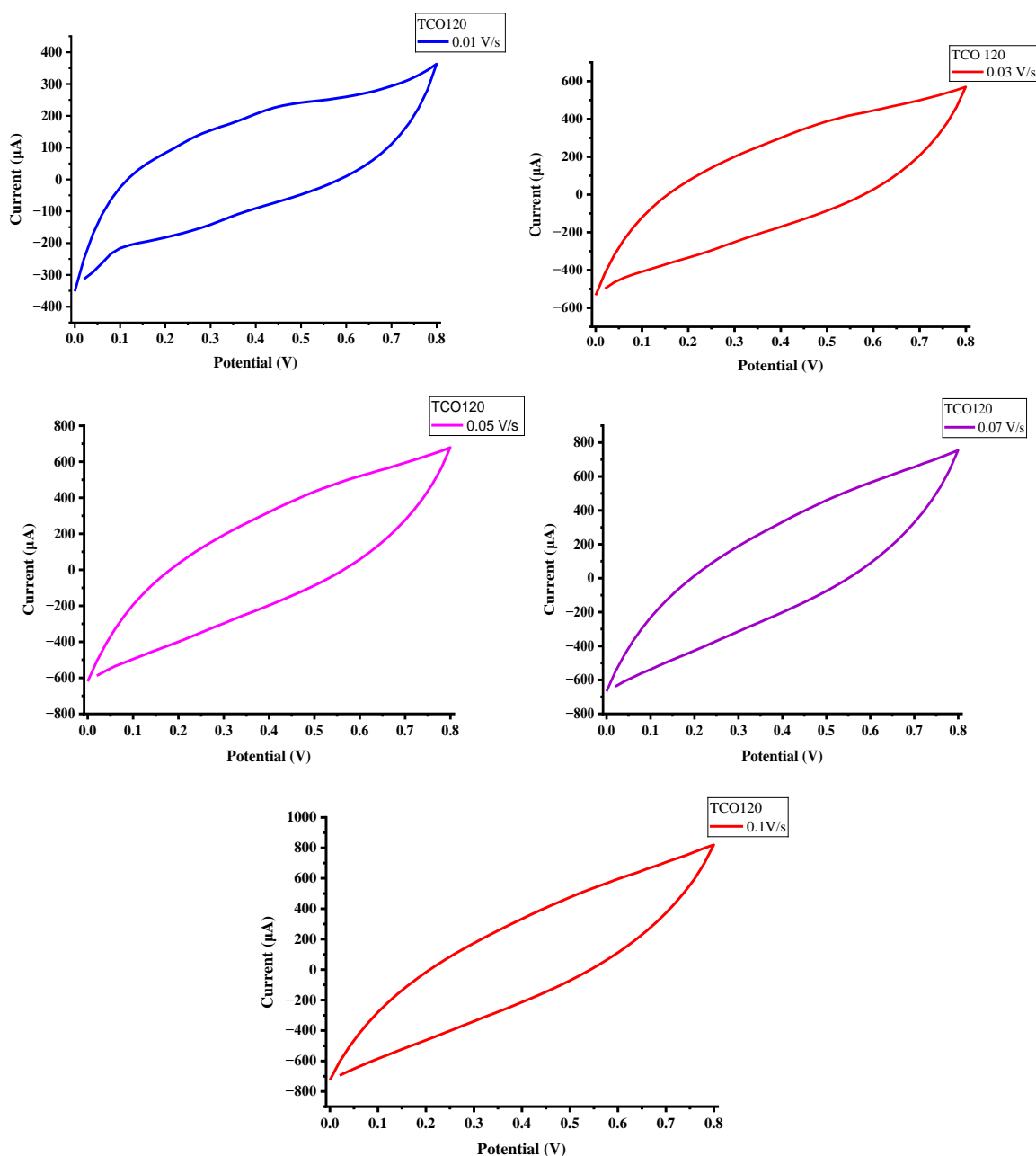


Fig. 2 Cyclic Voltammetry curves of TCO120 at a scan rate of 0.01, 0.03, 0.05, 0.07, and 0.1 V/s, respectively, in a potential window of 0.8 V.

3.2 Galvanostatic charge-discharge (GCD)

The GCD curve of the TCO120 electrode, respectively at the current density of 0.3, 0.5, 0.7, and 1 mA/g within the potential window 0V to 0.8V. The C_p of the TCO120 electrode can be calculated following equation

$$C_{p(GCD)} = \frac{i\Delta t}{m\Delta V}$$

Where i - Current density (A/g), t - discharging time (sec.), m - mass of the active material (gm), V - potential window (volts). The calculated $C_{p(GCD)}$ values are 32.3, 22.5, 14.12, and 8.1 F/gfor TCO120 at current densities of 0.3, 0.5, 0.7, and 1 mA/g, respectively.

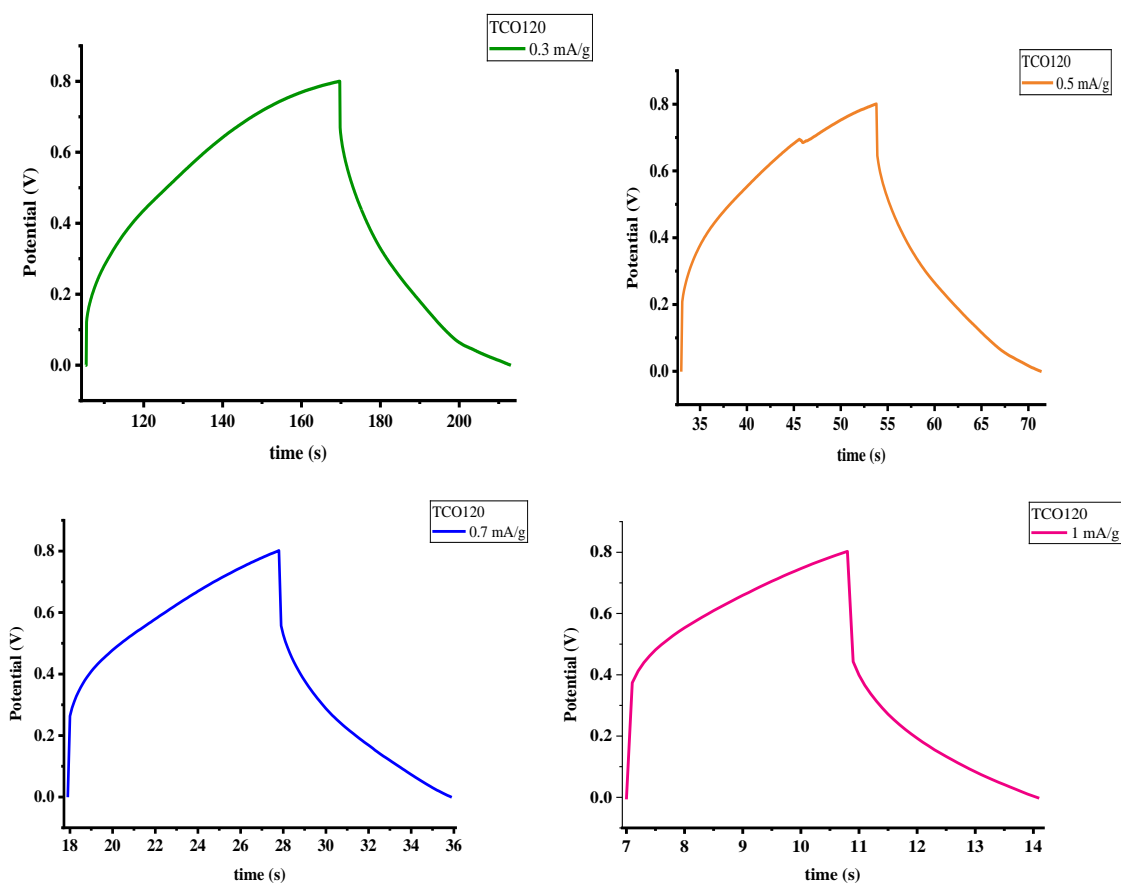


Fig. 3 GCD curves of TCO120 at a scan rate of 0.3, 0.5, 0.7, and 1 mA/g, respectively, in potential window 0 V to 0.8 V.

Conclusion

In this work, tin-doped copper oxide (TCO120) nanoparticles were synthesised using the solvo-combustion method. The electrochemical properties were analyzed by CV and GCD data. The prepared samples were used as supercapacitor electrodes with 0.1M H₂SO₄ electrolyte. The specific capacitance value has been calculated from CV and GCD data. The prepared electrodes exhibit a maximum specific capacitance of 91.5 with 0.1M H₂SO₄ electrolyte at a scan rate of 0.01 V/s.

REFERENCES

- [1]. Aalim, M., Altaf, U., Rashid, A., Ahmad, R., Sohail, A., Mir, A. and Shah, M.A., 2024. Tin (Sn)-doped hematite (α -Sn_xFe_{2-x}O₃) nanostructures as high-performance electrodes for supercapacitor application. *Journal of Solid State Electrochemistry*, 28(1), pp.1-18.
- [2]. B. Akkinapally, I. Neelakanta Reddy, C. Lee, T.J. Ko, P. Srinivasa Rao, J. Shim, Promising electrode material of Fe₃O₄ nanoparticles decorated on V₂O₅ nanobelts for high-performance symmetric supercapacitors, *Ceram. Int.* 49 (4) (2023) 6280–6288.
- [3]. Chelladurai, A., Veerasingham, M., Kesavan, T., Alotaibi, N.H., Sangaraju, S., Muthusamy, K.K., Sonaimuthu, M. and Sakkarapani, S., 2025. Facile synthesis of Bi₂WO₆-NiO nanocomposite for supercapacitor application. *Materials Science and Engineering: B*, 313, p.117939.

- [4]. Chernysheva, D.V., Smirnova, N.V. and Ananikov, V.P., 2024. Recent trends in supercapacitor research: Sustainability in energy and materials. *ChemSusChem*, 17(5), p.e202301367.
- [5]. Kannan, K., Chinnaiah, K., Gurushankar, K., Krishnamoorthi, R., Chen, Y.S., Murphin Kumar, P.S. and Li, Y.Y., 2024. Investigation of the electrochemical behavior of CuO-NiO-Co₃O₄ nanocomposites for enhanced supercapacitor applications. *Materials*, 17(16), p.3976.
- [6]. Liu, B., Liu, B., Wang, Q., Wang, X., Xiang, Q., Chen, D. and Shen, G., 2013. New energy storage option: toward ZnCo₂O₄ nanorods/nickel foam architectures for high-performance supercapacitors. *ACS applied materials & interfaces*, 5(20), pp.10011-10017.
- [7]. Liu, W., Zhang, Z., Zhang, Y., Zheng, Y., Liu, N., Su, J. and Gao, Y., 2021. Interior and exterior decoration of transition metal oxide through Cu⁰/Cu⁺ Co-doping strategy for high-performance supercapacitor. *Nano-micro letters*, 13, pp.1-14.
- [8]. N. Abbas et al., "Glycerol-mediated synthesis of copper-doped zinc sulfide with ultrathin nanoflakes for flexible energy electrode materials," *Journal of Alloys and Compounds*, vol. 919, p. 165701, Oct. 2022, doi: <https://doi.org/10.1016/j.jallcom.2022.165701>.
- [9]. Z. Cai, F. Zhang, D. Wei, B. Zhai, X. Wang, and Y. Song, "Ni_xCo_{1-x}S₂@N-doped carbon composites for supercapacitor electrodes," *Journal of Energy Storage*, vol. 72, pp. 108231–108231, Nov. 2023, doi: <https://doi.org/10.1016/j.est.2023.108231>.

An Investigation of Nanocrystalline Transition Metal Complexes using XANES, EXAFS, UV and IR spectroscopic technique: A review

Humera Khan¹, P.K. Malviya²

¹School of Studies in Physics, Ujjain, Madhya Pradesh, India

²Govt Madhav Science P.G College, Ujjain, Madhya Pradesh, India

ARTICLE INFO

Article History:

Published : 30 April 2025

Publication Issue :

Volume 12, Issue 13

March-April-2025

Page Number :

195-203

ABSTRACT

An element's valence state can be determined by looking at its X-ray absorption edge position. The damped periodic fine structure of the expanded region of the X-ray absorption edge is dependent on the amount of ligand atoms present, particularly their distance from one another. The superposition of the photoelectrons released during the absorption process and the incoming X-ray beam is the quantum mechanical action responsible for this extended X-ray absorption fine structure (EXAFS). Near-edge structure is defined as X-ray absorption; the upper limit is typically established arbitrarily at a voltage of about 50 eV above the absorption edge. This low photoelectron energy area has a long elastic mean free path and an electron scattering factor that is typically significant. Multiple scattering is therefore quite significant. Determining the chemical makeup of nanomaterial is made possible using X-ray-based spectroscopies. These methods involve X-ray absorption scattering (XAS), including energy-dispersive X-ray (EDX) spectroscopy, X-ray photoelectron spectroscopy (XPS), X-ray fluorescence (XRF) spectroscopy, and X-ray absorption near-edge structure (XANES) in addition to others.

Keywords: XAS, XPS, EXAFS, XANES etc.

INTRODUCTION

X-ray absorption fine structure (XAFS) spectroscopy refers to the details of how X-rays are absorbed by an atom at energies near and above the core-level binding energies of that particular atom. At certain energy, the absorption increases drastically and gives rise to an absorption edge. Although most of the absorption spectrum is quite smooth, oscillatory features called X-ray absorption fine structure (XAFS) is found directly above an edge. Traditionally, this fine structure is split into two energy regions. The first, termed as X-ray absorption near edge structure (XANES), occurs in the region from the edge to approximately 40 eV above the edge, while the

second, termed as the extended X-ray absorption fine structure (EXAFS), extends from 40 eV to 1000 eV above the edge. XANES is strongly sensitive to formal oxidation state and coordination chemistry of the absorbing atom, while the EXAFS is used to determine the distances, coordination number, and species of the neighbors of the absorbing atom.

The significant advantage of X-ray absorption spectroscopy over the X-ray crystallography is that the local structural information around the element of interest can be obtained easily and quickly even from disordered samples, such as powders and solutions. To be specific, single crystals of samples are not required in XAS spectroscopy as are necessary in the case of X-ray crystallography. This versatility allows it to be used in a wide variety of disciplines: physics, chemistry, biology, biophysics, medicine, engineering, environmental science, materials science, and geology [1].

UV-Vis spectroscopy is an analytical technique that measures the amount of discrete wavelengths of UV or visible light that are absorbed by or transmitted through a sample in comparison to a reference or blank sample. This property is influenced by the sample composition, potentially providing information on what is in the sample and at what concentration. Since this spectroscopy technique relies on the use of light, let's first consider the properties of light. Light has a certain amount of energy which is inversely proportional to its wavelength. Thus, shorter wavelengths of light carry more energy and longer wavelengths carry less energy. A specific amount of energy is needed to promote electrons in a substance to a higher energy state which we can detect as absorption. Electrons in different bonding environments in a substance require a different specific amount of energy to promote the electrons to a higher energy state. This is why the absorption of light occurs for different wavelengths in different substances. Humans are able to see a spectrum of visible light, from approximately 380 nm, which we see as violet, to 780 nm, which we see as red. UV light has wavelengths shorter than that of visible light to approximately 100 nm. Therefore, light can be described by its wavelength, which can be useful in UV-Vis spectroscopy to analyze or identify different substances by locating the specific wavelengths corresponding to maximum absorbance (see the Applications of UV-Vis spectroscopy section) [2].

The rays, which were below the red rays "non colorific rays" or invisible rays, which were called later "infrared rays" or IR light. This light is not visible to human eye. A typical human eye will respond to wavelengths from 390 to 750 nm. The IR spectrum starts at 0.75 μm . The Infrared spectrum is divided into, Near Infrared (NIRS), Mid Infrared (MIRS) and Far Infrared (FIRS). The first region (NIRS) allows the study of overtones and harmonic or combination vibrations. The MIRS region is to study the fundamental vibrations and the rotation-vibration structure of small molecules, whereas the FIRS region is for the low heavy atom vibrations (metal-ligand or the lattice vibrations). Infrared (IR) light is electromagnetic (EM) radiation with a wavelength longer than that of visible light: $\leq 0.7 \mu\text{m}$. One micrometer (μm) is 10^{-6}m . Experiments continued with the use of these infrared rays in spectroscopy called, Infrared Spectroscopy. IR Spectroscopy expanded rapidly in the study of materials and for the chemical characterization of materials that are in our planet as well as beyond the planets and the stars. The studies showed that IR spectroscopy could also be used to study biological molecules, such as proteins, DNA and membranes and could be used in biosciences, in general. Infrared spectroscopy can provide information on isolated materials, biomaterials, such as biopolymers as well as biological materials, connective tissues, single cells and in general biological fluids to give only a few examples. Such varied information may be obtained in a single experiment from very small samples. Clearly then infrared spectroscopy is providing information on the energy levels of the molecules in wave numbers (cm^{-1}) in the region of electromagnetic spectrum by studying the vibrations of the molecules, which are also given in wavelengths (μm) [3].

Discussion

T. Bartoli and co-workers have synthesized Nano crystalline $\text{PrCo}_{3-x}\text{Fe}_x$ ($x < 1$) powder samples by high energy milling and subsequent annealing at 1023K for 30min. Consequently, they give in this study the characterization of the local structure by X-ray absorption spectroscopy (EXAFS) at the iron K edge. By this method, and if they assume a unique preferential site, it was determined that Fe atoms preferably occupy the site. In order to obtain this result, a coordination sphere around Fe sites of $R = 5.2 \text{ \AA}$ had to be considered in order to find sufficient local differences between the possible sites. Furthermore, they provide complementary magnetic properties measurements for $(\text{PrCo}_{3-x}\text{Fe}_x)$ such as the coercive field, which decreases with iron content from 12kOe for PrCo_3 to 1.5kOe for $\text{PrCo}_{2.25}\text{Fe}_{0.75}$ [4].

E. Voronina and co-workers have been studied the EXAFS (Fe, Sn and Ge K-edges) of disordered by mechanical activation binary super saturated nano crystalline solid solutions Fe–Al, Fe–Ge, Fe–Sn and Fe–Si is presented. The EXAFS-spectra are processed by solving the inverse binary problem, using the EXAFS-spectrum of the Fe K-edge only or combining the EXAFS-spectra on two K-edges, Fe and Ge or Fe and Sn. The parameters of partial correlation functions indicate chemical short-range ordering, high local static distortions in the lattice, increasing with metalloid content. The macrostructure of other type is forming through an initial, “local” stage within the bcc lattice [5].

Seong-Ju Hwang and Jin-Ho Choy have been reported the local crystal structure and electronic configuration of transition metal in X-ray amorphous MnO_2 and CrO_2 nanocrystals by using X-ray absorption (XAS) spectroscopy at Mn K and Cr K-edges. The Mn K-edge XAS study reveals that tetravalent manganese ions are stabilized in $\alpha\text{-MnO}_2$ -type local atomic arrangement consisting of the intergrowth of edge- and corner-shared MnO_6 octahedra. On the other hand, it is found from Cr K-edge XAS results that nanocrystalline CrO_2 possesses two different kinds of local structures around chromium, that is, Cr_2O_3 -type with octahedral site and CrO_3 -type with tetrahedral site. This work can be regarded as a strong evidence for the usefulness of XAS to study nanocrystalline electrode materials [6].

Nazish Qadeer and co-workers have been studied the synthesize new cerium oxide-based nano- additives to minimise emissions from spark ignition (SI) engines fueled with gasoline blends, such as carbon monoxide (CO), unburned hydrocarbons (HC) and oxides of nitrogen (NO_x). To investigate the effect of transition metal dopant on their respective catalytic oxidation activity, nano-sized CeO_2 catalysts co-doped with Mn, Fe, Cu and Ag ions were successfully produced by a simple hydrothermal technique. The addition of transition metal ions to the CeO_2 lattice increased the concentration of structural defects like oxygen vacancies and Ce^{3+} ions, which are advantageous for the catalytic oxidation reaction, as also supported by XAFS and RAMAN analysis. The results demonstrated that harmful exhaust pollutants such as CO, HC and NO_x were significantly reduced. The high surface area, better redox characteristics and presence of additional oxygen vacancy sites or Ce^{3+} ions have been linked to the improved catalytic performance of the synthesized catalyst [7].

Justus Just and co-workers have been studied the copper chalcogenide nanocrystals. They reveal insights in the nucleation and growth during synthesis of anisotropic $\text{Cu}_2\text{ZnSnS}_4$ nanocrystals by simultaneously performing in situ X-ray absorption spectroscopy (XAS). Real-time XAFS reveals that upon thiol injection into the reaction flask, a key copper thiolate intermediate species is formed within fractions of seconds, which decomposes further within a narrow temperature and time window to form copper sulfide nanocrystals. These nanocrystals convert into $\text{Cu}_2\text{ZnSnS}_4$ nanorods by sequentially incorporating Sn and Zn. Their work demonstrates how combined in situ X-ray absorption and small-angle X-ray scattering enables the understanding of mechanistic pathways in colloidal nanocrystal formation [8].

A. Anspoks and co-workers have been studied nanocrystalline NiO samples using the Ni K-edge extended x-ray absorption fine structure (EXAFS) spectroscopy and recently developed modeling technique, combining classical molecular dynamics with ab initio multiple-scattering EXAFS calculations (MD-EXAFS). Conventional analysis of the EXAFS signals from the first two coordination shells of nickel revealed that (i) the second shell averaged distance $R(\text{Ni-Ni}_2)$ expands in nanocrystalline NiO compared to microcrystalline NiO, in agreement with overall unit cell volume expansion observed by x-ray diffraction; (ii) on the contrary, the first shell averaged distance $R(\text{Ni-O}_1)$ in nanocrystalline NiO shrinks compared to microcrystalline NiO; (iii) the thermal contribution into the mean-square relative displacement σ^2 is close in both microcrystalline and nanocrystalline NiO and can be described by the Debye model; (iv) the static disorder is additionally present in nanocrystalline NiO in both the first Ni-O₁ and second Ni-Ni₂ shells due to nanocrystal structure relaxation [9].

Alevtina Smekhova and co-workers have been studied the multi-edge X-ray absorption spectroscopy (extended X-ray absorption fine structure (EXAFS), X-ray absorption near edge structure (XANES), and X-ray magnetic circular dichroism (XMCD)) to probe the structural, electronic, and magnetic properties of all individual constituents in the single-phase face-centered cubic (fcc)-structured nanocrystalline thin film of Cr₂₀Mn₂₆Fe₁₈Co₁₉Ni₁₇ high-entropy alloy on the local scale. A homogeneous short-range fcc atomic environment around the absorbers of each type with very similar statistically averaged interatomic distances (2.54–2.55 Å) to their nearest-neighbors and enlarged structural relaxations of Cr atoms were revealed. XANES and XMCD spectra collected at the L_{2,3} absorption edges of all principal components at low temperature from the oxidized and in situ cleaned surfaces were used to probe the oxidation states, the changes in the electronic structure and magnetic behavior of all constituents at the surface and in the sub-surface volume of the film. The spin and orbital magnetic moments of Fe, Co, and Ni components were quantitatively evaluated [10].

Y.V. Zubavichus and co-workers have been studied the MoS₂ intercalated with Mn, Co, Ni, and Ru species, prepared from single layer MoS₂ dispersions in water by x-ray absorption spectroscopy. M. K-edge EXAFS results (M = Mn, Co, Ni) are consistent with an alternating MoS₂-M(OH)₂ layered structure. For the Mn and Co intercalates the MoS₂ layers were found to be very similar to that of the parent crystalline MoS₂ with trigonal prismatic coordination of the Mo atoms. For the Ni and Ru intercalates, Mo K edge EXAFS revealed structural rearrangement of MoS₂ layers similar to that observed for MoS₂ single layers, with octahedral coordination of Mo. S K edge XANES spectra reveal that the rearrangement is coupled with a change in the electronic structure of the S atoms in the matrix. These changes can be associated with charge transfer between 'host' and 'guest' layers. In addition, SO₄²⁻ and Mo⁶⁺ were detected in some of the intercalated materials, presumably due to exposure to air, suggesting that transition metal intercalation may increase the susceptibility of the MoS₂ layers to oxidation [11].

A. Anspoks and A. Kuzmin have been analyzed atomic structure at the nanoscale is a challenging task, complicated by relaxation phenomena and thermal disorder. In this work, the x-ray absorption spectroscopy at the Ni K-edge was used to address this problem in nanocrystalline NiO (nano-NiO). The expansion of the average lattice but contraction of the Ni-O bonds in the first coordination shell were determined in nano-NiO at 300 K in comparison with bulk material. Accurate EXAFS analysis, based on a combination of classical molecular dynamics and ab initio multiple-scattering EXAFS theory, allowed us to interpret full EXAFS spectrum. In particular, the effect of magnetostriction effect was elucidated in bulk NiO, and the effect of the thermal disorder in outer coordination shells was studied in both bulk and nano-NiO [12].

Seong Ju Hwang and Jin-Ho Choy have been studied the local crystal structure and electronic configuration of transition metal in X-ray amorphous MnO₂ and CrO₂ nanocrystals by using X-

ray absorption (XAS) spectroscopy at Mn K and Cr K-edges. The Mn K-edge XAS study reveals that tetravalent manganese ions are stabilized in α -MnO₂-type local atomic arrangement consisting of the intergrowth of edge- and corner-shared MnO₆ octahedra. On the other hand, it is found from Cr K-edge XAS results that nanocrystalline CrO₂ possesses two different kinds of local structures around chromium, that is, Cr₂O₃-type with octahedral site and CrO₃-type with tetrahedral site. This work can be regarded as a strong evidence for the usefulness of XAS to study nanocrystalline electrode materials [13].

J. Daniel Bryan and co-workers have been reported the colloidal cobalt-doped TiO₂ (anatase) nanocrystals. These nanocrystals were synthesized and studied by electronic absorption, magnetic circular dichroism, transmission electron microscopy, magnetic susceptibility, cobalt K-shell X-ray absorption spectroscopy, and extended X-ray absorption fine structure measurements. The nanocrystals were paramagnetic when isolated by surface-passivating ligands, weakly ferromagnetic ($M_s \approx 1.5 \times 10^{-3} \mu_B/\text{Co}^{2+}$ at 300 K) when aggregated, and strongly ferromagnetic (up to $M_s = 1.9 \mu_B/\text{Co}^{2+}$ at 300 K) when spin-coated into nanocrystalline films. X-ray absorption data reveal that cobalt is in the Co²⁺ oxidation state in all samples. In addition to providing strong experimental support for the existence of intrinsic ferromagnetism in cobalt-doped TiO₂, these results demonstrate the possibility of using colloidal TiO₂ diluted magnetic semiconductor nanocrystals as building blocks for assembly of ferromagnetic semiconductor nanostructures with potential spintronics applications [14].

N. Sivakumar and co-workers have been studied the nanocrystalline cobalt ferrite particles of 8 nm grain size. They were synthesized by co-precipitation technique and subsequently suitably heat treated to obtain higher grain sizes. The experimentally observed changes in the dc electrical conductivity and Curie temperature with heat treatment have been attributed to the changes in the cation distributions as obtained from the Mossbauer and extended x-ray absorption fine structure (EXAFS) measurements and to the grain size. The activation energies for conduction as determined from the Arrhenius plots suggest that the conductivity is due to hopping of both electrons and holes. The observed decrease in conductivity when the grain size is increased from 8 to 92 nm is clearly due to the predominant effect of migration of some of the Fe³⁺ ions from octahedral to tetrahedral sites, as is evident from in-field Mossbauer and EXAFS measurements. [15].

Matthias Niedermaier and co-workers have been reported the identification and manipulation of transition-metal ion impurities in oxide nanoparticles require an in-depth understanding of their stability, segregation behavior and at the same time, knowledge about their surface reactivity. The very different behavior of Co and Fe ions in the MgO host lattice, their changes in the local environment, and the different trends in segregation have been investigated by means of X-ray absorption and photoelectron spectroscopies and structure characterization techniques. Abundance and energetics of the defects and defect complexes were determined within the framework of the density functional theory and enabled us to explain consistently the reported experimental observations. Oxidation state and nature of the defect cluster have a significant impact on particle size and annealing-induced morphology evolution, which determine their material properties as components in heterogeneous catalysis and functional ceramics [16].

G. M. Chow and co-workers have been studied the nanocrystalline Co_xCu_{100-x} powders. The structure of powders was characterized by x-ray diffraction (XRD), extended x-ray absorption fine structure (EXAFS) spectroscopy. As-synthesized powders were composites consisting of nanoscale crystallites of face-centered cubic (fcc) Cu and metastable face-centered cubic (fcc) Co. Complementary results confirmed that there was no metastable alloying between Co and Cu. The results suggested that during preparation the nucleation of Cu occurred first, and the Cu crystallites served as nuclei for the formation of Co [17].

In this work, Yu Chen and co-workers have been studied the five nanocrystalline first transition- metal (Ti, Mn, Co, Ni and Zn) oxide nanofibers. The results reveal that the obtained nanofibers have a continuously twisted three-dimensional scaffold structure and are composed of neat nanocrystals with a necklace-like arrangement. All the samples possess high specific surface areas, which follow the order of NiO nanofiber (393.645 m²/g) > TiO₂ nanofiber (121.445 m²/g) > ZnO nanofiber (57.219 m²/g) > Co₃O₄ nanofiber (52.717 m²/g) > Mn₂O₃ nanofiber (18.600 m²/g). Moreover, the photocatalytic degradation of methylene blue (MB) in aqueous solution was investigated in detail by employing the five kinds of metal oxide nanofibers as photocatalysts under ultraviolet (UV) irradiation separately. The results show that ZnO, TiO₂ and NiO nanofibers exhibit excellent photocatalytic efficiency and high cycling ability to MB, which may be ascribed to unique porous structures and the highly efficient separation of photogenerated electron-hole pairs. In brief, this paper aims to provide a feasible approach to achieve five first transition- metal oxide nanofibers with excellent performance, which is important for practical applications [18].

Fahad Ahmed Alharthi and co-workers have been reported the discharge of pharma products such as paracetamol (PCT) into water has resulted in great harm to humans and emerged as a potential threat requiring a solution. Various spectroscopic techniques, such as XRD, FTIR, UV TEM, SEM-EDX and XPS were utilised to determine the lattice, structural, optical, and morphological information of the solid nanomaterial upon heterojunction formation. The results obtained suggested that the heterojunction nanocomposite NiWO₄/CoWO₄ exhibited enhanced photocatalytic efficiency (97.42%) with PCT as compared to its precursors - 96.50% for NiWO₄ and 97.12% for CoWO₄. It was observed that NiWO₄/CoWO₄NC with enhanced optical properties affected a higher rate of PCT degradation due to the improved band gap energy upon heterojunction formation. The material was found to be highly stable and reusable for the degradation of PCT at optimized reaction conditions [19].

K. S. Siddhapa and D. V. Shah have been studied the transition metal (Mn, Fe, Co,) doped TiO₂ nanoparticles. All the prepared samples were calcined at different temperatures like 200°C to 800°C and characterized by XRD and EDX. The studies revealed that transition metal (TM) doped nanoparticles have smaller crystalline size and higher surface area than pure TiO₂. Dopant ions in the TiO₂ structure caused significant absorption shift into the visible region. The results of photo degradation of formaldehyde in aqueous medium under UV light showed that photocatalytic activity of TiO₂ nanoparticles was significantly enhanced by the presence of some transition metal ions. Chemical oxygen demand (COD) of formaldehyde solutions done at regular intervals gave a good idea about mineralization of formaldehyde [20].

L. Kernazhitskya and co-workers have been reported the effect of nanocrystalline TiO₂ doping with transition metal cations (Cu⁺², Fe⁺³, Co⁺², Cr⁺³) on their optical absorption and photocatalytic properties. The obtained metal-doped TiO₂ samples were characterized by X-ray diffraction, scanning electron microscopy, and UV-vis absorption spectroscopy. It is shown that doping effect on anatase (A) and rutile (R) properties is quite different, being much stronger and complicated on A than on R. Contrary to doped R, doped A revealed a significant red shift of the absorption edge along with the band gap narrowing. Photocatalytic activity of anatase increases upon doping in the order: A₀A/Co > A₀A/Cu > A₀A/Fe. On the contrary, photocatalytic activity of rutile samples decreases upon doping in the series R₄R/Co > R₄R/Cu > R₄R/Fe > R₄R/Cr, indicating the inhibitory effect of impurity cations. This fact correlates with the decrease in the UV absorption of the doped rutile in the region of the Hg-lamp irradiation at 4.88 eV [21].

The requirement for materials which exhibit good second and third order non-linear optical properties and also for materials which could sense metals in trace quantities has kindled renewed investigations. Organometallics

and coordination compounds show a lot of promise as new NLO materials combining the variety of organic moieties with the strength and variable oxidation states of metals. Especially ligands which selectively detect industrial pollutants like Cd and biologically significant metals like Zn are necessary. In the current work the ligand 1,10-phenanthroline-2,9-di(carboxaldehyde phenylhydrazone) (L) and its Ni²⁺, Co²⁺, Fe²⁺, Zn²⁺, Cd²⁺ and Ir³⁺ complexes were synthesized. These were characterized by UV-Vis, FT-IR, ¹H NMR, MS and CHN microanalysis techniques. The complexes were shown to have the formula [ML]₂⁺. The second and third order NLO of the ligand and its complexes were recorded. These new compounds were found to have same order of third order nonlinear optical susceptibility as that of CS₂ and their second hyperpolarizability was an order of magnitude greater than that of C₆₀. Furthermore the ligand also displays selective luminescence sensing of metals ions Fe²⁺ and Ir³⁺ even in the presence of other metal ions [22].

K.H. Praveen and co-workers have been studied the nanocrystalline copper (II) oxide. This oxide was synthesized through hesperidin mediated phytochemical reduction method and post annealed at 600°C for 4 hrs. Various analytical results obtained after characteristic measurements such as XRD, FESEM, UV-visible spectroscopy and Photoluminescence studies have been discussed. Tauc' plot of UV-visible spectrum employing Kubelka-Munk function provided a direct optical band gap of 1.61 eV. The photoluminescence spectrum using 280 nm optimal excitation wavelength and the related CIE plot revealed that the optical emission occurs at blue region as indicated by the chromaticity coordinates [23].

Peter A and co-workers have been reported the synthesis and structural studies of copper sulfide nanocrystals from copper (II) dithiocarbamate single molecule precursors. The optical properties of the nanocrystals studied using UV-visible and photoluminescence spectroscopy showed absorption band edges at 287 nm that are blue shifted and the photoluminescence spectra show emission curves that are red-shifted with respect to the absorption band edges. These shifts are as a result of the small crystallite sizes of the nanoparticles leading to quantum size effects [24].

James T. Brewster and co-workers have been studied the reaction between dipyrromethin and copper(II) acetate [Cu(OAc)₂] afforded what is, to our knowledge, the first transition metal- dipyrromethin complex. Molecular and electronic characterization of this binuclear Cu(II) complex via EPR, UV-vis, and single crystal X-ray diffraction analysis revealed marked differences between the present constructs and previously reported binuclear copper(II) hexaphyrin species. UV-vis titration analyses provided evidence for a homotropic positive allosteric effect, wherein the binuclear species is formed without significant intermediacy of a monomeric complex [25].

Paritosh K. Rana and co-workers have been studied these semicarbazone derivatives of 2,4-dihydroxyacetophenone is synthesized and characterized by physico-chemical techniques such as melting point, Ultra Violet-Visible Spectrophotometer, Fourier Transform Infra-Red (FTIR), proton nuclear magnetic resonance (¹H NMR) spectroscopy and used as a chelating agent to form complex with Copper as Copper (II) semicarbazone derivative. The synthesized Copper (II) semicarbazone complex was also studied for its complex formation IR analysis, decomposition studies using TGA. The synthesized Copper (II) semicarbazone complex was successfully employed as precursor for synthesis of nano crystalline Copper oxide and its formation was confirmed by UV-Visible spectroscopy and XRD analysis. The method successfully employed use of Copper (II) semicarbazone complex for synthesis of nano Copper oxide [26].

Conclusion

The above review analysis reveals the application and importance of different techniques of measurements of different parameters of given complexes. Each technique plays an important role in their respective field. When

one technique is unable to do any analysis, then by using another technique in its place, we can get the necessary information as well as we can compare the parameters of the samples obtained by different techniques. We can also prove overmeasured parameters of the samples by different techniques and methods. With the help of EXAFS and XANES studies of any complexes or compounds, we can easily analyze the changing effect of the ligand in a given complexes, like change in bond length, change in geometrical structure around the nuclear atom and other information we can collect like effect on chemical shift, effective nuclear charge, magnetic properties measurements (such as the coercive field) and coordination number etc. in solid, liquid or any form of complexes. UV spectroscopy is a other unique tool for analysis of other parameters of a sample like DNA and RNA analysis, Pharmaceutical analysis, Bacterial culture etc. This technique may also be used in industrial work like measuring a color index, in medical science to determine hemoglobin concentrations, in wastewater treatments. It also finds great utility in food authenticity analysis and air quality monitoring. Infrared spectroscopy is used in chemistry and industry for identification and characterization of molecules. Infrared spectroscopy is a nondestructive method and it is useful to study the secondary structure of more complicated systems such as biological molecules proteins, DNA and membranes. In medical science it is used to characterize healthy and non- healthy human tissues. Samples in solution can also be measured accurately. IR spectroscopy has been highly successful in measuring the degree of polymerization in polymer manufacture.

REFERENCES

- [1]. BDS Shrivastava, 2012, J. Phys.: Conf. Ser., vol. 365.
- [2]. Justin Tom, 2021, UV-Vis Spectroscopy: Principle, Strengths and Limitations and Applications, Technology networks analysis and separations.
- [3]. Theophile (Theo) Theophanides, 2012, Infrared Spectroscopy - Materials Science, Engineering and Technology, Chapter -1 Introduction to Infrared Spectroscopy.
- [4]. T. Bartoli, K. Zehani, J. Moscovici, A. Michalowicz and L. Bessais, 2019, Journal of Magnetism and Magnetic Materials, vol. 473, pp. 253-261.
- [5]. E. Voronina, T. Miyanaga, A. Deyev, V. Kriventsov, G. Konygin and E. Yelsukov, 2007, Nuclear Instruments and Methods in Physics Research Section A: Accelerators, Spectrometers, Detectors and Associated Equipment, vol. 575, Issues 1-2, pp. 189-192.
- [6]. Seong-Ju Hwang and Jin-Ho Choy, 2003, J. Phys. Chem. B, vol. 107(24), pp. 5791-5796.
- [7]. Nazish Qadeer, Naila Jabeen, Latif U. Khan, Manzar Sohail, Muhammad Zaheer, Muhammad Vaqas, Afia Kanwal, Fatima Sajid, Samina Qamar and Zareen Akhter, 2022, RSC Adv., vol. 12, pp. 15564-15574.
- [8]. Justus Just, Claudia Coughlan, Shalini Singh, Huan Ren, Oliver Müller, Pascal Becker, Thomas Unold and Kevin M. Ryan, 2021, ACS Nano., vol. 15(4), pp. 6439-6447.
- [9]. A. Anspoks, A. Kalinko, R. Kalendarev and A. Kuzmin, 2012, Physical Review B, vol. 86.
- [10]. Alevtina Smekhova, Alexei Kuzmin, Konrad Siemensmeyer, Chen Luo, James Taylor, Sangeeta Thakur, Florin Radu, Eugen Weschke, Ana Guilherme Buzanich, Bin Xiao, Alan Savan, Kirill V. Yusenko, Alfred Ludwig, 2023, Nano Research, vol. 16(4), pp. 5626-5639.
- [11]. Y.V. Zubavichus, A.S. Golub, Y.N. Novikov, Y.L. Slovokhotov, A.N. Nesmeyanov, P.J. Schilling and R.C. Tittsworth, 1997, J. Phys. IV France 7, pp. 1057-1059.
- [12]. A. Anspoks, A. Kuzmin, 2011, Journal of Non-Crystalline Solids, vol. 357, pp. 2604-2610.
- [13]. Seong Ju Hwang and Jin-Ho Choy, 2003, J. Phys. Chem. B, vol. 107 (24), pp. 5791-5796.

- [14]. J.DanielBryan, SteveM.Heald,Scott A.ChambersandDaniel R.Gamelin,2004,J. Am. Chem.Soc., vol.126 (37), pp.11640–11647.
- [15]. N. Sivakumar, A. Narayanasamy, K. Shinoda, C. N. Chinnasamy, B. Jeyadevan, J.M. Greneche,2007, Journal of Applied Physics, vol.102, 013916.
- [16]. Matthias Niedermaier, Thomas Schwab, Paolo Dolcet, Johannes Bernardi, Silvia Gross, MichelBockstedte and Oliver Diwald, 2019, J. Phys. Chem. C, vol.123 (42), pp. 25991– 26004.
- [17]. G. M. Chow, L. K. Kurihara, K. M. Kemner, P. E. Schoen, W. T. Elam, A. Ervin, S. Keller,Y.D.Zhang,J.Budnick&T.Ambrose,1995,JournalofMaterialsResearch,vol. 10, pp. 1546–1554.
- [18]. Yu Chen, Weipeng Lu,Yanchuan Guo,Yi Zhu, Haojun Lu and Yeping Song, 2019,Appl.Sci.,vol. 9(1), pp.8.
- [19]. FahadAhmedAlharthi, AlanoudAbdullahAlshayiqi,WedyanSaudAl-Nafaei,Adel ElMarghany, Hamdah Saleh Alanazi and Imran Hasan, 2023, Catalysts, vol.13(1), pp. 152.
- [20]. K. S. Siddhapara and D. V. Shah, 2014, Advances in Materials Science and Engineering, ArticleID 462198, 4 pages.
- [21]. L.Kernazhitskya,V.Shymanovskaa,T.Gavrilkoo,V.Naumova,V.Kshnyakinb,T. Khalyavkaca,2013,Journalof solidstatechemistry,vol.198,pp. 511-519.
- [22]. G.KrishnaPrasad,S.S.P.Prashanth,S.Srivastava,G.NageswaraRaoandD.Rajesh Babu, 2017,Open Chemistry, vol. 15, no. 1, pp. 283-292.
- [23]. K.H.PraveenandArunS.Prasad,2021,Materialstoday:proceeding,vol41,Part3,pp. 520-524.
- [24]. PeterA.AjibadeandNandiphaL.Botha,2017,Nanomaterials,vol.7(2),pp.32.
- [25]. James T. Brewster, Harrison D. Root,Hadiqa Zafar, Gregory D. Thiabaud, Adam C. Sedgwick,JiamingHe,VincentM.LynchandJonathanL.Sessler,2020,Molecules,vol. 25(6), pp. 1446.
- [26]. Paritosh K. Rana, Suhas P. Janwadkar and Dilip K. Yadav, 2021, Asian Journal ofresearch inchemistry, vol. 14(4).

Sustainable Utilization of Seafood Discards and By-products for the Production of Nutraceuticals and Pharmaceuticals

A. Mathivanan^{1*}, A.U. Pagarkar², S. Dhariniswara¹, S.B. Satam², K.M. Shinde², A.N. Sawant², Urviben M Patel¹, R.B. Hajare¹

¹College of Fisheries, Shirgaon, (Dr.B.S.K.K.V. Dapoli), Ratnagiri, Maharashtra, India

²Marine Biological Research Station, (Dr.B.S.K.K.V. Dapoli), Ratnagiri, Maharashtra, India

ARTICLE INFO

Article History:

Published : 30 April 2025

Publication Issue :

Volume 12, Issue 13

March-April-2025

Page Number :

204-215

ABSTRACT

Global seafood consumption has increased because of growing awareness of its health benefits. Marine organisms live in different environments and have special bioactive compounds that make them unique compared to land-based organisms. These bioactive compounds help to improve health, lower the risk of diseases, reduce healthcare costs and exhibit wide range of biological activities. Processing seafood creates a lot of waste including fish scales, shells, bones, heads, skin, liver, fins, internal organs, etc. Commercial fishing operations discard million tonnes of whole fish every year and creating more environmental pollution. These wastes were traditionally converted into low value products (fish meal, fertiliser, biofuel, etc.) and also it was thrown directly in land. Instead of converting valuable discards and by-products into low value products, utilize them for producing high value nutraceuticals and pharmaceuticals. This review presents various high value compounds derived from seafood discards and by-products including protein hydrolysates, enzymes, bioactive peptides, collagen, gelatin, squalene, fish oil, chitin, chitosan, glucosamine, bone powder, cuttlebone powder, hydroxyapatite, hyaluronic acid, etc. and outlines their practical applications in different fields is discussed in the paper.

Keywords: seafood discards, seafood by-products, bioactive compounds, nutraceuticals, pharmaceuticals

INTRODUCTION

People around the world are eating more seafood nowadays because they have learned more about its health benefits. Marine organisms inhabit diverse environments and possess unique bioactive compounds that distinguish them from terrestrial organisms. In the last 20 years, scientists have discovered thousands of new natural products from the sea, leading to increased research, development, and sales of functional food

ingredients, health supplements, and nutraceuticals. These products help improve health, lower the risk of diseases, and reduce healthcare costs. Fish has traditionally been known as the "protein for the poor" and is considered a key solution to protein malnutrition in developing countries.

Seafood includes both finfish and shellfish from marine, estuarine, brackish, and freshwater environments and makes up a significant part of global food production. Major finfish species include anchovies, mackerel, tuna, herring, cod, whiting, etc. and shellfish are divided into two main groups: crustaceans and molluscs. Crustaceans encompass a variety of species including shrimp, lobster, crayfish, crab and krill. Molluscs consist of bivalves (such as mussels, oysters, clams and scallops), cephalopods (like squid, cuttlefish and octopus) and gastropods (such as abalone, sea snails and whelks).

According to the FAO (2024) State of World Fisheries and Aquaculture report, the global seafood supply in 2022 was 185.4 million metric tons (MMT), corresponding to an average annual per capita consumption of 20.7 kilograms. However, a significant portion of the total catch is discarded annually as by-catch or processing waste, including trimmings, fins, frames, heads, skins, viscera and other parts (Caruso et al. 2020). In 2022, 89% of the total aquatic animal production was directly consumed by humans and the remaining portion was utilized for non-food purposes, mainly for the production of fishmeal and fish oil (FAO, 2024).

The fishing industry prioritized catching high-value species like shrimp for export to earn foreign exchange. As a result, low-value fish caught along with shrimp were often discarded, as they were seen as taking up unnecessary storage space on fishing vessels. Traditionally, fish waste has been turned into low-value products like fish meal, fertilizer and biofuel. In many countries, a large amount of this waste is either thrown into landfills or used in small quantities for making animal feed and leather. Poor disposal of fishery waste creates serious environmental problems.

Despite being discarded, it should be used for a variety of purposes because by-catch and seafood waste contain valuable nutrients such as peptides, essential amino acids, long-chain omega-3 polyunsaturated fatty acids (PUFA), carotenoids, vitamins (A, B3, B6, B12 and D) and important minerals like calcium, copper, zinc, sodium, potassium, selenium and iodine. These wastes also contain various nutraceuticals including proteins like collagen and gelatin, protein hydrolysates, bioactive peptides, PUFA-rich lipids, hydrocarbons such as squalene, carotenoids, and polysaccharides like chitin, chitosan and glycosaminoglycans. Mineral-based compounds, such as bone powders, also offer health benefits (Mathew and Tejpal, 2018).

Biologically active compound from seafood waste and discards provide various health benefits such as antioxidant, anti-inflammatory, anti-allergic, antitumor, anti-obesity, anticoagulant, antimicrobial and immune-boosting effects. In addition to that, processing seafood waste can help to reduce environmental pollution while creating valuable ingredients for multiple industries (Remya et al. 2019). Large quantities of by-products such as shells from crustaceans and shellfish are generated by marine processing industries. Considering the limited availability of marine resources and the escalating global environmental pollution, the sustainable utilization of these by-products has become increasingly crucial. Fish and shellfish waste can be effectively utilized through the production of novel food ingredients, nutraceuticals, pharmaceuticals, biomedical materials, fine chemicals and other value-added products (Ferraro et al. 2010).

Bioactive compounds from seafood wastes have promising applications in functional foods, natural food additives, medicinal drugs and as encapsulation or carrier materials for nutraceuticals. With increasing consumer preference for natural bioactive compounds and advancements in biotechnology, seafood by-products offer great potential for the extraction of valuable nutraceuticals. Utilising seafood waste for human consumption can also help minimize environmental issues related to seafood production (Mathew and Tejpal, 2018).

Profile of global waste generation in seafood

In the seafood industry, the edible meat portion is typically regarded as the main product, while the remaining parts such as the head, trimmings, skin, viscera, scales, and bones were traditionally considered as leftovers. However, they are now referred to as "rest raw material" or "secondary raw material." Waste generation in the seafood sector starts right at the harvest site. For decades, the FAO has estimated post-harvest losses in the seafood industry to be around 20-35% of the total catch at different stages of the value chain. Each year, commercial fishing activities result in the discarding of approximately 17.9 to 39.5 million tonnes of whole fish. In capture fisheries, a substantial share of the marine catch is returned to the sea, either as untargeted bycatch or as processing discards from onboard operations.

2.1 Typical composition of secondary raw materials from fish processing operations (Binsi, 2018)

Waste Component	% of whole fish	Active component
Head	15 - 25	Protein, PUFA, Minerals, Plasmalogens, glycosaminoglycans
Frame Meat	~10%	Protein
Skin	3-5	Protein
Scale	6-7	Protein, Minerals
Bone	8-10	Protein, Minerals, Chondroitin
Viscera	5 - 12	Protein, Enzyme, fat
Gill	4-5	Protein, Fe

2.2 Composition of fish waste (Esteban et al. 2007)

<i>Nutrient</i>	<i>Fish waste</i>
Crude protein (%)	57.92 ±5.26
Fat (%)	19.10 ±6.06
Crude fiber (%)	1.19 ±1.21
Ash (%)	21.79 ±3.52
Calcium (%)	5.80 ±1.35
Phosphorous (%)	2.04 ±0.64
Potassium (%)	0.68 ±0.11
Sodium (%)	0.61 ±0.08
Magnesium (%)	0.17 ±0.04
Iron (ppm)	100.00 ±42.00
Zinc (ppm)	62.00 ±12.00
Manganese (ppm)	6.00 ±7.00
Copper (ppm)	1.00 ±1.00

Values in % or mg/kg (ppm) on a dry matter basis.

Classification of Nutraceuticals (Mathew and Tejpal, 2018)

Based on the bio-functional properties of bioactive compounds from terrestrial and marine sources are classified into following,

- Dietary Supplements

- Functional foods
- Medicinal food

3.1 Dietary Supplements

The Dietary Supplement Health and Education Act (DSHEA) of 1994 in the USA defines dietary supplements as products containing "dietary constituents" that are taken orally to enhance nutritional intake. These constituents include bioactive components such as amino acids, vitamins, minerals, fibers, essential metabolites, and specific enzymes. Dietary supplements are available in various forms, including tablets, capsules, powders, liquids, and other dosage forms (Radhika et al. 2011).

3.2 Functional foods

Functional foods are naturally derived foods enriched with nutrients and fortified with essential components. According to Health Canada, functional foods are regular foods that contain ingredients with specific therapeutic effects in addition to their nutritional value. In Japan, functional foods are evaluated based on three key criteria:

- (1) They must come from natural sources and be consumed in their original form rather than as processed supplements like tablets or powders
- (2) They should be part of a regular daily diet, and
- (3) They must play a role in both disease prevention and management while supporting biological processes (Mathew and Tejpal, 2018).

3.3 Medicinal food

Medical foods are specially designed for internal consumption under a doctor's supervision to help manage specific diseases with unique nutritional requirements that cannot be met through a regular diet alone. Unlike dietary supplements and functional foods, medical foods must meet these strict criteria and are classified separately (Radhika et al. 2011).

Nutraceuticals from seafood discards and waste

4.1 Major nutraceuticals and bioactive components from seafood (Venugopal, 2018)

<i>Finfish</i>	<i>Shellfish (crustaceans and molluscs)</i>
Bioactive peptides	Bioactive peptides
Biological calcium	Carotenoids
Carotenoids	Chitin, chitosan, chitosan derivatives
Enzymes	Enzymes
Glycosaminoglycans including chondroitin sulfate, dermatan sulfate and hyaluronic acid	Glucosamine
Long-chain omega-3 polyunsaturated fatty acids (PUFA)	Mussel polysaccharides, lipids and other products
Phosphopeptide from fish bone	
Protein hormones such as calcitonin	
Protein isolates including collagen and gelatin	
Squalene	

4.2 According to their chemical origin, can be classified into four groups (Remya et al. 2019)

4.2.1 Nitrogenous compounds

- Proteins
- Protein hydrolyzates
- Enzymes
- Bioactive peptides

4.2.2 Lipid-derived compounds

- Omega-3 PUFA
- Squalene
- Carotenoids

4.2.3 Polysaccharide-based compounds

- Chitin, Chitosan & its derivatives - Glucosamine
- Glycosaminoglycans (Chondroitin sulfate, Hyaluronic acid, Dermatan sulfate, Heparin, or Keratin sulphate)

4.2.4 Mineral-based compounds

- Bone Powders
- Cuttlebone powder
- Hydroxyapatite

4.2.5 Nitrogenous compounds

i. Proteins

Seafood processing waste contains valuable functional proteins that can be extracted using various techniques. These methods include extraction with dilute acids or bases as well as iso-electric solubilization and precipitation which help isolate the proteins for further use. On a dry weight basis, seafood waste typically contains 60% protein. Up to 65% of proteins can be found in shrimp head waste (Liu et al. 2021). Studies have shown that soluble powders obtained from Alaska pollock processing discards contain protein levels ranging from 65% to 79%. Fish protein isolates generally retain their properties for about six months when stored at 5°C. rotein isolate from striped bass (*Morone saxatilis*) has shown potential in controlling cardiovascular diseases, highlighting its nutraceutical value (Remya et al. 2019).

ii. Fish protein hydrolysates (FPH)

Fish protein hydrolysates (FPH) offer a valuable way to utilize proteins from seafood processing waste. They are produced by breaking down fish meat using proteolytic enzymes providing an alternative to using fish discards and byproducts. FPH is highly nutritious and have applications in both the food and pharmaceutical industries due to their balanced amino acid composition, easy digestibility, rapid absorption and bioactive peptide content. FPHs are combined with omega-3 fatty acids, they work together to reduce TNF- α levels more effectively than either FPH or omega-3 fatty acids alone (Remya et al. 2019). Peptides from FPH exhibit various bioactivities including antimicrobial, antihypertensive, antitumor, and antioxidative properties (Ortizo et al. 2023). FPH displayed α -amylase inhibitory activity (IC₅₀: 5.70–84.37 mg/mL) and strong ACE inhibitory activity, making them promising candidates for functional food and nutraceutical applications (Henriques et al. 2021).

iii. Collagen

Fish processing waste including discarded frames, fins, scales, air bladders and fish heads, is a rich source of collagen. Extracting collagen from fish bones, a major byproduct of filleting, involves removing lipids with acetone for 12 hours at room temperature, drying the material and then decalcifying it using hydrochloric acid for a day.

Fish skin and scales from seafood processing waste are excellent sources of collagen and gelatin. Collagen from marine sources is widely used in different industries due to its compatibility with the human body, ability to break down naturally, strong cell-binding properties and low risk of triggering allergic reactions (Yamada et al. 2014). Collagen peptides have been found to possess various bioactive properties, including antioxidant, antimicrobial, antihypertensive, metal-chelating, tyrosinase-inhibiting, immunomodulatory, neuroprotective, antifreeze, wound-healing and cell-proliferation activities (Zhuang et al. 2009; Chi et al. 2014).

Collagen extracted from fish skin and airbladder is used in dentistry and as artificial skin. When combined with chitosan, collagen films become highly effective in controlling blood loss, preventing fluid loss, and reducing the risk of infections. These films are absorbable and do not cause allergic reactions, making them ideal for medical applications (Devadasan, 2004).

Nutraceutical Applications of Collagen

- **Bone & Joint Health:** Reduces arthritis symptoms, strengthens bones.
- **Skin & Hair Health:** Improves elasticity, reduces wrinkles.
- **Muscle Growth:** Supports muscle recovery and strength.
- **Cardiovascular Benefits:** Helps maintain blood vessel integrity.
- Supports wound healing and tissue regeneration.

iv. Bioactive peptides

Peptides derived from marine by-products have significant nutraceutical potential in addressing major public health concerns such as obesity, stress and hypertension. Their beneficial effects stem from their unique bioactive properties which are influenced by their amino acid composition and sequence. These peptides exhibit a wide range of biological activities including antimicrobial, antiviral, antitumor, antioxidant, antihypertensive, cardioprotective, anti-amnesic immunomodulatory, analgesic, antidiabetic, anti-aging, appetite-suppressing and neuroprotective effects.

4.2.6 Lipid-derived compounds

i. Fish lipids

Omega-3 polyunsaturated fatty acids (PUFAs) from aquatic sources primarily include eicosapentaenoic acid (EPA) and docosahexaenoic acid (DHA), while docosapentaenoic acid (DPA) is found in much smaller amounts in fish oils. The oil from fish such as Atlantic mackerel, shark, anchovies, menhaden, and Atlantic sardines can contain up to 35% omega-3 fatty acids with EPA and DHA making up around 10% of the total oil content. Consuming adequate amounts of fish oil (omega-3 PUFA) is known to offer several health benefits. It helps in managing cardiovascular diseases, cancer, high blood pressure, Alzheimer's disease, diabetes, arthritis and autoimmune disorders. Additionally, it supports brain function and improves retinal health (Cole et al. 2009).

The European Academy of Nutritional Sciences (EANS) and the International Society for the Study of Fatty Acids and Lipids (ISSFAL) recommends a daily intake of 0.2 g of EPA and 0.65 g DHA respectively (Dedeckere et al. 1998). Fish oil is a highly effective and cost-efficient source of omega-3 PUFAs. Cod liver, in particular, is rich in fat-soluble vitamins and essential lipids, especially EPA, making it a valuable ingredient for developing nutraceutical products (Mondello et al. 2006).

ii. **Squalene** Squalene is a hydrocarbon ($C_{30}H_{50}$). The livers of deep-sea sharks contain high amounts of squalene. It helps sharks to maintain buoyancy since they do not have swim bladders. Shark liver oils especially from *Centrophorus* species found in the Pacific, North Atlantic and Indian Oceans contain around 85–90% unsaponifiable matter, mostly made up of squalene. Squalene is known for its skin-rejuvenating properties and also helps lower lipid levels and stabilize cell membranes. Senthilkumar et al. (2006) reported that administering squalene orally (0.4 ml per day per rat) effectively protects against toxicity in the liver, kidney and heart tissues. Research by Das et al. (2003) showed that squalene specifically safeguarded normal bone marrow cells from the toxic effects of cisplatin and other anticancer drugs. Its hydrogenated form squalane is widely used in the nutraceutical, pharmaceutical and cosmetic industries (Remya et al. 2019).

Squalene is naturally found in sources like wheat germ, rice bran, shark liver and olive oil. Among these, shark liver oil is the richest source, making up about 40% of its weight. Recently, squalene has gained interest for its various health benefits, including antioxidant, cholesterol-lowering, heart-protective, anti-aging and anti-cancer properties (Passi et al. 2002; Ko et al. 2002). Squalene is thought to shield the skin from UV radiation due to its high concentration (12%) in sebum. Squalene helps repair damaged body cells and supports cell regeneration. Its main protective function is preventing cell oxidation. (Sumi et al. 2018).

4.2.7 Polysaccharide-based compounds

Polysaccharides are becoming important ingredients in combating chronic diseases. These large, biodegradable molecules have unique properties such as water and fat binding, gelation, and viscosity, making them useful in both biomedical and food applications. In food and medicine, they serve various functions including acting as adhesives, coatings, emulsifiers, encapsulants, film formers, foam stabilizers and thickening agents. Its unique properties make them valuable in medicine for drug delivery, tissue regeneration, wound healing, dental implants, blood plasma expansion, vaccines and non-viral gene delivery among other applications

i. Chitin, Chitosan & its derivatives - Glucosamine

Chitin is a natural polysaccharide that was first discovered in 1821 by Henri Braconnot, the director of a botanical garden in France. The term "chitin" originates from Greek, meaning "a coat of mail." Chitin was first utilized in 1823, and by the late 1830s, it was successfully isolated from insects. In 1859, scientists developed chitosan, a derivative of chitin, marking a significant advancement in its applications. Chitin is produced by a vast number of living organisms and is the second most abundant natural polymer after cellulose. In crustaceans like lobster, crab, krill, shrimp, and prawn, chitin forms a protective outer layer by creating a strong, covalent bond with proteins.

The dry shells of crab, shrimp, and lobster can contain up to 70% chitin by dry weight, while the chitin content in dried squid skeleton pens and deproteinized krill shells is lower, at around 40%. Chitin is a cationic polymer made up of N-acetyl-D-glucosamine units linked by β -bonds. Its structure, β -(1–4)-N-acetyl-D-glucosamine, is a modified form of cellulose where the hydroxyl group at the C-2 position is replaced by an acetyl amino group. Chitosan derivatives exhibit a wide range of bioactivities depending on their chemical composition. These include antioxidant, anti-inflammatory, anti-allergic, antitumor, anti-obesity, antidiabetic, anticoagulant, antiviral, immunomodulatory and cardioprotective properties. Due to these diverse benefits, chitosan and its derivatives have valuable applications in various fields, including food, nutrition, medicine, agriculture, biotechnology, and material science. Chitosan films serve as an effective packaging material for food preservation. In medicine, chitosan and its derivatives have potential applications in drug delivery, hemodialysis membranes, artificial skin, hemostatic agents, hemoperfusion columns, wound healing, blood coagulation and gene therapy. Its ability to form a gel in slightly acidic conditions also provides antacid and anti-ulcer benefits. Additionally, chitosan, along with other polysaccharides like hyaluronic acid has gained

attention in regenerative medicine and tissue engineering as an ideal material for artificial extracellular matrices (Remya et al. 2019).

ii. Glucosamine Hydrochloride

Glucosamine is typically derived from crustacean waste, such as shrimp, crab, and lobster shells (Xu and Wang, 2004). Glucosamine is a key component of structural polysaccharides like chitin and chitosan found in the exoskeletons of crustaceans and other arthropods. Although it was discovered long ago, the market for glucosamine has gained popularity due to its health benefits. Dietary supplements containing glucosamine, such as glucosamine sulfate, glucosamine hydrochloride and N-acetyl-glucosamine, have shown promise in treating osteoarthritis, knee pain, and back pain (Mathew and Tejpal, 2018). Glucosamine is also recognized for its unique properties including anti-cancer, anti-inflammatory and antibacterial effects (Nagaoka et al. 2011).

Nutraceutical Application:

- **Dietary Supplements:** Glucosamine hydrochloride is widely incorporated into dietary supplements aimed at supporting joint health and alleviating symptoms of osteoarthritis. It serves as a building block for glycosaminoglycans, essential components of cartilage structure.

Pharmaceutical Application:

- **Osteoarthritis Treatment:** Glucosamine is utilized in pharmaceutical formulations to manage osteoarthritis, providing relief from joint pain and improving mobility.

iii. Hyaluronic acid (HA)

Hyaluronic acid (HA) can be extracted from bio-waste sources such as fish eyeballs and is also found in the cartilage matrix of fish. It has various biomedical applications, including use in osteoarthritis treatment through viscosupplementation, aiding in eye surgery and promoting wound healing. HA is utilized in drug delivery, tissue engineering, gene therapy, targeted drug delivery, cancer treatment, environmental applications and sensor technology (Mathew et al. 2017).

Nutraceutical Applications:

1. **Joint Health Supplements:** HA plays a crucial role in maintaining synovial fluid viscosity, which cushions and lubricates joints. Incorporating HA derived from fish by-products into supplements provides a natural alternative for supporting joint function.
2. **Skin Hydration Products:** Due to its exceptional moisture-retaining properties, HA is utilized in nutraceuticals aimed at enhancing skin hydration and elasticity (Graciela et al. 2023).

4.2.8 Mineral-based compounds

i. Bone powder

Marine organisms, particularly fish are rich sources of essential minerals like sodium, potassium, calcium, phosphorus, and magnesium. Fish bones, which are often discarded after protein removal, are an excellent source of calcium and hydroxyapatite. Due to their high mineral content, fish bone powder can be added to various food products for fortification. However, to make it suitable for consumption, the bone structure needs to be softened through treatments like hot water, hot acetic acid, or superheated steam. Calcium powder extracted from tuna bones is recognized as a valuable nutraceutical for combating calcium deficiency in children. Fortifying foods with this calcium source can support daily nutritional needs and potentially lower the risk of osteoporosis. Moreover, seafood provides higher levels of essential minerals like selenium, potassium, iodine, zinc and magnesium compared to meat, with a seafood-rich diet particularly beneficial for maintaining adequate iodine levels (Mathew and Tejpal, 2018).

Nutraceutical Applications:

- **Calcium Supplementation:** Fish bone powder is a natural source of calcium, essential for bone health. Studies have shown that calcium derived from fish bones is more bioavailable than traditional calcium carbonate supplements, making it a promising alternative for dietary supplementation.
- **Functional Food Ingredient:** Incorporating fish bone powder into food products can enhance their nutritional profile by increasing mineral content, particularly calcium and phosphorus. This fortification can aid in addressing dietary deficiencies and promoting overall health (Perez et al. 2024).

Pharmaceutical Applications:

- **Bone Tissue Engineering:** Due to its high hydroxyapatite content, fish bone powder has been explored for use in bone grafts and implants, supporting bone regeneration and repair (Anwar et al. 2025)
- **Calcium Supplements:** Fish bone powder is utilized in the production of calcium tablets or medicines aimed at treating conditions like osteoporosis.

ii. Cuttlebone powder

Studies on antimicrobial activity provide important insights into antibiotic discovery and the extraction of bioactive compounds from natural sources. One such natural resource gaining attention is marine mollusks. Among them, cuttlefish, a cephalopod belonging to the order Sepioidea, is being explored for its potential bioactive properties (Yazdanpanah et al. 2021).

Cuttlebone powder is rich in calcium and has been incorporated into herbal teas and other formulations for its potential health benefits. Calcium & mineral supplements (bone health), antacid formulations.

Nutraceutical Applications:

- **Calcium Supplementation:** Cuttlebone powder serves as a natural source of calcium, essential for bone health and metabolic functions. Its high calcium content makes it suitable for dietary supplements aimed at preventing osteoporosis and supporting overall skeletal health (Huey et al. 2021)

Nutraceutical Compounds from Marine Resources	Properties	References
Chitin, chitosan, glucosamine	Antimicrobial, anti-inflammatory, antioxidant, antitumor, antiulcer, immunoenhancing, weight and cholesterol reduction	Shahidi (2005), Rasmussen and Morrissey (2008), Kim et al. (2008)
Carotenoids, collagen, gelatin, peptides, carteno-proteins, halogenated compounds	Antioxidant, immunoenhancing	Shahidi (2005), Kim et al. (2008), Trung (2010), Riccioni et al. (2011)
Omega-3 fatty acids	Prevention of cardiovascular disease, macular degeneration, inflammatory disorders	Shahidi (2005)
Chondroitin sulfate	Anti-inflammatory, osteoarthritis treatment	Shahidi (2005), Ronca et al. (1998)
Minerals (calcium)	Strengthening of teeth and bones, nerve function, and many enzymatic reactions that require calcium as a cofactor	Shahidi (2005), Jung et al. (2008)

Conclusion

The sustainable utilization of seafood discards and byproducts for the production of nutraceuticals and pharmaceuticals presents a promising approach to addressing environmental concerns while adding value to the seafood industry. With the increasing demand for natural and functional health products, seafood waste which

is often discarded or underutilized can be transformed into valuable bioactive compounds such as collagen, chitin, omega-3 fatty acids, peptides, etc. These compounds exhibit numerous health benefits including anti-inflammatory, antioxidant, antimicrobial and cardioprotective properties, making them ideal ingredients for dietary supplements, functional foods and pharmaceutical applications. The processing of seafood waste into nutraceuticals and pharmaceuticals not only reduces environmental pollution but also promotes a circular economy by converting byproducts into high-value health-promoting products. Advanced extraction technologies including enzymatic hydrolysis, fermentation, and supercritical fluid extraction, have significantly improved the recovery of bioactive compounds from fish scales, bones, skin, shells and other seafood byproducts and discards. These methods ensure the preservation of bioactivity while enhancing the efficiency and sustainability of production. It also aligns with global sustainability goals by minimizing waste promoting resource efficiency and reducing dependence on synthetic additives. However, challenges such as proper waste collection, standardization of processing techniques, regulatory approval and consumer acceptance must be addressed to maximize the potential of seafood waste-derived nutraceuticals and pharmaceuticals. With growing awareness and investment in sustainable practices, the future of seafood waste utilization in nutraceuticals and pharmaceuticals is promising, paving the way for a more resource-efficient and health-conscious world.

REFERENCES

- [1]. Al-Rawe RA, Al-Rammahi H M, Cahyanto A, Maamor A, Liew Y M, Sukumaran P, and Hassan W N W (2024) Cuttlefish-bone-derived biomaterials in regenerative medicine, dentistry, and tissue engineering: A systematic review. *Journal of Functional Biomaterial*.15(8): 219.
- [2]. Anwar A I, Ruslin M, Marlina E, and Hasanuddin H (2025) Physicochemical analysis and application of sardinella fimbriata-derived hydroxyapatite in toothpaste formulations. *BMC Oral Health*.25: 195.
- [3]. Benavente M, Arias S, Moreno L, and Martínez J (2015) Production of glucosamine hydrochloride from crustacean shell. *Journal of Pharmacy and Pharmacology*.3(1): 20-26.
- [4]. Binsi P K (2018) Overview of waste generation in fish and shellfish processing industry. ICAR-Central Institute of Fisheries Technology, Cochin.
- [5]. Caruso G, Floris R, Serangeli C, and Di Paola L (2020) Fishery wastes as a yet undiscovered treasure from the sea: Biomolecules sources, extraction methods and valorization. *Marine drugs*.18(12): 622.
- [6]. Chi C F, Cao Z H, Wang B, Hu F Y, Li Z R, and Zhang B (2014) Antioxidant and functional properties of collagen hydrolysates from Spanish mackerel skin as influenced by average molecular weight. *Molecules*.19(8): 11211-11230.
- [7]. Cole G M, Ma Q L, and Frautschy S A (2009) Omega-3 fatty acids and dementia. *Prostaglandins, Leukotrienes and Essential fatty acids*. 81(2-3): 213-221.
- [8]. Coppola D, Oliviero M, Vitale G A, Lauritano C, Ambra I, Iannace S, and de Pascale D (2020) Marine collagen from alternative and sustainable sources: Extraction, processing and applications. *Marine drugs*.18(4): 214.
- [9]. Das B, Yeger H, Baruchel H, Freedman M H, Koren G, and Baruchel S (2003) In vitro cytoprotective activity of squalene on a bone marrow versus neuroblastoma model of cisplatin-induced toxicity: implications in cancer chemotherapy. *European Journal of Cancer*.39(17): 2556-2565.
- [10]. Devadasan K (2004) Fish-based pharmaceuticals and nutraceuticals and their applications.

- [11]. Elfahmi and Chahyadi A (2020) The diversity of ursodeoxycholic acid precursors from bile waste of commercially available fishes, poultry and livestock in Indonesia. *Brazilian Journal of Pharmaceutical Sciences*.56: e18094.
- [12]. Esteban MB, Garcia AJ, Ramos P, and Marquez M C (2007) Evaluation of fruit- vegetable and fish wastes as alternative feedstuffs in pig diets. *Waste Manag.* 27: 193-200.
- [13]. FAO (2024)The State of World Fisheries and Aquaculture 2024. Blue Transformation in action. Rome. <https://doi.org/10.4060/cd0683en>, pp 1- 115.
- [14]. Ferraro V, Cruz I B, Jorge R F, Malcata F X, Pintado M E, and Castro P M (2010) Valorisation of natural extracts from marine source focused on marine by-products: A review. *Food Research International*.43(9): 2221-2233.
- [15]. Ghaly A E, Ramakrishnan V V, Brooks M S, Budge S M, and Dave D (2013) Fish processing wastes as a potential source of proteins. Amino acids and oils: A critical review. *J. Microb. Biochem. Technol*, 5(4): 107-129.
- [16]. Graciela C Q, Jose Juan E C, Gieraldin C L, Xochitl Alejandra P M, and Gabriel A A (2023) Hyaluronic Acid—extraction methods, sources and applications. *Polymers*.15(16): 3473.
- [17]. Henriques A, Vazquez J A, ValcarcelJ, Mendes R, Bandarra N M, and Pires C (2021) Characterization of protein hydrolysates from fish discards and by-products from the North-West Spain fishing fleet as potential sources of bioactive peptides. *Marine Drugs*.19(6): 338.
- [18]. Huey Y W, Zulkipli AS, Tajarudin H A, and Salleh R M (2021) Physicochemical properties of pre-treated cuttlebone powder and its potential as an alternative calcium source. *Journal of Food Processing and Preservation*.45(10): e15831.
- [19]. Idrus N H, Azmi N S, and Palliah J V (2016) Waste to wealth: Alternative source of glycosaminoglycans (GAGs) from sea food waste *IIOAB J*.7: 543-547.
- [20]. Jafari A, Tabarsa M, Naderimanesh H, Ahmadi Gavlighi H, and You S (2024) The Preparation, Anti-inflammatory, and Antioxidant Properties of Glucosamine Hydrochloride from the Waste of *Litopenaeus vannamei* Processing Plant. *ECOPERSIA*. 175-188.
- [21]. Kim S K, Mendis E, and Shahidi F(2008) Marine fisheries by-products as potential nutraceuticals: An overview. In *Marine Nutraceuticals and Functional Foods*, C. J. Barrow and F. Shahidi (eds). Boca Raton, FL: Taylor & Francis Group. pp. 1–22.
- [22]. Kim S K, Mendis E (2005) Bioactive compounds from marine processing byproducts – A review. *Food Research International*. 39: 383-393.
- [23]. Kristinsson H G, and Rasco B A (2000) Fish protein hydrolysates: production, biochemical, and functional properties. *Critical reviews in food science and nutrition*.40(1): 43-81.
- [24]. Liu Z, Liu Q, Zhang D, Wei S, Sun Q, XiaQ, and Liu S (2021) Comparison of the proximate composition and nutritional profile of byproducts and edible parts of five species of shrimp. *Foods*.10(11): 2603.
- [25]. Mathew S, and Tejpal C S (2018) Nutraceuticals from fish and fish wastes: scopes and innovations. ICAR-Central Institute of Fisheries Technology, Cochin.
- [26]. Mathew S, Tejpal C S, Kumar L R, Zynudheen A A, and Ravishankar C N (2017) Aquaceuticals for developing high value noble foods and dietary supplements. *Indian Journal of Agricultural Biochemistry*.30(1): 1-9.
- [27]. Mondello L, Tranchida P Q, DugoP, and Dugo G (2006) Rapid, micro-scale preparation and very fast gas chromatographic separation of cod liver oil fatty acid methyl esters. *Journal of pharmaceutical and biomedical analysis*.41(5): 1566-1570.

- [28]. Mostoufi A (2016) New applications of cuttlebone (CB) as a natural marine compound. *Jundishapur J. Nat. Pharm. Prod.*11: e41762.
- [29]. Nagaoka I, Igarashi M, Hua J, Ju Y, Yomogida S, and Sakamoto K (2011) Recent aspects of the anti-inflammatory actions of glucosamine. *Carbohydrate polymers.*84(2): 825-830.
- [30]. Ortizo R G G, Sharma V, Tsai M L, Wang J X, Sun P P, Nargotra P, and Dong C D (2023) Extraction of novel bioactive peptides from fish protein hydrolysates by enzymatic reactions. *Applied Sciences.*13(9): 5768.
- [31]. Perez A, Ruz M, Garcia P, Jimenez P, Valencia P, Ramirez C, and Almonacid S (2024) Nutritional properties of fish bones: Potential applications in the food industry. *Food Reviews International.*40(1): 79-91.
- [32]. Radhika P R, Singh R B M, and Sivakumar T (2011) Nutraceuticals: An area of tremendous scope. *Int. J. Res. Ayurveda Pharmacy.*2: 410-415.
- [33]. Rajabimashhadi Z, Gallo N, Salvatore L, and Lionetto F (2023) Collagen derived from fish industry waste: progresses and challenges. *Polymers.*15(3): 544.
- [34]. Remya S, Renuka V, Jha AK, and Joseph T C (2019) Nutraceuticals from Secondary Raw Materials of Aquatic Origin. In: (Toms C. Joseph., Ashish Kumar Jha., Renuka, V., Remya, S., Eds.). *FishTech-19, Fishery Waste Management: Challenges and Business Opportunities in Gujarat- Souvenir*. Veraval Research Centre of ICAR-CIFT, Veraval, Gujarat, 10 July, 2019, pp. 73-115.
- [35]. Ronca, F., L. Palmieri, P. Panicucci, and G. Ronca. 1998. Anti-inflammatory activity of chondroitin sulfate. *Osteoarthritis Cartilage* 6 (Suppl A):14-21.
- [36]. Shahidi F (2005) Nutraceuticals from seafood and seafood by-products. In *Asian Functional Foods*, J. Shi, C.-T. Ho, and F. Shahidi (eds). Boca Raton, FL: Taylor & Francis Group, pp. 267-288.
- [37]. Senthilkumar S, Devaki T, Manohar B M, and Babu M S (2006) Effect of squalene on cyclophosphamide-induced toxicity. *Clinica Chimica Acta.*364(1-2): 335-342.
- [38]. Sumi E S, Anandan R, Rajesh R, Ravishankar C N, and Mathew S (2018) Nutraceutical and therapeutic applications of squalene.
- [39]. Veeruraj A, Liu L, Zheng J, Wu J, and Arumugam M (2019) Evaluation of astaxanthin incorporated collagen film developed from the outer skin waste of squid *Doryteuthis singhalensis* for wound healing and tissue regenerative applications. *Materials Science and Engineering.*95: 29-42.
- [40]. Yamada S, Yamamoto K, Ikeda T, Yanagiguchi K, and Hayashi Y (2014) Potency of fish collagen as a scaffold for regenerative medicine. *BioMed research international.* 2014(1): 302932.
- [41]. Yazdanpanah G, Javid N, Honarmandrad Z, Amirmahani N, and Nasiri A (2021) Evaluation of antimicrobial activities of powdered cuttlebone against *Klebsiella oxytoca*, *Staphylococcus aureus*, and *Aspergillus flavus*. *Journal of Environmental Health Management and Engineering.*8(1): 39-45.
- [42]. Zhuang Y L, Zhao X, and Li B F (2009) Optimization of antioxidant activity by response surface methodology in hydrolysates of jellyfish (*Rhopilema esculentum*) umbrella collagen. *Journal of Zhejiang University Science.*10(8): 572-579.

Synthesis and Characterization of Cu₂S Thin Films by Novel Arrested Precipitation Method

S. M. Karape^{1,2}, D. M. Sirsat², S. S. Jadhav³, S. T. Sankpal¹

¹Department of Chemistry, Athalye Sapre Pitre College, Devrukh, Ta-Sangameshwar, Dist-Ratnagiri, 415804, Maharashtra, India

²Department of Chemistry, AnandibaiRaorane Arts, Commerce and Science College, Vaibhavwadi, Tal-Vaibhavwadi, Dist.-Sindhudurg, 416810, Maharashtra, India

³P.G. Department of Chemistry, Sadguru Gadage Maharaj College, Karad, Tal-Karad, Dist.-Satara, 416004, Maharashtra, India

ARTICLE INFO

Article History:

Published : 30 April 2025

Publication Issue :

Volume 12, Issue 13

March-April-2025

Page Number :

216-224

ABSTRACT

Nanogranular thin films of copper sulfide (Cu₂S) were deposited through the arrested precipitation technique (APT). The prepared Cu₂S films were characterized to evaluate their optical, structural, and morphological properties. The optical absorption analysis indicated that the band gap energy decreased from 2.91 eV to 2.26 eV with increasing precursor concentration. The X-ray diffraction (XRD) analysis confirmed that APT is a favorable technique for synthesizing pure nanocrystalline Cu₂S thin films with a monoclinic crystal structure. Electrochemical impedance spectroscopy (EIS) measurements revealed the charge transfer resistance and electron lifetime characteristics of the films. Furthermore, X-ray photoelectron spectroscopy (XPS) indicated stochastic variations in the valence states of Cu in Cu₂S.

Keywords: Arrested precipitation technique, Copper sulfide, Thin films, Band gap, and Electrochemical impedance spectroscopy.

INTRODUCTION

Recently, the nanotechnology-enhanced thin film solar cell is a promising and potentially important emerging technology [1], designing stochastic nanoscopic inorganic semiconductor coatings, which is better alternatives for the depleting energy sources, such as fossil fuels, natural gas, and coal oils has led to the fabrications of new energy sources [2]. However, most of the semiconductor solar cell suffers from photo corrosion with the I⁻/I₃⁻ redox couple, and the polysulfide mediator chemisorbs on the platinum surface and induces undesirable effects on the electrochemical performance [3]. Hence, the copper containing chalcogenides semiconductor compound focused on the as extremely thin absorber layers [4] and counter electrodes like Cu₂S [5] and CuSe [6].

The metal chalcogenide thin film materials are deposited on the substrates such as glass, plastic, stainless steel, etc. especially suitable for solar building integration as optoelectronic devices, and PEC solar cell devices [6], due to easy junction formation with redox mediator [7]. The increasing popularity of IB-VIA and II-VIA group chalcogenides is their high absorption coefficient in visible radiation and electron-hole separations during the working of solar cells [8]. The copper sulfide (CuS, 2.9 eV) [9] is a visible photo-active and semiconducting in nature. But its wide applicability is limited due to complicated and sophisticated synthesis approaches, and during the chemical synthesis of copper chalcogenide materials use of toxic reducing agents, surfactants, solvents, and high temperature [10]. Contrary, the solution-processed APT method, simple and cost-effective [11], has comparable structural, compositional, and opto-electrical properties over other sophisticated deposition techniques [12].

In the present investigation, we have selected triethanolamine (TEA) as a polydentate ligand, which form a complex with copper metal ions to arrest the bulk precipitation. The invention in this report is to optimize the growth mechanism conditions especially reduction of copper metal ions through mild reducing agents (Na_2SO_3), which lead to form uniform, highly adherent, nanogranular structured Cu_2S thin films at ambient temperature.

The APT approach is a hybrid chemical bath deposition method in combination with the controlled chemical growth process (CCGP) for chemosynthesis of ternary nanoalloys [11]. Thus, smaller crystallites serve as nucleation sites to further grow the crystallites in inorganic metal chalcogenide coating thin films [13]. To the best of our knowledge, the novel chemosynthesis of Cu_2S thin films using TEA as a surface-active growth controller yet not reported.

Materials and method

2.1 Experimental details

All chemicals were of analytical reagent (AR) grade and used without further purification. Copper sulfate pentahydrate ($\text{CuSO}_4 \cdot 5\text{H}_2\text{O}$, 98%, S-D Fine Chem.), thiourea ($\text{H}_2\text{N}-\text{CS}-\text{NH}_2$, 99%, S-D Fine Chem.), ammonia hydroxide solution (NH_4OH , 30%, Thomas Baker), and triethanolamine ($\text{N}(\text{CH}_2\text{CH}_2\text{OH})_3$, 99%, Merck, TEA) were used as precursors and growth-controlling agent. The glass substrates were initially cleaned using a chromic acid solution heated to 50°C for 5 minutes, followed by ultrasonic cleaning in a mixture of isopropanol and deionized water. Subsequently, Cu_2S thin films were deposited onto the bare glass substrates using a facile deposition technique.

2.2 Synthesis of Cu_2S thin films

In the synthesis, a series of simple chemical reactions were employed. Copper sulfate solutions with concentrations ranging from 0.03 to 0.05 M were used to form a coordination complex with TEA, a polydentate ligand, resulting in a clear and transparent precursor solution. The $\text{Cu}^{2+}-(\text{TEA})_2$ complex subsequently reacted with sulfide ions (S^{2-}), which were gradually released via the alkaline hydrolysis of thiourea ($\text{H}_2\text{N}-\text{CS}-\text{NH}_2$) at a maintained pH of 10.5. The deposition of Cu_2S thin films proceeded via a combination of nucleation and Ostwald ripening mechanisms. These growth processes were found to be strongly influenced by various preparative parameters, including ligand concentration, Cu^{2+} precursor concentration, solution pH, deposition time, single-phase system conditions, agitation speed (RPM), and bath temperature. Accordingly, these parameters were carefully optimized during the initial phase of thin film deposition to ensure consistent film quality. In this study, the Cu^{2+} precursor concentration was varied between 0.03 and 0.05 M, while other deposition conditions such as deposition time, ambient temperature, and stirring speed were kept constant. After the formation of the Cu_2S films, their thickness was measured using a surface profilometer. It was

observed that an increase in Cu^{2+} concentration accelerated the film growth rate, resulting in thicker films. However, beyond a certain concentration, overgrowth led to peeling of the film from the substrate without a significant increase in film thickness. Therefore, the effect of Cu^{2+} precursor concentration on the deposition process was thoroughly investigated. In the final growth stage, all deposited thin films were found to be uniform, strongly adherent, and displayed a transparent blackish appearance. The prepared thin films were symbolized as C1, C2, and C3 corresponding to the 0.03, 0.04, and 0.05 M concentrations, respectively.

2.3 Characterizations

The optical absorption spectra of the Cu_2S thin films were recorded using a UV-Vis-NIR spectrophotometer (Shimadzu, UV-1800). Film thickness measurements were carried out using a surface profilometer (AMBIOS XP-1). The structural properties of the films were investigated using X-ray diffraction (XRD) analysis with a Bruker AXS D8 diffractometer employing $\text{Cu K}\alpha$ radiation ($\lambda = 1.5418 \text{ \AA}$) over a 2θ angle range of 20 to 80° . The surface morphology and elemental composition of the deposited films were examined using field-emission scanning electron microscopy (FE-SEM) and X-ray photoelectron spectroscopy (XPS, Thermo Scientific, Multilab-2000). The XPS system is equipped with a multi-channel detector capable of detecting photon energies in the range of 0.1 to 3.0 keV . Specific surface area and porosity of the films were analyzed using the Brunauer–Emmett–Teller (BET) method with a Quantachrome Instruments analyzer. Electrochemical impedance spectroscopy (EIS) measurements were performed using an Autolab PGSTAT 100 equipped with an FRA32 module to study the charge transfer characteristics and impedance behaviour. Fourier-transform infrared spectroscopy (FT-IR) was employed to investigate the chemical bonding and functional groups present within the scratched powder materials from C1, C2, and C3.

Results and Discussion

3.1 Growth mechanism of thin films formation

To understand the shape evolution of nanostructures, it is essential to investigate the morphological and crystalline properties of the deposited material. In the present study, Cu^{2+} metal ions were complexed with TEA and formed a stable coordination complex. These complexes facilitate slow and controlled release of Cu^{2+} ions under optimized conditions of precursor concentration, pH, and temperature. Aqueous ammonia was used to adjust the pH of the reaction solution. The increased concentration of OH^- ions enhanced the hydrolysis of thiourea, thereby promoting the gradual release of chalcogen ions (S^{2-}) into the solution [11]. However, it was observed that at elevated temperatures, the release rate of metal ions increased excessively, accelerating the reaction and leading to uncontrolled bulk precipitation rather than the formation of high-quality thin films.

Therefore, the deposition conditions were optimized at ambient temperature (300 K), Cu^{2+} precursor concentrations ranging from 0.03 to 0.05 M , and $\text{pH} = 10.5$. These controlled reaction conditions were successfully synthesized uniform and high-quality Cu_2S thin films. The mechanism of film growth follows the nucleation and Ostwald ripening processes, which form the basis of the APT. At ambient temperature, an increase in Cu^{2+} concentration within the 0.03 – 0.05 M range resulted in a favourable reaction rate. This facilitates the formation of small particulate and crystalline thin films with the optimized nucleation and growth.

The nucleation and growth of thin film initiated as soon as the ionic product (K_{IP}) exceeded the solubility product (K_{SP}) of the solution. The nucleation proceeded through an ion-by-ion condensation of Cu^{2+} and S^{2-} ions directly on the substrate surface [11]. Typically, a slower reaction rate leads to improved stoichiometry, crystallinity, and adhesion of the resulting thin films [15]. Thus, the hybrid optimized APT approach is more

effective than conventional chemical bath deposition methods, offering better control over film quality and uniformity.

3.2 Morphological studies

The FE-SEM micrographs were employed to investigate the surface morphology of Cu_2S thin films, which are synthesized at different precursor concentrations. The **Fig. 1** displays the FE-SEM images of C1, C2, and C3 thin films at both low and high magnifications. The C1 Cu_2S thin film exhibits a beaded nanogranular morphology with relatively small grain size of about 50 nm, see **Fig. 1(a) and (b)**. These nanograins are uniformly distributed across the substrate, indicating homogeneous nucleation and growth at this concentration. Whereas, the surface morphology of C2 thin film, reveals a more interconnected nanograins within the size of ~ 70 to 80 nm, as seen in **Fig. 1(c) and (d)**. The nanograins formed at 0.04 M concentrations are more closely interconnected than at 0.03 M. This increase in grain size and degree of aggregation is likely attributed to a higher deposition rate and film thickness resulting from the increased precursor concentration.

Further increasing the concentration to 0.05 M, see **Fig. 1(e) and (f)**, results in a denser and more continuous film morphology. The nanograins appear fully assorted and fused, with grain sizes in the range of ~ 90 to 100 nm. This compact morphology suggests a transition from individual nanograins to a more unified film structure, likely due to enhanced grain growth and aggregation at higher precursor concentrations. The films developed through the self-assembly and interlinking of nanograins, enhances surface area and improve electron transport. The formation of a uniform nanogranular texture through interlinked grains is beneficial for reducing charge transfer resistance and enhancing photoelectrochemical performance.

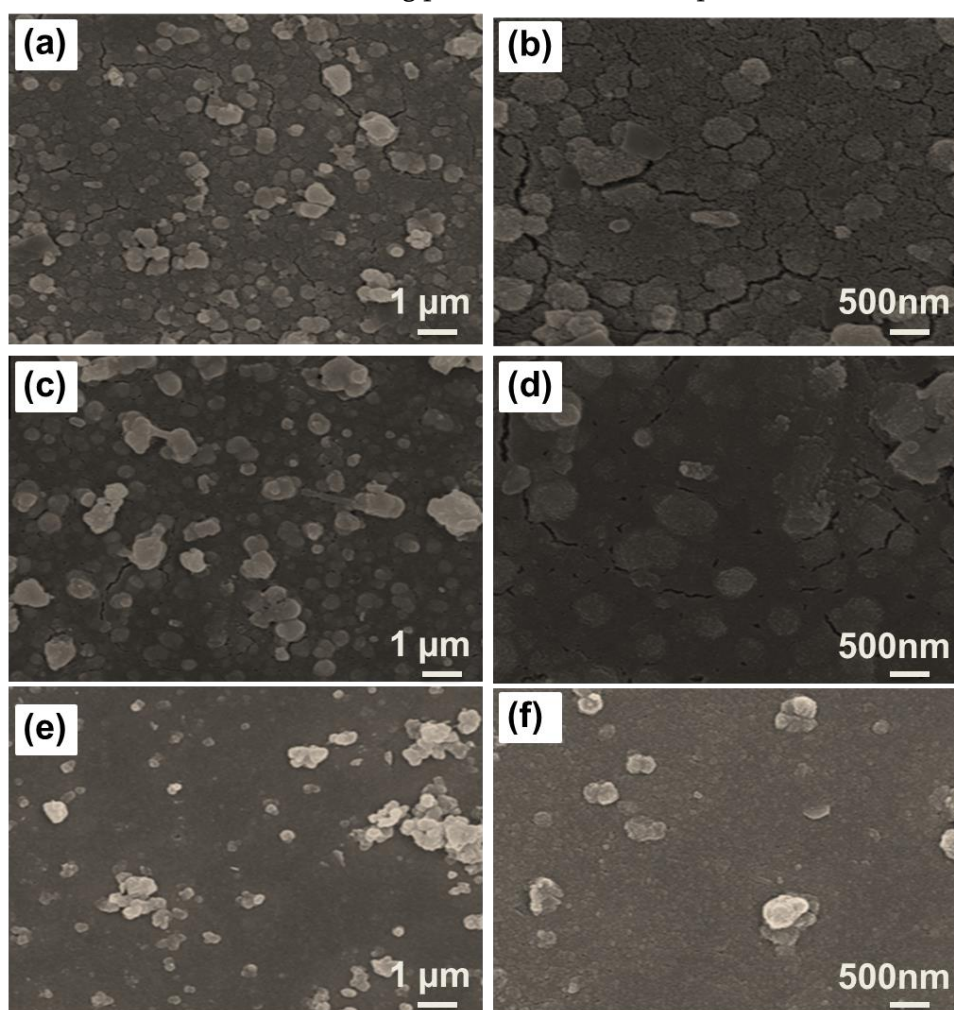


Figure 1. The FE-SEM micrographs of the (a,b) C1, (c,d) C2, and (e,f) C3 Cu_2S thin films.

3.3 Optical studies

The Fig. 2 shows the UV-Vis-NIR absorption spectra of C1, C2, and C3 thin films in the wavelength range 300 – 900 nm. The optical absorption spectra showed the maximum visible absorption peak at the wavelength range of 400–550 nm. The enhancement in the absorption is due to the considerably improved thickness and decreasing band gap value of Cu₂S thin films. The electron excitation from the valance band to the conduction band can be used to determine the value of the optical band gap energy. The optical absorption coefficient is estimated using the equation (1).

$$\alpha = \frac{A(h\nu - E_g)^n}{h\nu} \dots\dots\dots (1)$$

Where A is a parameter that depends on the transition probability, h is the Planck constant, E_g is the optical band gap energy of the material, and the exponent (n) depends on the type of transition. The values of (n) for the direct allowed, indirect allowed, direct forbidden and indirect forbidden transitions are 1/2, 2, 3/2 and 3 respectively.

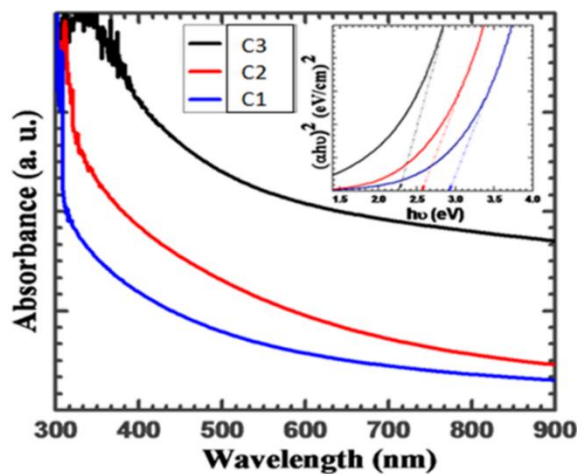


Figure 2. The Optical absorption spectra and inset figure contain Tauc plots of the C1, C2, and C3 Cu₂S thin films.

The linear increase in absorption intensity with decreasing the band gap energy (eV) with increase in thickness of films suggests a direct and allowed type of transition. The band gap energy decreases from 2.91 – 2.26 eV with increase in Cu²⁺ precursor concentration (0.03 - 0.05 M), due to the uniform compact nanogranular thin films. The optical band gap energy values of the Cu₂S thin films were obtained by plotting the graph (b) of (αhν)² (eV/cm)² Vs (hν)(eV) as shown inset of Fig. 2. The obtained optical band gap values very well match with the reported values [16]. The variations of thickness, band gap (E_g) with a concentration of copper precursor are depicted in Table 1.

Table 1. Variation of thickness and optical band gap (E_g) with concentration of copper.

<i>Sr. No.</i>	<i>Sample code</i>	<i>Concentration of Cu²⁺ (M)</i>	<i>Thickness (nm)</i>	<i>Band gap (E_g) (eV)</i>
1	C1	0.03	406	2.91
2	C2	0.04	446	2.55
3	C3	0.05	502	2.26

3.4 Structural studies

The crystal structural analysis and nature of samples were analyzed by X-ray diffraction pattern in the 2θ range of 20 to 80°, as shown in Fig. 3(a). The X-ray diffraction patterns of the Cu₂S thin films (C1, C2, and

C3) exhibits the broad and intense peaks for all the samples, which confirms the Cu₂S pure phase and nano-crystallinity [16]. The major diffraction peaks centered at 2θ values 27.44, 43.82, 51.34, 51.81, 54.44 A° and can be indexed as (111), (220), (311), (311), (222) for cubic crystal system. The experimentally calculated values are good agreement with JCPDS card no.79-1841, 84-1770 and indicate pure crystal structure.

In a typical X-ray diffraction analysis of the Cu₂S thin films, peaks appear at identical positions with amendments to the intensity and broadening the diffraction peaks, which indicates the creation of pure phase materials with an improved crystallinity with increasing thickness of the film. Some of the small intensity peaks reveal the nature of the films amorphous due to glass beads are presents with materials. In addition, no other peaks are observed which reveals that the material has a pure phase. The observed broadening of the diffraction peaks may be due to strain or micro-strain. Further, the crystallite size was calculated using the Debye Scherer formula equation (2)

$$D = \frac{0.9\lambda}{\beta \cdot \cos\theta} \dots \dots \dots (2)$$

Where D is the crystallite size, λ is the wavelength of X-ray radiation (1.5406 Å), β is the fullwidth-at-half-maximum (FWHM) in radians, and θ is Bragg's angle. The calculated crystallite size is improved from 22-34 nm with concentration. This crystallite size with the minimum interfacial energy is beneficial for improving the photon conversion efficiency [17–19].

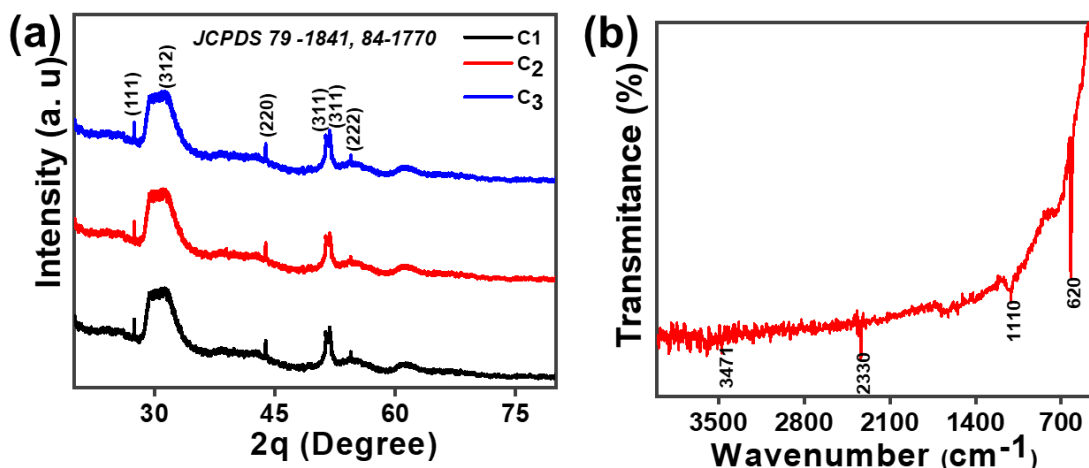


Figure 3.(a) X-ray diffraction patterns of the C1, C2, and C3 Cu₂S thin films.(b) FT-IR Spectrum of C3 Cu₂S material.

3.5 Chemical Characterization

The typical FT-IR spectrum of C3 Cu₂S scratched powder were performed to understand the chemical functional groups present within the sample, as shown in Fig. 3(b). FT-IR spectrum recorded at range 400 - 4000 cm⁻¹ shows the peak at stretching frequency 1134, 2330, 2900 & 3100, 3471 cm⁻¹ are related to the CuS, CN, CH, NH₂ [20]. Although some other peaks are also present due to the surface contamination, remain at a lower proportion [21]. To confirm the surface elemental composition of the C3 thin film, the XPS survey and high-resolution core level measurement has been taken, as shown in Fig. 4(b). The two prominent peaks confirm the presence of Cu, and S elements respectively. Furthermore, elements valance state and the existing form of the Cu₂S thin film was investigated by XPS study as shown in Fig. 4(a), peaks along with C and O in the sample. The core level spectrum of copper Fig. 4(b) shows prominent peaks of Cu2p which can be distinguished. These two peaks located at binding energies of 932.98 eV and 952.99 eV and are assigned to Cu2p_{3/2} and Cu2p_{1/2}, confirming the presence of Cu⁺ in the sample. However, weak satellite shake-up peaks were

also observed at binding energies around 942.3 eV. Moreover, two peaks with binding energies of 932.98 eV and 952.99 eV were assigned to $\text{Cu}2p_{3/2}$ and $\text{Cu}2p_{1/2}$, confirming the presence of Cu^+ with splitting energy of 20.1 eV [22] [23]. The core level spectrum of sulfur **Fig.4 (c)** indicates two strong peaks at binding energies 160.65 eV and 161.9 eV and are assigned to $\text{S}3p_{3/2}$ and $\text{S}3p_{1/2}$ respectively, which is consistent with the S^{2-} in sample with a splitting energy of 1.25 eV. However, the weak peak shown at 166.2 eV at core level indicates that the surface contamination with S^{2-} oxidation state ($\text{S}2p_{1/2}$). The values of the binding energies for Cu and S are at their respective positions for the Cu^+ and S^{2-} valence states. It means that Cu^+ and S^{2-} exists in the stochastic formula of deposited Cu_2S thin film.

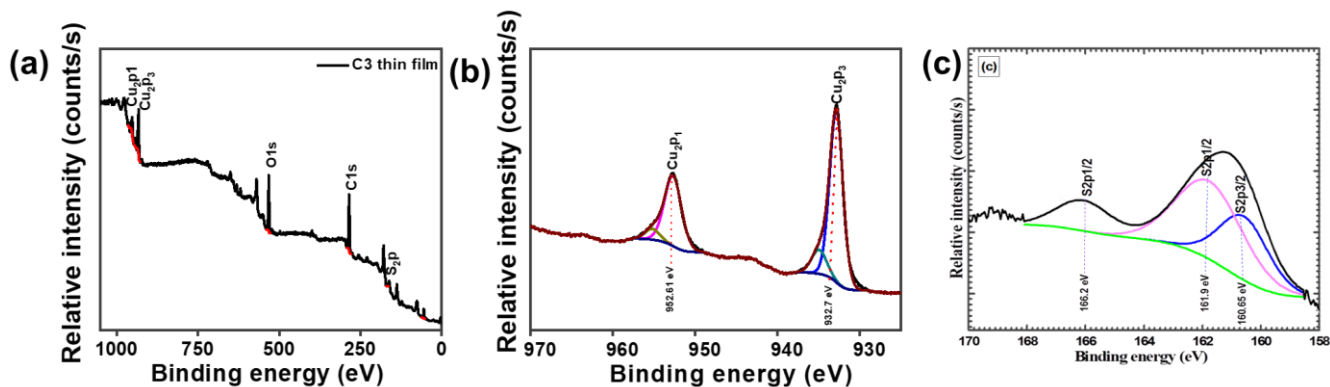


Figure 4. (a) XPS survey spectrum of Cu_2S counter electrode, (b) high-resolution core level XPS spectrum of Cu, (c) high-resolution core level XPS spectrum of S.

3.6 Surface Area Measurement

The specific active surface area and porosity of the C3scratched nanograins powder sample was evaluated by the Brunner, Emmett and Taylor (BET) isotherm, as shown in **Fig.5**. Typical isotherm reveals the adsorption and desorption branch of type II and IV pattern, indicating the presence of micro with mesoporous material having a three-dimensional (3D) intersection classification [24]. It confirms the formation of a multilayer along with monolayer adsorption and desorption hysteresis loop. The obtained specific surface area of nanogranular thin films is $30.840 \text{ m}^2/\text{g}$, as shown in **Fig.5**. This result indicates that the synthesized material has a wider micro-mesoporous structure. The pore radius of 1.8 nm was investigated by desorption branch of the BJH method. This kind of porous and high surface area containing thin film is best choice for a solar cell application. Hence, C3 type of mesoporous structure can be useful for efficient electrolyte diffusion into the electrode in semiconductor solar cells [25].

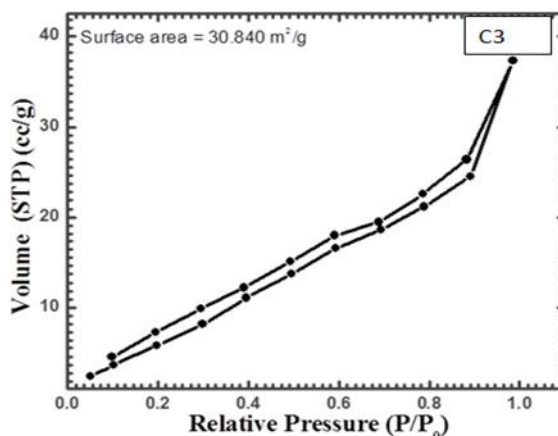


Figure 5. Nitrogen adsorption and desorption isotherm of C3 Cu_2S thin film material

3.7 Electrochemical impedance spectroscopy (EIS) measurement

The EIS measurement was employed to study the kinetics of charges within the Cu₂S thin films. In order to study the effect of concentration on conversion efficiency. EIS measurements were conducted in dark using the 0.2 M polysulfide mediator with applied forward bias voltage - 0.5 V, within the frequency range was 0.1 Hz to 1000 Hz. The Fig.6 (a) reveal the Nyquist plot of C1, C2, and C3 Cu₂S thin films, the equivalents circuit fit the spectra are shown inset of Fig.6 (a). Various parameters obtained for Cu₂S thin films from circuit fitting are listed in Table 2. The solution resistance (R_s), R₁ is the charge transfer resistance between the Pt-FTO counter/electrolyte interface and charge transfer resistance (R₂) related to photo-excited electron hole recombination at Cu₂S/mediator. The electron lifetime (τ_e) value calculated by using formula shown in Eqn.(3), [26] also indicates the electron hole recombination during the PEC operation and obtained from bode plot Fig. 6 (b). From these results we can conclude that electron lifetime increases and the recombination decreases with increase in thickness.

$$\tau_e = \frac{1}{2\pi f} \dots \dots \dots (3)$$

Table 2 Parameters obtained from EIS for Cu₂S electrode systems

Sample code	R _s (Ω/cm ²)	R ₁ (Ω/cm ²)	CPE ₁ (μF)	R ₂ (Ω/cm ²)	CPE ₂ (μF)	τ _e (ms)
C1	71.7	470.6	721.6	778.1	16.12	0.054
C2	77.4	343.1	272.2	845.1	696.8	0.056
C3	74.2	413.1	293.7	526.4	262.6	0.061

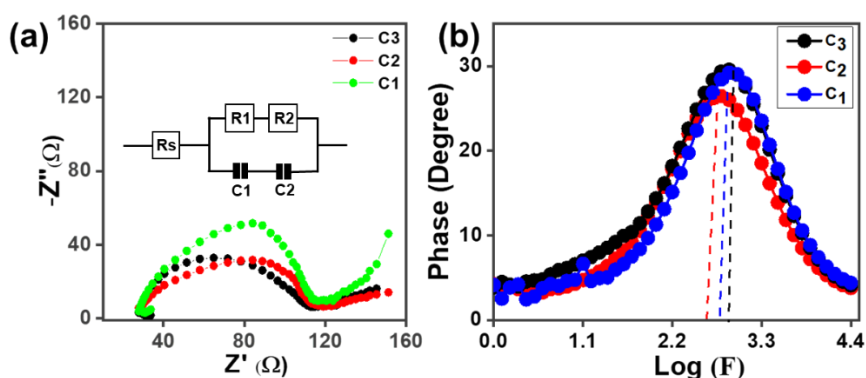


Figure 6 (a) Nyquist plot of Cu₂S samples, inset shows its fitted equivalent circuit and (b) Bode plot of the Cu₂S samples.

Conclusions

Concisely, nanogranular Cu₂S thin films have been synthesized using single-solution phase arrested precipitation technique. The effect of Cu⁺ ion concentration on the morphology has been studied systematically. Opto-structural and morphological studies reveal Cu₂S thin films have controls over the directional crystal growth due to crucial role containing TEA, tuning of band gap energy 2.92 - 2.26 eV. XRD pattern results the crystalline nature with pure monoclinic crystal structure, which controls the ion insertion kinetics leading to a charge transfer reaction. Stochastic Cu₂S thin film at chemical valance state is confirmed by XPS. BET study reveals that the nanograins have micro-mesoporous nature of the C3 sample with highest surface area of 30.840 m²/g. It was demonstrated that the deposited Cu₂S counters have hold potential and exhibit good electronic properties for optoelectronic device fabrication.

REFERENCES

- [1]. G. Chen, J. Seo, C. Yang, and P. N. Prasad, *Chem.Soc. Rev.* 42, 8304 (2013).
- [2]. K. V. Khot, S. S. Mali, N. B. Pawar, R. R. Kharade, R. M. Mane, V. V. Kondalkar, P. B. Patil, P. S. Patil, C. K. Hong, J. H. Kim, J. Heo, and P. N. Bhosale, *New J. Chem.* 38, 5964 (2014).
- [3]. X. Yu, J. Zhu, F. Liu, J. Wei, L. Hu, and S. Dai, *Sci. China Chem.* 56, 977 (2013).
- [4]. M. Page, O. Niitsoo, Y. Itzhaik, D. Cahen, and G. Hodes, *Energy Environ. Sci.* 2, 220 (2009).
- [5]. H. K. Jun, M. A. Careem, and A. K. Arof, *Nanoscale Res. Lett.* 9, 69 (2014).
- [6]. X. Song, X. Ji, M. Li, W. Lin, X. Luo, and H. Zhang, *Int. J. Photoenergy* 2014, 1 (2014).
- [7]. J.-W. Shiu, Z.-J. Lan, C.-Y. Chan, H.-P. Wu, and E. Wei-Guang Diao, *J. Mater. Chem. A* 2, 8749 (2014).
- [8]. E. Dilena, D. Dorfs, C. George, K. Miszta, M. Povia, A. Genovese, A. Casu, M. Prato, and L. Manna, *J. Mater. Chem.* 22, 13023 (2012).
- [9]. P. Vas-Umnuay and C-H Chang, *ECS J. Solid State Sci. Technol.* 2, 120 (2013).
- [10]. P. Zhang and L. Gao, *J. Mater. Chem.* 13, 2007 (2003).
- [11]. A. R. Patil, V. N. Patil, P. N. Bhosale, and L. P. Deshmukh, *Mater. Chem. Phys.* 65, 266 (2000).
- [12]. A. D. Dhondge, S. R. Gosavi, and N. M. Gosavi, *World J. Condens. Matter Phys.* 5, 1 (2015).
- [13]. H. Zhang, R. L. Penn, Z. Lin, and H. Cölfen, *CrystEngComm* 16, 1407 (2014).
- [14]. F. Liu, J. Zhu, L. Hu, B. Zhang, J. Yao, M. K. Nazeeruddin, M. Grätzel, and S. Dai, *J. Mater. Chem. A* 3, 6315 (2015).
- [15]. S. P. Patil, R. M. Mane, R. R. Kharade, and P. N. Bhosale, *Dig. J. Nanomater. Biostructures* 7, 237 (2012).
- [16]. N. B. Pawar, S. S. Mali, S. D. Kharade, M. G. Gang, P. S. Patil, J. H. Kim, C. K. Hong, and P. N. Bhosale, *Curr. Appl. Phys.* 14, 508 (2014).
- [17]. S. S. Jadhav, C. K. Hong, P. S. Patil, P. N. Bhosale, and G. N. Mulik, *J. Mater. Sci. Mater. Electron.* 4, 3812 (2016).
- [18]. S. S. Jadhav, S. S. Mali, C. K. Hong, P. S. Patil, P. N. Bhosale, and G. N. Mulik, *Mater. Lett.* 217, (2018).
- [19]. R. M. Mane, V. B. Ghanwat, V. V. Kondalkar, K. V. Khot, S. R. Mane, P. S. Patil, and P. N. Bhosale, *Procedia Mater. Sci.* 6, 1285 (2014).
- [20]. P. Roy and S. K. Srivastava, *Growth Lett.* 6, 6 (2006).
- [21]. J. Coates, *Encycl. Anal. Chem.* 10815 (2000).
- [22]. D. Li, Z. Zheng, Y. Lei, S. Ge, Y. Zhang, Y. Zhang, K. W. Wong, F. Yang, and W. M. Lau, *CrystEngComm* 12, 1856 (2010).
- [23]. J. Wang, D. Xue, Y. Guo, J. Hu, and L. Wan, *J. Am. Chem. Soc.* 18558 (2011).
- [24]. R. Govindaraj, M. S. Pandian, P. Ramasamy, and S. Mukhopadhyay, *Int. J. ChemTech Res.* 6, 5220 (2014).
- [25]. D. Susanti, M. Nafi, H. Purwaningsih, R. Fajarin, and G. E. Kusuma, *Procedia Chem.* 9, 3 (2014).
- [26]. T. L. P. Nguyen, X. T. L. Binh, A. R. Andersen, P. E. Hansen, *Eur. J. Inorg. Chem.* 2, 2533 (2011).

Renewable Energy Technology: Bridging Chemistry and Physics for a Sustainable Future

Shaikh Mohd. Azhar¹, Shaikh Baseer², Takale S.N.², Shaikh Kabeer Ahmed²

¹Department of Physics Sir Sayyed College, Aurangaabad-431001, Maharashtra, India

²Department of Chemistry, Sir Sayyed College, Aurangaabad-431001, Maharashtra, India

ARTICLE INFO

Article History:

Published : 30 April 2025

Publication Issue :

Volume 12, Issue 13

March-April-2025

Page Number :

225-227

ABSTRACT

The convergence of chemistry and physics has the potential to revolutionize our approach to sustainability. The integration of chemistry and physics plays a pivotal role in advancing renewable energy technologies essential for achieving sustainability. This paper explores how fundamental principles from both disciplines converge to drive innovations in solar energy, hydrogen fuel, battery storage, and carbon-neutral technologies. By leveraging interdisciplinary approaches, researchers can address energy efficiency, scalability, and environmental impact. The paper discusses recent advancements, practical applications, and future directions, emphasizing the potential of renewable energy to mitigate climate change and foster sustainable development.

Keywords: approach to sustainability, Renewable Energy, mitigate climate change, Carbon neutral technology, scalability

INTRODUCTION

The transition to renewable energy sources is critical for addressing global energy demands while reducing carbon emissions. Chemistry and physics, as foundational sciences, provide the theoretical and experimental frameworks necessary for developing efficient and sustainable energy technologies. This paper examines how these fields intersect to advance renewable energy systems, including solar photovoltaics, hydrogen fuel cells, and energy storage solutions.

Theoretical Foundations

2.1 Quantum Mechanics in Energy Conversion

Quantum mechanics explains the behaviour of electrons and photons, crucial for understanding photovoltaic systems and photocatalytic processes. Quantum tunnelling and band gap engineering are key concepts in optimizing solar cell efficiency.

2.2 Thermodynamics and Energy Efficiency

Thermodynamic principles govern the efficiency of energy conversion and storage systems. Concepts such as Gibbs free energy, enthalpy, and entropy are central to designing effective fuel cells and batteries.

2.3 Electromagnetic Interactions

Physics provides insights into light-matter interactions, which are fundamental for designing solar cells and photochemical reactors. Techniques such as plasmonics enhance light absorption and conversion efficiency.

RENEWABLE ENERGY TECHNOLOGIES

3.1 Solar Energy

3.1.1 Photovoltaics

Advancements in Materials: Perovskite solar cells demonstrate how chemical synthesis and physical characterization lead to high-efficiency, cost-effective solutions. Physics of Light Absorption: Band gap optimization ensures maximum photon absorption and electron excitation.

3.1.2 Solar Fuels

Photocatalysis: Chemistry enables the design of catalysts that utilize sunlight to split water into hydrogen and oxygen. Artificial Photosynthesis: Mimicking natural processes to produce chemical fuels from CO₂ and water.

3.2 Hydrogen Fuel Technologies

3.2.1 Electrolysis

Catalyst Development: Chemistry focuses on developing robust and efficient electrocatalysts, such as platinum-based and non-metallic alternatives.

Physics of Ion Transport: Understanding ion conductivity and membrane performance enhances electrolysis efficiency.

3.2.2 Fuel Cells

Chemical Reactions: Hydrogen and oxygen combine to produce electricity, with water as the by-product. Physical Optimization: Proton exchange membranes (PEMs) and electrode materials are critical for performance and durability.

3.3 Energy Storage Systems

3.3.1 Batteries

Lithium-ion Technology: Chemistry contributes to developing high-capacity anodes and cathodes, while physics focuses on charge transport and thermal management. Next-Generation Batteries: Solid-state and flow batteries promise higher energy densities and safety.

3.3.2 Super capacitors

Material Innovation: Nanostructured materials bridge chemical synthesis and physical properties, enhancing energy storage and discharge rates.

3.4 Carbon-Neutral Technologies

3.4.1 Carbon Capture and Utilization (CCU)

Chemical Absorption: Developing solvents and adsorbents for efficient CO₂ capture.

Physical Processes: Compressing and storing CO₂ using advanced materials.

3.4.2 Synthetic Fuels

Catalytic Conversion: Using heterogeneous catalysts to convert captured CO₂ into hydrocarbons. Energy Inputs: Combining renewable electricity with chemical processes.

CHALLENGES:

- i. To develop abundant and recyclable materials for solar cells, batteries, and fuel cells.
- ii. To enhance energy conversion efficiency and scaling technologies for global deployment.

CONCLUSION

Combining photovoltaic panels with hydrogen production units creates a sustainable cycle for energy generation and storage. Small-scale solar and wind systems integrated with battery storage and fuel cells provide reliable energy for remote areas. Renewable technologies are being adopted in industries such as transportation and manufacturing. Bridging chemistry and physics is vital for driving innovations in renewable energy technologies. By addressing technical challenges and fostering interdisciplinary collaboration, these fields will play a central role in achieving a sustainable future. Advances in materials, energy conversion, and storage will enable the widespread adoption of clean energy solutions, reducing reliance on fossil fuels and mitigating climate change. Governments must support renewable energy through policy frameworks and investments in infrastructure.

REFERENCES

- [1]. Lewis, N. S., & Nocera, D. G. (2006). Powering the planet: Chemical challenges in solar energy utilization. *Proceedings of the National Academy of Sciences*, 103(43), 15729-15735.
- [2]. O'Regan, B., & Grätzel, M. (1991). A low-cost, high-efficiency solar cell based on dye-sensitized colloidal TiO₂ films. *Nature*, 353(6346), 737-740.
- [3]. Turner, J. A. (1999). A realizable renewable energy future. *Science*, 285(5428), 687-689.
- [4]. Goodenough, J. B., & Park, K. S. (2013). The Li-ion rechargeable battery: A perspective. *Journal of the American Chemical Society*, 135(4), 1167-1176.
- [5]. Wang, Q., & Medlin, J. W. (2020). Heterogeneous catalysis at the bio-interface: Improving performance in renewable energy systems. *Chemical Society Reviews*, 49(14), 5086-5105.
- [6]. Crabtree, G. W., Dresselhaus, M. S., & Buchanan, M. V. (2004). The hydrogen economy. *Physics Today*, 57(12), 39-44.
- [7]. Zhang, Z., & Wang, X. (2018). Sustainable hydrogen production from water electrolysis: Advances in high-temperature electrolysis technology. *Chemical Engineering Journal*, 337, 203-225.
- [8]. Manthiram, A. (2020). An outlook on lithium ion battery technology. *Nature Communications*, 11(1), 1550.
- [9]. Hunt, A. J., & Farmer, T. J. (2020). Renewable feedstocks for green chemistry: Unlocking value from waste. *Green Chemistry*, 22(19), 5195-5207.
- [10]. Chu, S., & Majumdar, A. (2012). Opportunities and challenges for a sustainable energy future. *Nature*, 488(7411), 294-303.

Role of Some Fused Pyrimidine compounds in Medicinal Chemistry

Prashant N. Ubale

Department of Chemistry, Late Babasaheb Deshmukh Gorthekar College, Umri-431807, Maharashtra, India

ARTICLE INFO

Article History:

Published : 30 April 2025

Publication Issue :

Volume 12, Issue 13

March-April-2025

Page Number :

228-230

ABSTRACT

Pyrimidines and its fused compounds with other heterocyclic ring are essential biochemical components in living organisms. It is a heterocyclic organic compound contains multiple heteroatom and carbon atoms. Pyrimidines and its related fused derivatives plays crucial role in biological system as they are the backbones of several important biomolecules, including nucleic acid. Pyrimidine is the building block of vitamins, amino acids, proteins etc. It plays important role against vital diseases. Pyrimidines are present in vitamins like thiamine and riboflavin which are found in milk, egg and liver, folic acid, barbituric acid, coenzymes, purines, nucleotides, pterins alkaloids from coffee, tea etc.

Keywords: Pyrimidine, Biological importance, fused compounds, drugs, heterocycles etc.

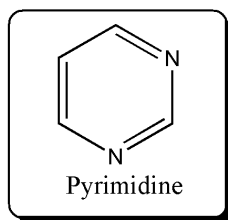
INTRODUCTION

Heterocyclic compounds are cyclic rings of atoms that contain at least one heteroatom. The most commonly used hetero-atoms are nitrogen, oxygen, and sulfur, selenium etc. Heterocyclic chemistry is the interesting branch of organic chemistry and interesting practical and theoretical importance. Heterocycles are the most important traditional division of research because of their medicinal, anti-microbial, and industrial applications. As a result of this a great deal of research conducted in chemistry is devoted to heterocyclic chemistry.

Heterocycles are widely distributed in nature. It is an expanding and vast field in chemistry because of use of compounds derived from heterocycles in pharmacy, medicine, agriculture, plastics, polymers, and other areas. Due to their biological importance heterocycles are employed in the treatment of infectious diseases. Various heterocycles prepared in laboratories are successfully used as clinical agents. The heterocyclic compounds such as pyridine, pyrimidine, quinoline, Isoquinoline, pyrazole, Pyrrole, benzimidazole, Benzothiazole, fused heterocycles – pyrimido-pyrimidine, pyrimido-benzothiazole, Pyrido-pyrimidine, thiazolo-pyrimidine, imidazolo[1,2-a]pyrimidine etc. shows the remarkable biological activity.

One of the heterocyclic compound which is important constituents in living organism is Pyrimidine. Pyrimidines are 6-membered heterocyclic ring compounds composed of two nitrogen and four carbon atoms.

Pyrimidine is a colourless crystalline solid with melting point is 22°C and boiling point 123-124°C. It dissolve in water and give a neutral solution. The molecular formula is – C₄H₄N₂ with molar mass 80gm.



Pyrimidine is a basic core skeleton in many naturally occurring biological compounds. It naturally occurs in Vitamins such as riboflavin, thiamine found in milk, egg liver, folic acid from liver and yeast, barbituric acid. Pyrimidine is the basic building block of nucleic acid components such as uracil, cytosine and thymine etc. It is also found in coenzymes, purines, nucleotides, alkaloids from tea, coffee and cocoa. The pyrimidine ring system has wide existence in nature as substituted ring fused compounds. The pyrimidine derivatives such as uric acid and alloxan were known in the early 19th century.

Pyrimidines occupy a distinct and remarkable place in biological system. A large extensive array of pyrimidine drugs possesses a variety of medicinal properties such as anti-inflammatory, antiherpes virus, anti-infective, selective human A₃ adenosine receptor antagonistic, antifungal, antioxidant and antitumor, herbicidal, anticancer, antiplasmodial, anticonvulsant¹⁰, herbicidal¹¹ and many pyrimidines derivatives are reported to possess calcium channel blockers.

Fused Pyrimidine Compounds:

1. **Pyrimido-Benzimidazole:** Benzimidazole is a fused heterocyclic aromatic compound. It is the combination of benzene ring and imidazole ring. Benzimidazole moiety shows a prominent importance in medicinal chemistry. The application of pyrimido benzimidazole widely used of in medicinal chemistry. Different substituted pyrimido benzimidazole shows remarkable activity which are very much important against life threatening diseases. pyrimido benzimidazole have very good medicinal value.
2. **Pyrazolo-Pyrimido-Benzimidazole:** When pyrimido benzimidazole fused with pyrazole to form pyrazolo pyrimido benzimidazole. This moiety contain three basic heterocyclic ingredients as pyrazole, pyrimidine and benzimidazole which contain five nitrogen in the fused ring system. Literature survey reveals that very little work is carried on synthesis of pyrazolo pyrimido benzimidazole.
3. **Pyrimido-Pyrimidine:** Pyrimido pyrimidine is the three to four nitrogen atoms containing fused heterocyclic compound. Pyrimido pyrimidines are important category of annelated uracils with pharmacological significance because of resemblance with purine pteridine. Substituted pyrimido pyrimidines are used against multiple severe diseases.
4. **Pyrazolo-Pyrimidine:** In the field of nitrogen containing heterocycles, pyrazole and fused pyrimidines bearing polycyclic compounds has prominent importance in medicinal science. Pyrazolo pyrimidine is one of them fused polycyclic compounds. Pyrazolo pyrimidines show the similarity in structure with biogenic purine which shows the same properties as antimetabolites in biochemical reactions.
5. **Pyrimido-Benzothiazole:** Pyrimido benzothiazoles are also the nitrogen and sulphur containing 3-4 ring heterocyclic compounds. Pyrimido benzothiazole is one of the most essential class of fused heterocycles where it shows potential role in drug synthesis.
6. **Pyrimido Quinoline:** When Pyridine ring fused with benzene is called quinoline and quinoline fused with pyrimidine then it is called pyrimido quinoline. Pyrimido quinoline recognized as an intriguing scaffold in

drug discovery. Researchers appreciate its fused heterocyclic framework, which offers diverse interactions with biological targets for making it a valuable lead structure for various therapeutic areas.

7. **Thiazolo Pyrimidine:** Thiazolopyrimidine is a bicyclic heterocyclic compound formed by the fusion of thiazole and pyrimidine ring. Thiazolo pyrimidines and its derivatives are well known moiety in various drugs moiety.

Biological Significance:

The compound containing pyrimidine nucleus fused with other heterocycles possess broad spectrum of biological activity like 5-fluorouracil as anticancer agent, trimethoprim, sulphamethiazine as antibacterial agent, zidovudine and stavudine as anti-HIV agent, idoxuridine and triflouridine as antiviral agent, phenobarbitone as sedative agent. Fused pyrimidine antagonists acts as block pyrimidine nucleotides synthesis and also leads to the stoppage of DNA synthesis and inhibition of cell division.

Conclusion:

Naturally Pyrimidine ring is the building blocks in living organism whether it may be in nucleic acid or vitamins. Pyrimidine is a core skeleton in many naturally occurring biological compounds. Fused compounds of pyrimidine with other ring used as drugs in several vital diseases as we discussed above. Because of its versatile use in medicinal chemistry, pyrimidine skeleton grabbed attention of scientist in medical field.

REFERENCES

- [1]. B. Tozkoparan, M. Ertan, P. Kelicen and R. Demirdamar; *Farmaco*, 1999, 54, 588–593.
- [2]. S. Shigeta, S. Mori, F. Watanabe, K. Takahashi, T. Nagata, N. Koike, T. Wakayama and M. Saneyoshi; *Antiviral Chemistry & Chemotherapy*, 2002, 13, 67–82.
- [3]. Moni Sharma, Vinita Chaturvedi, Y. K. Manju, Shalini Bhatnagar, Kumkum Srivastava, S. K. Puri, Prem, M. S. Chauhan; *Eur. J. Med Chem.*, 2009, 44, 2081–2091.
- [4]. Pier Giovanni Baraldi, Barbara Cacciari, Stefano Moro, Giampiero Spalluto, Giorgia Pastorin, Tatiana Da Ros, Karl-Nobert Klotz, Katia Varani, Stefania Gessi, Pier Andrea Borea; *Eur J. Med Chem.*, 2003, 38, 367–382. Chapter – II Synthesis of Pyrimido Benzimidazole Derivatives.
- [5]. Essam Mohamed Sharshira, Nagva Mohamed, Mahrous Hamada; *American J. Org Chem.*, 2012, 2(2), 26–31.
- [6]. A. A. Abu-Hashem, M. M. Youssef, and H. A. R. Hussein; *Journal of Chinese Chemical Society*, 2011, 58(1), 41–48.
- [7]. Y. Nezu, M. Miyazaki, K. Sugiyama; *Pesticide Science*, 1996, 47, 103–113.
- [8]. F. Xie, H. Zhao, L. Zhao, L. Lou, and Y. Hu; *Bioorganic and Medicinal Chemistry Letters*, 2009, 19(1), 275–278.
- [9]. Hardeep Kaur, Kamaljit Singh et.al.; *European Journal of Medicinal Chemistry*, 2015, 101, 52–62.
- [10]. A. K. Gupta, H. P. Kayath, A. Singh, G. Sharma, and K. C. Mishra; *Indian Journal of Pharmacology*, 1994, 26(3), 227–228.
- [11]. Y. Nezu, M. Miyazaki, K. Sugiyama, and I. Kajiwara; *Pesticide Science*, 1996, 47, 103–113.
- [12]. B. Kumar, B. Kaur, J. Kaur, A. Parmar, R. D. Anand, and H. Kumar; *Indian Journal of Chemistry B*, 2002, 41(7), 1526–1530.

Review Article on Application of Zeolite Nanomaterial for Environmental Remediation

Sadiya Patel¹, Surabhi Chourey²

¹Assistant Professor, Department of Chemistry, Government Degree College, Timarni Dist- Harda-461228, Madhya Pradesh, India

²Assistant Professor, Department of Physics, Government Degree College, Timarni Dist- Harda-461228, Madhya Pradesh, India

ARTICLE INFO

Article History:

Published : 30 April 2025

Publication Issue :

Volume 12, Issue 13

March-April-2025

Page Number :

231-237

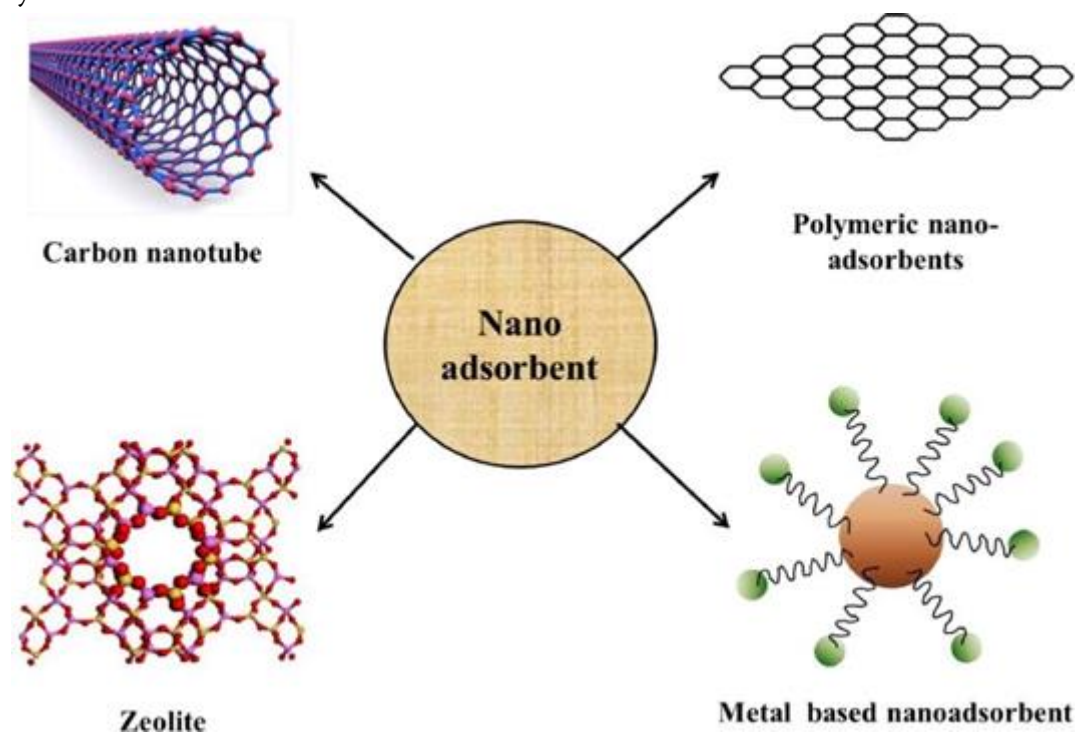
ABSTRACT

Environmental remediation techniques have been completely transformed by nanomaterials, which provide economical, sustainable, and effective ways to address the growing pollution problems. Among these, zeolites—crystalline, microporous aluminosilicates—stand out for their exceptional adsorption, ion-exchange, and molecular sieving capabilities. Heavy metals, ammonia, radioactive elements, medicines, and organic pollutants from air, water, and soil can all be selectively captured and retained to their special three-dimensional network of channels and cavities. While synthetic zeolites can be designed for specific uses and improved performance. Natural zeolites, like clinoptilolite, are much esteemed for their availability, affordability, and environmentally favourable profile. Zeolite nanomaterials have emerged as versatile and effective tools in environmental remediation due to their unique structural properties, including high surface area, tunable pore sizes, and ion-exchange capabilities. This paper focuses the modification, and application of zeolite-based nanocomposites in treatment of various environmental pollutants such as heavy metals, dyes, ammonia, microplastics, and radioactive contaminants. The review highlights recent advancements, mechanisms of pollutant removal, and future prospects in the field. Research into zeolite and their application will further strengthen their role as a cornerstone of nanomaterial-based environmental remediation in the current era.

Keywords: - Nanomaterial, Zeolites, Microporous materials, Aluminosilicates, Contaminants

INTRODUCTION

Both developed and developing nations are now worried about environmental degradation. The main causes of air, water, and land contamination are intensive farming practices and widespread industrialization. Environmental pollution, particularly water contamination, poses significant threats to ecosystems and human health. For the environment remediation various traditional methods have been used from many years. Less popularity of these methods due to high costs and inefficiency. Numerous conventional techniques used for treating various environmental contaminants has certain drawbacks and limitations. As a result, a different approach that is more efficient, less harmful, and yields superior results is needed. When it comes to environmental clean-up, nanomaterials have generated a lot of interest. Zeolite nanomaterials, owing to their nanoscale dimensions and inherent properties, offer promising alternatives for sustainable and efficient pollutant removal. Surface alterations increase the zeolites' adaptability by increasing their attraction for particular contaminants and expanding their remediation range. Zeolites are notable for their potent regenerative properties, which enable repeated use and long-term remedial effectiveness. Their effective use in nuclear waste management, wastewater treatment, and mining site rehabilitation highlights their applicability and versatility.



Classification of nanoadsorbent © Ningthoujam, R. et. al. (2022) [1]

Characterization methods of zeolites

Characterization is also very important step to study the zeolite structure and identify it for further use. Different experimental methods like XRD, IR, AES ICP, SEM-EDX, TGA DTG and N₂ ADSORPTION will be used to characterize the zeolite. [2]

Infrared Spectroscopy is used to provide information about the the major structural groups present in zeolite . Especially mid IR region [400 – 4000 cm⁻¹] is used for the determination of zeolite structure type, groups, and for secondary building units. Finger printing region of zeolites ranges from 1500 – 400 cm⁻¹ in infrared spectroscopy.

Structural information of the zeolite can be obtained by X Ray-Diffraction. XRD explain transformation in the structure due to many reasons.

Trace elements present in zeolite are studied by AES ICP method.

In zeolite mainly different sizes of pores and structures of zeolites are responsible for the various applications. . Nitrogen adsorption/desorption is highly efficient technique determine the pore size, surface area of mesopores and distribution of it.

SEM is a powerful tool for morphological studies of zeolite, which gives complete knowledge of structure and distribution of particle size. In SEM different images of zeolites are taken by the help of different signals produced by various energy sources. These energy sources fall on the surface of zeolite and by the help of signals, images of zeolite surface are produced which give idea of morphology and distribution of particles.

To characterize zeolite more precisely SEM is used in the combination with EDX. Energy - dispersive X-ray spectroscopy (EDX, EDS, XEDS) or Energy-dispersive X-ray analysis (EDXA). It is an analytical technique used for the elemental analysis and chemical characterization of zeolites. [3]

Properties of Zeolite Nanomaterials

Zeolites possess a 3D network of channels and cavities, functioning as molecular sieves. Key properties include:

3.1 Structural Characteristics

Zeolites are crystalline aluminosilicates with a microporous structure. At the nanoscale, zeolites exhibit enhanced surface area and reactivity, which are crucial for adsorption and catalytic processes. Their uniform pore sizes allow selective adsorption of pollutants based on molecular dimensions. [4]

3.2 High surface area: Enhances adsorption of contaminants like heavy metals (e.g., As, Cd, Pb)

3.3 Ion-Exchange Capacity: The ion-exchange properties of zeolites enable them to replace harmful cations in polluted water with less toxic or benign ions, facilitating the removal of heavy metals and other contaminants. This property is very useful for the treatment industrial effluent which causes water pollution. [5] Replaces harmless ions (e.g., Na⁺) with toxic ions (e.g., Hg²⁺, Pb²⁺) [6]

3.4 Thermal/chemical stability: Retains functionality under extreme conditions. [7]

3.5 Modifiability: Surface functionalization (e.g., nanoparticles, polymers) improves selectivity and efficiency [8]

CATION EXCHANGE CAPACITY OF DIFFERENT ZEOLITES								
CATION EXCHANGE CAPACITY (CEC%)							CONDITION	REFERENCES
IONS	TYPE OF ZEOLITES							
	CLI	MOR	CHA	STI	HEU	SCO		
Ca ²⁺	87-98	87-98					Conc. Of NH ₄ ⁺ +150gm/L	[9] M.L.Nguyen,(1998)
NH ₄ ⁺	86.4			54.8	76	20	Conc. Of NH ₄ ⁺ 25 ppm	[10] S.D. Ghan,(2005)
NH ₄ ⁺	95						Conc.of NH ₄ ⁺ +50gm/L	[11] M.Z.Swiatek,(2010)
Cr ³⁺						96	In standard conditions	[12] K.Margeta,(2013)
Ni ²⁺	75		98			40		
Cd ²⁺	90					59		
Zn ²⁺	85		98					

Cu ²⁺	90		98					
Cr ³⁺						73.55	Conc. Of metal ions 20 ppm	[13] B.Salunkhe,(2012)
Ni ²⁺						63.63		
Cr ³⁺						91.5	Concentration of metal ions 50gm/L	[14] W.A. Carvalho, (2005)
Ni ²⁺						96		
Cd ²⁺						84		
Mn ²⁺						75		
Ni ²⁺						96		
Cd ²⁺						84		
Mn ²⁺						75		
Cr ³⁺	16.6						Conc. Of sorbent 5gm/50ml	[15] Sh.V.Khachatryan ,(2014)
Cd ²⁺	20							
Zn ²⁺	13.6							
Cu ²⁺	45							
Mn ²⁺	11.1							
Ni ²⁺	10							
Pb ²⁺	90		77				Conc. Of ions 50 gm/L	[16] B.K.Payne,(2004)
Cu ²⁺	66.1						Conc. Of metal ions 100-400mg/L	[17] E.Erdem,(2004)
Zn ²⁺	45.96							
Mn ²⁺	19.84							
Co ²⁺	77.96							
Zn ²⁺	86			97			Conc. Of ions 25gm/L	[18] M.Golomeova(2014)
Cu ²⁺	98			100				
NH ₄ ⁺	95.2						Conc. Of ions 50 gm/L	[19] M.Lebedynets(2004)

Applications in Environmental Remediation

4.1 Heavy Metal Removal

Zeolite nanocomposites have shown high efficiency in adsorbing heavy metals such as lead (Pb), copper (Cu), and nickel (Ni) from contaminated water. Activated carbon-zeolite composites demonstrate an outstanding capacity of 213.3 mg/g for Pb removal, showcasing the effectiveness of hybrid materials.

4.2 Dye and Organic Pollutant Degradation

Zeolite-based composites, such as chitosan/zeolite, exhibit an adsorption capacity indigo carmine dye, demonstrating excellent potential for dye removal. [20]

4.3 Ammonia and Phosphate Removal

Zeolite composites like TiO₂/zeolite nanocomposites have been developed to remove ammonium and phosphate ions from wastewater, addressing issues related to eutrophication. These composites exhibit significant adsorption capacities, making them effective in nutrient removal. [21]

4.4 Microplastic and Trace Metal Removal

Zeolites are modified with different ions, metals, metal oxides, carbon materials, and polymers. These modified zeolites are very effective for separating and adsorbing multiple contaminants from water. These composites offer enhanced mechanical, catalytic, adsorptive, and porosity properties necessary for sustainable water purification techniques compared to individual composite materials. [22]

4.5 Radioactive Contaminant Removal

Synthetic nano-zeolites, including zeolite A, zeolite Y, zeolite X, CHA, and MOR, have been investigated for the removal of radioactive contaminants. These zeolites, when modified with magnetic or polymeric matrices, demonstrate effective adsorption capacities for radioactive ions, offering a promising approach for mitigating radioactive pollution. [23]

Mechanisms of Pollutant Removal

5.1 Adsorption

Zeolite nanomaterials remove pollutants through physical adsorption, where contaminants adhere to the surface of the zeolite. The adsorption capacity of zeolite can be enhanced by the high surface area and microporous structure. [24]

5.2 Ion Exchange

Zeolites facilitate ion exchange, replacing harmful cations in polluted water with less toxic ions, thereby removing heavy metals and other contaminants. [25]

5.3 Photocatalysis

Modified zeolite composites, such as $\text{TiO}_2/\text{zeolite}$, can degrade organic pollutants under light irradiation, breaking down complex molecules into simpler, less harmful substances. [26]

5.4 Bioremediation

Zeolite composites can support microbial activity, aiding in the degradation of organic pollutants. For example, immobilized enzymes on zeolite surfaces enhance the breakdown of specific contaminants. [27]

Mechanisms of Action

6.1 Ion Exchange: Zeolites swap innocuous ions (e.g., Na^+) for toxic ions (e.g., Pb^{2+}) [6]

6.2 Adsorption: Contaminants bind to zeolite surfaces via electrostatic interactions or van der Waals forces

6.3 Catalytic Degradation: Nanoparticle-doped zeolites generate reactive oxygen species to decompose organic pollutants

Challenges and Future Directions

7.1 Regeneration and Reusability

The ability to regenerate zeolite nanomaterials after pollutant adsorption is crucial for sustainable applications. Research into efficient regeneration methods is ongoing to enhance the practicality of zeolite-based remediation technologies.

7.2 Scale-Up and Commercialization

Translating laboratory-scale successes to industrial-scale applications involves addressing challenges related to cost, scalability, and integration into existing treatment systems.

7.3 Environmental Impact

Assessing the environmental impact of zeolite nanomaterials, including potential toxicity and lifecycle analysis, is essential to ensure their safe and sustainable use.

Conclusion

Zeolite nanomaterials offer a promising solution for environmental remediation, with applications spanning heavy metal removal, dye degradation, nutrient removal, and radioactive contaminant mitigation. Their unique properties and versatility make them valuable components in the development of sustainable water treatment technologies. Continued research and development are essential to overcome existing challenges and fully realize the potential of zeolite-based nanocomposites in environmental remediation.

REFERENCES

- [1]. Rina Ningthoujam, Yengkhom Disco Singh, Punuri Jayasekhar Babu, Mrinal Kumar Sarma, Nanocatalyst in remediating environmental pollutants ; *Chemical Physics Impact*, Vol 4, (2022), 100064
- [2]. Ho Soon Min; Zeolite: review of characterization and applications; *International Journal of Chemical and Biochemical Sciences* (2023) pp 704-715
- [3]. Sophie H. van Vreeswijk and Bert M. Weckhuysen; Emerging analytical methods to characterize zeolite-based materials ; *Natl Sci Rev.* (2022) Vol. 9, pp 1-20
- [4]. Sheetal Kumari , Jyoti Chowdhry , Manish Kumar , Manoj Chandra Garg , Zeolites in wastewater treatment: A comprehensive review on scientometric analysis, adsorption mechanisms, and future prospects *Environ Res.* (2024), 260,119782.
- [5]. Fernando Morante-Carballo, Néstor Montalván-Burbano, Paúl Carrión-Mero and Kelly Jácome-Francis, *Worldwide Research Analysis on Natural Zeolites as Environmental Remediation Materials by Sustainability* (2021), 13(11), 6378;
- [6]. Neelma Munir , Ayesha Javaid , Zainul Abideen , Bernardo Duarte , Heba Jarar , Ali El-Keblawy , Mohamed S Sheteiwy The potential of zeolite nanocomposites in removing microplastics, ammonia, and trace metals from wastewater and their role in phytoremediation; 2023.
- [7]. Giuseppe Cruciani , Zeolites upon heating: Factors governing their thermal stability and structural changes ; *Journal of Physics and Chemistry of Solids* 67 (2006) 1973–1994
- [8]. Sunaryo, Suyitno, Zainal Arifin, Muji Setiyo, and Febi Panji Diharja , Thermal Stability and Surface Area Modification of Natural Zeolite Through HCl & NaCl Treatment to Apply in Pyrolysis Systems ; *E 3S Web of Conferences* 465, 01026 (2023), <https://doi.org/10.1051/e3sconf/202346501026>
- [9]. M.L.Nguyen, C.C. Tanner; *New Zealand Journal of Agriculture research*, Vol. 42, pp.427-446, (1998)
- [10]. S.D. Ghan, H.V. Baksh and B.T. Bhoskar; *Asian Journal of Chemistry* Vol.13, pp.634-636, (2005)
- [11]. M. Zabchnick-Swiatek, K. Malinska; Removal of Ammonia by Clinoptilolite; *Global NEST Journal*, Vol.12, pp.256-261, (2010)
- [12]. Karmen Margeta, Nataša Zabukovec Logar, Mario Siljeg and Anamarija Farkas, *Natural Zeolites in Water Treatment – How Effective is Their Use*; book, pp.81-112, (2013)
- [13]. B. Salunkhe, S. Raut; Removal of heavy metal Ni (II) and Cr (VI) from aqueous solution by scolecite natural zeolite ; *International Journal of Chemical Science*, Vol.10, pp.1133-1148, (2012)
- [14]. W.A. Carvalho, G.S. Alves, A.O. Souza, Z. Fontana, C. Vignado; Removal of Heavy Metals from Wastewater by Brazilian Natural Materials ; *Revista CENIC Ciencias Quimicas*, Vol. 36, (2005)
- [15]. Sh.V. Khachatryan; *Proceeding of the Yerevan State University*, vol. 2 pp. 31 – 35, (2014)
- [16]. B.K. Payne, M.A. Fateh Tarek; *Journal of Environmental Science and Health*, Vol.39, pp.2275-2291, (2004)
- [17]. E. Erdem, N. Karapinar, R. Donat; *Journal of colloids and interface science*, Vol.280, pp.309-314, (2004)

- [18]. M.Golomeova,A.Zendeiska,K.Blazev,B.Golomeov;International Journal of Engineering Research and Technology,Vol.3,pp.1029-1035,(2014)
- [19]. M.Lebedynets,M.Sprynskyy,I.Sakhnyuk,R.Zbypniewski,R.Golembiewski,B.Buszewski;Adsorption science and technology,Vol.22,pp.731-741,(2004)
- [20]. Fatemeh Bahmanzadegan, Ahad Ghaemi , A comprehensive review on novel zeolite-based adsorbents for environmental pollutant Journal of Hazardous Materials Advances 17 (2025)
- [21]. Muhammad Hamza Ashfaq1Sammia Shahid Mohsin Javed Shahid Iqbal Othman Hakami Samar O. Aljazzar Urooj Fatima1Eslam B. Elkaeed5Rami Adel Pashameah Eman Alzahrani7Abd-ElAzim Farouk H. H. Somaily Controlled growth of TiO₂/Zeolite nanocomposites for simultaneous removal of ammonium and phosphate ions to prevent eutrophication; Front. Mater.,(2022) Vol 9
- [22]. Neelma Munir , Ayesha Javaid , Zainul Abideen , Bernardo Duarte , Heba Jarar , Ali El-Keblawy , Mohamed S Sheteiwy ,The potential of zeolite nanocomposites in removing microplastics, ammonia, and trace metals from wastewater and their role in phytoremediation; (2023)
- [23]. Rehab O. Abdel Rahman,* ,Ahmed M. El-Kamash 1 and Yung-Tse Hung, Applications of Nano-Zeolite in Wastewater Treatment: An Overview ; Water (2022), 14(2), 137;
- [24]. Álvaro de Jesús Ruíz-Baltazar 1 Álvaro de Jesús Ruíz-Baltazar Advancements in nanoparticle-modified zeolites for sustainable water treatment: An interdisciplinary review; Sci Total Environ . (2024)
- [25]. Tosha Pandya, Shruti Patel,Mangesh Kulkarni,Yash Raj Singh,Akruti Khodakiya,Sankha Bhattacharya,Bhupendra G. Prajapati, Zeolite-based nanoparticles drug delivery systems in modern pharmaceutical research and environmental remediation ; Heliyon (2024) Vol. 10, no. 16
- [26]. Na Liu1,, Ruilin Qi , Xiang Sun , Naoki Kawazoe , Guoping Chen3 and Yingnan Yang , Synthesis and characterization of 3D-zeolite-modified TiO₂-based photocatalyst with synergistic effect for elimination of organic pollutant in wastewater treatment ; Frontiers in Environmental Science, (2022) pp 1-12
- [27]. Arpita Roy, Apoorva Sharma , Saanya Yadav , Leta Tesfaye Jule,and Ramaswamy Krishnaraj Review Article Nanomaterials for Remediation of Environmental Pollutants, Hindawi Bioinorganic Chemistry and Applications Volume (2021), pp 1-16

Preparation And Structural Characterization of Transition Metal Complexes Derived from Hydrazone Schiff Base Ligands

Bhagat S. M.

Department of Chemistry, I.C.S. College of Arts, Comm. and Science, Khed, Dist. Ratnagiri- 415 709, Maharashtra, India

ARTICLE INFO

Article History:

Published : 30 April 2025

Publication Issue :

Volume 12, Issue 13

March-April-2025

Page Number :

238-242

ABSTRACT

Metal complexes is one of the most important field due to its versatile application. Certain metal complexes are used in Industries 1,2 , for synthesis, It work as catalyst 3 , they have some application in Agriculture 4. Particularly hydrazine metal complexes are bio-active compound and can used as anti-tubercular⁵, antimicrobial⁶ Antifungal⁷, anticancer⁸, Anti-convulsant⁹ and antiinflammatori¹⁰ activity. Particularly, the antibacterial and antifungal properties of hydrazone and their complexes with some transition metal ion is reported in letarature. The chelating agent like hydrazine contain C=N linkage is essential for biological activity. Several azomethazines were reported to possess remarkable antibacterial, antifungal, anticancer active.

In present study I reported some transition metal ion complex and charecterised them.

Keywords: Transition metal complexes, hydrazone ligands, chelation, Schiff base, biological activity, azomethine compounds.

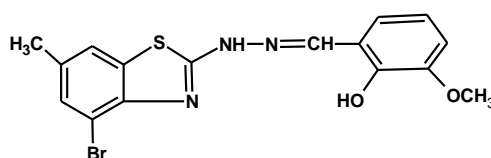
INTRODUCTION

Synthesis of ligand

2-(2'-hydroxy-3'-methoxy phenyl)-4-bromo-6-methyl benzothiazolyl hydrazones

2.48 of gm 4-bromo-2-hydrazino-6-methyl benzothiazolyl hydrazones is dissolved in alcohol and alcoholic solution of 2-hydroxy-3- methoxy benzaldehyde were refluxed for 1 hour using water condenser. The reaction solution were cooled and filtered, the product was recrystallized using alcohol in hot condition. The purity of compound is confirmed by TLC and melting point.

Structure of ligand



2-(2'-hydroxy-3'-methoxy phenyl)-4-bromo-6-methyl benzothiazolyl hydrazon.

Melting point-175 °C, Empirical formula- $C_{16}H_{14}N_3BrSO_2$, Exact mass -392

This ligand is referred as HMPBMBTH

Synthesis of complexes.

i) Synthesis of 2-(2'-hydroxy-3'-methoxy phenyl)-4-bromo-6-methyl benzothiazolyl hydrazones Fe^{III} chloride complex

100 ml 0.1 M $FeCl_3 \cdot 4H_2O$ were prepared in alcohol and 2-(2'-hydroxy-3'-methoxy phenyl)-4-bromo-6-methyl benzothiazolyl hydrazones 0.2 M solution were prepared in ethyl alcohol. These two solutions were mixed and transfer into 500 ml round bottom flask attached water condenser, the pH is of the reaction mixture were adjusted by adding basic buffer solution pH-10. Reaction mixture were refluxed for one hour in water bath. The precipitate was obtained. it is digested, after cooling it is filtered through Buckner funnel , the precipitate of complex were purified by washing with ethyl alcohol, the complex were dried by keeping it in oven. The product was packed into sample bottle.

iv) Synthesis of cobalt complex

Cobalt chloride and ligand 2-(2'-hydroxy-3'-methoxy phenyl)-4-bromo-6-methyl benzothiazolyl hydrazone (HMPBMBTH) were dissolved separately in ethanol so as to prepare 0.1 molar solution with constant stering. A clear solution of cobalt chloride was mixed in ligand solution in 1:2 proportion and pH is adjusted to 6.5 with buffer solution and refluxed on water bath for one hour and allowed to cool . the contents were diagedsted for one hour and filtered. Pale pink coloured solid is obtained it washed with ethanol and dried and stored in bottle.

Physical parameter and elemental analysis .

Melting point of complexes are determined with the help of melting point apparatus by open capillary method. Chlorine is estimated by Mohr's method. Metal ion percentage in a complexes is determined by E.D.T.A. titration. M:L ratio is determined by heating known weight of complexes in platinum crucible. Physical parameter and analytical data of the $Fe(II)$, $Co(II)$, complexes and ligand HMPBMBTH are given in table 2.1. metal ligand ratio and empirical formula were assigned on the basis of TGA measurements and elemental analysis (table 2.2.)

3.5 Characterization of complexes. :-

U.V. and visible spectra of complexes and ligand recorded on U.V. SHIMADZU UV3600 spectrophotometer at range 200-800 nm by using D.M.S.O. solvent at P.G. department of chemistry Shivaji University Kolhapur. I.R. spectra of ligand were recorded at Yeshwant Mahavidyala Nanded and I.R. spectra of complexes are recorded at PERKIN ELMER spectrum-100/79720 by KBr platelate method at Shivaji University Kolhapur. Thermo gravimetric analysis (T.G./D.T.A.) measurement are recorded on thermo gravimetric analyzer on TA model S.T.D-2960 at Shivaji University Kolhapur in Nitrogen atmosphere. XRD pattern of the complexes recorded on PW-3719/1710 Philips -Holland spectrometer at Shivaji University Kolhapur and E.S.R. is recorded at IIT, pawai, Mumbai.

Result and discussion

The complexes of $Fe(III)$, $Co(II)$, are prepared with the ligand HMPBMBTH . This complexes are coloured. These complexes are soluble in D.M.S.O. but insoluble in water, alcohol, chloroform, and D.M.F. Decomposition point of complexes are in the range of 240-300°C . It suggest that they have good thermal stability at room temperature.

Table.2.1: physical property of HMPBMBTH metal complexes.

Complex	color	D.P.	Yield%	%Cl
[Fe(HMPBMBTH) 2Cl H ₂ O] Cl	Faint brown	272-280	68	18.607
[Co(HMPBMBTH) ₂]Cl ₂ .H ₂ O	Pale pink	243-249	64	7.615

Table.2.2: Percent C,H,N and metal ion in HMPBMBTH metal *complex*

compound	M.wt	Empirical formula	%C	%H	%N	%M
HMPBMBTH	392.17	C ₁₆ H ₁₄ N ₃ BrSO ₂	49.005	3.569	10.714	-
[Fe(HMPBMBTH)2Cl H ₂ O] Cl	572.52	C ₁₆ H ₁₆ Cl ₃ FeN ₃ SBrO ₃	33.568	2.794	7.339	9.755
[Co(HMPBMBTH) ₂] Cl ₂ . H ₂ O	932.28	C ₃₂ H ₃₀ Cl ₂ CoN ₆ S ₂ Br ₂ O ₅	44.228	3.217	9.053	6.322

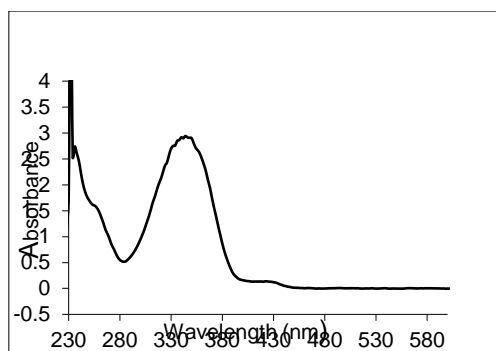
Electronic spectra :-

The ligand 2-(2'-hydroxy-3'-methoxyphenyl)-4-bromo-6-methyl benzothiazolyl hydrazones (HMPBMBTH) has exhibited one characteristic maxima in U.V. region at 344 nm while in [Ni(HMPBMBTH) H₂O] Cl₂ complex it is shifted towards blue shift i.e. lower region and observed at 324nm. While in [Cu(HMPBMBTH) Cl] Cl₂.H₂O complex the band is shifted towards red shift and observed at 352 nm . This shifting of bands indicate that there is complexation in metal and ligand.

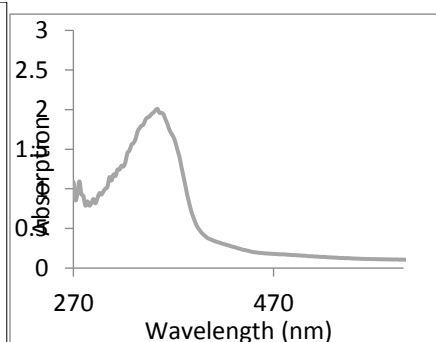
Table.2.3Electronic data of ligand HMPBMBTH metal complexes.

Compound	Wavelength	Log E
Ligand HMPBMBTH	344	2.942
[Fe(HMPBMBTH) 2Cl H ₂ O] Cl	324	1.936
[Co(HMPBMBTH) ₂] Cl ₂ . H ₂ O	352	2.009

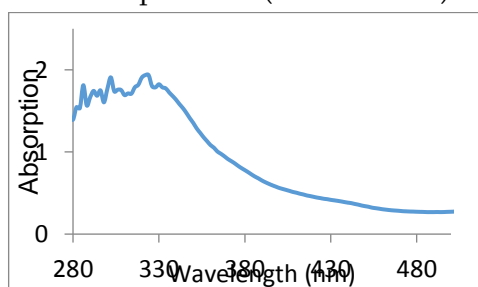
U.V. of HMPBMBTH



U.V. of Fe(III) complex wit HMPBMBTH



Co complex with (HMPBMBTH)



I.R. Spectra :-

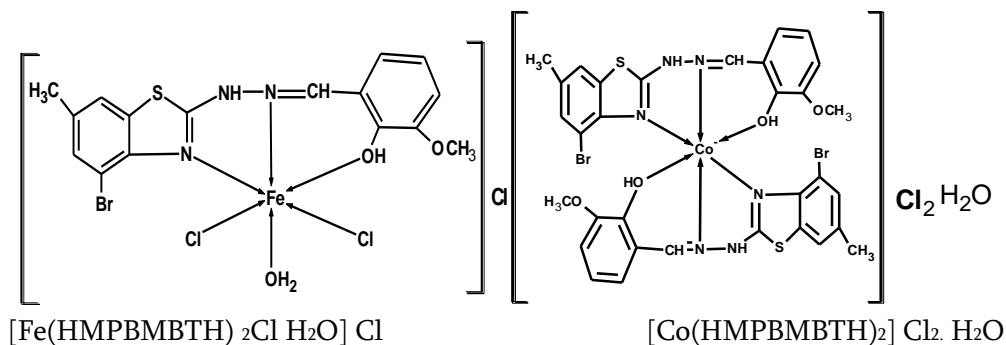
The ligand 2-(2'-hydroxy-3'-methoxy phenyl)-4-bromo-6-methyl benzothiazolyl hydrazones exhibit a sharp strong band at 3533 cm⁻¹ in I.R. spectra which may be assign to phenolic hydroxyl group In [Fe(HMPBMBTH) 2Cl H₂O] Cl complex broad strong is observed at 3435 and in [[Co(HMPBMBTH)₂] Cl₂. H₂O complex broad band is observed at 3456 cm⁻¹. The shifting of band indicate that the coordination of metal ion through 'O' of phenolic OH group. In I.R. spectra of one band is observed at 1616 cm⁻¹ it is due to C=N (ring) but in but in [Fe(HMPBMBTH) 2Cl H₂O] Cl it is observed at 1600 cm⁻¹ this shifting of band in complex clearly indicate that Nitrogen of benzothiazine ring is involved in the complex formation. The band is observed at 1605 cm⁻¹ in [Co(HMPBMBTH)₂] Cl₂. H₂O this shifting of band is indicate that 'N' of thiazol ring is involved in the complex formation. One band is observed at 1580 cm⁻¹ in ligand it may be due to the C=N (azomethine) group this band is shifted to lower region in [Fe(HMPBMBTH)₂Cl H₂O] Cl and observed at 1560cm⁻¹ it indicate that azomethine nitrogen is involve in the formation of coordinate bond with Fe⁺³. In [Co(HMPBMBTH)₂] Cl₂. H₂O complex band is observed at lower region and it appear at 1530 cm⁻¹ is indicate that the azomethine nitrogen is involved in the complex formation. Another band is observed at 3163 in I.R. spectra of ligand which may assign N-H stretching but in [Fe(HMPBMBTH)₂Cl H₂O] Cl and [Co(HMPBMBTH)₂] Cl₂. H₂O it is not observe because it may merged in the broad peak of OH group and water molecule this indicate that N-H is not involve in the complex formation. Another band is 595 in [Fe(HMPBMBTH)₂Cl H₂O] Cl] Cl₂ and [Co(HMPBMBTH)₂] Cl₂. H₂O complexes but not observed in ligand it indicate that there is formation of M-O bond in both complexes. One band is observed at 515 cm⁻¹ in both complex which is absent in ligand this indicate that the formation of M-N coordinate band. Thus 2-(2'-hydroxy-3'-methoxy phenyl)-4-bromo-6-methyl benzothiazolyl hydrazones act as tridentate in both complexes and coordinate through ring nitrogen, azomethine nitrogen and oxygen of phenolic OH. I.R. spectral data with probable is given in the table 2.4

Table.2.4 I.R. data of ligand HMPBMBTH metal complex

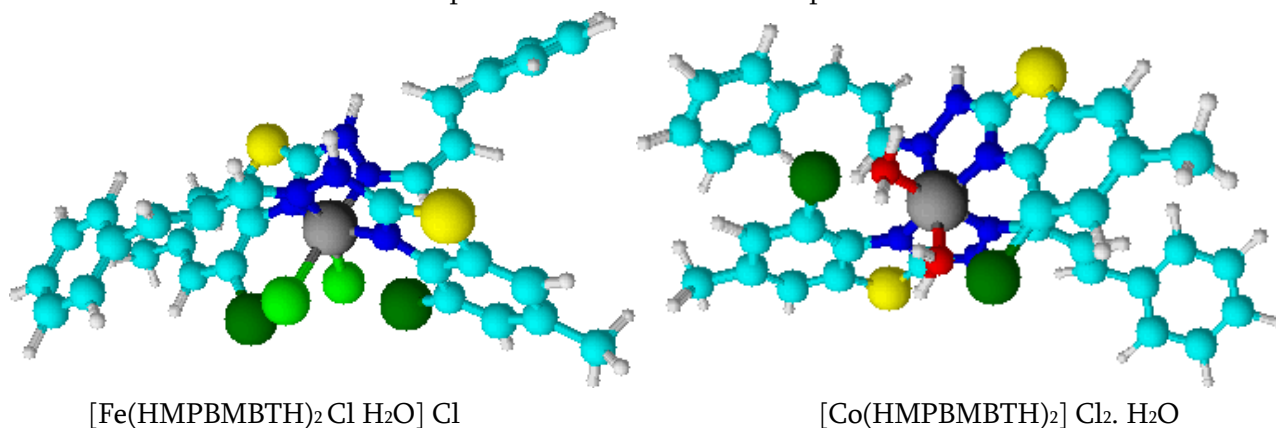
compound	O-H cm-1	N -H cm-1	C=N ring cm-1	C=N azomethine cm-1	M-O cm-1	M-N cm-1
HMPBMBTH	3533	3163	1515	1580	--	--
[Fe(HMPBMBTH) 2Cl H ₂ O]Cl	3435	-	1600	1560	595	515
[Co(HMPBMBTH) ₂] Cl ₂ .H ₂ O	3458	-	1605	1530	658	523

Electron spin Resonance Spectroscopy.

The X-band E.S.R. spectrum of the powder Fe(II) and Co(II) complexes was recorded at room temperature. The calculated values of Fe(II) is $g_{||}$, g_{\perp} , g_{avg} , and G are 2.227, 2.03674, 2.10016, 4.26374 respectively. And Co(II) is $g_{||}$, g_{\perp} , g_{avg} , and G are 2.23474, 2.01126, 2.0857533, 4.246 respectively. The values are typical for one unpaired electron in an orbital of mostly d_{xy} character. If $g_{||}$ value is less than 2.3 the compound is covalent and $g_{||}$ value is greater than 2.3 then it is ionic. Present values indicate that the complexes are covalent. G value is greater than 4 it indicate that the ligand is weak field ligand.



Proposed 3D structure metalcomplexes.



REFERENCES

- [1]. A. Gursoy, N.Teezioglu and G.Otuk, *J.Med.Chem*, 1997, 32, 753-757.
- [2]. F.D. Popp, *J. Heterocyclic chem.*, 1984,21,1641-1645
- [3]. N.K. Singh, N.Agrawal and R.C. Agrawal, *Indiand J. Chem.*, 1984,23A,1011-1015.
- [4]. Y.Kumar and P.D.Sethi. *J. Indian chem. Sco.*, 1990,67,796-799.
- [5]. M. Mohan, M.P. gupta, L. Chandra and N.K. Jha. *Inorganic Chem. Acta*.1988,151,61-68.
- [6]. M. Mohan, A. Kumar and M.Kumar, *Inorg. Chem. Acta*. 1987,136,65-74.
- [7]. R.C. Sharma, J. Ambwani and V.K. Varshney. *J. Indian Chem. Soc.*, 1992,69,770-772.
- [8]. N.K. Singh and D.K. Singh, *Synth. React, Inorg. Met-org. Chem.*,2002,32,203-218.
- [9]. Z.H. Chohan, K.M. Khan and C.T. Supuran, *Appl. Organomet Chem.*,2004, 18, 305-310.
- [10]. L. Sumalan, d. Macarovici, m. Neamtu and M.Coman, *Rev. Roum, Chem.*,1997,42,297-280.
- [11]. I. Yilmaz and A. Cukurovali, *Polish J. Chem.*, 2004,78,663-772.
- [12]. L. Katz. *J. Amer. Chem. Soc.*1951
- [13]. E. Carp and A. Toma. *Analele univ. Stiint. All. Cuza, Iasi, Sect. I.*, 196511c,67-72 .
- [14]. C.V. Gheorghiu and E. Carp, *Analele univ. Stiint. Al. I. Cuza, Iasi, Sect. I.*, 1957,3,367-372
- [15]. G.D. Tiwari, Ar. Tripathi, An. Tripathi, O. Kumari and M.V.B. Reddy, *J. Indian Chem.*, 50 C. 1994. 71, 755-756
- [16]. A. Shaikh Kabeer, M.A. Baseer and N.A. Mote, *Asian J. Chem.*, 2001,13, 496-500.

Fe₂O₃-g-C₃N₄ Nanocomposites for Photocatalysis: A Comprehensive Review on Synthetic Approaches, Characterization Techniques, Mechanistic Insights, and Environmental Applications

Babasaheb T. Shinde^{1,2}, Hemant V. Chavan^{1*}

¹Department of Chemistry, A.S.P. College (Autonomous), Devruk, Dist. Ratnagiri-415 804, Maharashtra, India

²Department of Chemistry, S.K.S.V. College, Lanja, Dist. Ratnagiri-, Maharashtra, India

ARTICLE INFO

Article History:

Published : 30 April 2025

Publication Issue :

Volume 12, Issue 13

March-April-2025

Page Number :

243-268

ABSTRACT

This review compiles and critically analyses recent developments in the synthesis, characterisation, and photocatalytic applications of g-C₃N₄-Fe₂O₃ nanocomposites. As a promising class of heterostructure materials, these composites integrate the visible-light activity of graphitic carbon nitride (g-C₃N₄) with the redox-active, magnetically separable iron oxide (Fe₂O₃) to improve photocatalytic degradation of organic pollutants. The present study emphasises the influence of various synthesis approaches, ranging from conventional chemical methods to eco-friendly strategies involving plant extracts, industrial waste, and laterite soil, on the materials' structural properties as well as their functional performance. Particular focus is placed on the formation of heterojunctions and their pivotal role in promoting efficient charge separation. Based on recent studies, supported by band structure analysis and spectroscopic evidence, the mechanistic pathways, such as Type II, Z-scheme and S-scheme, are thoroughly examined. Although these nanocomposites demonstrate >90% degradation efficiency for various dyes, long-term stability, environmental impact, and large-scale production remain. This article aims to provide a comprehensive understanding of the current state of research on g-C₃N₄-Fe₂O₃ nanocomposites and their potential for sustainable photocatalytic applications.

Keywords: Iron oxide nanoparticles, Graphitic carbon nitride, Photocatalysis, Nanocomposites, Wastewater treatment.

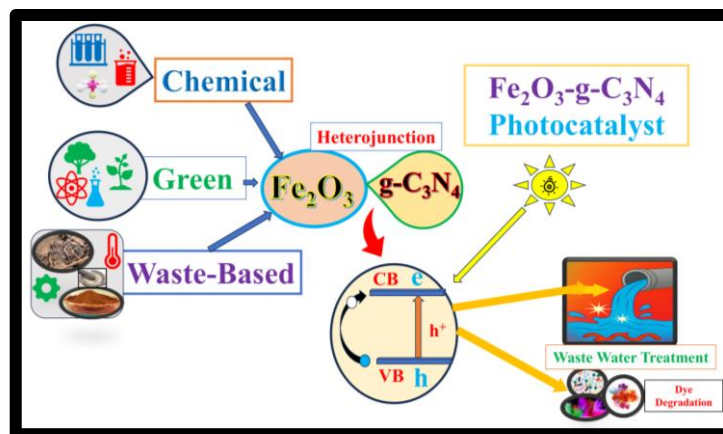


Fig.1. Graphical Abstract

INTRODUCTION

1.1 Environmental Challenges and the Rise of Photocatalytic Solutions

In recent years, extensive research has highlighted the growing burden of water pollution caused by industrial dyes, pharmaceuticals, pesticides, and other persistent organic pollutants (POPs)[1]. Conventional wastewater treatment technologies, although widely used, are often insufficient to address these complex contaminants due to limitations in efficiency, selectivity, and sustainability[2]. Photocatalysis has been extensively explored in the literature as a sustainable and green approach for degrading hazardous pollutants in wastewater[3]. Unlike physical or biological treatment methods, photocatalysis enables direct mineralization of pollutants using light energy, without generating harmful byproducts[4].

Iron oxide (Fe₂O₃) and graphitic carbon nitride (g-C₃N₄) have been extensively studied as photocatalysts due to their distinct properties[5]. Fe₂O₃ offers narrow band gap energy (~2.1 eV), magnetic separability, chemical stability, and earth abundance, making it cost-effective and environmentally benign[6]. On the other hand, g-C₃N₄ is a visible-light-active, metal-free polymeric semiconductor with a moderate band gap (~2.7 eV), good thermal stability, and facile synthesis from inexpensive precursors like urea or melamine[7]. Numerous studies have reported that their individual photocatalytic performance is limited by the rapid recombination of photogenerated charge carriers. However, their integration into a heterojunction system can mitigate these limitations, which justifies the growing interest in these materials as components of nanocomposite photocatalysts[8].

Recent literature highlights the strategic use of various dopants and modifiers to enhance the photocatalytic performance of Fe₂O₃-based systems. Carbonaceous materials such as graphene, reduced graphene oxide (rGO), and graphene oxide (GO) have been frequently employed to improve electrical conductivity and facilitate charge carrier mobility, thereby suppressing electron-hole recombination. Metal oxide dopants like TiO₂ and ZnO are valued for their oxidative strength and photostability, although their photocatalytic activity is typically confined to the UV region due to wide band gaps. To extend their response into the visible range, these oxides are often combined with Fe₂O₃ in heterostructured systems. Other modifiers, including SnO₂, carbon nanotubes (CNTs), Ag/AgCl, and biochar, contribute to enhanced surface area, improved charge separation, and localized surface plasmon resonance (LSPR) effects. Such modifications significantly improve light-harvesting capability, charge transfer efficiency, and overall degradation performance of Fe₂O₃.

composites. Nevertheless, achieving optimal photocatalytic efficiency often requires rational design and synergistic integration within a multi-component nanocomposite framework, as outlined in **Table 1**.

Table 1. Comparative analysis of Fe₂O₃ composite materials based on structural features, photocatalytic performance, and electronic properties

Composite Material	Type	Typical Band Gap (eV)	Key Advantages in Composites	Limitations	References
g-C ₃ N ₄	Polymeric semiconductor	~2.7	Visible light response, suitable band alignment with Fe ₂ O ₃ , thermal stability, metal-free	Low surface area, fast charge recombination	[9], [10]
Graphene	2D Carbon (semimetal)	~0	High conductivity, large surface area, fast electron transfer	No band gap (not ideal alone in photocatalysis), requires hybridization	[11], [12]
GO	Oxidized Graphene	~2.2–3.5	Tunable band gap, surface functional groups aid dispersion	Poor conductivity, unstable under light	[13], [14]
rGO	Partially reduced GO	~0.5–1.5	Better conductivity than GO, facilitates charge transfer	Residual oxygen can limit performance, structural defects	[15], [16]
TiO ₂	Metal oxide semiconductor	~3.2 (anatase)	High stability, strong oxidizing ability	UV-active only, wide band gap limits solar efficiency	[17]
ZnO	Metal oxide semiconductor	~3.2	High exciton binding energy, easy synthesis	Photocorrosion, UV-active	[18]
SnO ₂	Metal oxide semiconductor	~3.6	High mobility, good optical transparency	Limited visible light absorption	[19]
CNTs	Carbon-based nanostructure	~0–1	High conductivity, strong mechanical properties	Poor light absorption unless hybridized	[20]
Ag/AgCl	Plasmonic composite	~3.25 (AgCl)	Plasmon-enhanced visible absorption, strong oxidation	Stability issues under light, cost	[21]
Biochar	Carbon-rich porous material	Variable	Low cost, high surface area, eco-friendly	Low conductivity, limited electronic interaction	[22], [23]

The formation of Fe₂O₃/g-C₃N₄ nanocomposites is motivated by the need to overcome each material's intrinsic drawbacks and exploit synergistic interactions for enhanced photocatalytic performance. Reviewed studies consistently report that coupling these semiconductors leads to improved charge carrier separation, broader light absorption, and higher reactive oxygen species (ROS) generation. The heterojunction interface whether

traditional, Z-scheme, or S-scheme is crucial in driving efficient charge dynamics. Moreover, the magnetic property of Fe_2O_3 facilitates catalyst recovery, while $\text{g-C}_3\text{N}_4$ enhances surface area and dye adsorption. Together, they create a platform that addresses key challenges in environmental photocatalysis, particularly in degrading resistant organic dyes under visible or solar light[24].

This review aims to provide a thorough overview of recent studies on the synthesis of iron oxide (Fe_2O_3) nanoparticles derived from low-cost, abundant, and sustainable sources, including industrial waste, laterite soil, and plant extracts as well as some biogenic methods with a specific emphasis on their combining with graphitic carbon nitride ($\text{g-C}_3\text{N}_4$) to generate multifunctional nanocomposites. It also discusses characterization techniques essential for a detailed understanding of the structural, morphological, compositional, optical, magnetic, and surface properties of Fe_2O_3 nanocomposites, which directly influence their performance in catalytic applications. Particular focus is directed on comprehending the improved photocatalytic performance of $\text{Fe}_2\text{O}_3/\text{g-C}_3\text{N}_4$ nanocomposites under UV-visible and sunlight exposure, also clarified through heterojunction mechanisms like Type II, Z-scheme, and S-scheme. This review also highlights the environmental applications of $\text{Fe}_2\text{O}_3\text{-g-C}_3\text{N}_4$ nanocomposites, thus providing future guidance for the strategic development of sustainable, high-performance nanocomposite catalysts (Fig. 1).

Synthesis Methods of Iron Oxide (Fe_2O_3) Nanoparticles

The synthesis of Fe_2O_3 nanoparticles from sustainable sources involves a broad spectrum of techniques. These methods can be broadly categorized into chemical, green/biological, and physical approaches. Each synthesis pathway offers unique scalability, morphology control, environmental impact, and application specificity advantages (Fig. 2).

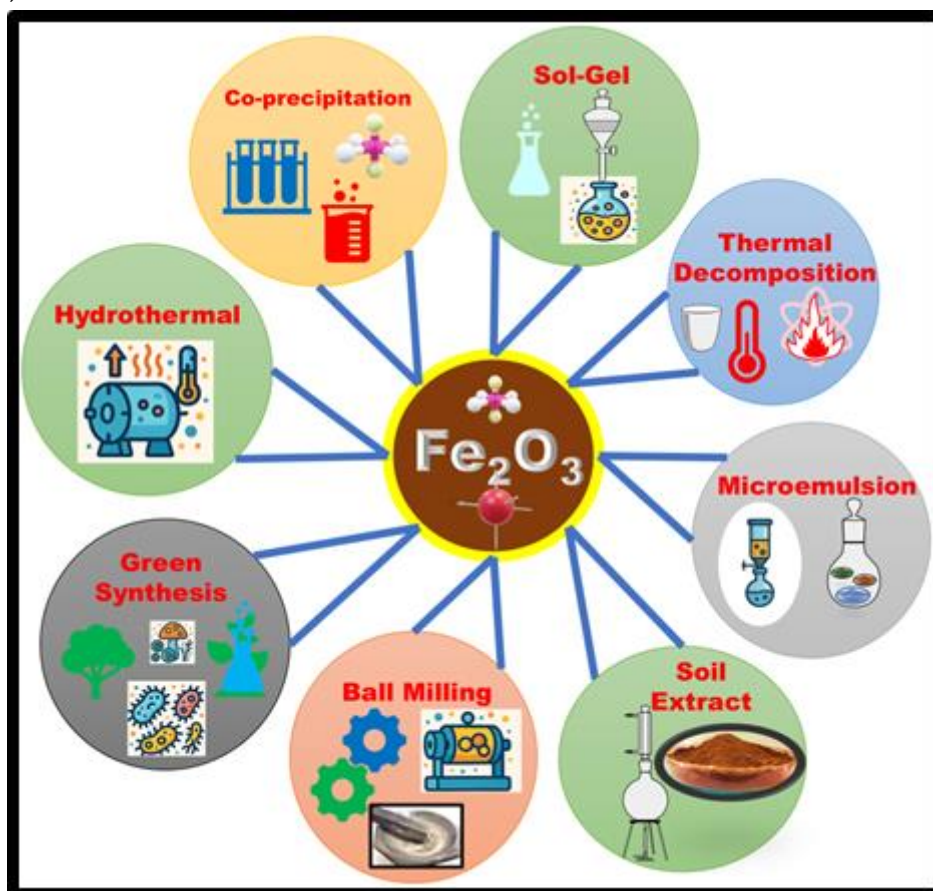


Fig.2 Various Synthetic Methods

2.1 Chemical Synthesis Methods

2.1.1 Co-precipitation Method:

The co-precipitation technique is one of the most efficient and widely used methods for synthesising iron oxide nanoparticles. It involves the simultaneous precipitation of Fe^{2+} and Fe^{3+} salts by adding a base such as NaOH or NH_4OH under controlled pH (typically around 9–11) and temperature conditions. The reaction leads to forming iron hydroxide precursors, which are then subjected to filtration, washing, and drying. Subsequent calcination at elevated temperatures enhances crystallinity, removes residual organics, and ensures phase purity, yielding well-defined Fe_2O_3 nanoparticles. This method is cost-effective, scalable, and suitable for chemical and green synthesis routes.

2.1.2 Sol-Gel Method

The sol-gel process involves the hydrolysis and polycondensation of iron precursors such as iron alkoxides or salts to form a colloidal suspension, which gradually evolves into a three-dimensional gel network. This gel is then aged, dried to remove solvents, and calcined at elevated temperatures to produce Fe_2O_3 nanoparticles. The method allows excellent control over composition, particle size, and morphology. It yields highly uniform, porous, and thermally stable nanoparticles, making it suitable for catalytic and electronic applications.

2.1.3 Hydrothermal/Solvothermal Method:

This method involves the crystallization of iron precursors in sealed autoclaves at elevated temperatures (typically 120–200°C) using water (hydrothermal) or organic solvents (solvothermal) as reaction media. The high-pressure environment promotes the formation of highly crystalline Fe_2O_3 nanoparticles with controlled size, morphology, and phase. Various nanostructures like rods, sheets, spheres, and cubes can be synthesized by tuning parameters such as temperature, time, pH, and solvent type. This method is especially advantageous for producing uniform, monodispersed particles with enhanced surface properties.

2.1.4 Thermal Decomposition:

This technique involves the thermal analysis of iron-based organometallic precursors in organic solvents, typically in the presence of surfactants or stabilizing agents. These surfactants help control nanoparticle growth, prevent aggregation, and enable the formation of highly monodisperse Fe_2O_3 nanoparticles. The method yields uniform particles with excellent crystallinity and allows fine control over size and morphology, making it suitable for biomedical and electronic applications.

2.1.5 Microemulsion and Reverse Micelle Techniques:

These methods use thermodynamically stable, surfactant-stabilized nanoscale emulsions (microemulsions) as nanoreactors for the controlled synthesis of Fe_2O_3 nanoparticles. In reverse micelles, water droplets dispersed in an organic solvent act as confined reaction zones where nucleation and growth occur, offering precise control over particle size and distribution. The approach enables the synthesis of ultra-small, monodisperse nanoparticles with uniform morphology. Despite being limited by low yield and complex separation, these techniques are valuable for fundamental studies and applications requiring high uniformity.

2.2 Green Synthesis (Eco-friendly/Biogenic Routes)

2.2.1 Plant Extract Mediated Synthesis:

This green synthesis approach employs bioactive compounds such as flavonoids, polyphenols, alkaloids, and proteins in plant extracts as natural reducing and stabilizing agents. Iron salts are typically reacted with the extract at room or mildly elevated temperatures, leading to the formation of Fe_2O_3 nanoparticles under eco-friendly conditions. The method is cost-effective and sustainable, avoiding toxic chemicals, aligning with green chemistry principles. It also offers tunable morphology and functional properties depending on the phytochemical composition of the extract.

2.2.2 Bacteria, Fungi, and Algae Mediated Synthesis:

In this biogenic approach, microorganisms like bacteria, fungi, and algae facilitate the reduction of iron ions into Fe₂O₃ nanoparticles through enzymatic and metabolic pathways. These microbes secrete enzymes, proteins, and other biomolecules that act as natural reducing and capping agents. The synthesis can occur intracellularly or extracellularly, depending on the organism and conditions. Although this method is eco-friendly and yields stable nanoparticles, it demands sterile environments, careful culture maintenance, and longer reaction times.

2.2.3 Soil and Mineral Source Extraction:

This method uses naturally abundant, iron-rich sources such as laterite or red soil for the synthesis of Fe₂O₃ nanoparticles. The process typically involves acid leaching to extract iron ions, followed by controlled precipitation using a base and subsequent calcination to obtain crystalline nanoparticles. It offers a sustainable and low-cost route by converting natural or waste materials into valuable nanomaterials. The approach aligns well with circular economy principles and is suitable for large-scale, eco-friendly applications.

2.2.4 Biowaste-Derived Synthesis:

This eco-friendly approach involves using iron-containing biowaste materials such as rusty iron tools, iron slag, or plant ashes as precursors for synthesizing Fe₂O₃ nanoparticles. The iron is typically extracted through acid or base treatment, followed by precipitation and calcination steps. This method promotes waste valorisation, reduces environmental burden, and supports sustainable nanomaterial production. It also aligns with green chemistry and circular economy frameworks, offering a low-cost and scalable synthesis route.

2.3 Physical Methods

2.3.1 High-Energy Ball Milling

High-energy ball milling is a top-down approach that involves the mechanical grinding of iron-containing materials, such as iron powders or ores, in a high-energy ball mill. The repeated collisions of grinding media break the bulk material into smaller particles, facilitating the formation of nanostructures. This method enables precise particle size and morphology control, producing highly dispersed Fe₂O₃ nanoparticles. It is particularly advantageous for fabricating nanoparticles with uniform size distributions, although it may require post-milling treatment to remove surface defects and improve crystallinity.

The comprehensive overview of the synthetic methods for Fe₂O₃ nanoparticles is given in Table 2.

Table 2. Comparative Overview of Synthesis Techniques and Methods

Method	Precursor	Conditions	Advantages	Limitations	Ref.
Co-precipitation	(Ferric nitrate and Oxalic acid)	water as a solvent, 250-450°C	High surface area, porous structure	Requires calcination,	[25]
Sol-gel	Fe(NO ₃) ₃ ·9H ₂ O, Epoxypropane	Hydrolysis in non-aqueous solvent; supercritical CO ₂ drying; calcination <300°C.	High surface area; good pore structure; environmentally friendly reagents.	Complex setup for supercritical fluid process; high cost of equipment.	[26]
Hydrothermal	FeCl ₃ ·6H ₂ O	Solvent variation (water/ethanol), 160–180°C, 6–24 hours.	Morphology control (nanoplates, nanorods); no surfactants required.	Agglomeration risks; require precise solvent control.	[27]

Method	Precursor	Conditions	Advantages	Limitations	Ref.
Thermal Decomposition	Iron acetate ($\text{Fe}(\text{CH}_3\text{COO})_3$)	Heated to 400°C in air; followed by annealing for mesoporous structure.	Produces mesoporous $\alpha\text{-Fe}_2\text{O}_3$ films directly on substrates; scalable for large-area applications.	Requires post-synthesis annealing for pore formation and crystallinity.	[28]
Microemulsion	$\text{FeCl}_3 \cdot 6\text{H}_2\text{O}$, NaOH	n-heptane as oil phase, AOT as surfactant, 1-butanol as co-surfactant; calcination at 500°C.	Produces plate-like $\alpha\text{-Fe}_2\text{O}_3$ nanoparticles (~13.1 nm); homogeneous dispersion; optical band gap ~3.2 eV.	Requires calcination; surfactant removal necessary; limited scalability.	[29]
Plant Extract (Green)	$\text{FeCl}_3 \cdot 6\text{H}_2\text{O}$	Methanol extract mixed with FeCl_3 solution; heated at 80°C for 2 hours.	Rapid heating profile for hyperthermia applications; SAR values ~62.75 W/g at low NP concentration.	Requires methanol extraction and sodium acetate addition; limited scalability for larger volumes.	[30]
Bacterial/Fungal	FeSO_4	Incubation with Bacillus sp. GMS10 at 37°C for 24–36 hours under aerobic conditions.	Eco-friendly, low-cost, and scalable; produces $\alpha\text{-Fe}_2\text{O}_3$ nanoparticles (~30 nm) with antibacterial and anti-biofilm properties.	Requires precise bacterial culture conditions; potential contamination risks.	[31]
Laterite soil extraction	Acid-treated laterite	5M HCl + 650°C calcine	Abundant source, waste valorization	Purity and reproducibility issues	[32]
Biowaste/rust	Scrap iron, rust	Rust dissolved in HCl, followed by precipitation with NaOH; dried at 110°C.	Simple and scalable; converts waste rust into $\alpha\text{-Fe}_2\text{O}_3$ nanoparticles (~20–50 nm).	Requires acid treatment; potential environmental concerns with acid disposal.	[33]
Ball Milling	Fe_2O_3 powder	Milling at 300–600 rpm for 5–10 hours under inert atmosphere; sintering at 600–800°C.	Produces nanoscale Fe_2O_3 with lattice distortion; improves mechanical and magnetic properties.	Requires high-energy equipment; risk of contamination from milling media.	[34]

A comprehensive table of data on synthetic methodologies has been developed for the preparation of Fe₂O₃ nanoparticles, each method offering unique significance in terms of morphology, surface area, and functional applicability. Conventional chemical routes such as co-precipitation, sol-gel, and hydrothermal synthesis provide reasonable control over particle characteristics but often require high-temperature treatments or complex setups. Green and biogenic approaches, including plant extract and microbial-assisted synthesis, present environmentally friendly and scalable alternatives with added biological functionalities. Waste-derived methods utilizing laterite, rust, or industrial by-products offer sustainable, cost-effective routes aligned with circular economy goals. Ultimately, the choice of synthesis method should be guided by the desired application, scalability, cost, and environmental impact.

Characterisation Techniques and Their Importance

There are various characterization techniques in confirming the synthesis, structural integrity, and functional properties of Fe₂O₃, g-C₃N₄, and their g-C₃N₄-Fe₂O₃ nanocomposites. These techniques are essential for understanding the materials' phase, morphology, optical properties, surface characteristics, magnetic behaviour, and thermal stability, directly influencing their photocatalytic degradation performance. A detailed discussion of each technique will follow in the next section.

3.1 X-ray Diffraction (XRD)

The X-ray diffraction (XRD) analysis of the synthesized materials provides clear evidence of their crystallinity and phase identification. For Fe₂O₃, the presence of well-defined peaks at 24.2°, 33.1°, and 35.5° corresponding to the (110), (113), and (024) diffraction planes confirms the formation of hematite (α-Fe₂O₃), indicating a highly crystalline structure[35]. Similarly, the g-C₃N₄ material shows characteristic peaks at 12.15° and 27.4° corresponding to the (100) and (002) planes, confirming the successful synthesis of graphitic carbon nitride[36]. In the case of the g-C₃N₄-Fe₂O₃ composite, the XRD pattern exhibits a combination of peaks from both Fe₂O₃ (at 24.2°) and g-C₃N₄ (at 13.0° and 27.4°), indicating the successful formation of the composite material[37]. The observed overlapping peaks suggest that the two components have been effectively integrated, maintaining their individual crystal structures, and confirming the synthesis of a composite material with distinct phases of Fe₂O₃ and g-C₃N₄ a Table 3. Highlighted various Phases, Peak position and its diffraction planes.

Table 3. XRD data of g-C₃N₄, Fe₂O₃ and g-C₃N₄-Fe₂O₃ nanocomposite

Material	Phase Identified	Peak Position (2θ)	Corresponding Diffraction Planes	Remarks
Fe ₂ O ₃	Hematite (α-Fe ₂ O ₃)	24.2°, 33.1°, 35.5°	(110), (113), (024)	Well-defined peaks confirming crystallinity
g-C ₃ N ₄	Graphitic Carbon Nitride	13.0°, 27.4°	(100), (002)	Characteristic peaks for g-C ₃ N ₄ structure
g-C ₃ N ₄ -Fe ₂ O ₃ Composite	Mixture of Hematite and g-C ₃ N ₄	13.0°, 24.2°, 27.4°	(100), (110), (002), (113)	Composite shows combined peaks of Fe ₂ O ₃ and g-C ₃ N ₄ , indicating successful synthesis

3.2 Fourier Transform Infrared Spectroscopy (FTIR)

The FT-IR spectra of Fe_2O_3 , $g\text{-C}_3\text{N}_4$, and their composite ($g\text{-C}_3\text{N}_4\text{-Fe}_2\text{O}_3$) reveal characteristic functional group vibrations that confirm the formation of each material and their composite. For Fe_2O_3 , prominent peaks at $\sim 3430\text{ cm}^{-1}$ and $\sim 1620\text{ cm}^{-1}$ correspond to O-H stretching and bending vibrations, while a peak at $\sim 530\text{ cm}^{-1}$ indicates Fe-O stretching, characteristic of hematite[38]. In $g\text{-C}_3\text{N}_4$, the key peaks at $\sim 3115\text{ cm}^{-1}$ and $\sim 1600\text{ cm}^{-1}$ are attributed to N-H stretching and C=N stretching, respectively, while the peaks at $\sim 1200\text{ cm}^{-1}$ and $\sim 800\text{ cm}^{-1}$ correspond to C-N stretching and C-C bending, confirming the presence of the triazine ring structure[39]. In the $g\text{-C}_3\text{N}_4/\text{Fe}_2\text{O}_3$ composite, the FT-IR spectrum shows a combination of peaks from both Fe_2O_3 and $g\text{-C}_3\text{N}_4$, including O-H and C-N stretching vibrations, alongside the Fe-O stretching vibration, indicating successful incorporation of both components into a composite material. These FT-IR results validate the successful synthesis of the $g\text{-C}_3\text{N}_4/\text{Fe}_2\text{O}_3$ nanocomposite with distinct phases[40]. Table 4. Listed various peaks and vibration modes of FT-IR peaks of $g\text{-C}_3\text{N}_4$, Fe_2O_3 , and $g\text{-C}_3\text{N}_4\text{-Fe}_2\text{O}_3$ nanocomposite

Table 4. FT-IR data of $g\text{-C}_3\text{N}_4$, Fe_2O_3 and $g\text{-C}_3\text{N}_4\text{-Fe}_2\text{O}_3$ nanocomposite

Material	FT-IR Peaks (cm^{-1})	Vibration Mode	Remarks
Fe_2O_3	3430, 1620, 530	O-H stretching, O-H bending, Fe-O stretching	Characteristic peaks for the Fe_2O_3 structure
$g\text{-C}_3\text{N}_4$	3115, 1600, 1200, 800	N-H stretching, C=N stretching, C-N stretching, C-C bending	Characteristic peaks for graphitic carbon nitride
$g\text{-C}_3\text{N}_4\text{-Fe}_2\text{O}_3$ Composite	3430, 1620, 1600, 530, 1200	O-H stretching, O-H bending, C=N stretching, Fe-O stretching, C-N stretching	Peaks from both Fe_2O_3 and $g\text{-C}_3\text{N}_4$ indicate successful composite formation

3.3 UV-Vis Diffuse Reflectance Spectroscopy (DRS)

UV-Vis Diffuse Reflectance Spectroscopy (DRS) is a crucial technique to evaluate semiconductor photocatalysts' optical properties and bandgap energies. Fe_2O_3 shows strong absorption in the visible region with an absorption edge around 520–580 nm and a bandgap of approximately 2.0–2.2 eV. However, its photocatalytic performance is limited by rapid electron-hole recombination. In contrast, $g\text{-C}_3\text{N}_4$ exhibits a slightly higher bandgap ($\sim 2.6\text{--}2.8\text{ eV}$) and absorbs up to 460 nm, offering good stability but restricted activity due to low surface area and fast charge recombination[41]. The formation of a $g\text{-C}_3\text{N}_4\text{-Fe}_2\text{O}_3$ nanocomposite leads to a redshift in the absorption edge ($\sim 540\text{--}580\text{ nm}$) and a reduced bandgap ($\sim 1.9\text{--}2.2\text{ eV}$), indicating improved visible-light absorption. This enhancement is attributed to forming Z-scheme or S-scheme heterojunctions, which promote efficient charge carrier separation and suppress recombination, making the composite a promising material for photocatalytic applications[42]. Table 5 highlights various peaks, band gap, and nature of transition of UV-Vis DRS peaks of $g\text{-C}_3\text{N}_4$, Fe_2O_3 , and $g\text{-C}_3\text{N}_4\text{-Fe}_2\text{O}_3$ nanocomposite.

Table 5. UV-Vis DRS peaks of $g\text{-C}_3\text{N}_4$, Fe_2O_3 , and $g\text{-C}_3\text{N}_4\text{-Fe}_2\text{O}_3$ nanocomposite

Material	Absorption Edge (nm)	Bandgap (eV)	Nature of Transition	Critical Remarks
Fe_2O_3	$\sim 520\text{--}580$	2.0–2.2	Indirect (d-d)	- Strong visible-light absorption capability.

Material	Absorption Edge (nm)	Bandgap (eV)	Nature of Transition	Critical Remarks
				<ul style="list-style-type: none"> - Suffers from rapid electron-hole recombination. - Limited photocatalytic efficiency when used alone.
$g\text{-C}_3\text{N}_4$	~440–460	2.6–2.8	Direct ($n\text{-}\pi^*$)	<ul style="list-style-type: none"> - Good thermal and chemical stability. - Absorbs visible light up to ~460 nm. - Low surface area and fast recombination restrict activity.
$g\text{-C}_3\text{N}_4\text{-Fe}_2\text{O}_3$	~540–580	1.9–2.2	Mixed (Z-/S-scheme)	<ul style="list-style-type: none"> - Redshift in absorption edge enhances light utilization. - Heterojunction formation improves charge separation. - Suitable for Z-/S-scheme photocatalytic applications.

3.4 X-ray Photoelectron Spectroscopy (XPS)

XPS spectra provide essential insights into the elemental composition, chemical states, and interfacial interactions within nanocomposites (Table 6.). In the case of Fe_2O_3 , characteristic Fe 2p peaks at ~710.8 eV (Fe 2p_{3/2}) and ~724.5 eV (Fe 2p_{1/2}), along with a satellite peak near 719 eV, confirm the Fe³⁺ oxidation state typical of $\alpha\text{-Fe}_2\text{O}_3$ [43]. For $g\text{-C}_3\text{N}_4$, the presence of C 1s peaks at ~284.6 eV (C–C) and ~288.2 eV (N–C=N), and N 1s peaks around 398.6 eV and 400.1 eV, indicates the dominance of sp²-hybridized C–N frameworks and bridging nitrogen atoms within triazine or heptazine units. Upon composite formation ($g\text{-C}_3\text{N}_4\text{-Fe}_2\text{O}_3$), notable shifts in the binding energies of N 1s and C 1s spectra and the consistent presence of Fe³⁺ peaks suggest strong electronic interaction at the heterojunction interface[44]. These shifts indicate chemical bonding, likely through Fe–N or Fe–O–C linkages, which enhance charge transfer and contribute to the improved photocatalytic performance of the composite system[45].

Table 6. XPS peaks and binding energy of $g\text{-C}_3\text{N}_4$, Fe_2O_3 , and $g\text{-C}_3\text{N}_4\text{-Fe}_2\text{O}_3$ nanocomposite

Material	Key Binding Energies (eV)	Observed Elements & States	Critical Remarks
Fe_2O_3	Fe 2p _{3/2} : ~710.8 eV Fe 2p _{1/2} : ~724.5 eV Satellite: ~719 eV	Fe ³⁺ oxidation state confirmed Presence of satellite peak supports $\alpha\text{-Fe}_2\text{O}_3$	<ul style="list-style-type: none"> - Fe³⁺ state confirms hematite phase. - Strong satellite peak indicates good crystallinity. - No significant Fe²⁺ detected.
$g\text{-C}_3\text{N}_4$	C 1s: ~284.6 eV (C–C), ~288.2 eV (N–C=N) N 1s: ~398.6 eV (C–N=C), ~400.1 eV (N–(C) ₃)	sp ² C–N frameworks and bridging nitrogen species	<ul style="list-style-type: none"> - Peak positions confirm triazine/heptazine units. - High N/C ratio indicates polymeric structure. - Minor C–C peak may arise from adventitious carbon.

Material	Key Binding Energies (eV)	Observed Elements & States	Critical Remarks
g-C ₃ N ₄ -Fe ₂ O ₃	Fe 2p similar to Fe ₂ O ₃ N 1s: slight shift to lower BE C 1s: shift in N-C=N	Coexistence of Fe ³⁺ , C-N, and N-Fe interactions	<ul style="list-style-type: none"> - Binding energy shifts suggest chemical interaction at interface. - Presence of Fe-N bonding confirms strong coupling. - Synergistic electronic structure favors charge transfer.

3.5 Field Emission Scanning Electron Microscopy (FE-SEM)

SEM provides high-resolution images of surface morphology and the distribution of Fe₂O₃ and g-C₃N₄ within composites (Table 7). It is essential for visualizing particle size, shape, and the homogeneity of the composite. The FE-SEM analysis reveals that Fe₂O₃ nanoparticles show agglomerated spherical morphology (~30–80 nm), while g-C₃N₄ displays layered, sheet-like structures. In the g-C₃N₄-Fe₂O₃ composite, Fe₂O₃ particles are uniformly dispersed over the g-C₃N₄ sheets, improving interfacial contact and reducing agglomeration. This morphology enhances surface area and facilitates better charge separation, supporting superior photocatalytic activity [46].

Table 7. SEM images and Morphology of g-C₃N₄, Fe₂O₃, and g-C₃N₄-Fe₂O₃ nanocomposite

Material	Observed Morphology	Particle Size / Shape	Critical Remarks
Fe ₂ O ₃	Agglomerated, irregular spherical particles	~30–80 nm	<ul style="list-style-type: none"> - Shows uniform nanoscale grain formation. - Some degree of aggregation observed. - Porous texture beneficial for surface reactions.
g-C ₃ N ₄	Layered, flaky sheet-like structure	Nanosheets or stacks	<ul style="list-style-type: none"> - Exhibits lamellar structure with wrinkled morphology. - High surface area but prone to stacking. - May limit photocatalytic efficiency due to low conductivity.
g-C ₃ N ₄ -Fe ₂ O ₃	Fe ₂ O ₃ particles dispersed over g-C ₃ N ₄ sheets	Fe ₂ O ₃ embedded in g-C ₃ N ₄ matrix	<ul style="list-style-type: none"> - Uniform dispersion of Fe₂O₃ enhances active sites. - Improved interfacial contact supports charge transfer. - Reduced agglomeration and enhanced surface roughness aid catalysis.

3.6 High resolution-Transmission Electron Microscopy (HR-TEM)

HR-TEM used to analyse morphology and lattice spacing of material (Table 8) images show that Fe₂O₃ nanoparticles exhibit well-defined spherical morphology with sizes ranging from ~30 to 60 nm and distinct lattice fringes corresponding to the (104) plane. g-C₃N₄ appears as crumpled nanosheets with a thickness of ~3–5 nm, showing limited crystallinity at the edges. In the g-C₃N₄-Fe₂O₃ composite, Fe₂O₃ particles are uniformly

dispersed on the g-C₃N₄ sheets, with particle sizes around 20–40 nm and similar lattice spacing[47]. This uniform dispersion improves the composite's charge separation and photocatalytic efficiency by facilitating enhanced interfacial contact between the two phases[48].

Table 8. HR-TEM images and lattice space of g-C₃N₄, Fe₂O₃, and g-C₃N₄-Fe₂O₃ nanocomposite

Material	Morphology / Structure	Particle Size / Lattice Spacing	Critical Remarks
Fe ₂ O ₃	Well-defined spherical particles	~30–60 nm, lattice spacing ~0.29 nm (101)	- High crystallinity with distinct lattice fringes. - Uniform nanoparticle size with good stability.
g-C ₃ N ₄	Crumpled nanosheets, amorphous at edges	Nanosheet thickness ~3–5 nm	- Shows irregular sheet formation. - Limited crystallinity and higher porosity.
g-C ₃ N ₄ -Fe ₂ O ₃	Fe ₂ O ₃ particles dispersed on g-C ₃ N ₄ sheets	Fe ₂ O ₃ particles ~20–40 nm, lattice spacing ~0.29 nm (101)	- Fe ₂ O ₃ uniformly dispersed over g-C ₃ N ₄ . - Enhanced interfacial contact facilitates efficient charge transfer.

3.7 Photoluminescence Spectroscopy (PL)

Photoluminescence (PL) Spectroscopy is another important tool used to study the significant differences in charge carrier dynamics across the materials (Table 9). Fe₂O₃ exhibits a broad emission band around 650–750 nm, indicative of high charge recombination rates, which hinder its photocatalytic performance. g-C₃N₄ shows a moderate PL intensity with emission peaks around 450–500 nm, suggesting a lower rate of charge recombination and better charge carrier retention, making it a promising photocatalyst. The g-C₃N₄-Fe₂O₃ composite demonstrates a redshifted emission peak (~550–600 nm) and a reduction in PL intensity, indicating enhanced charge separation and minimised electron-hole recombination, thus improving its photocatalytic efficiency[49].

Table 9. PL spectra of g-C₃N₄, Fe₂O₃, and g-C₃N₄-Fe₂O₃ nanocomposite

Material	PL Emission Peaks (nm)	PL Intensity / Features	Critical Remarks
Fe ₂ O ₃	Broad emission ~650–750 nm	High intensity, indicating charge recombination	- Strong PL emission suggests significant electron-hole recombination. - Not ideal for photocatalytic applications without modification.
g-C ₃ N ₄	Emission peaks ~450–500 nm	Moderate intensity, smaller peak width	- Lower PL intensity implies reduced charge recombination. - Shows good photocatalytic potential due to better charge carrier separation.
g-C ₃ N ₄ -Fe ₂ O ₃	Emission peaks ~550–600 nm, redshifted	Reduced PL intensity, enhanced separation	- Reduced PL intensity indicates effective charge separation. - Improved photocatalytic activity due to reduced electron-hole recombination.

3.8 Nitrogen Adsorption-Desorption Isotherms (BET Surface Area Analysis)

Nitrogen Adsorption-Desorption Isotherms (BET Surface Area Analysis) provide key insights into the materials' surface area and pore structure (Table 10). Fe_2O_3 exhibits a moderate BET surface area ($\sim 45\text{--}65 \text{ m}^2/\text{g}$) with mesoporous characteristics, which are suitable for catalysis but could be optimized for higher efficiency. $\text{g-C}_3\text{N}_4$ shows a higher surface area ($\sim 60\text{--}90 \text{ m}^2/\text{g}$) and microporous structure, making it an excellent candidate for photocatalytic applications due to its ability to retain charge carriers [50]. The $\text{g-C}_3\text{N}_4\text{-Fe}_2\text{O}_3$ composite shows a significant increase in both surface area ($\sim 90\text{--}120 \text{ m}^2/\text{g}$) and pore volume, which enhances its catalytic and photocatalytic performance, as the improved porosity allows for better diffusion of reactants and more active sites for reaction [51].

Table 10. BET surface and pore analysis of $\text{g-C}_3\text{N}_4$, Fe_2O_3 , and $\text{g-C}_3\text{N}_4\text{-Fe}_2\text{O}_3$ nanocomposite

Material	BET Surface Area (m^2/g)	Pore Volume (cm^3/g)	Pore Size Distribution	Critical Remarks
Fe_2O_3	$\sim 45\text{--}65 \text{ m}^2/\text{g}$	$\sim 0.1\text{--}0.2 \text{ cm}^3/\text{g}$	Mesoporous ($\sim 2\text{--}50 \text{ nm}$)	<ul style="list-style-type: none"> - Moderate surface area with mesoporous structure. - Pore volume indicates potential for catalytic applications, but could be optimized for better efficiency.
$\text{g-C}_3\text{N}_4$	$\sim 60\text{--}90 \text{ m}^2/\text{g}$	$\sim 0.2\text{--}0.3 \text{ cm}^3/\text{g}$	Microporous ($\sim 1\text{--}2 \text{ nm}$)	<ul style="list-style-type: none"> - Relatively high surface area suitable for photocatalytic applications. - Micropores provide a good framework for charge carrier retention.
$\text{g-C}_3\text{N}_4\text{-Fe}_2\text{O}_3$	$\sim 90\text{--}120 \text{ m}^2/\text{g}$	$\sim 0.3\text{--}0.4 \text{ cm}^3/\text{g}$	Mixed (micro- and mesoporous)	<ul style="list-style-type: none"> - Increased surface area and pore volume after composite formation. - Enhanced catalytic and photocatalytic properties due to improved porosity.

3.9 Thermogravimetric Analysis (TGA)

Thermogravimetric Analysis (TGA) reveals essential information about the materials' thermal stability and decomposition behaviour (Table 11). Fe_2O_3 demonstrates excellent thermal stability with only a minor weight loss ($\sim 5\text{--}10\%$) occurring between $200\text{--}300^\circ\text{C}$ due to the removal of adsorbed water, remaining stable up to 700°C [52]. $\text{g-C}_3\text{N}_4$, on the other hand, undergoes a significant weight loss ($\sim 20\text{--}30\%$) between $300\text{--}500^\circ\text{C}$, indicating decomposition of the organic framework, with stability up to 500°C . The $\text{g-C}_3\text{N}_4\text{-Fe}_2\text{O}_3$ composite shows a two-step weight loss, the first corresponding to water and surface group removal ($200\text{--}300^\circ\text{C}$), and the second associated with the thermal decomposition of $\text{g-C}_3\text{N}_4$ ($500\text{--}600^\circ\text{C}$). The composite's thermal stability is improved compared to pure $\text{g-C}_3\text{N}_4$, highlighting the interaction between the components [53].

Table 11. TGA of $\text{g-C}_3\text{N}_4$, Fe_2O_3 , and $\text{g-C}_3\text{N}_4\text{-Fe}_2\text{O}_3$ nanocomposite

Material	Initial Weight Loss ($^\circ\text{C}$)	Total Weight Loss (%)	Thermal Stability ($^\circ\text{C}$)	Critical Remarks
Fe_2O_3	$200\text{--}300^\circ\text{C}$	$\sim 5\text{--}10\%$	Stable up to	- Fe_2O_3 shows excellent thermal stability.

Material	Initial Weight Loss (°C)	Total Weight Loss (%)	Thermal Stability (°C)	Critical Remarks
			700°C	- Minor weight loss at lower temperatures due to surface adsorbed water.
g-C ₃ N ₄	300–500°C	~20–30%	Stable up to 500°C	- Noticeable weight loss due to decomposition of organic material. - Thermal degradation occurs within a specific range, indicating moderate stability.
g-C ₃ N ₄ -Fe ₂ O ₃	200–300°C and 500–600°C	~10–20%	Stable up to 600°C	- Composite shows a two-step weight loss. - First loss is attributed to water removal and surface groups, second to decomposition of g-C ₃ N ₄ .

3.10 Vibrating Sample Magnetometry (VSM)

Vibrating Sample Magnetometry (VSM) measurements reveal distinct magnetic behaviours in the materials (Table 12). Fe₂O₃ shows weak paramagnetic behaviour, with a saturation magnetisation of ~15–30 emu/g, making it suitable for magnetic separation in photocatalytic applications. g-C₃N₄ is non-magnetic, contributing no magnetic properties to the composite but offering a stable platform for Fe₂O₃ integration. The g-C₃N₄-Fe₂O₃ composite exhibits superparamagnetic behaviour, with a higher saturation magnetisation (~25–45 emu/g), indicating that the composite's magnetic response is significantly enhanced, which is beneficial for efficient separation and recycling after photocatalytic reactions[54].

Table 12. Magnetic measurement of g-C₃N₄, Fe₂O₃, and g-C₃N₄-Fe₂O₃ nanocomposite

Material	Magnetic Properties	Saturation Magnetization (emu/g)	Critical Remarks
Fe ₂ O ₃	Paramagnetic behavior	~15–30 emu/g	- Exhibits weak magnetism, typical for Fe ₂ O ₃ . - Potential for magnetic separation in photocatalytic applications.
g-C ₃ N ₄	Non-magnetic	0 emu/g	- g-C ₃ N ₄ is inherently non-magnetic, providing a stable platform for composite formation. - No contribution to magnetic properties.
g-C ₃ N ₄ -Fe ₂ O ₃	Superparamagnetic behaviour	~25–45 emu/g	- g-C ₃ N ₄ -Fe ₂ O ₃ composite exhibits superparamagnetic properties. - Enhanced magnetic response facilitates easy separation after catalytic processes.

Mechanism of Photocatalytic Activity in g-C₃N₄-Fe₂O₃ Nanocomposites

The graphitic carbon nitride (g-C₃N₄) has garnered particular attention due to its unique combination of visible-light activity, suitable band structure, and chemical versatility, making it a highly promising candidate for forming efficient Fe₂O₃-based heterojunction photocatalysts. In photocatalytic degradation, mechanisms play a very significant role in improving the efficiency of composite materials. There are various types of

mechanisms studied in the literature for composite materials, viz. Type-II, Z-scheme, and S-scheme are discussed, along with their identification techniques and advantages.

Table 13: Photocatalytic Performance and Mechanisms of Fe₂O₃/g-C₃N₄ Composites

No.	Composite Material	Mechanism Type	Target Pollutant / Activity	Photocatalytic Performance	Reference
1	Fe ₂ O ₃ /g-C ₃ N ₄	Z-scheme	Rhodamine B (RhB)	Rate constant 2.5 times higher than g-C ₃ N ₄ alone under visible light	[55]
2	Fe ₂ O ₃ /g-C ₃ N ₄	Z-scheme	H ₂ generation	13-fold enhancement in H ₂ evolution rate under visible light with Pt as co-catalyst	[56]
3	Fe ₂ O ₃ /g-C ₃ N ₄	Type-II	Phenol	Achieved 94% degradation in visible light conditions	[57]
4	g-C ₃ N ₄ /α-Fe ₂ O ₃ /Co ₃ S ₄	S-scheme	H ₂ production	Hydrogen evolution rate of 191.41 μmol, ~30 times higher than Co ₃ S ₄ alone	[58]

4.1 Type-II Heterojunction Mechanism

In the Type II heterojunction mechanism of the g-C₃N₄-Fe₂O₃ composite, mainly photogenerated electrons (e⁻) in the conduction band (CB) of g-C₃N₄ transfer to the CB of Fe₂O₃, while holes (h⁺) from the valence band (VB) of Fe₂O₃ migrate to the VB of g-C₃N₄. This spatial separation promotes effective charge transfer and reduces recombination, enhancing hydroxyl radical (·OH) generation crucial for photo-Fenton activity (**Fig.3**). Unlike the Z-scheme, which retains strong redox potentials by recombining less energetic charge carriers, and the S-scheme that selectively directs high-energy charges while filtering low-energy ones, the Type II system sacrifices some redox power for better charge separation and stability[44].

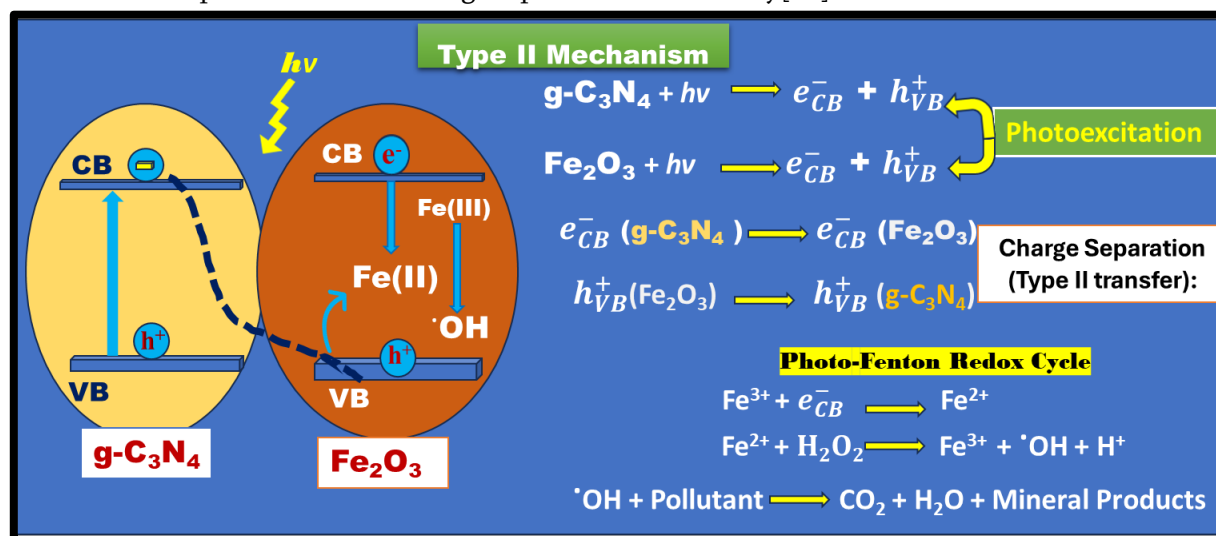


Fig.3 Type II Photocatalytic Mechanism

g-C₃N₄ and Fe₂O₃ form a Type-II heterojunction in which the band alignment enables directional charge separation:

- Electrons from the g-C₃N₄ conduction band (CB, ~-1.1 eV) transfer to the Fe₂O₃ CB (+0.3 eV).
- Holes from the Fe₂O₃ valence band (VB, +2.6 eV) move to the g-C₃N₄ VB (+1.6 eV).

Redox limitations arise due to the energy positions of the bands:

- Electrons in the Fe_2O_3 CB (+0.3 eV) are insufficient to reduce O_2 to $\cdot\text{O}_2^-$ (-0.33 eV).
- Holes in the g- C_3N_4 VB (+1.6 eV) cannot oxidize OH^- to $\cdot\text{OH}$ (+1.99 eV).

This limited redox potential hinders the formation of reactive oxygen species (ROS), essential for effective photocatalytic degradation.

Identification of the Type-II mechanism is supported by:

- UV-DRS and UPS measurements that confirm band alignment.
- Moderate photocurrent and high photoluminescence (PL), indicating charge recombination.
- Weak ESR signals for $\cdot\text{OH}$ and $\cdot\text{O}_2^-$, indicating low ROS production.

4.2 Z-Scheme Heterojunction Mechanism

The Z-scheme mechanism allows recombination of low-energy carriers, preserving high-energy electrons and holes with strong redox ability. This mechanism is preferred in Fe_2O_3 -g- C_3N_4 systems (Fig.4) [59].

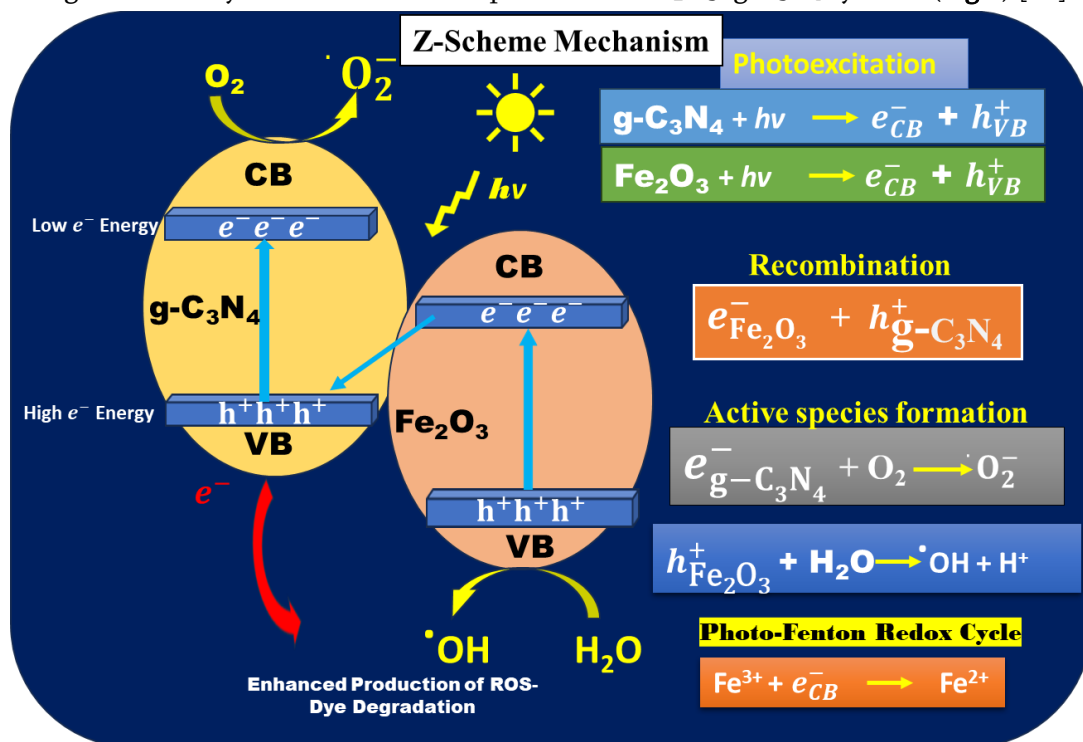


Fig.4. Z Scheme Photocatalytic Mechanism

Mechanism Details:

- e^- in Fe_2O_3 CB (+0.3 eV) recombines with h^+ in g- C_3N_4 VB (+1.6 eV)
- High-energy e^- in g- C_3N_4 CB (-1.1 eV) reduce $\text{O}_2 \rightarrow \cdot\text{O}_2^-$
- High-energy h^+ in Fe_2O_3 VB (+2.6 eV) oxidize $\text{H}_2\text{O}/\text{OH}^- \rightarrow \cdot\text{OH}$
- Enhanced production of ROS \rightarrow dye degradation

Advantages:

- Retains full redox potential
- Effective for the degradation of various dye pollutants

Identified by:

- Band edge analysis via XPS/UPS
- Strong signals of $\cdot\text{O}_2^-$ and $\cdot\text{OH}$ via ESR spectroscopy
- Efficient charge carrier dynamics (low PL, high photocurrent)

4.3 S-Scheme Heterojunction Mechanism

The S-scheme (step-scheme) is a new-generation heterojunction model that retains the high redox ability like Z-scheme but incorporates built-in electric field (IEF) and band bending to enhance charge carrier separation further (Fig.5) [60].

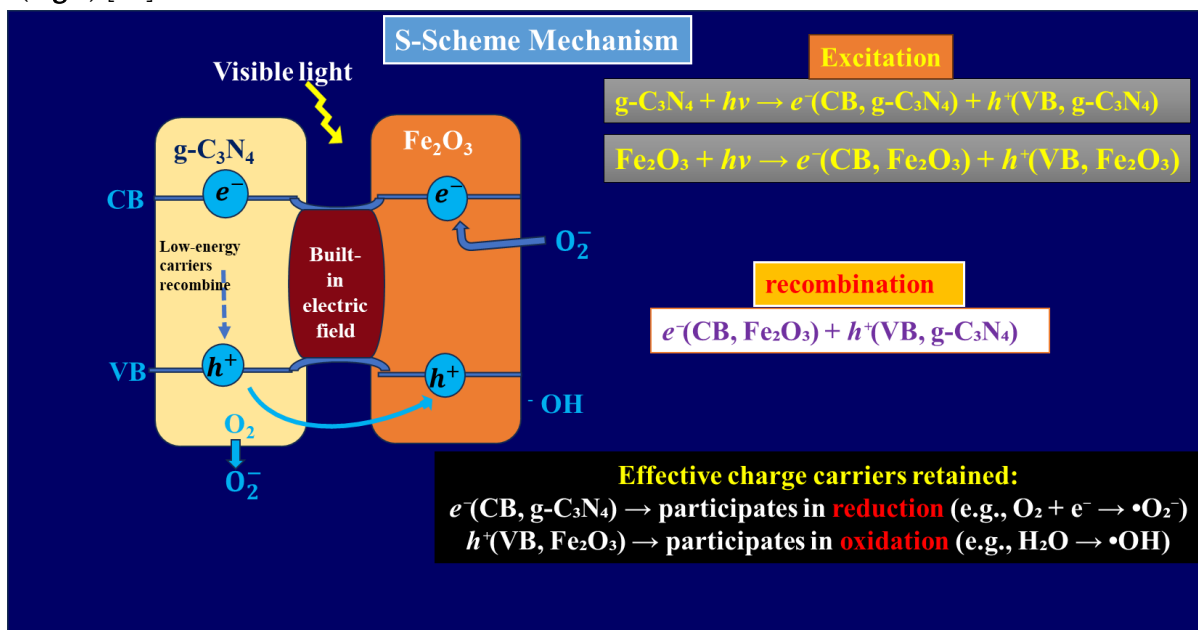


Fig.5

Mechanism Details:

- Upon contact, band bending and IEF form at the interface
- Low-energy carriers recombine at the interface
- High-energy e^- from CB of $g\text{-C}_3\text{N}_4$ and h^+ from VB of Fe_2O_3 are spatially separated
- Facilitates formation of $\cdot\text{O}_2^-$ and $\cdot\text{OH}$ radicals, key for dye degradation

Advantages:

- Strong internal field promotes ultrafast carrier migration
- Effective under visible light due to narrow bandgap and synergistic behavior

Identified by:

- Mott-Schottky plots (to determine flat band positions)
- Time-resolved PL spectroscopy
- XPS depth profiling (evidence of Fermi level alignment)
- Transient photocurrent, lower charge transfer resistance in EIS

Table 14 summarizes the comparison of charge transfer mechanisms and photocatalytic efficiencies among Type II, Z-scheme, and S-scheme heterojunctions.

Table 14. of Mechanisms, ROS, and Dyes Degraded.

Feature	Type II	Z-Scheme	S-Scheme
Charge Flow Direction	CB ($g\text{-C}_3\text{N}_4$) \rightarrow CB (Fe_2O_3), VB (Fe_2O_3) \rightarrow VB ($g\text{-C}_3\text{N}_4$)	CB (Fe_2O_3) \rightarrow VB ($g\text{-C}_3\text{N}_4$) (recombination)	Similar to Z-scheme but with a built-in electric field aiding separation
Redox Potential Retention	Reduced (lower redox ability)	Retained (strong oxidation/reduction retained)	Retained with added driving force via internal field

Feature	Type II	Z-Scheme	S-Scheme
Main Advantage	Efficient charge separation	High redox potential maintained	Strong charge separation + high redox ability
Suitable for	Mild reactions (e.g., dye degradation via Fenton)	Reactions needing strong redox power	High-efficiency photocatalysis with enhanced selectivity

5Fe₂O₃-g-C₃N₄ Nanocomposites for Sustainable Environmental Application

Iron oxide graphitic carbon nitride nanocomposites have emerged as auspicious materials for various environmental remediation applications, particularly for degrading organic pollutants from wastewater. The synergistic integration of iron oxide (Fe₂O₃), known for its strong redox properties, with graphitic carbon nitride (g-C₃N₄), valued for its high surface area, visible light response, and chemical stability, results in enhanced photocatalytic performance. These nanocomposites efficiently degrade persistent contaminants such as dyes, pharmaceutical residues, and pesticides under visible or solar irradiation, often achieving rapid degradation rates due to improved charge carrier separation and extended light absorption capacity[61]. Additionally, they are used for hydrogen production via water splitting and CO₂ reduction, contributing to clean energy solutions. Notably, the nanocomposites achieve substantial dye degradation in markedly shorter reaction times under UV-visible or sunlight. This confirms the enhanced interfacial charge transfer and wider light absorption achieved through composite formation (Table 15). Their reusability, cost-effectiveness, and ability to function under solar irradiation make them attractive for sustainable environmental remediation.

Table 15. Photocatalytic degradation of organic dyes using Fe₂O₃, g-C₃N₄, and their composites

Pollutant (Dye)	Material	Light Source	Photocatalytic Efficiency	Reaction Time	Performance of Composite vs. Individual	Reference
Methyl Orange (MO)	Fe ₂ O ₃	Sunlight	~60%	90 min	–	[62]
	g-C ₃ N ₄	Sunlight	~65%	120 min	–	
	Fe ₂ O ₃ /g-C ₃ N ₄	Sunlight	96.5%	60 min	Significant enhancement	
Methylene Blue (MB)	Fe ₂ O ₃	Visible light	~53%	120 min	–	[63]
	g-C ₃ N ₄	Visible light	~38%	120 min	–	
	Fe ₂ O ₃ /g-C ₃ N ₄	Visible light	89%	120 min	Strong enhancement	
Rhodamine B (RhB)	Fe ₂ O ₃	Sun light	~58%	150 min	–	[64]
	g-C ₃ N ₄	Sun light	~64%	150 min	–	
	Fe ₂ O ₃ /g-C ₃ N ₄	Sun light	93%	150 min	Excellent improvement	
Methyl Orange (MO)	Fe ₂ O ₃	Visible light	39.33%	60 min	–	[32]

Pollutant (Dye)	Material	Light Source	Photocatalytic Efficiency	Reaction Time	Performance of Composite vs. Individual	Reference
	$g\text{-C}_3\text{N}_4$	Visible light	45.33%	60 min	–	
	$\text{Fe}_2\text{O}_3/g\text{-C}_3\text{N}_4$	Visible light	97.66%	60 min	Superior activity	
Orange II	$\alpha\text{-Fe}_2\text{O}_3$	Visible light	~40%	150 min	–	[65]
	$g\text{-C}_3\text{N}_4/\alpha\text{-Fe}_2\text{O}_3$	Visible light	~60%	150 min	–	
	$g\text{-C}_3\text{N}_4/\alpha\text{-Fe}_2\text{O}_3/\text{Fe}_3\text{O}_4$	Visible light	79%	150 min	Significant enhancement	
Crystal Violet (CV)	Fe_2O_3	Sun Light	72%	150 min	–	[66]
	$g\text{-C}_3\text{N}_4$	Sun Light	85%	150 min	–	
	$g\text{-C}_3\text{N}_4/\text{Fe}_2\text{O}_3$	Sun Light	95%	1500 min	Significant enhancement	

5.1 Factors Influencing Photocatalytic Performance

Several key parameters, including the $\text{Fe}_2\text{O}_3:g\text{-C}_3\text{N}_4$ ratio, surface area, doping, and morphology, influence the efficiency of $\text{Fe}_2\text{O}_3/g\text{-C}_3\text{N}_4$ nanocomposites. Optimal ratios improve interface contact and charge transfer, while porous structures enhance dye adsorption. Metal or non-metal doping suppresses recombination and extends visible-light absorption. Environmental factors such as pH, light source, and dye type also impact performance. Tailoring these factors can significantly boost photocatalytic outcomes, though long-term stability still needs improvement. These key factors, which are critical for enhancing real-world efficacy, are summarized in Table 16.

Table 16. Influencing factors of dye degradation performance

Factor	Influence on Performance
Composite Ratio ($\text{Fe}_2\text{O}_3/g\text{-C}_3\text{N}_4$)	Affects interface contact, electron transfer, and light absorption. Too much Fe_2O_3 may shield light; too little reduces.
Morphology and Surface Area	Higher surface area = more active sites. Porous/hollow structures improve dye adsorption and light scattering.
Doping with Metal/Non-metals	Enhances conductivity, suppresses recombination, and tunes bandgap.
Co-catalysts	Noble metals (Ag, Pt) or graphene can act as electron sinks, enhancing charge separation.
pH of Solution	Affects surface charge, dye ionization, and ROS generation. Optimal pH is often dye-specific.
Light Source	$g\text{-C}_3\text{N}_4$ is visible-light active; Fe_2O_3 absorbs in both regions. The composite shows good

Factor	Influence on Performance
(UV/Visible)	performance under sunlight.
Reusability and Stability	Reusability is essential for practical use. Magnetic Fe ₂ O ₃ allows easy separation; stability ensures long-term use.

5.2 Comparative Analysis with Other Photocatalysts

Fe₂O₃/g-C₃N₄ composites outperform many conventional photocatalysts like TiO₂ and ZnO due to their broader light absorption and efficient charge separation via Z-/S-scheme mechanisms. While TiO₂ and ZnO are UV-active, the composite works efficiently under visible and solar light, often achieving >90% dye degradation. Its magnetic recoverability adds practical value. Moreover, green synthesis routes make it cost-effective and sustainable, although real wastewater conditions and reusability under field conditions need further evaluation.

Photocatalyst	Light Absorption	Charge Separation Efficiency	Photodegradation Efficiency (e.g., Methyl Orange)	Reusability	Cost & Sustainability	Limitations
TiO ₂ (P25)	UV-active only ($\lambda < 380$ nm)	Moderate	~60–70% in 120 min (UV)	Moderate (5 cycles)	Cheap, abundant	Limited visible light use
ZnO	UV-active	Fast recombination	~65–75% in 120 min (UV)	Moderate	Simple synthesis	Photo corrosion under light
g-C ₃ N ₄	Visible-light active ($\lambda \sim 450$ nm)	Low (fast recombination)	~50–60% in 120 min (visible)	Good	Green, metal-free	Needs heterojunctions to improve
Fe ₂ O ₃ alone	Visible ($\lambda \sim 550$ nm)	Poor (recombination)	~40–55% in 120 min	Limited	Earth-abundant	Low surface area, slow kinetics
Fe ₂ O ₃ /g-C ₃ N ₄	Wide range (UV + visible)	High (via Z-/S-scheme)	>90% in 90–120 min (visible or sunlight)	High (easy recovery via magnetism)	Eco-friendly (green synthesis possible)	Slightly lower activity under weak indoor light

Conclusion and Future Outlook

Iron oxide (Fe₂O₃)–graphitic carbon nitride (g-C₃N₄) nanocomposites represent a compelling class of visible-light-responsive photocatalysts that synergistically merge the magnetic, redox-active nature of Fe₂O₃ with the narrow bandgap and high stability of g-C₃N₄. Their integration forms effective Z-scheme or S-scheme heterojunctions, enhancing charge carrier separation and extended light absorption, attributes vital for efficiently degrading toxic organic dyes and pollutants.

This review has illustrated that the synthetic approaches, characterization techniques, mechanisms, and environmental applications of Fe₂O₃-g-C₃N₄ nanocomposites are closely aligned with green chemistry

principles for sustainable nanomaterial production. These materials have demonstrated more than 90% degradation of various dyes such as methyl orange, methylene blue, rhodamine B, Orange II, crystal violet, and congo red under UV-visible and sunlight, facilitated by advanced charge-transfer mechanisms and surface reactivity. However, a critical scientific analysis reveals notable limitations and research gaps: Incomplete mechanistic validation is often based solely on photoluminescence or UV-DRS without the support of TRPL, ESR, XPS, or scavenger-trapping experiments. Poor reproducibility of green-synthesized composites due to non-uniform precursor sources. Over multiple cycles, there is limited data on long-term photocatalyst stability, iron leaching, and reusability. Scarcity of real-effluent degradation studies, which are crucial for practical wastewater treatment. Inadequate monitoring of toxic degradation intermediates poses risks despite high decolorization efficiency.

To bridge these gaps, future research must focus on:

- Mechanistic studies using multi-spectral characterizations (e.g., TRPL, EIS, ESR, XPS) to gain deeper insights into charge transfer and active site dynamics.
- Standardized synthesis protocols for reproducible and scalable nanocomposite development, critical for real-world applications.
- Testing in real industrial wastewater and multi-component pollutant systems (dyes, antibiotics, heavy metals) to assess practical performance.
- Integration of ternary or doped systems (e.g., $\text{Fe}_2\text{O}_3/\text{g-C}_3\text{N}_4/\text{Ag}$) to boost photocatalytic and biological efficiency.
- Device-level implementation, such as coated membranes, 3D sponges, and magnetically retrievable platforms, to facilitate field applications.
- Expanding composite applications into energy storage devices and electrochemical sensing enhances multifunctionality.

Based on the comprehensive analysis of existing literature, future studies should prioritize scalable green synthesis methods, advanced mechanistic investigations through in-depth characterization, and expansion of application domains beyond dye degradation to include real wastewater treatment, hydrogen production, CO_2 reduction, and a stronger emphasis on energy storage devices aligning with global sustainability goals.

Acknowledgments

Mr. B.T. Shinde would like to extend our sincere appreciation to the Research Centre, Department of Chemistry, A.S.P. College (Autonomous), Devrukh, and S.K.S.V. College, Lanja, Ratnagiri, Maharashtra, India, for their valuable assistance and provision of essential resources for the successful execution of this research work.

Author Contributions:

Babasaheb T. Shinde: Conceptualization, literature review, writing original draft preparation, and data analysis. Dr. Hemant V. Chavan: Supervision, guidance throughout the research and writing process, critical revision of the manuscript, and final approval of the version to be submitted.

Conflicts of Interest:

The authors declare that there is no conflict of interest regarding the publication of this article.

REFERENCES

- [1]. F. Yang and P. Boulet, "DFT Investigation of a Direct Z-Scheme Photocatalyst for Overall Water Splitting: Janus $\text{Ga}_2\text{S}_5/\text{Bi}_2\text{O}_3$ Van Der Waals Heterojunction," 2025.

- [2]. H. W. Ahmad, H. A. Bibi, M. Chandrasekaran, S. Ahmad, and G. L. Kyriakopoulos, "Sustainable Wastewater Treatment Strategies in Effective Abatement of Emerging Pollutants," 2024.
- [3]. S. B. Babar et al., "An efficient fabrication of ZnO-carbon nanocomposites with enhanced photocatalytic activity and superior photostability," *J. Mater. Sci. Mater. Electron.*, vol. 30, no. 2, pp. 1133–1147, 2019, doi: 10.1007/s10854-018-0382-5.
- [4]. M. A. Hassaan, M. A. El, and N. Marwa, *Principles of Photocatalysts and Their Different Applications : A Review*, vol. 381, no. 6. Springer International Publishing, 2023. doi: 10.1007/s41061-023-00444-7.
- [5]. S. P. Keerthana et al., "A strategy to enhance the photocatalytic efficiency of α -Fe₂O₃," *Chemosphere*, vol. 270, p. 129498, 2021, doi: 10.1016/j.chemosphere.2020.129498.
- [6]. Y. L. Pang, S. Lim, and H. C. Ong, "Research progress on iron oxide-based magnetic materials: Synthesis techniques and photocatalytic applications," *Ceram. Int.*, vol. 15, no. August, pp. 01670–3, 2015, doi: 10.1016/j.ceramint.2015.08.144.
- [7]. N. Farooq, M. Imran, A. Mahmood, M. Ahmad, A. Shanableh, and S. Anjum, "Fe₂O₃ / g-C₃N₄ / CNTs based nanocomposites incorporated with neodymium and samarium nanoparticles for efficient photocatalytic vitiation of organic pollutants," vol. 259, pp. 71–81, 2022, doi: 10.5004/dwt.2022.28444.
- [8]. S. S. Yi, J. M. Yan, and Q. Jiang, "Carbon quantum dot sensitized integrated Fe₂O₃@g-C₃N₄ core-shell nanoarray photoanode towards highly efficient water oxidation," *J. Mater. Chem. A*, vol. 6, no. 21, pp. 9839–9845, 2018, doi: 10.1039/c8ta01908h.
- [9]. W. J. Ong, L. L. Tan, Y. H. Ng, S. T. Yong, and S. P. Chai, "Graphitic Carbon Nitride (g-C₃N₄)-Based Photocatalysts for Artificial Photosynthesis and Environmental Remediation: Are We a Step Closer to Achieving Sustainability?," *Chemical Reviews*, vol. 116, no. 12. pp. 7159–7329, 2016. doi: 10.1021/acs.chemrev.6b00075.
- [10]. Y. Wang, X. Wang, and M. Antonietti, "Polymeric graphitic carbon nitride as a heterogeneous organocatalyst: From photochemistry to multipurpose catalysis to sustainable chemistry," *Angew. Chemie - Int. Ed.*, vol. 51, no. 1, pp. 68–89, 2012, doi: 10.1002/anie.201101182.
- [11]. K. S. Novoselov et al, "Electric Field Effect in Atomically Thin Carbon Films," vol. 306, no. 5696, pp. 666–669, 2016.
- [12]. A. K. G. A. K. S. NOVOSELOV, "The rise of graphene," *Nat. Mater*, vol. 6, pp. 183–191, 2007, doi: 10.1007/978-3-319-70329-9.
- [13]. S. Pei and H. M. Cheng, "The reduction of graphene oxide," *Carbon N. Y.*, vol. 50, no. 9, pp. 3210–3228, 2012, doi: 10.1016/j.carbon.2011.11.010.
- [14]. D. R. Dreyer, S. Park, C. W. Bielawski, and R. S. Ruoff, "The chemistry of graphene oxide," *Chem. Soc. Rev.*, vol. 39, no. 1, pp. 228–240, 2010, doi: 10.1039/b917103g.
- [15]. G. Eda and M. Chhowalla, "Chemically derived graphene oxide: Towards large-area thin-film electronics and optoelectronics," *Adv. Mater.*, vol. 22, no. 22, pp. 2392–2415, 2010, doi: 10.1002/adma.200903689.
- [16]. D. Konios, M. M. Stylianakis, E. Stratakis, and E. Kymakis, "Dispersion behaviour of graphene oxide and reduced graphene oxide," *J. Colloid Interface Sci.*, vol. 430, pp. 108–112, 2014, doi: 10.1016/j.jcis.2014.05.033.
- [17]. X. Pan, M. Q. Yang, X. Fu, N. Zhang, and Y. J. Xu, "Defective TiO₂ with oxygen vacancies: Synthesis, properties and photocatalytic applications," *Nanoscale*, vol. 5, no. 9, pp. 3601–3614, 2013, doi: 10.1039/c3nr00476g.
- [18]. Y. Song, P. C. D. Mendes, and S. M. Kozlov, "Tunable properties and composition of ZnO films supported on metal surfaces," *J. Mater. Chem. A*, vol. 11, no. 25, pp. 13665–13676, 2023, doi: 10.1039/d3ta01940c.

- [19]. L. Yang et al., "Fabrication of semiconductor ZnO nanostructures for versatile SERS application," *Nanomaterials*, vol. 7, no. 11, 2017, doi: 10.3390/nano7110398.
- [20]. X. Zhang, W. Lu, G. Zhou, and Q. Li, "Understanding the Mechanical and Conductive Properties of Carbon Nanotube Fibers for Smart Electronics," *Adv. Mater.*, vol. 32, no. 5, pp. 1–21, 2020, doi: 10.1002/adma.201902028.
- [21]. P. Udomkun, T. Boonupara, S. M. Smith, and P. Kajitvichyanukul, "Green Ag/AgCl as an Effective Plasmonic Photocatalyst for Degradation and Mineralization of Methylthioninium Chloride," *Separations*, vol. 9, no. 8, pp. 1–17, 2022, doi: 10.3390/separations9080191.
- [22]. F. R. Oliveira, A. K. Patel, D. P. Jaisi, S. Adhikari, H. Lu, and S. K. Khanal, "Environmental application of biochar: Current status and perspectives," *Bioresour. Technol.*, vol. 246, pp. 110–122, 2017, doi: 10.1016/j.biortech.2017.08.122.
- [23]. A. Sánchez, "Editorial: Innovative uses of biochar in environmental applications," *Front. Chem. Eng.*, vol. 6, no. September, pp. 1–2, 2024, doi: 10.3389/fceng.2024.1474937.
- [24]. L. Zhou, L. Wang, J. Zhang, J. Lei, and Y. Liu, "Well-Dispersed Fe₂O₃ Nanoparticles on g-C₃N₄ for Efficient and Stable Photo-Fenton Photocatalysis under Visible-Light Irradiation," *Eur. J. Inorg. Chem.*, vol. 2016, no. 34, pp. 5387–5392, 2016, doi: 10.1002/ejic.201600959.
- [25]. P. Dhull, R. K. Lohchab, M. Kumari, K. Singh, and A. K. Bhankhar, "A Facile Method for Synthesis of α -Fe₂O₃ Nanoparticles and Assessment of Their Characterization," *Nat. Environ. Pollut. Technol.*, vol. 23, pp. 321–330, 2024.
- [26]. S. Sundar and G. Venkatachalam, "Nanostructures for the Selective and Sensitive Determination of Uric Acid and Dopamine," *Catalysts*, vol. 8, no. 11, p. 512, 2018, doi: 10.3390/catal8110512.
- [27]. J. Ma, J. Lian, X. Duan, X. Liu, and W. Zheng, "r-Fe₂O₃: Hydrothermal Synthesis, Magnetic and Electrochemical Properties," pp. 10671–10676, 2010.
- [28]. M. Diab and T. Mokari, "Thermal Decomposition Approach for the Formation of α -Fe₂O₃ Mesoporous Photoanodes and an α -Fe₂O₃/CoO Hybrid Structure for Enhanced Water Oxidation," *pubs.acs.org/IC Therm.*, vol. 53, p. 2304–2309, 2014.
- [29]. P. C. Implementation, "Synthesis and Characterization of α -Fe₂O₃ Nanoparticles by Microemulsion Method Gamze BOZKURT 1* 1," *J. Sci. Technol.*, vol. 13, no. 2, pp. 890–897, 2020, doi: 10.18185/erzifbed.742160.
- [30]. V. C. Karade et al., "Heliyon A green approach for the synthesis of α -Fe₂O₃ nanoparticles from *Gardenia resinifera* plant and its In vitro hyperthermia application," *Heliyon*, vol. 5, no. February, p. e02044, 2019, doi: 10.1016/j.heliyon.2019.e02044.
- [31]. H. J. Fatih, M. Ashengroph, and A. Sharifi, "potent antibacterial, anti-biofilm and anti-virulence agent against pathogenic bacteria," *BMC Microbiol.*, vol. 24, no. 535, pp. 1–13, 2024.
- [32]. B. T. Shinde, S. B. Babar, U. V. Shembade, A. V. Moholkar, and H. V. Chavan, "Efficient chemical synthesis of g-C₃N₄-Fe₂O₃ nanocomposites as a photocatalyst for superior photocatalytic degradation," *Res. Chem. Intermed.*, vol. 51, no. 3, pp. 1511–1535, 2025, doi: 10.1007/s11164-025-05514-7.
- [33]. Q. Tao, J. Bi, X. Huang, R. Wei, T. Wang, and Y. Zhou, "Chemosphere Fabrication, application, optimization and working mechanism of Fe₂O₃ and its composites for contaminants elimination from wastewater," *Chemosphere*, vol. 263, p. 127889, 2021, doi: 10.1016/j.chemosphere.2020.127889.
- [34]. B. Chen, S. Hatamie, P. Garu, P. Heravi, J. Chen, and B. Liu, "Synthesis of iron-oxide magnetic nanoparticles coated with dextran of varied molecular mass using a facile ball-milling method," *Micro Nano Lett.*, vol. 15, no. 10, pp. 645–650, 2020, doi: 10.1049/mnl.2019.0811.

- [35]. S. Babar et al., "Evolution of Waste Iron Rust into Magnetically Separable g-C₃N₄-Fe₂O₃ Photocatalyst: An Efficient and Economical Waste Management Approach," *ACS Appl. Nano Mater.*, vol. 1, no. 9, pp. 4682–4694, Sep. 2018, doi: 10.1021/acsnm.8b00936.
- [36]. S. B. Shinde, O. S. Nille, A. H. Gore, N. B. Birajdar, G. B. Kolekar, and P. V Anbhule, "Valorization of Waste Tungsten Filament into mpg - C₃ N₄ - WO₃ Photocatalyst: A Sustainable e - Waste Management and Wastewater Treatment," *Langmuir*, vol. 38, no. 44, p. 13543–13557, 2022, doi: 10.1021/acs.langmuir.2c02171.
- [37]. B. Palanivel et al., "Green synthesis of Fe₂O₃ deposited g-C₃N₄: Addition of rGO promoted Z-scheme ternary heterojunction for efficient photocatalytic degradation and H₂ evolution reaction," *Mater. Res. Bull.*, vol. 162, no. January, p. 112177, 2023, doi: 10.1016/j.materresbull.2023.112177.
- [38]. S. Vasantharaj, N. Sripriya, M. Shanmugavel, E. Manikandan, A. Gnanamani, and P. Senthilkumar, "Surface active gold nanoparticles biosynthesis by new approach for bionanocatalytic activity," *J. Photochem. Photobiol. B Biol.*, vol. 179, pp. 119–125, 2018, doi: 10.1016/j.jphotobiol.2018.01.007.
- [39]. L. Luo, A. Zhang, M. J. Janik, C. Song, and X. Guo, "Mesoporous graphitic carbon nitride functionalized iron oxides for promoting phenol oxidation activity," *RSC Adv.*, vol. 6, no. 94, pp. 91960–91967, 2016, doi: 10.1039/c6ra19455a.
- [40]. M. Ashraf et al., "Heliyon Fabrication and characterization of novel , cost-effective graphitic carbon nitride / Fe coated textile nanocomposites for effective degradation of dyes and biohazards," *Heliyon*, vol. 9, no. 10, p. e20822, 2023, doi: 10.1016/j.heliyon.2023.e20822.
- [41]. K. C. Christoforidis et al., "Synthesis and photocatalytic application of visible-light active α -Fe₂O₃ / g-C₃N₄ hybrid nanocomposites".
- [42]. S. Al, S. Thangavel, Y. Kim, and R. Selvaraj, "Enhanced photocatalytic activity of a α -Fe₂O₃ / g-C₃N₄ composite materials for degradation of toluene in aqueous solution under visible light irradiation," vol. 254, pp. 94–103, 2022, doi: 10.5004/dwt.2022.28350.
- [43]. D. Mhamane, H. K. Kim, V. Aravindan, K. C. Roh, M. Srinivasan, and K. B. Kim, "Rusted iron wire waste into high performance anode (α -Fe₂O₃) for Li-ion batteries: An efficient waste management approach," *Green Chem.*, vol. 18, no. 5, pp. 1395–1404, Mar. 2016, doi: 10.1039/c5gc01747e.
- [44]. F. Ge, X. Li, M. Wu, H. Ding, and X. Li, "RSC Advances PAPER A type II heterojunction α -Fe₂O₃ / g-C₃N₄ for the," *RSC Adv.*, vol. 12, pp. 8300–8309, 2022, doi: 10.1039/D1RA09282K.
- [45]. X. Hu, J. C. Yu, J. Gong, Q. Li, and G. Li, " α -Fe₂O₃ nanorings prepared by a microwave-assisted hydrothermal process and their sensing properties," *Adv. Mater.*, vol. 19, no. 17, pp. 2324–2329, Sep. 2007, doi: 10.1002/adma.200602176.
- [46]. V. Gaikwad, U. Kumar, F. Pahlevani, A. Piadasa, and V. Sahajwalla, "Thermal Transformation of Waste Toner Powder into a Value-Added Ferrous Resource," *ACS Sustain. Chem. Eng.*, vol. 5, no. 12, pp. 11543–11550, 2017, doi: 10.1021/acssuschemeng.7b02875.
- [47]. N. Farooq et al., "A comparative study of cerium- and ytterbium-based GO/g-C₃N₄/Fe₂O₃ composites for electrochemical and photocatalytic applications," *Appl. Sci.*, vol. 11, no. 19, 2021, doi: 10.3390/app11199000.
- [48]. N. X. D. Linh et al., "Facile Fabrication of α -Fe₂O₃/g-C₃N₄ Z Scheme Heterojunction for Novel Degradation of Residual Tetracycline," *Top. Catal.*, vol. 66, no. 1–4, pp. 139–148, Jan. 2023, doi: 10.1007/s11244-022-01751-x.

- [49]. A. Kheradmand, A. Wainwright, L. Wang, and Y. Jiang, "Anchoring Iron Oxides on Carbon Nitride Nanotubes for Improved Photocatalytic Hydrogen Production," *Energy & Fuels*, vol. 35, no. 1, pp. 868–876, 2021, doi: 10.1021/acs.energyfuels.0c03901.
- [50]. D. R. Paul, S. Gautam, P. Panchal, S. P. Nehra, P. Choudhary, and A. Sharma, "ZnO-Modified g-C₃N₄: A Potential Photocatalyst for Environmental Application," 2020, doi: 10.1021/acsomega.9b02688.
- [51]. R. Khurram, Z. U. Nisa, A. Javed, Z. Wang, and M. A. Hussien, "Synthesis and Characterization of an α -Fe₂O₃-Decorated g-C₃N₄ Heterostructure for the Photocatalytic Removal of MO," 2022.
- [52]. E. C. Spencer, N. L. Ross, R. E. Olsen, B. Huang, I. Alexander, and B. F. Woodfield, "Thermodynamic Properties of α -Fe₂O₃ and Fe₃O₄ Nanoparticles," pp. 1–19, 2008.
- [53]. S. Babar et al., "An innovative transformation of waste toner powder into magnetic g-C₃N₄-Fe₂O₃ photocatalyst: Sustainable e-waste management," *J. Environ. Chem. Eng.*, vol. 7, no. 2, Apr. 2019, doi: 10.1016/j.jece.2019.103041.
- [54]. G. I. Tovar, S. Briceño, J. Suarez, S. Flores, and G. González, "Biogenic synthesis of iron oxide nanoparticles using *Moringa oleifera* and chitosan and its evaluation on corn germination," *Environ. Nanotechnology, Monit. Manag.*, vol. 14, no. June, p. 100350, 2020, doi: 10.1016/j.enmm.2020.100350.
- [55]. J. Hu, Shaozheng and Jin, Ruirui and Lu, Guang and Liu, Dan and Gui, "RSC Advances," *RSC Adv*, vol. 4, no. 47, pp. 24863–24869, 2014, doi: 10.1039/c4ra03290j.
- [56]. Q. Xu, B. Zhu, C. Jiang, B. Cheng, and J. Yu, "Constructing 2D/2D Fe₂O₃/g-C₃N₄ Direct Z-Scheme Photocatalysts with Enhanced H₂ Generation Performance," *Sol. RRL*, vol. 2, no. 3, pp. 1–10, 2018, doi: 10.1002/solr.201800006.
- [57]. Y. Zhang, J. Wan, C. Zhang, and X. Cao, "MoS₂ and Fe₂O₃ co-modify g-C₃N₄ to improve the performance of photocatalytic hydrogen production," *Sci. Rep.*, vol. 12, no. 1, pp. 1–12, 2022, doi: 10.1038/s41598-022-07126-2.
- [58]. T. Yan, H. Liu, and Z. Jin, "g-C₃N₄/ α -Fe₂O₃ Supported Zero-Dimensional Co₃S₄ Nanoparticles Form S-Scheme Heterojunction Photocatalyst for Efficient Hydrogen Production," *Energy and Fuels*, vol. 35, no. 1, pp. 856–867, 2021, doi: 10.1021/acs.energyfuels.0c03351.
- [59]. Y. pei Li et al., "Z-scheme electronic transfer of quantum-sized α -Fe₂O₃ modified g-C₃N₄ hybrids for enhanced photocatalytic hydrogen production," *Int. J. Hydrogen Energy*, vol. 42, no. 47, pp. 28327–28336, 2017, doi: 10.1016/j.ijhydene.2017.09.137.
- [60]. H. Lv et al., "Multishelled hollow CaTiO₃ cubes decorated with Co_{0.2}Cd_{0.8}S nanoparticles for efficient photocatalytic H₂ evolution via S-scheme charge transfer," *Sep. Purif. Technol.*, vol. 345, p. 127429, Oct. 2024, doi: 10.1016/J.SEPPUR.2024.127429.
- [61]. M. A. Ahmed and A. A. Mohamed, "Recent progress in semiconductor/graphene photocatalysts: synthesis, photocatalytic applications, and challenges," *RSC Adv.*, vol. 13, no. 1, pp. 421–439, 2022, doi: 10.1039/d2ra07225d.
- [62]. S. Babar et al., "Evolution of Waste Iron Rust into Magnetically Separable g-C₃N₄-Fe₂O₃ Photocatalyst: An Efficient and Economical Waste Management Approach," *ACS Appl. Nano Mater.*, vol. 1, no. 9, pp. 4682–4694, 2018, doi: 10.1021/acsnm.8b00936.
- [63]. A. Ali et al., "g-C₃N₄/Fe₃O₄ composites synthesized via solid-state reaction and photocatalytic activity evaluation of methyl blue degradation under visible light irradiation," *Front. Mater.*, vol. 10, no. May, pp. 1–11, 2023, doi: 10.3389/fmats.2023.1180646.
- [64]. S. Kumaravel et al., "Rational construction of MOF derived α -Fe₂O₃/g-C₃N₄ composite for effective photocatalytic degradation of organic pollutants and electrocatalytic oxygen evolution reaction,"

Spectrochim. Acta - Part A Mol. Biomol. Spectrosc., vol. 310, no. November 2023, p. 123972, 2024, doi: 10.1016/j.saa.2024.123972.

- [65]. Z. Wang et al., "Novel magnetic g-C₃N₄/α-Fe₂O₃/Fe₃O₄ composite for the very effective visible-light-fenton degradation of Orange II," RSC Adv., vol. 8, no. 10, pp. 5180–5188, 2018, doi: 10.1039/c7ra13291c.
- [66]. T. Wang et al., "Facile one-step hydrothermal synthesis of α-Fe₂O₃/g-C₃N₄ composites for the synergistic adsorption and photodegradation of dyes," RSC Adv., vol. 9, pp. 29109–29119, 2019, doi: 10.1039/c9ra05100g.

Use of different sensors in Aquaculture

*Shinde K.M. Satam.S.B, Pagarakar A.U, Chogale N.D, Sawnt A.N, Sadavarte V.R, Sadawarte R.K., Dhamagaye H.B,
Mohite A.S, Golvankar A.P

DBSKKV, Marine Biological Research Station, Zadgaon, Ratnagiri, Maharashtra, India

ARTICLE INFO

Article History:

Published : 30 April 2025

Publication Issue :

Volume 12, Issue 13

March-April-2025

Page Number :

269-274

ABSTRACT

Sensors the name itself indicates the tool which sense. Sense may be changes in the property may be physical, chemical or biological. Now a days we are surrounded by many sensors. They are proved to be indispensable tool in many areas. The main concern is about modernization. Now a days the sensors are becoming appropriate tool for innovative aquaculture techniques improving farm productivity and sustainable aquaculture. Sensors in aquaculture sector provide real-time data of the environmental conditions that can useful for improving farm management tactics, increase in productivity, reduce environmental impact, and beneficial to aquatic species by monitoring water quality, fish health, and feeding behavior. This data allows for proactive adjustments to optimize conditions and minimize losses. The effective sensors used in aquaculture are Dissolved oxygen (DO) sensors measures the oxygen concentration in water. pH Sensors counts the pH of water as it is important parameter regarding the health of aquatic specimen. Ammonia sensors detect the concentration of ammonia (NH₃) in water, while Salinity sensors work on conductivity or refractive index, and provide real-time data on salinity levels of media. Temperature sensors, works with thermocouples or thermistors, continuously measure water temperature and send real-time data to a central control system. Electrical Conductivity (EC) sensors counts the ability of water to conduct electricity, directly related to the concentration of dissolved ions. Total Dissolved Solids (TDS) indicates the combined content of all dissolved substances, both inorganic and organic present in the water.

Keywords: sensors, indispensable tool, parameters, real time data, concentration,

INTRODUCTION

World population is increasing as anything but the resources are limited. Aquaculture is a word comprising of aquatic animal breeding, rearing, harvesting the grow outs. Many environmental parameters plays vital role in different phases of aquaculture. These parameters should be in range for better results which leads to high yields beneficial for the culturist. Some problems of aquaculture water quality monitoring systems, such as wiring difficulties, low performance-price ratio and short of flexibility, still exist. This paper analyzes the limitations of the existing aquaculture water quality monitoring systems and the new aquaculture water quality monitoring systems based on wireless sensor networks.

There are many parameters that affects the quality of culture water and in terms affects the growth and survival of the cultured specimen. Viz. Physical, chemical and biological or in combine form.

Physical parameters:

Physical parameters, including dissolved oxygen (DO), temperature, pH level, salinity, and turbidity which are known to be basic parameters that has to be monitored and keep under controlled in aquaculture system [1]. Fluctuations in these parameters may directly or indirectly affects not only health of the animals but also feed utilization, growth rates, and carrying capacities [2].

Various sensors used for Aquaculture:

Dissolved oxygen (DO) sensors:

One of the most important sensor from aquaculture point of view. Oxygen is essential for the survival of fish and other aquatic species. Aquatic species took oxygen directly from the water through their gills, the lower oxygen levels in water can lead to stress, hamper growth, and may leads to mortality. Regulating oxygen levels is therefore critical to maintaining a healthy aquaculture system. These sensors typically operates on techniques that measure the amount of oxygen dissolved in the water. The accurate and appropriate information of dissolved oxygen in water by the sensors allows farmers to ensure about oxygen levels lies within the optimal range needed for the farmed species. They can also be automated and linked to the aerators so that if oxygen levels fall too low, aeration systems can be activated to increase oxygenation in the water automatically. The level of DO in water, and hence the amount of oxygen consumed, is directly linked to the size of fish, feeding rate, activity level, and pond temperature [3].

pH Sensors:

The pH level of water affects the solubility of oxygen and other essential minerals. So pH is another crucial parameter for the health of aquatic species.

Some Aquatic organisms have specific pH requirements, so the shift in pH above the optimal range can lead to stress and reduced growth rates and vice versa. Some fish species such as salmon are particularly sensitive to changes in pH levels. These sensors measure the water acidity or alkalinity and provide continuous data which can be used to adjust the water conditions. Continuous monitoring of pH in real time, fish farmers may take appropriate actions to adjust the water quality, by adding buffers to stabilize the pH or adjusting the composition of the water to improve fish health and enhance the production.

Phytoplankton present in culture water breaks down toxic ammonia into harmless forms. This organism thus plays an indirect part in maintaining the pH level of the water as well. The acceptable range of pH for fish culture is usually between pH 6.5 and 9.0.

Salinity Sensors:

In aquaculture salinity plays a vital role, especially in marine fish farming. Salinity levels on too higher or too lower sides can prove harmful for the fish, which affects their growth and survival rates. Salinity sensors are used to measure the concentration of salts in the water, Unit for this is *ppt* i.e. *parts per thousand*. It is especially important for species that require specific salinity levels, such as shrimp or marine fish.

These sensors work on various principles, refractive index or conductivity. It also provides real-time data on salinity levels. With the help of this data received from these sensors, fish farmers can regulate salinity levels by adding fresh water if salinity rises and ensure optimal conditions for different species.

Ammonia detecting sensors:

Ammonia is a complex result of metabolic waste, feed waste and excreta of cultured species. If the concentration of ammonia increases in water can prove toxic to the aquatic species cultured and causes respiratory issues.

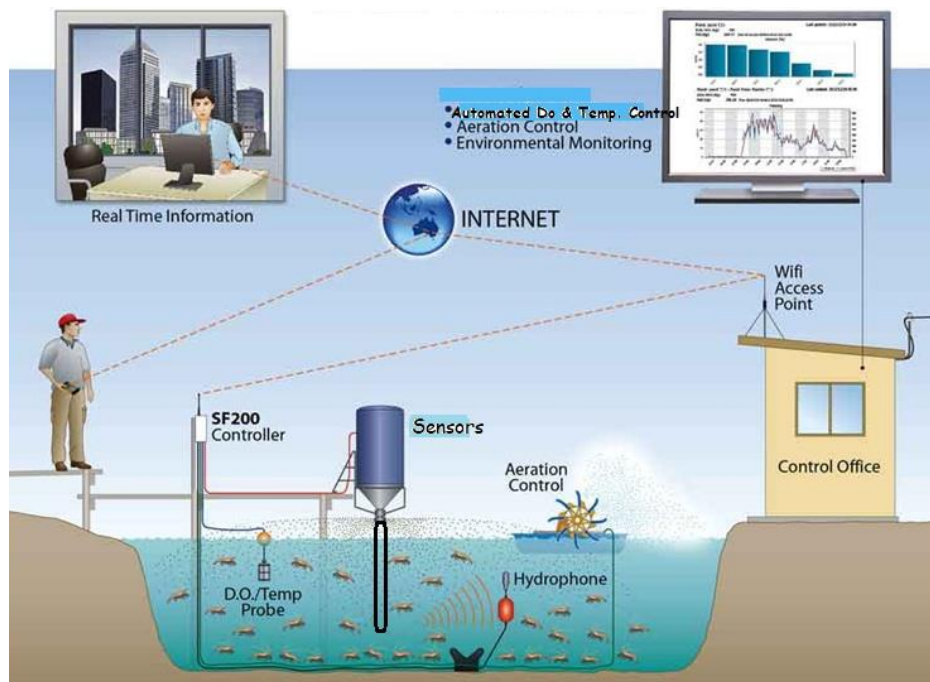
Ammonium (NH_4^+) in the water is converted to toxic ammonia (NH_3), a compound that is lethal to fishes. On the other hand, when the pH level goes below 5, acidic water would leach metals from rocks and sediments. These metals would adversely affect fishes' metabolism rates and their ability to take in water through their gills, resulting in a fatality as well.

Ammonia sensors detect the concentration of ammonia (NH_3) in water, typically using ion-selective electrodes (ISE) or chemical sensors. Continuous monitoring of ammonia levels helps fish farmers to prevent formation of ammonia reaches the harmful levels and cause toxicity in water. Use of bio filters and circulatory aquaculture system with incorporation of bio filtration system can reduce the concentration of ammonia in culture water.

The need of Wireless Sensor Network (WSN):

WSN is referred as wireless network system which ensures hassle-free operations of sensors. In older days fish farmers used handheld sensors for water quality measurement. The aforementioned physical parameters are commonly required to maintain acceptable levels for fish growth regardless the type of fishes. While handheld instruments or sensors can provide onsite measurement by the staff during office hours, the variation of one of the key water parameters beyond a safe level can occur out of office hours, unseen by the staff. When the bad situation is persistent, it will lead to undesirable effects, such as poor growth, undetected disease symptoms, or abnormal behavior of the fish [4, 5].

WSN is composed of many self-organized sensors deployed in a monitoring region that measure, collect, transmit, and process information in real time. The information measured is then displayed on a computer or conveyed in the form of a message to farmers for the real-time update. This real-time remote monitoring technology allows the streamlining of the information accumulation process, which conceivably minimizes human lapses and time delays, hence increasing the quantity and quality of data on temporal and spatial scales [6].



Various versatile research were conducted to study different water parameters and develop WSN for use in aquaculture [6–11]. Most of these technologies which are boosting the ability to measure the majority of the important physical parameters in real-time and the capability of informing the necessary people at the facility whenever a problem arises, allowing for quick and immediate resolution. Espinosa-Faller and Redón-Rodríguez [8] presented a WSN-based water monitoring system that transmits the gathered information and stores them in a database. The system is also able to measure temperature, pressure, and DO throughout the day. When a problem was detected, an SMS or an E-mail was forwarded to alert the person responsible for the facility. Zhang et al. [9] proposed another WSN-based water monitoring system that was able to measure pH, water temperature, water level, and DO. The data collected was forwarded to a database that provided the information to the software to be monitored in real time. In their system, the software used was able to separate logic, display, and data layers to improve scalability and reusability. Warnings could also be forwarded via SMS to the users. Lastly, Huang et al. [10] presented a WSN-based system that gathered data on pH, temperature, and DO. It contains a real-time interface that displays the data numerically and graphically. More recently, Luo et al. [11] reported a real-time remote monitoring system for aquaculture water quality using solar cells and lithium cells for power supply. In their system, they have integrated the commercial YCS-2000 DO sensor, pH electrode, Pt1000 temperature sensor, and ammonia nitrogen sensor.

Many combo equipment wired or wireless are available in market which bridges the gaps of multiple parameter systems covering a wider range of parameters (physical, chemical, biochemical, and biological). Utmost the chemical, biochemical, and biological sensors must reach to the desired level of portability. After repeated operations, trials and their outcomes we can assured their accuracy. After that we have to decide how to make them advanced by adopting advanced WSN technology. This can be decided on the nature of the need to cover not only the physical parameters but also chemical parameters and biohazards. The first thing to be taken into consideration while designing the same is that the sensor technologies must be highly robust because the aquatic environment and changes taking place from time to time. The factors such as extreme condition, drastic changes in environmental conditions maybe a problem in the reliability of the sensors and their sensing performance. The outer core or inner material of the sensor and their probes as the situation case may be

seaworthy, water resistance and to be stand in unstable chemical conditions. In future we have to think about the incorporation of nano- technology in this sensing world with microelectronics with cost effective platform. This advancement in sensors aquaculture industry may get boost and be proven a stake to the fish farmers operating their farms in remote areas. This will also give a touch of hi-tech aquaculture farming and may be fruitful for better and bio safe aquaculture production as due to this all parameters will remain in control and no need of external material to the aquaculture environment.

Applications of sensors in aquaculture:

1. Real time water quality monitoring.
2. Feed management and optimization.
3. Disease preventing and health management.
4. Atomization of environmental conditions.
5. Monitoring of water parameters in closed looped system.

Conclusion:

We are on the edge of the atomization of aquaculture and need to enter into this atomized world for sustain aquaculture production which is the need of the future food. It will also resolve the issues of monitoring aquaculture farms. The sensors and their WSN will boost the aquaculture production by controlling all environmental parameters within their optimum range. This edge cutting technology will be a milestone in aquaculture industry.

REFERENCES

- [1]. Mwegoha W. J. S., Kaseva M. E., Sabai S. M. M. Mathematical modeling of dissolved oxygen in fish ponds. *African Journal of Environmental Science and Technology*. 2010;4(9):623–638. [Google Scholar]
- [2]. Africa A. D. M., Aguilar J. C. C. A., Lim C. M. S., Pacheco P. A., Rodrin S. E. C. Automated aquaculture system that regulates pH, temperature and ammonia. 2017 IEEE 9th International Conference on Humanoid, Nanotechnology, Information Technology, Communication and Control, Environment and Management (HNICEM); December 2017; Manila, Philippines. pp. 1–6. [DOI] [Google Scholar]
- [3]. Chunkiew S., Jaroensutasinee M., Tina F. W., Jaroensutasinee K., Koad P. Physical factors affecting oyster diversity and distribution in Southern Thailand. *Journal of Environmental Biology*. 2019;40(1):03–08. doi: 10.22438/jeb/40/1/MRN-788. [DOI] [Google Scholar]
- [4]. Shifeng Y., Jing K. E., Jimin Z. Wireless monitoring system for aquiculture environment. 2007 IEEE International Workshop on Radio-Frequency Integration Technology; December 2007; Rasa Sentosa Resort, Singapore. pp. 274–277. [DOI] [Google Scholar]
- [5]. Yang S., Li Y. Dissolved oxygen remote monitoring system based on the internet. *Electronic Measurement Technology*. 2011;7:88–90. [Google Scholar].
- [6]. Glasgow H. B., Burkholder J. M., Reed R. E., Lewitus A. J., Kleinman J. E. Real-time remote monitoring of water quality: a review of current applications, and advancements in sensor, telemetry, and computing technologies. *Journal of Experimental Marine Biology and Ecology*. 2004;300(1-2):409–448. doi: 10.1016/j.jembe.2004.02.022. [DOI] [Google Scholar]
- [7]. Cario G., Casavola A., Gjanci P., Lupia M., Petrioli C., Spaccini D. Long lasting underwater wireless sensors network for water quality monitoring in fish farms. *OCEANS 2017 - Aberdeen*; June 2017; Aberdeen, UK. [DOI] [Google Scholar]

- [8]. Espinosa-Faller F. J., Rendón-Rodríguez G. E. A ZigBee wireless sensor network for monitoring an aquaculture recirculating system. *Journal of Applied Research and Technology*. 2012;10(3):380–387. doi: 10.22201/icat.16656423.2012.10.3.391. [DOI] [Google Scholar]
- [9]. Zhang M., Li D., Wang L., Ma D., Ding Q. Design and development of water quality monitoring system based on wireless sensor network in aquaculture. In: Li D., Liu Y., Chen Y., editors. *Computer and Computing Technologies in Agriculture IV*. Springer; 2011. pp. 629–641. [DOI] [Google Scholar]
- [10]. Huang J., Wang W., Jiang S., Sun D., Ou G., Lu K. Development and test of aquacultural water quality monitoring system based on wireless sensor network. *Transactions from the Chinese Society of Agricultural Engineering*. 2013;29(4):183–190. [Google Scholar]
- [11]. Luo H., Li G., Peng W., Song J., Bai Q. Real-time remote monitoring system for aquaculture water quality. *International Journal of Agriculture & Biological Engineering*. 2015;8(6):136–143. [Google Scholar]
- [12]. <https://google.com>

Viability of weed Biomass as an Alternative Source of Substrate for Biogas production

Sangita A. Ghadge

Department of Botany, Loknete Gopinathji Munde, Arts, Commerce and Science College, Mandangad Dist.
Ratnagiri, Maharashtra, India

ARTICLE INFO

Article History:

Published : 30 April 2025

Publication Issue :

Volume 12, Issue 13

March-April-2025

Page Number :

275-282

ABSTRACT

Biomass energy or bioenergy refers to all forms of renewable energy that are derived from plant materials produced by photosynthesis. Biomass fuels can be derived from wood, agricultural crops and other organic residues such as animal waste, weeds etc. Biogas is a promising clean source of energy. Many workers have explored various substrates for biogas production. Easily available source are need to find out. Weeds are the plant grows luxuriantly everywhere without any care. Nobody cultivate them but found dominant over other cultivated plant. Utilization of this natural resource as biogas substrate is novel practice.

In present investigation attempts have been made to utilize biomass of two most common weeds as a source of biogas. The weeds utilized for biogas production are *Daturainoxia* Mill.(Dhotra), *Ipomoea carnea*Jacq sub sp. *fistulosa*(Mart. ex Choisy) D.Austin (Beshram) along with dung and biogas slurry. The result shows that the weed plants acts as good source of substrate. *Ipomoea carneafistulosa*, pulp and *Daturainnoxia* plant pulp produce more amount of gas compare to only Dung and Slurry.

Keywords- Biomass, Renewable energy, *Ipomoea*, *Datura*, Biogas

INTRODUCTION

Biomass is the most common form of renewable energy sources. The Biomass which accounts for nearly 33% of a developing country's energy needs. In India it meets about 75% of the rural energy needs (Ramchandra, 2008). The potential of biomass to meet the domestic and industrial energy requirements of India has been well recognized. Biomass fuels are promising, non-toxic and eco-friendly clean fuels (Ravindranath and Hall, 1996, Varma and Basant, 2003). Biomasses in various forms are suitable as energy feed stock. They can be either burned directly in a furnace or converted into high energy content fuels using biochemical or thermo chemical conversion processes (Varma and Basant, 2003). Among different biomasses, wood has received the most attention because of its long and continuing precedent as a fuel and biomass feed stock (Jain, 1992, Senelwa, and Sims, 1999)However, due to stringent government policies, which are largely aiming towards protection of

native forests, there is hardly any supply of fuel wood from the forest. The burning of wood, cattle dung and agricultural waste in our village has been a traditional practice but still it's continuing. Incomplete combustion of plant parts generates lot of smoke vitiating the atmosphere and adversely affecting the health of the people. The Government of India provide subsidy for biogas plants under National Biogas Development Scheme and other related program, though there is very little response by people due to the failure of biogas plants. Thereasons behind are several, like high initial investment cost for large scale biogas plant, operational problems, structural defect & insufficient availability of suitable substratum. Therefore it is necessary to find out alternative biomass resources for meeting the substrate requirement of biogas plant.

Alternate feedstocks:

Animal wastes and agriculture wastes are generally used as feedstock in biogas plants. Conventional biogas digesters require 10 kg of cattle waste to produce an equivalent quantity of biogas (Anonymous, *Urja*, 1992) but the availability of these substrates is one of the major problems hindering the successful operation of biogas digesters. The availability of cattle waste can support only 12–30 million family-size biogas plants against the requirement of 100 million plants. A significant portion of 70–88 million biogas plants can be run with fresh/dry biomass residues (Khendelwal, 1990).

Many workers have explored various substrates for biogas production. The two most important parameters in the selection of particular plant feed stocks are the economic considerations and the yield of methane for fermentation of that specific feedstock (Smith, *et al* 1992). They assessed the methane yield from fresh-water aquatics, forage grasses, roots, tubers and marine species and reported that highest yield was obtained from root crops followed by forage grasses and fresh-water aquatics (Smith, *et al* 1988). Radhika *et al.* (1983) reported that a mixture of coir pith and cattle waste at 3: 2 ratio gave a better gas output and that the methane content was in the range of 80–85 per cent. Later, Jagadeesh (1990) reported that calcium-hydroxide-treated coir pith mixed with cattle waste slurry to adjust to a total solids content of 9.2 percent gave a biogas yield of $0.152 \text{ m}^3 \text{ kg}^{-1}$ of dry matter d^{-1} . However, Deivanai and Kasturi Bai (1995) observed that biomethanation of coir pith was slow, attributing this to higher lignin content of the waste. De oiled castor-oil cake as an alternate feedstock at a loading rate of $8 \text{ kg TS m}^{-3} \text{ d}^{-1}$ was reported by Gollakota and Meher (1988). Nagamani *et al.* (1992) also studied the potential of biogas production from different de oiled cakes like castor, neem, groundnut, and coconut and reported that accumulation of long-chain fatty acids, and propionate after four weeks of digestion inhibited the methanogenic process.

Biomass of Weeds as substrate:

Chynoweth *et al.* (1993) postulated that methane yield and kinetics were generally higher in leaves than in stems. Results of Sharma *et al.* (1988 and 1989) confirmed the above concept, using *Ipomoea fistulosa* as substrate. Observations on biogas production from food industry wastes (Krishnanand 1994) and from different biomass (Gunaseelan 1997) have shown that pretreatment of feedstock improved the biogas yield and methane content from biomass-fed digesters. Gunaseelan (1997) observed that succulent leaves such as *Mirabilis* sp., *Ipomoea fistulosa*, etc. can be fed without any shredding. Ramasamy *et al.* (1995) evaluated the biogas potential of *Gliricidia* sp., *Albizia* sp., and *Parthenium* sp. in plug flow digester and observed that biogas yield from these feedstocks improved with specific inoculum. Gunaseelan (1994) reported that pretreatment with NaOH increased the gas production from parthenium-fed digesters ($0.46 \text{ m}^3 \text{ m}^{-3} \text{ d}^{-1}$ and the methane yield was $0.11 \text{ m}^3 \text{ kg}^{-1}$ VS). Mathew *et al.* (2014) recorded Biogas amount from *Salvia* 552 L/Kg volatile solid 221L/Kg. Water hyacinth is a promising feedstock for producing alternative energy in the form of biogas. An experiment was conducted using an anaerobic digester with an HRT of 14 days. The results showed that the water hyacinth composition influences the biogas production. During 35 days, the NWH-W feedstock achieved the highest

cumulative biogas production (1229.83 l), followed by CDW (686.10 l), TWH-D (628.50 l), and TWH-W (370.46 l); it also exhibited the highest maximum production yield per day (0.398 l/g VS), followed again by CD-W (0.239 l/g VS), TWH-D (0.2198 l/g VS), and TWH-W (0.115 l/g VS). The NWH-W composition was as follows: 70.57% CH₄, 12.26% CO₂, 1.32% H₂S, and 0.65% NH₃ (Soeprijanto et al. 2021). Dar and Tandon (1987) reported a 62 per cent higher yield in biogas fed with NaOH-pretreated *Lantana camara* along with cattle waste. *Lantana camara* and *Eupatorium* species are two important weed species, which grow in the wild throughout India. They are widely available and dominating weed species, reported as potential biomass sources (Murali and Setty, 2001). With simple techniques these weeds can be converted into bio dung which could release cow dung to be utilized in some other purposes. These can also help to arrest deforestation (Ghatnnekar, 1980). Aim of the present experiment is to evaluate the potential of various weed pulp alone and mixed with Cattle dung for biogas production. Hence in this investigation attempts have been made to study biogas production by using two terrestrial weeds which are not grazed by the animals, sometimes toxic to human beings and cattle are used as the source for biogas production.

MATERIALS AND METHODS:

The materials used for this experiment was *Ipomoea carnea* Jacq subsp. *fistulosa* (Mart. ex Choisy) D. Austin. and *Datura innoxia* Mill. (Dhotra) weeds, dung and biogas slurry.

Experimental site:

The experiment was conducted in the research laboratory of botany department with four treatments and three replicates. The fresh green weeds were collected from different sites. The aerial biomass was first washed with water. The plant material was weighed accurately 100 gms and crushed in mixer. At the time of crushing 15 ml water was added. Pulp a paste product of fresh green weed was obtained which was used as feedstock with combination of slurry. Simultaneously analyses of weed samples were done (Table.1). The slurry is the byproduct of biogas plant was used as starting material. The active biogas slurry was collected from a working biogas plant which serves as the culture of microorganism. The equipment used for this type of laboratory scale biogas experiment, big (50ml) plastic syringe was utilized. The equipment made it possible to registrar the amount of gas produced. These have been used earlier for the same. The potential of biogas production in the plant pulp and mixture of plant pulp plus dung, dung plus slurry and only slurry as a control were investigated. Simultaneously samples from each treatment were kept in oven at 90°C for further analysis (Table.2 and 3).

Composition of sample:

The experiment was conducted with four treatments and three replicates of each.

Treatments:

1. Plant pulp + slurry + water, in the proportion of 10+5+5=20 gm.
2. Plant pulp + dung + slurry + water, in the proportion of 5+5+5+5=20 gm.
3. Dung + slurry + water, in the proportion of 10+5+5=20 gm.
4. Slurry + water (control), in the proportion of 15+5=20 gm.

Slurry from working biogas plant was used as common starting material in all treatments. The experiment was carried out in the month of May-June 2009. The room temperature was in the range of 38-42°C. The biogas production was measured at the intervals of 6 hours by volume displacement method in milliliters (ml).

Analyses of sample:

The chemical analyses were done by adopting standard analytical methods. Ash values were obtained by burning the moisture-free samples in a muffle furnace at 600°C for 2 hours. Nitrogen (N) was estimated by

micro-kjeldahl method after digesting the sample according to Bailey (1967). The pH of the sample was determined with the help of pH meter.

Statistical analysis-

All the results were means of three replicates statistically analyzed using analysis of variance (ANOVA) test and treatments means were compared using the least significant difference (CD, $P \leq 0.05$) which allowed determination of significance between different applications (Mungikar, 1997).

RESULTS AND DISCUSSION:

Table.1. Analysis of weed

Sr.no	Weed Plants	Percentage				C/N ratio
		DM	N	Ash	C	
1	Ipomoea carnea	26.02	2.58	12.4	7.19	2.79
2	Daturainnoxia	19.10	3.33	26.5	15.37	4.61

Table 1. Shows the Dry matter, Nitrogen percentage, Ash percentage and C: N ratio of weed sample. Dry matter percentage of *I. carnea* was more 26.02 than 19.10 percentage in *Datura* weed. Nitrogen percentage was maximum in *Daturainnoxia* 3.33% and minimum in *I. carnea* 2.58%, while Ash, Carbon percentage was more in *Datura* weed. C/N ratio of *Datura* was more than *I. carnea*.

Table. 2 Analysis of weed plant pulp (Mixing =Pulp+Slurry=10+5gm)

Sr.no	Weed Plants pulp	PH	Percentage				C/N ratio
			DM	N	Ash	C	
1	Ipomoea carnea	6.2	9.73	1.75	14.77	8.57	4.90
2	Daturainnoxia	5.9	10.47	3.17	19.2	11.14	3.52

Table No.2 shows the analysis of weed pulp. Dry matter percentage was 9.73 in *Ipomoea carnea* weed pulp shows the highest and followed by *Datura* pulp 10.47. Nitrogen % was recorded more in *Datura* pulp followed by *Ipomoea* pulp. Ash and Carbon percentage was maximum in *Datura* pulp and minimum in *Ipomoea* pulp. C: N ratio was more from *Ipomoea* than *Datura* pulp than other treatments.

Table. 3 Analysis of plant pulp (Mixing =Pulp+ Dung + Slurry = 5+5+5gm)

Sr.no	Weed Plants	PH	Percentage				C/N ratio
			DM	N	Ash	C	
1	Ipomoea carnea	7.6	14.27	1.17	22.9	13.28	11.39
2	Daturainnoxia	7.0	10.93	1.67	24.6	14.27	8.56
3	Slurry +Dung	7.6	12.00	1.00	26.9	15.60	15.61
4	Slurry (Con)	7.4	5.40	0.83	18.0	10.44	12.53

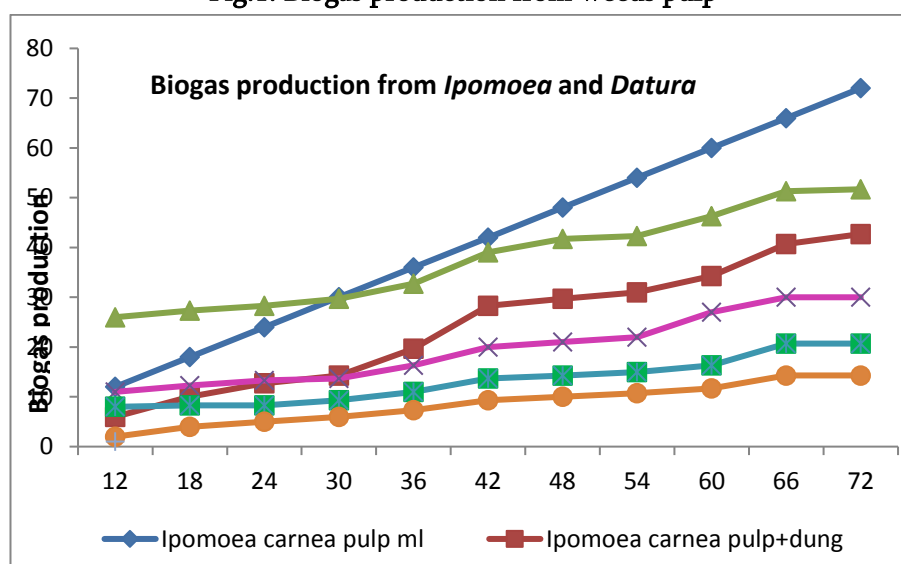
Table 3. shows the weed Pulp + dung, dung + slurry and only slurry composition treatments. DM percentage was more from *I. carnea* 14.27 in pulp plus dung treatment. Followed by Slurry + Dung and *Datura* + Dung and less in Slurry treatments. Shivraj and Seenayya (1994) and Ranade *et al.*, (1990) reported that digesters fed with

8% percent total solid of poultry waste gave better biogas yield. The N percentage was maximum in *Datura*+Dung, than *Ipomoea* + Dung, Slurry + Dung and less in Slurry (Control) treatments. The Ash and Carbon percentage was more in Slurry + Dung treatment followed by *Datura*+Dung, *Ipomoea* + Dung and less in Slurry (control) combination treatment. All the treatments show low C: N ratio due to high N percentage and low Carbon percentage. According to Mital (1996) 25-30 is optimum C: N ratio for biogas production. But the yield of biogas depends on various factors such as biogas potential of feedstock, installation technique for getting optimum temperature condition (Anand and sing, 1993; Bansal, 1988; Tiwari, *et al.*, 1988; Desai, 1988), digester design, temperature (Haque and Sharma, 1980; Zanaaki *et al.*, 1996). Loading rate (Sundrarajan, *et al.* 1997). The pH of pulp sample was ranged from 5.9 of *Datura* sample while to 6.2 of *I. carnea*. while in pulp plus dung combination high pH rang was observed i.e. *I. carnea* and Slurry + Dung same as 7.6. *Datura* pulp and *Datura* pulp plus Dung show low pH. Methane producing bacteria require a neutral to slightly alkaline environment i.e. 6.8 to 8.5 (Dennis and Burke 2001).

Table 4 Analysis of plant pulp (Pulp + Slurry=10+5gm) and Pulp+Dung (Pulp+ Dung + Slurry = 5+5+5gm) treatments

Weed Plants	Combination	PH	DM%	Percentage			C/N ratio
				N	Ash	C	
Ipomoea	Pulp	6.2	7.73	1.75	14.77	8.57	4.90
	Pulp+Dung	7.6	14.27	1.17	22.90	13.28	11.39
Datura	Pulp	5.9	10.47	3.17	19.20	11.14	3.52
	Pulp+Dung	7.0	10.93	1.67	24.60	14.27	8.56
Slurry + Dung		7.6	12.00	1.00	26.90	15.60	15.61
Control (slurry)		7.4	5.40	0.83	18.00	10.44	12.53

Fig.1. Biogas production from weeds pulp



Biogas production (ml) from weed Pulp, Pulp + Dung, Dung and Slurry alone after 72 hours .

Fig 1. Demonstrated that the gas production in milliliters at the time intervals as 12, 18, 24, 30,36,42,48,54,60,66 and after 72 hours. The mean value of treatments showed that the pulp (10gm) + slurry

(5gm) + water produced highest biogas in the weed combination as 14.3 to 63 ml in *Ipomea* followed by dung + pulp combination. The Production of gas in the control was less throughout the experiment. Fig 2 and 3 illustrates the comparative account of biogas production from two weeds with their combinations.

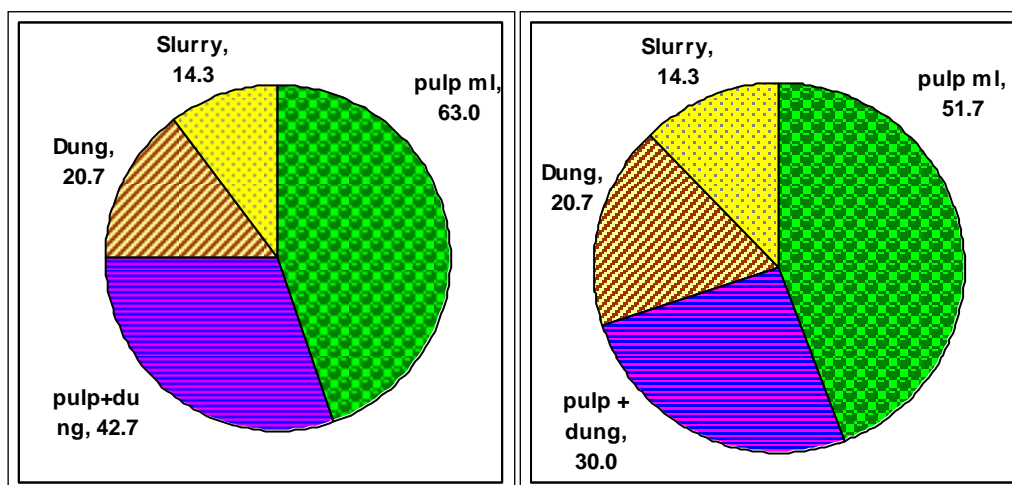


Fig.2. *Ipomoea carnea*

Fig. 3. *Daturainnoxia*

Among two weed treatments highest biogas was produced by pulp of *Ipomoea* weed and P^H was also optimum. Shilpkaret *al*(2007) also recorded significantly higher biogas production (109.82% increases) in weed *Calotropis* digesters than control digesters. The higher N, available P and K, organic carbon, calcium and magnesium content in sample provide sufficient nutrients to microbial community. Increased microbial activity may result into increased biogas production in *Calotropis* pulp and pulp plus Dung than controls. Presence of easily degradable compounds and various enzymes in the latex of may also increase the digestion rate of feeding material (Shilpkaret *al* 2007). *Ipomoea carnea*. The *Ipomoea* pulp produced 63 ml and pulp plus Dung 42.7 ml biogas after 72 hours. Sharma *et al.*, (1989) reported $0.361 \text{ m}^3\text{kg}^{-1}$ vs methane yield from stem of *Ipomoea*. *Ipomoea* was followed by *Daturainnoxia* produced 51.7 and 30ml biogas in *Daturapulp* and *Dung plus Daturapulp* respectively (Table.4). In present experiment Control *i.e.* slurry produces less biogas as compared to other samples. Dung treatment produced 20.7 ml biogas while in slurry (control) treatment showed less *i.e.* 14.3ml biogas after 72 hours. Biogas production was increased with increase in time. (Fig.1) shows the retention time for biogas production from different weed pulp and samples.

Positive effects of co-digestion of cattle dung and agricultural wastes were also reported by Somayaji and Khanna (1994); Kaparaju, and Rintala, (2005); Kivaisi, and Rubindamayugi, (1996).

Conclusion-

I. On the basis of statistical analysis it has been observed that all the values of biogas produced by *Ipomoea carnea* subsp. *fistulose* weeds were statistically significant over control and Dung plus slurry treatment. That can be concluded that addition of selective weeds like *Ipomoea carnea* enhance the biogas production capacity if biogas digester.

Biogas is produced by means of a process known as anaerobic digestion. It is a process whereby organic matter is broken down by microbiological activity and as the name suggests it is a process which takes place in the absence of air. Optimum temperature, P^H needs to maintain there. Weed biomass found to be good substrate for biomethanation but some weeds when admixed with industrial and agro-industry based wastes like distillery,

sugar, dairy and farmhouse wastes, its biomethanation potential may increase. Amongst two different selected common weeds and slurry and dung combinations as a substrate for biogas production, untreated *Ipomoea* biomass was found to be the best one weed biomass available free and in huge amount.

REFERENCES

- [1]. Anand, R.C. and Singh, R. (1993). *Bioresour. Technol.* 45, 151.
- [2]. Anonymous, *Urja*, 1992, 31, 7.
- [3]. Bansal, N.K. (1988) *Energy Res.* 10:216.
- [4]. Bailey R.L. (1967). (*Techniques in Protein Chemistry*” II Edition Elsevier Publication Co., Amsterdam.
- [5]. Chynoweth, D. P., Turik, C. E., Owens, J. M., Jerger, D. E. and Peck, M. W. (1993). *Biomass Bioenergy*, 5, 95–111.
- [6]. Dar, G. H. and Tandon, S. M. (1987) *Biol. Wastes*, 21, 75–83.
- [7]. Deivanai, K. and Kasturi Bai, R. (1995). *Biores. Technol.*, 52, 93–95.
- [8]. Dennis A. Burke P.E. (2001), *Dairy Waste Anaerobic Digestion Handbook* Environmental Energy Company 6007 Hill Street Olympia, WA 98516. © Environmental Energy Company www.makingenergy.com 360-923-2000.
- [9]. Desai, C.K. (1988). *Proceedings of the National Seminar on Solar Energy and Rural Development*, Shivaji University Kolhapur, 83.
- [10]. Ghatanekar, S.D. (1980). *Khadi Gramodyog. J. Rural Economy.* 27(3):209.
- [11]. Gollakota, K. G. and Meher, K. K., (1988). *Biol. Wastes*, 24, 243–249.
- [12]. Gunaseelan, V. N., (1994). *Biomass Bioenergy*, 6, 391–398.
- [13]. Gunaseelan, V. N., (1997). *Biomass Bioenergy*, 13, 83–114.
- [14]. Haque M.A. and Sharma S. (1980) *Science Reporter* 17:756
- [15]. H. V. Deshmukh, G. R. Pathade* and P. K. Goel (2007). *SCREENING OF COMMON PLANT WEEDS FOR THEIR POTENTIAL OF BIOGAS GENERATION ALONE AND IN COMBINATION WITH SOME AGRO-INDUSTRIAL WASTES* *Nature Environment and Pollution Technology* © Technoscience Publications Vol.6 No.2 page-263-270.
- [16]. Jagadeesh, K. S., (1990) *Curr. Res.*, 19, 189.
- [17]. Jain, R. K., (1992). *Fuel wood characteristics of certain hard wood and soft wood tree species in India.* *Bioresour. Technol.*, 41, 129–133.
- [18]. Kaparaju, P. and Rintala, J., (2005). *Resour. Conserv. Recycling*, 43, 175–188.
- [19]. Khendelwal, K. C., (1990) *Proceedings of the International Conference on Biogas Technology Implementation Strategies* (ed. Borda), held at Pune,.
- [20]. Kivaisi, A. K. and Rubindamayugi, M.T., *Renewable Energy*, (1996), 9, 917.
- [21]. Krishnanand., (1994). *Indian Food Ind.*, 13, 33–35.
- [22]. Mathew, Anil Kuruvilla, Bhui, Indranil, Banerjee, Sambhu Nath, Goswami, Ramansu, Chakraborty, Amit Kumar, Shome, Arunima, Balachandran, Srinivasan, and Chaudhury Shibani (2014). *Biogas production from locally available aquatic weeds of Santiniketan through anaerobic digestion.* *Clean Technologies and Environmental Policy*, DOI 10.1007/s10098-014-0877-6.
- [23]. Mital, K. (1996). *“Biogas Systems Principles and Applications”*. New age International Ltd.

- [24]. Murali, K. S. and Setty, R. S. (2001) Effect of weeds *Lantana camara* and *Chromola odorata* growth on the species diversity, regeneration and stem density of tree and shrub layer in BRT sanctuary. *Curr. Sci.* 80, 675–678.
- [25]. Mungikar, A. M. (1997). “An Introduction to Biometry”, Saraswati Printing press, Aurangabad.
- [26]. Nagamani, B., Chitra, V. and Ramasamy, K., (1992) 32nd Annual Conference of Association of Microbiologists of India held at Madurai Kamaraj University, Madurai, pp. 176.B33, 189–194.
- [27]. Radhika, L.G., Seshadri, S.K. and Mohandas, P. N., (1983). *J. Chem. Technol. Biotechnol.*
- [28]. Ramchandra, T.V. (2008). “Geographical information system Approach for Regional Biogas Potential Assessment”. *Research Journal of Environmental Science* 2(3):170-184, ISSN 1819-3412. Academic Journals Inc.
- [29]. Ramasamy, K., Ilamurugu, K., Sahul Hameed, M. and Maheswari, M. (1995). *Tech. Bull.* 5, 36.
- [30]. Ranade D.R., Nagarwala N.N, Dudhbhate J.A. Gadre R.V. and Godbole S.H. (1990) *Ind.J. Environ. Health.* 32:63.
- [31]. Ravindranath, N. H. and Hall, D. O., (1996). *Biomass, Energy and Environment: A Developing Country Perspective from India*, Oxford University Press.
- [32]. Senelwa, K. and Sims, R. E. H., (1999). Fuel characteristics of short rotation forest biomass. *Biomass Bioenergy*, 17, 127–140.
- [33]. Sharma, S. K., Mishra, I. M., Sharma, M. P. and Saini, J.S. (1988), *Biomass*, 17, 251–263.
- [34]. Sharma, S. K., Saini, J. S., Mishra, I. M. and Sharma, M. P. (1989) *Biol. Wastes*, 28, 25–32.
- [35]. Shilpkar Shilpkar, Mayur Shaha, D.R. Chaudhary, (2007). “An alternate use of *Calotropis gigantea*: Biomethanation”. *Current Science*, vol.92, (4, 25):435-437.
- [36]. Shivraj, D. and Seenayya, G. (1994). *Indian J. Environ. Hlth.*, 36:115.
- [37]. Smith, W. H., Wilkie, A. C. and Smith, P. H. (1992). *TIDE*, 2, 1–20.
- [38]. Smith, P. H., Bordeaux, F. M., Wilkie, A., Yang, J., Boone, D., Mah, R. A., Chynoweth, D. and Jerger, D. (1988) in *Methane from Biomass: A Systems Approach* (eds Smith, W. H. and Frank, J. R.), Elsevier Applied Science, London, p. 500.
- [39]. Soeprijanto Soeprijanto, I Dewa Ayu Agung Warmadewanthi, Melania Suweni Muntini, Arino Anzip (2021). “The Utilization of Water Hyacinth for Biogas Production in a Plug Flow Anaerobic Digester). *Int. Journal of Renewable Energy Development* 10 (1) 2021: 27-35..
- [40]. Somayaji, D. and Khanna, S. (1994) *World J. Microbiol. Biotechnol. (Hist. Arch.)*, 10, 521–523.
- [41]. Sundrarajan, R., Jayanthi, A. and Elango, R. (1997) *Indian J. Environ. Health* 39(3):193.
- [42]. Tiwari, G.N., Rawat, D.K. and Chandra, A. (1988) *Energy Conserv. Manage.* 28(1)1.
- [43]. Varma, A. and Basant, B., (2003) *Green Energy: Biomass Processing and Technology*, Capital Publishing Company, New Delhi.
- [44]. Zannaki, B.Z., Zadi, A., Lamini, H., Aubinear, M. and Boulif, M., (1996). *Tropicultura* 14 (4):134.

Synthesis Of Pyrimidine and It's Derivatives: A Review

Mr. Sharif. A. Kazi¹, Pradip R. Kate², Mr. Sandip A. Nirwan¹

¹Department of Chemistry, Loknete Gopinathji Munde Arts, Commers & Science College, Mandangad, Dist. Ratnagiri 415203, Maharashtra, India

²Department of Chemistry, Shri. Shivaji Mahavidyalaya, Barshi, Dist.-Solapur, 413401, Maharashtra, India

ARTICLE INFO

Article History:

Published : 30 April 2025

Publication Issue :

Volume 12, Issue 13
March-April-2025

Page Number :

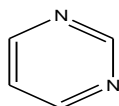
283-289

ABSTRACT

Pyrimidine, a six-membered heterocyclic aromatic compound containing two nitrogen atoms at positions 1 and 3, is a privileged scaffold found in numerous natural compounds, including nucleotides (cytosine, thymine, uracil), vitamins, and antibiotics. Its structural similarity to nucleotide bases in DNA and RNA underpins its significance in medicinal chemistry, particularly for anticancer, antiviral, antimicrobial, and other pharmacological applications. This review comprehensively examines recent advancements in the synthesis of pyrimidine and its derivatives, focusing on efficient and sustainable methodologies such as multicomponent reactions, transition metal-catalysed processes approaches. The synthetic strategies discussed include condensation, cyclization, and coupling reactions. The biological activities, particularly anticancer and antiviral potentials, are highlighted, emphasizing structure-activity relationships (SAR) and the role of fused pyrimidine derivatives in enhancing efficacy. The review aims to provide insights for researchers to develop novel pyrimidine-based therapeutics with improved potency and selectivity.

INTRODUCTION

Pyrimidine is six membered heterocyclic compounds containing two Sp^2 hybridized nitrogen atom in the ring at 1,3 positions with molecular formula $C_4H_4N_2$. Adolf pinner was a German chemist first proposed the name of pyrimidine in 1885. Pyrimidine is structurally similar to pyridine but has two nitrogen atoms instead of one. Structure of pyrimidine is planar, π bond in conjugation (alternating double and single bonds) & aromatic it obeys Huckel rule of aromaticity $4n+2\pi$ [1].

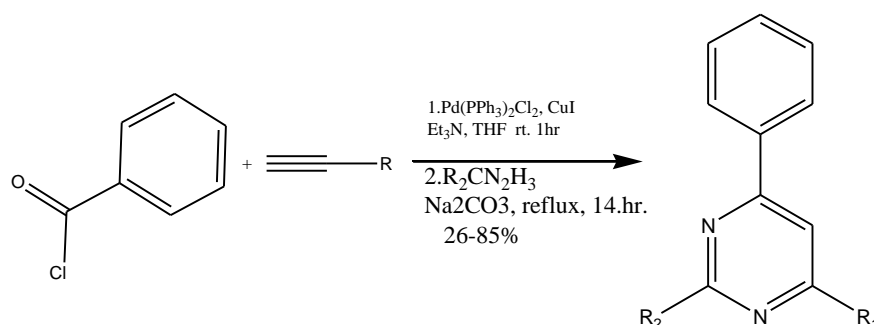


Pyrimidine

Pyrimidine is naturally occurring colorless compound soluble in water. It is weakly basic & can participate in hydrogen bonding due to nitrogen atom. Boiling point of pyrimidine is 123°C. Pyrimidine is most important naturally occurring diazines bases Uracil, Thymine & Cytosine which are obtained from hydrolysis of the nucleic acids. It undergoes various chemical reactions depending on the reaction conditions and substituents on the ring [2].

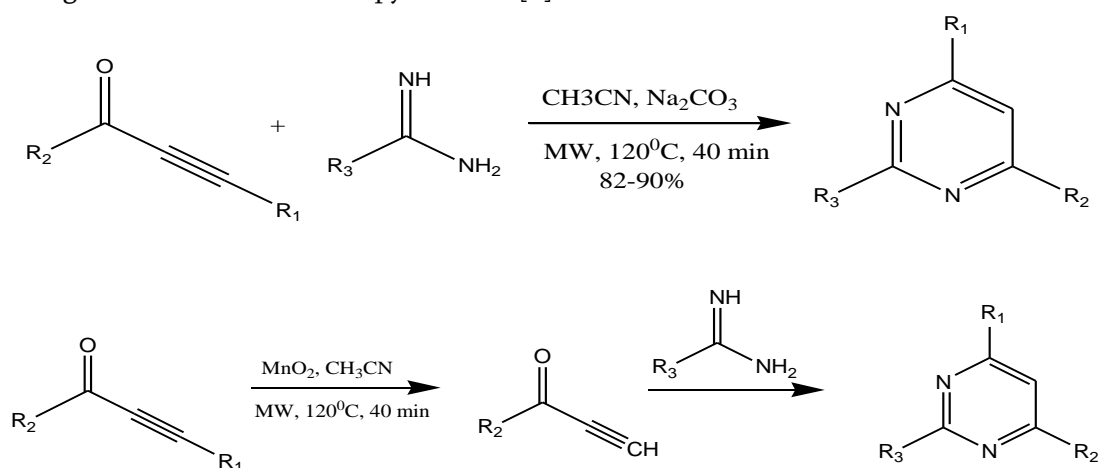
The most interesting approach developed so far for the convergent synthesis of highly functionalized pyrimidine can be classified according to the nature of the fragments that are joined together during the closure of the pyrimidine nucleus.

1. Karpov & Muller's et al synthesis of 2,4-disubstituted and 2,4,6-trisubstituted pyrimidines. In this synthesis coupling of Acid chloride with terminal alkynes by using Et₃N in stoichiometric amount followed by addition of aminium salt in the presence of sodium carbonate under reflux gave 2,4,6- trisubstituted Pyrimidine [3].



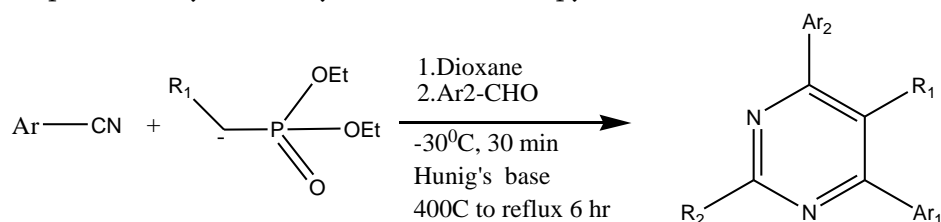
Scheme 1 Müller's synthesis of 2,4-disubstituted and 2,4,6-trisubstituted pyrimidines.

2. Bagley's proposed microwave assisted condensation reaction of alkynones with excess hydrochloric salt of substituted amidines. After cooling & filtration 2,4,6- trisubstituted pyrimidine is obtained. Bagley's proposed another microwave assisted reaction of oxidation of propargylic alcohol with MnO₂ provided corresponding alkynones at intermediate position which is immediately react with substituted amidines gave 2,4,6- trisubstituted pyrimidine [4].



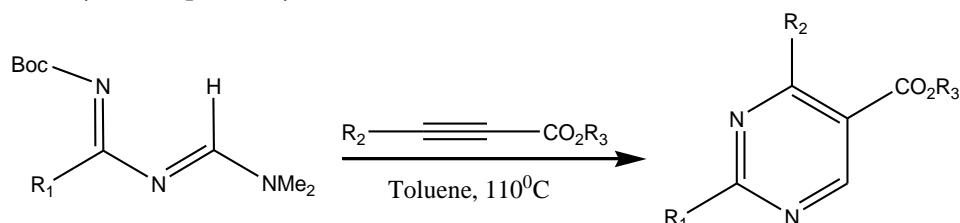
Scheme 2. Bagley's synthesis of 2,6-disubstituted and 2,4,6-trisubstituted pyrimidines.

3. Kiselyov's Synthesis for the preparation of 2,4,6- trisubstituted & 2,4,5,6- tetrasubstituted pyrimidines. Reaction of alkyl or benzyl- phosphate with aryl nitriles to formed unstable aza compound react with aromatic aldehyde & which are converted in to α , β -unsaturated imines further it is react with bidentate nucleophile usually amidine yield is substituted pyrimidine [5].



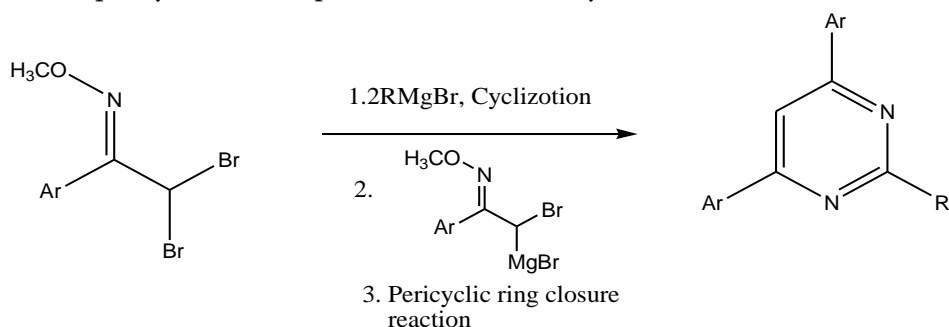
Scheme 3. Kiselyov's synthesis of 2,4,6-trisubstituted and 2,4,5,6 tetrasubstituted pyrimidines.

4. Muchowski's et al synthesis of 2,4,5- trisubstituted pyrimidine derivative based on $[4\pi+2\pi]$ cycloaddition reaction of 1,3 diazadienes with electron deficient acetylenes. N1-Boc protected 1,3 -diazadienes were converted into 2,4,5-trisubstituted pyrimidine by heating with ethyl propiolate or dimethyl acetylene dicarboxylate respectively.[6].



Scheme 4. Muchowski's synthesis of 2,4,5-trisubstituted pyrimidines.

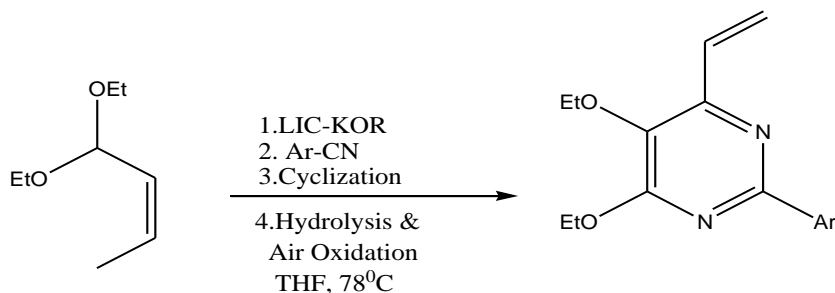
5. Kakiya's et al synthesis of 2,4,6-trisubstituted pyrimidines. In this synthesis reaction of α , α - dibromo oxime ethers with two equivalent of Grignard reagent at 42°C & warming reacting mixture up to room temperature yield is 2,4,6- trisubstituted pyrimidine. In first step of synthesis exchange of Br with Mg & second step alkylation at α - position, further it is cyclization as a result substituted pyrimidine [7].



Scheme 5. Kakiya's synthesis of 2,4,6-trisubstituted pyrimidines.

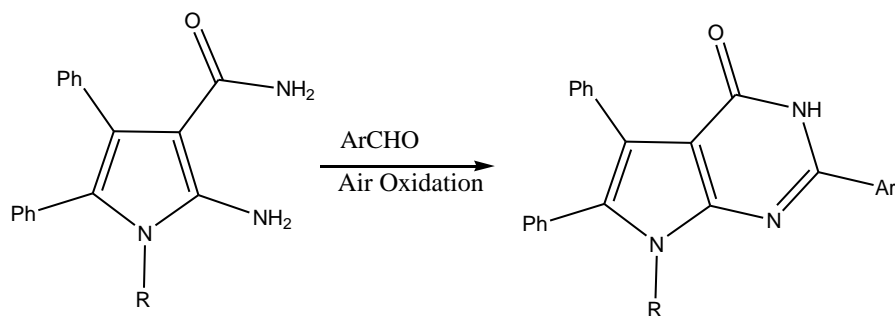
6. Blangetti's et al prepared 2,4,5,6- tetrasubstituted pyrimidine when reacting of crotonaldehyde acetate with 2 equivalents of nitriles in presence of Schlosser's superbase (LIC-KOR) yield is tetra-substituted

pyrimidine. In first step of synthesis methylation & addition of the first molecule of nitrile gave the N-metalketimine followed by cyclization & acid hydrolysis product is 2,4,5,6- tetrasubstituted pyrimidine [8].



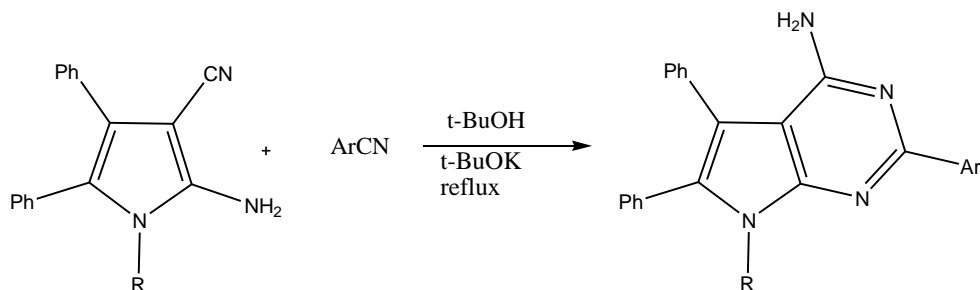
Scheme 6. Blangetti's synthesis of 2,4,5,6-tetrasubstituted pyrimidines.

7. A. Davoodnia et al synthesis new heterocyclic compound with biological activities that is 2- aryl-3,7-dihydro-4H-pyrrolo[2,3-d] pyrimidin-4- ones (7-deazapurines) using 3-methyl-1-(4-sulfonic acid) butylimidazolium hydrogen sulphate, Bronsted-acidic ionic liquid as a green and reuseable catalyst through cyclo-condensation of 2- amino-1H-pyrrol-3-carboxamides with aromatic aldehydes followed by air oxidation [9].



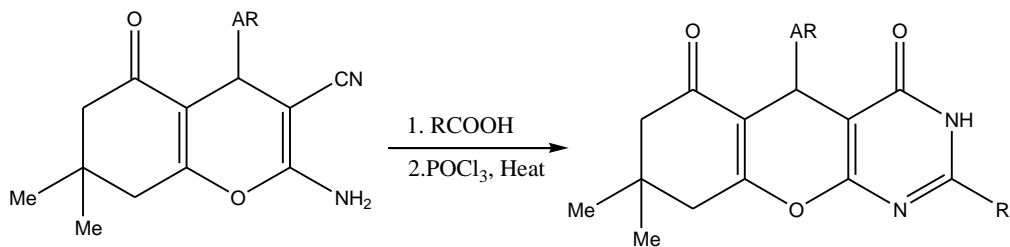
Scheme 7. Synthesis of pyrimidine derivative from 2- amino-1H-pyrrol-3-carboxamides

8. Abolghasem et al synthesis new 7-deazaadenine derivative that is 2-aryl-7H-pyrrolo[2,3-d] pyrimidin-4-amine by reaction of 2-amino-1H-pyrrole-3-carbonitriles with aryl nitriles in presence of t-butoxide in boiling t-butanol [10].



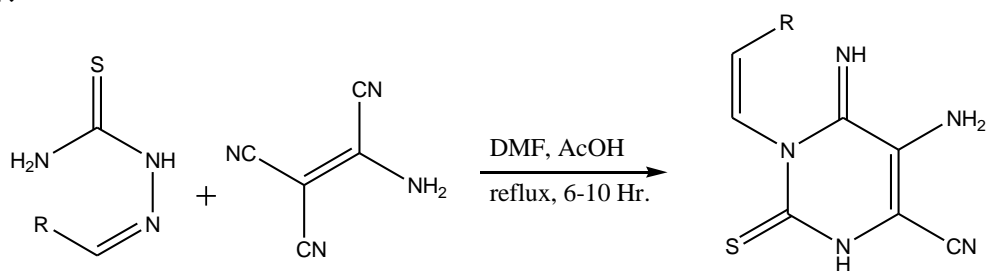
Scheme 8. Synthesis of 2-aryl-7H-pyrrolo[2,3-d] pyrimidin-4-amine

9. Nasrin Karimi et al synthesis derivative from 2-amino-4-aryl-7,7-dimethyl-5-oxo-5,6,7,8-tetrahydro-4H-chromene-3-carbonitriles with excess aliphatic carboxylic acid in the presence of phosphoryl chloride POCl_3 give pyrimidine derivative 2-alkyl-5-aryl 8,8-dimethyl-8,9-dihydro-3H-chromeno[2,3-d]pyrimidine-4,6(5H,7H)-diones with high yields.[11]



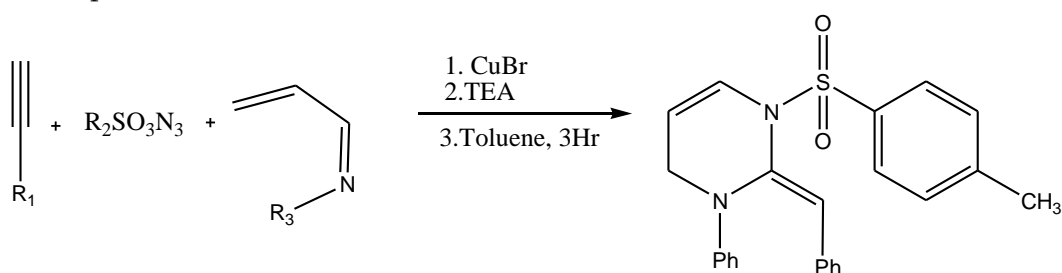
Scheme 9. Synthesis of 2-alkyl-5-aryl 8,8-dimethyl-8,9-dihydro-3H-chromeno[2,3-d] pyrimidine-4,6(5H,7H)-diones

10. A. elkanzi et al. synthesis of new pyrimidine when reaction occurred between thiosemicarbazones & 2-amino-1,1,2-ethanetricarbonitrile in the presence of DMF & few drops of glacial acetic acid to give pyrimidine-2-thiones[12].



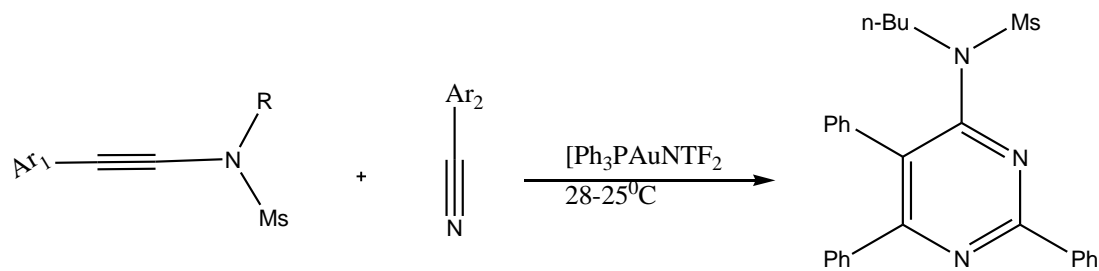
Scheme 10. Synthesis of pyrimidine-2-thiones

11. Wang et al was developed one pot synthesis of N-sulfonyl-2-alkylidene-1,2,3,4-tetrahydropyrimidine by using highly selective & copper catalysed multi-components reaction of sulfonyl azides, terminal alkynes, & alpha, beta-unsaturated imines.[13]



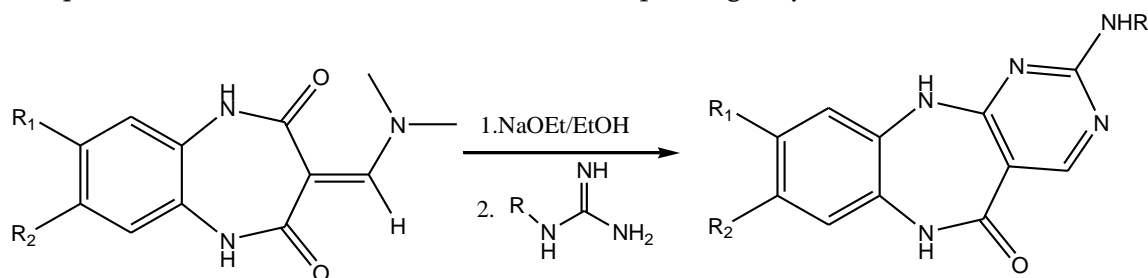
Scheme: 11. Synthesis of N-sulfonyl-2-alkylidene-1,2,3,4-tetrahydropyrimidine

12. Karad et al synthesis of monomeric 4-aminopyrimidines from gold-cycloaddition reaction between n-methyl-n-(phenylethynyl) methanesulfonamid & benzonitrile. This is commonly found in many bioactive molecules.[14]



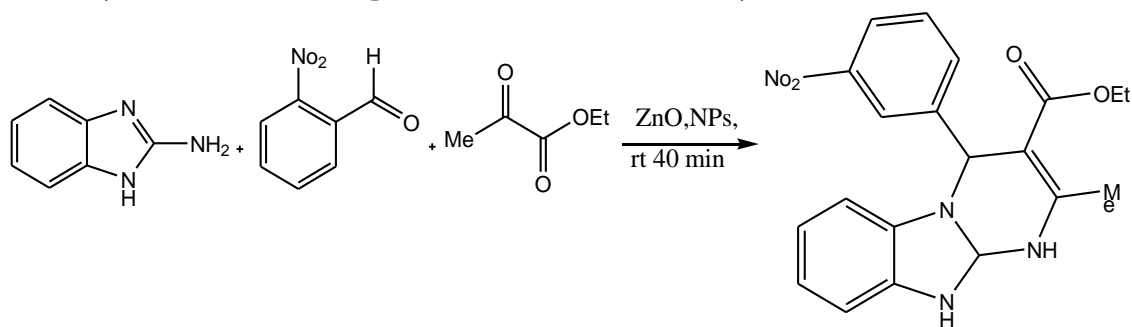
Scheme: 12. Synthesis of monomeric 4-aminopyrimidines

13. Qomi et al reported that some good yields method for the synthesis of some pyrimidine derivatives. In this method the intermediate were condensed with guanidine derivatives under reflux with ethanol in the presence of sodium ethoxide to form the corresponding tricyclic derivatives.[15]



Scheme 13. Synthesis of tricyclic pyrimidine derivatives

14. Sharma et al reported the synthesis of ethyl 2-methyl-4-(2-nitrophenyl)-1,4-dihydrobenzo [4,5] imidazo[2-a] pyrimidine-3-carboxylate when the reaction between 2-aminobenzimidazole, 2-nitrobenzaldehyde & ethyl acetoacetate in the presence of ZnONPs as a catalyst for 40 minutes.[16]



Scheme 14. synthesis of ethyl 2-methyl-4-(2-nitrophenyl)-1,4-dihydrobenzo [4,5] imidazo[2-a] pyrimidine-3-carboxylate

Conclusion

The synthesis of pyrimidine and its derivatives has witnessed significant progress, with diverse methodologies enabling the construction of complex molecular frameworks with potent biological activities. Multicomponent reactions, transition metal-catalysed processes and eco-friendly approaches like microwave-assisted synthesis have improved the efficiency, selectivity, and sustainability of pyrimidine synthesis. These advancements,

coupled with SAR studies, have positioned pyrimidine as a versatile scaffold for drug discovery. The review underscores the tremendous potential for further research to explore pyrimidine derivatives as lead molecules for developing novel therapeutics with improved pharmacological profiles and reduced side effects.

REFERENCES

- [1]. Theivendren Panneer Selvam*, Caiado Richa James, Phadte Vijaysarathy Dniandev, Silveira Karyn Valzita, *Research in Pharmacy* 2012, 2 (4) 01-09.
- [2]. Kaushik S. Patel*, Kishor N. Raval, Shivani P. Patel, Aswin G. Patel, Snehal V. Patel, *IJPBS*, Volume 2, Issue 3, 2012, 170-182
- [3]. A. S. Karpov and T. J. J. Muller, *Org. Lett.*, 2003, 5, 3451.
- [4]. 4.M.C. Bagley, D. D. Hughes and P. H. Taylor, *Synlett*, 2003, 2, 259.
- [5]. A. S. Kiselyov, *Tetrahedron Lett.*, 2005, 46, 1663.
- [6]. A. Guzmán, M. Romero and F. X. Talam, *J. Org. Chem.*, 1996, 61, 2470.
- [7]. H. Kakiya, K. Yagi, H. Shinokubo and K. Oshima, *J. Am. Chem. Soc.*, 2002, 124, 9032.
- [8]. M. Blangetti, A. Deagostino, C. Prandi, C. Zavattaro and P. Venturello, *Chem. Commun.*, 2008, 14, 1689.
- [9]. A. Davoodnia, M. Bakavoli, R. Moloudi, M. Khashi, N. Tavakoli-Hosseini, *Chinese Chemical Letters* 21 (2010)1-4
- [10]. Abolghasem Davoodnia, Maryam Khashi, Niloofar Tavakoli-Hoseini, Raheleh Moloudi, Hassan Ali Zamani, *Monatsh Chem* 2013, 144, 677-680
- [11]. Nasrin Karimi, Abolghasem Davoodnia and Mehdi Pordel, *Heterocycle Commun.* 2018; 24(1): 31-35
- [12]. N. A. A. Elkanzi, Nesrin M. Morsy, Ashraf A. Aly, Alan B. Brown, and Mohamed Ramadan J. *Heterocyclic Chem.*, 00, 00 (2015)
- [13]. Lu W., Song W., Hong D., Lu P., and Wang Y., *Adv. Synth. Catal.*, 2009, 351 (11-12) 1768-1772.
- [14]. Karad S. N., and Liu R. S., *Angew. Chem. Int. Ed.*, 2014, 53 (34), 9072-9076.
- [15]. Qomi H. R., and Habibi A., *Tetrahedron*, 2017, 73 (21), 2991-3001.
- [16]. Zaelin'ski W., and Kudelko A., *Monatsh. Chem.*, 2000, 131 (8), 895-899
- [17]. Raj T., Sharma H., Pharm M., Thammarat A. S., Navneet Kaur A., Singh N., and Jang D. O., *ACS Sustainable Chem. Eng.*, 2017, 5 (2), 1468-1475.
- [18]. Sasada T. Kobayashi F., Sakai N., and Konakahara T., *Org. Lett.*, 2009, 11 (10), 2161-2164.
- [19]. Satoh Y., Yasuda K., and Obora Y., *Organometallics*, 2012, 31 (15), 5235-5238.
- [20]. Rostamizadeh S., Nojavan M., Aryan R., Sadeghian H., and Davoodnejad M., *Chinese Chem. Lett.*, 2013, 24 (7) 629-632
- [21]. Xing Y., Cheng B., Wang J., Lu P., and Wang Y., *Org. Lett.*, 2014, 6 (18), 4814-4817
- [22]. Mahdavi M., Kianfard H., Saeedi M., Ranjbar P. R., and Shafiee A., *Derivatives Synlett*, 2016, 27 (11), 1689-1692.
- [23]. Gore R. P., and Rajput A. P., *Drug Invent. Today*, 2013., 5 (2), 148-152.
- [24]. Selvam T. P., James C. R., Dniandev P. V., and Valzita S. K., *Indian Journal of Pharmaceutical Sciences*, 2012, 74 (3), 275-283.
- [25]. Venkatesan K., Satyanarayana V. S. V., and Sivakumar A, *Bull. Chem Soc. Ethiop.*, 2016, 30 (1) 119-127.

Optoelectronic Properties of Strained Perovskite Crystals: A Review of Theoretical Perspective

Surabhi Chourey¹, Sadiya Patel²

¹Department of Physics, Govt. Degree College Timarni, Dist. Harda-461228, Madhya Pradesh, India

²Department of Chemistry, Govt. Degree College Timarni, Dist. Harda-461228, Madhya Pradesh, India

ARTICLE INFO

Article History:

Published : 30 April 2025

Publication Issue :

Volume 12, Issue 13

March-April-2025

Page Number :

290-295

ABSTRACT

Perovskite materials have emerged as key candidates for next-generation optoelectronic applications due to their tunable band gaps, high absorption coefficients, and long carrier diffusion lengths. Strain engineering in perovskites has been found to significantly influence their optoelectronic properties, providing a powerful tool for optimizing device performance. A thorough theoretical examination of the optoelectronic behaviour of strained perovskite crystals is given in this paper. We summarize recent developments in theoretical modelling approaches, including density functional theory (DFT), tight-binding models, and quantum hydro dynamic models, and discuss their implications for the electronic band structure, exciton dynamics, charge carrier mobility, and light absorption in strained perovskites.

Keywords: Perovskite crystal, Piezo electric Material, Opto electronic properties, DFT, QHM.

INTRODUCTION

Perovskite materials have emerged as promising candidates for next-generation optoelectronic devices owing to their exceptional absorption coefficients, tunable bandgaps, and long carrier diffusion lengths. Strain engineering offers an effective tool to further modulate their optoelectronic properties, opening avenues for tailored device performance. This review aims to provide an in-depth theoretical perspective on how mechanical strain influences the electronic and optical characteristics of perovskite crystals, with an emphasis on both static and dynamic effects. Metal halide perovskites, particularly lead-based organometallic compounds such as $\text{CH}_3\text{NH}_3\text{PbI}_3$, have revolutionized the field of photovoltaics and optoelectronics. The ability to tune their electronic properties through compositional engineering and external stimuli, such as strain, has opened up new avenues for device innovation [1][21][22]. This paper reviews the theoretical framework employed to analyze the effect of mechanical strain on the optoelectronic properties of perovskites and discusses how strain can enhance or degrade device performance. A basic overview of strain in semiconductors, covering its properties, characterization methods, and impacts on the

electrical, optical, and crystalline structures of semiconductors. then gave a summary of the evolution of our understanding of strain formation, categorized by global and local strains, and their impact on the different aspects of MHPs (Metal Halide Perovskite), such as phase stability, photostability, and other optoelectronic characteristics. On these equalities, both beneficial and detrimental effects have been noted [11]. Strain has been successfully used in other semiconductor systems (e.g., silicon, III-V compounds) to enhance carrier mobility and band alignment [4]. Its application to perovskites, however, is relatively new and underexplored. Theoretical studies suggest that strain can significantly modulate the optoelectronic properties of perovskites by altering bond angles, orbital overlap, and lattice constants [5]. Perovskite will always experience strains throughout the production and use of solar panels made of this material. Many perovskite compositions that would ordinarily exhibit thermodynamically stable photoinactive phases at room temperature have had their photoactive phases stabilized by the widespread use of strain. A summary of the strain-induced properties of several PVK materials is also provided, along with an explanation of the pressure-induced changes in structural and optoelectronic properties [12]. In the world of solar technology, inorganic perovskite materials have garnered a lot of interest because of their remarkable optical, electrical, and structural characteristics. First-principles density-functional theory (FP-DFT) was used to extensively examine how compressive and tensile strain affect the structural, optical, and electrical characteristics of the inorganic cubic perovskite Sr_3AsI_3 . According to band characteristics, this component has a high capacity for absorption in the visible range, as demonstrated by optical indicators such as dielectric functions, absorption coefficients, reflectivity, and electron loss functions [14].

Crystal Structure and Strain Types

Hybrid perovskites are materials that combine organic and inorganic compounds, usually following the ABX_3 structure. A means organic cation, B means metal cation and X means the halide anion. Their ideal cubic structure is susceptible to distortions under applied mechanical strain, leading to symmetry breaking and electronic structure modifications. Perovskites adopt an ABX_3 crystal structure, where B is a divalent metal ion, X is a halide anion, and A is a monovalent cation. Strain can be classified as compressive, tensile, biaxial, or uniaxial, depending on the nature of the mechanical deformation. The theoretical treatment of strain requires a detailed understanding of lattice deformation and its influence on atomic positions and orbital overlaps. Strain in perovskites may be introduced during growth or by external mechanical stress. Biaxial strain (in thin films) affects in-plane lattice constants. It is often seen in thin films grown on mismatched substrates. Stretches/compresses the film in two dimensions. Uniaxial strain influences band anisotropy and polarization. Applied along one crystallographic axis. Hydrostatic strain can occur under pressure in bulk crystals. Equal compression from all directions like underwater pressure [6][11][16].

Theoretical Modelling of Strained Perovskites

It entails modelling the effects of stress (strain) on their structure and characteristics. This is essential for comprehending and managing how well they work in solar cell applications. To help with the design of optimal perovskite materials, researchers can use computational tools to predict how strain affects bandgap, electrical structure, and other aspects.

3.1 Density Functional Theory (DFT)

It is the most popular theoretical technique for comprehending a material's electrical characteristics. The application of DFT to strained perovskites has revealed significant changes in the band structure,

including band gap narrowing or widening depending on the strain direction and magnitude. DFT serves as the primary theoretical tool for predicting the electronic band structure of strained perovskites. Various exchange correlation functionals (PBE, HSE06, SCAN) are employed for different accuracy levels. The electrical and optical characteristics of strained perovskites are commonly modelled using DFT-based first-principles computations. Biaxial strain and the resulting structural distortions affect the energy landscapes, band gaps, and band edges of the perovskite photovoltaic materials CsSnI₃ and CsPbI₃ using calculations based on density functional theory (DFT). Additionally, demonstrate how temperature-controlled octahedral rotations further widen band gaps, whereas biaxial stresses within $\pm 3\%$ of the corresponding cubic lattice parameters can change band gaps by several tenths of an electron volt, mostly through the tuning of antibonding interactions in the valence band maximum [15]. Tight-Binding and Effective Mass Models provide semi-analytical insights into the strain-induced modifications in electronic states, particularly near the band edges. Effective mass theory helps in estimating carrier mobility under strain.

3.2 Quantum Hydrodynamic Model (QHM)

Quantum Hydrodynamic Model incorporates quantum corrections such as Bohm potential and Fermi pressure, offering a macroscopic perspective on carrier dynamics under strain. This model is particularly useful for analysing high-frequency optoelectronic responses and nonlinear interactions in perovskites. QHM is used for describing collective carrier behaviour in strained perovskites, incorporating quantum pressure, Bohm potential, and exchange-correlation effects. It is especially useful for studying wave modulation, absorption, and nonlinear optical phenomena in materials with strain-dependent dielectric properties. QHM captures collective behaviour of electrons including quantum pressure and quantum Bohm potential important for understanding very small scale (nanoscale) or high-energy processes.

Optoelectronic Properties under Strain

Applying tensile or compressive stress to materials under strain modifies their optical and electrical properties. The material's band gap, which is essential for uses like solar cells and optoelectronic devices, can be altered by this strain modification. Band Gap Engineering Strain alters the bond angles and bond lengths, leading to changes in the orbital hybridization and electronic band gap. Theoretical studies have shown that tensile strain can decrease the band gap, enhancing visible light absorption. Compressive strain narrows the band gap, enhancing light absorption at longer wavelengths. Tensile strain widens the band gap, which can be useful for multi-junction solar cells where a broader range of band gaps is beneficial. Charge Carrier Mobility Strain impacts the scattering mechanisms and effective mass of carriers. QHM and DFT studies have reported both enhancement and suppression of carrier mobility, depending on the nature of the applied strain. Excitonic Effects and Recombination Rates Strain modifies the exciton binding energy and the dielectric environment of the material. High strain can even cause phase transitions. Theoretical frameworks predict changes in radiative and non-radiative recombination pathways under strain. Optical Absorption and Photo luminescence, the absorption edge shifts with strain due to band gap modulation. Theoretical absorption spectra computed from first-principles calculations provide key insights into these shifts. Under compressive strain, the absorption edge red-shifts, enhancing sensitivity to longer wavelengths. The overall absorption increases in the visible region (400–800 nm), which is crucial for solar energy conversion. Tensile strain caused a blue shift in absorption onset, which may benefit tandem cells with broader light harvesting ranges [10].

Comparative Analysis of Theoretical Results and Experimental Trends

Although this review emphasizes theoretical approaches, we compare selected theoretical predictions with available experimental data to highlight consistencies and discrepancies. Such comparisons validate the models and guide future theoretical improvements. Theoretical predictions are increasingly being validated within-situ strain-dependent photoluminescence, Raman, and XRD measurements. Agreement between DFT-predicted bandgaps and ellipsometry experiments under strain confirms the robustness of theoretical models. The simulated electrical, structural, and optical properties of the perovskite materials CsPbX_3 were examined in order to assess their feasibility for photodetector and solar cell systems. The greatest dielectric constant, electric energy storage capacity is found in CsPbI_3 . For CsPbCl_3 , the loss function's maximum value was discovered. CsPbI_3 and CsPbCl_3 perovskites were discovered to have the highest and lowest reflectivity's, respectively. The best options for producing solar cells, LEDs, and photodiodes are CsPbI_3 and CsPbBr_3 , according to the determined band gap, optical, and mechanical properties of CsPbX_3 [17]. Wide bandgap $\text{CH}_3\text{NH}_3\text{Pb}(\text{Br}_{1-x}\text{Cl}_x)_3$ ($x=0, 0.33, 0.66, \text{and } 1$) 3D hybrid perovskite materials were studied using first-principles calculations and experimentation. The bandgap of these materials was tuned from 2.4 eV (green emissive) to 3.2 eV (blue (UV) emissive) by substituting Cl for Br. Additionally, establish a connection between experimental findings and first-principles theory, offering valuable insights into critical parameters such as dielectric constant, electronic structure, lattice constants, excitonic binding energy and reduced effective mass of charge carriers in these perovskite [18]. Over the past few years, a lot of researchers have become interested in the use of organic-inorganic hybrid perovskite materials in solar cell applications. These materials are excellent options for low-cost solar cell technologies and optoelectronic devices because of their remarkable photoelectric qualities and quick efficiency gains. Additionally, formamidinium (FA)-based perovskites are among the most promising materials due to their high power conversion efficiency (PCE), cost-effectiveness, gap tunability, longer charge diffusion length, and significantly increased photochemical and thermal stability [19].

Challenges and Future Perspectives

Modelling strain in perovskites remains complex due to their structural flexibility, presence of defects, and dynamic disorder. Overtime, strained films may relax, forming defects that degrade performance. Including strain effects with temperature, field and light interaction is very complex. Multiphysics coupling is required for accurate real world predications. Future research should focus on multiscale modelling, combining atomistic and continuum approaches. Integration of machine learning with first-principles calculations also offers promising pathways for rapid screening of strain effects. Using AI/ML techniques can help predict optimal strain configurations. Designing tandem solar cells (Multiple layer with different absorption spectra) using strain engineering. Exploring lead-free perovskites (e.g. tin based) with strain-tuning for better environmental safety.

Conclusion

A better grasp of the idea and its impact on halide perovskites is required and crucial to research in order to regulate its influence on the optoelectronic characteristics and device stability. A review of the definition, history, several strain-probing characterization techniques, effects on perovskite films, and control methodologies for strain engineering to enhance the long-term stability and device performance of PSCs. In perovskites, strain is typically produced by: internal stress brought on by the crystal lattice's non-periodicity; and external stress brought on by a mismatch between lattice and thermal expansion or external stressors such as light, pressure, temperature, or applied

bias. Numerous characterization techniques can identify this strain, including macro-scale methods with high spatial averaging (XRD/GIXRD, Raman spectroscopy, PFM, TEM, GIWAXS, PL, TRPL, TPC) and micro-/nano-scale methods (SED, nano-XRD, and CDI) that enable highly-resolved analysis of strain. In terms of its impact on bandgap, charge carrier transport, defect characteristics, non-radiative recombination, and crystal film stability, an overview of the many consequences of strain on perovskite films has also been provided [13]. This review underscores the significant role of mechanical strain in tuning the optoelectronic properties of perovskite crystals. Through a variety of theoretical approaches, including DFT, k - p theory, and QHM, researchers have unveiled rich physics that can be harnessed for advanced device applications. Continued progress in theoretical modelling, paired with experimental validation, is critical for the rational design of strain-engineered optoelectronic systems. Without adding additional chemicals, strain is a potent tool for manipulating the characteristics of perovskites. Theoretical studies like DFT, QHM are crucial for guiding experiments. To create better optoelectronic devices, theory and practice must be integrated in the future. Important information on how strain impacts the optoelectronic characteristics of perovskite crystals can be gained from theoretical investigations. Strain engineering, when guided by predictive modelling, holds great promise for optimizing perovskite-based devices in photovoltaics, LEDs, and photodetectors.

REFERENCES

- [1]. C., Zhu., et al. "Strain engineering in perovskite solar cells and its impact on carrier dynamics", Nature Communications, Feb 2019.
- [2]. J. Even, L. Pedesseau, C. Katan, "Understanding quantum confinement of charge carriers in layered 2D hybrid perovskites," Chem Phys Chem, 2014.
- [3]. S.S. Shin et al., "Strain Engineering for High-Performance Perovskite Solar Cells," Nature Communications, 2020.
- [4]. F. Brivio et al., "Lattice dynamics and vibrational spectra of the orthorhombic, tetragonal, and cubic phases of methylammonium lead iodide," Phys. Rev. B, 2015.
- [5]. Y. Yuan et al., "Quantum Hydrodynamic Modelling of Strained Perovskites," Journal of Applied Physics, 2023.
- [6]. M. Wang, et al. Strain engineering in metal halide perovskite materials and devices: Influence on stability and optoelectronic properties, Chem. Phys. Rev. 2021.
- [7]. The Book "Quantum Hydrodynamic Equation and Its Mathematical Theory, by Boling Guo (2023)".
- [8]. AR Oganov, et. al. "Comparative study of quasiharmonic lattice dynamics, molecular dynamics and Debye model applied to MgSiO₃ perovskite" Physics of the Earth and Planetary Interiors, Dec 2000.
- [9]. Snaith, H. J. Perovskites: The Emergence of a New Era for Low-Cost, High-Efficiency Solar Cells, J. Phys. Chem. Lett. 2013.
- [10]. Chen, Q. et al. Planar heterojunction perovskite solar cells via vapor-assisted solution process, J. Am. Chem. Soc. 2014.
- [11]. Wang, M. et al. Strain engineering in metal halide perovskite materials and devices: Influence on stability and optoelectronic properties, Chem. Phys. Rev. 2021.
- [12]. S. Attique et al. "An overview of the pressure- and strain-induced changes in the structural and optoelectronic properties of organometal halide perovskites" Elsevier, Solar Energy, Volume 239, June 2022.

- [13]. B. Yang, et al. "Strain effects on halide perovskite solar cells", *Chem. Soc. Rev.*, 2022.
- [14]. A Ghosh et al. "Inorganic novel cubic halide perovskite Sr_3AsI_3 : Strain-activated electronic and optical properties", *Heliyon*, 9, (2023).
- [15]. C. Grote and R. Berger, "Strain Tuning of Tin–Halide and Lead–Halide Perovskites: A First-Principles Atomic and Electronic Structure Study", *The Journal of Physical Chemistry C*, 2015.
- [16]. Li, Y. et al. "Strain engineering in functional 2D materials", *Nat. Rev. Mater.* 2020.
- [17]. SMJ Zaidi et al., "A comparative DFT assessment of the mechanical, elastic, electronic, and optical parametric study of perovskites CsPbX_3 for opto-electronic applications", *Digest Journal of Nanomaterials and Biostructures*, September 2024.
- [18]. N K Kumawat et al., "Structural, Optical, and Electronic Properties of Wide Bandgap Perovskites: Experimental and Theoretical Investigations", *The Journal of Physical Chemistry A*, May 2016.
- [19]. M. Raeisian Asl, "A review on theoretical studies of structural and optoelectronic properties of FA-based perovskite materials with a focus on FAPbI_3 ", *International Journal of Energy Research*, May 2022.
- [20]. Y. Jiao et al., "Strain Engineering of Metal Halide Perovskites on Coupling Anisotropic Behaviors", *Advanced Functional Material*, October 2020.
- [21]. S. Yun et al., "Theoretical Treatment of $\text{CH}_3\text{NH}_3\text{PbI}_3$ Perovskite Solar Cells", *Angew. Chem. Int. Ed.* 2017.
- [22]. C Huo, et al. "Two-Dimensional Metal Halide Perovskites: Theory, Synthesis, and Optoelectronics", *Adv. Sci. News, Small Methods* 2017.

An Efficient Green Synthesis of Isoindolindione Derivatives Containing Pyrimidine as A Template Using Citrus Acid as Catalyst

Bhau A. Bulakhe¹, Kiran D. Dhawale¹, Dnyaneshwar G. Karpe²

¹Department of Chemistry, Maharaja Jivajirao Shinde Arts, Science & Commerce College, Shrigonda-413701, Maharashtra, India

²Department of Chemistry, Shri Chhatrapati Shivaji College, Shrigonda- 413701, Maharashtra, India

ARTICLE INFO

Article History:

Published : 30 April 2025

Publication Issue :

Volume 12, Issue 13

March-April-2025

Page Number :

296-299

ABSTRACT

Nitrogen based fused heterocyclic moiety can be seen in naturally occurring and synthetic bioactive molecules. Isoindolindione derivatives are crucial in pharmaceutical applications like their biological activities, including antiviral, anticancer, and anti-inflammatory properties. Use of environmentally benign catalysts and solvents in this synthesis align with the principles of green chemistry, falling the reliance on unsafe reagents and minimizing waste generation. A common strategy has been used of phthalimides or phthalimidines to synthesize the desired isoindolindione derivatives. While this strategy does help the access to diversely tinted isoindolindione. It can require multistep methodologies to achieve the target compound. During the past decade, a variety of catalytic methodologies have been investigated in order to minimize the number of reaction steps and to maximize the direct operation of commercially available compounds for the synthesis of isoindolindione based structures.

Keywords: Pyrimidine derivatives, Citrus acid catalyst, isoindolindione green chemistry, sustainable synthesis.

INTRODUCTION

The pursuit of eco-friendly and efficient synthesis methods has become a cornerstone of modern organic chemistry, driven by the need to minimize environmental impact and enhance sustainability. This synthesis focuses on the green chemistry of its derivatives, which are complex heterocyclic compounds with significant applications in pharmaceuticals, materials science, and catalysis.

The use of environmentally benign catalysts and solvents in this synthesis aligns with the principles of green chemistry, reducing the reliance on hazardous reagents and minimizing waste generation. The incorporation of anthracene and thiophene moieties into the pyrimidine framework introduces unique electronic and structural

properties, making these derivatives valuable for advanced applications such as organic semiconductors and drug development.

Heterocyclic compounds are abundant in nature and are of great significance to life because their structural subunits exist in many natural products such as vitamins, hormones, and antibiotics hence, they have attracted considerable attention in the design of biologically active Pyrimidines and Thiazole Derivatives in advanced organic chemistry. Also, in the family of heterocyclic compounds nitrogen containing heterocycles are an important class of compounds in the medicinal chemistry.

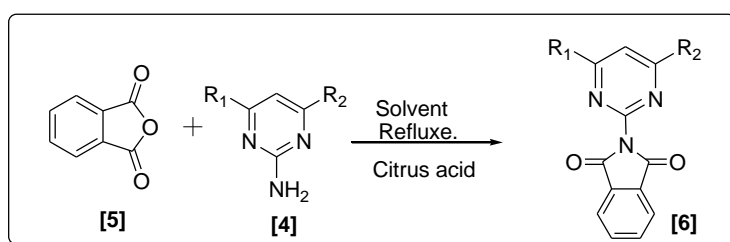
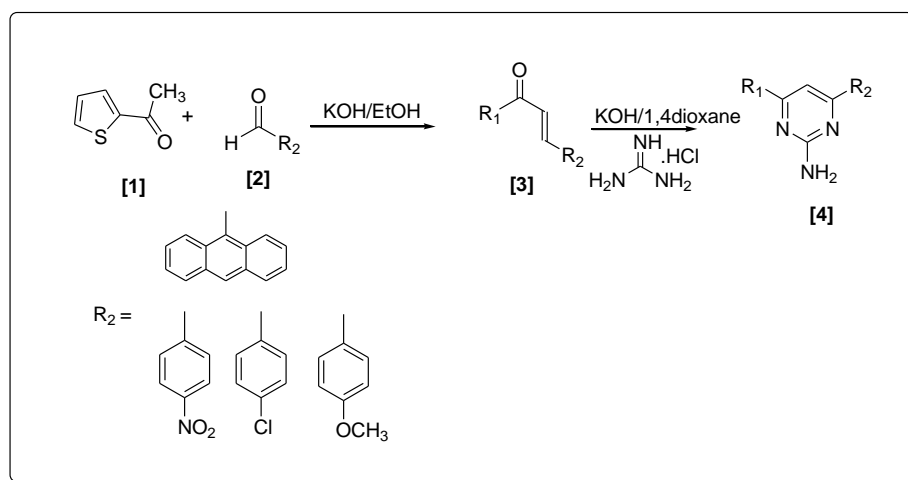
The pyrimidines derivatives represent an essential group of natural as well as synthetic products and some of them possess wide range of pharmacological activity such as antimicrobial [1], antitumor [2], anticancer [3], antitubercular [4], anti-inflammatory [5], antioxidant [6], antimalarial [7], antileishmanial [8]. etc.

MATERIALS AND METHODS

The reactions were monitored by thin layer chromatography. Thin layer chromatography was performed with silica-gel G (suspended in CHCl_3 -EtOH) and plates were viewed under UV Chamber. Melting points were determined in open capillaries and are uncorrected. Thin layer chromatography was used to reach completion of reaction and purity of compounds synthesized, using silica gel as stationary phase and Petroleum ether ethyl acetate as solvent system (2:4) and visualized by U.V. visualizing cabinet. All solvents used were analytical grade. The chemicals used were obtained from sigma –Aldrich.

Experimental Methods :

The following is representative methodology that will be undertaken in the work. In this methodology, we propose to undertake the synthesis of pyrimidine derivatives from chalcone.



Experimental work Synthesis of Pyrimidinone derivatives.

Compound [1] and [2] on heating with alcoholic KOH in the formation of [3]. The compound [3] reacts with guanidine hydrochloride to gives pyrimidine derivatives. Which on reacts with compound 5 and 4 and to gives the products 6.

Compound [1] and [2] on heating with alcoholic KOH in the formation of compound [3]. The compound [3] reacts with Guanidine hydrochloride and KOH gives corresponding pyrimidine derivatives [4]. This further on reaction with different aldehydes and other reactants gives final product [5] Place a Compound of 1gm 2-acetal thiophenene in beaker add 1.96 gm of 9-antraldehyde and add 0.66 gm of KOH in it and stir well for 45-60 min at room temperature until reaction gets completed. add cold water to it and filter it with funnel. Yellowish solid product will obtain having single spot TLC, and MP of product is 172°C and practical yield of the product is 88 %.

¹H NMR (400 MHz, Chloroform-d) δ 8.04 (d, J = 12.2 Hz, 1H), 7.04 (d, J = 12.2 Hz, 1H), 7.68 (d, J = 4.0 Hz, 1H), 7.55 – 7.38 (m, 8H), 7.16 (d, 1H), 7.11 (t, J = 4.4 Hz, 1H).

¹³C NMR (100 MHz, Chloroform-d) δ 134.2, 131.3, 130.5, 129.4, 129.1, 128.7, 128.5, 128.3, 126.6, 125.6, 125.5, 108.9.

STEP 2:- Synthesis of Pyrimidine from chalcone, Guanidine hydrochloride and KOH.

2.0 gm of chalcone in R.B. flask and add 1.82gm of guanidine hydrochloride and add 1.07gm KOH. Add 10ml of alcohol and placed condenser with heating and continuous stirring with help of magnetic stirrer. Reaction will be completed in 25-30 minutes, and it will conform from TLC. Until reaction get completed add little amount of alcohol whenever necessary to it. When reaction gets completed transfer the mixture into beaker with help of water. Add ice cold water into beaker the solid crystal will form out filter it with funnel single spot TLC is obtained and melting point of product is 260°C and practical yield of product is 40.23%

¹H NMR (400 MHz, Chloroform-d) δ 8.54 (s, 1H), 8.33 – 8.25 (m, 1H), 8.04 (d, J = 8.2 Hz, 2H), 7.79 (d, J = 8.5 Hz, 2H), 7.68 (d, J = 4.0 Hz, 1H), 7.55 – 7.38 (m, 8H), 7.16 (s, 1H), 7.11 (t, J = 4.4 Hz, 1H).

¹³C NMR (100 MHz, Chloroform-d) δ 176.2, 166.8, 163.1, 161.1, 142.4, 141.4, 134.2, 131.3, 130.5, 129.4, 129.1, 128.7, 128.5, 128.3, 126.6, 125.6, 125.5, 108.9.

STEP III: – synthesis of isoindolindione derivatives

Take 0.20 gm of Pyrimidine in R.B. flask and add 0.09gm Phthalic anhydride in R.B. flask and add 2-3 drop of Acetic Acid to carry out reaction. Heat reaction mixture with continuous stirring with magnetic stirrer at 45-50°C for 5-10 min. a single spot of TLC, we will confirm that reaction is completed. After transfer reaction mixture into beaker and add ice cold water to it. The solid crystals will come out filter it with help of funnel and recrystallize the product with alcohol. Single spot TLC, will obtained and MP of recrystallized product is 282°C and yield of product is 66.66 %.

¹H NMR (400 MHz, Chloroform-d) δ 8.54 (s, 1H), 8.33 – 8.25 (m, 1H), 8.04 (d, J = 8.2 Hz, 2H), 7.79 (d, J = 8.5 Hz, 2H), 7.68 (d, J = 4.0 Hz, 1H), 7.55 – 7.38 (m, 8H), 7.16 (s, 1H), 7.11 (t, J = 4.4 Hz, 1H).

¹³C NMR (100 MHz, Chloroform-d) δ 176.2, 166.8, 163.1, 161.1, 142.4, 141.4, 134.2, 131.3, 130.5, 129.4, 129.1, 128.7, 128.5, 128.3, 126.6, 125.6, 125.5, 108.9.

Result and Discussion:

The condensation reaction involving Pyrimidine Derivatives and Phthalic anhydride and *using Citrus lemon* by stirring with magnetic stirrer at 45-50°C for 2-3 hrs Resulted the formation of final product having practical yield 66.66% and having MP 132°C. [Scheme 1].The profound biological activities possessed by Pyrimidine derivatives their potential to be used as synthons for the synthesis of large number of heterocyclic compounds.

synthesis of large number of heterocyclic compounds have generated considerable interest in the synthesis of a large number of substituted isoindolindione derivatives.

Conclusion

In medicinal chemistry Isoindilonedione derivatives have been very well known for their therapeutic applications. The presence of a pyrimidine base in thymine, which exhibit useful biological activities cytosine and uracil, which are the essential binding blocks of nucleic acids, DNA and RNA is one possible reason for their activity. The literature indicate that compounds having Isoindilonedione nucleus possess broad range of biological activities As a result of remarkable pharmacological efficiency of pyrimidine derivatives, intensive There is still scope for more research work to be done in this field to find a novel pharmacological agent. This study would be useful for the researchers working in this field. All the newly synthesized substituted Pyrimidine derivatives were evaluated for their pharmacological activity. All the products have been achieved under mild conditions in good excellent yields using lemon juice as an eco-friendly catalyst.

Acknowledgement

I am grateful to Maharaja Jivajirao Shinde Mahavidyalaya Shrigonda and all Member of management Council, for their constant stimulus during my research work.

I am specially obliged to the Principal Dr. M.R. Jare for his continuous encouragement and timely co-operation during the course of my work. I would like to acknowledge to Dr. N.M. Thorat Head Department of chemistry for allocating resources and providing a conducive environment for us to carry out our research. I am sincere thanks to my guide Dr. L.R. Patil and Coguide Dr. D. G. Karpe for his guidance, valuable help, humanity and constant encouragement. My thanks to Department of Chemistry, Maharaja Jivajirao Shinde Mahavidyalaya, Shrigonda for providing library and laboratory facilities.

REFERENCES

- [1]. M.B. Hogale, N.P. Dhore, A.R. Shelar, P.K. Pawar, *orient J. Chem.*, 1986, 2, 55-57.
- [2]. Singh, H and Kapoor, V.K. 2003. *Medicinal and pharmaceutical chemistry*, 29.
- [3]. Cave G W. Raston C L & Scott J L, *Chem Commun*, 21(2001) 2159.
- [4]. Pal R, *Int J Org Chem*, 3(2) (2013) 136.
- [5]. Kajal A, Bala S, Kamboj S, Sharma N & Saini V, *J Catal*, 1 (2013).
- [6]. Abignente E, Arena F, De Caprariis P, Nuzzetti R, Marmo E, Lampa E, Rosatti E & Ottavo R. *Farmaco: Edizione Scientifica*, 36(1) (1981) 61.
- [7]. Bonnet P A, Michel A, Laurent F. Sablayrolles C. Rechencq E, Mani J C, Boucard M & Chapat J P, *J Med Chem*, 35(18) (1992) 3353.
- [8]. Azam F, Rajab IA & Alruiad A A, *Pharmazie*, 64(12) (2009) 771.
- [9]. Kikkeri P H, Kikkeri N M & Mallesha L, *Org Chem International*, 1 (2013).
- [10]. Fales H M, Blums M S. Southwick E W. William D L, Roller P P & Don A W, *Tetrahedron*, 44(16) (1988) 5045.
- [11]. Wheeler J W, Avery J, Olubajo O, Shamin M T, Storm C B & Duffiel... Maul C. Sundermann B. Hennies H. Schneider J & Gerlach M, *Tert-butyl-(7-methylimidazo[1,2-a]-pyridin-3 yl)-amine-derivative*, PCT Int Appl WO 027109 (2001). 7.1
- [12]. T. Vamakawa, H. Kagechika, E. Kawachi, Y. Hashimoto, K. Shudo, *J. Med. Chem.*, 1987 26B, 384-386.

Catalysis, Medicine and Biology : The Versatile Application of Coordination Compounds

¹Shaziya Mohammed Irfan Momin, ²Tahreem Ashraf Momin

^{1,2} Department of Chemistry, G.M.Momin Women's College, Bhiwandi, Dist Thane, Maharashtra, India
(Affiliated to University of Mumbai)

²Department of Chemistry, Shri Chhatrapati Shivaji College, Shrigonda- 413701, Maharashtra, India

ARTICLE INFO

Article History:

Published : 30 April 2025

Publication Issue :

Volume 12, Issue 13

March-April-2025

Page Number :

300-303

ABSTRACT

Coordination chemistry plays an important role in catalysis, particularly in systems where catalysts and reactants are in same phase. Metal complexes often act as catalysts or catalyst precursors, with their reactivity, selectivity, and stability largely governed by the surrounding ligands. By tuning the electronic and structural properties of these ligands, chemists can precisely influence catalytic performance. This ligand design strategy enables the development of more efficient, selective, and stable catalytic systems, making coordination chemistry a key foundation in advancing modern catalytic processes.

Keywords : Coordination compounds, Catalysis, Polymerization, CO₂ reduction

I. INTRODUCTION

Coordination compounds are crucial in various fields due to their unique properties and diverse applications. These compounds play a crucial role in biological systems, with haemoglobin and chlorophyll being prominent examples iron and magnesium-based coordination compounds vital for human and plant life, respectively. In addition to their biological significance, coordination compounds have notable medicinal applications, with complexes of platinum, palladium, and ruthenium being used in anti-cancer treatments. Many coordination compounds also exhibit antibacterial properties and have shown effectiveness in treating diseases such as Alzheimer's, malaria, and viral infections, including COVID-19. Furthermore, these compounds are critical in catalytic processes, enhancing the efficiency of various chemical reactions. This explores the versatile roles of coordination complexes in catalysis, medicine, and biological functions. Transition metals exhibit a unique capacity to create coordination complexes, attributed to their advantageous charge-to-mass ratio and the presence of d-orbitals. This ability has propelled significant progress in coordination chemistry, resulting in the development of a wide array of complex compounds with various functionalities. These compounds are essential in multiple industries, including metallurgy,

medicine, and industrial catalysis. For instance, in hydrometallurgy, coordination compounds enhance the effective extraction of metals such as nickel, cobalt, and copper from their ores. Additionally, they serve as effective catalysts in the polymerization processes of organic materials like polyethylene and polypropylene[1]. The impact of coordination chemistry reaches well beyond these applications, significantly influencing areas such as environmental science, material innovation, and pharmaceuticals. Below are several key sectors where coordination compounds have demonstrated their critical importance.

A) Medicine & Pharmaceuticals:

1. Cancer Treatment: Cisplatin and related platinum complexes are widely used in chemotherapy to treat various cancers.
2. Imaging Agents – Gadolinium (Gd^{3+}) complexes are used as contrast agents in MRI scans[2].
3. Antibacterial & Antiviral Agents – Some coordination compounds show antimicrobial properties and are being explored for drug development.
4. Metal-based diagnostics – Complexes can act as molecular probes or sensors in biological systems.

B) Catalysis:

1. Industrial Catalysts – Transition metal complexes (like those of rhodium, nickel, or palladium) are vital in catalytic converters, hydrogenation, and polymerization reactions [3][4].
2. Homogeneous Catalysis – Many organic reactions are catalyzed by metal complexes in solution [5][6].
3. Enzyme Mimics – Synthetic coordination complexes can mimic the active sites of metalloenzymes for biochemical research [7][8].

C) Environmental Applications:

1. Water Treatment – Coordination compounds are used to bind and remove toxic metals from wastewater.
2. Pollution Monitoring – Metal complexes serve as sensors to detect pollutants, like heavy metals or gases, in the environment.
3. CO_2 Reduction – Some complexes are being developed to catalyze the reduction of carbon dioxide into useful fuels.

D) Material Science:

1. Molecular Magnets – Some metal complexes exhibit magnetic behaviour and are studied for use in data storage.
2. Dye-sensitized Solar Cells (DSSCs) – Ruthenium complexes are used as light-absorbing dyes in solar energy technologies.
3. Conductive Materials – Coordination polymers and metal-organic frameworks (MOFs) have applications in electronics, sensors, and batteries.

E) Biological Systems:

1. Metalloenzymes – Many enzymes contain metal ions coordinated by ligands (e.g., hemoglobin has iron in a porphyrin ring).
2. Oxygen Transport and Storage – Complexes like hemocyanin (with copper) or myoglobin Hydrogenation Reactions.

Application of coordination compounds in Catalysis reactions:

1) Wilkinson's Catalyst: $RhCl(PPh_3)_3$

Catalyzes the hydrogenation of alkenes to alkanes under mild conditions.

Important in fine chemical and pharmaceutical industries. Wilkinson's Catalyst, formally known as chloridotris (triphenylphosphine)rhodium(I), is a coordination complex of rhodium with the formula $[RhCl(PPh_3)_3]_2$. It is widely used as a homogeneous catalyst for the hydrogenation of alkenes [9][10].

Properties:

- Appearance: Reddish-brown solid.
- Solubility: Insoluble in water but soluble in organic solvents like benzene and tetrahydrofuran.
- Structure: Slightly distorted square planar geometry.

Applications:

- Catalysis: Coordination compounds act as effective catalysts in hydrogenation reactions, facilitating the efficient conversion of alkenes to alkanes through the selective addition of hydrogen.
- Organometallic Chemistry: Played a key role in the development of asymmetric hydrogenation catalysts.

Wilkinson's Catalyst is named after Sir Geoffrey Wilkinson, a Nobel Prize-winning chemist who contributed significantly to organometallic chemistry [11].

2. Hydroformylation (Oxo Process)

- Uses rhodium or cobalt complexes to convert, alkenes + CO + H₂ → aldehydes.
- Application in the production of plasticizers, alcohol, and surfactant.

3. Polymerization

- Ziegler–Natta Catalysts: TiCl₄ with Al(C₂H₅)₃

They are crucial catalysts for the polymerization of ethene and propene, facilitating the efficient production of common plastics like polyethylene and polypropylene[12].

Metallocene Catalysts: (e.g., Cp₂ZrCl₂ with MAO)

Allow for stereocontrol and fine-tuning of polymer properties.

4. Cross-Coupling Reactions

- Palladium-based catalysts (e.g., Pd(PPh₃)₄)

Used in Suzuki, Heck, and Stille couplings to form C–C bonds.

Critical in the synthesis of pharmaceuticals, agrochemicals, and organic materials.

5. Water Splitting and CO₂ Reduction

- Coordination complexes of Ru, Fe, Co, etc., act as catalysts for:

a) Water oxidation to O₂.

b) CO₂ reduction to CO, formate, or even methanol.

c) Important in renewable energy and artificial photosynthesis.

6. Olefin Metathesis

Grubbs' Catalysts: Ruthenium-based complexes.

Enable exchange of alkene fragments via C=C bond rearrangement.

Used in organic synthesis, materials science, and pharmaceuticals.

7. Biomimetic Catalysis

Coordination complexes mimic metalloenzymes like nitrogenase, hydrogenase, or cytochrome P450.

Useful in understanding biological processes and designing green catalysts.

Coordination Complexes are very Effective in Catalysis:

Tunability: The design of ligands can be deliberately adjusted to optimize the reactivity and selectivity of coordination complexes, facilitating personalized catalytic efficiency.

Activation of Substrates: The metal center can coordinate to reactants, activating them for transformation.

- Stability: Chelating ligands can stabilize reactive metal centres.
- Regeneration: Many catalytic cycles rely on oxidation/reduction states of metals (e.g., Fe²⁺ ⇌ Fe³⁺).

II. CONCLUSION

Coordination compounds and organometallics have emerged as powerful tools in advancing scientific understanding and practical applications across various disciplines. Their intricate structures and adaptable properties make them indispensable in fields ranging from medicine and catalysis to environmental and materials science. These compounds play critical roles in life processes, such as oxygen transport and enzymatic activity, while also contributing to modern therapies for cancer and infectious diseases. In the realm of catalysis, coordination complexes drive essential industrial transformations with remarkable efficiency and selectivity. Moreover, their applications in pollution control, renewable energy, and smart materials highlight their importance in addressing contemporary global challenges. The continued

exploration and development of coordination chemistry promise not only deeper insights into molecular function but also innovative solutions for sustainable technologies and future scientific breakthroughs.

III. REFERENCES:

- [1] Malinowski J, Zych D, Jacewicz D, Gawdzik B, Drzezdzon J. Application of coordination compounds with transition metal ions in the chemical industry-a review. *Int J Mol Sci.* 2020 Jul 30;21(15):5443. doi: 10.3390/ijms21155443. PMID: 32751682; PMCID: PMC7432526.
- [2] Pessoa J.C., Correia I. Salan vs. salen, Metal complexes in catalysis and medicinal applications: Virtues and pitfalls. *Coordin. Chem. Rev.* 2019;388:227–247. doi: 10.1016/j.ccr.2019.02.035. - DOI
- [3] Eric Marceau, Laurent Bonneviot, Stanislaw Dzwigaj, Jean-Francois Lambert, Catherine Louis, Xavier Carrier, Interfacial coordination chemistry for catalyst preparation, *Journal of Catalysis*, Volume 396, 2021, Pages 104-121, ISSN 0021-9517. <https://doi.org/10.1016/j.jcat.2021.02.002>. (<https://www.sciencedirect.com/science/article/pii/S0021951721000427>)
- [4] Kundig EP, Catalysis with complexes containing stereogenic metal centers, *Chimia (Aarau).* 2014;68(5):312-4. doi: 10.2533/chimia.2014.312. PMID: 24983806
- [5] Reek JNH, de Bruin B, Pullen S, Mooibroek TJ, Kluwer AM, Caumes X, *Chem Rev.* 2022 Jul 27;122(14):12308-12369. doi: 10.1021/acs.chemrev.1c00862. Epub 2022 May 20. PMID: 35593647 Free PMC article. Review.
- [6] Xie JH, Zhu SF, Zhou QL, Recent advances in transition metal-catalyzed enantioselective hydrogenation of unprotected enamines, *Chem Soc Rev.* 2012 Jun 7;41(11):4126-39. doi: 10.1039/c2cs35007f. Epub 2012 Apr 16. PMID: 22509499 Review.
- [7] Schaper LA, Hock SJ, Herrmann WA, Kuhn FE, Synthesis and application of water-soluble NHC transition-metal complexes, *Angew Chem Int Ed Engl.* 2013 Jan 2;52(1):270-89. doi: 10.1002/anie.201205119. Epub 2012 Nov 9. PMID: 23143709 Review.
- [8] Sureshkumar D, Ganesh V, Kumagai N, Shibasaki M, Direct catalytic addition of alkyl nitriles to aldehydes by transition-metal/NHC complexes, *Chemistry.* 2014 Nov 24;20(48):15723-6. doi: 10.1002/chem.201404808. Epub 2014 Sep 22. PMID: 25252112
- [9] Adam R., Mon M., Greco R., Kalinke L.H., Vidal-Moya A., Fernandez A., Winpenny R.E.P., Domenech-Carbo A., Leyva-Perez A., Armentano D., et al. Self-Assembly of Catalytically Active Supramolecular Coordination Compounds within Metal–Organic Frameworks. *J. Am. Chem. Soc.* 2019;141:10350–10360. doi: 10.1021/jacs.9b03914. - DOI - PubMed
- [10] Glaser F., Wenger O.S. Recent progress in the development of transition-metal based photoredox catalysts. *Coordin. Chem. Rev.* 2020;405:213129. doi: 10.1016/j.ccr.2019.213129. - DOI
- [11] Yetra S.R., Rogge T., Warratz S., Struwe J., Peng W., Vana P., Ackermann L. Micellar Catalysis for Ruthenium(II)-Catalyzed C–H Arylation: Weak-Coordination-Enabled C–H Activation in H₂O. *Angew. Chem. Int. Ed.* 2019;58:7490–7494. doi: 10.1002/anie.201901856. - DOI - PubMed
- [12] Bohm L.L. The Ethylene Polymerization with Ziegler catalysts: Fifty years after the discovery. *Angew. Chem. Int. Ed.* 2003;42:5010–5030. doi: 10.1002/anie.200300580. - DOI – PubMed

International Conference on Bridging Chemistry and Physics for a Sustainable Future



Organized By

Savitribai Phule Shikshan Prasarak Mandal's
Department of Chemistry, Physics & IQAC
Loknete Gopinathji Munde Arts, Commerce & Science College,
Mandangad, Dist- Ratnagiri 415203, India

Publisher

Technoscience Academy

Website : www.technoscienceacademy.com